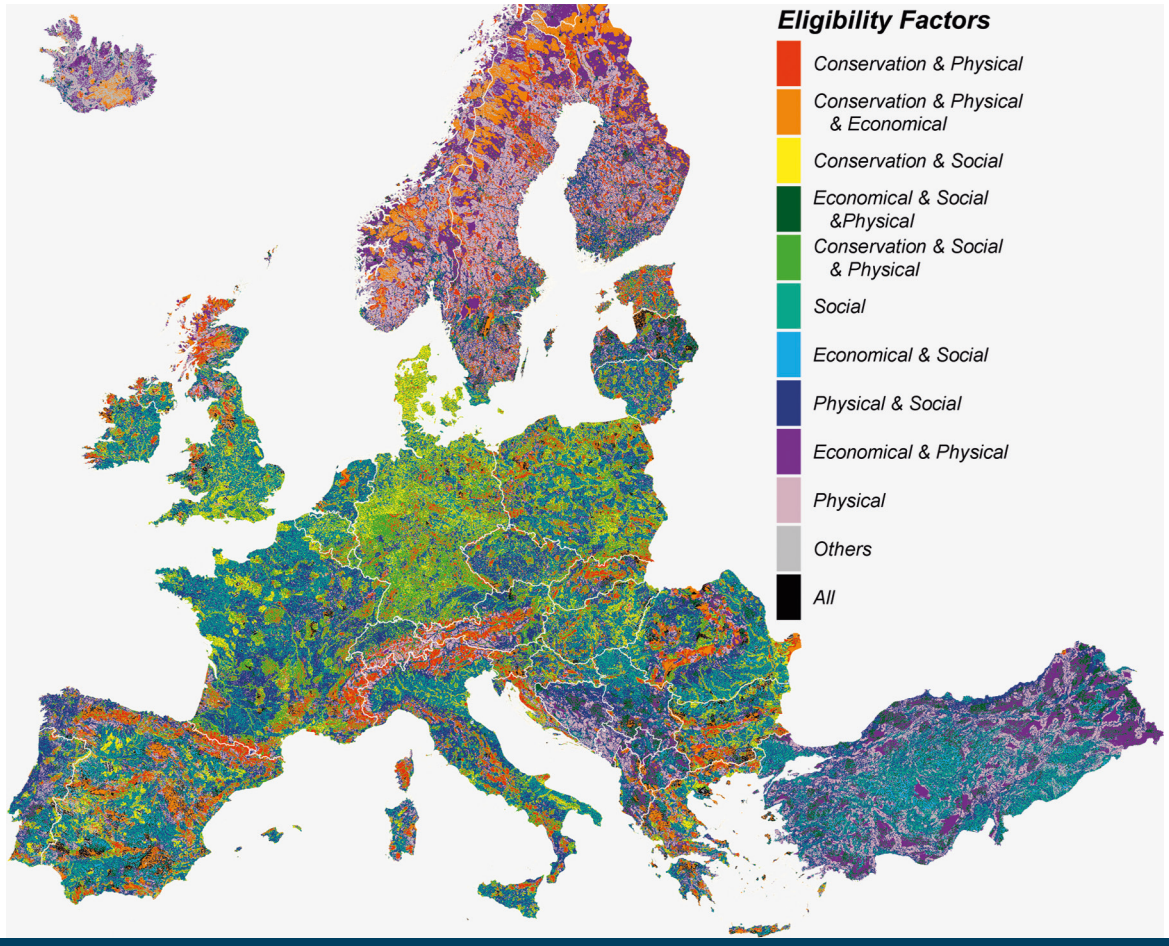

Generation Lulls from the Future Potential of Wind and Solar Energy in Europe

David Severin Ryberg

Energie & Umwelt / Energy & Environment
Band / Volume 521
ISBN 978-3-95806-513-0

Mitglied der Helmholtz-Gemeinschaft

JÜLICH
Forschungszentrum

Schriften des Forschungszentrums Jülich
Reihe Energie & Umwelt / Energy & Environment Band / Volume 521

Forschungszentrum Jülich GmbH
Institut für Energie- und Klimaforschung
Techno-ökonomische Systemanalyse (IEK-3)

Generation Lulls from the Future Potential of Wind and Solar Energy in Europe

David Severin Ryberg

Schriften des Forschungszentrums Jülich
Reihe Energie & Umwelt / Energy & Environment Band / Volume 521

ISSN 1866-1793 ISBN 978-3-95806-513-0

Bibliografische Information der Deutschen Nationalbibliothek.
Die Deutsche Nationalbibliothek verzeichnet diese Publikation in der
Deutschen Nationalbibliografie; detaillierte Bibliografische Daten
sind im Internet über http://dnb.d-nb.de abrufbar.

Herausgeber und Vertrieb:	Forschungszentrum Jülich GmbH Zentralbibliothek, Verlag 52425 Jülich Tel.: +49 2461 61-5368 Fax: +49 2461 61-6103 zb-publikation@fz-juelich.de www.fz-juelich.de/zb
Umschlaggestaltung:	Grafische Medien, Forschungszentrum Jülich GmbH
Druck:	Grafische Medien, Forschungszentrum Jülich GmbH
Copyright:	Forschungszentrum Jülich 2020

Schriften des Forschungszentrums Jülich
Reihe Energie & Umwelt / Energy & Environment, Band / Volume 521

D 82 (Diss. RWTH Aachen University, 2020)

ISSN 1866-1793
ISBN 978-3-95806-513-0

Vollständig frei verfügbar über das Publikationsportal des Forschungszentrums Jülich (JuSER)
unter www.fz-juelich.de/zb/openaccess.

Abstract

A future European energy system that primarily relies on variable renewable energy sources (VRES) such as wind turbines and photo-voltaic (PV) modules is becoming increasingly conceivable. Nevertheless, the role that VRES could play in future energy systems is still uncertain. Besides the well-known uncertainties resulting from the intermittency of these technologies, other questions remain in relation to their future design, spatial distribution, and expected operation. Additionally, there is a possibility that generation lulls could occasionally align across a broad region and, as a result, cast the energy system into an energy deficit. Little is known of these VRES lulls, primarily in regards to where and how often they might occur, how long they will last, and how deep their deficits will be. Before the optimal future energy system can be designed, both VRES potential and the lulls that can occur need to be understood at deeper level. Therefore, the aim of the current work is to evaluate the potential of future wind and PV generation in Europe by considering in detail their spatial, temporal, and future design characteristics, and furthermore to use the developed methods to investigate the occurrence of VRES lulls within the context of an exemplary future European energy system.

To perform this work, projections are made of the spatially-sensitive future design of onshore wind turbines, open-field PV parks, and rooftop PV systems by observing past trends and evaluating optimal system configurations. Geospatial land eligibility constraints are uniquely incorporated for these technologies over the entire European context, after which individual turbines, PV parks, and rooftop areas in residential zones are identified. Computationally efficient simulations tools are also developed to perform hourly-resolved simulations of all potential turbines, parks, and rooftop areas for the weather years 1980 until 2016. With these tools, the total capacity and generation potential of onshore wind, open-field PV and rooftop PV across Europe are found. VRES lulls are at last investigated by reconstructing a literature-sourced scenario of a future European energy system designed for $100\,\%$ reliance on renewable energy sources. Lull investigations are performed for three contexts considering: only the VRES generation, electricity demand without grid limitations, and finally the full operation of the energy system complete with grid limitations and backup orchestration via power flow optimization.

As a result of this work, total annual generation potential from onshore wind, open-field PV, and rooftop PV generation in Europe amounts to $58\,\mathrm{PWh}$, of which slightly over $20\,\mathrm{PWh}$ will be available at a cost below $4\,\mathrm{ct_{€}\,kWh^{-1}}$. In terms of VRES lulls, it is seen that wind and PV offer complementary generation leading to lull lengths around $80\,\%$ shorter than when any technology is evaluated independently. When aggregated at the European level without grid congestion, uninterrupted generation from VRES sources is found equal to $11\,\%$ of the hourly average over all years; indicating that a base generation from VRES sources in Europe is conceivable. Nevertheless when considering electricity demand then, without grid limitation, lulls are always observed at the European level until a back-up capacity of $102\,\%$ of the average hourly demand is available. With full energy system operation, lulls occurring in $1\,\%$ of years were consistently seen around 20 days at the national level, and total energy deficits across Europe were found up to $8.56\,\mathrm{TWh}$. Similarly, in these rare years, total VRES backup capacity across Europe of $501\,\mathrm{GW}$, with full regional cooperation, up to $738\,\mathrm{GW}$, with regional self-reliance, is needed.

Kurzfassung

Ein zukünftiges europäisches Energiesystem, das in erster Linie auf variable Erneuerbare Energien (VRES) wie Windkraftanlagen und Photovoltaikmodule (PV-Module) setzt, wird immer greifbarer. Dennoch könnte die Rolle, die VRES in Zukunft spielen könnte. Energiesysteme ist noch ungewiss. Neben den bekannten Unsicherheiten, die sich aus den folgenden ergeben von der Unterbrechung dieser Technologien, bleiben andere Fragen im Zusammenhang mit der ihr zukünftiges Design, ihre räumliche Verteilung und ihren erwarteten Betrieb. Zusätzlich gibt es dort ist eine Möglichkeit, dass sich Generationsschwächen gelegentlich über eine breite Region ausbreiten könnten. und damit das Energiesystem in ein Energiedefizit verwandeln. Es ist wenig bekannt über diese VRES wiegen, vor allem in Bezug darauf, wo und wie oft sie auftreten können, wie lange sie dauern werden und wie tief ihre Defizite sein werden. Vor der optimalen Zukunft Das Energiesystem kann entworfen werden, sowohl das VRES-Potenzial als auch die auftretenden Flauten. müssen auf einer tieferen Ebene verstanden werden. Daher ist das Ziel der aktuellen Arbeit, Folgendes zu erreichen das Potenzial der zukünftigen Wind- und PV-Erzeugung in Europa zu bewerten, indem sie Folgendes berücksichtigen ihre räumlichen, zeitlichen und zukünftigen Gestaltungsmerkmale detailliert darzustellen und darüber hinaus verwenden Sie die entwickelten Methoden, um das Auftreten von VRES-Lulls innerhalb der Kontext eines exemplarischen zukünftigen europäischen Energiesystems.

Um diese Arbeit durchzuführen, werden Projektionen der räumlich sensiblen Zukunftsgestaltung von Onshore-Windturbinen, Freiflächen-PV-Parks und Aufdachanlagen unter Beobachtung von Trends der Vergangenheit und die Bewertung optimaler Systemkonfigurationen. Geographische Eignung von Flächen Einschränkungen werden für diese Technologien über die gesamte Lebensdauer hinweg eindeutig berücksichtigt. Europäischer Kontext, danach einzelne Turbinen, PV-Parks und Dachflächen in den Bereichen Resistenzgebiete werden identifiziert. Berechnungseffiziente Simulationswerkzeuge sind auch die Grundlage für die entwickelt, um stündlich aufgelöste Simulationen aller potentiellen Turbinen und Parks durchzuführen, und Dachflächen für die Wetterjahre 1980 bis 2016. Mit diesen Tools wird die Gesamtsumme der Kapazität und Erzeugungspotenzial von Onshore-Wind, Freiflächen-PV und Dach-PV in ganz Europa gefunden werden. VRES-Lulls werden schließlich durch die Rekonstruktion eines Szenario aus der Literatur für ein zukünftiges europäisches Energiesystem, das auf $100\,\%$ ausgerichtet ist. die Abhängigkeit von erneuerbaren Energiequellen. Wiegenuntersuchungen werden für drei verschiedene Arten von Kontexte unter Berücksichtigung: nur die VRES-Erzeugung, Strombedarf ohne Netz Einschränkungen und schließlich der vollständige Betrieb des Energiesystems mit Netzanschluss. Einschränkungen und Backup-Orchestrierung durch Leistungsflussoptimierung.

Als Ergebnis dieser Arbeiten beträgt das jährliche Gesamterzeugungspotenzial aus Onshore-Wind-, Freiflächen-PV- und Dach-PV-Erzeugung in Europa $58\,\mathrm{PWh}$, von denen etwas mehr als $20\,\mathrm{PWh}$ zu Kosten unter $4\,\mathrm{ct_{€}\,kWh^{-1}}$ verfügbar sein werden. Im Hinblick auf die VRES-Schlafphasen zeigt sich, dass Wind und PV eine komplementäre Erzeugung bieten, die zu einer etwa $80\,\%$ kürzeren Schlaflänge führt, als wenn eine Technologie unabhängig bewertet wird. Bei einer Aggrega-

tion auf europäischer Ebene ohne Netzüberlastung ergibt sich eine ununterbrochene Erzeugung aus VRES-Quellen in Höhe von $11\,\%$ des Stundenmittelwertes über alle Jahre; dies zeigt, dass eine Basisgeneration aus VRES-Quellen in Europa realisierbar ist. Dennoch werden bei der Betrachtung der Stromnachfrage ohne Netzbegrenzung auf europäischer Ebene immer Flauten beobachtet, bis eine Reservekapazität von $102\,\%$ des durchschnittlichen Stundenbedarfs zur Verfügung steht. Bei vollem Betrieb des Energiesystems wurden die in $1\,\%$ der Jahre aufgetretenen Flauten auf nationaler Ebene durchgehend um die 20 Tage beobachtet, und es wurden europaweite Gesamtenergiedefizite von bis zu $8.56\,\mathrm{TWh}$ festgestellt. Ebenso wird in diesen seltenen Jahren eine gesamte VRES-Backup-Kapazität in ganz Europa von $501\,\mathrm{GW}$, bei voller regionaler Zusammenarbeit, bis zu $738\,\mathrm{GW}$, mit regionaler Eigenständigkeit, benötigt.

Contents

List of Figures

List of Tables

Nomenclature

CLC	Corine Land Cover
GWA	Global Wind Atlas
MERRA	Modern Era-Retrospective Analysis for Research and Applications

AC	Alternating Current
DC	Direct Current
EC	European Commission
ECF	European Climate Foundation
EES	Electrical Energy Storage
EU	European Union
EWEA	European Wind Energy Association
FLH	Full Load Hour
GCM	Global Climate Model
GISCO	Geographic Information System of the Commission
GLAES	Geospatial Land Eligibility for Energy Systems
GWEC	Global Wind Energy Council
IEA	International Energy Agency
IEC	International Electrotechnical Commission
IRENA	International Renewable Energy Agency
JRC	Joint Research Center
MCDA	Multi Criteria Decision Analysis
NREL	National Renewable Energy Laboratory
NRW	North Rhine-Westphalia
PHS	Pumped Hydro Storage
RCM	Regional Climate Model
RES	Renewable Energy Source
ROR	Run off River Hydro
UBA	Germany Environmental Agency
VRES	Variable Renewable Energy Source(s)

α	Elevation Angle
β	Surface Tilt
δ	Declination Angle
ω	Hour Angle
ϕ	Latitude
ψ	Solar Azimuth
ψ_s	Surface Azimuth
θ	Incidence Angle
I_{mp}	Current at the maximum power point on a PV module's I-V curve
I_{sc}	Short-circuit current on a PV module's I-V curve
P_{mp}	Maximum power point on a PV module's I-V curve
V_{mp}	Voltage at the maximum power point on a PV module's I-V curve
V_{oc}	Open-circuit voltage on a PV module's I-V curve
z	Zenith Angle
G_{sc}	Solar Constant ($1367\,W\,m^2$)
AM	Air Mass
c-Si	Crystalline Silicon
CdTe	Cadmium Telluride
CIGs	Copper Indium Gallium Selenide
DHI	Diffuse Horizontal Irradiance
DNI	Direct Normal Irradiance
GaAs	Gallium Arsenide
GHI	Global Horizontal Irradiance
GSA	Global Solar Atlas
mc-Si	Multi-crystalline Silicon
MPPT	Maximum Power Point Tracking
OSC	Organic Solar Cells
POA	Plane of Array
SAPM	Sandia Array Performance Model
STC	Standard Test Conditions
TOA	Top of the Atmosphere

λ	Weibull distribution scale parameter
ρ	Air density
k	Weibull distribution shape parameter

v	Wind speed
BOS	Balance of System
LRA	Long-Run Average
PBL	Planetary Boundary Layer
TCC	Turbine Capital Cost
TI	Turbulence Intensity

Chapter 1

Introduction

The culmination of climate research has lead to the scientific community's consensus on anthropogenic climate change [1–3]. Consequences of this are well communicated and include warming temperatures, rising sea levels, dryer heat waves, and more frequent forest fires; the effects of which may have already begun to be witnessed [4]. Global temperature has reportedly already risen at least $1.0\,°C$ since the beginning of the 20th century, and, following the current trajectory, is projected to rise another $5\,°C$ by 2100 [1]. Green house gas emissions from humanity's carbon-intensive energy systems are without a doubt the primary culprit of this, and thus the reimagining of these energy systems holds the key to averting Climate Change's most dire impacts. To combat this issue, the Paris Agreement in December of 2015 marked a milestone in the global initiative to limit the rise in temperature to well below $2.0\,°C$ above pre-industrial levels via the wide-spread reduction of green house gas emissions [5]; which has been ratified by 184 nations that collectively comprise $89\,\%$ of global emissions. Towards this goal, nations are encouraged to employ their own "nationally determined contributions" which, for the European Union (EU), translates to the target of 80 to $95\,\%$ reduction in overall green house gas emissions, relative to 1990, by 2050 [6]. Until 2017, the EU has achieved a $23\,\%$ reduction [7] which, while commendable, nevertheless leaves a long road ahead. Despite this, the ultimate form of a 2050 energy system that achieves these emission reduction targets remains uncertain, as are the new challenges that Europe will face in order to provide the same standards of energy availability today.

1.1 Motivation

One issue which appears certain in any future European energy system scenario is the proliferation of renewable energy sources (RES) [8]. To some extent this is sure to include established technologies such as biomass, geothermal, and hydro, and also developing technologies such as wave power, concentrated solar power, and solar heaters. More famously, the world has recently witnessed a meteoric rise in the wind energy and solar photovoltaic (PV) industries [9, 10]. As a result the cost of electricity generated from these technologies has, for many areas of the world, reduced beyond the point that they are competitive with conventional generation options [11]. In 2017 for instance, PV had the highest proportion of additionally installed capacity worldwide, at $98\,\mathrm{GW}$, while wind energy ranked in second place at $52\,\mathrm{GW}$ [8, 12, 13]. Beneath these two technologies, gas turbines were the next most installed generation technology at $38\,\mathrm{GW}$. Despite this, the

total contribution of RES[1] to cumulative global electricity demand remains a mere $8.42\,\%$, which is further reduced to $6.80\,\%$ when considering the primary energy demand [9]. Nevertheless, since there is no foreseeable end to this momentum in either the wind or PV industry, their significant contribution to the emission reduction targets of European countries is assured.

Despite this growth in the wind and PV industries, multiple well-known issues complicate the design of a future energy system reliant on these technologies. These issues include the temporal intermittency of their generation profiles, as well as their spatial distribution across the landscape. Intermittency arises from weather's chaotic nature, leading to rapid fluctuations in wind speeds and cloud coverage that are directly translated to fluctuating wind and PV generation. To ensure a stable electricity supply, this intermittency must be constantly monitored and instantaneously counteracted. For this reason, wind and PV energy are collectively referred to in the current work as variable renewable energy sources (VRES)[2]. Furthermore, the spatial distribution of individual wind turbines and PV modules results from a complex overlapping of sociotechnical drives; including public attitude, technical suitability, conservation concerns, and economic viability. The intermittent generation from a single VRES generator is difficult enough to predict within a future context, and, with each potential installation location contributing its own generative fluctuations, understanding the precise behavior of Europe's optimal future energy system presents a monolithic challenge that policy makers and stakeholders must nonetheless overcome in the coming years [14].

Unlike the established issues of VRES intermittency and spatial dependency, another prime concern to policy makers and stakeholders is the long-term security of electricity supply; which, due to the technical difficulties involved, has been the subject of much discussion in both the academic and political spheres [14]. In the German language, "Kalte Dunkelflaute" is a well known term referring to an extended period of time in which the weather is cold, dark, and windless. This artifact of various weather phenomena resonates strongly within the energy community since *cold* and *dark* typically equate to more energy demand[3], while *dark* and *windless* correspond to poor VRES resource availability. Put together, this arrangement potentially creates a lull in the VRES generation profile which could not come at a worse time for a VRES reliant energy system. Although there is no equivalent term in the English language, the consequences of these VRES lulls - *extended time spans where low VRES availability is likely to leave an energy system, or a subregion therein, in a state of energy deficiency* - are just as real and must be better understood in order to ensure a successful decarbonization of Europe's energy system [15].

[1] Excluding hydro.
[2] Hydro run-off-river can also be considered as a VRES technology, however this is not dealt with in detail in this thesis.
[3] Depending on region.

1.2 Research Question

Thankfully, advancements in multiple realms have brought the scientific community to the point that many of these uncertainties surrounding VRES generation can be directly investigated. Climate science, for one, is continually improving its capability to model the Earth's climate and weather systems, and the products of this can be used to specify the weather parameters that drive VRES generators [16, 17]. Besides this, the explosion of data collection efforts and their increased frequency towards open availability has provided a wealth of geospatial information relating to the sociotechnical issues inherent to VRES distribution [18]. Some of the previously existing uncertainties still remain, notably in the future evolution of social attitudes, land-use, and RES industries, and additional uncertainties are introduced by the use of climate model and geospatial datasets, such as in reference to their accuracy and completeness [19]. Nevertheless, the stage is set for an in-depth yet far-reaching evaluation of VRES in the future Europe which begins with the placement and operation of single VRES units, and ends with their operational dynamics on the European scale. This, therefore, formulates the scope of the current thesis, in which the following overarching research questions are directly addressed:

- Considering the spatially-varying sociotechnical constraints relating to VRES, what is the technical capacity potential of wind and PV energy in Europe in 2050?
- How much electricity can be expected from these units? At what cost? And how will these quantities vary temporally and spatially?
- When distributed across Europe to form the basis of a fully RES based energy system in 2050, how often could VRES lulls occur? How long will they span? And how deep could their energy deficits be?

1.3 Analysis Requirements

Answering these overarching research questions will require a detailed consideration of certain issues for each point. For the first question, to identify total VRES capacity potential, the dominant role of geospatial analysis necessitates the identification of the relevant geospatial criteria unique to each VRES technology and the collection of corresponding and highly-detailed datasets that span the entire European scope. A trade off between geospatial precision and computational limitations must also be kept in mind due to the broad spatial scale of this analysis. Also important to this question is a projection of the wind and PV industries, since their state is certain to develop over the coming decades.

For the second question of generation and cost potentials, the roles of weather parameter estimation and VRES simulation schemes are of highest importance. Although weather parameters can be sourced from climate models, their spatial resolution relative to the local context of individual VRES units are still extremely

low and, therefore, adjustments to these inputs will be necessary to localize them to each VRES unit being simulated. Likewise, the simulation schemes translating weather parameters to electricity generation profiles should consider the elementary operating principals of these technologies as much as possible. Once again, however, a trade off between simulation realism and computational limitation must be considered. Ultimately, an adequate resolution to this question hinges upon the accurate construction of VRES generation profiles; involving both their spatial relationships across the European context, as well as their temporal intermittency on both short and long time scales.

Addressing the last question regarding the occurrence of VRES lulls builds on top of the previous items and thus is responsive to the same drivers. In addition, however, the specific design of the energy system under investigation is key. To best fit emission reduction targets, the considered energy system design scenario should describe a Europe who's electricity is predominatly supplied by VRES generation and which incorporates a projection of current and future electricity demand sectors. Additionally, the measures used to define and evaluate VRES lulls beyond the general definition provided above should allow for the extraction of actionable conclusions in the minds of energy system decision makers and researchers.

1.4 Structure

To address these questions, this thesis is structured according to the diagram of Figure 1.1.

Following this introduction, the second chapter of this thesis will discuss the considerations made in this work that relate to the geospatial distribution of VRES generators. The chapter begins with an overview of the background of this topic, where the foundational geospatial concepts that are applied throughout this work are introduced. In the end, the relevant geospatial distribution issues are manged via the development of a general model that can be parameterized uniquely for any VRES technology. The general model is described in detail, including the evaluation of land eligibility via the exclusion of technology-relevant exclusion constraints, a placement algorithm that distributes the maximum number of placements possible within the eligible areas, and finally the unit selection convention that identifies the subset of all placements which should constitute a desired capacity. Technology-dependent exclusion constraints used within this general model are discussed in later chapters as they become relevant.

Background and methodologies related to wind energy modeling are then provided in the third chapter. The background topics will provide an overview of the most relevant fundamental working principals of wind energy and wind turbines, and will also discuss trends in the wind industry, future expectations, and at last modeling methodologies employed by other researchers. Ultimately the introduction of these topics serve to distinguish the most important wind energy dynamics that should be incorporated into the final model, and how the approaches of previous researchers

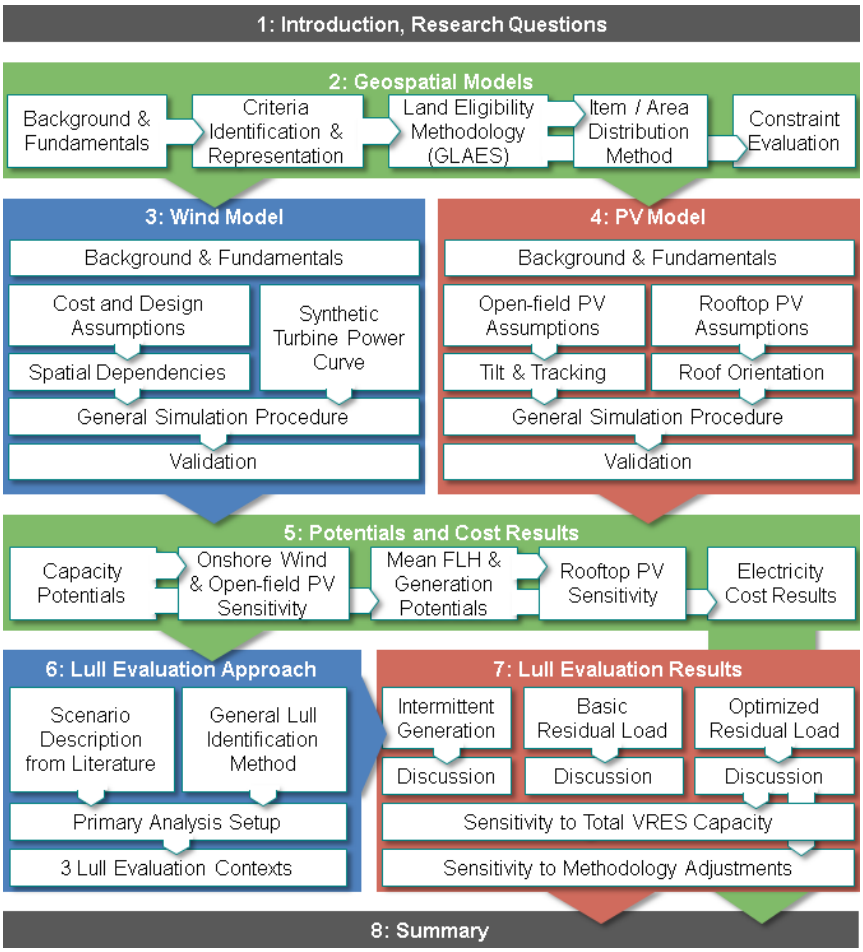

Figure 1.1: Overview of thesis

are improved upon in the current work. Methodology discussions focus on the exogenous assumptions that fit this model to a spatially-sensitive 2050 European context, wind-relevant parameterizations of the previously mentioned geospatial models, and finally the general turbine simulation scheme. In the end of this chapter a discussion regarding validation against other research efforts as well as historical observations is provided.

Following this same structure, PV energy background and methodologies are discussed in the fourth chapter. Once again, background topics will touch on the most relevant fundamental working principals of solar energy and PV modules, trends in the PV industry, future expectations, and at last modeling methodologies employed

by other researchers. As with wind, introducing these topics serves to identify important dynamics which should be considered to capture realistic PV behavior as well as to point out the improvements of this work in comparison to previous researchers. For methodology, focus is placed on the future-oriented PV module assumptions, PV-relevant geospatial model parameterizations, and finally a general PV simulation scheme. Moreover, the differing domains of open-field PV and rooftop PV in residential areas are handled separately, resulting in parallel sets of assumptions, parameterizations, and, eventually, results. As before, this chapter concludes with a discussion regarding validation.

The chosen approach to VRES lull evaluation is covered in the fifth chapter. A short background discussion introduces the issue of VRES lulls in a detailed manner, mentions some of the weather phenomena which likely lead to lull occurrence, and then reviews how this topic has appeared in the literature. Methodology topics revolve around the description of a selected European energy system scenario from the literature, the generalized method to identify VRES lulls, the analysis method used to recreate the selected scenario, and finally the explicit definition of three evaluation contexts in which to VRES lulls will be measured. The lull evaluation contexts are as follows: lulls measured in reference to only the intermittent VRES generation, in reference to VRES generation's correlation to electricity demand without grid restrictions, and finally in reference to the full operation of an electricity system.

Capacity, generation, and cost potentials across Europe for onshore wind, open-field PV, and rooftop PV are presented in the sixth chapter. By providing potentials for each VRES technology, the first two overarching research questions presented above are addressed here, and comparisons to literature are provided to put these results into perspective. Furthermore, multiple sensitivity results are presented to exemplify how the results might change in response to differing assumptions such as, for example, the enforced spacing in between turbines or the expression of land eligibility constraints.

Chapter seven provides the results of the VRES lull analysis, thus addressing the third and final overarching research question of this thesis. This chapter discusses the outcome of the analysis within each of the lull evaluation contexts, and, when appropriate, performs sensitivity analyses to explore how sensitive these outcomes are to key inputs. For each context, discussion of their results in comparison to the literature is provided. At the end of this chapter, the sensitivity of the overall approach to total VRES capacity is tested, as is the response of the analysis to fundamental adjustments of the overall VRES-lull evaluation method.

A conclusion to this work is at last supplied in chapter eight. In addition to reiterating the main outcomes of this work, this chapter serves to speculate on how alterations to the current work might affect the results that have been produced. Furthermore, an outlook of the role these outcomes can play in later research efforts is touched upon as well.

Chapter 2

Geospatial Considerations

Evaluating VRES dynamics across large spatial domains inherently involves a geospatial consideration of their distribution. As a result, common themes related to VRES distribution come up repeatedly in this work and therefore their background principles and the methods developed will be discussed here in a general sense and then applied in later chapters. In regards to background, a brief overview of the role geospatial analyses play in the context of this work is given, followed by a description of the commonly employed geospatial approaches of land eligibility, VRES generator distribution, and Multi Criteria Decision Analysis (MCDA). Afterwards, methods developed for this thesis are detailed, including: the identification of requisite geospatial criteria, selection and preprocessing of representative datasets for these criteria, implementation of a land eligibility methodology, and, finally, implementation of a placement algorithm to explicitly distribute single VRES units. All of the topics introduced in this chapter are given in a general manner, except when providing representative examples from the literature, since they can be parameterized to fit both wind and PV energy[1]. The specific parameterizations of these approaches, such as the land eligibility constraints of either onshore wind turbine or open-field PV parks, will be provided in their respective methodology chapters by referring back here.

2.1 Background Principles

As energy system evaluations progress toward larger spatial scopes, the variability of VRES generation in connection to their spatial distribution quickly becomes a crucial quality to consider [20]. Yet, as it stands, the influence of sociotechnical criteria - such as natural conservation, disruptions to local populations, and unfit terrain - on the future VRES distribution are not a deeply understood topic. One main reason for this is that the response to these criteria are dependent on technology, and can vary significantly between geopolitical groups [21–23]. Moreover, a group's response to these criteria will likely change over time due to evolving social preferences and technological advances [24]. There are also numerous technical issues that plague the literature dealing with this topic, including manual evaluations prone to human-error, inconsistent usage of data sources, and inconsistent data preparation and processing techniques [19, 25]. These often lead to divergent and incomparable results between studies who consider spatial components even in the same regions and for the same technologies. It is therefore apparent that in

[1] Actually, these models are applicable to just about any application involving spatially-sensitive item placement.

order to evaluate the role of VRES over the European scope, and thus to address all of the overarching research questions of this thesis, a methodological development of the spatially-sensitive sociotechnical criteria governing VRES placement will need to play a central role.

The application of sociotechnical criteria to VRES distribution is inherently a geospatial question, which has received significant attention from the research community [19, 26, 27]. One simple avenue in which these criteria affect RES distribution is conveyed by the concept of land eligibility; which has been described by Iqbal [28] as one of the typical inputs in the generic energy resource allocation problem. Alongside land eligibility, where sociotechnical criteria are used to define exclusion constraints, sociotechnical criteria are also commonly employed as decision factors in MCDA schemes; which can be used to make relative comparisons between installation sites. MCDA is fundamentally different from land eligibility despite primarily relying on the same sociotechnical criteria. Examples of land eligibility analyses in the literature are common [29–33], where they are used to determine the total area available for a VRES technology. Furthermore, many studies perform both a land eligibility and MCDA analysis alongside one another to estimate a likely distribution of a desired VRES capacity with in a study region [34–41].

2.1.1 Land Eligibility

As the land available in a region for any particular VRES technology is directly related to its total potential, the treatment of this topic is directly related to the first primary research question. However, as it will be shown throughout this thesis, this issue is also implicitly related to the other two overarching research questions as well, since its outcomes are foundational to later work flows. In any case, the role of this specific discussion serves to introduce this topic in relation to VRES generators in a general way, and to provide a few representative examples of its appearance in the literature, but not to give a comprehensive review of this topic.

For the purposes of this discussion, the land eligibility for a VRES technology will be defined as the binary conclusion that the given technology is eligible for placement at a particular location. Land eligibility analyses are not generally concerned with the eligibility of a single location, however, but instead investigate an ensemble of locations that in total constitute a region. The rules that lead to a location being deemed available or ineligible are understood from a predefined set of exclusion constraints. Ideally, these should be derived from the preferences of local inhabitants and other stakeholders in the region, as well as from larger governmental and international organizations. Furthermore, exclusion constraint sets are, as mentioned, typically unique for different RES technologies and can be expected to differ between regions and to evolve over time.

Examples of land eligibility analyses in the literature are common and, among them, are notable examples that are comparable to the European scale investigated in this thesis. Some of these studies for onshore wind and open-field PV are summarized in Table 2.1, where indications of exclusion are given; missing fields are

either not considered by these authors or are explicitly included. The European Environmental Agency (EEA) [42], for example, investigated the land eligibility of onshore wind turbines in Europe where the avoidance of protected areas was the only exclusion constraint. McKenna [43] also analyzed onshore wind land eligibility in Europe, but with many more constraints and, additionally, more complex distance based constraints; such as excluding all locations within 200 m from roads. Zappa et al. [44] investigated both open-field PV and onshore wind and only allowed these technologies on certain types agricultural areas, grasslands and, for onshore wind, woodlands. Deng et al. [45] performed a global VRES potential estimation relying on a land eligibility analysis where, depending on the technology, they considered protected areas, urban areas, terrain slope and elevation, and average wind speed.

Table 2.1: Simplified overview of wind and PV eligibility studies in Europe. "Exc." stands for "excluded"

	EEA [42]	McKenna [43]	Zappa [44]		Deng [45]	
	Wind	Wind	Wind	PV	Wind	PV
Constraints						
Prot. Areas	Exc.	Exc.	Exc.	Exc.	Exc.	Exc.
Urban Areas		<0.7-1 km	Exc.	Exc.	Exc.	Exc.
Water ways		<400 m	Exc.	Exc.		
Harbors		<400 m	Exc.	Exc.		
Roads		<200 m	Exc.	Exc.		
Airports		<1000 m	Exc.	Exc.		
Construction		Exc.	Exc.	Exc.		
Agriculture				Some Exc.		
Woodlands		Exc.		Exc.		Exc.
Grasslands				Some Exc.		
Terrain Slope		>20°				>15°
Elevation					>2 km	
Wind Speed					<6 m s^{-1}	
Eligibility	86.3 %	23 %				
Distribution						
Suitability		10-50 %	6 %	1 %		
Power Density	8 $\frac{MW}{km^2}$	8.3-18.6 $\frac{MW}{km^2}$	4.2-6 $\frac{MW}{km^2}$	61 $\frac{MW}{km^2}$	7 $\frac{MW}{km^2}$	
Potential						
TW		11.52	0.543	0.895		
PWh a^{-1}	39.0	20.2			11.1	38.1

Unsurprisingly, although each of these studies investigate future wind or PV eligibility in Europe, the differing constraints sets can result in drastically different outcomes; seen, for example, in the EEA's [42] estimate that 86.3 % of Europe is available for onshore wind turbines, while McKenna only only finds 23 % [43]. The studies shown in Table 2.1 do not represent all land eligibility analyses, but are nevertheless representative for studies covering the whole of Europe. Numerous other examples can be found for both wind and PV technologies, however these generally investigate relatively small regional scopes in exchange for more detailed constraint

considerations. Later, in Section 2.2, a review of many of these other studies will be discussed in order to understand which criteria are the most important to consider.

2.1.2 Spatial Distribution of Generators

In addition to exclusion constraints, Table 2.1 also gives an idea of the typical VRES distribution assumptions that are applied over Europe. For all of these examples provided, the land eligibility analysis is used to estimate the total installable capacity by making an assumption of the power density of wind turbines and PV parks which could be distributed in the available areas. Zappa et al. [44], for instance, assumed between 4.2 and $6.0\,\mathrm{MW\,km^{-2}}$ for onshore wind turbines depending on turbine classification[2] and $61.1\,\mathrm{MW\,km^{-2}}$ for open-field PV. Due to their extremely low suitability factors, which are enforced on all available land, their resulting capacity estimations are low compared to other sources. Nevertheless, as can be seen throughout the literature where a large spatial context such as Europe is investigated, the use of such suitability and power density factors are wide spread. Furthermore, as a result of evolving VRES technologies and possible complex available land arrangements, it is likely that the use of such factors is highly uncertain.

On smaller spatial scales, a researcher will rarely follow their land eligibility analysis with a placement procedure which explicitly distributes turbines or PV parks within the eligible region. Compared to suitability and power density factors, the advantage of using a placement procedure is that it makes best use of the available area by conforming to whatever distribution this area has. Two examples of this are the works of Robinius [47] and Jäger et al. [48], who both investigated wind turbine placements in Germany. Robinius' method considered a tight, but nevertheless uniform, grid of turbines across the whole of Germany, with the distance between locations equaling a predetermined separation distance. Afterwards, those locations which were not placed in an eligible area were discarded. Jäger et al. applied a more involved algorithm over the state of Baden-Württemberg and considered the primary wind direction to allow for different separation distances in the axial and transverse directions. This is an important consideration since turbines are typically aligned in rows perpendicular to the dominant wind direction, with a large wind-parallel distance between rows [49].

To the author's knowledge, no work to date has performed an explicit placement algorithm across the whole of Europe. Therefore, in order to improve upon past VRES potential estimations, an explicit placement algorithm that is scalable to the European scope has been developed and is discussed in Section 2.5. By using this placement algorithm to help address the first two overarching research questions, a direct outcome of this work will not only include capacity and generation potentials for large regions, but will furthermore produce such potentials for individual turbines, open-field PV parks, and rooftop PV regions across Europe.

[2] This is in the range of current wind park power densities, found between 1.2 and $11.2\,\mathrm{MW\,km^{-2}}$ with a average near to $3.0\,\mathrm{MW\,km^{-2}}$ [46]

2.1.3 Multi-Criteria Decision Analysis

Investigating the third overarching research question is dependent on constructing a cohesive scenario of regional capacities across Europe. Therefore, in order to select the individual VRES generators which should be employed within this scenario, MCDA could be performed.

MCDA is a well established technique which combines multiple criteria to assist in decision making. Although there are many ways that a MCDA could be carried out, the general concept assigns subscores between 0 and 1 to multiple criteria, generally computed in each case from a piece-wise linear function, which are then combined via a weighted average. In the context of VRES distribution modeling, MCDA analyses are commonly performed after a land eligibility study to suggest the likely installation locations within the available area. One example of a MCDA scoring scheme is that of Tlili et al. [50], given in Figure 2.1. In this case, after performing land eligibility and placement evaluations, Tlili et al. scored individual turbine and open-field PV park locations in France in a manner similar to what will be used here. To compute the final score of each turbine and park location, subscores are determined and finally combined using the weighted equations 2.1, for onshore wind, and 2.2, for PV. Finally, within each of several geopolitical subregions, the top X scoring locations are selected in order to fulfill a scenario-determined capacity.

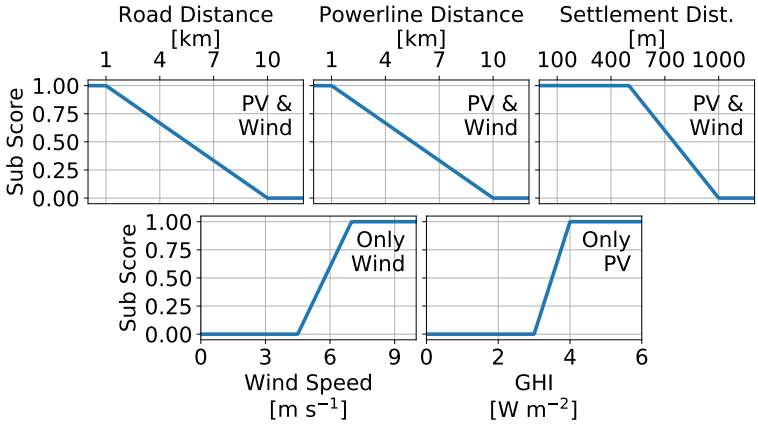

Figure 2.1: Exemplary MCDA scoring conventions suggested by Tlili et al. [50]. Figure is adapted from [50]

$$\text{Score}_{wind} = 0.4 * \text{wind} + 0.3 * \text{road} + 0.2 * \text{powerline} + 0.1 * \text{settlement} \tag{2.1}$$

$$\text{Score}_{PV} = 0.5 * \text{GHI} + 0.2 * \text{road} + 0.2 * \text{powerline} + 0.1 * \text{settlement} \tag{2.2}$$

A few other notable examples of this type of approach are given by Watson et al. [51] who investigated wind and PV distribution in the United Kingdom, Höfer et al. [38] for wind turbines in Western Germany, as well as Aydin et al. [36] and Atici et al. [40] who evaluated wind turbine installation sites in Western Turkey. In fact, the land eligibility plus MCDA pathway has been a common enough theme in the literature that it has been a central issue discussed in multiple literature reviews [26, 27, 52], and so is not greatly expanded upon here.

2.1.4 Summary and Outlook

It is clear that the VRES distribution issues of land eligibility, placement, and MCDA are directly related to all three overarching research questions of this thesis. Although the specifics of these issues change depending on technology, such as the need for wind-direction-dependence when placing wind turbines, their commonalities allow for a generalized implementation which can later be parameterized for each specific application.

In the following sections of this chapter, discussion will focus on how the relevant geospatial criteria for the onshore wind and PV contexts are identified and, afterwards, how datasets are selected and processed in order to represent these criteria across the European scope. Following these steps, the generalized land eligibility and placement algorithms are described. As mentioned, the technology-specific parameterizations, such as which exclusion constraints are applied for either wind turbines or PV parks, will be given in Chapters 3 and 4, respectively.

2.2 Criteria selection

In this section, the set of generalized criteria which can be used for land eligibility and MCDA analyses of wind turbines and PV parks are identified. This is performed by reviewing 54 publications [20,29,31–43,51,53–90] that each include one or more land eligibility analyses, and many which additionally consider an MCDA or similar analysis as well. While reviewing the literature sources, four overarching groups were identified that reflect the underlying motivation for considering each criterion: physical, sociopolitical, conservation and economic.

In the end, 28 general criteria were identified and a full description of each criterion can be found in Appendix A.1. Nevertheless Table 2.2 provides a summary of these criteria, where the self-descriptive name of each criterion is given as well its occurrence rate in the literature in one of four contexts: anywhere in the study, specifically as an exclusion constraint, as a constraint in a wind energy study, or finally as a constraint in a solar energy study. The 'Preference' column indicates the range of values which are generally preferred in the literature. Most criteria have a 'Far' preference, meaning that in the context of locating VRES generators, a large distance is most desirable; for example, the distance of a wind turbine from settlement areas or protected areas. Some criteria, such as the distance to the nearest grid connection point, are most commonly associated with a 'Low' preference, while

the others specifically favor locations within a specific range of values.

Table 2.2: Typical criteria employed for VRES Geospatial analyses as seen in the literature. Previously published in [25]

Criterion	Inclusion Rate [%]				Preference
	In General	As a Const.	Wind Const.	Solar Const.	
Sociopolitical					
Dist. from Settlements	85	84	95	54	Far
Dist. from Airports	55	51	59	15	Far
Dist. from Roadways	53	51	64	0	Far
Dist. from Agriculture	44	29	28	38	Far
Dist. from Railways	33	31	41	0	Far
Dist. from Power Lines	31	27	33	0	Far
Dist. from Historical Sites	27	25	31	15	Far
Dist. from Recreation Sites	20	18	23	0	Far
Dist. from Industrial Areas	18	18	23	0	Far
Dist. from Mining Sites	15	11	13	0	Far
Dist. from Radio Towers	9	7	10	0	Far
Dist. from Gas Lines	7	5	3	0	Far
Dist. from Power Plants	4	4	0	0	Far
Physical					
Terrain Slope	69	65	62	77	Low
Dist. from Water Bodies	64	64	62	62	Far
Dist. from Woodlands	40	33	38	15	Far
Dist. from Wetlands	31	27	28	23	Far
Terrain Elevation	18	15	21	0	Low
Dist. from Land Instability	16	15	10	8	Far
Ground Composition	15	7	5	15	-
Slope Aspect	7	5	0	15	South
Present Vegetation	15	0	0	0	-
Conservation					
Dist. from Protected FFH	82	75	82	46	Far
Dist. from Protected Areas	67	65	72	46	Far
Pseudo Economical					
Resource Availability	64	38	41	38	High
Access Distance	45	25	23	38	Near
Connection Distance	47	24	18	38	Near
Land Value	13	5	5	8	Low

The review performed to create Table 2.2 will be referred to at later points in this thesis to assist in the determination of which exclusion constraints should be applied to either wind of PV technologies. For example, the reviewed studies generally agreed that settlement areas, water bodies, steep terrain slopes and protected areas should always be excluded. However, wind related studies tended to be more restrictive than for PV studies in the sense of larger buffer distances and more numerous exclusion constraints. Nevertheless, PV related studies had a higher tendency towards including a lower terrain slope constraint, terrain aspect constraint,

and agricultural area constraint. As mentioned previously, the precise exclusion constraints which are applied to wind and PV for the evaluations made in this thesis will be discussed in their respective chapters.

2.3 Prior Dataset Construction

Information gathered for Table 2.2 indicated the geospatial criteria which are predominantly factored into VRES distribution studies. The next steps involved selecting datasets capable of representing these criteria across the European context, and furthermore on the preparation of this data into a form that can be efficiently applied on a large scale.

All criteria related to a land cover category, such as forests and industrial areas, are taken from the Corine Land Cover (CLC) dataset [91]; a land cover raster from Copernicus, the European Union's Earth Observation Program, specifying predominant land cover at $100\,\mathrm{m}$ resolution across Europe. This includes indications of settlement areas, however dense urban settlement were identified using the EC's Urban Clusters [92] dataset, which was developed as part of the Geographic Information System of the Commission (GISCO) initiative. GISCO also provided the airport transportation network dataset [93], used to identify airports and airfields, the EuroDEM [94] dataset, for identifying terrain elevation and slope, and the Hydrography [95] dataset, used to identify probable routes of small rivers. Larger water bodies were located using a combination of CLC and the HydroLAKES [96] dataset developed by the World Wildlife Fund (WWF). An extract of the OpenStreetMap [97] database was used to identify roads, power lines, camp sites, leisure areas, and touristic areas. Finally the World Database on Protected Areas (WDPA) [98] was used to identify all protected area designations according to IUNC categories [99].

Throughout this work, these criteria are repeatedly evaluated and the underlying datasets are highly detailed; resulting in the need for numerous computationally intensive operations applied across the European context. To exemplify this, the OSM road data constitutes nearly $50\,\mathrm{GB}$ of line data, representing millions of roadways, and so answering a question as simple as '*how far is this location from a roadway*' means sifting through the entire dataset and computing the nearest distance between the point in question and each line. Considering that this question is not asked just once but instead for every location across Europe and, additionally, for numerous other criteria as well, then it is clear to see why computational efficiency is a prime concern. The best solution to this problem was to preprocess these fundamental datasets using high performance computers, and as a result create a rasterized output which can be used to simply lookup a criterion's value for any location without the need for recalculating.

These preprocessed datasets will from hereon be referred to as 'Priors', and each represents exactly one criterion, or sub-criterion, shown in Table 2.2; ultimately totaling to 44 Priors. All Priors take the form of a single-banded, byte-valued raster dataset defined over the European context, expressed in the EPSG:3035 spatial

reference system and possess a 100 m resolution; chosen to match the CLC dataset as it is the fundamental raster dataset with the highest spatial resolution. Byte values were chosen to minimize the overall size of each individual dataset, but restrict the datasets to only containing integer values less than 256. Therefore, instead of representing criteria values directly, each value in a Prior dataset is associated with a given set of strictly increasing criteria thresholds, referred to as edges, indicating the minimal edge that includes the associated pixel. Figure 2.2 exemplifies the production of the 'distance from roads' Prior. In this case, roadways are seen throughout the scene, and the distance of each location from the nearest road is displayed on the left. The following set of 11 edges is then chosen: 0, 100, 200, 300, 400, 600, 800, 1000, 1200, 1600, and 2000 m. As a result, the processed data shown on the right gives the pixel value at each location. This dataset represents a simplified version of the original criteria, however the edges are carefully chosen to reflect the typical usage in the land eligibility literature (Appendix Table A.1). For an exact account of edges used, refer to Appendix Tables A.2, A.3, and A.4.

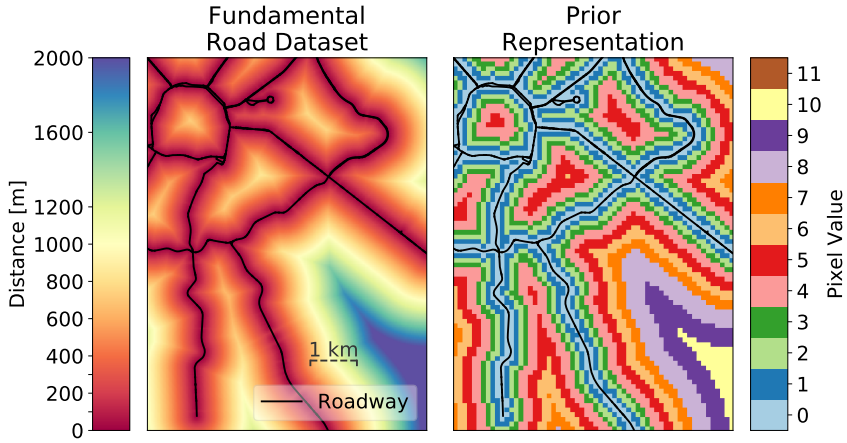

Figure 2.2: Example construction of data preprocessing to facilitate land eligibility and other geospatial analyses. Distance ticks represent edge values of each pixel. Figure is adapted from a version previously published in [25]

Of the 44 Prior datasets produced, a few are visualized here as they prove to be highly impactful in later portions of this work. The first of these, Figure 2.3, shows the distance from settlements. It is clear from this figure that much of central Europe is within 1 to 2 km from a settlement, while other areas, such as the Iberian Peninsula, Scandina and the Baltic regions are generally much further, although this is not represented clearly in the figure due to the color legend. Figure 2.4 shows the distance from agricultural areas, where again the entirety of Europe, with the exception of the Scandinavian countries and mountainous regions, is within 500 m of land used for crops or pastures. Figure 2.5 shows the distance from primary and secondary roads, although not including most small roadways. In this figure it can be seen that most of Europe is within 1 to 2 km of a roadway, except for the

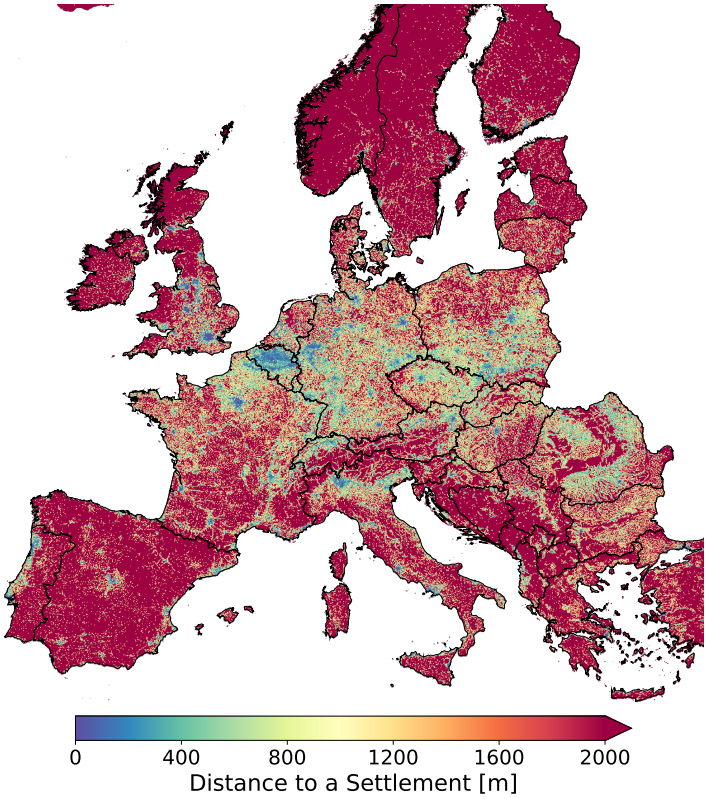

Figure 2.3: Prior Dataset: Distance from settlement areas in meters

Iberian Peninsula showing distances more in the range of 2 to 4 km. Much larger distances from roadways are seen in Scandinavia as well as in much of Eastern Europe. Finally, Figure 2.6 shows the distance from protected areas. The prevalence of this criteria is highly dependent on the country in question as, for example, all of Denmark is within 1 to 2 km of a protected area while there are almost no such designations within the Balkan countries. Turkey does not make its protected area designations available within the WDPA [98], unfortunately resulting in the exclusion of Turkey from the later evaluations made in this work. Along with Denmark, Germany is also highly impacted by protected area designations while most other countries show interspersed pockets of protected regions. Besides these four examples, the other Prior datasets are also highly impactful in the latter portions of this work, and so are visualized in Appendix B.

Due to the fundamental nature of this geospatial data to all three overarching research questions of this thesis, the availability of the data used to construct the Prior datasets therefore determines the geospatial scope of the latter analyses

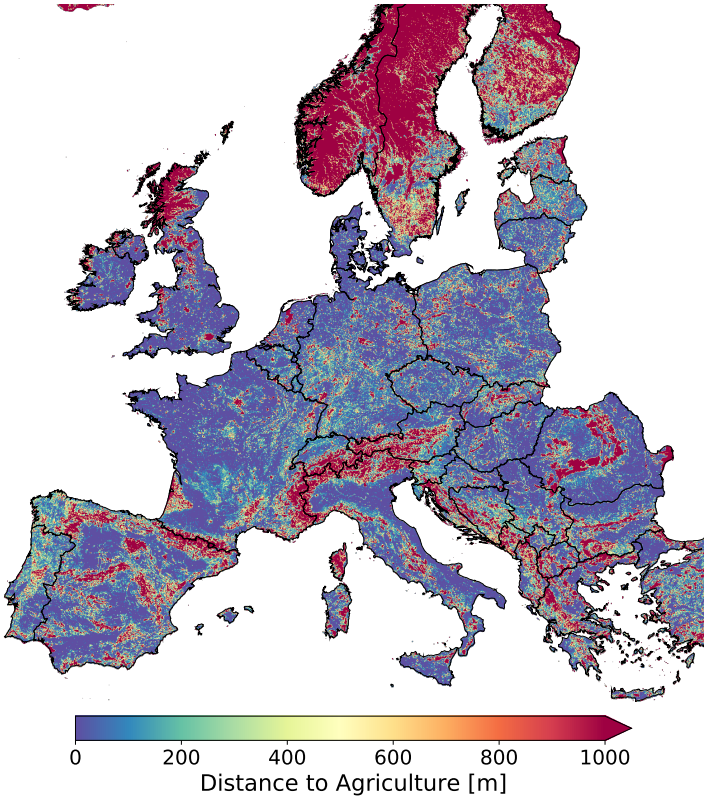

Figure 2.4: Prior Dataset: Distance from agricultural areas in meters

made here. Because of this, the following countries are included and for the rest of this thesis will be collectively referred to as 'Europe': Albania, Austria, Belgium, Bosnia and Herzegovina, Bulgaria, the Czech Republic, Croatia, Denmark, Estonia, Finland, France, Germany, Greece, Hungary, Ireland, Italy, Latvia, Lithuania, Luxembourg, Montenegro, the Netherlands, Northern Macedonia, Norway, Poland, Portugal, Romania, Serbia, Slovakia, Slovenia, Spain, Sweden, Switzerland, and the United Kingdom. As mentioned, Turkey is excluded on account of missing protected areas data, while Ukraine, Belarus, Moldova are excluded due to missing land cover data. Several smaller nation are also not included due to their size; including Lichtenstein, Andorra, the Vatican City, Monaco, Malta, and San Marino. Iceland is also not included in the later analyses of this work due to its large distance to the European mainland.

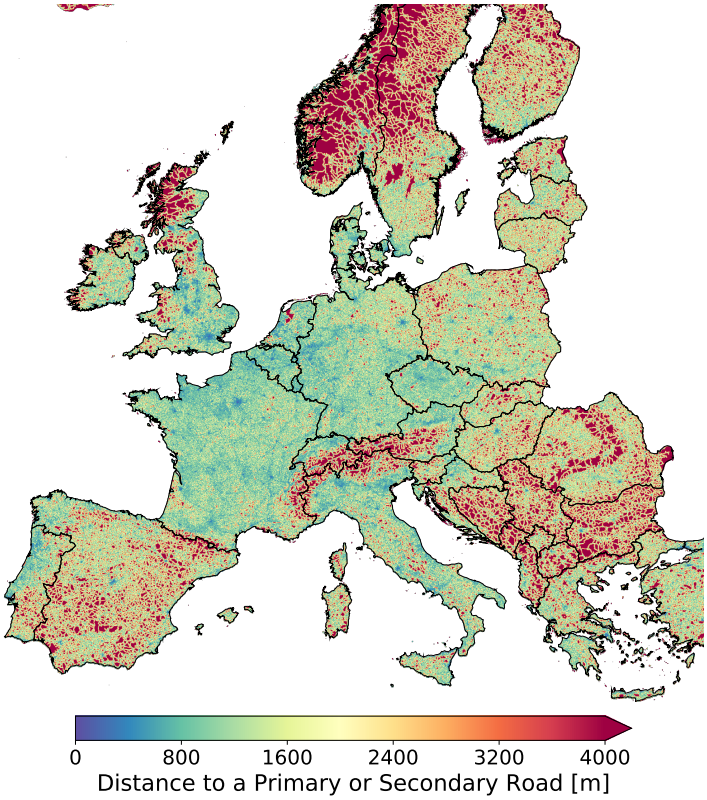

Figure 2.5: Prior Dataset: Distance from primary and secondary roads in meters

2.4 Land Eligibility

The land eligibility model which was developed in line with this work has been made open source on GitHub under the name Geospatial Land Eligibility for Energy Systems (GLAES) [100]. At the time of this writing, the GLAES model is already in use by multiple research groups within the energy modeling community; such as the Reiner-Limoine Institute[3] and the Institute for Automation and Applied Computer Science at the Karlsruhe Institute of Technology[4]. Furthermore, it has also been employed in publications beyond the work of this thesis; such as that of Heuser et al. [101], Tlili et al. [50], Caglayan et al. [102], and Weber [103]. The GLAES model is implemented in the Python 3 programming language, and its primary dependencies are the open-source projects Geospatial Data Abstraction Library (GDAL) [104] for geospatial operations and on the SciPy [105] ecosystem

[3] See `https://github.com/Ludee/glaes`
[4] See `https://github.com/PyPSA/glaes`

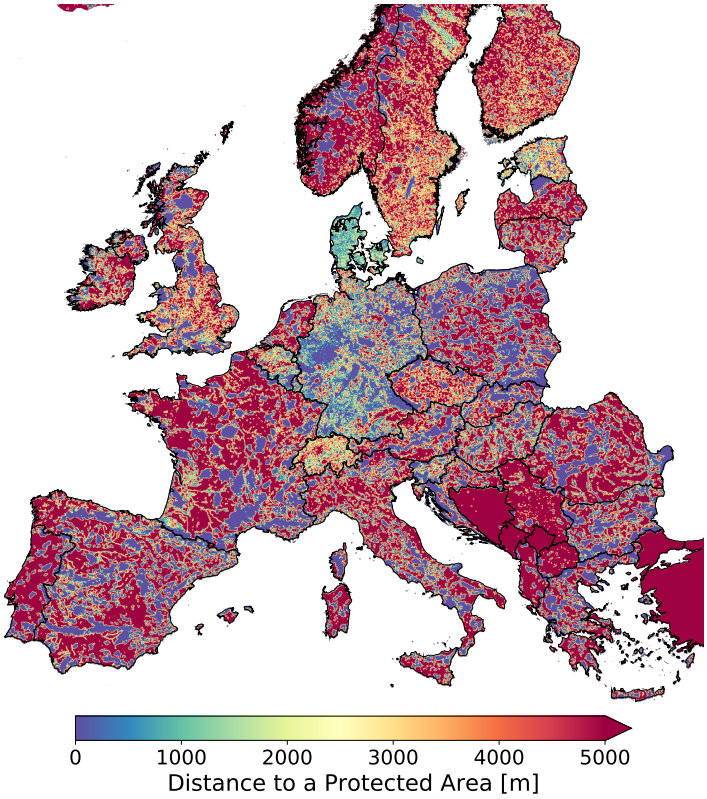

Figure 2.6: Prior Dataset: Distance from any protected areas in meters

for general numerical and matrix computations. GLAES was designed to be a fully transparent, automated, and general land eligibility model that can normalize the various land eligibility approaches used by researchers in the literature. In order to apply a collection of user-specified constraints, GLAES can be applied to any area in the world and can incorporate the vast majority of geospatial data formats. Since this model is described in detail in previous publications [25], with all code and detailed examples provided in the GitHub repository [100], its full description is available in Appendix A.5. Nevertheless, Figure 2.7 provides a flowchart describing how GLAES performs a land eligibility analysis.

In summary, land eligibility analyses with GLAES are comprised of 3 stages: region definition, exclusion, and finalization. In the first stage a region is decided upon, which can be a municipality, state, country, or any other boundary of interest. The spatial resolution and spatial reference system (SRS) in which the land eligibility analysis will take place must also be specified. At first, all area within the region is considered to be eligible. Beginning in the exclusion stage, geospatial datasets

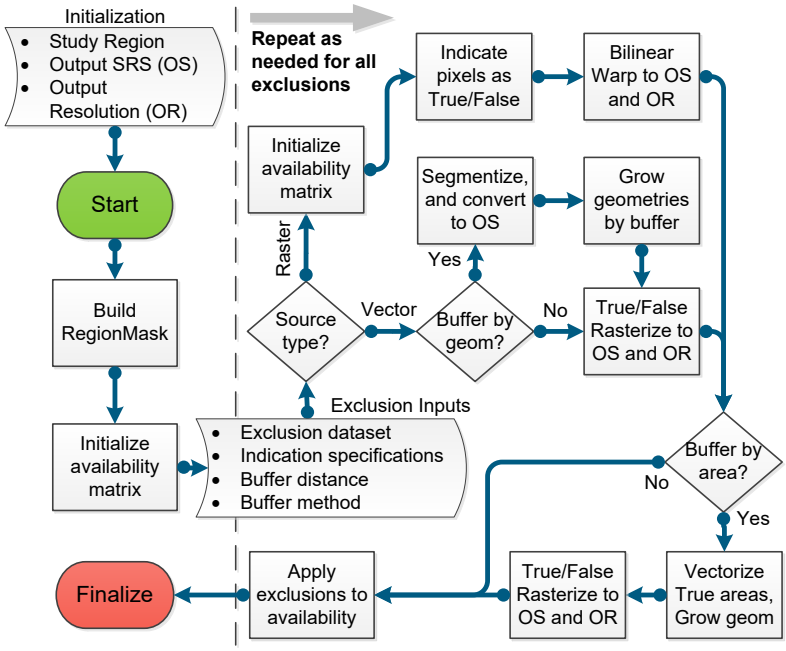

Figure 2.7: Land eligibility flow chart

can be used to apply constraints onto the region definition, setting the constrained areas as ineligible. These constraints are applied one at a time, and the various data-processing subroutines allow the most common raster and vector database formats to be used. As discussed, the Prior data sets can be used in place of other geospatial datasets, which primarily has the benefit of vastly improved computation time. In any case, as a result of the exclusion phase, an availability matrix defining the remaining eligible areas within the region can be finalized; meaning it can be saved as a new raster dataset or else used in further analyses. Figure 2.8 depicts this work flow on an exemplary region with a few sample exclusions.

In order to show the efficacy of using GLAES and the Prior datasets for land eligibility evaluations in Europe, a validation effort was performed by recreating results seen in the literature. Although this issue was of high importance during the development of the land eligibility procedures, its complete discussion would be a distraction from the main objective of this thesis, and as such it is provided in Appendix A.6. Nevertheless, in short, 10 studies [29–32,39,53,67,73] from the criteria review were selected on account of their analysis regions distributed around Europe and explicitly reported eligibility result. Nevertheless, differences in criteria definitions,

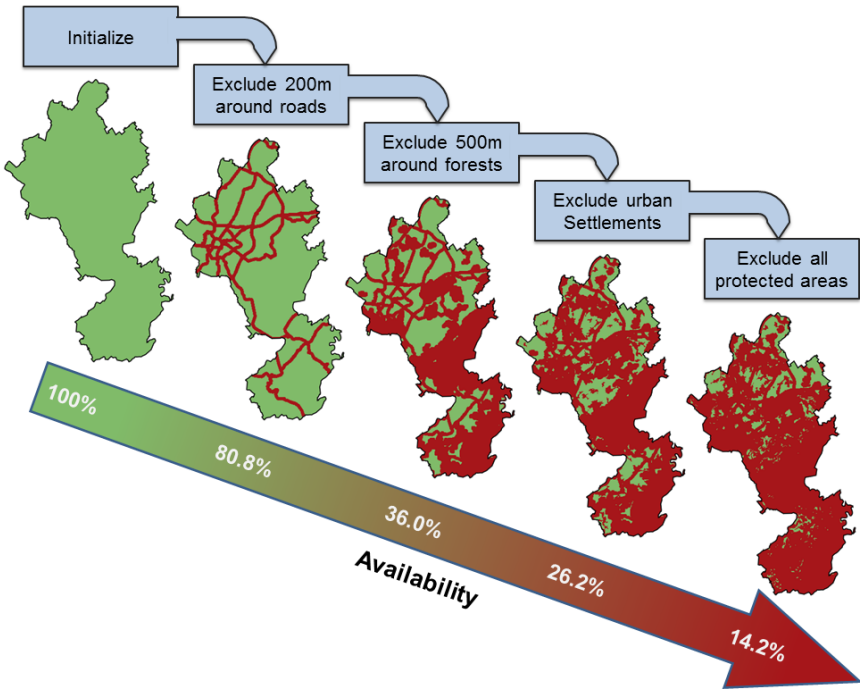

Figure 2.8: Exemplary land eligibility evaluation for the Aachen administration region in Germany. Constraints shown here are for descriptive purposes.

regional definition, and constraint inclusion could not be avoided. Despite this, land eligibility results were for the most part recreated well, with 6 of 10 comparisons being reproduced within $4\,\%$ of the reported excluded area [29–31, 67, 73], with the other four studies showing differences between 7 and $8.5\,\%$ of the reported values. For these latter studies, several issues were discussed, primarily relating to data availability and criteria definitions, which can explain the observed discrepancies.

In a final note concerning land eligibility analysis, the use of GLAES, and the Prior datasets, it should be mentioned that the outcomes of this work have been peer-reviewed and are published in the journal *Energies* [106]. The analysis conducted in this publication explored the value of each eligibility constraint represented by the 44 Prior datasets to the outcome of a land eligibility study. Multiple measures of "value" were considered, and it was found that some constraints, such as distance from forests and agricultural areas, are strong in all measures, while others, such as distance from airports or camp sites, do not have a large impact on land eligibility results[5]. Moreover other constraints, such as elevation and road access distance, are seen to have a high value in terms of the exclusivity of their respective

[5] This is not to say these constraints should not be considered in a land eligibility analysis, however.

exclusions while at the same time being of low value according to other measures. Nevertheless, the complete discussion of these results would distract from the objective of the current thesis and so are not presented further.

2.5 Placement Algorithm

Following the original release of the GLAES model, an additional feature was added which can identify the maximum number of placements within the identified eligible areas. In the basic use case of this placement algorithm an omnidirectional separation distance can be specified and the model will identify explicit placements such that no two locations are within the specified distance from one another. This is shown in Figure 2.9 where a distance of 2 km is selected for ease of visualization, which can be seen as the diameter of the circles around each placement. Moreover, four successive stages of the placement procedure are shown, and the placement ordering is also provided for clarification.

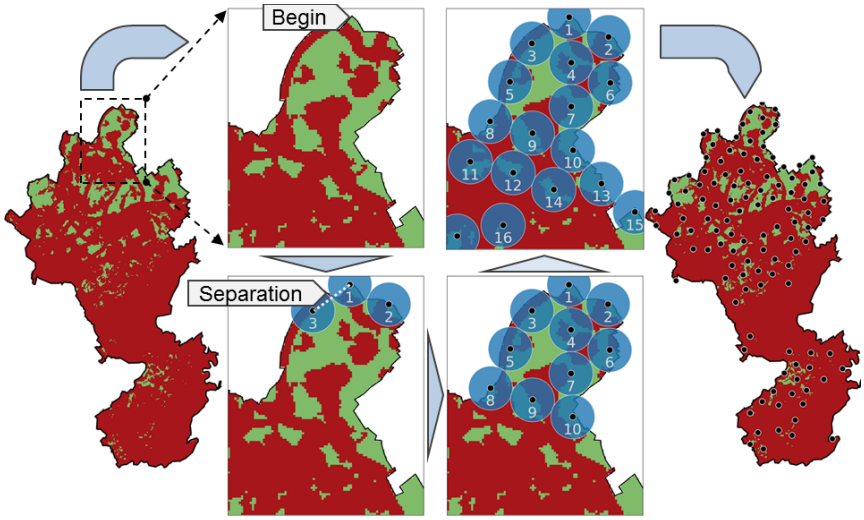

Figure 2.9: Overview of basic placement algorithm.

To determine these placement locations, the following procedure is followed. By consulting the availability matrix resulting from a land eligibility analysis performed in GLAES, the placement algorithm begins at the north-westernmost pixel and scans each row of the availability matrix recording which pixels are eligible for a placement. Then, beginning at the first eligible pixel, the algorithm scans the pixel from left-to-right and top-down looking for the first suitable location which is not in the vicinity of previously located placements. This scanning is performed for every 20 m within each pixel; meaning that a pixel corresponding to an area of 100 m by 100 m will constitute 25 potential placement locations. In each case, a circle with

radius equal to the separation distance is centered around the location, and if any other previously identified placement is within its radius the location is passed. This is continued until either a placement candidate is found, in which case it is selected and the algorithm moves on to the next eligible pixel, or else all subpixel locations have been checked. This procedure is continued until all available pixels have been considered, thereby finding the maximal number[6] of potential locations within the eligible region.

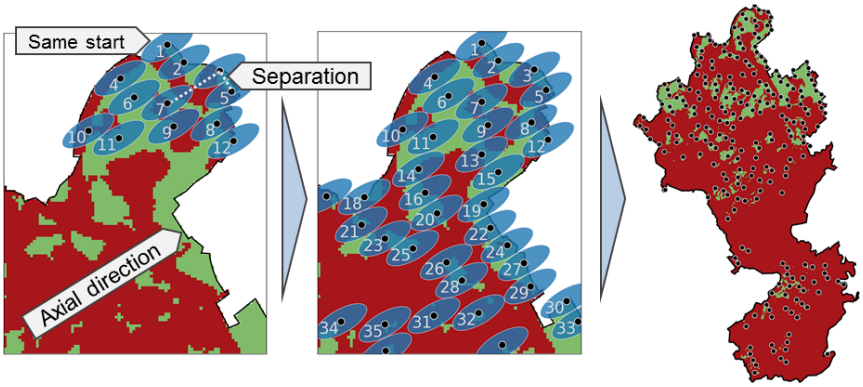

Figure 2.10: Direction dependent mode of the placement algorithm. Start point refers to that of Figure 2.9

Beyond the basic operation of the placement algorithm, two additions are made to better adapt the algorithm to the unique requirements of wind turbines and PV parks. As previously mentioned in Section 2.1.2, wind parks are typically aligned in rows in order to create a larger separation distance between turbines in the predominant downwind direction compared to the crosswind direction [49]. Therefore, it is important for the placement algorithm to capture this behavior. To do this, a small change is made to the basic placement algorithm which allows for the specification of both axial and transverse separation distances, in addition to the angle at which the axial direction is aligned. Furthermore, these separation distances and the axial direction can be given as constant values, or else in the form of a raster dataset in order to incorporate a spatial variability to these qualities. In any case, when evaluating eligible locations an ellipse oriented in the dominant wind direction is used to check for pre-existing placements instead of a circle. Besides this, however, the placement algorithm proceeds in the manner described previously. For reference, Figure 2.10 provides a depiction of this process for the same area and eligibilty result as Figure 2.9, but with an axial separation distance of 2 km, a transverse separation distance of 800 m, and an axial direction of 30° relative to figure's orientation. A clear difference can be seen between the basic placement algorithm and the axial version, in that the latter results in placement rows which

[6] In truth, this is not guaranteed to be the absolute maximum, however sensitivity testing showed that results are robust to changes in pixel scan order and pixel division, and so the results are likely very close to the absolute maximum.

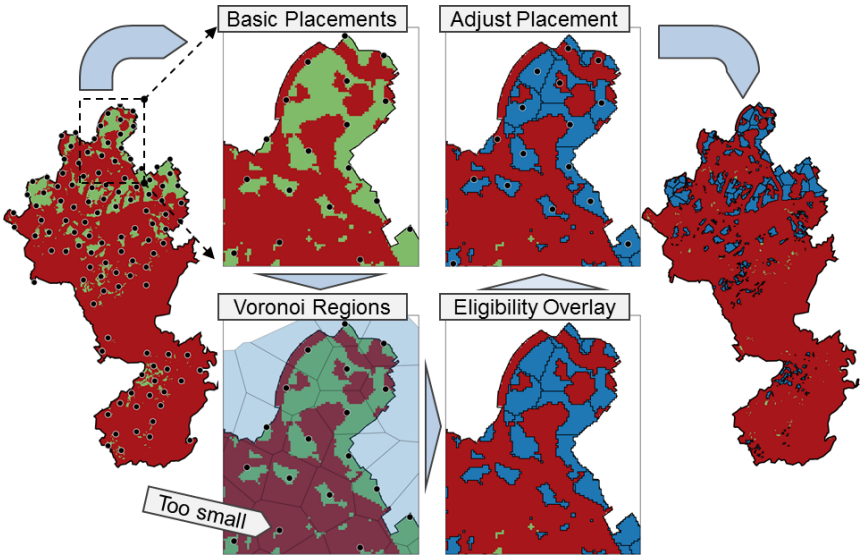

Figure 2.11: Depiction of the area assignment mode of the placement algorithm. Initial placements refers to those resulting from Figure 2.9

are summarily opposed to the axial direction.

The second advanced mode of the placement algorithm adapts it to context of PV parks, and is depicted in Figure 2.11. Since PV parks are much more spread out compared to wind parks, the available area surrounding each placement is an important consideration since it is directly related a park's potential capacity. Therefore, in addition to identifying placement locations, this second mode also decomposes and assigns the eligible area. This area assignment version of the placement procedure follows the basic placement procedure until all locations have been found, and then Voronoi polygons [107] are created around each identified location. These polygons are then rasterized, overlaid with the eligibility matrix, and finally re-vectorized. In effect, the adjacent and non-contiguous eligible area around each placement location is grouped together. As seen in the figure, this procedure also produces a distribution of area sizes which, if desired, can then be filtered according to their size. As a final step, the placement locations are updated to correspond to the centroid of each identified area.

2.5.1 Summary

This chapter has discussed the role and development of the geospatial distribution issues of wind turbines and PV generators in Europe. To address this issue, work conducted here has identified criteria relevant to the distribution of onshore wind turbines and PV parks, produced the Prior datasets for efficient criteria represen-

tation across Europe, and released the GLAES model [100] for conducting land eligibility analyses and performing item placement. Moreover, some of this work has been peer-reviewed and published in the journal *Energies* [106]. As mentioned throughout this chapter, these geospatial distribution models for land eligibility and item placement have been given in a general sense, and the parameterizations that fit their use to either the wind or PV case will be detailed in the following chapters. Although all of these issues have previously be considered in the available literature, the novel aspect of this thesis is two fold: First the emphasis of producing automated and computationally efficient models for the evaluation of land eligibility and item distribution has been accomplished and has already been used by the community for works beyond this thesis as well as outside of the European domain. Secondly, this thesis represents the first instance known to the author where these issues have been combined across the entire European scope for a single VRES technology. Of course, this thesis performs this task for both wind and PV energy and, as will be detailed in later chapters, further exercises the computation efficiency of these models to perform detailed sensitivity analyses over the European scope which also have not been seen over the European scope[7].

[7] As far as the author is aware.

Chapter 3

Wind Energy

In this chapter wind energy will be discussed, with excerpts from some the author's previously published works [108, 109]. An initial discussion is provided covering the basic principles of wind energy which are either directly related to the development of the simulation methods, or else are relevant to fully understand the potential estimation results. This introductory chapter is not meant to provide a comprehensive overview of all wind energy related topics, however, as doing so is beyond the scope of this thesis. Instead, background discussion will focus on: energy available in the wind, spatial and temporal wind variability, wind turbine mechanics, trends in the wind energy industry[1], and finally a summary of representative simulation approaches used in the literature. In all cases discussion highly emphasizes the context of onshore wind energy, however offshore wind energy, which is not dealt with in detail in this thesis, will occasionally be mentioned in brief for the sake of comparison.

Following the background discussion, the methods used in this work for simulating onshore wind turbines will be given in detail. This will begin with arguments for the assumptions made in regards to typical future turbine design and investment cost, after which the method used to incorporate spatial variability to these qualities is given. Following this, a method to generate a synthetic turbine power curve as a function of turbine capacity and rotor diameter is described. Next, the wind-specific parameterizations of the land eligibility and placement algorithms are provided. The simulation scheme is then discussed, covering the extraction of weather parameters from a climate model source, the adjustment of wind speeds to a turbine location's local context, and then estimation of electricity generation. Finally, a note is given in regards to the simulation scheme's validity.

3.1 Background Principles

Within the following section the relevant background information corresponding to wind energy will be covered. As mentioned in the introduction to this chapter, this section is not intended to provide a comprehensive overview of wind energy, as there are many preexisting sources which perform this function; for example, sources that contributed significantly to the authors knowledge of these topics include the works of Troccoli [110], Stull [111] and Kaimal [112], where general atmospheric principals relating to wind energy are explained, as well as that of El-Sharkawi [113], Manwell [114], Wagner [49] and Letcher [115], who all provide

[1] In terms of design, investment cost, and LCOE for both past observations and future estimations.

detailed accounts of wind energy specifically.

3.1.1 Energy in the Wind

The first topic under discussion covers the physical energy available in the wind which, from a fundamental perspective, is related to both the wind speed as well as the air density. Understanding the role played by these two quantities directly influences the wind energy aspect of this thesis' second overarching research question.

Kinetic energy in the wind is of course directly related to its speed. By means of aerodynamic interactions between this movement and a wind turbine's rotors, energy can extracted in exchange for increased rotor rotation speed as well as lowered wind speed and increased turbulence in the turbine's wake [115]. The power available from the wind can be easily calculated as an air-filled volume with cross-sectional area A, air density ρ, and moving at a speed of v, ultimately leading to the following equation.

$$P_{wind} = A * \rho \, v^3/2 \tag{3.1}$$

It is easy to see from Equation 3.1 why wind turbines with large rotor diameters could be preferred, as the pool of energy that can be extracted from is directly proportional to the cross sectional area that a wind turbine presents to the oncoming wind. More importantly, however, is that wind power has a cubic relationship with the wind speed, and thus a twofold increase in wind speed has an eightfold increase in available power. Using the Beaufort scale [116], provided in Appendix Table C.1, as a reference, a 'light breeze' where the wind speed is between 1.5 and $3.3\,\mathrm{m\,s^{-1}}$ would contain a power density of 4 to $43\,\mathrm{W\,m^{-2}}$, while a 'strong breeze', 10.7 and $13.8\,\mathrm{m\,s^{-1}}$, has a power density of 1500 to $3200\,\mathrm{W\,m^{-2}}$. Furthermore, it is clear to see that wind power is also directly proportional to air density, which can be calculated using the following equation [117].

$$\rho = \frac{pM_a}{ZRT}\left[1 - x_v\left(\frac{M_v}{M_a}\right)\right] \tag{3.2}$$

Where surface pressure (p), air temperature (T), the molar mass of dry air (M_a), the molar mass of water (M_v), the molar gas constant (R), the compressibility factor (Z), and finally mole fraction of water vapor (x_v) are all important factors to wind power. As shown in Figure 3.1, air density can change by as much as +16 % on a cold day with above average pressure to $-14\,\%$ on a warm day with below average pressure and high humidity. Furthermore, air density decreases at higher altitudes which, in the first few hundred meters from Earth's surface[2], can be modeled using the Barometric formula [111]. For this reason, air density is an important consideration for turbines in high altitude locations.

[2] The range relevant for wind turbines.

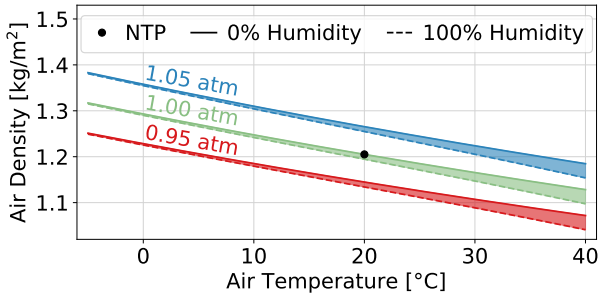

Figure 3.1: Air density sensitivity to temperature, pressure, and humidity. Normal temperature and pressure (NTP) [118] is also indicated.

3.1.2 Wind Variability

In the next discussion, the wind variability is touched upon, including the temporal variability in the wind as well as the spatial variability. Furthermore, spatial variability must be further broken down to its horizontal and vertical aspects. The purpose of this discussion introduces the reader to the basics of these principles, pointing out a few examples of past observations and identifying complex weather phenomena which, ideally, should be considered in order to best identify wind energy potential across Europe as well as to better identify the occurrence of VRES lulls. Ultimately, the topics discussed here give rise to the temporal and spatial differences seen in wind energy potential estimates and generation profiles. The spatial variability, alone, directly relates most to the second overarching research question of this thesis, while the combination of spatial and temporal variability leads to the generation patterns that can create VRES lulls and, hence, relates to the third overarching research question.

Wind is notoriously intermittent and spatially non-uniform due to the complex fluid dynamics involved with its propagation over the land [112]. If a measurement device were setup at some location and programmed to take many instantaneous wind speed measurements over a long time period, the observed wind speed distribution can be represented reasonably well by a Weibull distribution [119, 120]; which is uniquely defined by two parameters, k and λ, and is given by Equation 3.3, where v refers to wind speed.

$$f(v;\lambda,k) = \frac{k}{\lambda}\left(\frac{v}{\lambda}\right)^{k-1} e^{-(v/\lambda)^k} \tag{3.3}$$

Figure 3.2 shows multiple examples of Weibull distributions fitted to near-surface wind speed measurements made over several years in Europe [121]. Referring again to the Beaufort wind scale [116], the windiest of these locations, Kastrup, has an average wind speed of $6.9\,\mathrm{m\,s^{-1}}$ and likewise predominantly experiences

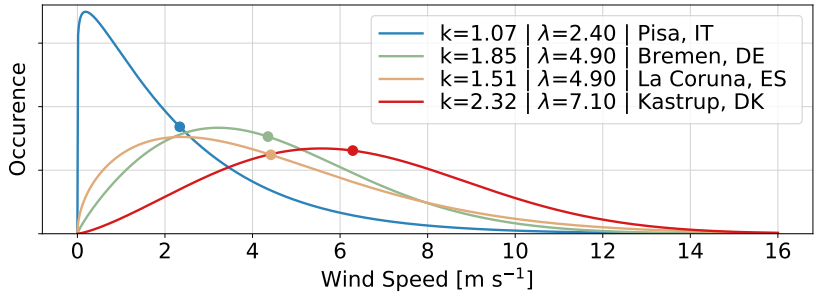

Figure 3.2: Example Weibull distribution of wind speeds for four locations in Europe [121]. The solid point on each line indicates the average wind speed value.

breezes, most notably gentle breezes and moderate breezes, but nevertheless infrequently experiences high winds. By comparison, the curve for Pisa has an average wind speed of $2.3\,\mathrm{m\,s^{-1}}$ and the vast majority of the winds seen there are in the light air range. The distributions observed at Bremen and La Coruna have average values quite close to each other, 4.35 and $4.42\,\mathrm{m\,s^{-1}}$, although the shapes of their distributions are quite different. Bremen, for example, would see a greater proportion of gentle breezes compared to La Coruna, however La Coruna has a slightly higher likelihood of observing strong breezes. How these differences would impact the behavior of a wind turbine at either of these locations is not a simple matter; and so it is not possible to exactly estimate the average performance of a wind turbine based off only the average wind speed. Therefore, in order to answer the second overarching research question in regards to wind energy, a temporally-resolved wind energy simulation procedure will be required.

In the end, to ensure that VRES lulls are properly evaluated in the final stage of this thesis, these temporal fluctuations at each turbine location must be recreated in a realistic manner. However, as the precise modeling of the atmosphere far beyond the scope of this work, the accurate representation of temporal wind fluctuations will be dependent on the chosen weather data source; the selection of which will be discussed in detail in the later portions of this chapter. Nevertheless, it is clear to see that the chosen weather data source should incorporate a high temporal resolution.

Regarding spatial variability, if a region is primarily flat and without many obstacles, such as over grasslands and water bodies, then disturbance of air movement will be minimal. On the other hand, if forests or cities are present, or if there is significant topographic variability, wind propagation will become much more convoluted [124, 125]. Transient issues also impact spatial variability of wind, such as high or low air pressure regions and surface heating due to solar irradiance. As a result, many intricate weather phenomena can be observed which greatly impact

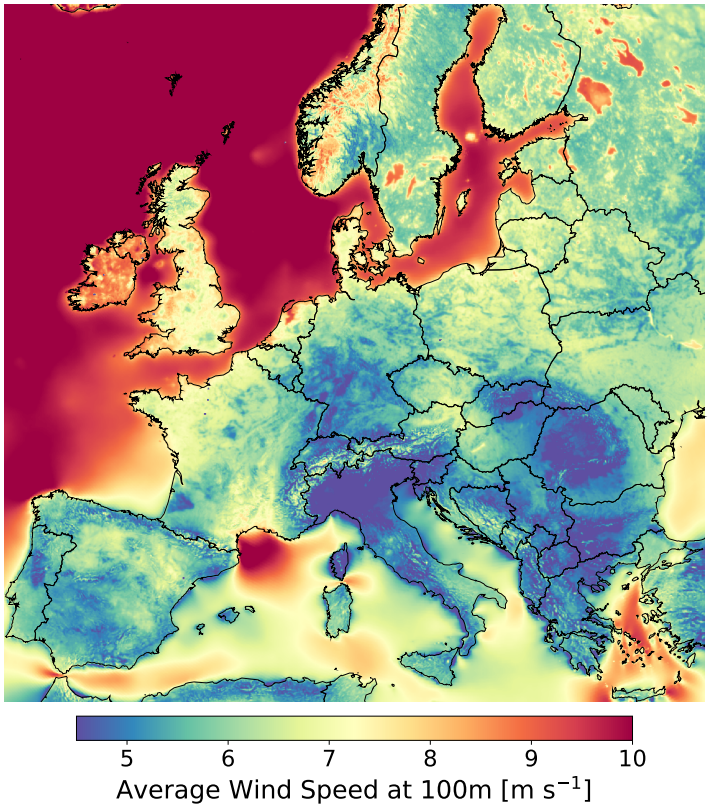

Figure 3.3: Average wind speed at 100 m altitude in Europe between 1980 and 2015 for onshore (Data from [122]) and 1995 until 2015 for offshore (Data from [123]).

wind speeds. One example of this is the low-level jet, a mesoscale phenomenon caused by night-time temperature gradients between the surface and the upper atmosphere, which can cause long corridors of several kilometers with high wind speeds, 10 and 20 m s^{-1}, and at altitudes similar to today's taller turbines [111, 126]. These and many other dynamics work in tandem to create a complex state of spatial variability that is always in transition. Ideally, all atmospheric phenomena should be precisely modeled in order to determine their impact on the energy system. However, as explicit climate modelling is not an aspect of this thesis, realistic representation of all atmospheric phenomena will be dependent on the chosen weather data source. Therefore, in addition to a high temporal resolution, the chosen weather data source should possess a high spatial resolution as well. To give the reader an idea of the long term trends of spatial variability in wind speeds, Figure 3.3 displays the average wind speed values at an altitude of 100 m over the European

scope [122, 123].

In regards to vertical variability, when viewed from basic fluid dynamic principals it is apparent that the wind represents a viscous fluid moving in reference to a static boundary; i.e. the surface. Clearly, then, the no slip condition implies that there must be some gradient between wind speeds near to the surface to those in the upper atmosphere. This zone where atmospheric dynamics are closely tied to surface interactions is called the planetary boundary layer (PBL)[3] and is typically found to extend to around $1\,\mathrm{km}$ above the surface [127]; although this height varies considerably with weather conditions, and can even be as low as a few tens of meters above the surface. In total, this vertical wind profile is collectively referred to as wind shear. Of course, the reality of weather dynamics are such that wind shear can be complex. Besides the aforementioned low-level jets, other examples of atmospheric phenomena which influence the vertical profile are weather fronts, a boundary separating air masses of differing densities, and micro bursts, intense but small-scale down drafts produced by storms. As before, the accurate representation of these phenomena in later stages of this work will be reliant on the selected weather source, leading to the third requirement of high vertical resolution.

Most measured wind speed data is taken from devices at around $10\,\mathrm{m}$ above the surface [128], however wind turbines can be built at heights up to $200\,\mathrm{m}$ and so it is often the case that known wind speeds must be projected to different altitudes. The two most typically used approaches for this are the power-law wind profile and the logarithmic wind profile. To note, both of these approaches represent simplifications which cannot precisely capture all wind shear phenomena [125]. The logarithmic wind profile, which is used later in this work, can be adjusted to the form given in Equation 3.4 [125]. Where v_o is a known wind speed at height h_{ref}, and $v(h)$ is the resulting wind speed at the desired height, h. Furthermore, d is the displacement height where wind speed is theoretically zero, z_o is the roughness factor determined by surface obstacles, and finally Ψ is a stability term depending on L, the Obukhov length defined according to Monin-Obukhov similarity theory [124]. Surface roughness values range from $0.0002\,\mathrm{m}$ over the ocean to $1.2\,\mathrm{m}$ over continuous urban fabric; additional roughness suggestions for different types of land cover are supplied in Appendix Table C.2 [129]. Under neutral stability conditions, which neglects most complex PBL phenomena, $h/L \approx 0$ and Ψ becomes insignificant. The logarithmic wind profile will play a key role later in this work when adjusting wind speeds to the height relevant to a wind turbine, and therefore contributes to answering both the second and third overarching research question. However, the fact that this representation of wind shear is a simplification of wind shear means that the weather data source should also provide 'known' wind speeds at a height close to that of the wind turbines being simulated.

$$v(h) = v_{ref} \cdot \frac{\ln\left(\frac{h-d}{z_o}\right) + \Psi(z, z_o, L)}{\ln\left(\frac{h_{ref}-d}{z_o}\right) + \Psi(z, z_o, L)} \tag{3.4}$$

[3] Also known as the atmospheric boundary layer.

3.1.3 Wind Turbine Mechanics

Next to knowing how much energy is stored in the wind, it is of course imperative to understand how much of that is actually extractable, which of course is a function of wind turbine mechanics. Discussions here will cover the basic limits and working principles of a wind turbine, and then will shift towards turbine classifications, followed by the expected generation response to wind speeds according to a turbine's power curve. As one might expect, the design and operation of wind turbines is fundamental to their performance and, thus, these topics relate directly to the second and third primary research questions. A final discussion is also provided in regards to generation uncertainty, which is directly used in the turbine simulation methods employed later. All in all, this discussion is meant to impart to the reader why the chosen wind simulation considerations are a necessity later on.

In recent years the wind energy industry has largely converged onto the upwind, three-bladed, horizontal-axis, and pitch-regulated turbine design [130]. Furthermore, the European Wind Energy Association (EWEA) predicts that this should remain the status-quo until the physical limitations of this design are reached [130]. They also suggest that a 20 MW wind turbine should be achievable in the future without significant issues.

For clarity, the operation and main components of a wind turbine are described. The rotors of a wind turbine are aerodynamically designed to generate a torque on the nacelle when exposed to oncoming wind. The pitch control system is composed of actuators within the nacelle that pivot the rotors around their longitudinal axes in order to change the angle of attack with the oncoming wind. This serves to regulate the turbine's response to strong winds. The diameter of the circle inscribed by the rotors as they revolve is referred to as the rotor diameter. The nacelle is connected to the hub via the drive train, which in turn either connects directly to the generator in direct drive wind turbines or else can be connected to an intermediate gear box in geared wind turbines [131]. While geared wind turbines generally make use of a doubly-fed induction motor, direct drive wind turbines employ a synchronous generator with a large number of poles allowing for low angular velocities to be translated to higher electrical frequencies [131]. The direct drive design has higher costs associated with the need for more permanent magnets[4], but the elimination of the gear box allows for reduced hub weight as well as lower and less frequent maintenance costs [131]. In either case, the maximum power of the generator is commonly referred to as the turbine's nameplate capacity, or simply the capacity. Specific power, computed from the turbine's capacity divided by the swept area, is often used to describe a specific wind turbine configuration and is given in units of $\mathrm{W\,m^{-2}}$. The hub, which sits atop the tower at the so-called hub height, is free to change its cardinal orientation via the yaw control system. Finally, power generated from the generator is transfered to an inverter usually placed near to the tower's base which then transforms to an alternating current the electricity such that it can be sent to the grid.

[4] Conventionally requiring rare earth materials.

The combination of turbine components chosen for a particular installation site depends heavily upon the stresses the turbine is expected to withstand over the course of its lifetime. As the International Electrotechnical Commission (IEC) suggests, wind turbines are currently categorized into various classes according to the installation site's expected time-averaged wind speed at the hub height, v_{avg}, as well as the expected turbulence intensity (TI) [132]. Table 3.1 displays a summary of these classes, differentiating between strong wind turbines, IEC I, and weak wind turbines, IEC III. Realistically, the choice of turbine design for any particular location depends on a variety of other factors, such as noise tolerance, failure probability, as well as the tendency for ice formation, lightning strikes, and atmospheric corrosion and abrasion [133]. However a common theme is that low wind speed areas tend to have turbines installed with smaller capacities and taller hub heights than high wind speed areas [113, 115]. Later in this work, this general theme will be replicated in order to ensure that a reasonable turbine design is considered at each simulation location.

Table 3.1: IEC Turbine classes

Turbine Class		I	II	III
v_{avg}	$\mathrm{m\,s^{-1}}$	10	8.5	7.5
Turbulence subclass		A	B	C
	TI	0.16	0.14	0.12

Generally speaking, since IEC III turbines are typically installed in less windy areas, they differ from IEC I turbines in that they must respond better to lower wind speeds in order to obtain the same averaged capacity factor. More specifically, a power curve or an efficiency curve is usually provided by a turbine's manufacturer to communicate the turbine's expected performance. Figure 3.4 provides an example of these curves for a contemporary turbine with a capacity of $3450\,\mathrm{MW}$ [134]. For this turbine design, the efficiency curve clearly shows that the maximal efficiency of $24.2\,\%$, achieved at a wind speed of $8\,\mathrm{m\,s^{-1}}$, falls far short of the ideal Betz limit of $\approx 59.3\,\%$ [135]. The wind speed at which rotor forces overcome internal friction, allowing the turbine to begin generating electricity, is called the cut-in wind speed and is found here around $2.5\,\mathrm{m\,s^{-1}}$. After the cut-in, the power generation and efficiency quickly rise until the maximal efficiency point is reached, after which the efficiency begins to fall despite the increasing power generation. This continues until the rated wind speed is reached, at which point the turbine has achieved it's maximal capacity and the pitch control systems activate to regulate further generation. The turbine will continue to generate electricity at its rated power until the cut-out wind speed, at which point the pitch control systems have altered the wind's angle of attack onto the rotors to $90°$ and no net torque is generated. For wind speeds above the cut-out, the turbine is kept in this shut down state in order to avoid mechanical damage.

Although power curves differ quite a bit between turbines, a relationship can be seen between a wind turbine's specific power value and its power curve; shown in

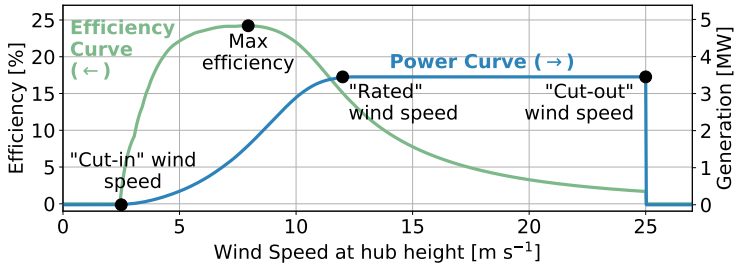

Figure 3.4: An example power curve shown for a contemporary 3450 MW wind turbine

Figure 3.5 [136]. Although the relationship is not ubiquitous, it is generally seen that a low specific power value corresponds to a lower rated wind speed value. Due to this, turbines with low specific power will have a higher average capacity factor than turbines with a larger specific power for the same wind speed distribution. It is also seen from Figure 3.5 that most of the power curves possess a cut-out wind speed at 25 m s^{-1}, although some extend to 30 m s^{-1}, while others (older) reach their cut-off between 20 and 25 m s^{-1}. Later in this work, the selection of an appropriate power curve for each simulation location will be a key consideration which contributes to answering both the second and third overarching research questions.

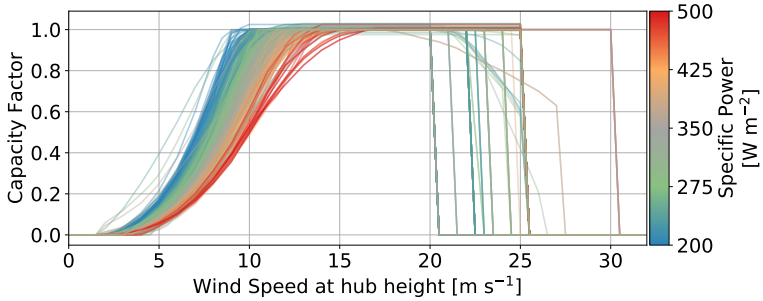

Figure 3.5: Normalized power curves (N=130), colored by specific power (data from [136]).

The presentation of power curves gives the impression that the generation from a wind turbine is explicitly defined for a given wind speed, but unfortunately this is not the case. Figure 3.6 displays observed 15 minute average power generation values for a wind park in western France [137, 138] behind the power curve for the park's turbines [136]. Especially for wind speeds between the cut-in and rated wind speed, it is clear to see that the ideal power curve is at best a suggestion of what the power generation could be, but that significant uncertainty is nevertheless present.

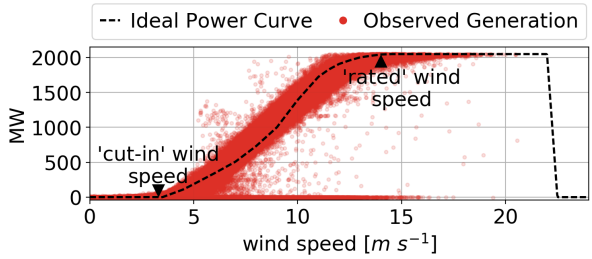

Figure 3.6: Power curve uncertainty (data from [137])

The reasons for this uncertainty are numerous. Some sources of uncertainty come from stochastic characteristics of the wind [139]; such as changing air density, turbulence in the wind [140], or the presence of strong wind shear effects [125]. To try and account for turbulence effects, IEC proposes a simple correction scheme dependent on an intensity factor [132], which has been enhanced by Ren et al. [141]. Other sources of uncertainty arise in the wind speed estimation process. For anemometers making measurements near to a turbine and at the hub height, wind speeds can be influenced in the turbine's wake. Measurements made far from the turbine must be spatially adjusted, and similarly measurements made at different altitudes must be projected to the hub height [142]. When considering the operation of a wind farm, the tendency for wind turbines to increase turbulence and decrease wind speed for other turbines downwind of the original must also be considered [143, 144]. This so-called wake effect will ultimately decrease the generation potential of downwind turbines and is dependent on the specific layout of the wind farm, wind speed, and wind direction. Archer [143] and Seim [144] both discuss the validity of various wake estimation models for use in wind farm simulations. Nevertheless, when only a single wind speed value is known without turbulence intensity, wind direction, or farm layout, each of these sources of uncertainty can be thought of as a stochastic fluctuation around the power curve [17]. Some of these issues will be addressed directly within the simulation scheme used in this work, such as the effect of air density and wind shear, however other issues will not. The effect of turbulence, for one, will not be explicitly modeled as turbulence intensity data is not available in the chosen weather data source. Similarly, the impact of turbine wake will not be explicitly modeled as doing so using the previously mentioned models is not feasible on the European scale. Therefore, a stochastic approach similar to the literature [17] will be used to account for these effects; which will be detailed in Section 3.6.4.

3.1.4 Turbine Design Trends

In the following section, key design trends seen in the wind industry are discussed. First, a discussion on past trends is provided, after which future trend estimations are given. Understanding these trends and estimations informs the selection of turbine design assumptions which fit the 2050 context investigated in this work,

and thus relates to the first overarching research question.

As a result of the wind industry striving to use lighter, cheaper, and more resilient materials alongside increasingly effective turbine designs, the typical configuration of turbine characteristics - capacity, rotor diameter, and hub height - which correspond to a specific turbine class are also shifting. This dynamic is clear to see and is summarized by Figure 3.7 where, for each IEC turbine designation, the average (line) and range (area) of specific power values for turbines erected in the years between 2000 and 2017 are shown [145]. It can be seen that a configuration that could only be installed in 'weak' wind conditions in the early 2000's could be used in 'strong' wind conditions at the end of 2017. Similarly, Figure 3.8 shows turbine characteristic trends for new turbine installations per year seen for several European countries, the EU-28, and the United States provided by the International Energy Agency (IEA) [146]. Therefore, while a spatial variability to turbine design should still be present in the future, it would be a mistake to assume that turbine designs of 2050 should be limited by the current IEC designations.

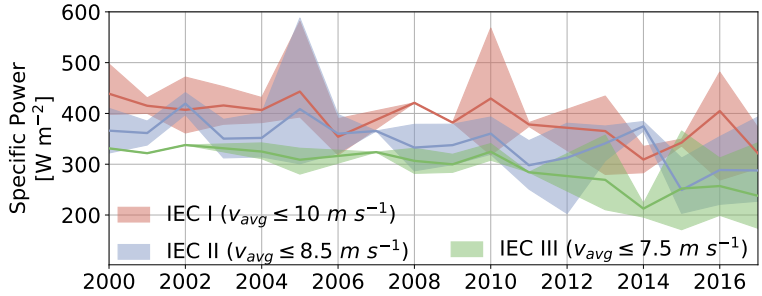

Figure 3.7: Wind turbine class trends seen in The Wind Power's Turbines database [145]. Solid lines show the average specific power of new turbines that belong to each IEC class, while areas refer to the range of values observed.

Various underlying causes of these design trends exist. In regards to rotor diameter, a typical rotor diameter of newly installed turbines in 2016[5] was between 100 and 110 m, and between 2007 and 2016 this has been increasing at a rate near to 2.5 m per year. More frequent use of carbon fiber [147] and advanced load reduction designs, via increase flexibility and better pitch control [131] is largely responsible for allowing this growth. Similarly, by means of conventional tubular steel towers, typical hub heights in 2016 could be found around 100 m and are increasing at a rate of about 2 m per year. Turbine capacity has also been increasing steadily, with a typical 2016 value of 2600 kW growing at a rate of nearly 70 kW per year. Increased use of direct drive wind turbines is partly responsible here [131, 148, 149]. Nevertheless geared wind turbines are also improving, seen by the use of a high-speed-stage gear box leading to improved system reliability and reducing downtime [131, 150]. Finally the growth in rotor diameters is out pacing the growth

[5] 2016 was chosen for this discussion since not all countries have reported values for 2017.

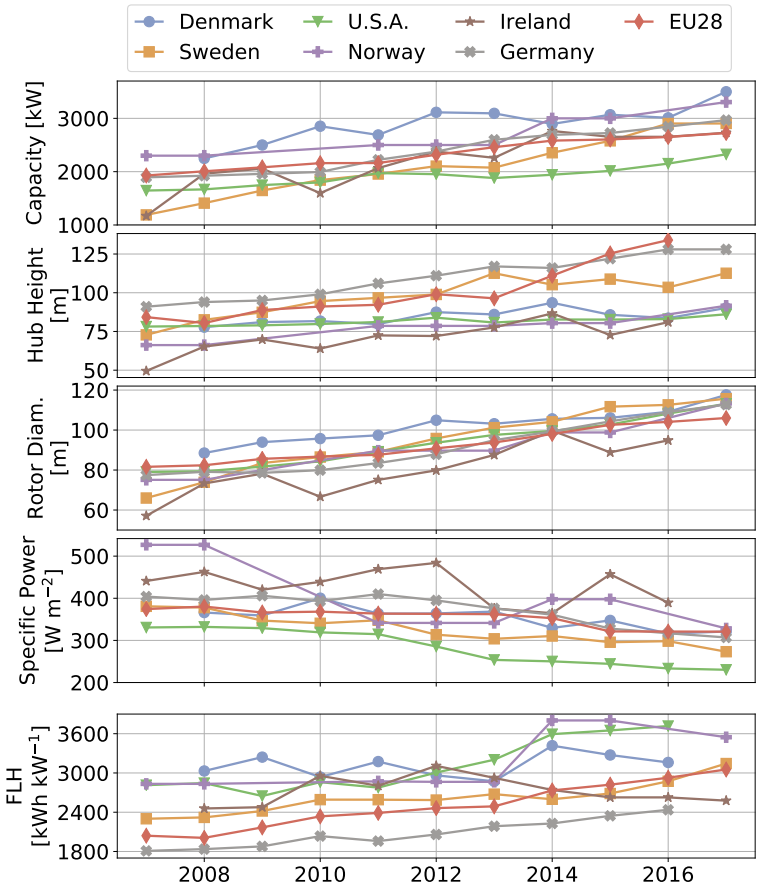

Figure 3.8: Wind turbine characteristic trends for multiple regions. Only onshore wind turbines larger than 1 MW that were connected to the grid within the indicated year are included in the averaging. Values are reported by IEA [146], and are not complete for all countries.

in capacities, resulting in decreasing turbine specific powers. In 2016, a typical specific power was $320\,\mathrm{W\,m^{-2}}$, decreasing at a rate of roughly $8\,\mathrm{W\,m^{-2}}$ per year. As discussed earlier in this section, turbines with lower specific powers are expected to produce better full load hours (FLH) compared to higher specific powers when exposed to the same wind speed distribution.

Due to the decreasing specific powers and increasing hub heights, an increasing trend in FLH should be expected, which as reported by IEA [146] is exactly what has been observed in the last decade; shown at the bottom of Figure 3.8. The

FLH trend in this figure shows the average 2017 performance of turbines greater than 1 MW that were connected to the grid within the indicated year. For turbines installed between 2008 and 2015[6], all regions have shown an increase in FLH, although the magnitude of this growth varies. Of the regions shown, Norway shows the highest growth of $138\,\mathrm{kWh\,kW^{-1}}$ per year, follow by the EU-28 and the USA both around with $115\,\mathrm{kWh\,kW^{-1}}$ per year, and Germany with $73\,\mathrm{kWh\,kW^{-1}}$ per year. Sweden and Denmark have lower FLH growths at 52 and $35\,\mathrm{kWh\,kW^{-1}}$ per year, respectively, while Ireland has only grown by $24\,\mathrm{kWh\,kW^{-1}}$. This growth clearly fluctuates between installation year and independently for each country, and Ireland, Denmark, and Norway are distinguishable in the fact that their FLH trends appear to be stagnating or even in slight decline for turbines installed in the last several years. These differences are potentially due to the changing turbine designs between years as well as to the wind resource quality at the specific installation locations. Furthermore, the number of turbines included in these averages for Ireland, Norway, and Denmark, around 40 to 100 turbines in each year-group, are far less than that of, for example, Germany which possess between 700 and 1700 turbines in each year-group [146][7]. For this reason, the stagnation seen in Ireland, Norway, and Denmark may not be as indicative of the overall momentum of the wind industry as the trends seen in Germany, the EU-28, and the USA; which all show a clear positive FLH progression.

The wind industry has clearly come a long way in the previous decades, and it is certain to continue doing so into the future. Many of the previously introduced historic growth drivers are still at play, however other opportunities are also available. Individual and collective pitching of turbine blades could reduce rotor loads, thereby permitting larger rotor diameters with current materials [151], and multi-piece blade designs can boost flexibility and enhance the rotor's reactions across various load scenarios [131]. Similarly, the continued use of typical tubular steel towers does not appear to be a viable option above a height of 100 m due to transportation limitations [131]. To get around this issue, several avenues are currently being explored: including hybrid or fully concrete tower designs as used by Enercon [152], an easily-erected steel rod lattice structure by GE [153], segmented large diameter steel towers by Vestas [154], or bolted steel shell towers developed by Siemens [155]. Hence, the momentum of the wind industry is apparent, however the precise realization of turbine design in the future remains uncertain. Nevertheless, in order to properly estimate Europe's wind energy potential as well as to properly evaluate VRES lulls, deciding on turbine designs which are in line with these trends is an important consideration to this thesis.

For reference, a few representative examples of future turbine design assumption seen in the literature are provided, and the lack of a clear consensus is a key observation. Robinius [156], for example, considered many turbine designs for individual sites within a 2050 energy system simulation of Germany, but ultimately made the most use of an advanced turbine design with $240\,\mathrm{W\,m^{-2}}$ specific power and 140 m

[6] This range is chosen here as all regions have a reported value.

[7] The USA values are found from between 2000 and 5000 turbines in each year-group, while the EU-28 values are derived from JRC statistics and so the exact number of included turbines is not known.

hub height. In comparison, and also considering 2050 Germany, the German Environmental Agency (UBA) [73] and McKenna et al. [43] both chose to use more conservative turbine designs in the range of $330\,\mathrm{W\,m^{-2}}$ specific power and $110\,\mathrm{m}$ hub height. In 2009, the European Energy Agency [42] concluded that $2\,\mathrm{MW}$ turbines with a specific power of $390\,\mathrm{W\,m^{-2}}$ and hub height of $80\,\mathrm{m}$ could be expected in 2030. Since both of the specific power and hub height heavily influence turbine performance, then, if all else was equal, the study of Robinius would show the most optimistic performance of wind energy, the EEA's study would show the most conservative performance, and UBA and McKenna's somewhere in the middle. This hypothesis will be directly tested later in this work when validating the wind energy simulation models. Looking to 2030, Wiser et. al [157] surveyed 163 of the world's foremost wind energy experts in order to estimate typical turbine parameters in the future, and they found that a median expectation of onshore turbines in 2030 would correspond to capacities between 3 and $4\,\mathrm{MW}$, hub heights between 110 to $120\,\mathrm{m}$, and rotor diameters between 120 to $140\,\mathrm{m}$. In terms of specific power, the experts estimated an average value of $260\,\mathrm{W\,m^{-2}}$, with a low of 155 and a high of 455.

3.1.5 Cost Trends

Next to changes in turbine design, changes in turbine cost are also of high relevance to this thesis. Here, the reader is informed of turbine investment cost and levelized cost of electricity (LCOE) in regards to both historic trends, and future projections seen in the literature. Especially in the case of investment cost, the importance of cost sensitivity to different turbine designs is also stressed. Within the scope of this thesis the discussion here is most relevant to the validation of later wind potential estimations, to ensure that the resulting turbine LCOEs are in the range expected by literature, and furthermore plays an integral role in the selection of wind generator units, thus relating strongly to the third overarching research question.

In terms of investment cost, Figure 3.9 shows future estimations (right) by several organizations next to actual reported cost values (left) reported by IEA [146][8]. Despite strong fluctuations in some countries, historical trends show that the specific cost of wind turbines has summarily decreased over the last decade. Nevertheless, at the time of this writing, viewing these trends supports the notion that a reasonable current investment cost for onshore wind turbines in Europe is around 1450 - $1500\,€\,\mathrm{kW^{-1}}$ [11, 158–161].

Future estimated trends also suggest a further decreasing trend until 2050, although it is apparent that there is not a clear consensus regarding this topic. The highest 2050 estimate shown is that made by the GWEC in 2016, at $1321\,€\,\mathrm{kW^{-1}}$ [162], while the lowest estimate shown was reported by the ECF in 2010 at 1000 € $\mathrm{kW^{-1}}$ [159]. The EC [163], JRC [160], and EMD International [161] all appear to agree on a value in the range of 1100 to $1160\,€\,\mathrm{kW^{-1}}$. The other data values shown in this figure originate from: the IEA [157], U.S. Department of Energy [164],

[8] For onshore turbines larger than 1 MW connected to the grid in each year.

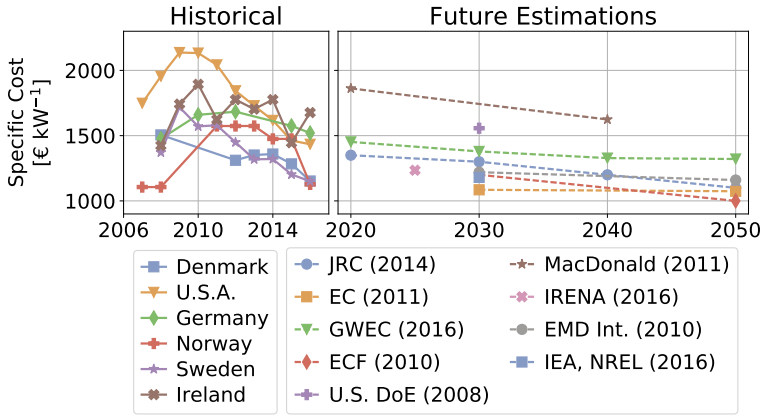

Figure 3.9: Onshore wind turbine investment cost trends and estimations. Sources are given in the text.

EWEA [165], Fraunhofer ISE [166], IRENA [11], and MacDonald [167]. For comparison, for offshore turbines in 2050, ECF [159] and IRENA [158] appear to agree that a cost around 2000 to 2300 € kW^{-1} is likely, and JRC [160] suggests a range between 1900 and 3300 € kW^{-1}.

NREL annually releases a report detailing the cost breakdown wind turbines in the United States [168], where costs are grouped into three categories. The first group, turbine capital costs (TCC), are simply the costs associated with the tower, rotor blades, and the nacelle. The second group, balance of system (BOS), are comprised of costs associated with constructing a turbine and connecting it to the grid. Costs found in this group are project development, engineering management, accessing and staging the installation site, setting the foundation, assembly and installation of the turbine, and finally grid connection. Financial, the third and final group, is simply broken down into construction financing and contingency costs. The breakdown of these costs categories proposed by NREL are shown in Table 3.2. Despite being derived from wind turbine costs in the United States, the breakdown proposed by NREL is in line with costs proposed by other sources within a European context [169, 170].

Of course the breakdown of turbine costs are highly dependent on the context of each installation. This can depend on local policies, land leasing costs, distances to the nearest grid connection point, the route taken when transporting materials, and other factors [169]. In order to estimate the sensitivity of turbine costs in response to changes in turbine characteristics, Fingersh et al. [171], in association with NREL, created a detailed cost model for turbine capital costs and balance of system costs of onshore wind turbines in the United States, which was later updated by Maples et al. [172]. This model assumes that individual component costs, such as the generator, individual rotors, and even the nacelle nose cap, are linked

Table 3.2: Onshore turbine cost breakdown proposed by NREL [168]

Category	Onshore
Turbine Capital Cost	67.3 %
Rotor	19.1 %
Tower	15.1 %
Nacelle	33.1 %
Balance of System	22.9 %
Development	1.1 %
Engineering and management	1.3 %
Foundation & substructure	4.1 %
Site access & staging	3.2 %
Assembly & installation	13.0 %
Electrical infrastructure	10.3 %
Financial	9.7 %
Construction finance	3.7 %
Contingency	6.0 %

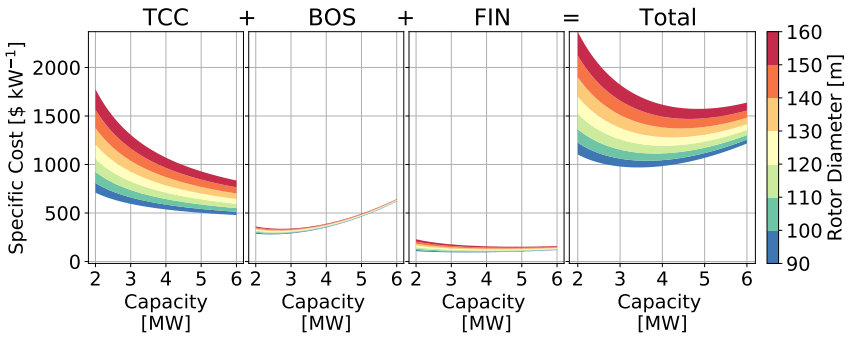

Figure 3.10: Sensitivity of onshore turbine costs to changes in capacity and rotor diameter for the NREL model [171,172]. For the values shown, hub height is always held constant at 125 m and financial costs are kept at 9.7 % of the total cost.

to their material mass. The resulting model estimates turbine capital cost and balance of system cost as non-linear functions of a turbine's capacity, rotor diameter, and hub height.

Figure 3.10 displays the sensitivity of costs estimated with this model for a range of capacities and rotor diameters, and, from this figure, it is again clear why the wind industry is moving toward larger turbines. A transition from 2 to 4 MW, for example, is not estimated to alter BOS costs significantly, however TCC would be reduced by around 30 % depending on rotor diameter and hub height. Conversely, increases

in rotor diameter and hub height[9] are expected to raise TCC, with a similar albeit much less effect on BOS. However, these cost increases are offset by improved turbine performance and can still lead to a reduction in the final cost of electricity.

Although the wind is free, there are nevertheless several operating costs associated with the generation of wind turbines. Some of these costs arise from the need for maintenance, while others result from other financial obligations such as, for example, land-lease costs, insurance, and taxes. In the former case, the past several years have seen a slight increase in service and maintenance contracts offered by turbine manufacturers [158], which have typically amounted to between 15 and $35\,€\,\mathrm{kW}^{-1}$. Land-lease, insurance, taxes, and other similar expenses depend heavily on the region in question and design context of the wind farm, and are quite hard to estimate due to rapidly changing landscape of the wind industry [11, 131, 169]. Nevertheless, distinct differences can be observed between countries when considering the net O&M costs. In 2015, for example, IEA Wind reported the O&M costs of several countries for data collected between 2002 and 2012, and is summarized in Table 3.3 [173]. Within this time period, and of the countries shown, Germany is seen to pay the highest O&M costs largely as a result of the more aged fleet. When reviewing cost data from Denmark, Jensen [174] shows how O&M costs are inversely related to turbine capacity when measured in $€\,\mathrm{kW}^{-1}$, and Manwell et al. [114] have discussed how O&M costs constituted $3\,\%$ of investment costs in 2006, but then fell to 1.5 - $2\,\%$ by 2009. Given the uncertainty of the sociotechnical landscape in the distant future, detailed estimations of future O&M expenses are difficult to produce. In general, however, it is not unreasonable to expect that, over the lifetime of a turbine, these costs can add up to as much as 15 to $25\,\%$ of the final cost of electricity [131].

In terms of the LCOE, a similar decreasing trend is expected on account of both the lower investment costs and improved performance of future turbines. Figure 3.11 shows future LCOE estimations by various research groups next to historical LCOE values for several countries [11]. For the case of onshore wind, IRENA [11] estimates that costs could range globally between 2.7 and $8.0\,\mathrm{ct}_€\,\mathrm{kWh}^{-1}$ in 2025, while JRC [160] expects a more narrow range of between 3.5 and $7.0\,\mathrm{ct}_€\,\mathrm{kWh}^{-1}$ for the same time context. Resulting from their expert survey, Wiser at al. [157] expects costs to be in a range of 3.5 to $5.0\,\mathrm{ct}_€\,\mathrm{kWh}^{-1}$. Conversely, in their 2016 reference scenario, the EC estimates a cost closer to $8.0\,\mathrm{ct}_€\,\mathrm{kWh}^{-1}$ [175]. In the more distant future of 2050, JRC and Wiser et al. appear to summarily agree on a range of 3.0 to $4.0\,\mathrm{ct}_€\,\mathrm{kWh}^{-1}$, with Wiser et al.'s estimates being slightly lower. Once again, the estimate used in the EC's 2016 Reference Scenario [175] is comparatively high at $7.3\,\mathrm{ct}_€\,\mathrm{kWh}^{-1}$. These cost estimations will be directly compared to the resulting values found in this work to ensure that they are within a reasonable range.

[9] Not shown in Figure 3.10

Table 3.3: Example total O&M costs for various countries. Data collected by IEA Wind [173], and presented in the format shown by IRENA

Country	Variable O&M [€$_{ct}$ kWh^{-1}]	Fixed O&M [€ kW^{-1} year^{-1}]
Germany	2.60	57.4
Denmark	1.74	
Ireland		64.3
Norway	2.60	
USA		46.1
Austria	3.48	
Finland		35.7
Italy		43.5
Japan		66.1
The Netherlands	0.87	
Spain	2.60	
Sweden	2.60	
Switzerland	4.35	

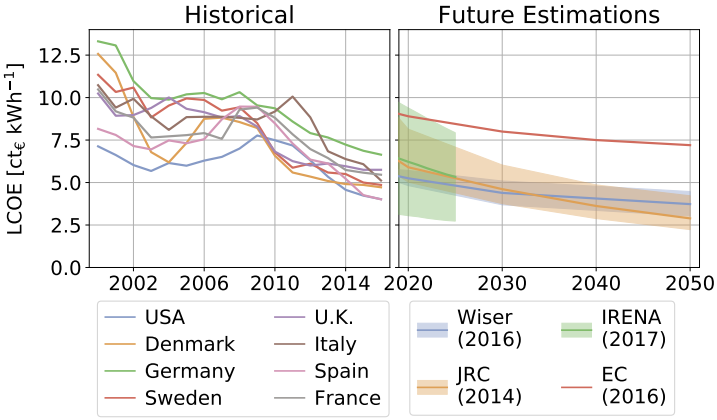

Figure 3.11: LCOE trends for onshore wind turbine, including historical values and future estimations. Sources are as follows: IRENA [11] for historical trends and future estimations until 2025, JRC [160], Wiser at al. [157] and the European Commission [175].

3.1.6 Wind Modeling in the Literature

The final background topic presented on wind energy discusses modeling approaches seen in the literature. The goal of this discussion is not to provide a full review of all wind-modeling-related research, as doing so is beyond the scope

of this thesis. Instead, this section serves to introduce the reader to a representative set of methods used in the literature that are relevant to the current work, to discuss their pros and cons, and to identify avenues to improve upon them. For this reason, extremely simplified methods which clearly will not capture the many wind energy dynamics discussed throughout this section, and extremely detailed methods such as those reliant on complex compressible fluid dynamics simulations [144] and whose use is not feasible across the European scope, are not discussed. Moreover, despite the efficacy of these approaches, studies who use emergent statistical learning-based approaches in their studies, such as Kalogirou et al. [176], are also not discussed. Ultimately, all of the sources discussed, in addition to others, have had a direct influence on the formulation of the wind distribution and simulation schemes used in this work, and as as result are closely related to all three overarching research questions.

Spatial Distribution

Beginning with the spatial domain, one very detailed example of considering wind energy's spatial characteristics is given by the study of McKenna et al. [29] where the wind potential of Germany is investigated. The study begins with a land eligibility evaluation that considers distances from settlement area, commercial and industrial areas, roadways, railways and airports, as well as buffer distances around protected zones. The classic implementation of land eligibility is then extended to consider land suitability; using land-cover dependent suitability factors based on the Corine Land Cover dataset [91]. As a result McKenna finds that only $11.3\,\%$ of the land in Germany is available for wind turbines. McKenna goes on to estimate the wind potential throughout Germany using $1\,\mathrm{km}$ resolved average wind speed data at several altitudes from the German weather service and computing the expected FLH and LCOE value of 12 different turbine designs. In the end, the expected FLH of the cheapest turbine at each $1\,\mathrm{km}$ point is found, after which it is combined with the previous suitability result to identify Germany's total potential. In this way McKenna found that $367\,\mathrm{GW}$ could be installed, and that an average of $855\,\mathrm{TWh}$ of electricity could be generated each year. On one hand, strengths of McKenna's approach are the treatment of land eligibility, the expected value analysis with high resolution weather data, and the LCOE computation. On the other hand, McKenna's approach assumes a simple packing factor when estimating how many turbines can be found in each of the German administrative regions and the origin of the suitability factors used is not expressly stated. Furthermore, while the average wind speed data used by McKenna is of high quality, a constant Weibull distribution is assumed for all locations; which, as seen by Figure 3.2, is not always accurate. Lastly, while this approach is nevertheless effective at estimating wind potentials for some region, it is not capable of providing any temporal information.

McKenna's approach was later expanded in two separate works. In the first of these, McKenna directly applied the German approach to the European context [43] and found that $23\,\%$ of the land was available, corresponding to a maximal average annual generation of $20.2\,\mathrm{PWh\,a^{-1}}$. As a trade off for the larger spatial scope, monthly-averaged and $80\,\mathrm{km}$ spatially resolved wind speed data had to be used,

and furthermore had to be projected to turbine hub height from a height of 10 m using the logarithmic wind profile. Once again, a capacity density factor is used to estimate the technical capacity potential and no temporal quality was produced. In the second extension of McKenna's original work, Jäger et al. [48], investigated the potential of the German state Baden-Württemberg. Although a narrower scope is considered compared to either of McKenna's works, Jäger's study improves on the other approaches by first expanding the land eligibility step to include green areas, observatories, agriculture, forests, and mining sites. Afterwards, Jäger then included a sophisticated turbine placement phase, which individually placed turbines across the state. Besides avoiding the ineligible areas, the placement scheme took into account the predominant wind direction and was thus able to ensure that no two turbines are closer than 8 times the rotor diameter in the longitudinal wind direction and 3 times the rotor diameter in the transverse direction. As with McKenna's original study, this analysis was performed while allowing for multiple turbine design options.

Further notable examples of approaches addressing the spatial quality of wind turbines can also be found. Robinius [47], for example, performed a land eligibility and turbine placement analysis for the whole of Germany, although the placement scheme was not as detailed as the one used by Jäger et al.. In comparison, however, as Robinius' goal was to design an energy system for Germany a temporal simulation was included. Atici [40], Aydin [36], and Höfer [38] are also notable in that they each first performed a land eligibility analysis using similar constraints, and then performed a MCDA analysis to estimate which of the available areas were most attractive for installation. Atici, for example, used an MCDA approach where membership function are assigned to multiple criteria; such as the distance to the nearest transmission line, wind speed, and terrain slope. Höfer, in comparison, used the Analytic Hierarchy Process (AHP) [177] by considering wind speed, road and transmission distance, slope, and other criteria. The AHP weights used by Höfer were found by surveying regional wind energy experts using AHP's typical relative-importance questionnaire. It is shown by Agora Energiewende in their report concerning new onshore installations in Germany in 2014 [178] and by Robinius et al. [47] that realistic turbine installation patterns do not purely reflect the best possible cost of generation. Therefore the MCDA analyses by Atici, Aydin, and Höfer share the strength of incorporating a more realistic site selection scheme. Compared to a European context, however, the study regions in each of these investigations were relatively small, with Atici and Aydin both investigating a piece of western Turkey and Höfer investigating the Aachen county in western Germany.

Time Series Generation

The previously mentioned study by Robinius [47] is the only study discussed here which inherently couples spatial concerns, including land eligibility and an individual turbine placement scheme, along with hourly-resolved turbine generation simulation. In order to arrive at hourly generation values, Robinius first extracted wind speed measurements from nearly 400 weather stations across Germany. Then, for each of the potential turbine locations identified from the land eligibility and place-

ment stages, the measured wind speed time series from the nearest weather station was scaled to match the average wind speed at that location as reported by a high resolution dataset from the German weather service. The locally-adjusted wind speeds were then projected to the hub height of the turbine model being simulated assuming a logarithmic profile and roughness factors suggested by Silva [129]. Finally, using a Fourier-series power curve representation and a $16\,\%$ holistic loss factor, the output generation of each location at each hour was estimated. This procedure was carried out for multiple turbine options, which were later filtered and selected according to the method suggested by Agora [178]. At last, Robinius then aggregated the time series generation values within each of Germany's over $11{,}000$ districts. The major strength of Robinius' approach is without a doubt the unified treatment of spatial and temporal modeling. Moreover, similar to McKenna's [29] and Jäger's spatial analyses, the localization of wind speeds using high resolution average wind speeds enhances the realism of the final result. With these qualities, Robinius's model showcased its ability to estimate the time series generation of wind energy in a region which is reflective of land use concerns, placement likelihood, and locally-contextual wind behavior. Weaknesses of Robinius' approach result primarily from the use of measured weather data, covering a span of only four years, which is likely not representative of all weather phenomenon observable in Germany. Moreover, the measured weather data was often incomplete for many stations meaning that, of the 402 available stations, only a fraction of them were useful for each year.

Staffell and Pfenninger [17] described another temporally-resolved simulation approach relying on climate model data from the Modern Era-Retrospective Analysis for Research and Applications (MERRA) dataset, a global climate model published by NASA with a resolution of $0.625°$ by $0.5°$ (roughly $60\,\mathrm{km}$) [179]. This climate model provides hourly wind speed estimates at each grid point at 2, 10, and $50\,\mathrm{m}$ altitude. In Staffell and Pfenninger's approach 10 and $50\,\mathrm{m}$ hourly wind speeds are spline-interpolated to any location of interest, and extrapolated to the desired hub height for each time step using these two known wind speeds to solve for the profile factor in the wind power-law profile mentioned in Section 3.1.2. Power estimation is performed by mapping these wind speeds to a 'smoothed' power curve, which is found by convolving a Gaussian kernel over the power curve defined by a standard deviation (σ) of $\sigma(v) = 0.2v + 0.6$, where v is the wind speed. Finally, country-specific loss and bias-correction factors are applied to the resulting time series generation values which were found by matching estimated FLH to historic grid-fed FLH reports. By using a publicly accessible global weather dataset along with a straight-forward simulation scheme, Staffel's approach has the strength that it is, ideally, applicable anywhere in the world. Additionally, in reference to turbine generation uncertainty shown in Figure 3.6, the use of a convoluted power curve should better capture the stochastic dynamics of a wind turbine's response to 'measured' wind speeds. Although Staffel's justification of the chosen convolution parameters is not clear, and are furthermore quite strong in comparison to Figure 3.6. At the same time, validation against grid fed generation data will inherently include many energy system dynamics and thus lead to an inaccurate representation of turbine's real generation potential. Furthermore, the development of country-specific cor-

rection factors limit the applicability of their approach to regions where this data is available. Lastly, simply interpolating wind speeds between MERRA grid points does not accurately account for wind development within the nearly $3600\,\mathrm{km}^2$ area allotted to each grid cell.

At last, the EMHIRES dataset commissioned by JRC [180] is introduced. Similar to Staffell and Pfenninger, JRC also utilized the MERRA climate model and their approach also begins by extracting 10 and $50\,\mathrm{m}$ hourly wind speeds and extrapolating to turbine hub height assuming a power wind shear profile. However, before performing this extrapolation, the wind speeds at both of these altitudes are adjusted to a location-specific context via a probability point matching technique relying on the Global Wind Atlas (GWA) dataset developed by the Technical University of Denmark [122]. This probability point matching procedure can be thought of as a more detailed version of the average value mapping procedure employed by Robinius [47], where instead of only scaling the wind speeds to match an expected average, the MERRA-modeled wind speeds are uniquely scaled so that the resulting wind speeds time series constitutes the expected Weibull at each location. Furthermore, by applying this procedure before using the 10 and $50\,\mathrm{m}$ wind speeds to project to a hub height, the projection procedure will better represent wind sheer dynamics as compared to the interpolation used by Staffell and Pfenninger [17]. Once the wind speed at the hub height is obtained, power generation is then estimated by the application of a power curve and holistic loss factor. Outputs of the EMHIRES dataset are computed in the context of contemporary turbine designs, and made publicly available for the NUTS2 European boundary definitions, and over 36 years worth of weather data. Therefore, this approach does not inherently include any spatially-sensitive eligibility characteristics.

3.1.7 Summary and Outlook

Evaluating wind energy's future role in the Europe, especially when focusing on the lulls which can occur, will require a detailed look at the behavior of its generation in this future context. On one hand, this should include the basic working principals of wind energy at high spatial and temporal resolution; such as changes in air density, spatial development, and vertical wind shear. On the other hand, this should also incorporate the momentum of the wind industry by means of considering futuristic turbine designs. Ultimately, electricity generation from wind turbines is expected to be available at LCOEs between 2 to $6\,\mathrm{ct}_{€}\,\mathrm{kWh}^{-1}$. Finally, many techniques have been developed in the literature to account for these dynamics, although there does not appear to be any single study which takes into account all of the requisite details on the European level. For the evaluation of VRES lulls that are made later in this work, this will require utilizing futuristic turbine designs, realistic turbine distribution resulting from land eligibility and explicit turbine placement, and hourly turbine simulation. In the remaining sections of this chapter, the methods used in this work to model the future operation of wind turbines in Europe will be described in detail.

3.2 Turbine Design Assumptions

In this section, the assumptions made in this work regarding future turbine design will be provided. First, the assumption of a baseline turbines design is discussed, which is meant to reflect the typical turbine configuration in 2050. Afterwards, the approach used to incorporate spatial variability around this baseline design is given.

As described in the background discussion of turbine mechanics (Section 3.1.3) and trends in the wind industry (Section 3.1.4), the design of onshore wind turbines in the far future is closely linked to the progression of the wind industry as well as the location-specific conditions that these turbines will be exposed to during their lifetime. As the IEC suggests, wind turbines are currently categorized according to the installation site's expected time-averaged hub heigh wind speed and the expected turbulence intensity [132]. In order to account for technological advancements, a detailed prediction would project turbine designs within each of these categories to their future context; where the application of new materials, construction schemes, and component cost estimations are all considered. However, such a detailed projection is out of scope for this thesis so instead a summary approach to determining future turbine designs is developed.

On average, historical design trends in Europe reveal that from 2007 until 2016 there has been a steady increase in turbine capacity, hub height, and rotor diameter, in addition to a steady decrease in turbine specific power [146] (see Section 3.1.3). These trends depend on the country in question and certainly cannot be expected to continue in this way indefinitely. With this in mind, a baseline turbine is chosen to represent the typical onshore wind turbine in 2050 and later location-specific designs will fluctuate around this baseline. In this way, both the future context and spatial variability of turbine design can be accounted for. Table 3.4 displays the chosen baseline turbine parameters, which are based on the currently available Vestas V136 wind turbine [134]; meaning this is a proven turbine configuration which can only be improved upon in the coming decades. Furthermore, this designs is well within the range of turbines expected as early as 2030, according to the expert solicitation conducted by Wiser et al. [157], as well in line with projections made by the IEA [181].

Considering that future turbine designers will still need to account for varying site-specific conditions by making decisions regarding their choice of materials and the allowable fatigue limits, the general relationship where low wind speeds sites correspond to taller and lower specific power turbines compared to high wind speed sites will likely still be seen. Therefore, in this work spatially varying turbine designs are incorporated around the baseline definition under the assumption that these relative differences remain nearly the same to what is observed today. To accomplish this, the World Wind Farms Database [182] is consulted to determine fitted relationships between real world turbine parameters versus the average wind speed at their installation site. Only onshore wind farms installed in Europe between 2013 and 2017 are included, and average wind speeds are taken from the GWA [122] at $100\,\mathrm{m}$, since this is the available height closest to the baseline turbine's hub height.

Table 3.4: Summary of assumptions for the baseline turbine. Note that location-specific turbine designs will fluctuate around these values.

Quality	Onshore Value
Design:	
Hub Height	120 m
Rotor Diameter	136 m
Capacity	4.2 MW
Specific Power	289 W m^{-2}
Economic:	
Capital Cost (capex)	1100 € kW^{-1}
Annual Operating Cost	2 % capex
Economic Lifetime	20 years
Interest Rate	8 %

Figure 3.12 displays the spread of observed hub height and specific power values, and the resulting fitted functions. The fit for these function is tenuous, which is in fact the expected outcome considering the discussion provided earlier (3.1.3) wherein it is mentioned that numerous factors besides wind speed contribute to turbine design selection in a real world setting. Nevertheless, the resulting fitting functions follow the expected general trend and are therefore deemed sufficient.

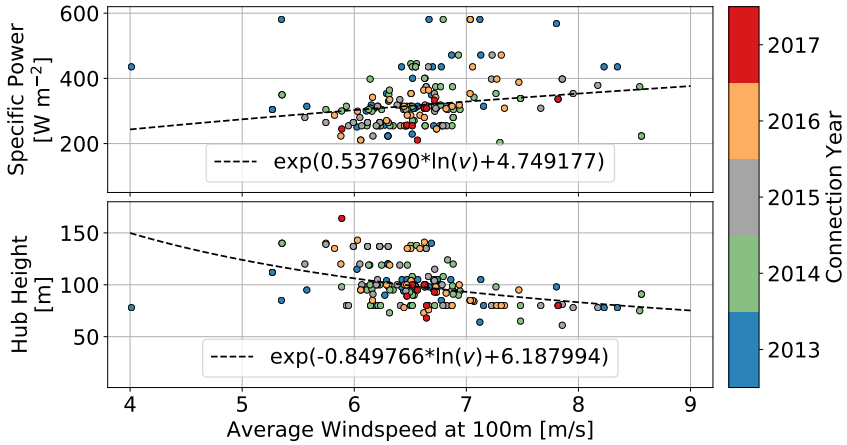

Figure 3.12: Design deviance of actual onshore wind turbines between 2013 and 2017 vs the 100 m average wind speed at the installation site. Adapted from Ryberg et al. [109].

To make the relative design relationships of Figure 3.12 match future turbine characteristics, the resulting functions are scaled such that the baseline onshore turbine's characteristics are returned when a site's average wind speed of 6.7 m s^{-1} is specified. This wind speed is chosen as it corresponded to the average installa-

tion sites wind speed for all sites observed in the previous step. These final design conventions, given in Equation 3.5, are furthermore adjusted to ensure that the hub height is not allowed to fall below 88 m; meaning a minimal ground-to-tip height of 20 m is maintained. Moreover, since this method can only specify two turbine characteristic parameters, hub height and one of either the capacity or the rotor diameter, rotor diameter is always held constant at the baseline turbine's 136 m. Finally, locations where the average wind speed exceeds 9.5 m s^{-1} are not considered as there are no large-scale wind parks installed beyond this value according to the World Wind Farms Database [182]. This restriction will not greatly effect the results in this thesis, however, since average 100 m wind speeds in onshore areas across Europe are generally far below this limit (Figure 3.3). Finally, since the GWA supplies wind speed data at a resolution of 1 km, an averaging kernel of 5 km, corresponding to a small wind farm of 10 to 20 turbines, is applied to the GWA wind speeds in order to suppress design fluctuations over short distances. Figure 3.13 displays the final distribution of turbine design employed across Europe.

$$\begin{aligned} \text{hub height} &= 1.240910 \cdot exp(-0.849766 \cdot ln(\text{wind speed}) + 6.187994) \\ \text{specific power} &= 0.900260 \cdot exp(0.537690 \cdot ln(\text{wind speed}) + 4.749177) \end{aligned} \tag{3.5}$$

3.3 Synthetic Power Curve

The previous section provides turbine design at any arbitrary location, but a turbine power curve must be decided on as well before simulations can be performed. As discussed in Section 3.1.4, current trends show that both rotor diameter and capacity are increasing on average, however increases in rotor diameter are out pacing increases in capacity resulting in the observed decreasing trend in specific power [146]. Furthermore, in Section 3.1.3, it was discussed how a turbine with low specific power is often correlated with a lower cut-in wind speed, a lower rated power wind speed, and, ultimately, higher FLHs compared to a turbine with larger specific power[10]. This effect is taken into account here via the development of a method to generate a synthetic power curve for each placed turbine as a function of specific power.

To accomplish this, the first step involved selecting approximately 130 power curves of three-bladed, horizontal-axis, upwind, pitch-regulated wind turbines with capacities larger than 1 MW from the Power Curve Database [136]. These filters were chosen in order to avoid including unrelated turbine power curves, such as those based on a stall-regulated design or those which are far too small compared to the designs considered in this work. The highest specific power amongst these turbines is from the Enercon E-126 7580 at 7.5 MW capacity and 127 m rotor diameter, resulting in a specific power of 592 W m^{-2}, while the smallest value of 199 W m^{-2} corresponds to the Siemens SWT-3.15-142 turbine with a 3.15 MW capacity and a 142 m rotor diameter. Considering the transition between the cut-in and rated wind

[10] When exposed to the same wind speeds.

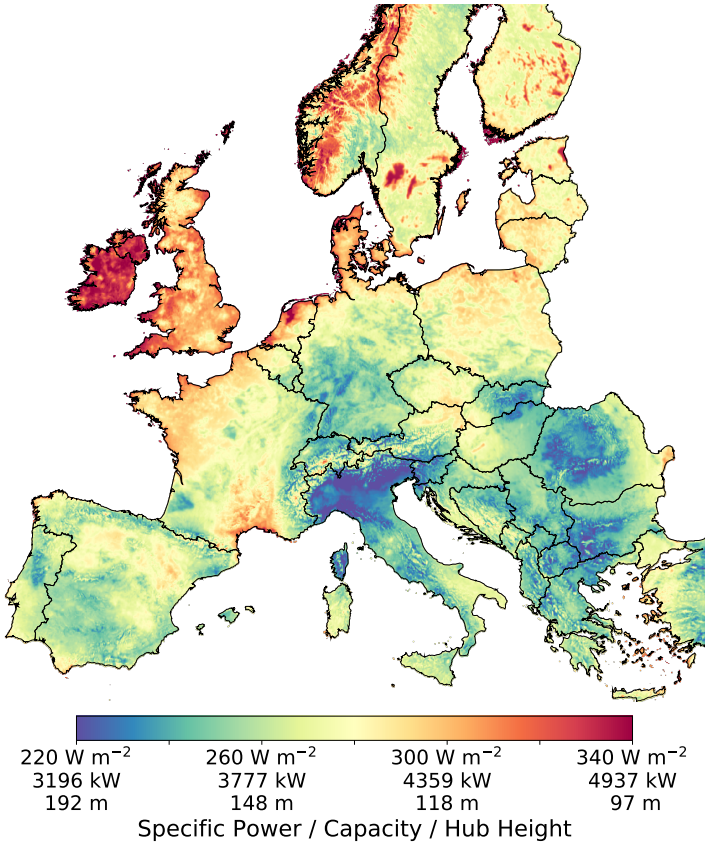

Figure 3.13: Turbine design conventions without land eligibility. Adapted from Ryberg et al. [109].

speed of the real power curves, then, for each $1\,\%$ increment in capacity generation[11], fitting functions in the form of Equation 3.6 were developed that map a given specific power to the wind speed at which that capacity factor is reached. In this equation, A_{cf} and B_{cf} are the resulting constants fit for each capacity factor, displayed in full in Appendix Table D.1, and v_{cf} is the corresponding wind speed. The logarithmic form of Equation 3.6 was chosen empirically, as it was seen to best agree with the shape of the observed relationships.

$$v_{cf} = exp\,(A_{cf} + B_{cf} \cdot ln(\text{specific power})) \tag{3.6}$$

Figure 3.14 displays example fitting results, where the values at capacity factors

[11] Chosen to give a high degree of fidelity to the resulting power curve.

of 30 and 70 % show the typical strong fit for all 1 % steps around and in between these values. Meanwhile, the 1 % and 99 %, which are just beyond the cut-in wind speeds and just before the rated wind speed respectively, show a larger spread of observations since these are the areas of the power curve most heavily influenced by minute differences in real turbine designs; such as the amount of internal friction or the rotor's specific shape.

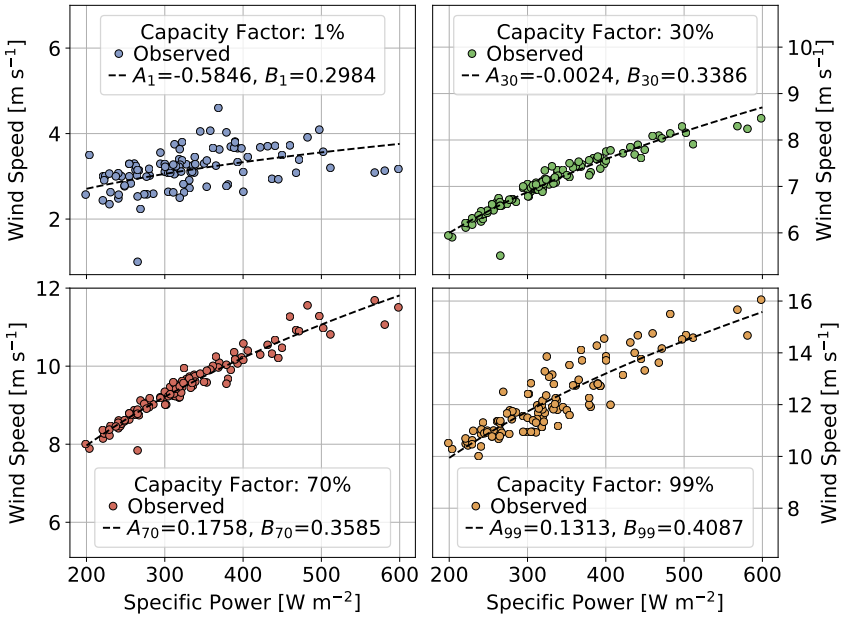

Figure 3.14: Example depictions of the fitting for each 1 % increase in capacity factor during the ramping phase of a wind turbine's power curve. Power curves supplied by the Power Curve Database [136]. Figure adapted from Ryberg et al. [109].

In the next step, a power curve is designed when given a specific power value by computing the wind speed of each capacity factor percentage between the cut-in and rated wind speeds using A_{cf} and B_{cf} values from Table D.1 in Equation 3.6. Cut-in and rated wind speeds are given directly by applying the 0 and 100 percentages constants. Then, the capacity factor for all wind speeds below the estimated cut-in wind are set to zero, while all capacity factor values between the rated and cut-out wind speeds, which for all analyses conducted in this work is always assumed to be 25 m s^{-1}, are set to one. This cut-out limit is chosen since it agrees with the vast majority of recent turbine designs seen in the Power Curve Database [136], and a clear outlook of this quality into the future could not be found in the available literature. Nevertheless, this limit will have a very small impact on the end results here, as even highly windy onshore areas rarely see sustained wind

speeds at this speed (See Figure 3.2). Finally, all capacity factors above the cut-out wind speed are set to zero. At this point, a power curve tailored to the turbine design in question has been produced and can be used for simulation. Figure 3.15 provides a sample output of this procedure for relevant onshore turbine designs.

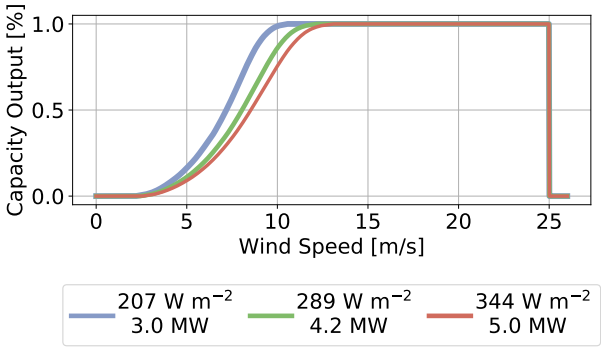

Figure 3.15: Exemplary synthetic power curves. Rotor diameter is held at 136 m.

3.4 Wind Turbine Cost Model

Wind turbines installation cost estimation is performed in this work by scaling the sensitivities of NREL's onshore [171,172] cost model, discussed in Section 3.1.5, to a 2050 context. This model, which is ultimately a function of turbine capacity, rotor diameter, and hub height, is chosen as it is the only example known to the author of a detailed cost model which is sensitive to the three primary turbine characteristics. Ideally, a turbine cost model should also include both grid connection costs as well as financial costs tailed to the country in question, however these issues will not be addressed here as no model for these quantities nor data on which to develop and validate such a model is known to the author. Ultimately, the NREL model is used to estimate both turbine capital cost and balance of system costs for any given turbine configuration.

To scale these functions to a 2050 context, factors are determined for each sub cost model such that an expected cost is returned when the baseline turbine's characteristics are specified. As Table 3.4 indicates, a summary cost of the onshore wind turbines in 2050 is assumed to be 1100 € kW^{-1}, which is in line with the estimates of ECF [159], JRC [160], and EMD International [161]. Furthermore, Table 3.2 provides NREL's latest cost breakdown of onshore turbines in 2016 and, despite the fact that these shares will certainly change in the far future, the exact nature of these changes are uncertain [157] and so they are still applied to the 2050 context in this work. Following this breakdown, the onshore baseline turbine should have a turbine capital cost of 741 € kW^{-1}, a balance of system cost of 252 € kW^{-1}, and additional financial costs of 107 € kW^{-1}. Ultimately, Equation 3.7 calculates turbine investment cost in € kW^{-1}, with scaling factors applied to the NREL onshore costs

models as shown in Equation 3.8.

$$CapEx = TCC(c, rd, hh) + BOS(c, rd, hh) + FIN(_{TCC}, _{BOS}) \tag{3.7}$$

$$\begin{aligned} TCC &= 0.918995 \cdot TCC_{nrel}(c, rd, hh) \\ BOS &= 0.644322 \cdot BOS_{nrel}(c, rd, hh) \\ FIN &= 0.108647 \cdot (TCC + BOS) \end{aligned} \tag{3.8}$$

When preceded by the turbine design conventions of Equation 3.5, onshore cost estimation ultimately becomes a function of the average 100 m wind speed, as shown by Figure 3.16. In this way the expected behavior is found where low wind speed turbines cost less than high wind speed turbines in terms of total cost, but also have a higher specific cost per capacity. By again taking wind speeds from GWA, and applying a 5 km averaging kernel for the same reasons provided earlier, the distribution of turbine cost across Europe presented in Figure 3.17 is found.

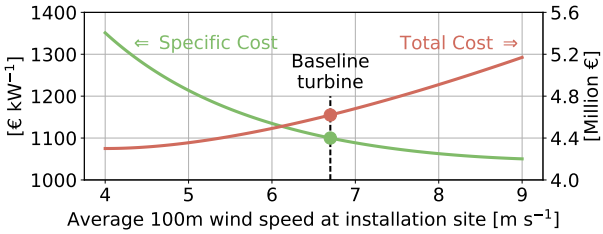

Figure 3.16: Estimated onshore wind turbine CAPEX in a 2050 context vs installation site wind speed. Adapted from Ryberg et al. [109].

3.5 Land Eligibility and Placement

To ensure that wind turbines are not placed in those areas which should be excluded, a land eligibility scenario is taken into account followed by turbine placement. This is performed using the GLAES model [100, 106] in the manner previously described in Section 2. To note, the outcomes of this land eligibility work have been peer-review and published in the journals *Renewable Energy* [108] and *Energy* [109], and therefore portions of these works are repeated here.

For land eligibility, the 30 constraints given in Table 3.5 are uniformly imposed across the European landscape. Most of these constraints were decided upon based on the land eligibility literature review discussed in Section 2.2, and cover

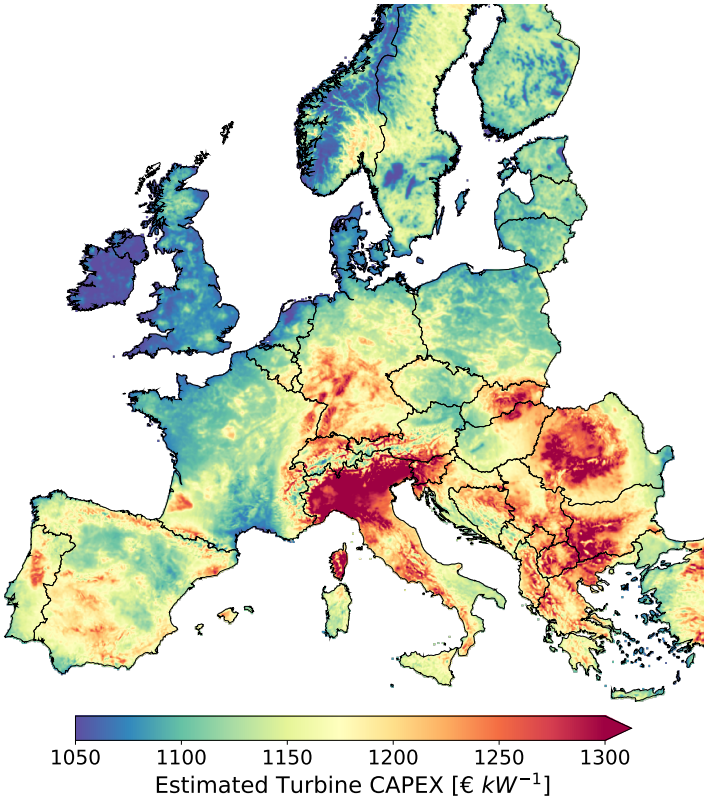

Figure 3.17: Wind turbine CAPEX in a 2050 context across Europe. Adapted from Ryberg et al. [109].

the most impactful constraints commonly considered by other researchers. This includes, for example, an 800 m security distance from settlements, 5 km security distance from airports, and 1 km security distance from designated bird habitats. In addition to these considerations, less-commonly considered constraints are also included; such as a 1 km security distance around camp sites, leisure areas, and recreational parks. These constraints are applied uniformly across Europe and, as such, they were specified to summarily fit a European perspective; judging from studies in the literature review where the study area was within Europe.

Once the distinction is made between available and excluded areas, individual turbine locations are identified within the available areas according to the placement algorithm detailed in Section 2.5. Based on the suggestions of Jäger et al. [48], Emami and Noghreh [183], and McKenna et al. [29], the separation distance of each turbine should correspond to 8 and 4 times rotor diameter of each turbine, ori-

Table 3.5: 31 land eligibility constraints applied for onshore wind turbines. Adapted from Ryberg et al. [108].

Constraint	Threshold	Source
Sociopolitical		
Distance from Settlements	>800 m	CLC
Distance from Urban Settlements	>1.2 km	EuroStat
Distance from Commercial Airports	>5 km	EuroStat
Distance from Airfields	>3 km	EuroStat
Distance from Primary Roadways	>300 m	OSM
Distance from Secondary Roadways	>200 m	OSM
Distance from Railways	>200 m	OSM
Distance from Power Lines	>200 m	OSM
Distance from Leisure Areas	>1 km	OSM
Distance from Camp Sites	>1 km	OSM
Distance from Touristic Areas	>1 km	OSM
Distance from Industrial Areas	>300 m	CLC
Distance from Mining Sites	>200 m	CLC
Physical		
Terrain Slope	<17°	EuroDEM
Distance from Water Bodies	>400 m	CLC
Distance from Rivers	>200 m	EuroStat
Distance from Coast Lines	>1 km	CLC
Wetlands	excluded	CLC
Terrain Elevation	<2 km	EuroDem
Distance from Sandy Areas	>1 km	CLC
Conservation		
Distance from Bird Areas	>1 km	WDPA
Distance from Habitats	>200 m	WDPA
Biospheres	excluded	WDPA
Wildernesses	excluded	WDPA
Landscapes	excluded	WDPA
Reserves	excluded	WDPA
Parks	excluded	WDPA
Distance from Natural Monuments	>500 m	WDPA
Pseudo-Economic		
Wind Speed	$<4\,\mathrm{m\,s^{-1}}$	GWA
Access Distance	<5 km	OSM
Connection Distance	<20 km	OSM

ented with the major axis parallel to the predominant wind direction[12]. Since rotor diameter is kept constant at 136 m, this allows for constant separation distances of

[12] Wind direction is determined using the input weather source, which will be introduced shortly.

1088 m in the dominant wind direction and 544 m in the transverse wind direction. To note, this spacing assumption will have an immediate impact on the number and distribution of turbine placements but, as seen in Figure 2.10, the exact outcome of this is not purely dependent on the available area; the distribution of the available areas is also an important consideration. Therefore, the sensitivity of this assumption to total capacity potential will be discussed later on.

3.6 Wind Turbine Simulation

In the next section, the novel wind turbine simulation scheme is described. As much as possible, a generalized scheme is developed so that it can be applied to a wide variety of turbine designs as well as with a variety of input weather sources. The issues discussed here relate to: the selection of weather data source, the method used to extract data from that source, the adjustment of wind speeds to a turbine's local context, and finally the estimation of electricity generation. Description of this simulation method is given in the context of a single turbine for a single hour, however in practice this method is designed to be applied simultaneously for many placements over an entire year in a computationally efficient manner. The placements that are simulated will be taken from the results of the land eligibility model, placement algorithm, and turbine design conventions described previously, and the year which is simulated will be controlled by the input weather data which is provided to the model. Together, these parameters define the spatial, temporal, and technological context of the wind energy simulation to be carried out. In the end, the result of this procedure is a single hourly generation time series from all wind turbine placements spanning a complete year. Although the described procedure is applicable for simulating single turbines, its intended purpose is to estimate the aggregated time series generation over a large area, such as a large wind park or an administrative area, since this is the context required for the later VRES lull evaluation. An overview of this wind simulation scheme is given in Figure 3.18

The model has been designed with flexibility and ease-of-use in mind and, at the time of this writing, has already been applied in works besides the scope of this thesis, peer-reviewed, and published. This includes the investigation of wind generation in Patagonia by Heuser et al. [101] in the *International Journal of Hydrogen Energy*, which required slight modifications due to data availability. Furthermore, this approach has been used by Welder et al. [184] in Germany and by Tlili et al. [185] in France, both within the journal *Energy*, and has been adapted to the offshore context and publish in the journal *Applied Energy* by Caglayan et al. [102]. Furthermore, the author of this thesis has published the work conducted in this thesis relating to wind energy potential in Europe [109]; some of which is repeated within the discussions included here.

To note, the development of a simulation model which can perform these simulations in a computationally efficient manner has been a significant accomplishment of this work. In summary, this efficiency is obtained by arranging all operations

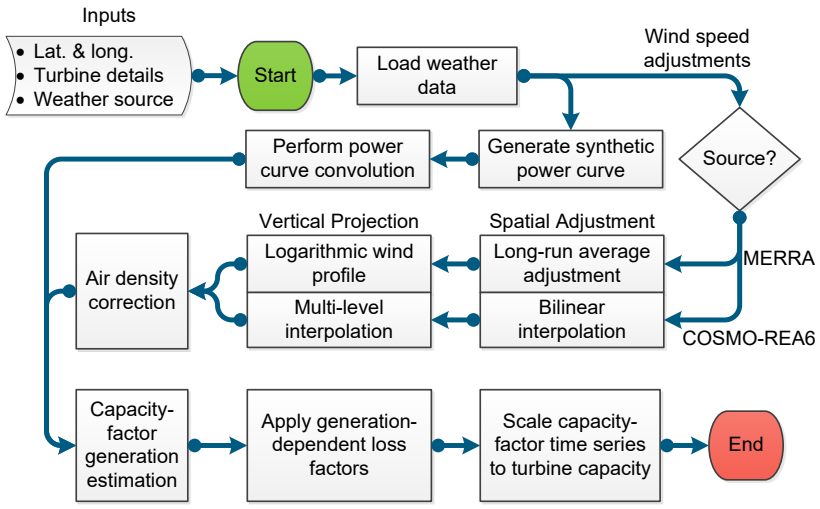

Figure 3.18: Overview of wind simulation scheme

as broad matrix operations that are executed directly in low-level libraries[13]. However, as mentioned in the discussion of power curve uncertainty (Section 3.1.3), wake effects could not be explicitly included into this model since this would need to be evaluated individually for each turbine and at each time-step, and thus would drastically undermine computational efficiency. This is the underlying reason for choosing the stochastic treatment of turbine uncertainty, which is discussed in detail shortly, to account for wake losses as well as other factors; such as the effect of turbulence or turbine misalignment.

3.6.1 Weather Source Selection

In the discussion of wind variability in Section 3.1.2, it was concluded that the ideal weather data source is one that incorporates a high degree of resolution in the temporal, horizontal and vertical dimensions. Furthermore, it was also mentioned that wind speeds should be available from this ideal source at altitudes already near to turbine hub heights and that air temperature and pressure, which are used to determine air density, should also be available. Nevertheless, since the explicit modeling of atmospheric phenomena is far outside the scope of this thesis, a selection of available sources must be made. Given the large spatial domain, the need for multiple weather parameters, and the need to evaluate wind generation over multiple years in order to best capture the wide variety of possible weather events, the only suitable option is the use of climate model output datasets. Of course, the use of climate model outputs in place of, for example, measured data or satellite-derived

[13] Such as BLAS and LAPACK.

data brings its own uncertainties and potential biases which must be accounted for [16, 17, 186, 187]. A more detailed summary of the construction of climate models, including the simplifications they tend to make and the way their outputs should be interpreted, is provided in Appendix C.3.

As mentioned in the discussion of past wind energy simulation approaches (Section 3.1.6), the use of the Modern Era-Retrospective Analysis for Research and Applications[14] (MERRA) dataset [179] for providing weather variables in wind energy simulations is quite common in the literature [17, 180, 188–193]. This global climate model (GCM) is evaluated with a time step of 5 to 10 minutes, but output is saved only hourly. Furthermore, this model has a spatial resolution of $0.625°$ by $0.5°$ ($\approx$60 km over Europe), and the atmosphere is divided into 72 distinct layers [179]. Lastly, MERRA's analysis period begins in 1980 and is updated regularly in monthly cycles; meaning that, at the time of this evaluation, 37 years of global weather data are available between 1980 until the end of 2016. Compared to other GCMs available at the time of this evaluation, the MERRA dataset is superior in both the spatial and temporal resolution and, given its common use in the literature and long time span, it is therefore selected as the primary weather source used in this work as well. In addition to providing all the required weather parameters, the MERRA data set also provides wind speeds at a height of 50 m which, while not equal to the turbine hub heights used in this work, is far better than the 10 m available in most other GCMs. Nevertheless, the $\approx$60 km spatial resolution is not fine enough, and so an adjustment must be made to bring these MERRA-grid-context wind speeds to the local context of each turbine.

Table 3.6: Overview of pros and cons of using the MERRA dataset [179] versus the COSMO-REA6 dataset [194].

	Variables	Output resolution	Available years	3D wind speeds	Fits for all validation sources
MERRA	Includes all necessary variables	1 hour $\approx$60 km	37	No	Yes
COSMO-REA6	Includes all necessary variables	15 minute 6 km	21	Yes	No

Another climate model dataset worth considering is the COSMO-REA6 [194], produced by the German weather service. The COSMO-REA6 dataset is produced from the COSMO Regional Climate Model (RCM) and only covers the European scope but, in turn, boasts a $\approx$6 km grid with outputs written in 15 minute time steps. Besides the drastically improved resolutions, COSMO-REA6 also provides three-dimensional wind speed data, meaning that wind speeds can be interpolated to a

[14] In this work, the second version of the MERRA dataset will be used.

turbine's hub height for each time step as opposed to relying on the constant assumption of a logarithmic wind profile in neutral stability conditions. The use of this dataset, therefore, would be much more capable of capturing the complex atmospheric phenomena mentioned in Section 3.1.2. Like MERRA, COSMO-REA6 is also capable of suppling all other necessary weather parameters, such a temperature and pressure, as well. Conversely, at the time of this writing, the COSMO-REA6 dataset is only available for years between 1995 and 2015 and its increased resolution and wind speed redundancy greatly enhance data handling challenges as well as overall simulation time. Furthermore, until very recently, this dataset has not been used commonly in the wind energy modeling literature [195–197]. For the purposes of this thesis the MERRA dataset is still preferred in order to avoid these drawbacks, however the additional consideration that one of the main validation sources for real wind park generation could only be obtained for the years of 2015 and 2016 also played a significant role in this decision. Nevertheless, the author recognizes the potential of using such a highly resolved weather dataset for the primary VRES lull analysis made in this work, and so in the end of this thesis a sensitivity will be performed by using generation profiles derived from COSMO-REA6 based simulations instead of MERRA.

3.6.2 Weather Data Extraction

Next, the extraction of weather data variables from either the MERRA or COSMO-REA6 dataset is discussed. Beginning with a set of turbine placements resulting from the land eligibility and placement algorithms, the smallest rectangular subset of the dataset's grid points that contain the placement locations is identified. and a three dimensional column of data is extracted. This subset of grid points will be common across all weather parameters. For each of the required weather parameters - wind speed, temperature, pressure - a three dimensional column of data is extracted consisting of a full year of hourly data. Table 3.7 specifies the variable selection for either climate model dataset, which also indicates how these variables differ from each other between sources.

Table 3.7: Climate model variables used for wind turbine simulations

Variable description	Variable Name	Unit	Height Context
MERRA			
Northerly wind speed	U50M	$\mathrm{m\,s^{-1}}$	50 meters
Easterly wind speed	V50M	$\mathrm{m\,s^{-1}}$	50 meters
Pressure near surface	PS	Pa	at surface
Temperature near surface	T2M	K	2 meters
COSMO-REA6			
Northerly wind speed	u	$\mathrm{m\,s^{-1}}$	variable
Easterly wind speed	v	$\mathrm{m\,s^{-1}}$	variable
Pressure near surface	sp	Pa	at surface
Temperature near surface	2t	K	2 meters

Since wind speeds from weather models are commonly provided as component vectors oriented according to the model's horizontal grid, these are always combined to find the magnitude. Similarly, temperatures are converted to °C, and pressure is kept in units of Pascals. Specifically for the COSMO-REA6 data, wind speed data is not provided at a static altitude, but rather at multiple heights which vary depending on location. To note, the MERRA dataset also offers wind speed variables at 10 and 2 m, however these are not used in the wind simulation scheme since, due to their close proximity to the surface, their use would incur a high degree of uncertainty [198].

3.6.3 Wind Speed Adjustment

Next, this raw weather data is combined in order to generate a wind speed time series that is adjusted to the hub height of each placement. In general this includes spatial adjustment, vertical projection, and finally pressure correction.

In the MERRA case, spatial adjustment of onshore wind speeds is performed by emulating the approaches of Robinius [156] and JRC [180], where the hourly profile provided by a slightly out-of-context source[15] is adjusted to the local context according to expected averages. Throughout the rest of this thesis, this will be referred to as the long-run average (LRA) adjustment, and is shown in Equation 3.9. A pre-analysis was performed to find the time-averaged wind speed of all 50 m wind speeds for each MERRA grid point around Europe and, from this, $v_{MERRA,avg}$ is extracted for the MERRA grid point closest to the turbine placement being simulated. Similarly, $v_{GWA,50m}$ represents the expected average wind speed at 50 m altitude at the placement's specific location according to the finely-resolved[16] GWA [122]. Finally, the raw wind speed time series from the placement's closest MERRA point, v_{MERRA}, is scaled such that the long-run average of the adjusted time series, v, should equal the value dictated by GWA.

$$v(t) = v_{MERRA}(t) \cdot \frac{v_{GWA,50m}}{v_{MERRA,avg}} \tag{3.9}$$

In comparison, when the COSMO-REA6 dataset is used as input, the naturally high spatial resolution and the fact that wind speeds are not provided at a constant altitude means that applying a similar long-run average adjustment procedure would be computationally expensive while not adding additional accuracy beyond basic interpolation. Therefore, spatial adjustment of onshore wind speed from COSMO-REA6 is performed via bi-linearly interpolating wind speeds at each time step to a placement's location using the values observed at the four surrounding grid points. This interpolation scheme was chosen due to it being less computationally intensive than, for example, cubic or spline interpolation, while at the same time resulting in

[15] Which, for Robinius is measured weather station data while for JRC and this work will be from MERRA.
[16] 1 km resolution.

minor differences[17]. Lastly, this horizontal interpolation is performed for wind speed variables on each of the bottom 6 model levels in the COSMO-REA6 dataset; representing altitudes of 0 to 200 m depending on the grid cell.

Vertical projection also differs when using MERRA versus COSMO. When using MERRA wind speeds, the adjusted values from the LRA spatial adjustment procedure are projected using the logarithmic wind profile described for Equation 3.4. Since stability conditions are not known, neutral stability conditions are assumed for lack of a better option. Furthermore, since the origin of wind speeds will always be 50 m and displacement height is typically negligible, Equation 3.4 will take the form given by Equation 3.10. Location-specific roughness values, z_o, are found by extracting the CLC land cover type, and matching it to the values suggested by Silva et al. [129]; provided in Appendix Table C.2. As mentioned previously, the COSMO dataset provides 4-dimensional wind speed values at non-uniform heights, allowing for wind speeds to be directly interpolated to nearly any altitude. Therefore, in a pre-processing stage, this interpolation is done component-wise to produce intermediate datasets containing net wind speeds at constant altitudes of 10, 50, 100, and 140 m. When simulating turbine placements, wind speed values at these altitudes are used to extrapolate to the relevant hub height.

$$v_{hub} = v_{ref} \cdot \frac{\ln\left(hub/z_o\right)}{\ln\left(50/z_o\right)} \tag{3.10}$$

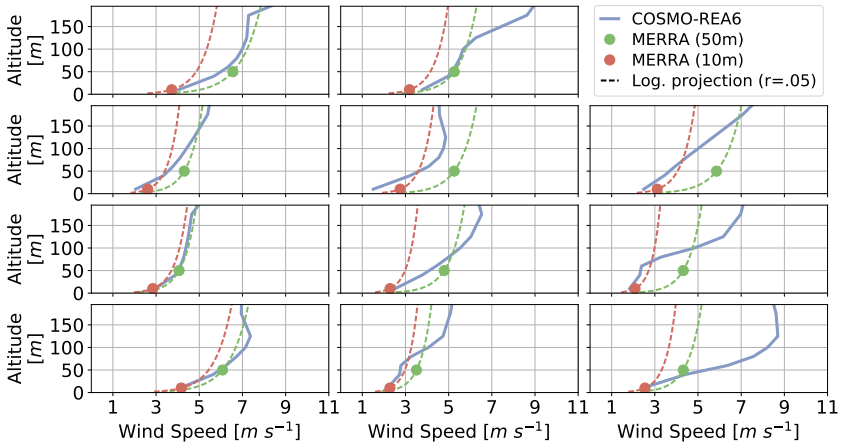

Figure 3.19: Vertical wind projection using MERRA versus COSMO-REA6 for arbitrary points in time in Denmark

It is not straight forward to predict how the use of the logarithmic wind profile for

[17] As in, much smaller differences than what is imposed later when accounting for power curve uncertainty

MERRA-derived wind speeds will impact the end result. To exemplify this point, Figure 3.19 displays a few instances of the vertical wind profile predicted by either dataset at a strong wind speed location in Denmark for arbitrary points in time. In these images, both the vertically-explicit trend from COSMO-REA6 is shown, and the corresponding 10 and 50 m wind speed estimates from MERRA, after applying the LRA adjustment, are indicated. Additionally, using the procedure detailed above, the estimated roughness length of 0.05 m is used to project the two MERRA wind speeds to other altitudes. As both of these sources represent estimations of the wind speed, neither can be necessarily considered as "the truth". Furthermore, these examples are not represent of all possible discrepancies between these two sources, since this is highly dependent on the location and weather state of the surrounding area. Nevertheless, these examples were specifically chosen to convey how the logarithmic wind profile can often represent wind shear in an approximate manner, especially when projecting from a higher altitude. However, these examples also show how the wind shear can, at times, be highly irregular leading to both over and under predictions of the high altitude wind speeds from the 50 m based logarithmic MERRA projections. The tendency of these over and under predictions are also clearly dependent on the height of the turbine in question. Therefore, at this stage of the thesis, it is not possible to tell how this issue will impact the resulting wind potentials throughout Europe, much less the occurrence of VRES lulls, and thus this is the main motivation for including a comparison between these two sources as a final sensitivity analysis.

In the final step of the wind speed adjustment phase, air density correction is applied. First an air density time series is computed for each simulation location using bilinearly interpolated near-surface pressure, P, and air temperature, T, values and applying Equation 3.2. As before, bilinear interpolation is chosen for both data sources over other options, such as cubic or spline interpolation, as it is more computationally efficient and resulted in only minor differences. Nevertheless, these subtle differences in air density due to interpolation method will not have a large impact on the resulting generation values. Once interpolated to the simulation location, this surface density is then projected to the turbine's hub height using the Barometric equation [111]. Finally, as suggested in IEC 61400-12 [199], wind speed correction factors are computed to a standard air density referenced wind speed (v_{std}) such that kinetic energy is maintained. Equation 3.11 contains these last two steps represented as a single equation; where $\rho(P,T)$ is the result of Equation 3.2[18], g represents gravitational acceleration, and M_a stands for the molar mass of dry air.

$$v_{std} = v \cdot \left[\frac{\rho(P,T)}{\rho_{std}} \cdot exp\left(\frac{-g\ M_a\ h_{hub}}{(R\ T)} \right) \right]^{1/3} \tag{3.11}$$

At the end of this step, density-corrected wind speed values have been generated that are localized to both the simulated turbine's location as well as its hub height.

[18] Relative humidity is assumed zero, since it is only impactful at high temperatures.

The next stage of the simulation scheme converts these wind speeds into electricity generation.

3.6.4 Generation Estimation

To predict a turbine's generation, the first operation is the creation of a synthetic power curve following the procedure detailed in Section 3.3. As described, this is ultimately a function of the simulated turbine's specific power.

Following this, before applying wind speeds to the power curve, the stochastic response of a turbine to wind speeds as discussed at the end of Section 3.1.3 needs to be accounted for. In addition to the issues brought up previously, such as reduced aerodynamic efficiency caused by turbulence, large wind speed gradients across the rotor blades, and short time-scale wind speed fluctuations, additional uncertainty is introduced from the wind speed extraction and adjustment procedures. On top of the uncertainty inherent to either the MERRA or COSMO-REA6 datasets [198], the spatial adjustment, altitude projection, and density correction methods detailed earlier are of course also imperfect and will introduce their own stochastic error when estimating the wind speed observed at the turbine. Quantifying the precise magnitude of these errors, however, would necessitate an in depth comparison of either procedure to measured wind speeds across the whole of Europe, which is far beyond the scope of this thesis. Therefore, in the end, all of these stochastic effects are treated as unpredictable fluctuations of a turbine's generation around the power curve estimate for any given wind speed. The approach used here follows the procedure described by Staffel and Pfenninger [17], where a Gaussian kernel is convoluted over a power curve. In effect, this procedure incorporates a spread of effective wind speeds around the estimated wind speed and averages the ideal power curve's responses, thus creating a 'smoothed' power curve. Equation 3.12 shows the general form of the standard deviation computation that defines the width of this kernel as a function wind speed (v). The constants $\sigma_{scaling}$ and σ_{base} were empirically determined by comparing simulation results against reported generation values for multiple wind parks and over multiple years. In the end, the values which were found to fit best were 0.1 for $\sigma_{scaling}$ and 0.06 for σ_{base}. Equation 3.13 details how this convolution is carried out, where $PC(v')$ refers to an input power curve's ideal capacity factor values over all possible wind speeds, v', and $PC_{conv}(v)$ is the resulting convoluted power curve.

$$\sigma(v) = \sigma_{scaling} \cdot v + \sigma_{base} \tag{3.12}$$

$$PC_{conv}(v) = \int_0^\infty \frac{1}{\sqrt{2\pi \cdot \sigma(v)}} \cdot exp\left(\frac{(v'-v)^2}{2\,\sigma(v)}\right) \cdot PC(v')dv' \tag{3.13}$$

Once the power curve is convoluted, the power output from a wind turbine is estimated by identifying the generation given by the new power curve in response to

the input wind speeds. Nevertheless, the theoretical power output of a wind turbine or a wind farm is different than the actual value because of losses such as turbine availability, electrical inefficiencies during transportation and conversion, wake effects and mechanical degradation. Quantifying each loss in detail with an accurate value is highly speculative, yet overall loss factors used in literature commonly vary between 5 to $20\,\%$ [17, 49, 200]. However, as previously discussed, convolution of the power curve already accounts for many stochastic effects which contribute heavily to these losses, so a holistic loss factor is not utilized in this work flow. Nevertheless, when compared against measured data, noticeable over-prediction of the generation was still observed mainly at low generation times. As a result, generation-dependent correction factors calculated using Equation 3.14 are used to specifically suppress the low generation periods. The shape of this correction factor is defined by two additional constants, $base$ and $sharpness$, that were empirically determined by comparing simulation estimates against measure values. The values found to produce the best results were 0.0 for $base$ and 5.0 for $sharpness$.

$$cF = (1 - base) * (1 - \exp(-sharpness \cdot capacity\ factor)) + base \tag{3.14}$$

Figure 3.20 shows the impact of including the convolution and low generation correction factors on an input power curve. Two areas of note should be pointed out: The first occurs between wind speeds above the cut-in and, for this particular power curve, until around $8\,\mathrm{m\,s^{-1}}$. In this area the generation is reduced significantly from the ideal generation and, since a large proportion of wind speeds will be found in this range (See Figure 3.2), will therefore greatly reduce the generation estimates. The second region worth discussing can be found around the cut-out wind speed, between 22 and $28\,\mathrm{m\,s^{-1}}$ which extends beyond the unconvoluted cut-off wind speed. In this area the original power curve's sharp cut-out is replaced with a more gradual fall off of generation. This can be thought of as a probabilistic likelihood that the effective wind speed is above the cut-out when the estimated wind speed is in this range, or vice-versa. Nevertheless, as sustained onshore wind speeds will very rarely be found at these speeds (See the Weibull distributions in Figure 3.2), then this will have a minor impact on the final wind generation estimates.

In the final step of the simulation scheme, the corrected capacity-factor values are multiplied by the simulated turbine's total capacity. This, then, completes the work flow of the wind simulation procedure. As a final note, when simulating multiple turbines at once, their generations are summed at each time step to form a single generation time series.

3.7 Simulation Validation

An in depth validation effort has been performed to ensure the accuracy of the developed model. These efforts focused on hourly comparison against measured generation data of two utility-scale wind parks, monthly comparison against tur-

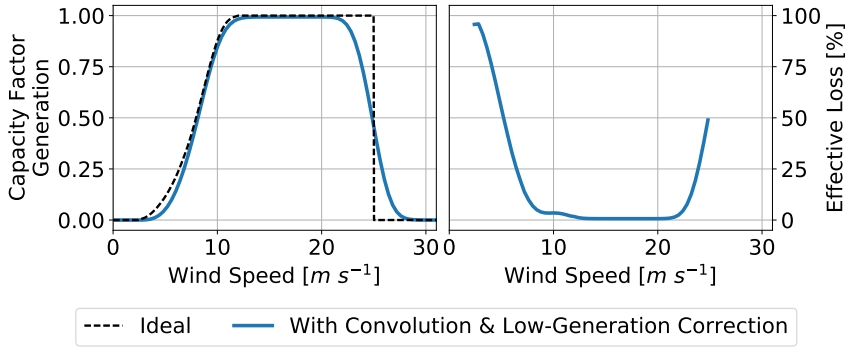

Figure 3.20: The effect of convolution and low generation correction for a typical power curve.

bines spread across Denmark, and finally a comparison against the annual German FLH estimated by several studies and reports. In all cases, these validation sources were chosen as they were the only ones available to the author during the time of the simulation scheme's development. In general it was seen that the model can reliably recreate measured generation reports at both the hourly scale as well as across a large region. The German comparison, in particular, suggests that the choice of turbine design made here will result in high FLHs compared to other studies but, more importantly, shows how these high FLHs are reached via a very reasonable progression of turbine design improvements. This result also clearly communicates the importance of using futuristic turbine designs when considering wind energy generation in future energy systems. Additionally, this latter comparison also showed that, when viewed from a comparable perspective, the current model is conservative compared to other models. The complete discussion is provided in Appendix D.2.

3.8 Wind Method Summary

This chapter has covered the background of wind energy and then discussed how this issue has been incorporated into the current thesis. All of these issue have been discussed as they ultimately relate to all three overarching research questions. The developed model stands out from past approaches seen in the literature by considering a detailed application of land eligibility and explicit turbine placement across Europe, location-specific turbine designs tailored to a 2050 context, automated generation of synthetic turbine power-curves, and the ability to perform full hourly simulation of each individual turbine over a 37 year time frame. In addition to the primary setup of the wind simulation scheme which has been described here, several sensitivity analysis have been promised which will be discussed in the later results sections; these include the sensitivity of total wind energy potential to the assumed distance between individual turbines, as well as the sensitivity to

using the COSMO-REA6 climate model dataset instead of the MERRA dataset.

In addition, portions of the wind energy related work conducted in this thesis have been peer-reviewed and published by the author in the journals *Renewable Energy* [108] and *Energy* [109]; some of which has been reiterated in this chapter as well as elsewhere in this thesis. Furthermore, studies conducted outside the context of this thesis have used the model developed here and are published or submitted to the journals *Energy* [184, 185], *Applied Energy* [102], and the *International Journal of Hydrogen Energy* [101].

Chapter 4

PV Energy

In the next chapter, the topic of solar PV simulations will be presented. Following the structure of Chapter 3, the discussions here will begin with an overview of the relevant background topics for PV, including: the dynamics which cause variability in the available solar irradiance, the physical mechanisms of a PV module as well as their typical configurations in the open-field and rooftop domains, trends seen in the PV industry, and finally the treatment of PV in the literature for studies with similar aspects to the current work. The goal of this introduction is not to provide a comprehensive overview of all PV related topics, but instead to introduce to the reader the main considerations that a European-wide PV simulation scheme should make, which considerations are important to PV in general but will require simplification, and finally how the resulting model compares against the work of other researchers. After the background discussion, the methods used in this work for simulating open-field and residential rooftop[1] PV will be provided. This will begin with the assumptions made for future module characteristics as well as system design, after which the PV-specific parameterizations of the land eligibility and placement algorithms are provided. The simulation scheme is discussed next, covering the extraction of weather parameters from a climate model source, the adjustment of irradiance values to a module's local context, estimating total irradiance on a tilted module's surface, and finally estimation of electricity generation. Finally, a note is given in regards to the PV simulation scheme's validity.

4.1 Background Principles

Ultimately, the Sun is responsible for all energy available on Earth, however it plays much more of a central role in the context of solar energy within the energy system. For reference, BP's estimate of the total global primary energy supply of $13{,}511\,\mathrm{Mtoe}$[2] in 2017 [9] constitutes only $0.0105\,\%$ of the total incident solar energy unto Earth over the course of a year; and thus it is quite apparent that an immense quantity of solar energy is available for energy generation. However, the amount of this energy which is accessible is subject to numerous dynamics of solar energy, which will be the subject of the following sections. As numerous accounts concerning solar energy are available in the literature, the only dynamics presented here will be those that are of the highest relevance to the current work as well as those which aid the discussion of later chapters. Key sources that inspired the formulation

[1] Commercial rooftop PV could not be considered in detail in this work due to lacking geospatial building data across the European scope.

[2] 157,133 TWh.

of this chapter are: Duffie and Beckman [201], Wenham et al. [202], Myers [203], and Santbergen [204].

4.1.1 Solar Energy Availability

Not all incident solar energy across Earth will be utilizable for electricity generation, and so it is important to determine how much is technically available. This section summarizes the notable sources of variability whose influences stack on top of one another to determine the final irradiance that can be harvested with a solar panel. These sources include the extraterrestrial variability in the incident irradiance onto the Earth, atmospheric path length, annual and daily periodicity, and the impact of PV module orientation. Additionally, as solar irradiance modeling is an imprecise science [201, 205], common methods to predict irradiance components will be introduced. Most of these variability sources have a spatial sensitivity and so, at last, an estimate of average annual irradiace on an optimally-oriented module derived in the literature [206] is provided.

The first variability source is the available extraterrestrial irradiance, the solar energy flux found at the top of the atmosphere (TOA). From the Sun itself, solar radiation is seen to vary cyclically over an 11 year period by $0.1\,\%$, and over a $27\,\mathrm{day}$ period by $0.2\,\%$ due to solar rotation [207]. Intense solar flares can also increase solar radiation by up to $0.015\,\%$. Much more importantly, however, the Earth's orbit around the Sun is slightly elliptical. Therefore, since solar radiation is proportional to the solar distance squared, the aphelion irradiance is $7.0\,\%$ less than the perihelion irradiance [208]. On average the TOA irradiance is estimated at $1367\,\mathrm{W\,m^2}$, and is known as the Solar Constant (G_{sc}) [209, 210]. This variability will be implicitly incorporated into the PV simulation scheme by the use of climate model weather dataset which have already incorporated the solar distance into their irradiance estimations.

The next variability source is a result of irradiance's path through the atmosphere, which ultimately reduces the collimated TOA irradiance to ground-level diffuse and direct components. In a typical scenario, the atmosphere only permits $55\,\%$ of the TOA irradiance to reach the earth's surface while $26\,\%$ is scattered or reflected back into space and $19\,\%$ is absorbed via thermalization [211]. Unless captured, $4\,\%$ is also reflected back into space from the ground [211]. Moreover, the specific impact of this journey can be seen in Figure 4.1, where the TOA irradiance spectrum, which is similar to that of a black body radiator at $5523\,\mathrm{K}$, is reduced to a much more complicated spectrum at sea level. This spectrum change is due to the absorption bands of the various atmospheric species; primarily molecular oxygen, ozone, water, and carbon dioxide [203]. In summary, this attenuation is exponentially related to the light's path length through the atmosphere and can be modeled with the Beer-Lambert law [212]. As a result, the attenuating effects of the atmosphere change in accordance with geospatial location, elevation, and solar orientation. This attenuation can also be affected by changes in atmospheric composition such as increased carbon dioxide or other pollutants [213–215]. To simplify the discussion of atmospheric absorption in the atmosphere, the airmass (AM) terminology is commonly

used in the community. AM0 refers to a zero-length path through the atmosphere, and so the AM0 spectrum is equal to that of the TOA irradiance shown in Figure 4.1. AM1 refers to a direct downward path through the atmosphere ending at sea level, and thus refers to the expected spectrum on a clear day at the beach with the Sun directly overhead. AM1.5, where '1.5' refers to the relative increase in optical path verses AM1, is commonly used as a reference spectrum spectrum as the extra path length is typical for latitudes in the range of $33°$ to $46°$ [216]. In the general sense, the attenuated portion of the TOA irradiance which reaches the surface unimpeded by the atmosphere is referred to as the direct irradiance.

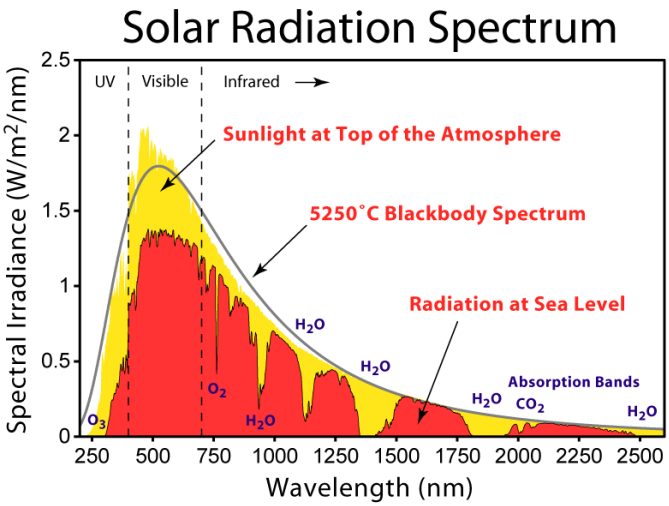

Figure 4.1: Solar spectrum at the TOA, sea level, and versus an idealized black body. Image retrieved from [217]

Yet absorption is not the only process by which the atmosphere alters incoming radiation. Reflectance off clouds and other particulates is a key factor determining how much irradiance reaches the surface, and cloud reflectivity can range from 40 to $90\,\%$ [211]. Rayleigh scattering can also occur, which has a tendency to scatter low wavelength photons (blue) at extreme angles than high wavelength photons (red) [212]; leading to both the blue day-time sky as well as the redish hue of the twilight horizon. Ultimately these dynamics create the diffuse irradiation seen at the surface, which can be thought of as an ensemble of random-walk paths occurring throughout the atmosphere that all happen to converge on a single location. Due to the differing path lengths through the atmosphere, as well as the wavelength dependence of Rayleigh scattering, the spectrum of diffuse irradiation has a higher proportion of visible-range photons than direct irradiation [218]. In the simulation scheme used here, some climate model datasets specify a direct and diffuse irradiance component at the surface, while others provide only the total irradiance. Therefore, in the latter case, irradiance decomposition models will need to be used to distinguish between these components for each location and at each time step.

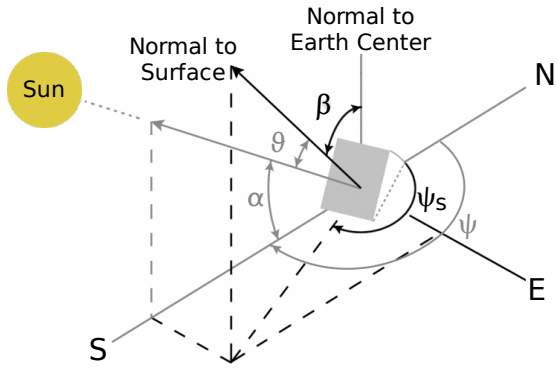

Figure 4.2: Visual reference of solar-relevant angles. Adapted from [219].

The next variability source of note is the temporally-explicit solar position. Due to to Earths 24 h day-night cycle, annual orbit, axial tilt of 23.45°, and its nearly spherical shape, determining the direct and diffuse irradiance at an arbitrary point on its surface is not a trivial task. Nevertheless, proper treatment of these issues is core to understanding the role of solar energy in the energy system. To introduce this issue further, the terminology given in Table 4.1 is provided will be used from this point forward; Figure 4.2 serves as a visual aid.

With these quantities, it is possible to compute the solar position relative to any geospatial location and at any time via trigonometric analysis [203]. The relevant steps of this will be returned to in the latter presentation of the simulation methodology. In summary, however, solving for these trigonometric equations in the context of a single location leads to an annually-repeating time-series for both the solar elevation angle and the solar azimuth. Figure 4.3 provides a chart showing the outcome of this if it were to be performed for Aachen, Germany. At this location the elevation angle reaches its maximum of 63° in the summer and, on December 21st, the Sun is only over the horizon for a period of 8 hours. Without accounting for the slight changes caused by elevation, co-latitudinal locations with Aachen will share similar solar position trajectories[3]. Meanwhile, locations south of Aachen will observe a larger maximum elevation angle in the summer and a longer minimum day span in the winter, and vice versa. Furthermore, beginning at around 68° latitude the minimum winter day span reaches zero; meaning that, at locations north of these latitudes, the Sun never rises for at least one day in the year. In order to estimate the direct and diffuse irradiance components, and furthermore for reasons introduced with the next section on variability due to orientation, the explicit solar position will be computed with respect each individual simulation location and at each time step.

Besides the variability of solar position, another important issue to consider is a PV

[3] Although offset in time due to differing longitude.

Table 4.1: Solar angle variables. See Figure 4.2 for a visual reference.

Name	Symbol	Description
ϕ	Latitude	The location's latitude
δ	Declination Angle	Angle between the Sun and the equatorial plane
ω	Hour Angle	Non-physical angle representing the time of day relative to solar noon
α	Elevation Angle	Angle between the Sun and the horizon
z	Zenith Angle	The angle between the solar vector and the vertical $(90 - \alpha)$
ψ	Solar Azimuth	Azimuth angle of the Sun's position ($180°$='south')
ψ_s	Surface Azimuth	Azimuth angle of collector surface's normal vector ($180°$='south')
β	Surface Tilt	Tilt angle of collector surface's normal vector relative to the vertical
θ	Incidence Angle	Incident angle between the collector's normal vector and the solar vector
GHI	Global Horizontal Irradiance	The total irradiance on a flat plane, given in $\mathrm{W\,m{-}2}$
DHI	Diffuse Horizontal Irradiance	The total diffuse irradiance on a flat plane, given in $\mathrm{W\,m{-}2}$
DNI	Direct Normal Irradiance	The total direct irradiance on a plane normal to the Sun, given in $\mathrm{W\,m{-}2}$
POA	Plane of Array	The total irradiance on an arbitrarily oriented plane, given in $\mathrm{W\,m{-}2}$

module's orientation. For obvious reasons, the orientation at which a PV module is installed will directly impact how much irradiance it will receive. With a clear view of the sky, the best surface azimuth angle would be pointed south in the northern hemisphere and vice-versa in the southern hemisphere [201, 203]. Optimal surface tilt, however, is highly dependent on the typical site-specific weather conditions, but can be determined empirically via a transposition factor analysis [220, 221]. When both the solar position and surface orientation are known, then the direct component of the POA irradiance can, again, be computed via trigonometric analysis [203]. In comparison, conventional methods to compute the diffuse POA irradiance component are inexact [205, 222, 223]. A multitude of independently derived and validated models exist in the literature for this purpose, and the choice of which one to use should be used depends on the availability of measured ir-

radiance data. For the situations encountered later in this work, where only GHI or else both GHI and DNI are known, the relevant methods are as follows. DHI can be estimated from GHI by means of empirical relationships dependent on atmospheric clearness, airmass, and water content [224, 225]. Following this, when DNI is not known, it can be estimated according to the trigonometric relationship $GHI = DNI * cos(z) + DHI$ [203]. Next, a library of transposition models exist which use GHI, DNI, and DHI in addition to the solar position to estimate the sky-diffuse[4] POA irradiance component. The transposition model developed by Perez et al. [226, 227] will be used later in this work as it is often found to perform slightly better than the other options [223]. At last, the ground-diffuse POA irradiance originating from surface reflections can be estimated by making an assumption of the surface reflectivity, known as the albedo [205]. In the end the direct, sky-diffuse, and ground-diffuse components are summed together to constitute the total POA irradiance. Overall, uncertainty when using these POA estimation approaches depends heavily on the region and weather conditions, although errors are often reported in the range of 10 to 20 % [227] In the latter PV simulation scheme, both the direct and diffuse components of the POA irradiance will need to be computed for each location and at each time step.

Ultimately, all of the dynamics mentioned throughout this section serve to impact the amount of solar irradiance which will be available for an arbitrarily-oriented PV module somewhere on the Earth's surface. It is clear that these fluctuations are primarily dependent on time of year, time of day, latitude, weather conditions, and the collector's orientation. With all of these dynamics combined, Figure 4.4 displays the average irradiance received for the European region on an optimally-oriented surface [206].

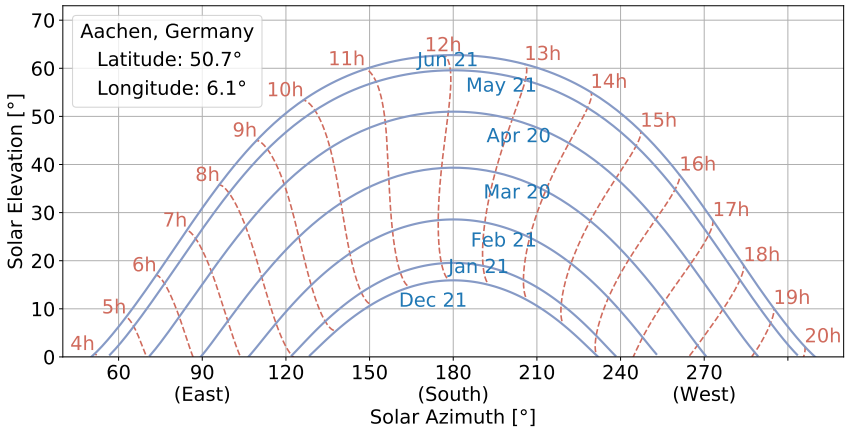

Figure 4.3: Annual variance of solar elevation and azimuth in Aachen, Germany.

[4] As in, the diffuse irradiance originating from the sky

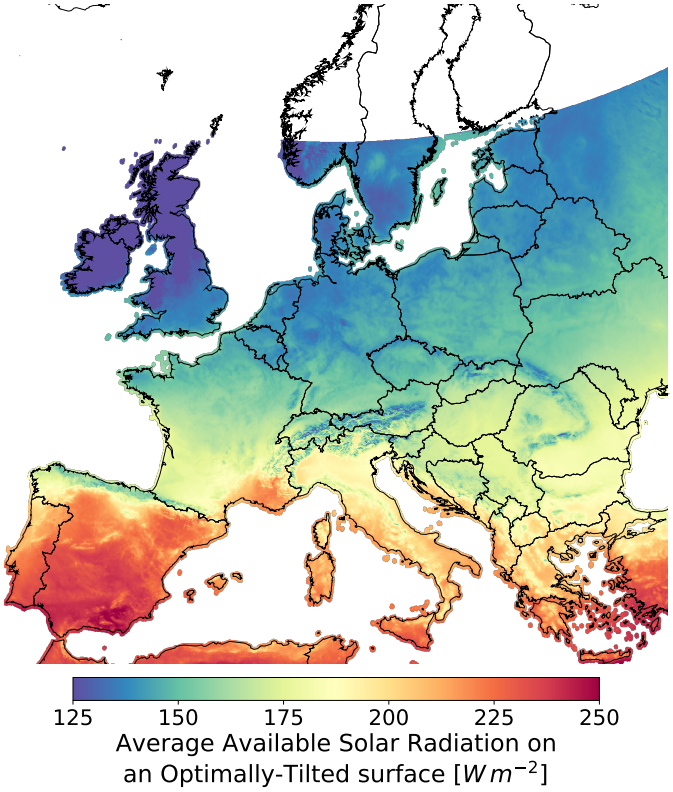

Figure 4.4: Average irradiation across Europe (data from [206])

4.1.2 Photovoltaic Solar Cells

After finding the available irradiance, the module must in some way harness that solar energy. Thus, this section introduces the reader to the basic operating principals of PV modules and points out how these concepts are incorporated into the latter simulation scheme. Although, as mentioned in the introduction to this section, the discussion here is not intended to provide a comprehensive overview of PV module design and operation. For such discussions, the reader is referred to the following sources [201–204, 228, 229]. The topics discussed here will include the basic configuration of a PV cell, the photovoltaic effect, differences between cell chemistries, mathematical representation, overall cell efficiency, and finally an account of common losses.

Figure 4.5 displays the typical configuration of a crystalline silicon PV cell, from which it is apparent that a P-N semiconductor junction lies at the heart of PV operation. This type of junction, referred to as a diode, is extremely well known and their use has become prominent within several industrial sectors [228, 229]. In short, the interface between the P-type and N-type semiconductor materials generates an electric field in the interface of the two semiconductors, called a space charge re-

gion. A PV cell begins with the typical diode configuration, and combines it with the photovoltaic effect.

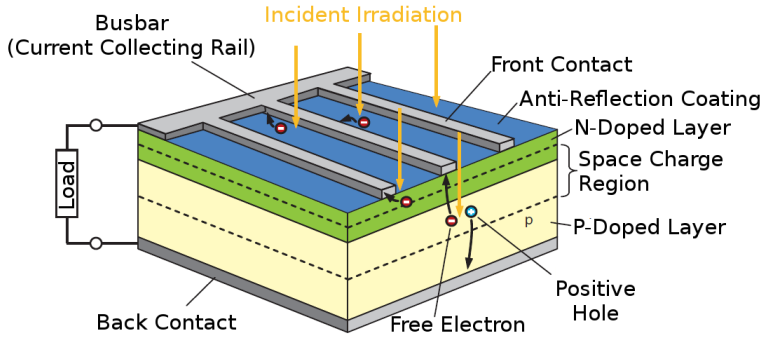

Figure 4.5: Configuration of a typical crystalline silicon PV cell. Adapted from [228].

The photovoltaic effect is a quantum process related to the allowable energies electrons can possess within a material. For non-conductive materials, the valance band[5] and the conductive band[6] are separate from one another by the so-called band gap; a span of electron energies that are forbidden within the material. In semiconductor materials, the band gap is small enough that visible-range photons have enough energy to excite an electron from the valence to the conductive band, and this event is referred to as the photovoltaic effect. Notice that a wide range of photon energies can perform this excitation and, when an electron is excited above the minimum allowed in the conductive band, it will typically diffuse the excess energy via thermalization [201]. Since crystalline silicon (c-Si) is a semiconductor with a band gap of $1.1\,\mathrm{eV}$, it is particularly well suited to absorb photons within the visible range [204]. In any case, when a PV cell is exposed to solar radiation there is a chance that a photovoltaic event will occur within the space charge region. When this happens, the free electron is separated from it's positive hole by the P-N junction's electric field, and the new charge imbalance can then be put to work.

While the photovoltaic effect is common to all PV module types, the precise behavior of a PV cell depends on the cell's chemistry. Multi-crystalline silicon (mc-Si), for instance, make use of an inhomogeneous crystalline silicon structure, and so are slightly less efficient than c-Si while being cheaper to produce [230]. In the PV industry, these c-SI and mc-SI account for nearly $95\,\%$ of new PV cells, and this trend is currently increasing [11, 158, 231]. Other chemistries include cadmium telluride (CdTe), copper indium gallium selenide (CIGS), and gallium arsenide (GaAs); which all fall into the 'thin-film' group on account of the deposition-based manufacturing process [232]. Some emerging cell chemistries include organic solar cells (OSC), dye-sensitive solar cells, and perovskite solar cells; all of which represent a plethora of cell configurations [233]. An important way in which PV cell chemistries differ

[5] Low energy states where electrons are trapped by the nuclear forces of a single molecule.
[6] High energy states where electrons are free to move around the material.

from each other is in their photovoltaic response to different wavelengths of light as a result of their differing band gaps. Figure 4.6 shows how most of the chemistries mentioned here are ideally expected to respond to different wavelengths of light. Since shifts in the solar irradiance spectrum are expected to alter the response of a PV module by around $5\,\%$ [218, 234–236], an ideal PV simulation scheme should consider this wavelength dependent response in detail. However, if explicit wavelength dependence were to be incorporated, it would come at an extremely high computational cost. King et al. [237] describe an empirical method to estimate a module's spectral response as a polynomial function of airmass, however the polynomial constants must be measured independently for each commercial module meaning that these factors are not available for most modules. Therefore all simulations performed in this work will assume an AM1.5 spectrum since uncertainties in this regard are small in comparison to the POA irradiance estimation procedures discussed previously, and thus are not expected to have a large influence on the final simulation results. Unfortunately, this also means that the spectral response differences between PV cell chemistries will not be resolvable. To note, other differences between chemistries, such as response to cell temperature, are included in the latter simulation scheme.

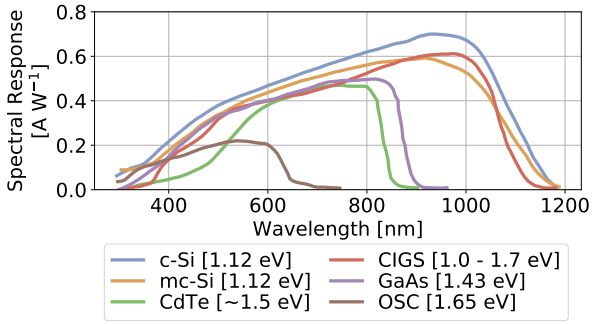

Figure 4.6: Spectral response of common PV cell chemistries (data from [238])

In order to mathematically represent the electricity generation of a PV cell in response to irradiation, a quasi-physical model can be used which represents the call as a light-current source in parallel with a single diode and shunt resistance in addition to a series resistance connected to the circuit's output [229, 239]. Equation 4.1 shows this equation, with Figure 4.7 as reference, where I_L is the current generated by incident light, I_0 is the diode's reverse saturation current, R_s is the series resistance, R_{sh} is the shunt resistance, k is the Boltzmann constant, q is the charge of an electron, and finally T_c is the cell temperature.

$$I = I_L - I_0 \left[exp\left(\frac{q(V + I \cdot R_s)}{n \cdot k \cdot T_c} \right) - 1 \right] - \frac{V + I \cdot R_s}{R_{sh}} \tag{4.1}$$

This equation results in a coupled relationship between the output current and the

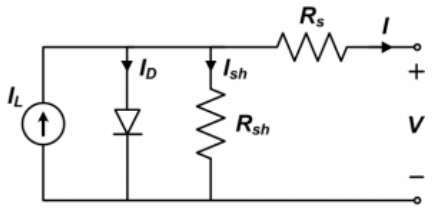

Figure 4.7: Single diode-equivalent circuit for a PV cell. Image adapted from [240].

output voltage, shown in Figure 4.8, which will vary depending on the load which completes the circuit. Additionally, it is also seen in Equation 4.1 that the response of a PV module is a function of the cell's temperature. Since cell temperature is computed according to a thermal balance between ambient temperature, irradiance, conduction, and convection, this means that Equation 4.1 is fundamentally also a function of air temperature, air pressure, and wind speed [241, 242]. Moreover, the manner by which a cell is encased, either with a glass or polymer backing, and the way it is mounted, either free standing or set closely to another surface such as a roof, will also impact heat dissipation and therefore performance [237]. For one exemplary c-Si PV cell, Tobnaghi et al. [243] discuss how the output power of a PV cell can be reduced by around 6 to 10 % as a result of a cell temperature difference of 10 °C. They then showed how this is primarily due to a drop in the cell's open circuit voltage. In order to compute cell temperatures in response to these variables, the cell temperature model developed by King et al. [237] will be employed in the latter simulation scheme.

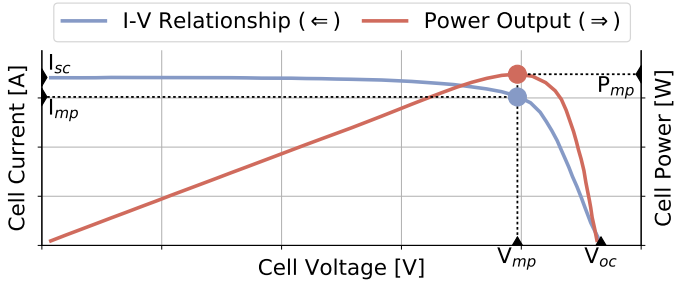

Figure 4.8: Example I-V curve and output power of a PV module

Determining the various quantities for equation 4.1 is not a simple task, however. De Soto [236] developed a procedure called the 5-Parameter Model which can estimate all unknown quantities in Equation 4.1 based off measured module behavior under standard test conditions (STC); cell temperature of 25 °C, irradiance of 1000 W m^{-2}, and an AM1.5 spectrum [218]. For the last two decades, a repository of performance measurements on commercially-available modules [244, 245] has

been compiled according to IEC-standardization [246, 247] which can be used in De Soto's model. Another approach, called the Sandia Array Performance Model (SAPM) [237], solves for I and V in Figure 4.7 by determining empirical relationships derived from cell measurements performed exactly for use in this model [248]. SAPM is easier to use and is more computationally efficient than the 5-Parameter model, however the SAPM database is far less up-to-date compared to that which is available for the 5-Parameter model. Nevertheless, each of these approaches depends on the total POA irradiance received by the cell, the cell temperature, and module characteristics. When applied to the same module configuration and under the same weather conditions, they give nearly identical results [249]. Therefore, the later simulation scheme will make use of the 5-Parameter Model on account of its more up-to-date module dataset and its more fundamental basis.

Figure 4.8 shows how different combinations of output current and voltage are possible, however only one combination gives the maximum power, P_{mp}. Always ensuring that a module is operating at the maximum power point, known as maximum power point tracking (MPPT), is a significant challenge that represents a real-world loss of power if not properly controlled. Therefore, although the overall efficiency of a PV cell is described as the ratio between the modules P_{mp} at STC to the total power of $1000\,\mathrm{W\,m^{-2}}$, this does not mean that the module is always operating at this efficiency. A well-known theoretical boundary of PV cell efficiency is that of the Shockley-Queisser limit originally set at $30\,\%$ [250], and later updated to $33.77\,\%$ when taking into account different cell configurations and an AM1.5 spectrum [251]. For c-Si and mc-SI cells, however, this limit may only be $29.4\,\%$ on account of silicon's imperfect band gap [252]. Exceeding this limit is possible via a more complicated multijunction PV cell structure, which uses multiple semiconductor layers that each have their own band gap and spectral response [253]. These layers can be carefully chosen to compliment one another and in effect greatly improve overall cell efficiency to a theoretical limit above $50\,\%$ [254, 255]. An important consideration for the PV simulation scheme used later in this work will be to predict the progression of future cell efficiencies; this issue will be returned to after discussing current trends in the PV industry in Section 4.1.4.

In reality, multiple dynamics serve to reduce the ideal cell efficiency, many of which depend strongly on the conditions the cell operates in. Since PV cells are housed in a rigid translucent material, most often glass, the reflectivity of the housing's external and internal interfaces can play a large role in reducing the irradiance received by the cell. Special coatings have been developed to reduce these reflections, and special texturing of the internal glass-semiconductor interface has been shown to greatly improve photon absorption [256]. Nevertheless, no coating is perfect and the chance for reflection is dependent on a light ray's angle of incidence [236, 257]. For direct radiation this loss can be estimated using Fresnel's law [203] and, for diffuse irradiation, an effective angle of incidence can suffice when given as a function of the cell's tilt angle [258]. Using these two approaches along with conventional coating and texturing performance [256], angle of incidence losses will be explicitly incorporated into the later PV simulation scheme. Ideally other loss sources should also be considered in detail, including shading

of the cell from nearby obstructions [259, 260], soiling of the cell by airborne particulates [261], snow coverage [262], recombination losses [233], power mismatch losses [263–265], and general electrical interconnect losses [266]. Nevertheless, performing location-specific estimations of these losses would require computationally expensive three-dimensional and state-based representations of each location, which are not feasible to apply across the European scope. As discussed in the various sources provided for each example, the impact of these losses over the course of a year are generally small, but nevertheless depend on location and the specifics of each installation site. Therefore, a holistic loss factor will need to be decided upon in the final PV simulation scheme to account for the general impact of these issues.

4.1.3 PV System Configuration

In the next section, the common configuration of PV systems will be discussed. This discussion will introduce the arrangement of PV systems from individual PV cells, and will mention how this is incorporated into the latter simulation scheme. In addition to this, this section will introduce how PV systems tend to differ according to the open-field or rooftop domains.

A PV system consists of one or more PV arrays, which themselves consist of multiple modules, which further consist of multiple PV cells (Figure 4.9). Although any electrical configuration of cells, modules, or arrays is possible, in general PV systems are configured according to a few conventions. Within modules, individual cells are arranged in series, but with a parallel bypass diode wired across every one or two dozen cells [202]. The configuration of these bypass diodes within a PV module are important as they determine the module's ability to cope with partial shading conditions [202]; however this dynamic will not be incorporated into the latter simulation scheme. In conventional system designs, modules are arranged into strings connected to a large string inverter which performs MPPT on a collective basis, and multiple strings are arranged into an array [267]. A more recent trend, however, is to provide each PV module with its own micro-inverter which has the advantage of performing MPPT on a per-module basis [267–270]. Despite coming at a higher cost, the use of micro-inverters over string inverters can reduce mismatch losses and are particularly well suited to complex rooftop configurations. In both cases, direct current (DC) to alternating current (AC) conversion is a highly efficient process typically seen around $98\,\%$ [202, 203]. Due to the extreme variety by which PV modules and larger PV systems can be arranged, along with the high efficiency of DC to AC conversion when properly implemented, the later PV simulation scheme will simulate the performance of a single PV cell and the resulting generation will be scaled in accordance with the capacity of the total system. Real world losses resulting from power conversion, including inverter inefficiency as well as the effect of AC clipping due to the optimal loading ratio [271], are therefore grouped together in the previously mentioned holistic losses. Especially in comparison to other losses, this simplification is not expected to have a significant impact on the resulting PV potential estimations made in this work.

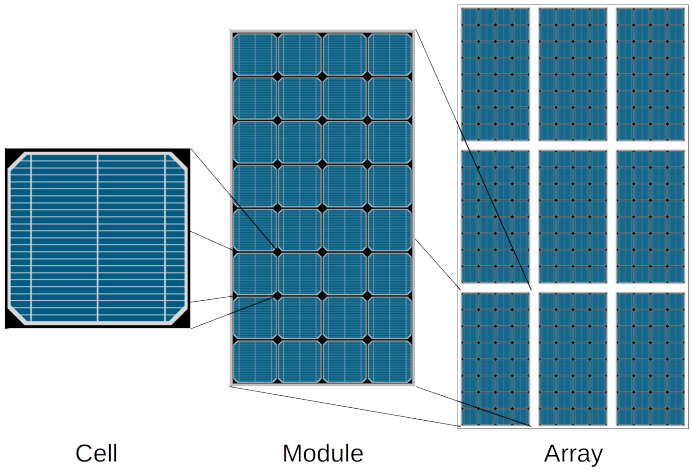

Figure 4.9: Example arrangement of PV cells in to PV arrays.

In the open-field domain, PV arrays are often organized into PV farms and operate at the utility scale. Since the construction of PV farms typically also mean the construction of support facilities, including buildings, roads, and fences, these farms can take up large land areas. Therefore, the most suitable location for construction of PV farms are flat brush lands that are distant from protected areas and settlements [272]. Furthermore, while installations of PV farms have been seen in agricultural zones, the potential conflict between these two resources is nevertheless of high concern [273–275]. Experimental solutions to this issue allowing co-use of agricultural areas, such as Fraunhofer's sparse-elevated-arrays [276], represent on-going research projects but are far from mainstream and so are not considered in this work. On average a conventional PV farm can be around 50 to 60 MW in capacity, however the smallest PV farms can have a capacity below 20 MW and the largest farms can extend beyond 700 MW [277]. Different tracking systems are also available for open-field farms. For these tracking installations, servos are built into the PV mounting structure that can be used to manipulate the panel's orientation in order to keep the module pointed towards the sun[7]. This can be either passively or actively controlled, and can incorporate one or two degrees of freedom [278]. For clarity, systems with no tracking capabilities will be referred to as fixed-tilt system. A significant difference between the generation profile of fixed-tilt versus tracking systems can be expected, especially in the early mornings and late evenings [279, 280], however the difference between single and dual-axis tracking is far less pronounced [281–283]. Therefore, in the latter evaluation of this work, a decision of which tracking type should be employed at each simulation location will need to be made.

In order to avoid self-shading of the PV modules in the farm, when one row of mod-

[7] Thus reducing the impact of angle of incidence losses

ules causes shading on the row behind it, tracking systems are typically spaced farther apart from each other than fixed-tilt systems, resulting in different packing factors [284]. Fixed tilt systems typically have a packing factor between 31 and 92 %, with an average of 47 %, which can be thought of as the ground coverage ratio of active module area to direct land area. Single-axis tracking systems generally fall between 20 and 51 %, with an average of 34 %, while double-axis tracking systems are generally around 25 % [277]. Therefore, in addition to costing more on account of the tracking motors and controllers, tracking systems also typically require a larger land area than fixed-tilt systems for the same capacity. Due to this spacing between panels, open-field PV farms[8] can require a direct land area equal to 24 to 33 $m^2\,kWp^{-1}$. Since module efficiency improvements also increase capacity without increasing the size of a module, land coverage factor will decrease for future module designs [285]. For farms larger than 20 MW, the additional need for access roads, fences, and other ancillary structures typically increases this land usage by between 10 and 30 % [277]. In the later evaluation of this work the available capacity of each park will be estimated using these packing factors in combination with the future-oriented module efficiencies.

Compared to open-field PV, two types of rooftop systems can be identified: residential and commercial. Residential systems are those installed on homes and primarily serve to offset local electricity usage. Depending on the area, these systems are generally mounted in-plane with the roofs they are connected to, and as such are often sub-optimally oriented. Furthermore, residential systems are typically in the range of 2 to 10 kW [286–288]. Commercial rooftop systems are those which are installed on large commercial or industrial buildings and, since they are generally installed on flat roof areas, they are free to choose the best orientation. Their size is directly proportional to the amount of rooftop area which their purchasers would like to use, and so a wide range of such systems exist; most of which are between 10 and 100 kW [286,287]. The rate at which rooftop PV systems are installed, particularly residential systems, is highly dependent on multiple sociotechnical variables [289]; generally in response to the solar resource, institutional incentives, electricity price, social attitude, and rooftop orientation. Due primarily to data availability limitations which will be discussed in more detail in the upcoming paragraphs, this work will focus on the residential rooftop PV domain rather than commercial.

Rooftop PV has several additional considerations compared to open-field PV which will need to be kept in mind. For one, while the potential of open-field PV is directly related to the available land, rooftop PV potential is related to the available rooftop area. On the scale of cities and small regions, explicit investigations of total rooftop area can be performed with a combination of satellite imagery data and light detection and ranging (LIDAR) data [290, 291]. However, as these types of approaches require extremely detailed[9] topographic data which, to the author's knowledge, simply does not exist across the entire European scope, this level of detail is not suitable for the current analysis. Similarly, neither building footprint data, such as those

[8] With a typical module efficiency of 11.7 % [277]

[9] On the order of 1 m resolution.

offered for select urban areas by state and national organizations or from publicly collected data such as the OpenStreetMap [97], offer complete European coverage and typically do not include roof orientation information. In comparison, other rooftop area estimation methods rely on empirically derived relationships between geospatial indicators and observed rooftop area. An example of this has been derived by the IEA [292], where nearly 1600 cities across the globe[10] were considered and a function for estimating PV-suitable rooftop area depending on population density was derived. After this, and especially for the case of residential rooftop, another key aspect is the consideration of rooftop orientations, which will depend on the region of study [293]. Considering over 30,000 reported rooftop PV installations in, primarily, the United Kingdom, France, and Belgium, Leloux et al. [288] report that most residential roofs have a tilt between 20 and 50° with a mean around 33°. In regards to azimuth, they find a slight tendency for roofs to be oriented between a south-east and south-west orientation, but nevertheless find that all azimuth orientations are present. For the state of Baden-Württemberg in Germany, Mainzer et al. [290] find that residential rooftop tilt angles have a Gaussian distribution centered around 35° with a standard deviation of 15°, and for azimuth they also find a full representation of azimuths with a slight preference towards roofs oriented east-to-west or north-to-south. Finally, for select urban areas in Spain and Italy, Ullah [294] and Bergamasco et al. [295], respectively, also observe a wide spread of rooftop azimuths, but report tilt angles more in the range of 20°.

To the author's knowledge there is no data source which allows for an explicit and comprehensive investigation of rooftop area, tilts, and azimuths across the whole of Europe for both the residential and commercial rooftop domains, nor is there a report claiming to have performed such an evaluation. Therefore, the empirical approach from the IEA will be used to estimate available residential rooftop area and, for orientation, a general distribution assumption will need to be decided upon based off the values seen in the literature. However, as the IEA's relationship is defined as a function of population density, it cannot be applied to the commercial rooftop PV domain; hence why the current work focuses on the residential rooftop PV domain. Nevertheless, it is worth noting that the freely-orientable quality of commercial rooftop PV means that the optimal tilt and azimuth can be selected and, as a result, the generation profile will be close to that of open-field PV while installation costs will be closer to that of residential rooftop PV [160]. Therefore, commercial rooftop PV LCOE should always be found between open-field PV LCOE and residential rooftop PV LCOE for a common area. Additionally, judging from Figure 4.10, it is quite clear that there is no common national theme in regards to the share between open-field and rooftop PV [12]. Therefore, this thesis' focus on the residential rooftop and open-field PV domains should already cover the dominant operational boundaries of PV generation, and thus a detailed consideration of commercial rooftop PV would not have a large impact on the combined generation profiles or LCOE estimates.

[10] A large portion of which are found in Germany

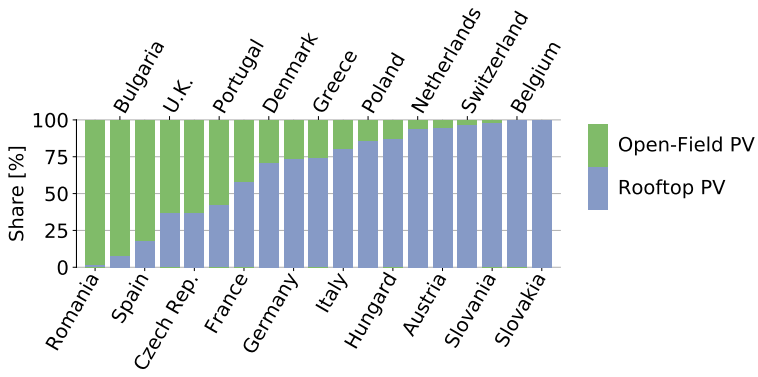

Figure 4.10: Shares between open-field versus rooftop PV in 2017 for European countries (data from [12]).

4.1.4 Trends in the PV Industry

The following section touches briefly on the trends seen in the PV industry which relate to the analyses performed in this work. Discussion here will begin with a presentation of recent PV installation trends and their rough projection into the future, followed by an overview of the improving performance of PV systems in terms of efficiency and FLH. At last, trends in regards to PV system installation costs and expected future LCOE are given.

Installation trends

Throughout the world total PV capacity grew by 99.1 GW in 2017 to reach a total of 404.5 GW [8, 12, 158]; continuing a roughly 30 % annual growth since 2015. 2017 was significant, however, in that more PV generation capacity was installed globally than any other electricity generation technology. Wind energy, with the second largest only constituted 53 % of PV's growth. China installed more than half of this new capacity (51.9 GW), followed by the US (10.6 GW), Turkey 2.6 GW, and Germany 1.7 GW [8, 158]. According to future projections, total PV capacity is expected to surpass 1 TW sometime around 2022 [12]. As seen in Figure 4.11, new PV installations in Europe for 2017 at 9.2 GW was an improvement over 2016, but still less than half of the peak in 2011. Of this total, the European Union added 5.89 GW. Within Europe's current sum of 113 GW, Germany maintains the top position with 43.0 GW, followed by Italy's 19.4 GW, the UK's 12.7 GW, France's 8.0 GW, and Spain's 5.6 GW.

Into the far future there is much speculation about how much PV capacity will be installed. As an example, the EU's E-Highway project [296] constructed 5 scenarios of future European electricity demand and generation capacity in the context of 2050 that each follow different sociotechnical trajectories, but which all satisfy

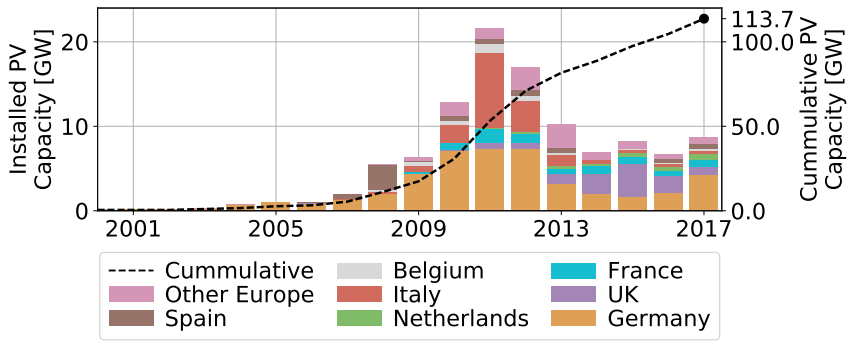

Figure 4.11: New PV capacity by country, and total European capacity (data from [12]).

an 80 % emission reduction target. Since these scenarios were developed from a consortium of research institutes across Europe, and additionally incorporated the feedback of stakeholders such as transmission system operators at several different stages, these scenarios are singled out here as they likely reflect a good estimate of the range of future PV capacity. In the "Fossil & Nuclear" scenario, where fossil fuels and nuclear energy are still heavily used, the total PV capacity in Europe reaches 190 GW; where the largest contributors are Germany (51.7 GW), Spain (35.8 GW), and Italy (28.3 GW). In the "100% RES", the scenario with the highest PV share, the total PV potential is set at 662 GW. Once again, the highest contributors are France (103.1 GW), Germany (98.6 GW), Spain (91.9 GW), and Italy (91.4 GW). In order to reach their targets within this latter scenario, Germany would need to install on average 1.79 GW of new PV per year; just shy of the installed capacity in 2017. France, meanwhile, would need to install 3.07 GW per year; far above their new 2017 capacity of only 873 MW [12].

Performance Trends

NREL annually publishes a trend of cell efficiencies measured in lab conditions, showing a wide range of 'record' PV cell efficiencies [297]. At the time of this writing, the current record for c-Si cells is 26.1 %, while ms-Si cells currently top out at 22.3 %. Without the use of a concentrator, the most efficient single-material cell is a thin-film GaAs cell with an efficiency of 28.9 %. Considering multijunction PV cell structures, NREL's efficiency trend [297] reports the highest non-concentrated efficiency at 39.2 %. For comparison, in 2010, the record efficiencies of c-Si and mc-Si cells were seen at 24.8 % and 20.7 %, respectively. Between 2010 and 2018, the largest increases in cell efficiency were seen in quantum dot cells (3.0 to 16.6 %) and Perovskite cells (14.1 to 23.7 %). Finally, the combination of Perovskite with typical c-Si cells has been shown to increase efficiency to 28 % [297]. Of course, as shown in Figure 4.12, these record cell efficiencies are significantly higher than the reported efficiencies of commercial PV modules [244]. In this figure, the average,

99th percentile, and 1st percentile of introduced PV modules in each half year are shown between 2008 and the beginning of 2017. Furthermore this trend is shown explicitly for c-Si and mc-Si based modules and collectively for thin-film modules, but do not show multijunction, quantum dot, organic, or perovskite trends since, at the time of this writing, no commercial modules of these types are reported [244]. Although module efficiencies are summarily increasing, a wide range are still seen since the efficiency at STC is not the only module parameter worth considering; temperature dependence, for example, which has previously been discussed would also be an important factor.

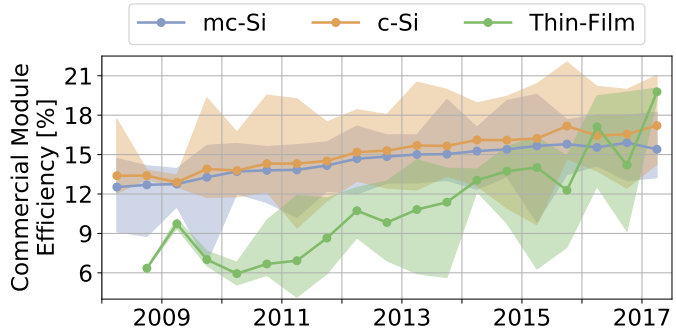

Figure 4.12: Average and 98 percentile spread of commercial PV module efficiencies introduced in each year (data from [244])

In terms of performance, a slight increase in FLH has been observed across the world [11]. However, this is not so much due to improving PV performance but rather more due to a higher installation tendency in developing countries with high solar-resource potential [11]. A slight shift towards cell chemistries, such thin-film cells, that perform better than c-Si cells in warm climates as well as an increased use of tracking systems in some areas has also contributed to this [11]. One way to understand this development is that cell efficiency improvements also increase a module's maximum power point, and thus its capacity. As a result, the increases in PV efficiency lead to greater generation per unit area, and thus larger power densities, but don't necessarily increase FLH.

Into the future, assumptions of module efficiency and FLH depend heavily on the dominant cell design [233]. As of 2018, c-Si and mc-Si continue to increase their current share of global PV capacity at 95 % [11, 158, 231]. By the end of the next decade, mass produced c-Si and mc-Si modules are expected to reach efficiencies between 20.5 and 25.7 % [298]. According to JRC [160], who do not specify a cell technology, typical module efficiency will reach 20 % in 2030 and 30 % by 2050. Similarly, an outlook study performed by Fraunhofer [285] predicts a conservative 2050 efficiency of ≈24 %, where c-Si and mc-Si modules remain dominant, as well as a median and optimistic efficiency of ≈30 % and ≈35 %, respectively, where dual-junction modules and triple-junction modules are readily available. For

performance, JRC [160] predicts slight but nevertheless noticeable FLH gains in Europe between now and 2050 depending on PV domain. In the case of residential rooftop, they predict that the current average of 1051 kWh kWp^{-1} would rise to 1226 kWh kWp^{-1}. Similarly, for fixed-tilt open-field systems they expect to see an increase from 1139 to 1490 kWh kWp^{-1} and, for tracking open-field systems they expect an increase from 1577 to 1840 kWh kWp^{-1}.

Cost Trends

For the cost of PV systems, the average cost on the world stage of electricity generated from PV systems has fallen below 0.10 USD$_{2016}$ kWh^{-1} (9.3 ct$_€$ kWh^{-1}) [158]. This achievement is largely a result of the falling module prices, shown in Figure 4.13 [231]. Following the current learning rate of 24 % and the estimate of 1 TW of global capacity by 2022, then it seems likely that module costs will fall to somewhere in the range 0.2 to 0.3 € Wp^{-1}. At that point it is apparent that module costs, at least for those which are silicon-based, would begin to approach their materials cost [285]. If thin film technologies begin to increase their capacity share, then this price could fall further.

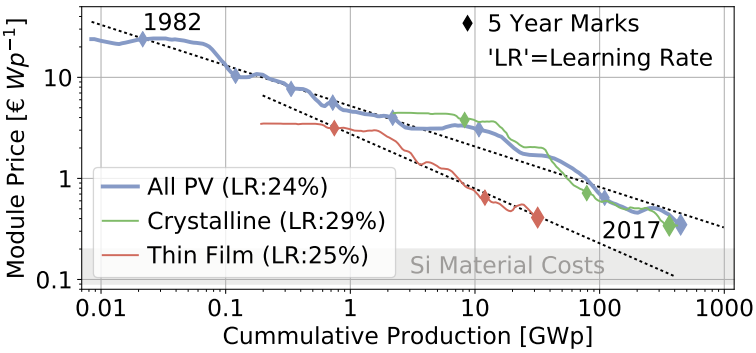

Figure 4.13: Global commercial PV module price trend until 2017. Values adjusted for inflation. Adapted from [231].

Within Europe, average PV costs are expected to reach between 4 and 6 ct$_€$ kWh^{-1} by 2025, and between 2 to 4 ct$_€$ kWh^{-1} until 2050 [285]. This cost trend can be dissected into the various PV domains, as well. From 2013 until 2017 utility scale open-field PV fell from 17.0 to 10.4 ct$_€$ kWh^{-1} in Germany - a 39 % decrease - from 25.9 to 8.2 ct$_€$ kWh^{-1} in France (68 %), from 14.6 to 7.7 ct$_€$ kWh^{-1} in Italy (47 %), and from 32.3 to 12.5 ct$_€$ kWh^{-1} in the United Kingdom (61 %) [158]. During this same time, rooftop costs fell from 42.3 to 11.3 ct$_€$ kWh^{-1} in Germany (73 %), from 40.0 to 16.3 ct$_€$ kWh^{-1} in France (59 %), from 16.7 to 10.4 ct$_€$ kWh^{-1} in Spain (37 %), from 28.4 to 22.1 ct$_€$ kWh^{-1} in Switzerland(22 %), and finally from 29.1 to 18.5 ct$_€$ kWh^{-1} in the UK (36 %) [158].

The underlying reason for these cost reductions is multi-dimensional. As men-

tioned, falling module costs play a large role, which is occurring in part due to improved silicon usage rates as well as reductions in ancillary manufacturing and shipping costs [231]. However other components such as inverters, frames, and wiring are becoming cheaper as well [12, 158]. Inverters, especially, have reduced in cost from about $1 €\,Wp^{-1}$ in 1990 to nearly a tenth of that in 2014 [285]. Inverters are also becoming 'smarter' by offering advanced monitoring and communicative interfaces which help to improve PV availability and MPPT performance [285]. Increasing efficiencies of PV modules also reduce total costs as it has a compounding effect within the BOS costs [285]. Put shortly, a more efficient panel means less module area for the same capacity, and less module area means less mounting and less wiring, all of which further ease material transportation costs. Moreover, less mounting and wiring infrastructure also means less manual labor and material costs.

Between the module, inverter, and BOS cost - which can be further broken down into various sub costs - a conservative total fixed-tilt open-field system cost in 2050 would be $606 €\,kW^{-1}$, while an optimistic cost would reach as low as $270 €\,kW^{-1}$ [11, 285]. A tracking system would likely still cost more, and is projected to be close to $710 €\,kW^{-1}$ [160]. Similarly, residential rooftop systems are projected to cost somewhere in the range of 760 to $1000 €\,kW^{-1}$ [160].

4.1.5 PV Modeling in the Literature

The final PV background item to be discussed revolves around the common methods used in the literature to simulate PV generation dynamics at the European scale. The aim of this discussion is not to provide a comprehensive review of the complete PV modeling literature, but rather to briefly present the key aspects of representative and relevant literature examples. This includes both estimations of total PV potential in Europe, which will ultimately be used for later result comparison, as well as temporally and spatially explicit simulation methods which have, in many cases, inspired the later simulation scheme used here. In comparison, methods used in the literature which are limited to small regional scales, such as those performing LIDAR-based rooftop potential analyses, will not be discussed since they cannot be extended to a European approach.

To determine the total PV potential in 2050, first an estimate of available land, in the case of open-field PV, and roof area, in the case of rooftop PV, would need to be made. Zappa and van den Broek [44] performed an example of this type of evaluation across Europe. For their open-field land availability phase, they exclude protected areas and all land cover categories besides sparse vegetation areas, pastures, and arable land. Afterwards they assume that $1\,\%$ of this land is actually available for PV farms, leading to a total of $15{,}849\,km^2$ across Europe. By assuming a module efficiency of $16.8\,\%$ and a coverage factor of $17.7\,m^2\,kWp^{-1}$ they arrive at a total open-field European Capacity of $865\,GWp$. Other examples of future open-field potential estimates in Europe include the work of Stetter [299] as well as that of the E-Highway project [300]. Stetter's included a detailed look at land eligibility, where PV is only allowed on shrub and grasslands, sparsely vegetated and other

bare areas, and furthermore excluded areas based on slope, settlement distance, and protected area designations. Stetter assumes a panel efficiency of $18\,\%$ and very small coverage factor of $6.57\,\mathrm{m^2\,kW^{-1}}$, leading to total European capacity estimate of $77.4\,\mathrm{TWp}$. In comparison, when developing the E-Highway scenarios [300], the total open-field PV potential was found by assuming that only $2\,\%$ of free natural lands and grasslands in addition to $1\,\%$ of agricultural lands are available for PV farms. Then, with a land coverage factor of $6.62\,\mathrm{m^2\,kW^{-1}}$, they find a total European capacity potential of $1071\,\mathrm{GWp}$. For both Zappa and van den Broek [44] as well as Stetter [299], the land eligibility constraints included for their European scale analysis are significantly less detailed than the regional PV eligibility studies reviewed to construct the exclusion criteria list in Table 2.2.

Slightly different approaches are taken to estimating the potential of European rooftop PV. Zappa and van den Broek [44] only consider rooftop PV in urban areas, estimate total rooftop area based on a constant land-cover factor derived from observations in the UK and Netherlands, and then assume a roof pitch angle of $35\,°$ and roof availability factor of $30\,\%$. The total rooftop area is estimated in Europe at $10{,}339\,\mathrm{km^2}$, which with a module efficiency of $21.5\,\%$ leads to a total rooftop capacity of $2187\,\mathrm{GWp}$. In the E-Highway study [300], a rooftop area is estimated assuming a constant factor of $24\,\mathrm{m^2\,capita^{-1}}$, $40\,\%$ rooftop availability, and a roof coverage factor of $6.62\,\mathrm{m^2\,kW^{-1}}$, leading to a total capacity of $815\,\mathrm{GWp}$. Defaix et al. [301] take a different approach, where national statistics of building types and floor area are combined with their own floor count assumptions. This leads to a total European rooftop area estimation of $7641\,\mathrm{km^2}$ which, with a $40\,\%$ availability factor and $19.7\,\%$ module efficiency, allows for $607\,\mathrm{GWp}$ of overall rooftop potential. Defaix et al. go on to assume a constant performance factor[11], but don't consider the impact of rooftop tilt and azimuth orientations, and report a total rooftop PV generation potential of $601\,\mathrm{TWh}$. Finally, Bódis et al. [302] applied IEA's population-based PV-suitable rooftop area estimator [292] to population density data at $1\,\mathrm{km}$ resolution across Europe. After assuming that north-facing roof portions are not suitable, thus reducing the overall availability by $50\,\%$, the total PV-suitable rooftop area is reported at $7582\,\mathrm{km^2}$. Without specifying a particular PV module efficiency or taking into account roof orientation, Bódis et al. [302] conclude their report with the estimation that these rooftop systems could generate up to $895\,\mathrm{TWh\,a^{-1}}$.

At last, a few methods used in the literature to simulate time series generation from arbitrary[12] PV systems are discussed. The PV-GIS tool developed by Šúri et al. [303] used monthly-averaged climate-model GHI and DHI data measured from 566 weather stations, which was temporally downscaled to the hourly level by computing solar position and airmass, and additionally used spatially-sensitive turbidity[13] observations. They also include shading effects from geological features such as hills and mountains by considering $1\,\mathrm{km}$ resolved elevation data. Šúri et al. then use their hourly irradiance values to estimate the optimal PV module orientation and at last determine the output of a PV module using a constant performance factor

[11] Amounting to $990\,\mathrm{kWh\,kWp^{-1}}$

[12] In the sense of module selection, system design, and location

[13] A measure of atmospheric 'cloudiness' or 'haziness'

which is not sensitive to temperature or incident irradiance. In a latter publication Šúri et al. [304] apply their approach over the European scope to investigate the FLH distribution of optimally-tilted PV modules, which will be compared against in the latter portions of this work. Huld et al. later expended on this method to include higher resolution satellite-derived irradiance data [305] as well as to use a variant of the SAPM PV simulation model which takes into account a linear temperature dependence [306, 307]. Ultimately, this forms the simulation model used in the previously mentioned estimate of Bódis et al. [302]. In comparison, the approach of Pfenninger and Staffel [16] developed a model which can use either MERRA-derived [179] GHI data, or else high resolution satellite-derived GHI and DNI data; both of which are hourly resolved. They then, at each hour, compute the solar position, angle of incidence, and DHI using an irradiance decomposition model known as the BLR method [308, 309]. An isotropic transposition model is chosen to estimate POA irradiance, which has been shown in several cases to perform poorly in overcast conditions [205, 222, 223]. The hourly generation of a PV module is at last estimated using the simulation approach of Huld et al. [307]. Pfenninger and Staffell [16] validate their complete approach against 1029 PV generation measurement sites across Europe and which span multiple years at an hourly time scale. They also offer nationally-averaged and hourly generation time-series data which will be used later in this work to validate the final PV simulation scheme.

4.1.6 Summary and Outlook

Evaluating PV energy's contribution to VRES lulls observed across Europe will require an approach which considers all of the dynamics presented in the preceding chapter. Since so much of the PV potential is a result of the available irradiance, hourly-resolved sun tracking will need to be performed and POA irradiance must be estimated individually for all locations across Europe. The ideal PV performance should then be evaluated in a manner which takes into account real-world losses such as the effects of angle of incidence, cell temperature, spectral response as well as shading and soiling. Of these examples, the first two will be dealt with explicitly in the latter simulation scheme, while the others would require detailed analysis which are not feasible when applied at the European scope; and therefore a holistic loss factor will be used. Following future trends, the PV modules simulated in a 2050 context should have efficiencies in the range of 25 to $35\,\%$. Summarizing the preexisting literature for PV potential at the European scale, it is apparent that open-field land eligibility procedures consider less detailed constraints compared to regional studies, heavily rely on suitability and land coverage factors, and tend to use low efficiency modules compared to what is expected in the future. For rooftop PV, there seems to be some agreement on a total rooftop area in Europe around 7500 to $10{,}000\,\mathrm{km}^2$, all studies operating at this scale have employed a simplified rooftop estimation procedure, and generally consider a single rooftop orientation or else don't include orientation in their analysis at all. In terms of PV simulation schemes which can operate at the European scope, all studies makes use of climate model data while some use satellite derived data in addition, and several key loss sources such as angle of incidence and temperature dependence are either non-existent or else simplified as a linear response.

4.2 Assumptions and design conventions

In the coming section, the reasonings behind several assumptions are given. These assumptions include the module selection, land or roof area usage, and finally system design in terms of orientation and tracking capabilities. Furthermore, as these assumptions will need to be adapted separately for either the open-field and rooftop PV domains, the discussion here will focus first on the open-field domain, and will then address rooftop.

4.2.1 Open-field PV

Module Selection

When describing PV module dynamics is Section 4.1.2 it was described how the efficiency of a PV module is measured by its STC performance but that several other factors can influence the real-world generation; such as incident irradiance, air temperature, and wind speed. Furthermore, it was also discussed how increased efficiency of a module primarily lowers the area required for a desired capacity without having a strong influence on FLHs. Therefore a pre-analysis is performed to identify location-specific PV modules for the open-field domain based on the expected FLH of competing module characteristics. Using the PV simulation scheme which will be described in fine detail later in this chapter, a simulation was performed at 100 locations across Europe representing all countries in the study area. This was performed for all PV modules in the most recent module database provided by Go Solar California [244], containing electrical characteristics of over $19{,}000$ modules available on the market that include c-Si, mc-Si, and various thin-film cell chemistries. The intnt of this was to identify the module with the highest FLH for each location, however the Winaico WSx-240P6 [244] module emerged as the best choice for all simulation points. Therefore this module was selected for all open-field applications. Table 4.2 provide the characteristics of this module in addition to the module selected for rooftop applications and various economic assumptions which are discussed later in this section.

It is seen in Table 4.2 that the selected module is a polycrystalline module with a max power efficiency of $14.46\,\%$. While this efficiency is reasonable for contemporary open-field modules, it certainly does not match the future outlook discussed in Section 4.1.4. Ideally the analysis conducted here would project the electrical characteristics of all PV cell configurations and chemistries to a future context, and choose that which is most cost-effective. However, making these projections while ensuring the feasibility of these configurations is a non trivial task which would nevertheless be highly speculative in regards to both the performance of these technologies as well as their relative costs. Nevertheless, Fraunhofer ISE [285], for example, propose a conservative 2050 crystalline module efficiency of $24\,\%$, after accounting for the progress of cell efficiencies; taking into account their theoretical limit [251] and the effects of imperfect junction connections and other intra-module losses. Therefore, this efficiency value is assumed here as well when determining open-field PV land usage and the total capacity of potential PV farms, while the rel-

Table 4.2: Chosen PV modules characteristics [160, 244, 285]

Parameter	Open-field	Rooftop
Module		
Module Name	Winaico WSx-240P6	LG 360Q1C-A5
P_{mp}	240.4 W	370.4 W
Area	1.663 m^2	1.673 m^2
Efficiency		
Actual	14.46 %	22.14 %
Used in model	24.00 %	30.00 %
Technology	Polycrystalline	Mono-crystalline
Coverage	20 m^2_{land} kWp^{-1}	6.67 m^2_{roof} kWp^{-1}
Economic:		
Capital Cost		
Fixed-tilt	500 € kWp^{-1}	800 € kWp^{-1}
Single-axis Tracking	700 € kWp^{-1}	-
Operating Cost	1.7 % capex	1.7 % capex
Economic Lifetime	25 years	25 years
Interest Rate	8 %	8 %

ative behavior is simulated using the current Winaico WSx-240P6 characteristics.

Land Usage

This future-oriented module efficiency leads to the coverage assumption employed for open-field PV parks. A module with 24 % PTC efficiency corresponds to a direct module coverage of 4.17 m^2_{module} kWp^{-1}. For reasons discussed in the background section on open-field system design (Section 4.1.3), a standard ground coverage ratio of 3/7 is assumed since it is observed for both fixed-tilt and single-axis tracking systems [277]. This is done in order to minimize self-shading and to permit maintenance access, and increases this coverage to 9.72 m^2_{land} kWp^{-1}. Additionally, the necessity to add service buildings, access roads, and surrounding area associated with a PV park to the coverage value, increases this total to 12.67 m^2_{land} kWp^{-1} [277]. Finally, the land eligibility procedure applied for open-field PV, as described in detail in the following section, excludes the primary land-constraining features - such settlements, forests, agricultural areas, and protected areas - but it does not exclude relatively small land features such as streams, roads, railways, and isolated buildings. It is chosen to not consider these smaller features in the land eligibility analysis since their exclusion would not be well represented on the 100 m resolution of the land eligibility analysis. Under the assumption that PV parks can be designed to conform around these features, a conservative final open-field PV coverage of 20 m^2_{land} kWp^{-1} is thus assumed.

System Configuration

Besides the module which is used and the resulting land coverage, a realistic open-field PV system design should also consider the tilt, azimuth, and tracking type for each potential installation location. A system's optimal azimuth is generally a function of surrounding obstacles such as trees, buildings, and mountains as well as cloud formation tendencies. However as all of this information is not known in a detailed three-dimensional manner, as would be required to determine the optimal azimuth angle, the industry-standard of a south-oriented azimuth is assumed for all open-field parks [203]. Tilt and tracking type, however, are each designed for all locations across Europe according to the results of the pre-analyses discussed next.

Optimal tilt angle is defined for all locations across Europe in a manner which follows the transposition factor approach of Umoette et al. [220], where the tilt angle which provides the best ratio of annual POA irradiance to GHI is found. In order to accomplish this, 37 years of weather data are extracted from the MERRA [179] climate model dataset and POA irradiance is computed on the tilted surfaces between $0°$ and $90°$. A complete description of this POA calculation will be covered later in this chapter when discussing the general PV simulation scheme, and so is not repeated here. This is performed on a $5\,\mathrm{km}$ grid spanning the European continent[14], and, in each case, the tilt angle which maximizes the ratio of annual POA to annual GHI is selected. Figure 4.14 shows an example result of this procedure, and the Europe-wide results are presented in Figure 4.15.

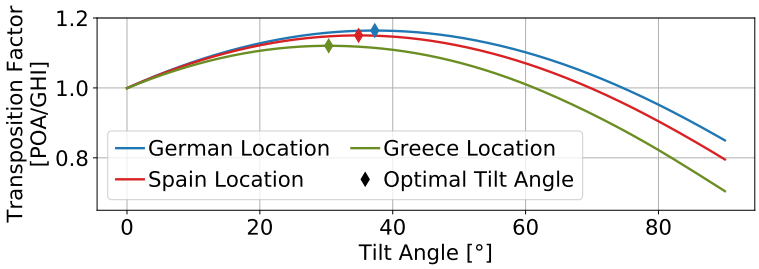

Figure 4.14: Optimal fixed tilt selection examples

Although a general correspondence of lower tilt angles to lower latitudes is observed, it is clear that sub-structure results from factors besides just the latitude. One example of this is given from the fact that the lowest optimal tilt angles of around $25°$ are actually found in predominantly mountainous areas, such as in the Alps or in central Norway. In these areas, it is clear that the maximization of POA irradiance from diffuse sources is more effective then from direct irradiance. To explain this in greater detail, modules in, for example, southern Italy and Greece can primarily expect to see clear skies and as such the optimal tilt angle in these

[14] Constituting 191,917 points

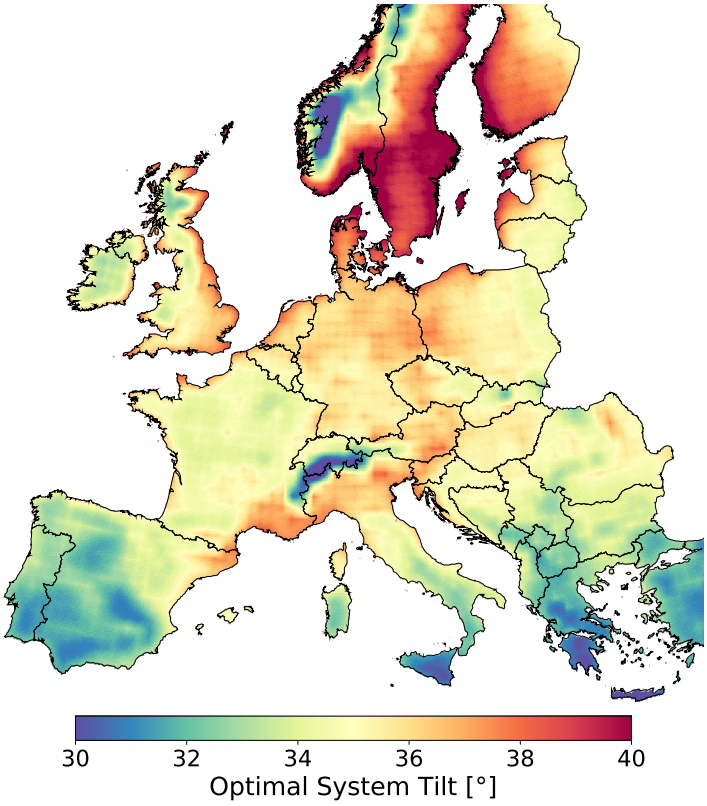

Figure 4.15: Optimal tilt angle of south-facing PV systems across Europe. Actual observed values ranged between 25° and 43° but are shown between 30° and 40° here to accentuate trends.

areas is strongly influenced by the angle which makes the best use of direct and circumsolar diffuse irradiance. In comparison, modules placed in the Alps and central Norway could be more often exposed to cloudy skies, meaning that a much higher proportion of the light they receive arrives from diffuse irradiance sources such as scattering from clouds. Therefore, despite the higher latitudes, modules in these areas are optimally oriented at low tilt angles in order to expose them to a larger view of the sky. For a country like Germany, where a mixture of these dynamics is observed, a typical optimal tilt angle around 36° is seen throughout the country; which is in close agreement with values expressed in the literature ranging from 35° to 37° [206, 221].

Tracking type is then defined for all locations across Europe by comparing the LCOE potential between fixed-tilt and single-axis tracking system designs, while dual-axis tracking is not investigated as it offers little additional benefit over single-

axis [281–283]. To accomplish this, the same $5\,\mathrm{km}$ grid and optimal tilt angle from the previous pre-analysis were used and a PV system using the Winaico WSx-240P6 module was simulated at each point for either tracking type. Once again, the simulation procedure used is discussed in greater detail further on in this chapter, and so it is not discussed here. Simulations were performed for all available weather years in the MERRA dataset, and the average FLH was found for each tracking type at each location wsa recorded. In the end, the ratio of single-axis tracking to fixed-tilt FLH was found, and the resulting distribution is displayed in Figure 4.16. As expected, it is seen that single-axis tracking system always perform better than fixed-tilt systems, however this only appears to range between a $5\,\%$ to $26\,\%$ improvement in annual FLH. Due to the LCOE computation used in this work, discussed in Appendix Section C.4, and the cost assumptions displayed in Table 4.2, a tracking system would only become the cost-optimal choice when the FLH improvement exceeds $40\,\%$ of the FLH of a fixed-tilt system. Since this is never observed in the pre-analysis performed here, only fixed-tilt systems are considered for the remainder of the open-field PV analyses made here.

4.2.2 Rooftop PV

The treatment of rooftop PV will focuses on dynamics related to residential rooftop sector. While commercial-scale rooftop will certainly be an important factor in the future solar industry, it is not dealt with in detail within this report for two primary reasons. On one hand, there is little data available concerning the rooftop area of commercial and industrial buildings. On the other hand, commercial-scale rooftop PV generally differs from residential rooftop PV in the sense that the flat roofs allow for optimal orientation of these modules. As a result commercial-scale rooftop PV should perform in a manner more similar to that of open-field PV systems, while the cost should always fall somewhere between that of open-field and residential rooftop [160]. Therefore, the detailed consideration of open-field and residential rooftop PV should already cover the operational boundaries in terms of generation costs and time-series profile. Given that there is much uncertainty in regards to the future shares of PV domains (see Figure 4.10), then a detailed consideration of commercial rooftop systems would not enhance the results this thesis. For these reasons, commercial scale rooftop PV is not specifically addressed in this work, and discussion instead focuses on the two opposing PV domains: open-field and residential rooftop.

Module Selection and Coverage

Compared to open-field PV, where the module with the best FLH is selected, the design of rooftop PV is constrained by the available roof area leading to the prioritization of module efficiency[15]. Therefore, the module LG360Q1C-A5 developed by LG is selected from the Go Solar California module database [244] as it possess the highest efficiency of $22.14\,\%$. However, as this efficiency value also does not match future expectations (Section 4.1.4), the moderate 2050 module efficiency estimated

[15] Therefore allowing for the most capacity per module area.

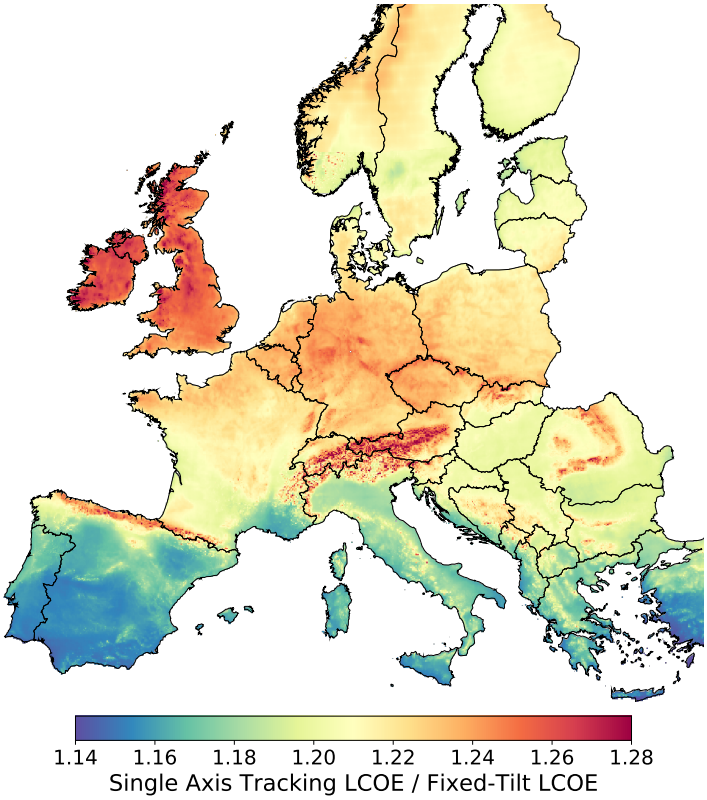

Figure 4.16: Performance of single-axis tracking LCOE divided by fixed-tilt PV LCOE across Europe. Land eligibility is not included.

by Fraunhofer [285] and JRC [160] of $30\,\%$ is used here as well. Therefore future rooftop simulations are treated in the same way as open-field simulations; where relative performance values are found by simulating the LG 360Q1C-A5 module with its current electrical properties, but with the total capacity scaled to match a module with $30\,\%$ efficiency.

Regarding rooftop coverage, the $30\,\%$ module efficiency used for the future context leads to a direct coverage of $3.33\,\mathrm{m}^2_{\mathrm{module}}\,\mathrm{kWp}^{-1}$ at PTC conditions. Normally, a rooftop utilization factor of $29\,\%$ can be used [310, 311] to account for imperfect roof layouts by subtracting area for chimneys, sky lights, and irregular roof shapes, as well as for a large north-facing portion. In this work, however, rooftop area estimations will be made which already provide the amount of PV-suitable rooftop area, and thus only a $50\,\%$ utilization factor is imposed to account for the portion of these roofs that are summarily facing northward. This increases the coverage factor for rooftop PV to $6.67\,\mathrm{m}^2_{\mathrm{roof}}\,\mathrm{kWp}^{-1}$.

System Orientation

As shown in Section 4.1.5, previous rooftop PV estimations over Europe performed in the literature all rely on statistical simplifications to determine the distribution of rooftops, since a detailed evaluation of this issue across the European scope is not feasible due, primarily, to data availability. This work will also need to make a similar simplification, but will nevertheless improve upon these previous approaches, who either use only a single rooftop orientation or else neglect roof orientation entirely, by evaluating a distribution of rooftop azimuths and tilt angles. Once simulated for each orientation, the resulting generation profiles are combined via an occurrence-weighted average to formulate a single time-series. This array of simulations will be performed for numerous representative rooftop zones across Europe, the identification of which will be described in the following section regarding land eligibility and distribution. Judging from reports of real rooftop PV systems throughout France, the UK and Belgium [288], a detailed LIDAR based investigation of roof orientations in Baden-Württemberg, and the assumptions made in similar investigations [44], the distribution of rooftop azimuths on which PV is installed is always assumed to be uniformly distributed between $90°$ and $270°$[16] and roof tilt angles are assumed to follow a Gaussian distribution defined by an average tilt of $35°$ and a standard deviation of $15°$.

4.3 Land Eligibility and Placement

4.3.1 Open-Field PV

Land exclusion and placement for open-field PV systems is performed using the GLAES model and 'Prior datasets' which represent 44 of the most commonly considered geospatial criteria in the literature[17] in the context of renewable energy generators (Section 2). In many ways, the land considerations made in this case reflect those which were used for onshore wind in Section 3.5, however they differ considerably in the exclusion of agricultural areas, forests, and north-facing slopes, as well in the specific security distances used; which should in total result in a smaller portion of available area. In the end, the 28 constraints presented in Table 4.3 were selected in light of the literature review conducted during the development of the GLAES model (Section 2.2), and are meant to represent a general European perspective. As a result, these exclusions might not include the specific preferences or extra considerations of each geopolitical region, but nevertheless capture the typical exclusions seen for studies conducted in Europe. Similar to the approach of JRC [312], a conservative position is taken when selecting these constraints, resulting in the expectation of extensive exclusion from four constraints in particular: settlement areas, forests, agricultural areas[18], and all designated protected areas. For reference, Figures 2.3, 2.4, 2.6 show this coverage in much greater de-

[16] Where $180°$ indicates a south-facing orientation.

[17] Including many studies who's scopes are small compared to Europe, but in exchange consider many more criteria compared to European-level studies.

[18] Including permanent crops, arable lands, and pasture lands, as defined by the CLC [91]

Table 4.3: 28 land eligibility constraints applied for open-field PV

Constraint	Threshold	Source
Sociopolitical:		
Distance from Settlements	>200 m	CLC
Airports	*excluded*	EuroStat, CLC
Airfields	*excluded*	EuroStat, CLC
Industrial Areas	*excluded*	CLC
Mining Sites	*excluded*	CLC
Distance from Touristic Areas	>1 km	OSM
Distance from Camp Sites	>1 km	OSM
Distance from Leisure Areas	>1 km	OSM
Agriculture	*excluded*	CLC
Physical:		
Distance from Sandy Areas	>1 km	CLC
Elevation	<1.75 km	EuroDEM
Slope: Total	<10°	EuroDEM
Slope: Northward	<3°	EuroDEM
Woodlands	*excluded*	CLC
Distance from Wetlands	>1 km	CLC
Distance from Coast Lines	>1 km	CLC
Distance from Water Bodies	>1 km	CLC
Conservation:		
Designated Parks	*excluded*	WDPA
Distance from Habitats	>500 m	WDPA
Designated Landscapes,	*excluded*	WDPA
Distance from Reserves	>500 m	WDPA
Distance from Natural Monuments	>1 km	WDPA
Distance from Wildernesses	>500 m	WDPA
Distance from Biospheres	>500 m	WDPA
Pseudo Economic:		
Connection Distance	<20 km	OSM
Access Distance	<10 km	OSM

tail across the European scope. Following the suggestion of JRC [312], however, non-agricultural vegetated areas are not excluded. Beyond these constraints, the immediate area around airports and air fields, touristic, camping, and leisure areas, and locations too near to coast lines and sandy terrains are also excluded. Furthermore, areas with a terrain slope angle above 10° or a north-facing slope above 3°[19] are also excluded. At last, a less restrictive access distance constraint is considered for open-field PV in comparison to onshore wind, on account of PV modules being easier to transport over non-ideal road conditions. As before, the realism of

[19] Since even slight northward slopes can result in a high degree of self-shading losses

this portion of the analysis could be improved upon by specifying unique exclusion definitions for each geopolitical subregion, however, as with wind, such a task is beyond the scope of the current work.

Placement of potential park locations is performed following the land eligibility analysis by employing GLAES' area distribution feature, as discussed in Section 2.5. A separation distance of $1\,\mathrm{km}$ is chosen during the item distribution phase, since this value leads to potential placement areas which are, at maximum, $1.2\,\mathrm{km}^2$, but due to the configuration of eligible land, most often in the range of $0.35\,\mathrm{km}^2$. Furthermore, as the land eligibility result produced many small and isolated pockets, all potential areas less than $0.05\,\mathrm{km}^2$ are discarded, since only a small fraction of open-field PV farms are near this value [277]. Using the open-field coverage factor discussed above, these land areas correspond to park sizes around $60\,\mathrm{MW}$ at maximum, $\approx 18\,\mathrm{MW}$ most often, and $2.5\,\mathrm{MW}$ at minimum. Open-field PV parks span a wide range of sizes, from less than $20\,\mathrm{MW}$ to as high as $720\,\mathrm{MW}$ [277], therefore the units placed in this analysis can be thought of as either small and independent parks, or else as sub units of much larger parks. Finally, as stated in Section 2.5, the geometric centroid of each potential area is then computed and used as the representative simulation location in each case.

4.3.2 Residential Rooftop PV

In order to identify residential rooftop simulation points and their associated rooftop areas, a similar procedure of land eligibility (Section 2.4) and area distribution (Section 2.5) is used. The rooftop land eligibility analysis has only a single constraint, areas which possess a non-zero population density, which relies on the EC's Global Human Settlement Layer [313] (Figure 4.17). As this population density data was developed according to 2015 data, it will not reflect changes due to future population growth and migration. It is not straight forward to predict how these population shifts could alter the final rooftop PV potential estimate since it is ultimately the change in building stock, such as single family homes or apartment complexes, which matters most. Nevertheless, area placement is again performed using GLAES, with a $10\,\mathrm{km}$ separation distance. This relatively large separation distance was chosen to offset the increased computational intensity of the rooftop simulation procedure which, as mentioned previously, will involve the explicit simulation of a two-dimensional distribution of rooftop orientations for each location.

After the land eligibility and area distribution phases, an additional step is taken to estimate the total residential rooftop area and capacity in each area. To accomplish this, the average population density and total population is computed for each placement area by again referring to the EC's population density data [313]. The relationship proposed by the IEA [292], shown in Equation 4.2, is then used to estimate the total PV-suitable rooftop area available in each placement area. Here $population$ is simply the total inhabitants in each placement area, $pop\_density$ is the population density given in $\mathrm{people\,km}^{-2}$, and the estimated PV-suitable rooftop area is given in m^2. As described by IEA [292], the constants used in this equation were derived via a trend fitted to GIS data of nearly 1600 cities across the globe.

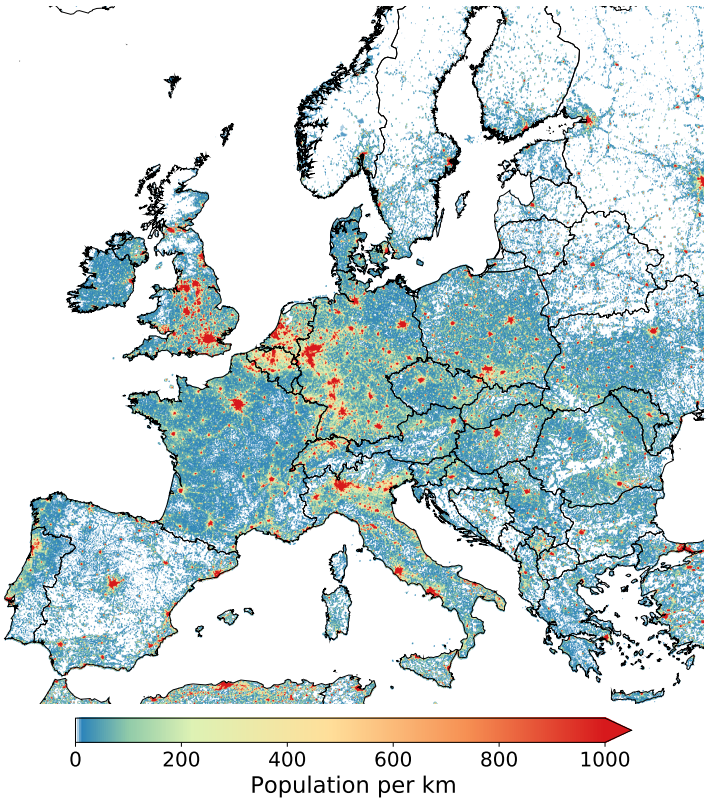

Figure 4.17: Population density visualized from the European Commission's Global Human Settlement Layer [313]

Finally, combining the total available rooftop area of each placement area and the rooftop coverage factor given in Table 4.2 leads to an estimate of the total available capacity.

$$PV\_suitable\_rooftop\_area = 172.3 \cdot population \cdot pop\_density^{-0.352} \tag{4.2}$$

The use of this equation implicitly takes into account the diminishing relationship where higher population densities lead to less rooftop area per capita; as a result of a higher proportion of people living in shared building complexes. For example, for a medium sized urban area such as Aachen, Germany, with a population density of around 4000 people per km^2 [313], Equation 4.2 suggests a PV-suitable rooftop area of $9.3\,m^2$ per capita. Meanwhile, for a densely populated city such as Paris, where population density can be found at 20,000 people per km^2 [313], Equation 4.2 suggests a PV-suitable rooftop area of $5.2\,m^2$ per capita. Note that these val-

ues include all rooftops in the residential area. Nevertheless, several unavoidable disadvantages exists as a result of using Equation 4.2 to estimate the total rooftop area availability. First and foremost, it cannot be used in areas which don't possess a population density and thus cannot estimate rooftop area in non residential areas. Furthermore, it does not account for differences in building type and building quality between geopolitical regions. Finally, use of Equation 4.2 does not take into account how building design may change in the future to better accommodate PV utilization. Nevertheless, as discussed in Section 4.1.3, the lack of data availability excludes the possibility of direct investigation of rooftop area via geospatial analysis[20] across the entirety of the European scope. For this reason, as discussed in Section 4.1.5, all previous European-scale analyses of rooftop PV potential have had to rely on simplified rooftop area estimations such as the one used here.

4.4 Simulation Procedure

A generic PV simulation scheme is developed for both open-field and rooftop applications, but is parameterized slightly differently in either case. Figure 4.18 presents a flow chart of the overall approach. For both domains, the model expects a latitude and longitude coordinate, a module definition, system tilt and azimuth, tracking capability, and climate model weather data, and as a result provides a time-series of capacity factors that can be scaled to a system's total capacity. The work flow begins by specifying a location at which the simulation will occur, detailed module characteristics, the system's tilt, azimuth, and tracking behavior, and finally specifying a set of climate model weather data. Locations can be specified at any point on the globe, so long as weather data is available, although in this work only locations within Europe are considered. Expected module characteristics are taken from the module database provided by Go Solar California [244] which, among other items, include the module chemistry, active area, current and voltage characteristics, and temperature dependence coefficients [245]. Lastly, the weather data source should contain gridded hourly time series data for GHI, air and dew-point temperature at or near to the surface, surface pressure, near-surface wind speed and, if available, DNI.

Considering the vast scale of this project in combination with the intricate individual-system level simulation, the significant effort spent on ensuring computational efficiency within the simulation process is worth mentioning. Similar to the computational efficiency note made when introducing the wind simulation scheme in Section 3.6, without making these considerations it would not have been possible to produced the latter simulation results within a reasonable time. As with the wind simulation scheme, this is primarily incorporated by formulating the steps described below as large matrix operations, processed using low-level libraries[21], that evaluate a large number of PV simulation locations and time steps at once. As much as possible, the PVLIB library [314] is used extensively to realize the described simulation scheme as it has previously implemented many of the requisite mod-

[20] Such as via a LIDAR analysis.
[21] Such as BLAS and LAPACK.

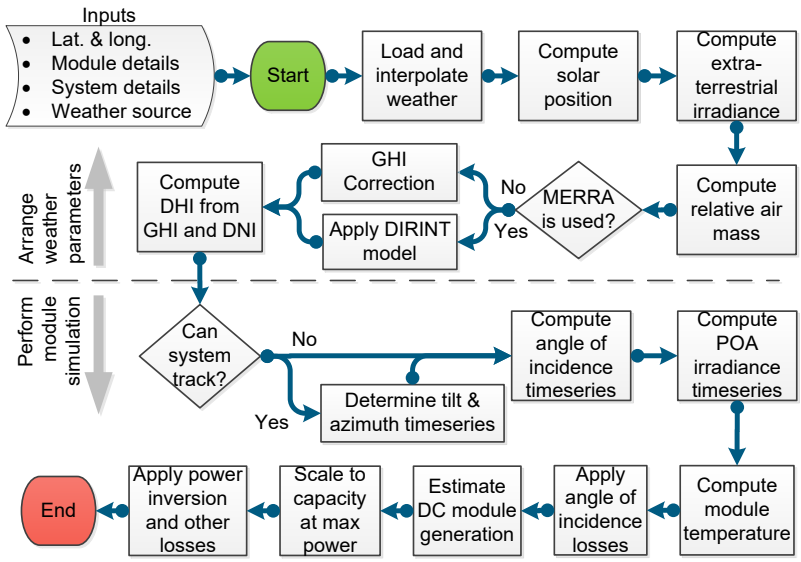

Figure 4.18: Flow chart of the general PV simulation scheme, which is parameterized uniquely for both open-field and rooftop applications.

ules in Python, but several slight alterations had to be made to its code base in order to accept this batch processing style. Due to this, many complex location-specific aspects of PV generation could not be factored in: including shifts in the solar spectrum and the chemistry-specific module response, the state-based loss resulting from soiling and snow coverage, and a three-dimensional awareness of shading culprits. As discussed in Section 4.1.2, however, over the course of a year the impact of these issues is small in comparison to the imprecise irradiance transposition methods and furthermore, in the case of the latter two examples, their impact can be actively minimized by means of frequently module cleanings as well as careful location selection with an unobstructed view of the sky.

4.4.1 Weather Source Selection

As with the wind models, the PV simulation procedure is also developed in such a way that it could make use of any climate model data, so long as irradiance, wind speed, temperature, and pressure data is available. The requirements of a weather sources have been described previously (Section 3.6.1) which, in summary, amount to the need for a high spatial and temporal resolution of all relevant weather parameters in order to best capture small scale weather phenomena which impact PV generation, as well as a large number of available weather years in order to better represent the possible climatic scenarios. Many examples of MERRA's

use for PV simulation can be found in the literature [16, 190, 312, 315–318], while examples which use the COSMO-REA6 dataset [187, 319] are less frequent. At the time of this writing, the MERRA dataset also contains 37 years of weather data while only 20 are found in COSMO-REA6. Conversely, the MERRA dataset's lower spatial resolution of $\approx$60 km over Europe means that it won't be able to capture small scale cloud formations and other small scale phenomena as well as COSMO-REA6, which has a 6 km spatial resolution. Nevertheless, in order to maintain consistency between the final wind energy and PV energy estimates, in this work the MERRA [179] dataset is used primarily and COSMO-REA6 [194] source is considered as a sensitivity in the latter stages of the VRES lull analysis.

4.4.2 Weather Data Extraction

The extraction of weather data variables from either the MERRA or COSMO-REA6 dataset follows the same procedure described for wind in Section 3.6.2. Beginning with a set of PV placements[22] resulting from the land eligibility and placement algorithms, the required weather parameters - irradiance, wind speed, temperature, pressure - are extracted for a full year of hourly data in the area around the placements. Table 4.4 specifies the variable selection for either climate model dataset, and also indicates the slight differences between these sources. To note, the MERRA dataset provides only GHI data, while the COSMO-REA6 dataset provides both DHI and the horizontal portion of the DNI. Therefore, when reading data from the COSMO-REA6 dataset, GHI is computed by adding these two irradiance variables together, and the direct irradiance component is converted to DNI in the later stage of the simulation once the solar position is known.

Table 4.4: Climate model variables used for PV simulations

Variable description	Variable Name	Unit	Height Context
MERRA			
Global Horizontal Irradiance	SWGDN	$\mathrm{W\,m^{-2}}$	at surface
Northerly wind speed	U2M	$\mathrm{m\,s^{-1}}$	2 meters
Easterly wind speed	V2M	$\mathrm{m\,s^{-1}}$	2 meters
Pressure near surface	PS	Pa	at surface
Temperature near surface	T2M	K	2 meters
COSMO-REA6			
Diffuse Horizontal Irradiance	dhi	$\mathrm{W\,m^{-2}}$	at surface
Direct Horizontal Irradiance	dni_flat	$\mathrm{W\,m^{-2}}$	at surface
Northerly wind speed	u	$\mathrm{m\,s^{-1}}$	10 meters
Easterly wind speed	v	$\mathrm{m\,s^{-1}}$	10 meters
Pressure near surface	sp	Pa	at surface
Temperature near surface	2t	K	2 meters

[22] Which can represent either open-field PV parks or else rooftop PV simulation areas

4.4.3 Computing Irradiance Components

The first stage, shown in the upper half of PV simulation flow chart given in Figure 4.18, serves to construct all necessary weather parameters irrespective of the module and system characteristics. This consists of determining the extra-terrestrial irradiance, airmass, and at last the three fundamental irradiance components[23]. Although these steps will be described in the context of a single location and at a single time step, the reader should be aware that these operations must be performed independently for all simulation locations and at all time steps in a given year in order to complete a simulation.

Beginning with reading raw weather data from the climate model source then, for all variables mentioned above, time-series data from the four surrounding grid points are extracted and bi-linearly interpolated to the desired simulation location. Following this, solar position is first computed for each time step using the NREL Solar Position Algorithm (SPA) [320], from which hourly time series for the zenith angle (z), elevation angle (α), and solar azimuth (ψ) are obtained for the exact location and times under consideration. For this, latitude, longitude, terrain elevation (retrieved from the EU-DEM [321] dataset for the simulation location), pressure and temperature are required. Other solar position algorithms were not tested since the NREL SPA has been shown to produce highly accurate estimations, with uncertainties in the range of $\pm 0.0003°$, and is expected to be highly dependable for the next several millennia [322]. Extraterrestrial irradiance and relative airmass time series are then estimated using the Fourier method proposed by Spencer [322,323] (Equation 4.3) and the approach of Kasten and Young [324] (Equation 4.4), respectively. In these equations, G_{sc} is the solar constant of $1367\,\mathrm{W\,m^2}$ [209,210], x is the annual periodicity ($x = hour\_of\_year * 360/8760$), TOA is the expected TOA irradiance, and AM is the airmass.

$$TOA = G_{sc} \cdot [1.00011 + 0.034221 \cdot \cos(x) + 0.00128 \cdot \sin(x) - 0.000719 \cdot \cos(2x) + 0.000077 \cdot \sin(2x)] \quad (4.3)$$

$$AM = \left[\cos(z) + 0.50572 \cdot (96.07995 - z)^{-1.6364}\right]^{-1} \quad (4.4)$$

At this point, a slightly different path is taken depending on weather data source. If MERRA data is provided, then, due to the low spatial resolution, GHI values are adjusted to a local context using the same long-run averaging approach as was applied to wind speeds in Equation 3.9. To do this, a pre-analysis was performed to compute the temporal average of MERRA's GHI variable[24] for each grid cell and saved as a raster dataset. These MERRA averages are then compared

[23] GHI,DHI, and DNI
[24] MERRA variable "SWGDN".

against the finely-resolved expected GHI averages provided in the Global Solar Atlas (GSA) [206]. This dataset is chosen for this purpose as it offers average GHI values across the Globe at $1\,\mathrm{km}$ resolution and claims to possess an error around $\pm 4\,\%$. These values are used in Equation 4.5 where $GHI_{GSA,50m}$ refers to the expected average irradiance from the GSA, $GHI_{MERRA,avg}$ is the average value predicted from MERRA in each grid cell, GHI_{MERRA} is the raw GHI time-series provided by MERRA for a single location, and finally GHI is the locally-adjusted GHI time-series used for further simulation.

$$GHI = GHI_{MERRA} \cdot \frac{GHI_{GSA,50m}}{GHI_{MERRA,avg}} \tag{4.5}$$

Since a DNI variable is not available when using MERRA, the next step is to estimated this value using the DIRINT model [224]. This model was selected for this simulation scheme since its use was compared against other similar models, such as the DISC [225], Erbs [325], and Liu & Jordan [326] model, and was found to behave best in terms of numerical stability. The DININT model is summarized by Equation 4.6, where DNI is estimated as a function of TOA irradiance, airmass (AM) and a clearness factor (Kb'). This clearness factor is determined from a 4-dimensional look up table of clearness regimes[25] based on altitude, solar zenith, dew-point temperature, and the ratio of TOA irradiance to GHI.

$$DNI = TOA \cdot Kb' \cdot \exp[-1.4/(0.9 + 9.4/AM)]/0.87291 \tag{4.6}$$

In comparison, when COSMO-REA6 is used as input a DNI-like variable is already present and so the use of DIRINT is not required. Despite this, Frank et al. [187] have shown that the use of COSMO-REA6 data source for PV simulations requires the bi-modal correction of GHI values depending on atmospheric transmissivity. Therefore, when a COSMO-REA6 source is used here, these corrections are applied in the manner suggested by Frank et al. In either case, once both the GHI and DNI are known the DHI is estimated using Equation 4.7, thereby concluding the first stage of the PV simulation scheme; where z refers to the zenith angle.

$$GHI = DNI * \cos(z) + DHI \tag{4.7}$$

4.4.4 Generation Estimation

In the next stage of the PV simulation scheme, shown in lower half of Figure 4.18, the electrical response of the PV system to the previously computed weather parameters is modeled. This consists of determining the tracking orientation if this capability is enabled, computing POA irradiance, cell temperature, angle of incidence losses, and finally module generation.

[25] 960 regimes in total

If the system is capable of tracking, then the approach of Lorenzo et al. [278] is employed to determine the system's preferred tilt and azimuth at each time step in response to the solar position. As input to this model, the previously indicated tilt and azimuth given during the initialization of the PV simulation serves as the systems base tilt and azimuth about which the tracking behavior can operate, in addition to the three irradiance components and time of day. Additionally, a ground coverage ratio of 3/7 is assumed in all cases for the reasons presented above, along with a maximum tilt angle of $60°$, the value suggested by Lorenzo et al., and with back tracking[26] enabled. When a fixed-tilt system is simulated, this step is of course not performed. In any case, at this point the tilt and azimuth of the system is known for each time step and so the angle of incidence is computed next by means of the dot product between the solar vector and the module's normal vector, shown in Equation 4.8. Where, as stated in Table 4.1, ϕ is the locations latitude, β and ψ_s are the PV system's surface tilt and surface azimuth[27], and finally ω is the hour angle.

$$\cos(\theta) = \cos(\beta) \cdot \cos(z) + \sin(\beta) \cdot \sin(z) \cdot \cos(\psi - \psi_s) \tag{4.8}$$

Following this, the POA irradiance is computed at each time step. For the direct irradiance and ground diffuse POA components, Equations 4.9 and 4.10 are used respectively [203]. In the latter case, a constant surface albedo of 0.2 is assumed [16, 303, 327]. For the sky diffuse portion of the POA irradiance, three commonly used transposition models were compared: the Perez model [226,328], Hay-Davies model [329] and the Reindl [330] model. The Perez model was generally found to perform better than the others when comparing against the validation sources which are discussed later in this chapter. Furthermore, similar evaluations made in the literature [205, 223] also agree that the Perez model often performs better than other transposition models, and so the impacts of these other models on the final PV potential results and VRES lull outcomes are not investigated. The Perez model, represented by Equations 4.11 - 4.13, takes into account the GHI, DNI, DHI, solar position, extraterrestrial irradiance, and airmass, and as a result estimates the sky diffuse irradiance incident on the plane of the module. In this equation, C, F_1, and F_2 are intermediate variables related to sky clearness, circumsolar brightening, and horizon brightening. Additionally, $F_{1,a}$, $F_{1,b}$, $F_{1,c}$, and $F_{2,a}$, $F_{2,b}$, $F_{2,c}$ are all constants found from a lookup table determined by Perez et al. [226, 328] which depend on the clearness regime.

$$POA_{direct} = DNI \cdot \frac{\cos(\theta)}{\cos(z)} \tag{4.9}$$

$$POA_{ground} = GHI \cdot albedo \cdot \frac{1 - \cos(\beta)}{2} \tag{4.10}$$

[26] The where a tracking system chooses a slightly sub-optimal orientation in order to minimize self shading.

[27] When simulating a tracking system, these will be a time series.

$$C = \left(\frac{DHI + DNI}{DHI} + 1.041 \cdot z^3 \right) / \left(1 + 1.041 \cdot z^3 \right) \tag{4.11}$$

$$\begin{aligned} F_1 &= F_{1,a}[C] + F_{1,b}[C] \cdot AM \cdot \frac{DHI}{TOA} + F_{1,c}[C] \cdot z \\ F_2 &= F_{2,a}[C] + F_{2,b}[C] \cdot AM \cdot \frac{DHI}{TOA} + F_{2,c}[C] \cdot z \end{aligned} \tag{4.12}$$

$$POA_{sky} = DHI \cdot \left(\frac{1 - F_1}{2} (1 + \cos(\beta) + F_1 \cdot \frac{\cos(\theta)}{\cos(z)} + F_2 \cdot \sin(\beta) \right) \tag{4.13}$$

Angle of incidence losses are applied next in order to account for reflections from the glass cover of the PV module. For this purpose, PVLIB's implementation of the AOI modifier suggested by De Soto [236] is utilized, and will be referred to as $\kappa_{\tau\alpha}$ here after the notation of De Soto. This modifier is in fact applied three times, once for each component of POA irradiance, and can be found for any arbitrary incidence angle (θ'). Equation 4.14 computes the refraction angle using the indexes of refraction for air (n_{air}) and glass (n_{glass}). Equation 4.15 then computes the ration of transmitted irradiance (τ) using Frensel's law multiplied by the effect module coatings, which is controlled by the coating's extinction coefficient (K) and thickness (L); assumed as $4\,\mathrm{m}^{-1}$ and $2\,\mathrm{mm}$, respectively, according to the suggestions of De Soto [236]. In Equation 4.16, the irradiance modifier $\kappa_{\tau\alpha}$ is then found as the ratio of τ at θ' to τ at a $0\,°$ incidence. To modify direct POA irradiance the direct application of $\kappa_{\tau\alpha}$ is used at the real angle of incidence (θ), as shown in Equation 4.17. For POA from sky diffuse and ground reflected sources, however, a full physical evaluation of this modifier would require integration over the module's entire view, and as a result would necessitate intense computation when applied across Europe. To avoid this, the effective incidence angle trends suggested by Brandemuehl and Beckman [258] and discussed by Duffie [201] are used, which depend only on the PV system's tilt angle (β). This leads to Equations 4.18 and 4.18. Ultimately, the total POA irradiance received by the module that is available for electricity conversion is found by summing these three components multiplied by their respective angle of incidence modifiers, shown in Equation 4.20

$$\theta_r = \sin^{-1} \left(\frac{n_{air}}{n_{glass}} \cdot \sin(\theta') \right) \tag{4.14}$$

$$\tau(\theta') = \left[1 - \frac{1}{2} \left(\frac{\sin^2(\theta_r - \theta')}{\sin^2(\theta_r + \theta')} + \frac{\tan^2(\theta_r - \theta')}{\tan^2(\theta_r + \theta')} \right) \right] \cdot \exp \left(\frac{-K \cdot L}{\cos(\theta')} \right) \tag{4.15}$$

$$\kappa_{\tau\alpha}(\theta') = \tau(\theta') \; / \; \tau(\approx 0) \tag{4.16}$$

$$\kappa_{\tau\alpha,\ direct} = \kappa_{\tau\alpha}(\theta) \tag{4.17}$$

$$\kappa_{\tau\alpha,\ sky} = \kappa_{\tau\alpha}(59.7 - 0.1388\beta + 0.001497\beta^2) \tag{4.18}$$

$$\kappa_{\tau\alpha,\ ground} = \kappa_{\tau\alpha}(90 - 0.5788\beta + 0.002693\beta^2) \tag{4.19}$$

$$POA = POA_{direct} \cdot \kappa_{\tau\alpha,\ direct} + POA_{sky} \cdot \kappa_{\tau\alpha,\ sky} + POA_{ground} \cdot \kappa_{\tau\alpha,\ ground} \tag{4.20}$$

The cell temperature of the module is determined next, using the method proposed by King et al. [237], where total POA irradiance, wind speed (v), and air temperature (T_{air}) are considered. Equation 4.21 shows this equation, where a, b, and c are the constants suggested by King et al. [237] which tailor the cell temperature response to that of an open-backed glass encased PV module versus that of a rooftop-backed glass encased module. These constants are provided in Table 4.5.

$$T_{cell} = POA \cdot \exp(a + b \cdot v) + T_{air} + \frac{POA}{1000} \cdot c \tag{4.21}$$

Table 4.5: PV domain cell temperature coefficients

	Open-field	**Rooftop**
a	-3.47	-2.98
b	-0.0594	-0.0471
c	3	1

The most crucial stage of simulation, time series estimation of the DC electricity generated by the module, is addressed next. During the development of this procedure, the SAPM [237] model and the Single Diode model [236], using the Lambert W-function based solution suggested by Jain [239], were compared in detail and found to produce nearly equivalent results when simulating the same panel in the same conditions. Ultimately, however, the single diode approach was selected for application here as it models a physical representation of PV cell behavior, while SAPM uses an empirical approach. Moreover, the coefficients required by the SAPM model are not readily available for most modules available today meaning the use of the single diode approach is more adaptable to varying simulation contexts. On the downside, the evaluation of the single diode approach is much more computationally intensive compared to the SAPM model since an iterative-search solution scheme is required at each time step in order to identify the maximum

power point. In any case, using this method the DC generation of the module is estimated in response to total effective POA irradiance, cell temperature, and of course the specific characteristics of the module under consideration. As a result, time series DC generation values are produced and given in Watts, which are finally adjusted to capacity factor value by dividing them by the module's maximum power value. At last, an $18\,\%$ holistic loss is applied to account for inversion, wiring, soiling, and other losses. This loss value was selected by comparing simulation results to those from other validated sources, primarily those of Pfenninger and Staffell [16] and the GSA [206].

4.5 PV Simulation Validation

As with wind modeling, a significant effort was put towards the validation of the developed PV model, and is provided in detail in Appendix E.1. As all major sub modules used in the total model have been independently validated throughout the last few decades, these fundamental issues are not readdressed here. Instead, the validation effort is spent on comparing the current model against the study of Pfenninger [16] and the GSA [206], since these approaches have been previously validated against measured generation data across Europe.

To make these comparisons, the full 37 years of MERRA data availability were simulated on a $5\,\mathrm{km}$ grid across Europe[28], using a conventional PV module and the optimal tilt angles found in this work. To compare against Pfenninger's method, the hourly outputs from these simulations were averaged across the European countries and compared against the results of Pfenninger. In all instances a good, if not extremely close, agreement with the current model was seen, with total errors generally found within $\pm 5\,\%$ and with correlation coefficients all equal to or above 0.988. Nevertheless, some relative deviations were observed most often in the early mornings and late evenings, when extremely low generation easily leads to large relative differences. These difference, however, are likely a result of Pfenninger's use of a different DHI estimation method compared to the one used here, as well as unknown details of Pfenninger's approach; such as the exact module characteristics, or the precise simulation locations. When comparing against the GSA, which provides the expected average FLH of an optimally-tilted PV module across the Globe, the simulation results were averaged at each testing point across the complete 37 year time frame. Once again, these comparisons were generally found to be very close to one another, with the vast majority of locations seeing an error within $\pm 5\,\%$ and the average bias error seen at $-0.551\,\%$. Slightly larger errors, near to $9\,\%$ were often seen in regions with high terrain complexity, such as in the Alps, however this is most likely a result of differences in the optimal tilt assumption.

Through these comparisons, it is concluded that the general PV simulation scheme is highly reliable in both the temporal as well as spatial contexts. Nevertheless, the reader is reminded that this scheme is dependent on the use of appropriate PV

[28] Chosen as it is a good trade-off between computation effort and a well resolved coverage over Europe (191,917 points)

system design parameters, such as module selection tilt and azimuth.

4.6 Summary

This chapter has detailed the background of PV energy, including the variability of solar energy in the temporal, spatial, and module-orientation domain. Additionally, the operation of PV modules from a physical standpoint, differences between the open-field and rooftop PV domains, and trends in the PV industry have been described. As the operation of PV distribution and generation is fundamental to all three overarching research questions, all of these issue which have been discussed are highly relevant to this thesis' aims. Finally, when discussing the treatment of PV modeling approaches in the literature to evaluate PV potential on the European stage, it was seen that no previous study has considered this issue in as much detail as is performed here.

The developed model stands out from past approaches seen in the literature by considering a detailed application of land eligibility and explicit PV park placement and the identification rooftop zones within residential areas across Europe. The treatment of rooftop orientations in the current thesis is not as advanced as that of studies which perform, for example, explicit LIDAR-based investigations of rooftop orientation and availability, however as this type of approach is not yet feasible on the European scale it could not be incorporated here. Nevertheless, the specification of module selection tailored to a 2050 context and the ability to perform full hourly simulation of each individual PV park and rooftop area over a 37 year time frame has, until now, not been seen in the literature. In addition to the primary setup of the PV simulation scheme which has been described here, several sensitivity analysis have been promised which will be discussed in the later results sections; these include the sensitivity to using the COSMO-REA6 climate model dataset instead of the MERRA dataset for simulation.

Chapter 5

VRES Lull Analysis

Building on top of the distribution and simulation methods for wind and PV generators found in the previous chapters, which serve to answer the first two overarching research questions of this thesis, the discussion at last focuses on the topic of the occurrence of VRES lulls; thus addressing the third and final overarching research question. In the current chapter, a brief background of VRES lulls is provided focusing on the physical phenomena and implications of their occurrence as well as how this issue has been considered in the literature. Afterwards, the methodologies chosen to investigate this topic in the current work are described. These include an introduction to the chosen energy system scenario which will be at the center of these evaluations, a general lull identification algorithm, the specific contexts in which lulls will be evaluated here, and finally a note on how the probabilistic results presented in the next chapter should be interpreted.

5.1 Background Principles

To aid the discussion of VRES lulls and furthermore to give the reader a clear understanding of one way they could be directly investigated, the exemplary study of Huneke et al. [331] is described. This serves to identify the ideal role such analyses could play and what information it should be able to provide to energy system decision makers and stakeholders.

In their work, Huneke et al. [331] investigate the possible occurrence and impact of VRES lulls on a simulated German energy system around the year 2050, which included the activity of fossil fuel, hydro, and other generators. In their scenario, the fleet of on- and offshore wind turbines and PV systems amounted to a total capacity larger than four times the current level, and these were simulated over many years of time series weather data. They also considered an increased future electricity demand as well, including 42 million electric cars, for multiple years of demand data time series. Scouring through the resulting data, they looked for VRES lull events which they define as the time periods where stored hydro and electricity import options were not available, and VRES generation was not enough to satisfy the demand. In the end, they located the single period when the German energy system would experience its deepest VRES lull, occurring, in their analysis, between the 24^{th} of January until the 7^{th} of February. Within this period, a total of $4.47\,\text{TWh}$ of electrical energy would have to be sourced from a ”non-renewable” technology in order to maintain the energy system’s operation, and the largest residual load was over $50\,\text{GW}$; amounting to $57.2\,\%$ of the average electricity demand.

Results from their lull investigation are provide actionable information to the energy community. On the one hand, although several energy sources could be tapped to fill this deficit, the 4.47 TWh deficit is a direct measure of how much electrical energy storage (EES) would have been necessary for the energy system to pass through this VRES lull. On the other hand, considering that Germany's average power demand today is in the range of 60 GW, the 50 GW of backup power needed at the most strenuous moment is by no means trivial. If a 100 % renewable system were sought after, one possibility is that this EES could come in the form of batteries [332]. The Hornsdale Power Reserve built in South Australia, the largest battery storage system to date at 100 MW and 129 MWh, is an example of the capabilities of conventional battery technologies within the energy system [333]. Yet this solution is a far cry from the storage requirements estimated by Huneke et al. to withstand the largest German lull [331]; where that at least 500 Hornsdale-like systems would need to be installed to cover Huneke's residual load, and over 36,000 Hornsdale-like systems would be needed to cover the estimated deficit. Another possible energy option would be the use of hydrogen salt caverns [334]. These artificial caverns can be built in deep geologic salt deposits within salt domes and thin-bedded salt formations. Surrounded by a malleable salt boundary, large quantities of hydrogen could be safely stored in these caverns and, due to their immense volume of 500,000-750,000 m^2 each, total storage potential of a single cavern is likely to be between 100 and 220 GWh [103].

There are also several drawbacks to Huneke et al.'s approach that limit the usefulness of their results. Most clearly, the results are only in context to Germany and therefore don't comment on similar lull events for other countries in Europe, much less for all of Europe. Moreover, the 14 day lull period underpinning the magnitude of their EES and backup estimates is an exogenous assumption; meaning that lulls which might have lasted longer or shorter are not considered. It is certainly possible for a VRES lull to extend beyond the two week period, but with less extreme residual loads or, conversely, to be shorter yet with very extreme residual loads. Moreover, Huneke et al.'s result says nothing about how likely such a lull event is to occur. Will it happen at least once every year? Or once in 100 years? Risk management considerations such as the likelihood of occurrence must be taken into consideration at the energy system planning level. While the implications of an in depth VRES lull investigation are quite clear in regards to future European energy system, a fundamentally-derived and probabilistic consideration of these lull occurrences has, until now, not been performed for the German scope, much less the European one.

5.1.1 Causes of Lulls

Here the reader is provided with a brief overview of the weather and climatic phenomena which could lead to VRES lulls. This is implicitly related to VRES occurrence and imparts unto the reader why a detailed spatial representation of these phenomena is a necessity for their evaluation.

As the Earth's climate system and stochastic weather phenomena are highly com-

plex, the causes of VRES lulls are widespread. On the mesoscale, localized events such a low pressure zone can cause surface winds to blow towards an updraft at its center, causing the formation of cloud coverage and, often, precipitation within the region. While the enhanced surface winds may be a boon to wind energy, the cloud coverage and precipitation will greatly hinder PV production [211, 335]. Similarly, depending on topography and the distribution of pressure differentials, developing wind patterns can result in a spatially complex wind speed arrangement [336, 337]. Turbines that are by chance in the resulting low wind speed zone will naturally generate less energy. Similar dynamic can occur for offshore wind turbines [338], for which mesoscale oceanic eddies have long been the focus of research [339]. However many of these dynamics are localized and, often, small in comparison to the overall electrical energy system, leading to the common speculation that their impact on VRES generation can be averaged out over a large enough area [340–342]. Especially when combined with a future scenario that includes demand flexibility, it is often concluded that these localized fluctuations can be effectively managed and that a fully renewable energy system is possible [343].

Nevertheless, larger synaptic scale developments can be observed that directly impact VRES generation on a continental scale. In the European context, some examples of which are known as North Atlantic Oscillations (NAOs) [344, 345]. These events can occur on annual to decadal cycles, are characterized by large pressure differentials over the Atlantic Ocean, and their impact on the energy system is of high concern [110, 346]. Grams et al. [15] discuss seven distinct NAO scenarios differentiated by the spatial positioning of low and high pressure regions and showed that each scenario can have a wide spread and lasting impact on a wind-based European energy system. They show that a ”European blocking” regime, where a broad high pressure anomaly is situated over the North Sea region while an equally broad low pressure anomaly is situated over Greenland, would be most disastrous to the European energy system as a whole; resulting in an estimated $20\,\%$ reduction in wind generation across the continent over the whole winter in comparison to a normal winter. The spatial implications are also quite interesting, since Grams et al. also conclude that the same event could lead to a significant increase in wind generation within the Balkan region. During a ”Greenland blocking” regime, another NAO scenario, where a high pressure anomaly over Greenland and Iceland is coupled with an elongated low pressure anomaly west of the Azores islands in the Atlantic Ocean, wind generation can be reduced by as much as 20 to $30\,\%$ in Central and Northern Europe. This scenario would have minor impact in the Balkans and Eastern Europe, and would increase generation in Italy and the Iberian peninsula. Holistically, a ”Greenland blocking” event could reduce European wind generation by around $15\,\%$ over an entire winter [15]. As a result of NAOs and other anomalous synaptic scale events, many researchers have concluded that VRES lulls would certainly be observed across a European scope [347–349], which can in turn impact the storage and backup needs [350, 351]. Furthermore, the effect of climate change on these anomalous events has been shown to increase EES storage and backup needs in comparison to today [352].

5.1.2 Presence in the Literature

When reviewing literature on the topic of VRES lulls, it is apparent that very few have addressed the topic in a manner directly comparable to the approach proposed in this work. For those that do offer comparable qualities, there are significant similarities between studies. Therefore only a representative set of these sources are discussed here for the primary purpose of identifying gaps in the literature, as well as to introduce quantities which can be directly compared to in the final chapters.

Besides the study of Huneke et al. [331], a few studies have delved into topics relating to VRES lulls, which includes the rate of lull occurrence, the time spans spent within a lull, or the energy deficits experienced during lull lifetimes. Handschy et al. [340], for instance, took a look at wind availability in the United States by simulating wind turbines at nine locations spread across the country. They clearly showed that with more interconnections between generators, the number of hours spent below a low capacity factor threshold becomes exponentially less. Looking to Europe, Weber et al. [352] modeled wind turbines across Europe using the outputs of multiple climate models and, assuming a fully interconnected Europe with no grid restrictions (e.g. "copper plate"), simulated an electricity system with a variable amount of EES. Weber et al. found an explicit relationship between the amount of EES versus the non-VRES backup that would be required over the course of a year. Even with EES storage totaling to $1\,\%$ of the total electricity demand, a truly massive amount of EES at the European scale, they expect that about $15\,\%$ of demand would still need to be satisfied by non-VRES sources. Using future-projected weather data with strong climate change forcing, they also show that this backup reliance would increase in the future by about $1\,\%$ for the same quantity of storage. Weber et al. also look at the distribution of time period durations where cumulative wind generation is below its average generation. They find that about one in ten wind energy lulls would last at least $100\,\text{hours}$, and that one in 100 lulls would last at least 350 to $600\,\text{hours}$ (14.6 to $25\,\text{days}$) depending on which weather source was used. Lastly, Weber et al. repeated their analysis over an autarkic Germany (no electricity exchange), and found that the relative backup necessity per EES fraction nearly doubles, and the "one in ten" lull duration increases to $6.25\,\text{days}$, on account of the smaller spatial scope. Similarly, the "one in a hundred" lull durations decrease for the German case to between 14.58 and $17.50\,\text{days}$.

Another prime example of VRES lull investigation is given by Raynaud et al. [347], where VRES lulls (or "droughts" as the authors refer to them) are evaluated over a copper plate Europe with a high share of onshore wind, PV, and hydro run-off-river capacities. They define two lull regimes, "severe" and "moderate", given as time periods where VRES generation falls below 20 and $50\,\%$ of the average generation. The VRES technology options are evaluated both independently as well as collectively, and results are reported on a per-country basis. Raynaud et al. find that countries experience, on average, 40 to 60 moderate wind energy lulls a year and 10 to 25 moderate PV energy lulls. In the case of wind, all countries are clustered around an average moderate lull length of $2\,\text{days}$ to $3\,\text{days}$, while for PV a large

spread is shown between 2.5 days, seen in Spain, to 13 days, in Finland and Norway. In the severe case, wind energy lulls last slightly shorter, 1 to 2 days, while frequency drops significantly for some countries, for instance Italy only observes 5 severe lulls per year, but hardly changes for most others. For these latter countries, Raynaud et al.'s result suggest that a large portion of all wind energy lulls experienced are severe. Severe PV lulls are much varied and show an asymmetric distribution. According to the authors Spain has the shortest severe PV lulls at a single one-day lull per year, while Norway and Finland show the same duration as for moderate lulls but with only 7 to 10 occurrences per year. The asymmetry quality comes from countries like Germany, where around 20 severe lulls lasting on average 2.1 days are found. Using the energy share mix determined in a previous analysis [353], the moderate and severe lulls are also evaluated collectively. In this case moderate VRES lulls are between 2 and 3 days for all countries and occur between 4 and 18 times per year depending on the country. Severe lulls, meanwhile, become nearly non existent except for Belgium and Finland who each see 3 1.5 day lulls per year.

While great additions to the literature, several drawbacks of these exemplary approaches can be seen. First and foremost, neither Weber et al. [352] or Raynaud et al. [347] considered the role of an electricity grid, meaning that grid limitations and VRES curtailment are not factored in to their analyses. On top of this, each study used fairly rudimentary VRES simulation techniques: The low temporally resolved data, 3-hourly for Weber et al. [352] and daily for Raynaud et al. [347], is also likely not detailed enough to capture shorter time scale weather events and are prone to longer lull estimations since short high generation hours will be averaged out. The spatially uniform and contemporary wind turbine and PV module design assumptions mean that their results do not reflect the expected future behavior of these technologies. And their overly-simplified distribution of VRES generators across the European landscape might not produce a realistic generation profile. Moreover, each study includes an assessment of lulls in comparison to temporal demand fluctuations, but the issue is not handled in a detailed manner in either case. Weber et al., for instance, do not consider how the demand time series may evolve into the future and only consider a single year of demand data, while Raynaud et al. only consider demand on a daily level. Both studies agree that the inclusion of demand into VRES lull occurrence evaluation does not have a large impact on the results; however this is most likely due to the framework of their studies where, in both cases, total annual VRES generation is scaled to match to the total demand. Finally, in specific regards to their results regarding lull occurrence, the outcomes of these analyses do not offer highly actionable information in the eyes of energy system planners and decision makers where risk management is a concern. For instance, as mentioned, Huneke et al. [331] give the largest lull span in Germany, but don't comment on how often it could occur. Raynaud et al. only specify lull lengths and occurrence on an average basis, which cannot communicate the most dire lulls around which an energy system will likely be designed, and the duration distributions Weber et al. provide only comment on lulls in reference to each other and are thus distinct from occurrence rates. Finally, neither Weber et al. or Raynaud et al. provide any information in regards to the depth of lull deficits.

Although they don't directly deal with the issue of VRES lulls, other studies of note which will come up again later in this thesis include: Wohland et al. [348], who considered low wind availability synchronism between national and European scopes. Ravestein et al. [349] who, similar to Grams et al. [15], also investigated the impact of NAOs to European wind and PV generation. In a fully renewable European energy system, Rodriguez et al. [354, 355] investigated transmission needs, and Rasmussen et al. [351] considered the relationship between storage and balancing needs. Finally, Schlachtberger et al. [356], Rodriguez et al. [357], Cebulla et al. [350], Child et al. [358], Becker et al. [359], and Zappa and van den Broek [44] each evaluated RES-based European energy system designs.

5.1.3 Summary and Outlook

A higher reliance on VRES within Europe's energy system is clearly expected into the future, and thus the unavoidable underlying climate and weather phenomena, such as NAOs, which give rise to VRES lulls will become more and more of a concern; and may even increase in intensity into the future due to climate change. Nevertheless, there has been frequent speculation that a broad enough geographic spread of VRES generators, a clever technology mix, and the encouragement of flexible demand measures could be enough to ensure supply stability in a predominantly VRES-based energy system. Recent investigations into VRES lull occurrence, however, seem to suggest that this may not be the case without large scale EES and backup measures alongside the VRES generators. A few issues that these studies tend to agree on are that: a larger spatial scopes reduces lull occurrences, a strong dependence on spatial context exists, a wind-PV combination produces less lulls than either separately, and finally that the lull occurrence shows little relation to demand and is thus primarily driven by the generation profile.

In order to improve upon the efforts previously made in the literature, several efforts could be made. Chief among them, an exquisitely detailed consideration of VRES generation could be employed to ensure a realistic generation profile. Intrinsically this would entail a detailed geospatial generator distribution that avoids ineligible locations and prefers economically-suitable locations; a role which is filled by the methods discussed in Chapter 2. Additionally this should include a projection of VRES technology designs such that the VRES lulls are evaluated in context of the energy systems wherein their occurrence is most relevant. And finally, detailed simulation of all VRES generators should be built on top of the fundamental operating principals of these technologies as well as high temporally and spatially resolved weather data. Both of these issues are addressed in the wind and PV simulation methods used in this work, as discussed in Chapters 3 and 4. Outside of the VRES generation, improvements should also focus on the lull evaluation procedure. Incorporation of grid dynamics is clearly a necessity, as is an improved comparison against demand profiles. Lastly, results could be formulated in such a way as to improve their actionable quality; such as by providing probabilistic occurrence rates for both the time spans and energy deficits of these lulls, as well their spatial relations.

Building atop the previous discussions, the remaining portions of this chapter

present the setup and evaluation procedures in the VRES lull analysis. The first section of this chapter will focus on the energy system scenario constructed for the purpose of this analysis. After this, the lull measurement methodologies will be given. Since this topic is not extensively researched in the literature, meaning a conventional measure of VRES lulls has not been established, and therefore several different measures will be investigated here in varying contexts. Finally, since results of the primary lull evaluation are explicitly tied to the constructed scenario, this section concludes by presenting the various sensitivity analyses which are performed to observe lull behavior under different analysis conditions.

5.2 Analysis overview

In order to investigate the future occurrence of VRES lulls in Europe, the scenarios developed in line with the European Commission's E-Highway 2050 project are suited best among other scenarios in the literature. This is because the E-Highway scenarios consider a relatively highly detailed regionalization of Europe (Figure 5.1), as well as projections of future electricity demand, renewable and non-renewable generator capacities, and grid development until 2050 [296,300]. In total, the E-Highway project developed 5 contrasting scenarios, each under fundamentally different future circumstances, which all achieve $80\,\%$ reduction of green house gas emissions compared to 1990.

Of the available E-Highway scenarios, the "100% RES" scenario is chosen for use here due to several reasons. Primarily, this scenario has the highest proportional reliance on VRES sources compared to the other E-Highway scenarios. Secondly, it has the second highest gross electricity demand and only a $3\,\%$ reliance on the surrounding areas. Put together, these characteristics should correspond to the most frequent and most exaggerated occurrence of VRES lulls. An explicit description of this scenario will be provided in the following section.

Since there is no clear convention as to how VRES lulls should be measured or compared, several lull evaluation contexts will be investigated in this work to span a range of interesting perspectives. In the general sense, a threshold is set for each of these contexts and the periods during which available VRES production falls below this threshold constitutes a VRES lull.These contexts differ in the VRES technologies which are considered and in the method by which the lull-threshold is set. Three lull evaluation contexts are therefore considered: "Generation Threshold" in which VRES generators are considered independent of demand and grid limitations, "Versus Demand and Average Backup" in which VRES generation is compared against demand and the average backup[1] without incorporating grid dynamics, and finally "Grid Limited and Backup Dispatch" in which VRES generation, demand, and grid limitations are all considered in concert with one another. Detailed descriptions of each of these contexts will follow in the upcoming sections.

Besides the lull evaluation contexts which could be considered when discussing

[1] In the form of Biomass, Hydro, Import and Export

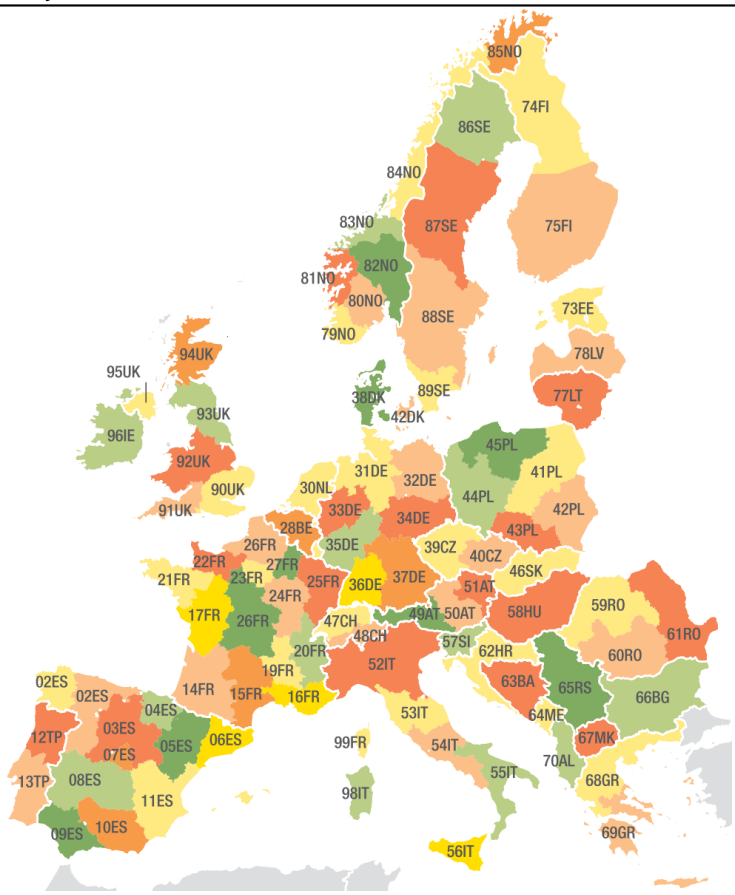

Figure 5.1: Regionalization used in the E-Highway 2050 study. Extracted from [296]

VRES lulls, the spatial context is also relevant. Since weather patterns evolve both spatially as well as temporally, several geospatial scopes are considered in order to observe how this effects the occurrence of VRES lulls. Therefore, the three lull evaluation contexts are evaluated once for the entirety of Europe, for a set of central European nations, for several leading nations in terms of future electricity demand[2], and finally for the North Rhine-Westphalia region in Germany on account of both its high industrialized activity and high population. The nations considered in the ”central” region are: Germany, France, Italy, Switzerland, Luxembourg, Belgium, and the Netherlands. Furthermore, the specific countries investigated are Germany, Spain, France, Italy, and the United Kingdom.

[2] Determined by E-Highway

5.3 Scenario Description

As with the other scenarios, the E-Highway's "100% RES" scenario [300] was contrived in accordance with a predefined set of energy-related circumstances and perspectives. As the name suggests, for the case of "100% RES" this included a communal European desire for a 100% renewable energy system, with some connections to North Africa, as well as the installation of both large and small scale storage technologies to ensure a balanced grid despite VRES variability. The scenario assumes that there is a very positive public attitude towards renewable technologies, while at the same time there is a very negative attitude towards nuclear and shale gas. In terms of electricity demand, the scenario includes a marked increase in energy efficiency, partial electrification of the heating and industrial sectors, electrified mobility via the use of battery electric vehicles, and a strong social drive towards "greener" behaviors. As a result of this, total annual electricity demand in Europe is expected to be around 4329 TWh; 31.2 % higher than the European electricity consumption in 2016 of 3300 TWh [10]. Demand-side management and flexible electric vehicle charging are also incorporated in E-Highway's pre-analysis stages by applying peak-shaving to the demand time series of each region.

Working within this framework, the E-Highway project performed a series of telescoping energy system optimizations alongside frequent stakeholder review sessions to ultimately lead to a final energy system design. Figure 5.2 shows the distribution of the resulting renewable energy capacities across Europe along with the designed grid's line capacities. Several renewable installation domains can be seen in this figure. Offshore wind energy, for instance, is only installed in the North Sea and around Denmark, while onshore wind can be found, to at least a small extent, in all regions. In total, wind energy possesses the predominant share of generation capacity throughout much of north-central Europe, North-Western France, the United Kingdom, the Baltic states plus Finland, and parts of Spain and Greece. Conversely, PV is also seen to have a significant portion of generation capacity across most of Europe, with the exception of Scandinavia. PV is also is the primary generator in most of Central and Southern Europe. Hydro generators, in the form of run-off-river (ROR), pumped hydro storage (PHS), and hydro reservoir possess the largest shares in Norway, most of Sweden, regions near to the Alps, Northern Greece, and Bulgaria. Biomass generators are also distributed across all of Europe to serve as a backup generator option, but are never seen as the dominant generator within a region. Full tabulation of generation capacities for each E-Highway region, as well national total, can be found in Appendix J.

Electricity demand distribution across Europe is shown in Figure 5.3. Northern Italy distinguishes itself as the region with the largest demand of 200 TWh, followed by the Netherlands (161 TWh), central England (162 and 158 TWh), and North Rhine-Westphalia (145 TWh). Nationally, Germany has the highest national demand at 666 TWh, followed closely by France with 649 TWh. For more detailed information, the annual demand of each E-Highway region is also tabulated in Appendix J.

In order to simulate the hourly operation of the European energy system, the E-

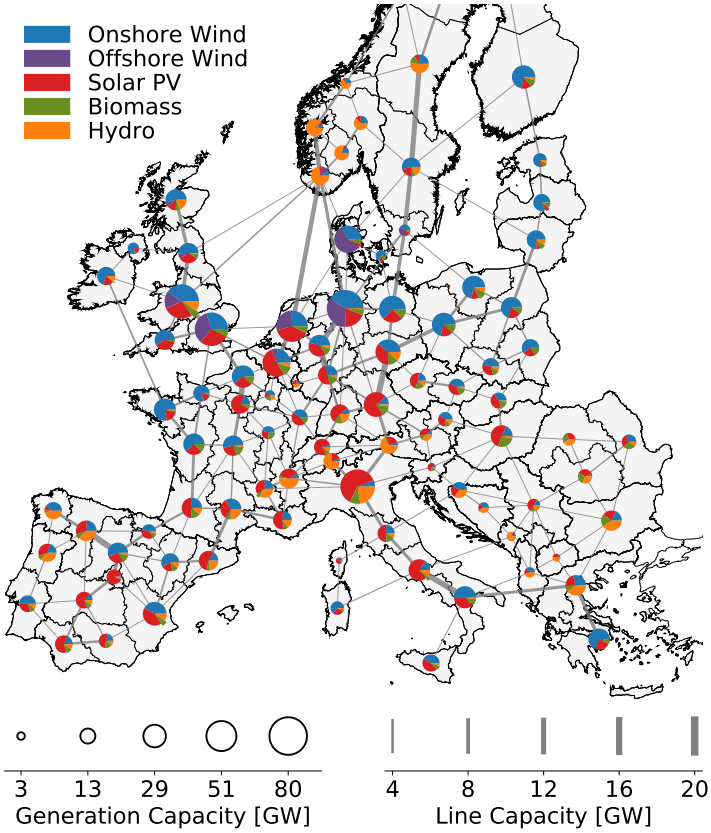

Figure 5.2: Renewable energy capacities and grid line capacities in the E-Highway's "100% RES" scenario. Plotted with data from E-Highway D2.1 [300]

Highway study makes use of ANTARES, the Monte-Carlo-based power system simulation tool discussed by Doquet et al. [360]. Three different sets of demand time series for all regions were created using ENTSO-E historical demand data between 2010 and 2012. Similarly, eleven generation time series sets for onshore wind, offshore wind, and PV were produced, as well as three generation time series for hydro technologies corresponding to dry, wet and average years. The simulation approach randomly selects a demand year and a generation year independently for each renewable technology; leading to over 20,000 possible combinations. These combinations are then simulated using the ANTARES software to check for system adequacy. As a result of this process, the E-Highway project found the typical energy balance for all countries which is summarized in Table 5.1; where only the results which are relevant to the discussion of this work is shown.

Several observations can be made from Table 5.1 which will become relevant later

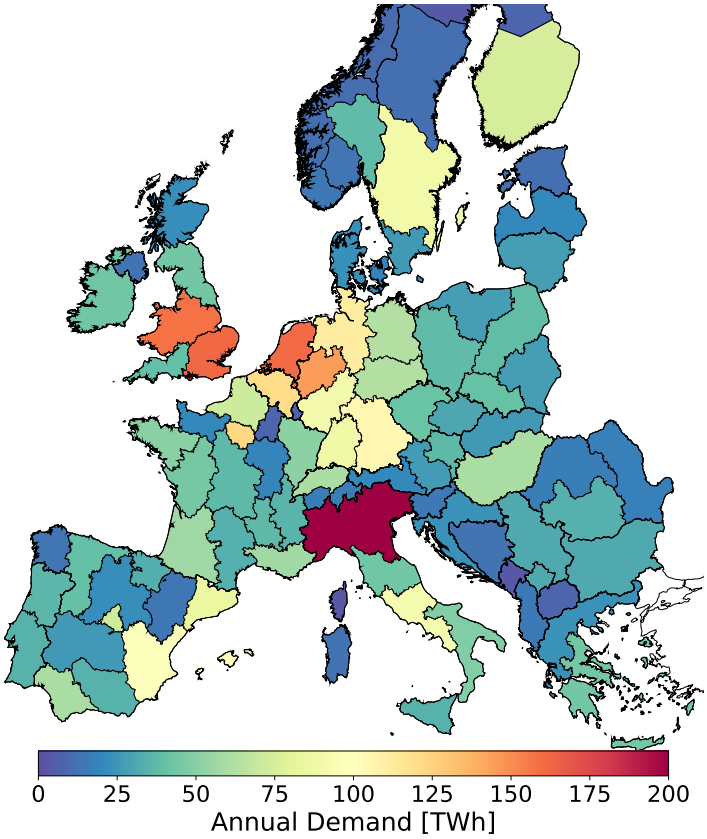

Figure 5.3: Annual demand per region in E-Highway's "100% RES" scenario [300]

on. For one, total curtailment across Europe reaches 273 TWh across Europe, which represents 6 % of total VRES generation. Additionally, it is clear that many nations are designed as net importers of electricity, while others are designed as net exporters. Germany, for example, has the 3rd most generation of all countries but still relies on imports for 26.8 % of its electricity demand. In contrast, Denmark and Norway are each net exporters of electricity with totals reaching to 52 and 57 %, respectively, of their average annual demand.

Table 5.1: Overview of results obtained by E-Highway in the ”100% RES” scenario [296, 300]

Region	Demand [TWh]	Generation [TWh]	Import (+) Export (-) [TWh]	Curtailment [TWh]
Europe	4297.59	4487.73	82.16	272.78
Germany	666.15	503.32	178.55	15.72
France	656.13	589.44	85.91	19.40
Spain	499.23	449.99	67.78	18.57
United Kingdom	438.92	583.90	−77.20	67.95
Italy	431.16	336.86	111.05	16.75
Poland	173.43	205.33	−22.01	9.88
Netherlands	160.24	137.84	34.33	11.94
Sweden	131.12	175.83	−36.20	8.51
Belgium	121.19	71.68	51.38	1.87
Norway	101.69	267.08	−152.55	12.85
Austria	91.42	94.54	−2.72	0.41
Finland	82.31	99.88	−8.98	8.59
Switzerland	80.62	63.05	17.82	0.27
Czech Republic	71.81	52.38	19.85	0.42
Portugal	71.35	87.68	−13.52	2.82
Romania	68.30	79.81	−10.36	1.16
Greece	68.23	115.83	−37.32	10.28
Hungary	59.41	52.85	7.48	0.92
Ireland	43.31	46.22	4.27	7.24
Denmark	42.53	169.92	−89.04	38.34
Bulgaria	32.01	37.33	−4.50	0.83
Serbia	31.71	27.79	4.53	0.61
Lithuania	28.99	41.20	−8.34	3.86
Slovakia	26.69	29.29	−1.98	0.62
Croatia	24.13	24.64	−0.32	0.19
Latvia	20.92	37.15	−8.86	7.37
Albania	14.97	19.67	−4.39	0.30
Slovenia	14.94	14.76	0.33	0.15
Bosnia & Herz.	12.75	28.95	−15.94	0.26
Estonia	12.67	20.59	−3.53	4.39
Macedonia	8.41	7.56	1.05	0.20
Luxembourg	7.63	3.28	4.40	0.05
Montenegro	3.21	12.08	−8.80	0.07

5.4 VRES Lull analyses

5.4.1 Scenario Deviations

The framework developed by E-Highway is, as much as possible, unaltered from its source as it represents an internally consistent scenario across Europe which has

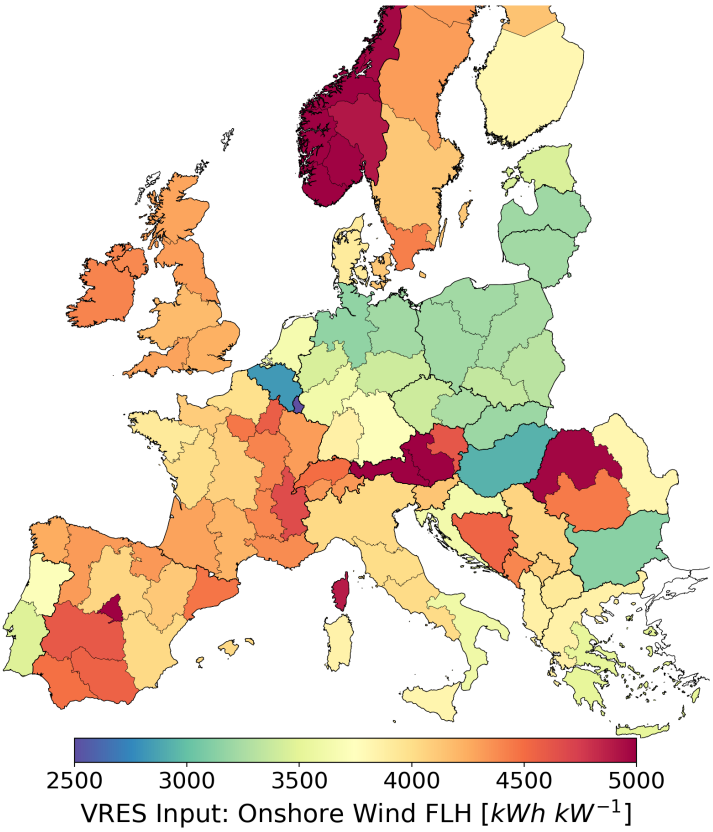

Figure 5.4: Average Onshore Wind FLH over E-Highway regions from the simulation schemes developed in this work

been vetted by the European Union and numerous independent research groups. Most notably, E-Highway's simplified grid topology as shown in Figure 5.2 is used, despite recent examples in the literature that much more detailed European grid simulations are possible [361, 362]. Also the total demand and total generation capacities for all regions as stated by E-Highway are left unchanged.

The only effective change which is made to the original scenario is the substitution of the highly detailed VRES generation time series from the methods developed and discussed previously in this work. Furthermore, LCOE sorting within each region is used to select individual turbine and open-field park locations as it constitutes a straight-forward and unbiased sorting mechanism. In this way, the results found for the VRES lull analysis will represent the best possible VRES performance, although it likely will not reflect the most realistic wind turbine and PV installation patterns. Because of this, a sensitivity to the sorting method will be considered to

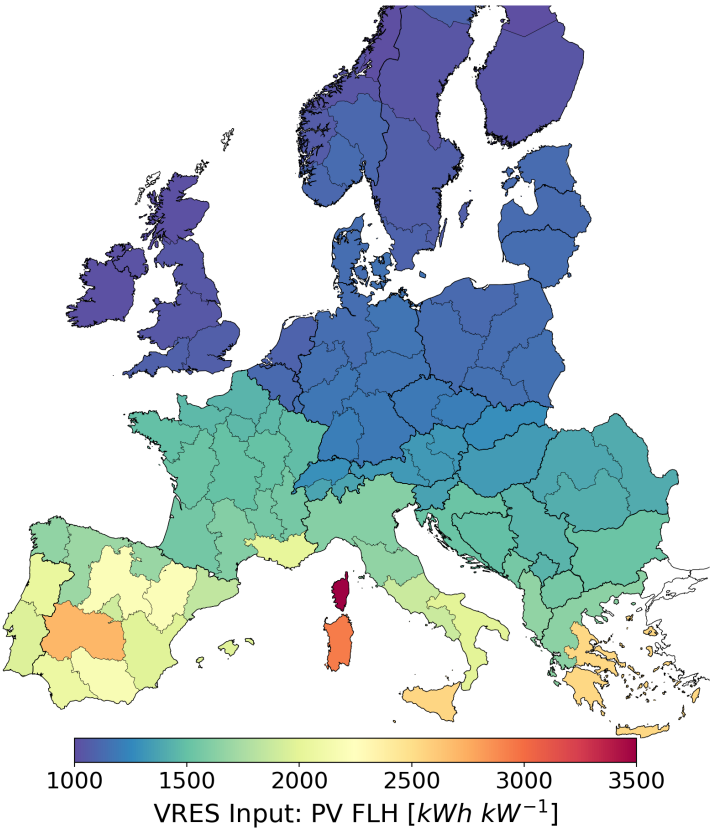

Figure 5.5: Average PV FLH over E-Highway regions from the simulation schemes developed in this work

look at this issue in more detail in the final chapter of this thesis. Moreover, area exclusivity is not enforced between open-field PV parks and onshore wind turbines as there are several examples of PV-Wind hybrid parks being considered in the literature [363, 364], and that extra shading losses onto the PV panels due to nearby turbines are expected to be small [365]. Meanwhile, for rooftop PV, the desired capacity is always assumed to be spread evenly in proportion to rooftop area across the associated region due to its unique market mechanisms. Lastly, since making a prediction on the final shares between open-field and rooftop PV would be highly speculative, the total PV capacity specified by E-Highway will be evenly split between these two PV domains; which is plausible considering the current shares given in Figure 4.10 [12]. In rare cases[3], however, $50\,\%$ of the E-Highway's prescribed PV capacity exceeded either the open-field or rooftop PV potential available

[3] For Switzerland and a few regions in Germany.

for that region. In these cases the full potential for the limited PV domain is utilized and the remaining reliance was placed on the other. Using this procedure, the average FLH derived for each E-Highway region are shown in Figure 5.4 for onshore wind and Figure 5.5 for PV. To note, the average FLH over Europe seen here comes out to 3815, 4487, and 1491 for onshore wind, offshore wind, and combined PV, respectively. Although these values are high compared to today's standards, they are perfectly in line with future estimates of, for example, JRC [160] who estimate that the average FLH observed in Europe in 2050 would be 3942, 4203, and 1489[4] for the same three technologies. Furthermore, due to the LCOE-sorting approach to turbine and PV park selection, these FLHs also represent the best possible FLH out of the full potential in each E-Highway region. A much more detailed discussion of these the full wind and PV potentials at the European and national levels will be provided in Chapter 6. As before, tabulation of the annual generation potentials which result from the use of this work's simulation models can be found in Appendix J for each E-Highway region and each country.

Besides this, the scenario framework provided by E-Highway does not include any time series data. Therefore, regional time series data for demand, ROR generation, and hydro inflows were recreated as much as possible in the manner described by E-Highway. As the precise implementation of these items are discussed at length by Syranidis [362], they are not repeated here. Furthermore, offshore wind generation is also produced in a manner similar to the onshore wind and open-field PV procedures used in this thesis. A full description of this is available from the publication of Caglayan et al. [102], and so is also not repeated here.

5.4.2 VRES lull algorithm

A general algorithm for determining VRES lulls is adapted to each lull evaluation context and regional scope. The process begins by defining a lull threshold which, when not satisfied by VRES generation, initiates a lull event. Depending on the context, this threshold can be either constant or time-dependent. Once a lull is initiated, two counters are initialized to zero: one for the *span* of time spent in the lull, and one accounting for the *deficit* energy throughout the lull. After each hour, the energy difference between the VRES generation and the lull threshold is found, the span counter is incremented by one hour, and the energy difference is added to the deficit counter. Once the deficit counter returns to zero, meaning VRES generation has offset the previous deficiency, the lull event is concluded.

With this algorithm, it is evident that a VRES lull is composed of both the time in which generated energy is less than a desired amount, and furthermore continues until that energy is recompensed to the energy system via VRES generation. During a lull period, it is possible that the deficient VRES generation could be supported by a fast-acting dispatchable generator option; such as from conventional gas turbine generators, or by means of re-electrification within a power-to-hydrogen energy scheme [366]. Nevertheless, this lull algorithm makes the most sense if

[4] Estimated for open-field PV.

one assumes that, within a single lull period, a lossless storage option is in place within the regional scope that is capable of providing back-up to VRES generators anywhere in the region. Whether this storage option is realized with batteries, chemical carrier storage in tanks or underground caverns, flywheels, or any other storage technology, is not investigated in detail here. It is clear that a later, more detailed, exploration of VRES lulls should also consider the dynamics of these storage options at sub-regional scales. For this reason, and along with the earlier point of LCOE-sorting, the current set-up should be viewed as an investigation into an optimistic case of lull occurrence.

5.5 Analysis Contexts

As mentioned, multiple lull evaluation contexts are investigated as there is no consensus in the literature regarding how VRES lulls should be quantified and, thus, a broad approach is taken here. Three contexts are considered, named "Intermittent Generation", "Residual Load with Basic Backup", and "Constrained Grid with Dispatchable Backup", and are summarized in Table 5.2. These will be described in greater detail in the following sections.

Table 5.2: Overview of lull evaluation contexts in which lulls will be evaluated

	Context	VRES Generation	Demand	Backup & Im/Export	Electricity Grid
1	**Intermittent Generation**	Time-series simulated in this work	None	None	Copper plate
2	**Residual Load with Basic Backup**	Time-series simulated in this work	E-Highway time-series	E-Highway hourly average	Copper plate
3	**Constrained Grid with Dispatchable Backup**	Time-series simulated in this work	E-Highway time-series	Power flow optimized	E-Highway interregional capacities

5.5.1 Context 1: "Intermittent Generation"

The "Intermittent Generation context investigates lulls originating from the VRES generators themselves, without any comparison against demand or trading in between regional scopes. In each case, the onshore wind, offshore wind, PV, and total VRES generation are all explicitly investigated by aggregating the sub-regional profiles. Furthermore, the lull threshold is chosen as $25\,\%$ of the average generation, meaning the threshold is, in this case, constant. As this threshold is arbitrarily chosen, a sensitivity will be performed to observe the impact of higher or lower values. Figure 5.6 displays an exemplary diagram for this context, in which the constant threshold is seen as the dashed line, around which an exemplary VRES generation

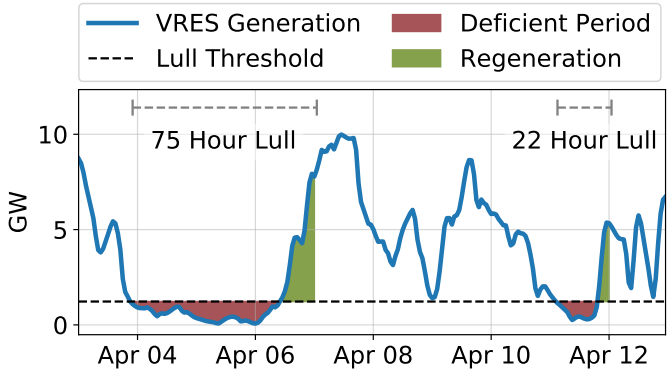

Figure 5.6: Lull diagram for the first lull evaluation context.

profile fluctuates. Once the generation falls below the lull threshold, for example on April 4^{th}, a lull event is initiated and continues until the deficit (shown in red) is offset by the super-threshold generation (shown in green), which in this case ends on April 7^{th}. For each lull event, the overall time span is recorded. Table 5.3 provides explicit threshold quantities for each VRES group and regional scope.

Table 5.3: Thresholds used for the "Intermittent Generation" context, broken down by VRES group and regional scope. In all cases, the threshold is determined as $25\,\%$ of the average generation.

Regional Scope	Average Performance [FLH]			Lull Threshold [GW]			
	Onshore Wind	Offshore Wind	PV	Onshore Wind	Offshore Wind	PV	All VRES
Europe	3815	4487	1491	82.74	14.71	28.18	125.63
Central	3735	4599	1468	31.11	6.05	14.89	52.05
France	4134	-	1599	14.65	-	4.70	19.36
U.K.	4255	4344	1056	11.31	4.61	1.81	17.72
Germany	3314	4720	1177	9.30	3.66	3.31	16.28
Spain	4204	-	2046	8.33	-	5.36	13.69
Italy	3810	-	1847	4.49	-	4.82	9.31
NRW	3444	-	1155	1.23	-	0.36	1.59

5.5.2 Context 2: "Residual Load with Basic Backup"

The "Residual Load with Basic Backup" context adds temporal interactions between VRES generation and the corresponding electricity demand. As before, when evaluating each regional context no active external trading is allowed and the lull computation is performed assuming a copper plate (i.e. region-wide time-series aggre-

gation). Lull thresholds are computed as constant values subtracted from the total time-series demand for the region in question; meaning that both the lull threshold and VRES generation fluctuate in time. Figure 5.7 depicts this set-up with exemplary demand and generation time series, where the total demand profile (shown in the background) is reduced by a constant amount to formulate the fluctuating lull threshold, given again as a dashed line. In the same way as before, the lull event is initiated when the total VRES generation profile falls below this threshold, and continues until the energy is recompensed by super-threshold VRES generation. In this case, however, both the span and largest deficit, seen in the top portion of Figure 5.7, are recorded for each lull event.

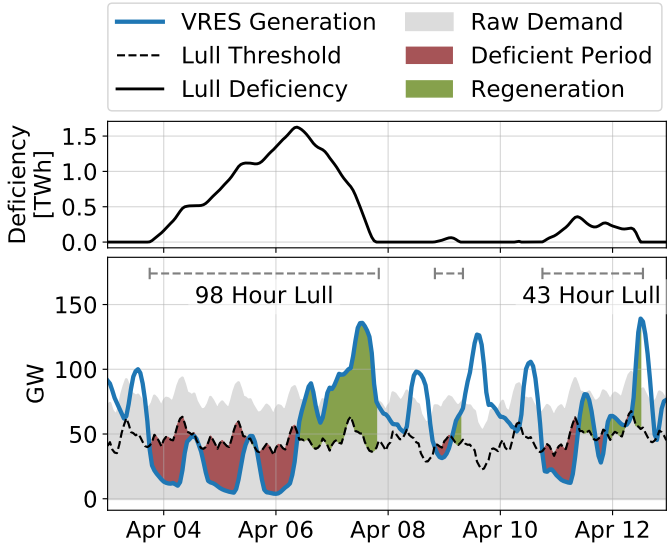

Figure 5.7: Lull diagram for the second lull evaluation context.

E-Highway's scenario was constructed with partial reliance on backup generation[5], as well as electricity imports and exports. However the E-highway scenario results only include the total annual usage and thus, without a simulation of the full energy system, it is not possible to predict their time-series utilization. Therefore, the lull threshold for each region is calculated using Equation 5.1; where $\overline{\mathrm{Biomass}}$ and $\overline{\mathrm{Hydro}}$ each represent hourly-averaged generation from these sources, and $\overline{\mathrm{Export}}$ and $\overline{\mathrm{Import}}$ each reflect the hourly-averaged exported and imported electricity. Note that some regions, such as Germany, were designed to be net importers of electricity while others, such as the United Kingdom, were designed as net exporters. Finally, as this threshold is only one example of backup capacity, the sensitivity of residual load lull occurrence as a function of the level of backup capacity will also be tested using Equation 5.2; where X is the overall backup percentage of a region and $\overline{\mathrm{Demand}}$ is the hourly-averaged electricity demand. Fur-

[5] In the form of biomass and hydro.

thermore, Equation 5.2 also shows how the lull threshold is strictly positive. Table 5.4 provides the average values for $\overline{\text{Biomass}}$, $\overline{\text{Hydro}}$, $\overline{\text{Export}}$, $\overline{\text{Import}}$, and $\overline{\text{Demand}}$ calculated from the E-Highway results [300].

$$\text{Lull Threshold}(t) = \text{Demand}(t) + \overline{\text{Export}} - \overline{\text{Biomass}} - \overline{\text{Hydro}} - \overline{\text{Import}} \tag{5.1}$$

$$\text{Lull Threshold} = \left\lfloor \text{Demand}(t) - \frac{X}{100} \cdot (\overline{\text{Demand}} + \overline{\text{Export}} - \overline{\text{Import}}) \right\rfloor_0 \tag{5.2}$$

Table 5.4: Average hourly utilization values used for Biomass, Hydro, Export, Import, and Demand [300].

Regional Scope	$\overline{\text{Biomass}}$ [MW]	$\overline{\text{Hydro}}$ [MW]	$\overline{\text{Export}}$ [MW]	$\overline{\text{Import}}$ [MW]	$\overline{\text{Demand}}$ [MW]
Europe	51,840	101,618	-	-	490,592
Central	24,963	24,886	-	55,187	242,366
France	9394	10,286	-	9807	74,901
United Kingdom	2308	2002	8813	-	50,105
Germany	7965	2816	-	20,382	76,045
Spain	5883	7276	-	7738	56,990
Italy	5168	6771	-	12,677	49,219
NRW	1735	613	-	4439	16,551

5.5.3 Context 3: "Constrained Grid with Dispatchable Backup"

At last, the "Constrained Grid with Dispatchable Backup" context simulates the constructed electricity system using the DC optimal power flow (DCOPF) approach. However, as this issue has received significant attention in the literature, such as by Syranidis et al. [362, 367], it is only vaguely summarized here. Figure 5.8 gives an exemplary setup of an electricity system that can be solved using DCOPF, and will be described in more detail in the coming paragraphs.

In essence, DCOPF solves the static power flow equations by relying on several simplifying assumptions of the electricity system. Within the temporal domain, DCOPF assumes a steady-state operation of the electricity grid, neglecting stability measures required on the millisecond to multi-minute timescale. Temporal evolution will then be solved for as independent snapshots of grid activity in steps of 1 hour, defined by the temporal resolution of the VRES inputs generated here. DCOPF also assumes linearization of the static power flow equations, bringing it closer to a simple representation of an ohmic circuit. The current work focuses on the transmission grid level, where the DC flow assumptions are most valid as a

result of small phase mismatches and higher line voltages [367]. Finally, DCOPF assumes a monopolist generation dispatch market, where all generation dispatch options across the entire electricity grid are controlled by a centralized authority whose objective could, for example, be the minimization of total annual cost or total emissions. While not a realistic scheme on the international scale, this assumption is crucial to allow for an unbiased and optimal electricity exchange solution to be found for each time step [367]. With these simplifications, the electricity system can thus be constructed as a graph where lines refer to the grid's transmission capacities, and nodes represent centralized demand centers. As seen in Figure 5.8, these centers can each have their own collection of consumers (such as residential, industrial, and commercial units) and producers (such as dispatchable conventional generators and nondispatchable VRES generators). Prosumers, here shown as a household with a rooftop PV system, as well as storage systems such as pumped hydro can also be included. Grid lines capacities can be specified between any two nodes, as shown by the largest transmission capability between nodes C and A. Generator options must each be given an operating cost in $€\,\mathrm{MWh}^{-1}$, which for VRES will equal 0. This allows the system to choose the order in which dispatch options are utilized. Once constructed, the entire system can be represented as a set of linear equations with constraints being the complete satisfaction of all electricity demand and maximal storage capacities, and with an objective function of minimizing total annual cost. This set of linear equation will be set up using the energy system analysis framework "PyPSA" [368], and will then be solved by means of the commercial optimization solver Gurobi [369].

As the objective of the power flow optimization is to minimize the total annual cost, cost parameters have to be provided for each generator option. For onshore and offshore wind, PV, and run-off-river the generation costs are set at zero so that

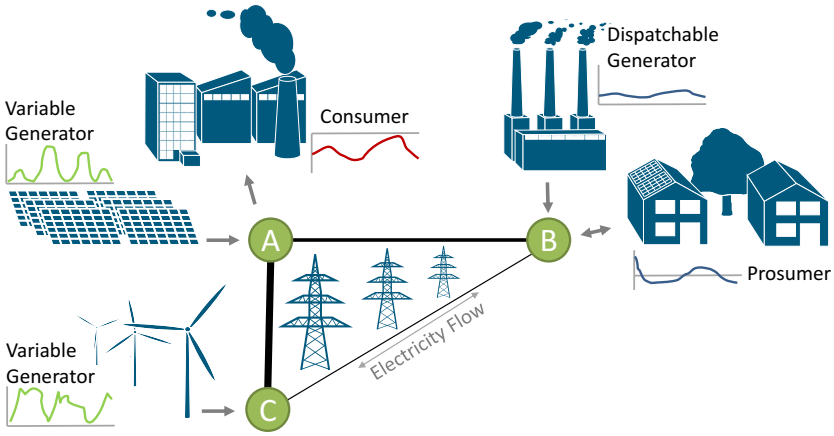

Figure 5.8: Exemplary power flow setup

these technologies are used as much as possible when they are available[6]. For biomass generation, a constant value of $11.3\,\mathrm{ct_{€}\,kWh^{-1}}$ [370] is assumed, while for hydro reservoir and pumped hydro generators a value of $2\,\mathrm{ct_{€}\,kWh^{-1}}$ is used [370]. Additionally, to ensure feasibility of the optimization, each E-Highway region is given an extra generator with an effectively infinite capacity which operates at a cost of $1000\,\mathrm{ct_{€}\,kWh^{-1}}$. Although total annual cost of the entire system becomes available by performing these optimizations, a proper simulation of the electricity market should consider dispatch options across multiple generator units in each region, each with their own operational cost, ramping rate and must-run requirements. As these issues are not dealt with in this work, cost results will not be discussed in detail so that emphasis can instead be placed on the primary issue of VRES lulls. Nevertheless, the reader is referred to the work of Syanidis [362] for a more comprehensive analysis of these issues on the European scale. In the end, the cost values chosen here are only in place to ensure that the proper dispatch order is followed, and are not expected to significantly influence the final outcome of this analysis.

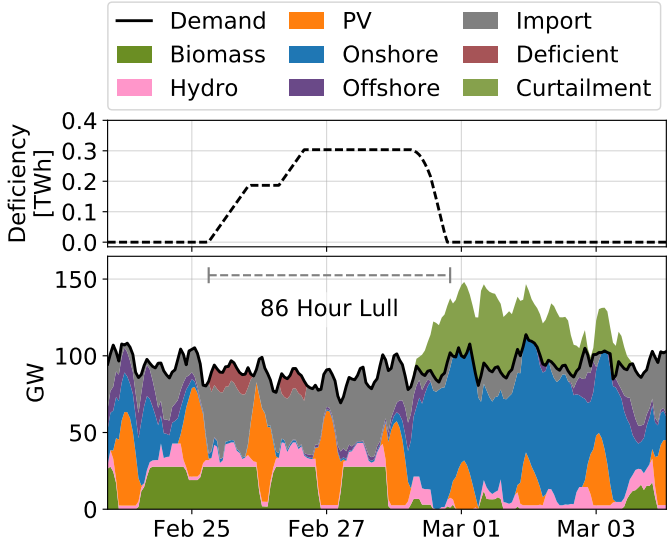

Figure 5.9: Lull diagram for the third lull evaluation context

As exemplified in Figure 5.9, the use of the power flow solver determines the time series dispatch of all available generators as well as active monitoring of imports and exports over grid connections. In the figure, the area labeled as ”Deficit” implies a reliance on the extra generator included for each region. Furthermore, the ”Curtailment” given here accounts for the total amount of wind, PV, and run-off-river generation which could not be utilized due to grid limitations and over production. Lull threshold is determined using Equation 5.3, where all quantities are

[6] Note that zero marginal cost does not equal zero LCOE.

time-variant. To note, subtracting the total VRES generation time series from this lull threshold simply results in the region's residual load. Ultimately, with this setup, a lull is initiated once a region must utilize the extra generator and continues until there is enough intraregional curtailment to offset that deficiency. Furthermore, so long as there is no curtailment, the lull threshold will be equal to or greater than the VRES generation, leading to a static lull period with positive yet unchanging deficiency. Finally, as with the "Residual Load" context, both the span and largest deficit are recorded for each lull event.

$$\mathrm{Threshold}(t) = \mathrm{Demand}(t) + \mathrm{Export}(t) - \mathrm{Biomass}(t) - \mathrm{Hydro}(t) - \mathrm{Import}(t) \quad (5.3)$$

5.6 Lull Occurrence Probability

To determine the likelihood of VRES lull occurrence, the approach of E-Highway is emulated by combining different sets of demand time series years and VRES generation time series years. In the process described by Syranidis [362], 5 *demand years* are developed using historical ENTSO-E demands for all involved countries between 2011 and 2015. Similarly, the weather data available in the MERRA [179] weather dataset is used in full, leading to 37 VRES *generation years*; corresponding to 1980 until 2016. Contrary to E-Highway's approach, generation years are not mixed between VRES technologies in order to avoid correlation inconsistencies.

By comparing demand years to generation years, a total of 185 demand-generation combinations are possible. As the development of a future demand estimation model was not within the scope of this thesis, this set-up unavoidably neglects correlations between demand time series and weather time series. Nevertheless, mirroring the approach of E-Highway, the full year of electricity system activity is determined within each demand-generation combination, but only the longest lull span and the deepest lull deficit within each lull evaluation context is retained for each regional scope in that year. At last, the question is posed "what percentage of years observe a single lull which has a span at least as long as, or a deficit at least as deep as, *X* hours or TWh". When 10 % of demand-generation years observe a specified lull, either by span or by deficit, then a lull of that magnitude can be expected to occur in one every ten years. Similarly, when 1 % of demand-generation years observe a specified lull, it can be expected once per hundred years. Without a doubt long and deep VRES lulls are probable to happen eventually, however it is their frequency of occurrence that allows for informed risk assessments. Therefore, this particular formulation of lull measurement provides actionable information to energy system planners and other stakeholders to make decisions regarding their future investments.

Chapter 6

Potentials and Cost Results

In this chapter, results of wind and PV potentials across Europe are discussed. First, land eligibility and placement results for each technology will be given, which includes land eligibility sensitivity analyses conducted for onshore wind, open-field PV and residential rooftop PV. Afterwards, simulation results are provided in the form of average FLH values across Europe. At last, cost estimations are provided in the same format as average FLH. Throughout this chapter, comparisons will be made against literature when it is helps to enhance the discussion.

6.1 Land Eligibility and Capacity Potentials

6.1.1 Onshore Wind

Figure 6.1 displays the remaining wind-eligible areas after applying the exclusion constraints shown in Table 3.5 across the European landscape. It can immediately be seen that available land in many central nations, the UK, and Greece are greatly dispersed across the countryside, while other countries such as Spain, Ireland, France and Scandinavia show much larger contiguous patches of available land. Table 6.1 summarizes the results for each country within the studied area as ordered by the their total available land. All in all, $1{,}352{,}000\,\mathrm{km}^2$ is found to be available across Europe, constituting $27.3\,\%$ of the total region. For comparison, after their land eligibility analysis Hoogwijk [371] estimates $10.8\,\%$ availability at the European level, while the EEA [42][1] was left with $82\,\%$. The constraints and methodology used in both of these studies differ significantly from the current one, however, as does the study region. Similarly, Stetter [299] estimates roughly $840{,}000\,\mathrm{km}^2$ over OECD Europe which, even with the addition of Turkey, is significantly less than the current value. McKenna [43], however, used similar constraints and datasets compared to the current work, and likewise $23\,\%$ of the study region is found to be available. Nevertheless the methodology of McKenna is not directly comparable to the one used here, as it has employed a slightly different study area in addition to using suitability factors on top on the land eligibility evaluation. In comparison to McKenna et al., Bosch et al. [372] and Eurek et al. [373] consider similar land eligibility constraints, use a coarser land cover dataset, do not consider buffer distances, and use a more restrictive set of suitability factors. While all of these sources use the World Database of Protected Areas [98] for their protected area exclusions, as is performed in this work, Bosch et al. and McKenna et al. do not distinguish between protected areas while Eurek et al. only excluded protected

[1] Who only exclude protected areas.

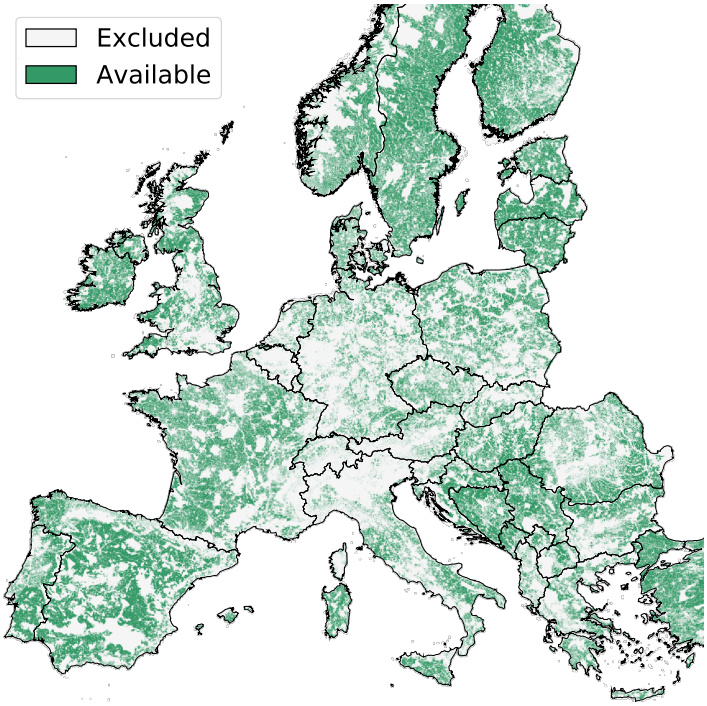

Figure 6.1: Land eligibility result for onshore wind turbines. Previously published in Ryberg et al. [108].

areas with an IUNC designation of "I-III". Furthermore, the chosen suitability factors for all three of these studies are based off the assumptions of Hoogwijk [371]. In the end Bosch et al. [372] report that $1{,}232{,}000\,\mathrm{km}^2$ is available for onshore wind turbines in Europe[2], while Eurek et al. [373] find $1{,}993{,}622\,\mathrm{km}^2$.

Within Europe, Spain is found to possess the highest share of total available area, with $168{,}000\,\mathrm{km}^2$, followed by Sweden ($161{,}000\,\mathrm{km}^2$) and then France ($149{,}000\,\mathrm{km}^2$). Sweden's estimate, corresponding to $35.7\,\%$ of its total area, is close to the estimate of Siyal et al. [374] who also used a GIS-based analysis and predicted $31\,\%$ land availability in their scenario which is most similar to the land eligibility assumptions used here. Germany is $10^{\,\mathrm{th}}$ in the current study, which is interesting considering its current leading position in terms of European installed onshore wind capacity [375]. Here, Germany is found with an available area of $54{,}017\,\mathrm{km}^2$, which is near to the land eligibility estimate of the German Environmental Agency (UBA) [73] who report $49{,}361\,\mathrm{km}^2$, but far below that of Robinius [47] who finds $113{,}115\,\mathrm{km}^2$. Unsurprisingly, smaller countries such as Luxembourg and several Balkan nations rank

[2] This value only includes generation locations which exceed a $15\,\%$ capacity factor. Bosch et al. do not report their unrestricted land eligibility potential.

Table 6.1: Onshore wind land eligibility results per country. Previously published in Ryberg et al. [108].

Region	Land Eligibility		Placements	
	%	km^2	*Count*	*GW*
Europe	27.3	1,352,260	3,404,700	13,508
Spain	33.1	167,679	397,220	1538
Sweden	35.7	160,684	390,497	1546
France	27.2	149,481	406,757	1644
Finland	32.4	109,044	266,919	1077
Poland	23.0	71,654	182,725	748
Romania	29.1	69,255	153,103	559
Norway	20.4	66,408	187,205	790
Italy	21.8	65,456	163,315	601
United Kingdom	24.1	59,276	154,105	693
Germany	15.1	54,017	160,792	620
Serbia	44.2	34,584	75,692	274
Portugal	33.5	30,805	74,375	284
Bulgaria	27.2	30,401	63,893	232
Hungary	31.2	28,991	71,572	270
Greece	21.4	28,326	75,540	281
Lithuania	42.3	27,512	64,539	268
Ireland	37.5	26,394	67,907	327
Latvia	39.9	25,807	58,382	239
Bosnia & Herz.	49.3	25,155	56,382	210
Estonia	38.8	17,630	43,614	179
Czech Republic	22.3	17,580	51,112	202
Croatia	26.2	14,973	36,518	136
Austria	15.6	13,112	43,575	166
Denmark	24.2	10,459	33,855	151
Slovakia	19.0	9342	23,168	86
Macedonia	32.6	8103	15,687	56
Montenegro	45.3	6040	14,623	56
Netherlands	15.6	5888	18,544	80
Albania	19.3	5536	16,033	58
Switzerland	10.0	4099	14,968	55
Slovenia	18.5	3698	8808	31
Kosovo	30.5	3328	7641	28
Belgium	4.4	1355	4937	20
Luxembourg	7.3	188	697	3

towards the bottom of the list. When ordering by the percentage available, Bosnia would be first, with 49 % of land available, followed by Montenegro (45 %) and Serbia (44 %). It is possible, however, that this outcome results from incomplete infrastruc-

ture and conservation data (Figure 2.6) for these areas which, once included, would certainly reduce the available land. Belgium and significant portions of the Netherlands and Germany are characterized by highly dispersed settlement areas (Figure 2.3) and, as such, are heavily impacted by security distances from these features. As a result, all of these countries have a relatively low availability percentage: Belgium is last, with $4.4\,\%$, Germany is fourth from last, with $15.1\,\%$, followed by the Netherlands at $15.6\,\%$.

The studies of McKenna et al. [43], Bosch et al. [372] and Eurek et al. [373] have all reported their land eligibility results at the national level. Therefore, Figure 6.2 directly compares the current work against these sources by showing the percent difference from the results found here. When taking the capacity weighted average of these differences, it is seen that the outcome of Eurek et al. [373] differs from the this work by $62.5\,\%$, McKenna et al.'s [43] result differs by $-26.2\,\%$, and Bosch et al.'s [372] result differs by $16.2\,\%$. The largest national discrepancy is seen in Belgium, where Eurek et al.'s and Bosch et al.'s results are nearly $806\,\%$ and $960\,\%$ of the result found here. Following this, Luxembourg and the Netherlands also show large discrepancies of at most $598\,\%$ and $377\,\%$, respectively. These large discrepancies are a result of Eurek et al.'s and Bosch et al.'s lack of an exclusive buffer distance around settlement areas, roads, railways, and water bodies.

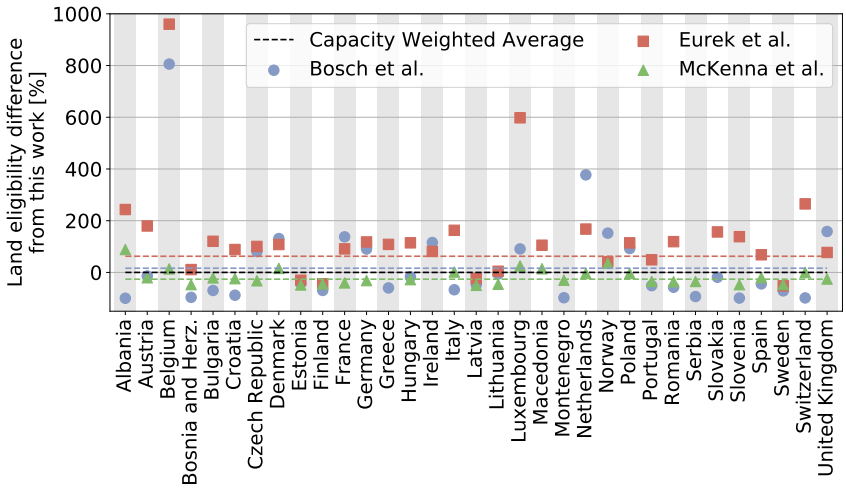

Figure 6.2: Comparison of onshore wind land eligibility results against McKenna et al. [43], Bosch et al. [372] and Eurek et al. [373]. Previously published in Ryberg et al. [108].

In terms of turbine placement, slightly over 3.4 million potential locations are identified across Europe constituting $13.5\,\mathrm{TW}$ of installable capacity; nearly 80 times the current total European wind capacity of $169\,\mathrm{GW}$ [8]. Per country, an obvious relationship exists wherein larger totals of available land correspond to larger maxi-

mum capacities, although this relationship is not absolute due to the turbine design convention, which maps turbine characteristics to the average wind speed, and the sparsity of eligible areas. Because of these relationships, observed national power densities are varied; for example, $9.17\,\mathrm{MW\,km^{-2}}$ is seen in Spain, $11.5\,\mathrm{MW\,km^{-2}}$ for Germany, and $9.99\,\mathrm{MW\,km^{-2}}$ on average across Europe. Ultimately, France is ranked top in available capacity at $1.64\,\mathrm{TW}$, followed by Sweden at $1.55\,\mathrm{TW}$ and Spain at $1.54\,\mathrm{TW}$. Similarly, Romania, which was ranked 6^{th} in terms of land availability, falls to 10^{th} in terms of capacity, while Germany, previously ranked 10^{th}, rises to 8^{th}.

The following observations can be made when comparing these results to literature. As a result of their use of power densities between 5 and $2.5\,\mathrm{MW\,km^{-2}}$, Siyal et al. estimate Sweden's technical capacity potential at around $520\,\mathrm{GW}$, nearly one-third of the value found here. In Germany, Robinius [47] estimates the total onshore wind potential at $253\,\mathrm{GW}$, while the UBA [73] finds $1188\,\mathrm{GW}$; representing $-59.2\,\%$ and $91.6\,\%$, respectively, of the $620\,\mathrm{GW}$ found in this work. The reduced capacity potential for Robinius is primarily due to the separation distances between turbines, where Robinius' use of 10 times the rotor diameter excludes $3.125\,\mathrm{x}$ times more area per turbine, and has a smaller packing density due to the circular shape, as compared to the elliptical 8 by 4 times the rotor diameter distances used here. In the case of UBA the opposite is true, where a turbine separation distance equal to roughly 4 times the rotor diameter separation distance between turbines excludes only $35.1\,\%$ of the area per turbine as in the current work; thus leading to the greatly increased capacity potential. For comparisons against other nations, the studies of McKenna et al. [43], Bosch et al. [372] and Eurek et al. [373] are again used. Figure 6.3 displays the direct comparisons of capacity potential in each country in comparison to the current work. In total, Bosch et al. reports a total[3] capacity potential in Europe at $12.9\,\mathrm{TW}$, while Eurek et al. find $10.0\,\mathrm{TW}$ and McKenna et al. find $8.4\,\mathrm{TW}$; leading to the average offsets seen in Figure 6.3 of $-7.29\,\%$, $-24.0\,\%$ and $-37.0\,\%$, respectively, from this work. As with the land eligibility result, Belgium, Luxembourg, and the Netherlands are distinguishable in the works of Eurek et al. and Bosch et al. as having high deviance from the current work on account of the lack of a security buffer around settlements, roads, railways, and water bodies. Besides this, as none of these three studies employed a placement algorithm, opting instead for an assumed power density factor, the present results will have a slight advantage since a portion of the 'exclusion area' caused by the separation distance between turbines can extend into the areas excluded by the land eligibility analysis (See Figure 2.10). As a result of this, the use of the placement algorithm in this work makes more efficient use of the eligible areas compared to McKenna et al., Bosch et al. and Eurek et al.. McKenna et al.'s power density factors average to $9.0\,\mathrm{MW\,m^{-2}}$, which are around $86\,\%$ of the effective power density factors that arise a result of the current work; which, when combined with McKenna's lower estimation of onshore land eligibility leads to the observed capacity discrepancy. Eurek et al. estimated far more eligible area than this work, however their small power density factor of $5.0\,\mathrm{MW\,m^{-2}}$ causes their capacity estimate to fall below the estimate

[3] This value only includes generation locations which exceed a $10\,\%$ capacity factor. Bosch et al. do not report their unrestricted capacity potential.

made here.

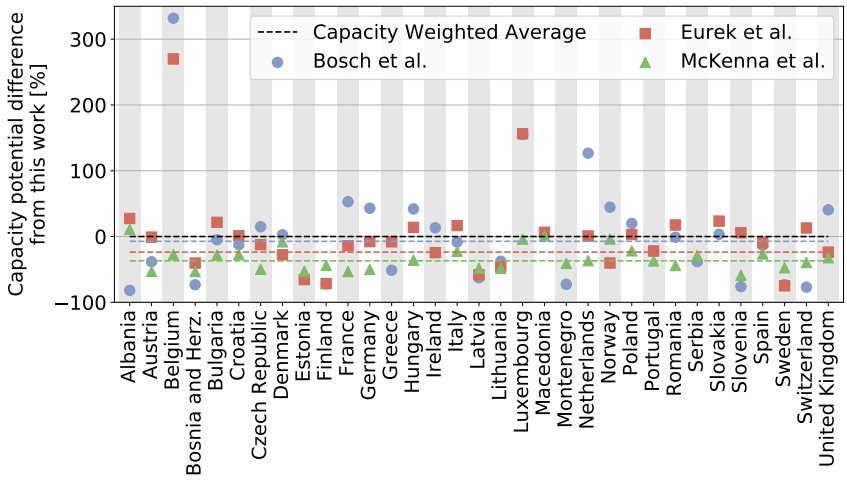

Figure 6.3: Comparison of onshore wind capacity potential results against McKenna et al. [43], Bosch et al. [372] and Eurek et al. [373]. Previously published in Ryberg et al. [108].

6.1.2 Onshore Wind Sensitivity

In order to understand the sensitivity of the previously presented potentials, a sensitivity analyses on available land was carried out. Furthermore, although this was performed for all constraints displayed in Table 3.5, as well as out for all countries, only a few are displayed and discussed here. Slope, distance to settlements, connection distance and distance from secondary roads are shown in Figure 6.4 due to their high ranking impact. Additionally distance from water bodies, protected habitats, airfields and airports on account of their noteworthy behavior are displayed in Figure 6.5.

Each line shown in Figures 6.4 and Figure 6.5 displays the resulting percentage of available land for the respective region as a function of the variable constraint, which was applied only after all other constraints shown in Table 3.5. The vertical dark gray line indicates the threshold value used in the primary land eligibility scenario, and is accompanied by a lighter gray zone, indicating $\pm 20\,\%$. Countries that are notoriously flat, such as Denmark, show a rapid saturation to a high-availability percentage for the terrain slope threshold, while countries that have many mountainous features, such as Austria, Greece, and Italy, appear to increase nearly linearly as the slope threshold grows. However, besides slope and connection distance, a general behavior of a high-availability starting point, monotonic decent and asymptotic approach to zero availability is found for the other constraints; exemplified especially well by the settlements constraint in the case of Germany. The specific character-

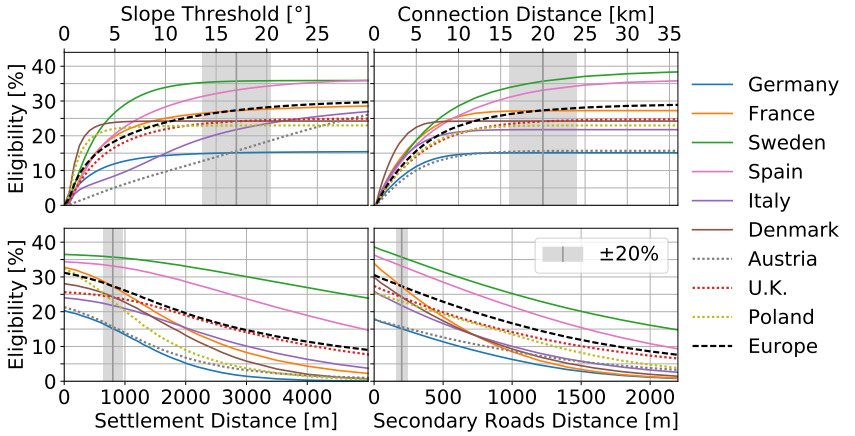

Figure 6.4: Onshore wind eligibility sensitivity to the terrain slope, distance to settlements, connection distance and distance to secondary roads constraints for Europe and selected countries. Adapted from Ryberg et al. [108].

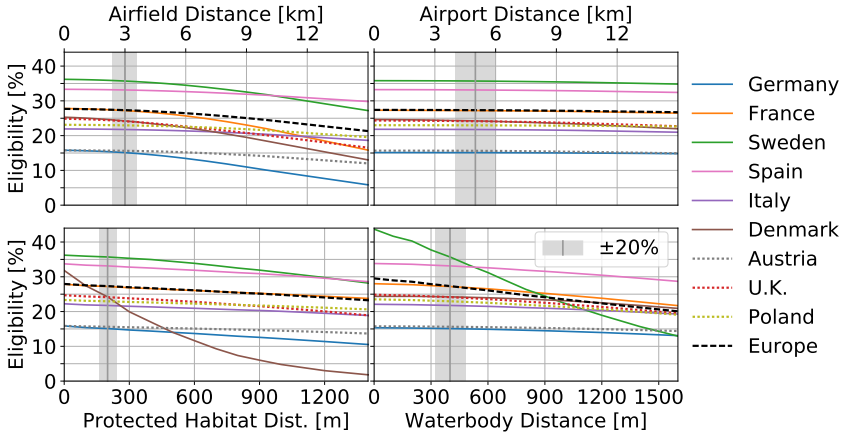

Figure 6.5: Onshore wind eligibility sensitivity to the distance to water bodies, habitats, airfields and airports constraints for Europe and selected countries. Adapted from Ryberg et al. [108].

istics of this general behavior strongly depends on both the constraint in question as well as the region in which it is evaluated. For example, in Figure 6.4, despite always having a larger percentage of available land, Poland is seen to be slightly more sensitive to settlement proximity than Germany. In connection to total potential, if the distance from settlement constraint for Germany were doubles the total

capacity potential would drop from 620 to 326 GW while Poland's would drop from 748 to 435 GW[4]. Similarly, a maximal connection distance constraint is particularly important for Sweden and Spain; where the general exclusion sensitivity trend is also seen, albeit in the reverse direction. For most of the displayed countries, this constraint is not impactful beyond a 10 km threshold, meaning that if this constraint were employed instead of the 20 km specified in Table 3.5, it would have little effect on the capacity potential. For Spain and Sweden, however, if such a constraint were to be used, their total potentials could fall from 1538 to 1197 GW and from 1546 to 1238 GW, respectively.

In Figure 6.5, proximity constraints from water bodies and protected habitats both share a characteristic wherein they consistently show a low-sensitivity for most countries, but then a remarkably strong sensitivity for a single country; Sweden and Denmark, respectively. For instance, the 200 m buffered exclusion of protected habitats alone reduces Denmark's land eligibility from 30 %, without a buffer, to around 24 %. If this constraint were increased to, for example, 1 km around protected habitats while keeping other constraints constant, then the total potential in Denmark would likely fall from 151 to around 29 GW. A discrepancy between Airports and Airfields is also investigated, and it is clear that neither of these constraints are large contributors to land eligibility until large thresholds are considered. Nevertheless, deviation from the high-availability point is observed much sooner for airfields than for airports. Deeper investigation reveals that this observation results from airfields being more numerous and having a greater likelihood of occupying remote locations than airports, and thus exclusions from airfields tend to have less overlap with exclusions from other constraints compared to exclusions from airports. As a result, a distance from airfields constraint is found to be more significant than distance from airports.

Finally, the sensitivity of these capacity potential results on the chosen turbine separation distance, 8 and 4 times the 136 m rotor diameter (8Dx4D) in the dominant wind direction, is tested. In comparison to the base separation, the following distances are tested: 6Dx3D, 6Dx4D, 10Dx4D, and 10Dx5D. In terms of their exclusive area, these distance sets correspond to 56.25 %, 75 %, 125 %, and 156.26 % of the base case's area. Figure 6.6 shows the outcome of this sensitivity test, where the percent change in total capacity for each country is given. A fairly typical trend is seen where, on average across Europe, changing the separation distance to 6Dx3D times the rotor diameter increases the total capacity to 164 % of its base value, 127 % for 6Dx4D, 84 % for 10Dx4D and finally 68 % for 10Dx5D. These values are slightly different than what would be expected if the total capacity potential was inversely dependent on the exclusive area[5]. For the case of 10Dx4D and 10Dx5D the resulting potentials are higher than what would be expected since only the turbine placement itself is required to be within the eligible area, meaning that some portion of the exclusion area around that turbine can be within the ineligible area[6]. For the case of 6Dx3D and 6xD4D the resulting potentials are less than the ba-

[4] When the average power density is held constant

[5] Expected changes: 178 % for 6Dx3D, 133 % for 6Dx4D, 80 % for 10Dx4D, 64 % for 10Dx5D.

[6] See Figure 2.9 for a visual example of this

sic expectation since, while the above statement is still true, a smaller portion of the exclusion area around each turbine will be in the ineligible areas on account of their smaller size. The differences seen between countries arise from their differing distributions of eligible areas as well as a result of the turbine capacities changing according to conventions outlined in Equation 3.5. This result highlights yet another reason why the wind industry is moving towards larger rotor diameter wind turbines since, even when separated by the same relative distances as smaller turbines, the larger separation distance would allow for more overall capacity with the same eligible area.

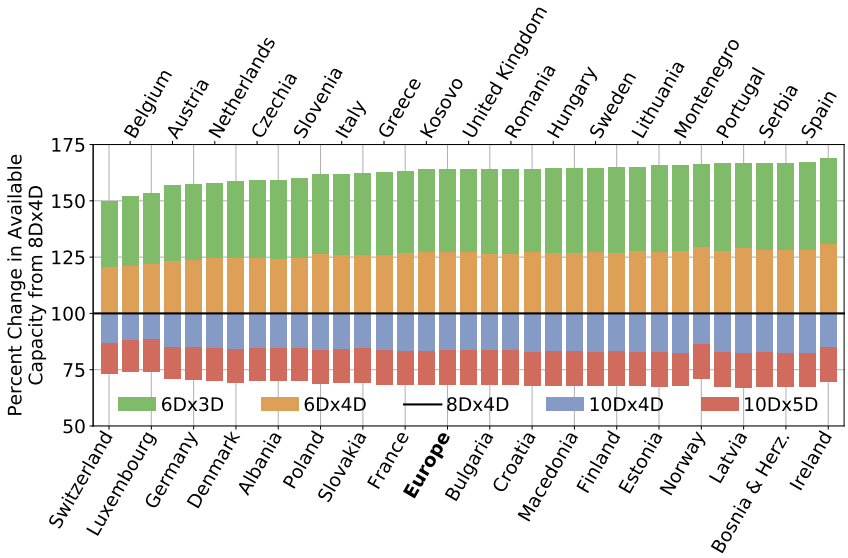

Figure 6.6: Sensitivity of wind capacity potentials to turbine separation distance

6.1.3 Open-Field PV

By applying the 28 constraints given in Table 4.3, the land eligibility result for open-field PV is found and presented in Figure 6.7. Large portions of availability are found primarily in Spain, France, and Portugal, however Lithuania, Latvia, Estonia, and many Baltic countries are also seen to possess dense patches of available land. Countries such as Italy, Poland, Romania, and Bulgaria also appear to have large overall quantities of available land, however the majority of the availability appears to be more sparse. In comparison, countries such as Germany, Switzerland, Denmark, and most of the United Kingdom are seen to possess very little available land. This is an outcome of the set of land eligibility constraints that was chosen to fit an unbiased European perspective according to the literature. In Germany, for instance, the complete exclusion of protected landscapes, all settlements, all forests, and most agricultural areas more or less excludes the entire country; leaving merely

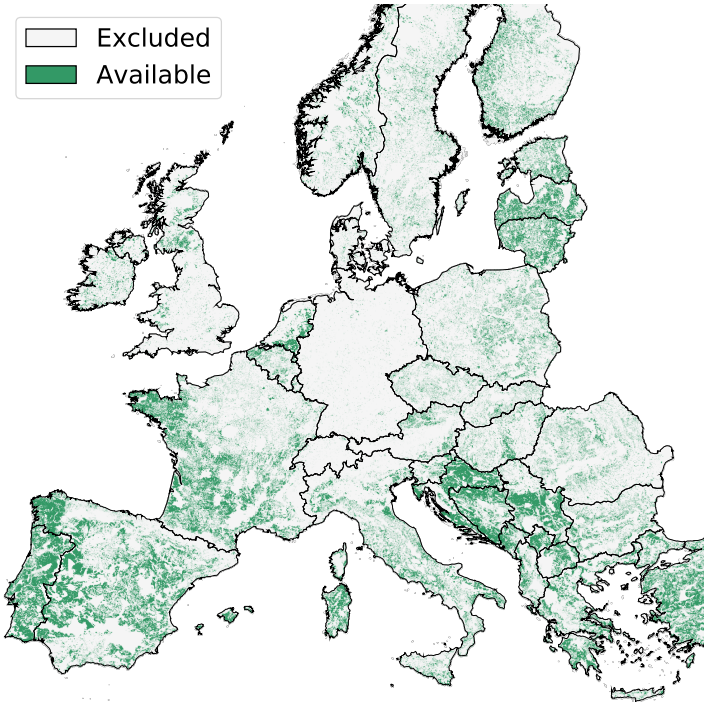

Figure 6.7: Open field PV land eligibility resulting from the application of 28 exclusion constraints

0.32 % of the land available. Meanwhile, in Switzerland, certainly settlement, forest, and agricultural exclusions are impactful in the northern portion of the country, however in the southern region, the total-slope and northward-slope constraints are the dominant exclusion; as a result leaving only 0.43 % of the land available. Nevertheless, even with these low proportions of available land, significant open-field PV potential can be found in all countries, as seen in Table 6.2.

On average it is found that 5.96 % of the land in Europe, 294,850 km^2, is available for open-field PV; constituting 14.5 TW of potential capacity. Spain and France are seen to possess the vast majority of the European open-field PV potential, at 2.87 and 2.09 TW respectfully, due to their combination of dense availability and relatively large landmass. Next to these two countries, Portugal's dense availability affords it a potential of 917 GW, falling closely behind Italy's potential of 995 GW. Despite it's very low availability, the open-field potential of Germany is found at 54 GW as a result of its large unconstrained landmass, followed by Denmark at 21 GW, Switzerland at 9 GW and finally Luxembourg at 6 GW.

As most studies operating at the European scale report a total PV potential, there

Table 6.2: Open field land eligibility results per country

Region	Land Eligibility		Placements	
	%	km^2	Count	GW
Europe	5.96	294,851	859,719	14,475
Spain	11.44	57,880	142,075	2871
France	7.65	42,035	122,452	2085
Italy	6.76	20,334	65,404	995
Portugal	20.04	18,411	40,968	917
Finland	3.67	12,382	41,884	601
Croatia	20.78	11,862	23,109	588
Greece	8.86	11,740	35,253	573
Poland	3.68	11,478	42,698	566
Serbia	14.43	11,292	28,461	559
Sweden	2.22	9986	38,098	486
Bosnia and Herz.	18.80	9601	23,403	474
Lithuania	13.43	8728	23,148	431
Latvia	12.67	8198	22,547	407
Norway	2.45	7967	23,389	327
Romania	3.08	7341	33,856	355
Bulgaria	4.73	5280	20,849	259
United Kingdom	2.10	5160	16,235	254
Hungary	4.36	4058	14,230	201
Netherlands	10.71	4033	6899	201
Estonia	8.74	3975	12,540	196
Macedonia	10.74	2667	7987	131
Czech Republic	3.29	2588	12,410	126
Austria	3.05	2561	10,513	125
Ireland	3.57	2511	7257	124
Albania	7.33	2107	6793	102
Kosovo	18.20	1987	4466	98.6
Montenegro	14.80	1974	5872	96.9
Belgium	6.23	1913	6676	94.0
Slovakia	3.43	1683	8023	81.4
Slovenia	6.13	1224	4267	59.9
Germany	0.32	1127	4946	54.4
Denmark	1.03	443	1758	20.9
Switzerland	0.47	194	853	8.98
Luxembourg	4.86	126	398	6.20
Andorra	0.58	2.62	2.00	0.01

are very few literature comparison candidates that perform a pan-European analysis with a specific focus on open-field PV potential. Two examples of such studies that provide a combined PV potential in Europe are that of Stetter [299], who finds

77.4 TW, and Pietzcker et al. [376], who finds 67.0 TW. In both cases, large differences in the land eligibility assumptions lead to their estimates being far larger than Europe's PV potential found in this work. Conversely, Zappa and van den Borek [44] performed an open-field PV potential analysis over Europe, finding only 14,672 km^2 and 895 GWp of total available land and installable capacity; which is far less than the European sum found here. Their result, which is an outcome of a highly restrictive land eligibility constraint set that only allows open-field PV in a subset of agricultural areas and grasslands in addition to a 1 % suitability factor, are largely incomparable to those found here. Focusing instead on studies conducted for Germany, for which slightly more open-field PV specific potential estimations have been made, it is seen that the estimates made here are low compared to estimates in the literature. The German Federal Ministry of Transport and Digital Infrastructure (BMVI) [377], for example, estimates the total available area for open-field PV at 3000 km^2 leading to a capacity potential of 143 GW. Although BMVI has employed similar constraints to what is used in this work, the extremely small percentage of the total available land in Germany makes these outcomes highly susceptible to slight differences in geospatial datasets and the implementation of the land eligibility methodology. Similarly, Fraunhofer IWES [378] estimates the total available land area to be between 1412 km^2 and 4384 km^2, 25.3 % and 269.3 % from the German land eligibility result in this work, leading to between 114 GWp and 875 GWp. In this case the discrepancy comes from both Fraunhofer's completely different land eligibility considerations than those used in this work, as well as their much smaller open-field PV coverage factors between 5 and 12 $m^2_{land}\,kWp^{-1}$. Fraunhofer's open-field eligibility is separated into three groups: built-up areas (54-134 GWp), areas around railways (45-556 GWp), and areas around highways (15-185 GWp). It is seen that the estimate made in this work are comparable to Fraunhofer's if only their potential within built-up areas is considered, but not when the additional areas around roads and railways are included. Besides these studies, Nitsch et al. [379] estimate 1300 km^2 and Robinius [47] estimates 40.13 GWp, which equate to 9.5 % and −25.7 % from the current work.

6.1.4 Open field PV Sensitivity

Judging from the E-Highway's 2050 capacity scenarios presented in Section 4.1.4, most countries presented above exhibit enough open-field area to cover any envisioned future PV potential. However the results found for Germany stand out as an exception to this, since its total open-field PV capacity is only seen at 54.4 GW while its future capacity envisioned by E-highway is found between 51 and 109 GW; although these projections do not specify between open-field and rooftop PV. Furthermore, when comparing the open-field German result in this work to Fraunhofer IWES [378], the lack of including road- and rail-side areas is apparent. Therefore, a side analysis is performed to investigate how much this land potential could be increased if these areas were to be added back in. Following the suggestion of Fraunhofer, a new Germany exclusion scenario is created wherein first the exclusions for agricultural, landscapes, parks, and reserves are enforced, after which all areas within 110 m of a major road or railway is re-indicated as eligible. Finally, the remaining constraints shown in Table 4.3 are excluded. With this ordering, the

additional road- and rail-side areas are only added back in to the eligibility result so long as they are within an area excluded due to the agricultural or protected area constraints. Road- and rail-side areas which are excluded due to other reasons, such as due to being in a forest, remain excluded.

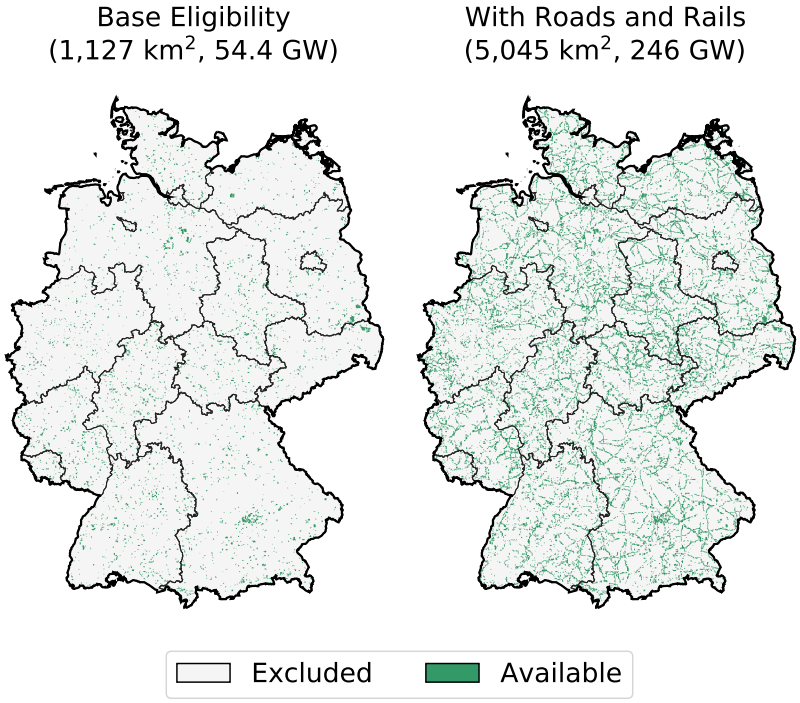

Figure 6.8: Open-field eligibility scenarios for Germany. Left: primary scenario applied to all countries. Right: addition of road- and rail-side areas back into the eligibility result.

The result is shown in Figure 6.8, where is can be seen that the addition of this extra area can increase Germany's available open-field PV area to $5045\,\mathrm{km}^2$ ($1.43\,\%$ of the total land area), or nearly 4.5 times its previous value. When applying the area distribution algorithm and the open-field PV coverage value of $20\,\mathrm{m}^2\,\mathrm{kWp}^{-1}$, this corresponds to a capacity potential of $246\,\mathrm{GWp}$. Since major roads and railways are fairly evenly dispersed across Germany, this additional capacity is also seen to be intermixed throughout the country, which could be advantageous to the electricity system. Referring to Fraunhofer's results discussed in the previous section, the total land eligibility in this adjusted scenario is $15.1\,\%$ above Fraunhofer's upper estimate for Germany but is well within Fraunhofer's range of capacity estimates. Despite this increase in potential and the improved capacity agreement with Fraunhofer, this extra land eligibility scenario is not considered for further analyses so as to maintain a homogeneous treatment of open-field potential between countries. In any case,

this sensitivity stresses the point that land eligibility results are highly scenario-bound, and that, while most countries may adopt open-field PV constraints similar to Table 4.3, countries such as Germany may need to make special consideration in the case of large future capacities.

6.1.5 Rooftop PV

Applying only the population density constraint results in the rooftop PV availability map given in Figure 6.9. In this figure, all major metropolitan areas are directly visible and are therefore likely to correspond to large rooftop PV potentials; including for example Paris, London, Madrid, Berlin, and Rome. The same can also be said for The Netherlands, Belgium, Northern Italy, and Western Germany, where large patches of eligible areas can be found. In comparison to the open-field eligibility result, it is interesting that these same areas are specifically lacking in open-field PV potential; meaning that rooftop PV and open-field compliment one another. Germany is perhaps the best example of this, as it possesses one of the lowest potentials for open-field PV, but, as given in Table 6.3, possesses the second most amount of land available for rooftop PV and the highest capacity.

Table 6.3 shows the summarized results for eligibility land, rooftop area, and finally capacity potential for all countries and for Europe. Concerning land eligibility, France takes the top position with $119{,}169\,\mathrm{km}^2$ constituting $21\,\%$ of the country's land mass. Due to the population distribution in these areas, and the application of Equation 4.2, an estimated rooftop area of $1069\,\mathrm{km}^2$ and capacity potential of $159\,\mathrm{GW}$ is found. Germany is in close second in terms of land eligibility at $110{,}162\,\mathrm{km}^2$ ($30.8\,\%$), but due to the more spread out and overall larger population, the estimated rooftop area and thus capacity, $1272\,\mathrm{km}^2$ and $189\,\mathrm{GW}$ respectfully, are larger than France's. A similar relationship can be seen between Poland and the United Kingdom, where despite similar available land areas of $53{,}370$ and $52{,}029\,\mathrm{km}^2$, respectfully, the United Kingdom possesses $123\,\mathrm{GW}$ of rooftop PV potential while Poland is only found to have $91\,\mathrm{GW}$. In total across Europe, $8119\,\mathrm{km}^2$ of rooftop area is estimated corresponding to a rooftop PV potential of $1211\,\mathrm{GW}$.

The results of Table 6.3 are of course strongly influenced by the use of Equation 4.2 as well as by the coverage value chosen for the rooftop PV context. However, when viewed from an equivalent perspective these results are not out of line with similar estimation made within the literature. In regards to estimated rooftop area, Figure 6.10 exemplifies that the current rooftop estimation procedure closely resembles the results of Bódis et al. [302] ($3.8\,\%$ on average compared to this work) and Nowak et al. [380] ($-1.4\,\%$), but is significantly more than that of Defaix et al. [301] ($-51.8\,\%$). Nowak et al. and Defaix et al. use statistical approaches that make use of national census and building stock data, and thus are not geospatially resolved. Meanwhile, Bódis et al. conducted a similar GIS based analysis and also made use of Equation 4.2, so it follows that the results are quite close to one another. Differing estimations between this work and Bódis et al. arise from the nonlinear nature of Equation 4.2 in combination with the manner by which population density data is handled. Beside these sources, when performing similar estimates in Spain,

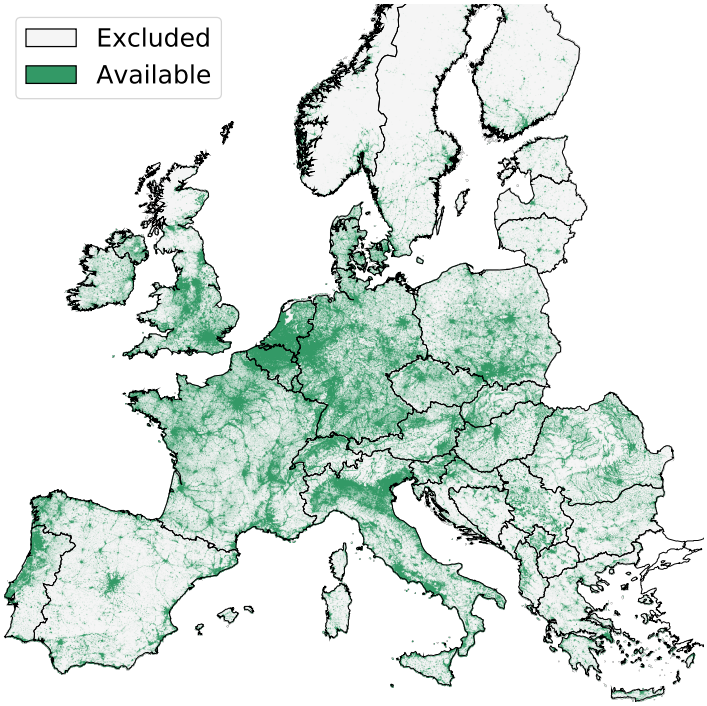

Figure 6.9: Rooftop PV eligibility after excluding all area with a population density below $1\,\text{person}\,\text{km}^{-2}$

Izquierdo et al. [381] found a total rooftop are of $571\,\text{km}^2$, Korfiati et al. [382] estimated $568\,\text{km}^2$, and Greenpeace [383] estimated $595\,\text{km}^2$; respectfully representing a $-2.2\,\%$, $-2.7\,\%$, and $1.9\,\%$ difference from the value found here. In Germany a wider range of total available rooftop area is seen in the literature, for example: $1045\,\text{km}^2$ by BMVI [377], $1064\,\text{km}^2$ by Grau et al. [384], $1200\,\text{km}^2$ by Fraunhofer IWES [378], $1464\,\text{km}^2$ by Korfiati et al. [382], $1470\,\text{km}^2$ by UBA [385], and $1687\,\text{km}^2$ by Mainzer et al. [310]. Although each of these sources differs slightly in regards to their definition of residential rooftop area, it is clear to say that the current estimate of $1272\,\text{km}^2$ is well placed in this group.

In terms of total capacity, UBA reports [385] concerning residential rooftop potential in Germany, a potential capacity of $275\,\text{GW}$ is found, although this value includes both north facing rooftops as well as building facades. If north facing roofs were not excluded in this work, a coverage factor of $3.33\,_{\text{roof}}\text{m}^2\,\text{kW}^{-1}$ could have been used, increasing the current estimation of Germany's potential to $378\,\text{GW}$, which, while far beyond of the UBA estimate, is explained by the differing assumptions of module efficiency. For their estimates, the UBA assumed a module efficiency of $17\,\%$ which, when scaled to the $30\,\%$ efficiency used here would correspond to

Table 6.3: Rooftop eligibility and total capacity results per country.

Region	Land Area km^2	Rooftop Area km^2	Placements Count	Capacity GW
Europe	730,425	8119	40,802	1211
France	119,169	1069	5702	159
Germany	110,162	1272	3790	189
Italy	75,536	904	3000	135
Poland	53,370	609	3035	91.0
United Kingdom	52,029	825	2249	123
Spain	47,131	584	4178	87.3
Romania	33,289	326	2112	48.7
Netherlands	20,692	257	421	38.5
Austria	17,693	149	872	22.3
Belgium	17,548	187	340	27.9
Portugal	17,333	160	834	23.9
Czech Republic	16,644	176	795	26.4
Hungary	14,705	158	865	23.6
Greece	14,381	149	1417	22.4
Serbia	13,587	134	767	20.1
Sweden	11,679	144	1765	21.5
Switzerland	10,646	125	422	18.8
Denmark	10,545	96.1	541	14.3
Ireland	10,015	82.2	744	12.3
Norway	9716	83.0	1373	12.4
Bulgaria	9401	108	910	16.3
Slovakia	9379	94.6	473	14.1
Croatia	7424	71.3	582	10.6
Finland	6357	79.8	1224	11.9
Slovenia	5161	40.6	215	6.06
Bosnia and Herz.	3734	54.0	387	8.05
Albania	3214	40.7	252	6.07
Lithuania	2599	38.8	486	5.8
Macedonia	2160	29.6	198	4.42
Estonia	1859	19.1	326	2.85
Latvia	1520	25.5	385	3.8
Luxembourg	973	9.56	34	1.43
Montenegro	759	9.26	108	1.38

485 GW. In the analysis of Mainzer et al. [310] where county-level building statistics and historical design criteria were considered, a total German rooftop PV potential of 380 GW is found with a module efficiency of 30 %. Once again this value does not consider the exclusion of north facing roofs, meaning that the estimation between this work and Mainzer et al. are in fact quite close to one another de-

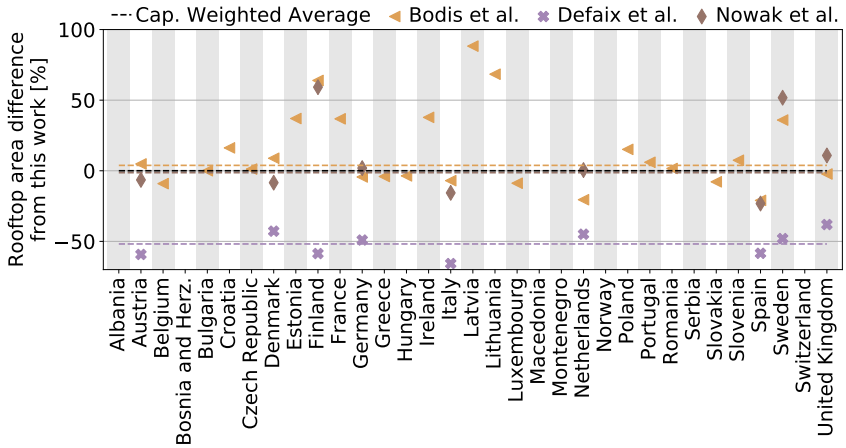

Figure 6.10: Comparison of national rooftop area estimations against Bódis et al. [302], Defaix et al. [301] and Nowak et al. [380].

spite using fundamentally different methodologies for determining overall rooftop area. Other rooftop PV capacity estimations in Germany include Robinius [47] with 79.2 GW, Kaltschmitt [386] with 121 GW, Quaschning [387] with 130 GW, BMVI [377] with 149 GW, Lödl et al. [388] with 161 GW, and Fraunhofer IWES [378] between 96 and 240 GW. Once again, many differences exist between these studies including the definition of residential rooftop areas, rooftop utilization rates, and assumed module efficiencies, but nevertheless the point is apparent that the current estimate is not out of range of the literature.

6.2 Simulation Results

When the wind and PV simulation schemes are applied across Europe using the MERRA [179] dataset as input, the following FLH distributions are shown in Figure 6.11 for onshore wind, Figure 6.14 for open-field PV, and finally Figure 6.16 for rooftop PV are found. To note, Figures 6.11 and 6.14 are created by simulating onshore turbines and open-field PV parks on a 2 km grid and do not include land eligibility in order to better display the trends. As a result, Figures 6.11 and 6.14 will not display many of the outliers which can be found when simulating explicit locations. Meanwhile, due to the computation intensity of the rooftop simulation scheme, Figure 6.16 is created using the 40,802 rooftop simulation locations identified via the land eligibility and area distribution methods discussed in Chapter 2. Comparison to literature sources will be performed throughout this section and, at the end, Table 6.4 is given summarizing the national FLH and generation potentials for all technologies.

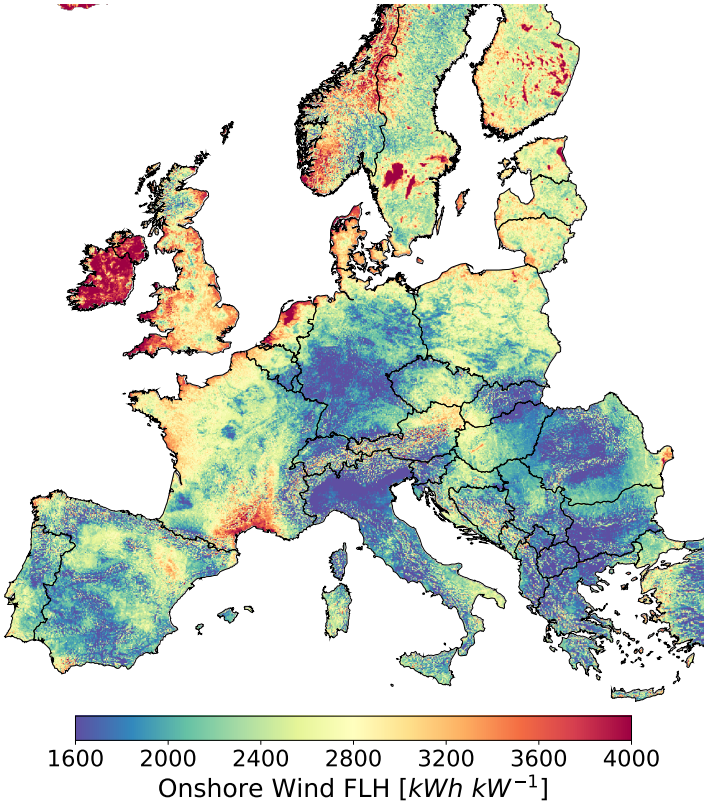

Figure 6.11: Average annual FLH for onshore wind turbines mapped across Europe. Land eligibility is not included. Previously published in Ryberg et al. [109].

6.2.1 Onshore Wind Full Load Hours

For the onshore wind FLHs in Figure 6.14, it is clear that Ireland is distinguishable as having many well-performing turbine locations; the majority of which are in excess of 3800 kWh kW^{-1}. To a slightly less degree, the United Kingdom and Denmark both posses a majority of strong turbine locations; predominantly ranging between 3400 and 4000 kWh kW^{-1}. Estonia, Latvia, and Lithuania also show semi-homogeneous FLH distributions around 2600, 2500, and 2800, respectively. Nevertheless, many other countries are seen to have certain sub-regions with strong wind energy locations. For the Netherlands, Belgium, and Germany, for instance, strong locations with around 3000 kWh kW^{-1} are found more frequently in proximity to the North Sea and, in the case of Germany, Baltic Sea. France appears to have strong locations in the south of the country near to the Mediterranean coast, where FLH can reach 4000, but a much larger region of FLHs around 3000 can be seen in the North. Yet the strong wind locations are not always associated with

close proximity to coasts; which can be observed in north-eastern Spain, central Poland, and North-Eastern Austria. The Nordic countries are observed to have a variety of FLH values, which primarily range from less than $2000\,\mathrm{kWh\,kW^{-1}}$ to above $4000\,\mathrm{kWh\,kW^{-1}}$.

In JRC's technology projections to 2050 [160], the projected design of onshore wind turbines is similar to the baseline turbine used here, with a nameplate capacity of $4.5\,\mathrm{MW}$, and the claim is made that an average of $3942\,\mathrm{kWh\,kW^{-1}}$ will be observed across Europe, with a maximum of $5694\,\mathrm{kWh\,kW^{-1}}$. These values are calculated assuming an average wind speed of 7 to $8.5\,\mathrm{m\,s^{-1}}$, and so when this wind speed is applied to this work's baseline turbine and simulation scheme[7], then an average of $3898\,\mathrm{kWh\,kW^{-1}}$ is found, which is in close agreement with the JRC estimate. Furthermore, the turbine location with the maximum average FLH which results from the current analysis is found in Northern Norway with $6033\,\mathrm{kWh\,kW^{-1}}$, which represents a $5.9\,\%$ discrepancy from the maximum JRC estimate. This maximum FLH is extremely uncommon, however, since $99\,\%$ of locations are found below $4278\,\mathrm{kWh\,kW^{-1}}$, and therefore this outcome is most likely a result of numerical fluctuations in the GWA as opposed to a physical reality for these particular locations. Across all onshore simulation locations, however, an average of $2561\,\mathrm{kWh\,kW^{-1}}$ is observed; which is significantly less than JRC's estimate. The explanation for this discrepancy lies in the fact that JRC's estimate is given in context of operating turbines in 2050, while the value found here results from the average of all available turbines. In a more comparable estimate, Stetter [299] suggested an average of $2471\,\mathrm{kWh\,kW^{-1}}$ across all available locations in 2050; which represents a $3.6\,\%$ difference to the value from this work. Besides the close agreement in FLH estimate, however, Stetter finds far less overall available generation, at $21.5\,\mathrm{PWh}$, as compared to the value from this work of $34.3\,\mathrm{PWh}$, resulting directly from the significantly smaller quantity of eligible land found by Stetter.

At the national level, the pan-European onshore wind potential estimation studies of McKenna et al. [43], Bosch et al. [372] and Eurek et al. [373] can be compared to this work. Figure 6.12 shows the differences of each of these studies in comparison to the average FLHs found here. The impact of the futuristic turbine designs employed in this work is immediately apparent, causing the national FLH results of these studies to be on average $14.9\,\%$ less for Eurek et al., $22.0\,\%$ less for McKenna et al., and $36.1\,\%$ less for Bosch et al. than the current work. Bosch et al.'s estimates are always between 20 and $60\,\%$ less than the values found here, however estimates from McKenna et al. and Eurek et al. can for some countries exceed the estimates made here; such as for Luxembourg, Latvia, Germany, and Belgium. Switzerland shows the largest discrepancy of all countries, where McKenna et al.'s estimate is $80\,\%$ less than the value here. Ultimately these differences stress the importance of using futuristic turbine designs in the European potential estimate.

Of course, an important point to keep in mind is that the average FLH only tells part of the story for each of these countries. To emphasize this point, Figure 6.13 shows the distribution of FLHs in Germany in both the current work as well as re-

[7] And assuming a Weibull shape parameter for the wind speed distribution equal to 2

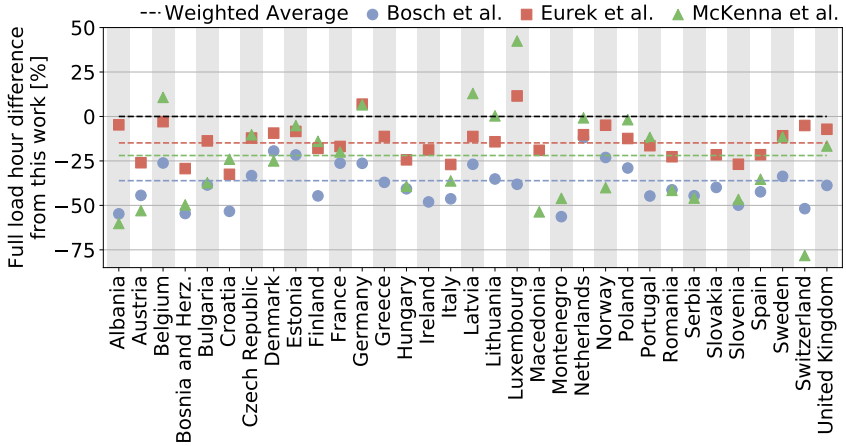

Figure 6.12: Comparison of onshore wind full load hour results against McKenna et al. [43], Bosch et al. [372] and Eurek et al. [373]. Previously published in Ryberg et al. [109].

ported from UBA [73]. Here it is seen that UBA has an average FLH in Germany of $2492\,\mathrm{kWh\,kW^{-1}}$ compared to the average of $2150\,\mathrm{kWh\,kW^{-1}}$ found here. For comparison, other estimates of FLH in Germany include $2329\,\mathrm{kWh\,kW^{-1}}$ by McKenna et al. [29] and $2536\,\mathrm{kWh\,kW^{-1}}$ by Robinius et al. [156]. As one might expect from these averages, the current work has a proportion of individual turbines with low FLH's in comparison to that of UBA. Nevertheless, the UBA distribution is slightly skewed to the left while the distribution from this work is heavily skewed to the right; resulting from the individual turbine simulation performed in this work. Despite its lower average FLH across Germany, this skewing leads to a slightly higher proportion of individual turbines in the current work than UBA with FLH's above $3200\,\mathrm{kWh\,kW^{-1}}$, which then extends up to $3900\,\mathrm{kWh\,kW^{-1}}$. Moreover, both distributions share the property that about $5\,\%$ of their overall potential is greater than or above $3000\,\mathrm{kWh\,kW^{-1}}$. In the end, this comparison shows that average FLH is not a comprehensive indicator of how wind energy will perform between studies as well as between countries.

6.2.2 Open-field PV Full Load Hours

Concerning open-field PV, as expected it is clear from Figure 6.14 that placements in southern Europe offer significantly better performance than placements in Central and Northern Europe. The highest FLHs, above $1900\,\mathrm{kWh\,kWp^{-1}}$, are found in much of Portugal, Spain, and Turkey. Meanwhile, in Greece, Italy, and Southern France, FLHs between 1600 and $2000\,\mathrm{kWh\,kWp^{-1}}$ can be seen. Further north, in Germany, the Netherlands, Belgium, Poland, and Northern France, FLHs between 1200 and 1400 are more typical. At higher latitudes, FLHs are generally found to be

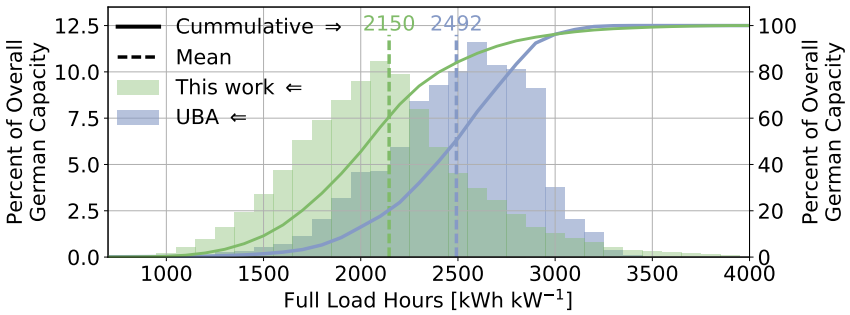

Figure 6.13: Comparison of onshore wind full load hour distribution in Germany to UBA [73].

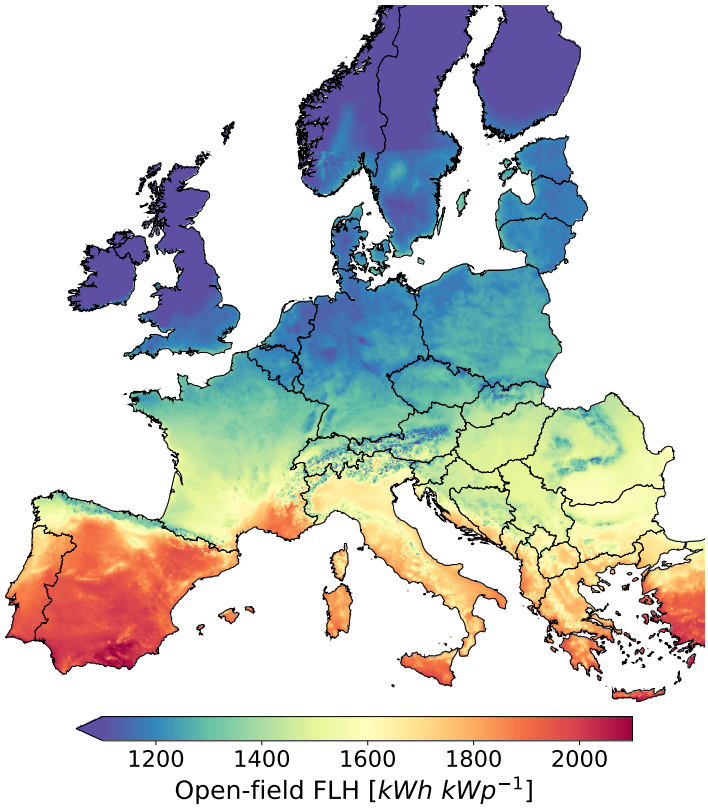

Figure 6.14: Open-field PV average FLH. Land eligibility is not included.

around 1100 and below. Despite this, micro-trends can be observed wherein slightly higher FLH can be found near-to coasts versus locations further inland; seen, for example, in Northern France and Central Italy. Nevertheless, these micro-trends are small compared to the spatial variability of onshore wind generation seen in Figure 6.11. The average open-field PV FLH of 1534 found here is roughly 3 % away from the JRC's [160] estimate of utility scale PV performance in 2050, given as 1489 kWh kWp^{-1}.

Figure 6.15 compares open-field PV FLH distribution differences for select countries considered in this work to that of Šúri et al. [304], the EMHIRES dataset [312], and the Global Solar Atlas (GSA) [206]. The simulation scheme of Šúri et al. has been previously described in Section 4.1.5 but, in short, primarily differs from the current approach by making use of monthly averaged irradiance data from 566 weather stations across Europe as opposed to the hourly climate model data used here. These results are also affected by Šúri et al.'s use of a constant module performance equal to 75 % of the plane-of-array irradiance. The EMHIRES dataset and the GSA both use an hourly PV simulation scheme, but employ standard PV modules to what is seen today. Taking the average FLH of each country[8], a typical FLH difference between this work and Šúri et al. is found at 386 kWh kWp^{-1}, compared to 343 kWh kWp^{-1} from the EMHIRES dataset and 229 kWh kWp^{-1} from the GSA. The PV validation discussion in Section 4.5 performed a comparison of this work's simulation scheme against the GSA when using a typical conventional silicon crystalline PV module for and, as a result, found a percent error of 0.551 % across the whole of Europe. The increased FLH in the results shown for Figure 6.15 is therefore purely an outcome of the module selected for this analysis on account of its strong FLH performance (See Table 4.2 and the surrounding discussion). Note that this does not imply that this module is unequivocally superior to all other modules, since its increased FLH comes at the cost of a smaller overall module efficiency. For the EMHIRES dataset and Šúri et al., it follows that the differences seen for these two sources are quite close to one another, since the simulation approach used to create the EMHIRES dataset is fundamentally built on top of Šúri et al.'s work. Nevertheless, it is seen that both of these sources under-predict compared to the GSA and, by extension, this work if these simulations were performed with the typical module selection used for validation.

6.2.3 Rooftop PV Full Load Hours

The FLH distribution seen for rooftop PV in Figure 6.16 closely follows that of open-field PV, albeit at lower FLH values. Slight differences can be seen, however, particularly in areas where diffuse irradiance is prevalent, such as in much of Northern Europe. While open-field PV still outperforms rooftop PV in these areas, the difference is much smaller than in the southern regions. Across Europe, an average of 1246 kWh kWp^{-1} is seen which, once again, is comparable to JRC's 2050 average residential rooftop performance estimate at 1226 kWh kWp^{-1} [160]. For Germany, an average rooftop PV FLH is seen in this work at 1093 kWh kWp^{-1}. Although the

[8] Including those not visualized in Figure 6.15

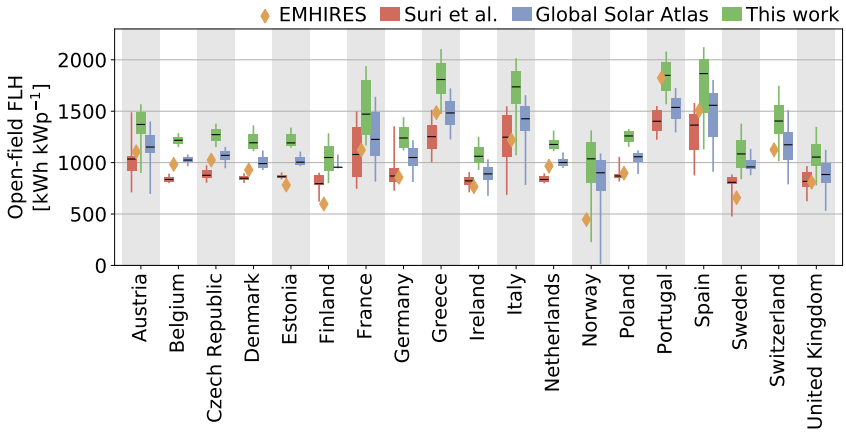

Figure 6.15: Comparison of open-field PV full load hour results against Šúri et al. [304], the EMHIRES dataset [312], and the Global Solar Atlas (GSA) [206]. Indicated values are the maximum FLH, 95thpercentile, mean FLH, 5th percentile, and the minimum FLH, except for the EMHIRES dataset, where only the mean is shown.

FLH value found for Europe is in agreement with the JRC estimate, this German FLH value is high compared to studies in the literature. For example, Mainzer et al. [310] finds 712 kWh kWp^{-1}, Kaltschmitt reports 813 kWh kWp^{-1}, Robinius [47] reports 862 kWh kWp^{-1}, Quaschning et al. [387] report 869 kWh kWp^{-1}, UBA [385] reports 902 kWh kWp^{-1}, BMVI [377] reports 943 kWh kWp^{-1}, and Nowak et al. find 990 kWh kWp^{-1}. None of these sources have employed a temporally explicit PV simulation scheme as is used in this work, however it is not possible to predict whether or not this would lead to the reduced FLHs without having full access the data sources used by these researchers. Furthermore, some of these studies also include building facades in their FLH calculation while other incorporate both south and north facing roofs[9], both of which would certainly lead to a low bias of the reported FLH.

6.2.4 Rooftop PV Sensitivity

As discussed in Section 4.2.2, a European-wide dataset describing roof orientations does not exist and performing a direct investigation of this issue via LIDAR analysis is not feasible on the European scale. Despite this, the robustness of the constant rooftop distribution is called into question and so a short sensitivity analysis was performed to investigate this further.

While determining the rooftop potential in Italy's Piedmont region, Bergamasco and

[9] This study only considers south facing roofs

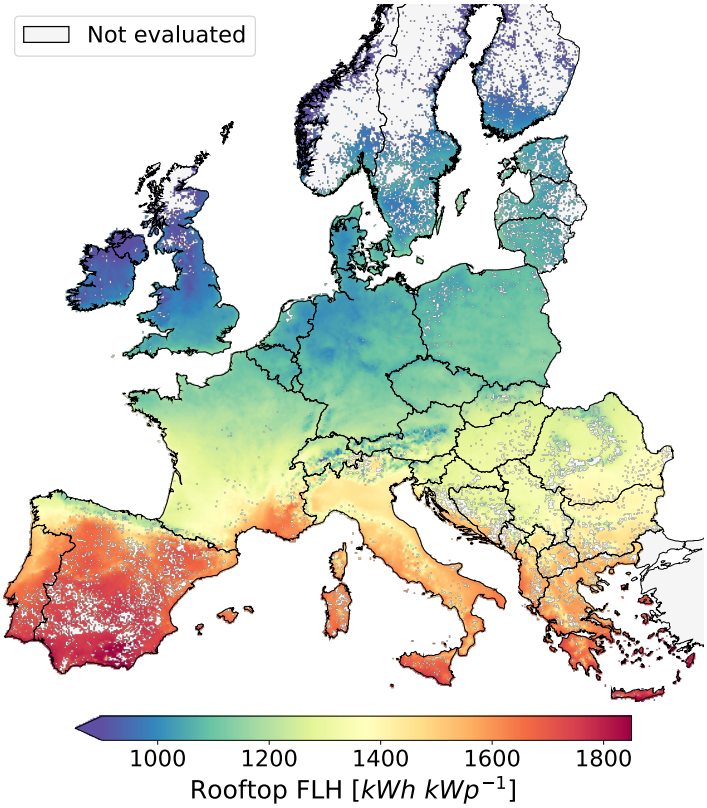

Figure 6.16: Rooftop PV average FLH. Note that the 2 km display resolution of this figure does not accurately represent land eligibility.

Asinari [295] note that the rooftop tilt angels found there are generally between 17° and 24°, with 20° as a representative value for the whole area. This is of course far from the average tilt angle used in this work of 37°. To test how these alternative tilt angles would impact the rooftop simulation results, the MERRA-based rooftop simulation scheme described in Section 4.4 is applied across Italy substituting the tilt range of Bergamasco and Asinari. Figure 6.17 shows the difference in average FLH between the two sets of assumptions.

Compared to the base rooftop tilt assumption, the tilt angles given by Bergamasco and Asinari [295] are much closer to the optimal tilt angles derived for Figure 4.15, suggesting that system performance should improve. In fact, this is exactly what is seen in Figure 6.17 where on average a 2.22 % increase in FLHs are seen compared to the base assumptions. Furthermore, a clear trend is seen wherein FLHs in the north are generally around 0.5 to 1.5 % higher, which transitions to increases

between 3.0 and 4.0 % in the south. These higher values are particularly clear on the island of Sardinia.

This change in FLH clearly suggests that a more detailed treatment of rooftop PV should be performed in the future when the requisite data becomes available, as it can have a measurable impact on estimated performance. Nevertheless, within the context that it is employed in this work, these results also suggest that this impact would be around 2 or 3 %. As a result, while the base assumption of a constant rooftop orientation distribution is not the most precise assumption, it is nevertheless still expected to produce reliable results.

6.2.5 Summarized Generation Potentials by Country

Table 6.4 provides a national summary of the average annual FLH and generation potential for onshore wind, open-field PV, and rooftop PV. Furthermore only the generation from eligible placements are counted, and countries are sorted by total generation potential. Spain is found to have the largest total potential of 9014 TWh; representing 15.6 % of the total generation potential found across Europe. France and Sweden are next at 7587 and 4541 TWh, respectively. Unlike Spain's potential,

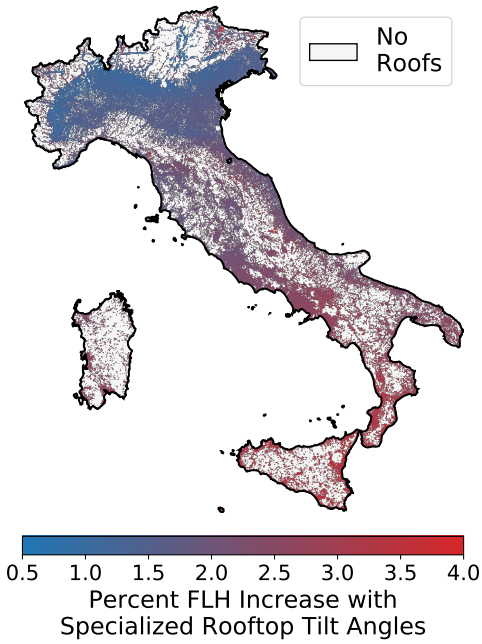

Figure 6.17: Percent change in rooftop PV FLH versus the base assumptions when specially defining roof tilt angles in Italy

Table 6.4: Total generation potentials at country level. Onshore wind results previously published in [109].

Region	Onshore Wind		Open-field PV		Rooftop PV		Total
	$\frac{kWh}{kW}$	TWh	$\frac{kWh}{kWp}$	TWh	$\frac{kWh}{kWp}$	TWh	TWh
Europe	2561	34,286	1534	22,161	1245	1509	57,957
Spain	2286	3496	1873	5375	1633	143	9014
France	2626	4306	1475	3078	1271	203	7587
Sweden	2583	3990	1077	528	1032	22.2	4541
Finland	2750	2940	1052	643	963	11.5	3594
Italy	2180	1309	1752	1749	1505	203	3261
Poland	2598	1941	1259	716	1111	101	2758
Norway	3053	2327	1030	373	953	11.8	2712
United Kingdom	3278	2262	1054	269	1010	124	2655
Portugal	2301	648	1862	1708	1608	38.5	2395
Romania	2098	1163	1483	526	1323	64.4	1753
Greece	2155	601	1814	1049	1641	36.7	1687
Germany	2150	1330	1238	67.3	1093	208	1605
Serbia	2074	567	1513	847	1357	27.3	1442
Ireland	3949	1254	1058	132	964	11.8	1397
Lithuania	2760	733	1209	525	1067	6.18	1264
Bosnia and Herz.	2417	505	1552	738	1328	10.7	1254
Croatia	2381	321	1546	913	1360	14.5	1249
Latvia	2676	637	1199	489	1065	4.05	1130
Hungary	2175	583	1467	294	1286	30.4	908
Bulgaria	1973	456	1599	414	1421	23.1	893
Estonia	2771	494	1191	235	1054	3.00	732
Czech Republic	2256	453	1270	160	1135	29.9	644
Austria	2611	434	1375	172	1215	27.1	633
Denmark	3331	501	1192	25.3	1062	15.2	542
Netherlands	3015	238	1176	237	1057	40.7	515
Macedonia	1935	107	1694	222	1492	6.60	336
Albania	2184	126	1780	182	1574	9.56	318
Slovakia	2202	188	1377	112	1214	17.1	317
Montenegro	2467	136	1637	159	1468	2.03	297
Belgium	2594	51.8	1218	114	1076	30.0	196
Slovenia	2144	65.7	1465	87.7	1287	7.79	161
Switzerland	2126	116	1407	12.6	1265	23.8	152
Luxembourg	2024	5.31	1248	7.72	1117	1.59	14.6

which is slightly PV-dominant, France's potential comes from a much closer share between onshore wind and PV, while Sweden's is heavily wind-dominant. Ireland and Denmark represent extreme examples of this availability biasing, where their

potential is comprised of 89.8 % and 92.4 %, respectively, from wind energy. As for PV, Croatia at 74.3 % and Portugal at 72.9 % show the most PV-dominant potentials. Note that comparison of these FLH results to literature sources has been provided in the preceding subsections, and so will not be repeated here.

To put these generation values into perspective, a short comparison was made against past and estimated future electricity demands for these countries. For this purpose, the 2016 electricity demand is taken from the IEA's "Key World Energy Statistics" from 2018 [10] and the E-Highway [296] project can be used for future demands. E-Highway projected future European electricity demand and generation capacity in 2050 at the end of 5 different sociotechnical trajectories[10]. Furthermore, these scenarios were developed from a consortium of research institutes across Europe, and incorporated the feedback of transmission system operators and other stakeholders at several different stages. Two of the E-Highway scenarios are considered here as they represent the highest and lowest demand scenarios proposed by E-Highway. The high demand E-Highway scenario is titled "Large Scale RES", in which a passive public attitude results in low energy efficiency and limited demand-side management. Conversely, the low demand scenario is titled "Small & Local" and instead emphasizes local solutions to decentralized generation and extensive energy efficiency improvements. In addition to changes in current electricity demands, taking into account GPD growth, population change, and improved efficiency of electrical devices, these demands also include an electrified mobility sector as well as prolific electric heating. As seen in Figure 6.18, all countries are observed to be able to produce more than its current or estimated future demand in either scenario. Countries known for denser populations or else heavy industry, such as Belgium and Germany, tend to rank towards the lower end of this list. Despite this, Belgium, in the last position, can still produce between 1.3 and 2.2 times its demand, and Germany can produce between 2 and 3.5 times its demand. On the other end of the spectrum, countries with lower population densities and less industrial activity see much larger multiplication factors. Bosnia and Herzegovina is found in the leading position with between 81 and 126 times its estimated demand, followed by Montenegro at between 75 and 116 times. Despite its large generation potentials, Spain is found in the 18$^{\text{th}}$ position, with between 15 and 25 times its projected demand.

Figure 6.19 shows average FLH trends for onshore wind, open-field PV, and rooftop PV for most countries; where placements are ordered by increasing LCOE. In this way, values towards the left of these figures correspond to the performance of only the best locations, and each trend ends at the maximum capacity and average FLH corresponding to the values provided in Tables 6.1, 6.2, 6.3, and 6.4.

These trends show that average FLH is closely related to the desired capacity. In Norway, for example, the average onshore wind FLH can be seen to start at nearly 5400 kWh kW^{-1} for the best 1 GW of placements, but reduces to 4900 kWh kW^{-1} when 10 GW is desired. The greatest spread of FLH is seen for wind turbines in Austria, which also starts at 5400 kWh kW^{-1} with 1 GW, but falls at rate of

[10] All of which satisfy an 80 % emission reduction target

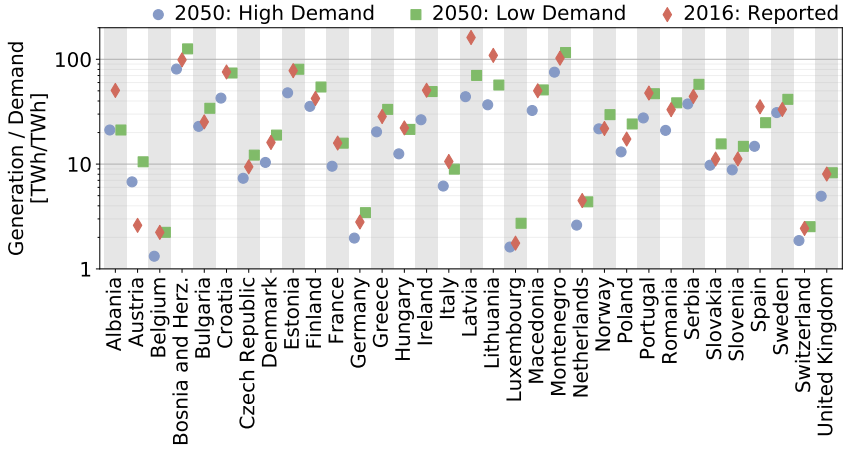

Figure 6.18: Ratio between total VRES generation potential in 2050 and total demand in 2016 [10] and 2 scenarios in 2050 [296]. Generation values do not include offshore generation potential.

380 kWh kW^{-1} for each doubling of the desired capacity until its encompassing values of 2611 kWh kW^{-1} at 166 GW. Switzerland also shows a similar FLH fall off rate, as does the ending portions of the trends for Norway and Greece; suggesting that the mountainous ranges in each of these countries can have a drastic impact on the expected performance of wind turbines. For most other countries, in particular France, Germany, Sweden, Belgium, and The Netherlands, a FLH fall of rate between 200 kWh kW^{-1} and 250 kWh kW^{-1} for each capacity doubling is seen.

Compared to onshore wind, this dynamic seems to affect PV installations much less as a result of the lower variability. For almost all countries, for instance, a FLH fall off rate between 100 and 150 kWh kW^{-1} is typical for the majority of their trends. Despite this, France and, to a lesser extent, Spain show a sharp transition in FLH fall off when approaching their encompassing FLH. This effect is due to the stark difference between the average performance in these regions versus a significantly large low-performance region. For Spain, the region can be clearly seen on the northern edge of the country, near to the Cantabrian and Pyrenees mountain ranges.

Of course, real-world location selection of wind turbines and PV parks does not necessarily favor the cheapest available option [178]. Moreover, for rooftop PV, sociopoltical incentives and limited roof availability lead to greater distribution of rooftop PV capacity [289]. Therefore, the trends shown in Figure 6.19 should be interpreted as the best FLH which could be achieved at each capacity from a cost-optimal perspective, but that realistic installation trends would certainly be lower until the maximum capacity is reached. As an example of how this ordering could

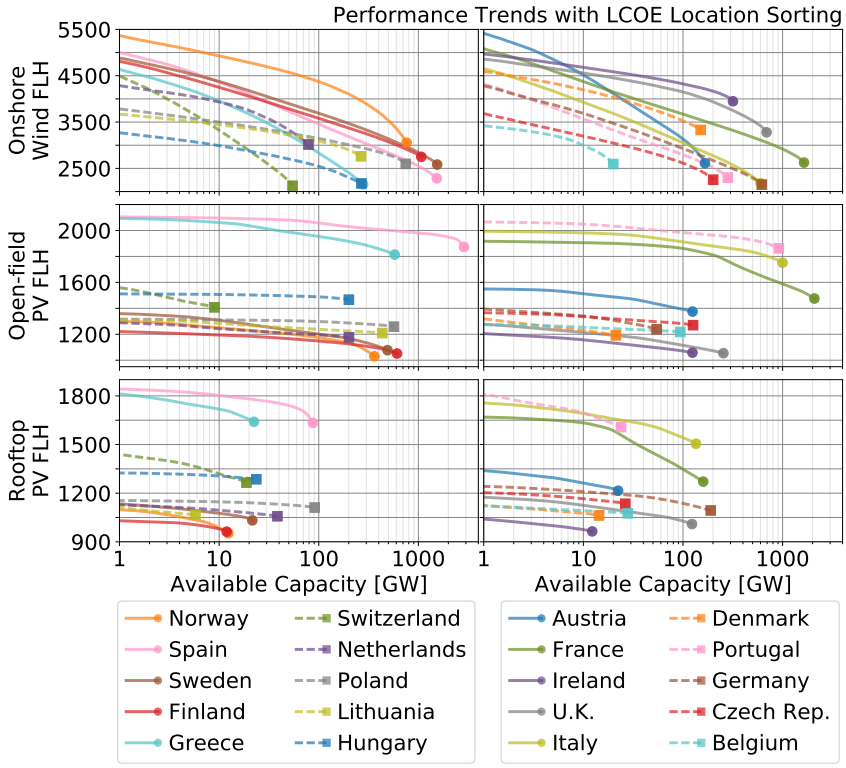

Figure 6.19: Average FLH trends for onshore wind, open-field PV, and rooftop PV versus installed capacity per country. Placements sorted by LCOE. Onshore wind figures adapted from Ryberg et al. [109].

change the trends for onshore wind and open-field PV, Figure 6.20 shows these same trends if they were constructed using the MCDA sorting approach of Tlili et al. [50], which has been previously described in Section 2.1.3. Notice that, with both LCOE-sorting and MCDA-sorting, the trends always end at the same total capacity and FLH average value for each country. On the other hand, the relatively low-capacity portions of these trends are most susceptible to the use of MCDA-sorting since the average wind speed or average GHI irradiance only account for a portion of each location's score. Because of this, countries such as Norway are heavily affected and the average FLH of its first $1\,\mathrm{GW}$ of onshore wind falls roughly $32.4\,\%$ to $3650\,\mathrm{kWh\,kW^{-1}}$. Onshore wind energy in Ireland is seen to maintain a FLH around $4000\,\mathrm{kWh\,kW^{-1}}$ for its entire potential. Finally, the MCDA-sorting is seen to have a much higher impact on the average performance of onshore wind turbines than on open-field PV parks.

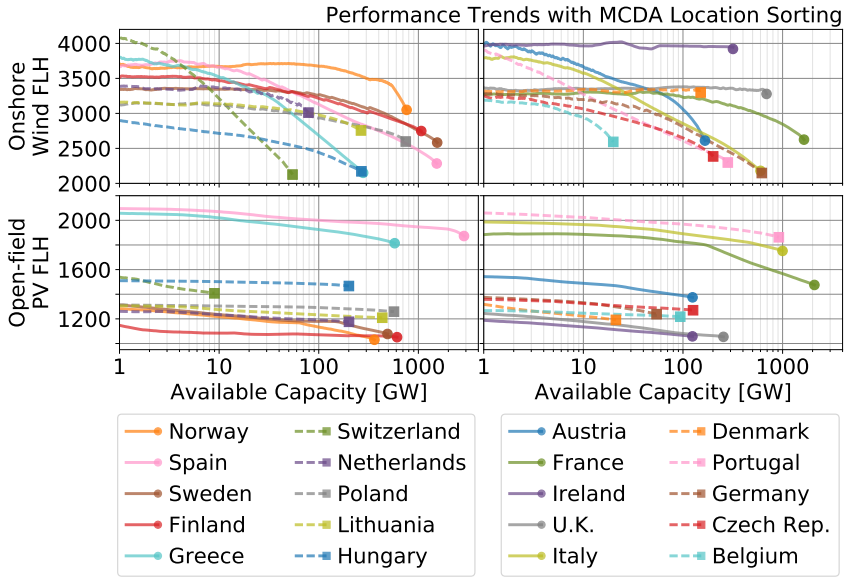

Figure 6.20: Average FLH trends for onshore wind, open-field PV, and rooftop PV versus installed capacity per country. Placements sorted by the MCDA approach of Tlili et al. [50], and previously discussed in Section 2.1.3.

6.3 Cost Estimations

After simulation results are obtained, estimates of the final generation costs can be found across Europe for each technology. A summary of the resulting LCOE values is given for select countries in Figure 6.21, which generally shows that onshore wind has the largest spread of observed LCOE values which generally encompasses the observed LCOEs of both open-field and rooftop PV. Furthermore, as expected, rooftop PV is always seen to be more expensive than open-field PV due both to its higher investment cost and lower FLH.

For onshore wind turbines, the capital cost is a function of turbine design, leading to a convoluted relationship between FLH and final LCOE. Therefore, the explicit distribution of onshore wind FLH is shown in Figure 6.22. Comparing Figures 6.11 and 6.22 shows that, in general, locations with high average FLH correlate to low LCOEs. As a result, all of the trends noted for FLH, such as the predominance of strong performance in Ireland, the United Kingdom, and Denmark also lead to cheap LCOE values. This result is not surprising considering that the high FLH locations often correspond to strong wind speeds and, as a result, the specific cost of turbines at these locations are cheaper owing to their higher capacity. As seen in Equation C.5, cheaper capital costs and higher FLHs support each other to result in cheaper LCOE. Despite this, there are still cheap generation options

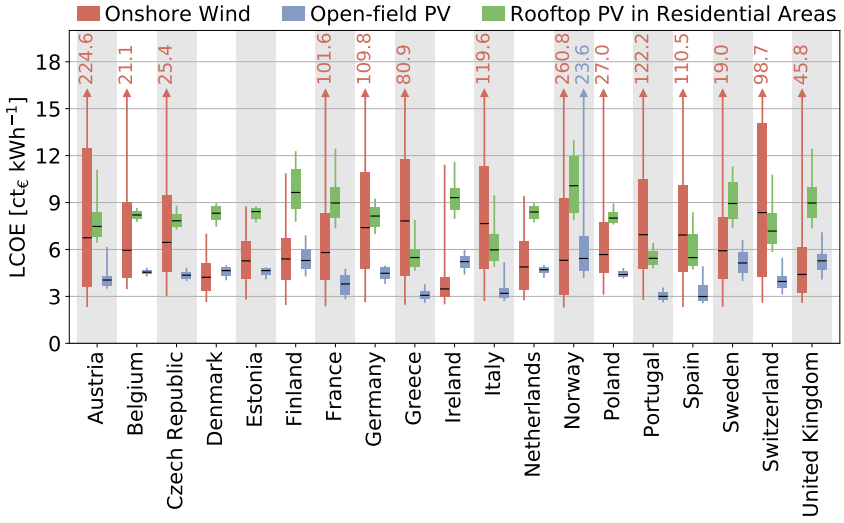

Figure 6.21: LCOE distribution of all technologies by country. Indicated values are the maximum LCOE, 95$^{\text{th}}$percentile, mean LCOE, 5$^{\text{th}}$ percentile, and the minimum LCOE.

in some surprising areas. For instance, the south eastern tip of Italy, the island of Sardinia, and much of Sicily are good examples of this. Almost all of Poland, Estonia, Lithuania, and Latvia, also show costs in the range of 4 to 6 $\text{ct}_{€}\,\text{kWh}^{-1}$.

Across all of Europe, a large spread of onshore wind LCOE values are observed, with 90 % found between 3.82 and 10.71 $\text{ct}_{€}\,\text{kWh}^{-1}$. Furthermore, an asymmetric distribution is observed, shown in Figure 6.23, wherein the cheapest cost is observed at 2.33 $\text{ct}_{€}\,\text{kWh}^{-1}$, the most probable value is found at 5.50 $\text{ct}_{€}\,\text{kWh}^{-1}$, and the average is found at 6.65 $\text{ct}_{€}\,\text{kWh}^{-1}$. Compared to the expert survey conducted by Wiser et. al [157], onshore wind generation costs in 2030 are expected to be between 3.03 and 4.47 $\text{ct}_{€}\,\text{kWh}^{-1}$, with a median estimate given at 3.73 $\text{ct}_{€}\,\text{kWh}^{-1}$; which, if achievable by 2030, should represent at least conservative estimates for 2050. In comparison, LCOE values derived from JRC's estimates [160], which are in context of 2050, suggest onshore wind LCOEs should be between 2.23 and 4.22 $\text{ct}_{€}\,\text{kWh}^{-1}$, with a 2.89 $\text{ct}_{€}\,\text{kWh}^{-1}$ median. Considering that these cost estimates are given in the context of operating wind turbines, as opposed to all potential turbines, then the values found in this work are arguably in close agreement with these estimates. Between the ranges given by either source, a total potential of 2.79 and 1.39 TW, respectively is found in the results of this work; which are both far larger than the largest envisioned future European onshore wind capacity of 760 GW in the aforementioned E-Highway scenarios [296].

Since relative capital costs for open-field PV is always assumed at 500 € kW^{-1}

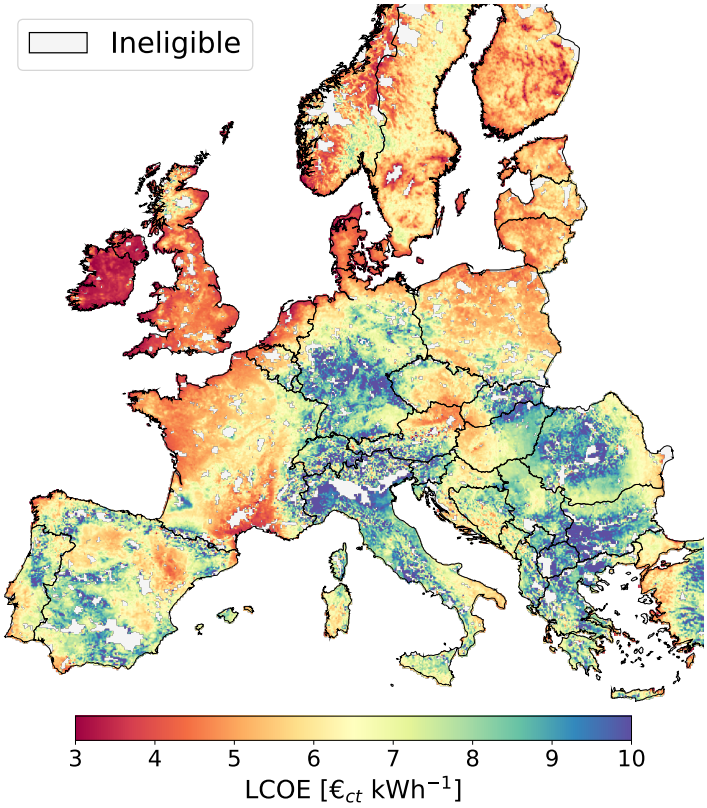

Figure 6.22: Average estimated LCOE for onshore wind turbines mapped across Europe. Previously published in Ryberg et al. [109].

(Section 4.2), the spatial distribution of these costs can be directly inferred from the open-field FLHs in Figure 6.14, and therefore this is mapped in Appendix Figures G.1. For reference, with the assumptions of Table 4.2, open-field PF locations with a FLH of $1000\,\mathrm{kWh\,kWp^{-1}}$ would correspond to an LCOE of $5.53\,\mathrm{ct_{€}\,kWh^{-1}}$, and $1500\,\mathrm{kWh\,kWp^{-1}}$ would lead to $3.69\,\mathrm{ct_{€}\,kWh^{-1}}$. Nevertheless, a similar pan-European distribution as the one shown for onshore wind can be made for open-field PV, which is given in Figure 6.24. For open-field PV, a trimodal distribution is seen, corresponding to peaks around 2.8, 3.7, and $4.7\,\mathrm{ct_{€}\,kWh^{-1}}$. The first peak corresponds to the darkest red areas of Figure 6.14 dominated by Spain, but also appears in Southern France, Sicily, and Greece. To note, while FLH values for areas in Turkey are shown in Figure 6.14, these are not factored into the distribution of Figure 6.24, since Turkey was not included in the latter VRES lull analysis on account of missing land eligibility data. The cheapest open-field LCOE is found at $2.65\,\mathrm{ct_{€}\,kWh^{-1}}$, while the average is found at $3.77\,\mathrm{ct_{€}\,kWh^{-1}}$. Open-field LCOE values are grouped much tighter compared to onshore wind, with $90\,\%$ of values

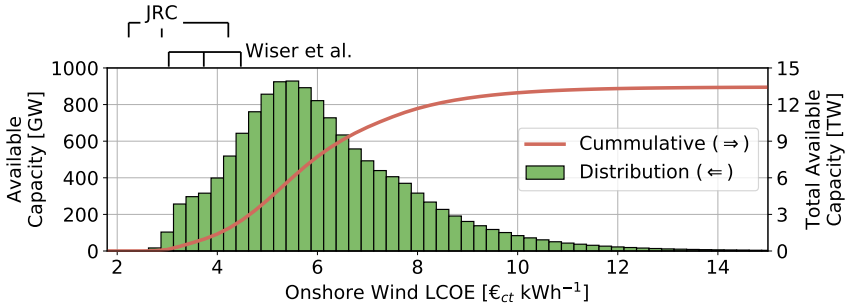

Figure 6.23: LCOE distribution of all available onshore wind turbines across Europe compared to estimates by Wiser et al. [157] and JRC [160]. Figure previously published in Ryberg et al. [109].

being found between 2.80 and 5.34 ct€ kWh^{-1}. As for rooftop PV, 90 % of LCOEs are found between 5.24 and 9.08 ct€ kWh^{-1}. In this case, a more spread out distribution is seen with a general peak around 8.2 ct€ kWh^{-1}, and a European average at 7.32 ct€ kWh^{-1}.

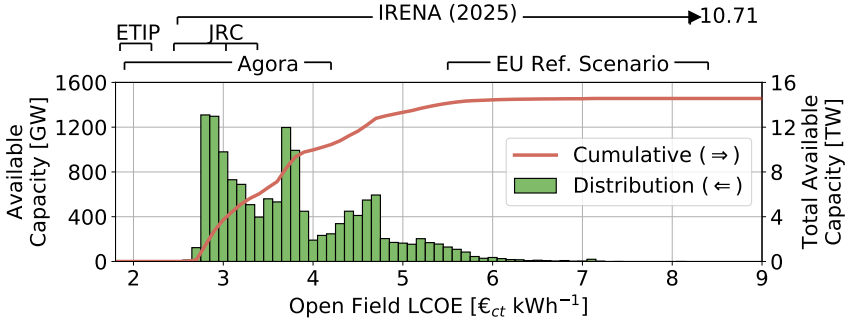

Figure 6.24: LCOE distribution of all available open-field PV placements across Europe compared to estimates by JRC [160], ETIP [287], Agora Energiewende [285], IRENA [11], and from the EU's 2016 Reference Scenario [175].

A range of conclusions can be drawn by comparing these values to literature. In the case of open-field PV, the estimates of JRC [160], who predict costs between 2.45 and 3.38 ct€ kWh^{-1}, and Agora [285], 1.90 and 4.20 ct€ kWh^{-1}, are arguably very well aligned with the estimates made here. The same could also be said for the estimates of IRENA [11], although these results are given for a global context and thus span a very broad range and, furthermore, are intended for 2025. ETIP [287] appears to come to very optimistic cost estimates between 1.85 and 2.20 ct€ kWh^{-1}, which are not supported by the results here. Finally, estimates from the EU's 2016

reference scenario [175], between 5.5 and 8.4 $ct_{€}\,kWh^{-1}$, appear high compared to both the results here as well as to other reports. This is most likely due to the EU's reference scenario being designed as a 'business as usual' scenario without much VRES development compared to today.

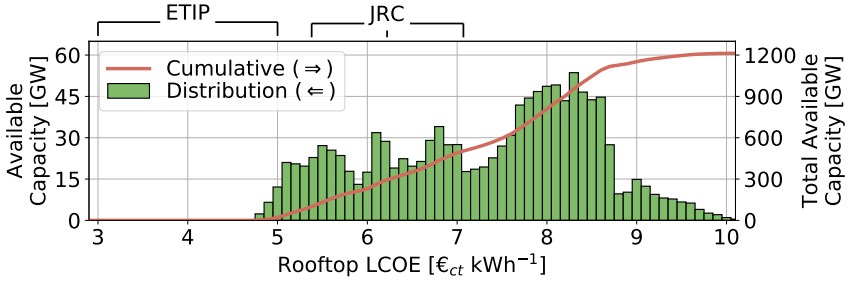

Figure 6.25: LCOE distribution of all rooftop PV simulation locations across Europe compared to estimates by JRC [160], and ETIP [287].

Rooftop PV LCOE values are also directly inferable from their FLH trend, and so this is supplied in Appendix Figure G.2. For reference, with a FLH of 1000 kWh kWp^{-1} rooftop PV LCOE would be calculated at 8.85 $ct_{€}\,kWh^{-1}$, and at 1500 kWh kWp^{-1} it would be 5.90 $ct_{€}\,kWh^{-1}$. Concerning the pan-European distribution of rooftop PV LCOE values in Figure 6.25, two comparisons are made. ETIP [287] estimate of 3.0 to 5 $ct_{€}\,kWh^{-1}$ is again quite low compared to the result here. However, JRC's [160] estimate of installed costs between 5.38 and 7.07 $ct_{€}\,kWh^{-1}$, with and average of 6.22 $ct_{€}\,kWh^{-1}$, is in close agreement with the results here as this range corresponds to 405 GW, roughly one third, of the full potential range.

At last, national generation cost trends in the same form as Figure 6.19 are provided in Appendix Figure G.3 for LCOE-sorted locations, and Appendix Figure G.4 for MCDA-sorted locations. As the relationships observed in these trends follow very closely to the observations made for Figure 6.19, they will not be repeated here. Furthermore, the effect of imposing economic limitations on the capacity potential on Europe and for each country is given in Appendix Tables G.1, G.3, and G.5 for onshore wind, open-field PV, and rooftop PV, respectively. In these tables, the remaining capacity potential after excluding all locations with an LCOE above X $ct_{€}\,kWh^{-1}$ are shown. Similarly, Tables G.2, G.4, and G.6 provide the impact of these same limitations on available generation. From all of these plots and figures, it is clear to see that all regions possess some amount of cheap onshore wind and PV generation locations; although this is much more drastic for onshore wind than for PV. It is also clear that the remaining potential below a given economic threshold constitutes a very non-linear relationship unique to each country. Nevertheless, in summary, it is seen that Europe as a whole has an onshore wind potential of 1177 GW and 4614 TWh and an open-field PV potential of 9599 GW and 15,546 TWh available below a threshold of 4 $ct_{€}\,kWh^{-1}$, while, for rooftop PV, a remaining po-

tential 513 GW and 674 TWh is seen below an $8\,\mathrm{ct}_{€}\,\mathrm{kWh}^{-1}$ threshold.

6.4 Summary

The capacity, generation, and cost potential results discussed in this chapter have exposed the full potential of European onshore wind, open-field PV, and rooftop PV generation. Total potential results seem to deviate from similar studies seen in the literature, however, as discussed throughout this report, much of this is a direct result of highly scenario-dependent land eligibility outcomes. Nevertheless, FLH results appear to match fairly well and, especially, the resulting LCOE distributions of all technologies are well within the ranges predicted by other research organizations.

Ultimately, these results set the stage for the forthcoming investigation into VRES lulls. On the one hand, these results have shown that, in principal, Europe is capable of satisfying its own electricity demands several times over by means of only VRES generation. Furthermore, it is shown that large portions of this generation potential will be available at extremely competitive costs. On the other hand, these potentials fail to communicate the temporal relationships inherent between regions and between VRES technologies. Considering the complexity which exists only in the spatial dimension, it is therefore clear to see why energy systems modeling remains such a complicated task.

Chapter 7

Lull Occurrence Results and Discussion

In this chapter the results of the VRES lull investigation will be discussed and in all cases the general lull evaluation algorithm described in Section 5.4.2 is always applied. Furthermore, since probability likelihoods are often discussed, the following notation will be used: P_{100} refers to a quantity which has a $100\,\%$ chance of being observed in any given year, P_{10} for a $10\,\%$ occurrence per year, P_1 for a $1\,\%$ occurrence, and finally P_{max} for the maximum observed value. P_{10} and P_1 values can also be thought of as referring to a quantity that is likely to occur 'once every 10 years' and 'once every 100 years', respectively.

For the primary analysis, result discussion will be presented in the order that they are described in Section 5.5, and in each case will compare lull occurrence differences between the following regional scopes: Europe as a whole, North Rhine-Westphalia (NRW), a central European area, and the countries Germany, France, Italy, Spain, and the UK. For the final context, "Constrained Grid with Dispatchable Backup", a more detailed discussion is provided for the E-Highway regions; including lull lengths and deficits, average curtailment, and backup generation. In all cases, a detailed tabulation of P_{100}, P_{10}, and P_1 lulls in each of the three lull evaluation contexts, as well as annual operational values[1] averaged across all demand-generation years can be found in Appendix J.

7.1 Context 1: Intermittent Generation

The first lull evaluation context to be discussed is the "Intermittent Generation" context, where only the generation from wind turbines and PV systems are considered without accounting for electricity demand or grid limitation. The following discussions will focus first on the occurrence of lulls in primary setup of this context, where a lull begins once the generation falls below a threshold equal to $25\,\%$ of the multi-year average. Afterwards, the sensitivity of lull occurrence to the lull threshold is explored. Finally, comparisons to literature sources with comparable features are discussed.

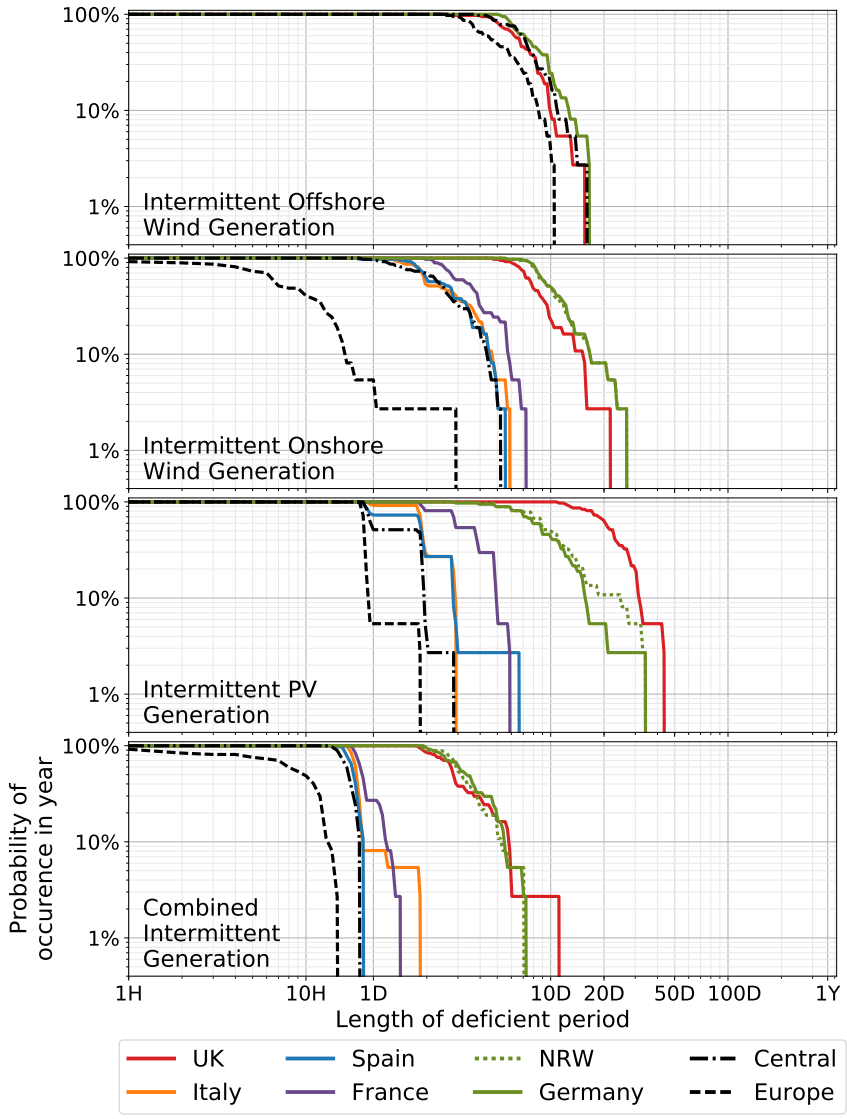

Figure 7.1: Length of VRES lulls in the ”Intermittent Generation” context.

7.1.1 Lull Occurrence

Figure 7.1 displays the length of VRES lull spans. At the top of this figure is the probabilities of observing intermittent generation lulls from offshore wind energy

[1] Such as the total biomass usage, total curtailment, total reliance on import, and largest residual load

(offshore lulls). Of the regional contexts shown, only Germany, UK, Central, and Europe have a contribution from offshore wind turbines. Furthermore, since all offshore generation in this scenario is placed in the North Sea, it follows that offshore lull lengths do not differ much between the various regional scopes. For example, all scopes have a P_{100} offshore lull lasting 2.4 days in any given year. For longer offshore lulls, there is a slight deviation between scopes where, for example, a P_{10} lull span lasting 8.5 days is seen across Europe, 9.8 for the UK, 10.8 for the Central region, and 12.5 days for Germany. At the end, the UK, Central, and Germany all appear to converge around a P_{max} lull length of 16 days, while the entirety of Europe only reaches to 10.5 days. Due to the region-wide generation aggregation, it makes sense that Europe as a whole shows the shortest lull lengths since it also corresponds to the largest area and, therefore, the most spatial variability in the offhore generation profiles.

Looking at intermittent generation lulls from onshore wind energy (onshore lulls), a much greater variability between regional scopes is observed compared to the offshore lulls. Onshore lulls in Germany and UK are, like offshore lulls, quite close to one another, seen by the fact that their largest P_{100} values are found at nearly the same points. At lower observation rates, however, onshore lulls in these areas are noticeably longer then they were for the offshore context; extending to 16.5 and 15.0 days, respectively, at P_{10}, and to 26.8 and 21.0 days at P_{max}. The onshore lull occurrence trend for NRW nearly exactly follows that of Germany, suggesting that onshore lull occurrence is not strongly affected by the spatial scope enlargement between NRW and the whole of Germany. However, since much more diversity contributes to the onshore generation at the European level, onshore lulls are significantly different when considering the Central and European scopes. For the Central scope, a maximum P_{100} onshore lull span of 19 hours is seen, roughly one-fifth of the P_{100} offshore lull span. Similarly, a P_{10} onshore lull span of 4.3 days, and a P_{max} of 5.0 days are seen; which are again much less than those seen in the offshore lulls. Italy and Spain both see onshore lulls trends that are extremely close to those described for the Central region, above which the trend for France is consistently around a factor of 1.3 times higher. At last, Europe as a whole shows the shortest onshore lulls, which actually never see a P_{100} value. For Europe, $10.9\,\%$ of years did not observe any onshore lull throughout the entire year; suggesting that a base load generation from onshore wind turbines in Europe up to $25\,\%$ of their average generation is possible when not considering grid limitations and concurrent demand, but would nevertheless not occur reliably. A P_{10} onshore lull for Europe of only 15 hours is seen, ultimately reaching to a P_{max} value of 2.8 days.

Compared to the previous discussions, intermittent generation lulls from PV energy (PV lulls) are more varied between regions. Beginning with the European scope, where once again the shortest lulls are seen, a P_{100} PV lull span of 19 hours is seen which naturally corresponds to lacking PV generation during the winter solstice. A steep transition to the P_{10} PV lull span value is then seen, at 21 hours, which ends at a P_{max} of 1.8 days. Comparing PV lulls to onshore lulls over the European scope is therefore quite complex. On the one hand onshore lulls are found to span shorter time periods than PV lulls around $95\,\%$ of the time, while on the other

hand onshore lulls also have the potential to be last almost twice as long as PV lulls in the most rare cases. After Europe, PV lulls for the Central region, Spain, France, and Italy each show trends with maximum P_{100} span values similar to that of their onshore lulls, and P_{10}'s and P_{max}'s which are noticeably shorter. More interestingly, PV lulls in Germany, the UK, and NRW are quite different from their onshore wind counterparts. Germany and NRW, which are once again very close to one another, have a maximum P_{100} PV lull of 2.83 and 3.71 days, respectively; almost half of their maximum P_{100} onshore lull. For a brief period around the P_{10} PV lull span value, Germany and NRW separate to show spans of 15.54 and 24.46 days, but then come together again to share a P_{max} PV lull span of 34.17 days; much longer than the corresponding values seen for onshore lulls. In this case, the relationship between onshore wind and PV generation is opposite to that which was described for Europe; where most of the time PV is the more reliable generation option compared to onshore wind, but also has a remote possibility of causing significantly longer lulls. For the UK, the entirety PV lull span trend is beyond that of their onshore lulls; with a maximum P_{100} PV lull span of 10.79 days, a P_{10} of 31 days, and a P_{max} of 43.58 days. The longest PV lulls observed in Germany and the UK are most likely an artifact of the 25 % lull threshold chosen for this phase of the analysis. Since Germany and the UK are not as sunny as countries such as Spain, Italy, and much of France, it follows that the few exceptionally sunny years in these two countries offset the average generation enough that generation profiles in typical PV years are much closer to the lull threshold, thus resulting in more frequent and longer lulls.

At last, attention is turned toward the intermittent generation lulls resulting from the combination of all VRES generators (combined generation lulls), shown at the bottom of Figure 7.1. In these trends, a constant relationship is observed in that, for all regional scopes, significantly shorter combined generation lulls are seen in comparison to any of offshore lulls, onshore lulls, or PV lulls. Similar to onshore lulls, combined generation lulls in Europe are not guaranteed to occur and, in fact, 16.22 % of years never see VRES generation fall below the lull threshold of 25 % of the average generation. Europe sees a P_{10} combined generation lull span of 12 hours and a P_{max} at only 14 hours. In the Central region, a maximum P_{100} combined generation lull of 12 hours is seen, which then drops rapidly to a P_{max} value of 19 hours. The trend for Spain closely follows the Central region, as does the trend for Italy until around the P_8 point; after which Italy's P_{max} increases significantly to 1.79 days. Germany, NRW, and the UK again observe the longest combined generation lulls that, for the most part, are quite close to one another. For these scopes, the maximum P_{max} combined generation lull is seen around 1.75 days, increases to a P_{10} of nearly 5.5 days, and then diverges as they approach the P_{max} point; with around 7.15 days seen for both Germany and NRW, and 11.13 days for the UK. Once again it is seen that the larger regional scope of Germany compared to NRW does not greatly influence the occurrence of combined generation lulls.

7.1.2 Sensitivity to Lull Threshold

Of course, all of the above discussion is dependent on the lull threshold definition of 25 % of the average generation. Figure 7.2 shows how the maximum P_{max}, P_{10} and P_{100} combined generation lull values change for each regional scope as a function of this threshold. It is clear that the outcome of these lull spans are closely linked to the lull threshold, which does not come as a surprise as a larger threshold leads to both more opportunities for the VRES generation to fall below the threshold as well as less opportunities to replenish the deficit from super-threshold generation. When the lull threshold factor reaches 100 % then, by definition, more of the generation is below the threshold than is above and as a result often leads to lulls which span all 8760 hours in a year. This is why all scopes converge on a full year at a 100 % lull threshold for the P_{10} and P_{100} values. Nevertheless, the same basic relationships seen in Figure 7.1 are again observed, albeit at different magnitudes; such as the tendency for Germany and the UK to have the longest lull spans while Europe and the Central region have the shortest.

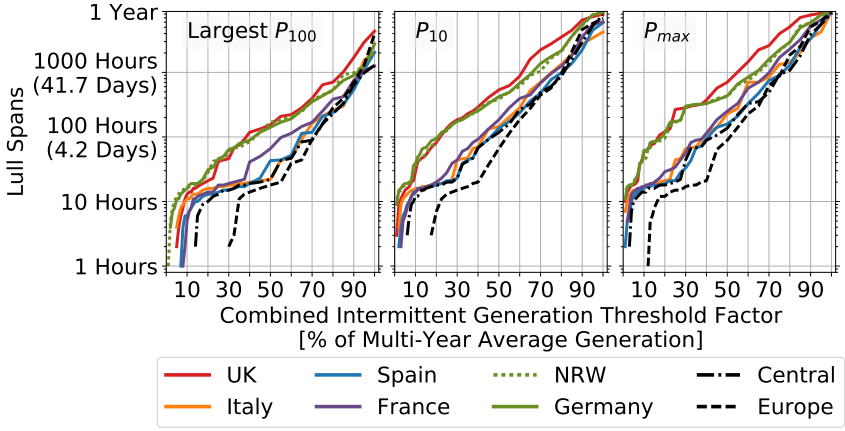

Figure 7.2: Sensitivity of combined generation lull spans to lull threshold

The initial left position of each trend in Figure 7.2 indicates the minimal VRES threshold where lulls begin to be observed, and thus comment on the possibility of uninterrupted wind and PV generation in these regions. For instance, all regions have a corresponding lull threshold at which no P_{100} value exists, meaning that at least some years[2] have the possibility of producing uninterrupted generation at that threshold. In Germany this threshold is seen at 1 % of the average generation, while for the UK and Italy it is seen at 4 %. Spain and France's minimal lull threshold at P_{100} can be found at 6 and 7 %, respectively. Finally, the Central region and Europe allow the largest lull thresholds at 13, and 27.5 %. A few of these regional scopes also show the potential for uninterrupted generation, where no combined generation lulls occur in any year; this can be found from the left most position of the P_{max}

[2] Typically in the range of 2 to 8 % of generation years

trend of Figure 7.2. These regions are France, corresponding to a lull threshold of $1\,\%$ of the average generation, the Central region with $2\,\%$, and finally Europe with $11\,\%$. Although this outcome is limited to the distribution of wind and PV capacities within the evaluated scenario along with the neglect of grid limitations, this suggests that uninterrupted VRES generation is possible across the European scope equal to $11\,\%$ of the multi-annual average of hourly wind and PV generation; which is in this case equal to a generation capacity of $55\,\mathrm{GW}$. It is possible that this potential for a uninterrupted generation could be improved via a tailored distribution of wind and PV generators as well as different share between these technologies.

7.1.3 Discussion

Comparing these outcomes to literature is not a one-to-one procedure as no study has taken a look into intermittent generation lulls in the same manner used here. Nevertheless, there are several studies whose scope is at least close to the current work and thus can be compared from a high level perspective. For example, Wohland et al. [348], looking only at onshore wind generation, investigated the likelihood of observing a national onshore wind generation lull coincidentally to a European onshore wind generation lull. Wohland's results suggest that Germany should have the most frequent lulls since the deficits also correspond to European deficits, France should be next, followed by Italy and finally the UK and Spain. Compared to the onshore lull trends of Figure 7.1, Wohland's national ordering is the same as the one found here with the exception of the UK's placement above Germany. Although Wohland et al. also argue that the inclusion of PV would not have a significant impact on the final results, which is not supported by the results of this work where the difference between combined generation lulls and onshore lulls is significant for all regions. In another study, Weber et al. [352] show that the average backup energy needed for a copper-plate Europe is much smaller than for individual countries due to the larger spatial scope; which is clearly backed up by all trends observed in Figure 7.1. It is also commonly concluded in the literature that, over large regional scopes, wind energy is less variable than PV energy [355, 356], and thus should generally produce shorter lulls. In contrast, many others have noted that wind energy is much more susceptible than PV energy to North Atlantic Oscillations, which can also induce significant lull periods [15, 349]. As discussed above, the relationship between onshore lulls and PV lulls are quite complex and could be interpreted to support either position depending on whether or not one focuses on the probability of observing frequent yet short lulls, where PV energy could be considered as less dependable, versus the probability of observing infrequent yet long lulls, where wind would be considered less dependable. Furthermore, the region of study also matters since, as discussed, the relationship between onshore lulls and PV lulls appears to be opposite for Germany and the UK compared to all of Europe.

For two studies in particular, a more detailed comparisons can be performed. The first of these, by Weber et al. [352], investigated the dependence of storage needs in a wind-dominated European energy system to weather shifts arising from to Climate Change. In this study, Weber et al. plot the relationship between the time duration when wind generation is less than the average versus their frequency of

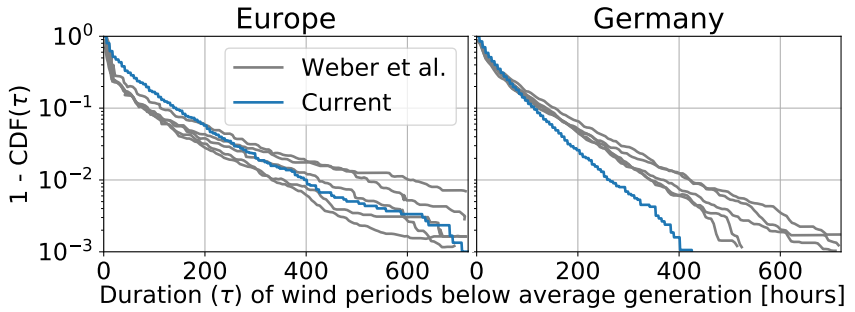

Figure 7.3: Length of onshore lull durations vs. Weber et al. [352]. Results are formulated in the cumulative distribution function (CDF) manner shown by Weber et al., including the aggregation of generation over 6 hour periods.

occurrence. Weber et al.'s lull threshold is far more restrictive than the $25\,\%$ of the average used in this work, although they do not require lull events to continue during a regeneration period. Furthermore, Weber et al. display these trends when using multiple weather datasets within the EURO-CORDEX initiative, as well as for both Germany and a copper plate Europe. Formulating the onshore lull results found here in the manner published by Weber et al. is straight forward, and the comparison is shown in Figure 7.3. In this figure it is seen that the lull durations calculated by Weber et al. and those produced from this work are quite close to one another; especially in the European scope for lull durations beyond 200 hours, and in Germany for lull durations until around 100 hours. In comparison to the current study, Weber et al. have a simpler wind simulation procedure which only considers a single turbine design at $100\,\mathrm{m}$ hub height, 3-hourly wind speed resolution, and a nearly uniform spatial turbine distribution. The larger occurrence of short lull durations across Europe seen in the current results are explainable on account of Weber et al.'s use of the EURO-CORDEX datasets. Since these datasets have a spatial resolution around $12.5\,\mathrm{km}$ across Europe, as opposed to the much larger resolution of the MERRA data used here[3], the more varied spatial mixing across large scopes decreases the occurrence of short lulls. For Germany, the deviation for large lulls is an artifact of Weber et al.'s use of 3-Hourly data when performing their simulations, as opposed to the hourly data used here. Due to the non-linear nature of turbine power curves, the use of 3-Hourly data in place of hourly data will under predict turbine generation during periods with wind speeds in the range of the cut-in wind speed. Weber et al.'s turbine definition, which is both shorter and appears consistent with a turbine with a specific power near to $320\,\mathrm{W\,m^{-2}}$, also plays a role here in that it would have less generation at lower wind speeds compared to the average German specific power used in this work, around $270\,\mathrm{W\,m^{-2}}$. For both of these reasons, it is more likely for Weber et al. to observe longer, unbroken, lull periods across Germany in comparison to the current results.

[3] $\approx$60 km over Europe.

Table 7.1: Lull occurrence comparison against Raynaud et al. [347]

	Average Span [Days]		**Days in Drought**	
	Current	Raynaud et al.	Current	Raynaud et al.
Onshore				
Moderate				
Germany	2.4	2.3	120.3	115.9
France	1.8	2.5	59.5	109.5
Spain	1.8	2.0	53.1	118.0
Italy	2.1	2.4	54.2	107.4
UK	2.3	2.7	86.5	127.2
Onshore				
Severe				
Germany	1.6	1.3	48.4	39.5
France	1.3	1.3	3.7	33.7
Spain	1.0	1.3	1.5	13.7
Italy	1.2	1.2	0.9	5.9
UK	1.7	1.6	26.0	47.6
PV				
Moderate				
Germany	2.9	7.0	68.9	119.5
France	1.7	5.1	38.2	100.9
Spain	1.5	2.4	22.6	44.0
Italy	1.5	5.4	27.2	82.0
UK	3.6	6.6	83.1	135.4
PV				
Severe				
Germany	1.5	2.1	14.7	39.6
France	1.2	1.2	5.1	5.7
Spain	1.0	1.1	0.9	3.1
Italy	1.0	1.5	1.0	21.2
UK	1.6	2.4	27.0	54.2

The second study where a comparison can be made is given by Raynaud et al. [347], who investigated the occurrence of onshore wind and PV generation lulls in Europe; which they refer to as ”Energy Production Droughts”. They measure their lulls against two thresholds referred to as ’Moderate’ and ’Severe’, identified as time durations where generation falls below $50\,\%$ and $20\,\%$, respectively, of the average daily generation. As before, the results produced from the current analysis are formulated to match the context of Raynaud et al., and are directly compared in Table 7.1 for Germany, France, Italy, Spain, and the UK. In terms of the average lull span, there is a very clear correlation between the current results and Raynaurd et al.’s; with the exception of lower average spans for moderate PV lulls. Besides this, all other values are within a small margin of error from the reported value

considering the imperfect extraction process. Total time spent in lulls, however, are significantly lower compared to Raynaud et al., which is an expected result considering the daily evaluation of wind and PV generation compared to the hourly evaluation performed here.

7.2 Context 2: Residual Load with Basic Backup

In the ”Residual Load with Basic Backup” context, VRES lulls are computed by comparing the total VRES generation to the demand profile of each regional scope and adjusted according to the hourly-averaged backup generation, import, and export as reported by E-Highway [300]. Similar to the previous context, this context assumes a copper-plate across Europe. Equation 5.1 displays how the temporally-explicit lull threshold is calculated for this evaluation context by subtracting a constant amount of biomass, hydro, and import utilization from the summation of time-series demand and constant export. The following subsections will first report the occurrence of the lulls which are found in this context, which will be referred to as ”basic residual load lulls”[4] to distinguish them from the combined generation lulls discussed in the previous section. After discussing the occurrence of both lull spans and lull deficits in the primary setup of this context, the sensitivity of these lull occurrences to the level of backup availability will be explored. In the end of this section comparisons against a few literature sources will be provided and the results will be further discussed.

7.2.1 Lull Occurrence

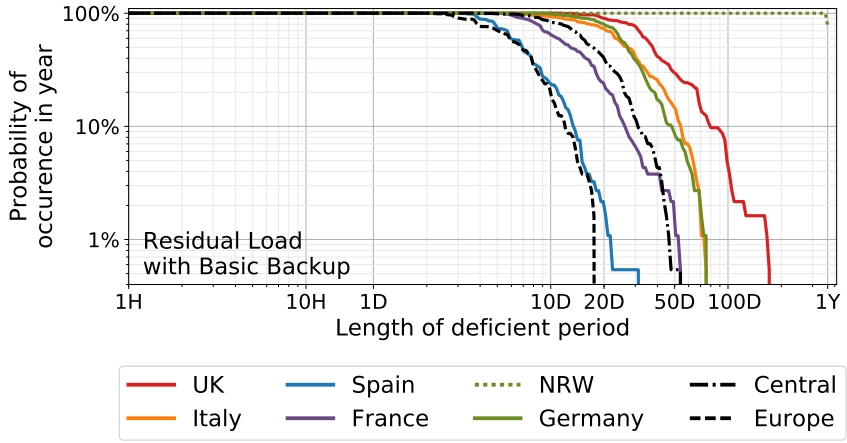

Figure 7.4: Length of VRES lulls in the ”Residual Load with Basic Backup” evaluation context

[4] on account of the copper plate and constant backup availability.

Figure 7.4 and 7.5 show the resulting spans and deficits of the VRES lulls observed in this context; which will be discussed in turn. Compared to the combined generation lulls from the "Intermittent Generation" context shown in Figure 7.1, it is clear that the inclusion of demand and average backup into the VRES lull computation has a drastic impact on lull occurrence. Depending on regional scope, it can be immediately seen that the length of lulls in this context increases by one to two orders of magnitude in comparison to the combined generation lulls. For the European scope, for example, the maximum P_{100} basic residual load lull span in this context is found at 1.92 days, P_{10} at 11.79 days, and P_{max} at 17.54 days. Lull spans for Spain are closely comparable to that of all of Europe; with the longest P_{100} span at 3.00 days, P_{10} of 12.92 days, P_1 at 21.67 days, and finally a P_{max} at 31.21 days. The Central region takes a median position of all the regional scopes shown; where the maximum P_{100} lull span is found at 3.83 days, P_{10} at 30.29 days, P_1 at 46.29 days, and finally P_{max} at 53.92 days. These values in the Central region are also very close to what is seen for France. Germany and Italy also show lull spans which are very close to one another; which, for Germany, a maximum P_{100} lull span is found at 9.54 days, P_{10} at 47.75 days, and finally P_1 and P_{max} at 75.25 days. At last, due to its position as a net electricity exporter, the UK has the most likely chance of the visualized regions to witness a lull. In this case, the maximum P_{100} basic residual load lull span for the UK is observed at 11.46 days, P_{10} at 77.58 days, and a P_{max} at 170.8 days.

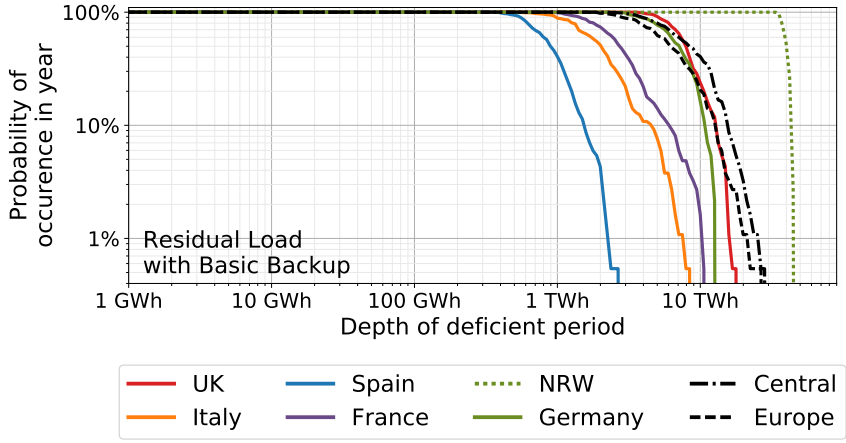

Figure 7.5: Size of VRES lull deficits in the "Residual Load with Basic Backup" evaluation context.

Figure 7.5 shows the basic residual load lull deficits, which correspond to the lull spans shown in Figure 7.4. To note, lull deficit trends shown for NRW is misleading in this figure since this region shows full-year lulls for some percentage of demand-generation years. Spain shows the least deficient lulls in this context as a result of having both the shortest spans next to Europe and much less overall demand. The maximum P_{100} basic residual load lull deficit in Spain is seen at 375.8 GWh, P_{10}

at 1.50 TWh, P_1 at 2.24 TWh, and a P_{max} of 2.66 TWh. Although far above Spain, Italy shows the second smallest lull deficits with the maximum P_{100} deficit found to be 530.9 GWh, P_{10} at 4.47 TWh, and P_{max} of 8.41 TWh. Germany and the UK show similar trends beginning at a maximum P_{100} lull deficit of around 3 TWh, P_{10} values near to 11 TWh, and P_{max} values at 12.59 and 17.78 TWh, respectively. The largest lull deficits in this context are of course seen for the European and Central scopes. Between these two, the entirety of Europe has much greater demand and does not expect any imports, but it has much more VRES generation and observes shorter lulls. In comparison, the Central region has less demand and receives help in the form of imports, but the reduced VRES generation and longer lull spans ultimately results in larger lull deficits. For Europe the maximum P_{100} basic residual load lull deficit is 1.58 TWh, P_{10} is 12.59 TWh, and P_{max} is 26.61 TWh. For the Central region the maximum P_{100} lull deficit is slightly higher, at 2.24 TWh, P_{10} at 14.96 TWh, and P_{max} is 28.18 TWh.

7.2.2 Sensitivity to Backup Capacity

The basic residual load lull spans and deficits discussed above are inherently linked to the amount of backup, import, and export which E-Highway reports for each region. Therefore, the sensitivity of the span and deficit occurrences was investigated for each regional scope wherein a range of fully-available backup capacities[5] were considered. The capacities considered range between zero up until a capacity equal to 100 % of the average hourly demand plus imports and exports[6]. Equation 5.2 shows how lull thresholds are computed in this sensitivity analysis for each backup percentage. The outcome of this sensitivity is given in Figure 7.6.

Figure 7.6 shows that basic residual load lulls occur in all regional scopes even when a fully available 100 % backup capacity is in place. For the European scope, these lulls with 100 % backup capacity can last at most 1 hour and would have deficits of only 20 GWh, which is insignificant on the European scale, but for a country like Germany they could last as much as 200 hours with deficits as high as 1 TWh. Furthermore, with 100 % backup capacity, Germany, France, Italy, and the UK are guaranteed to observe a basic residual load lull in all years lasting between 3 and 18 hours, and deficits in the range of 8 to 50 GWh, depending on the country. In comparison, Spain, the Central region, and Europe as a whole are only guaranteed to observe a lull with backup capacities of 95, 92, and 66 % respectively. Even when accounting for its average import, NRW is in a full-year lull for all years up until a 36 % backup capacity, but will continue to observe full-year lulls up until a backup capacity of 50 %. Finally for backup capacities factors above 90 % Europe no longer has a P_{10} value meaning that, with 90 % backup capacity, only around 10 % of years observe a basic residual load lull at the European level.

[5] Meaning that it is capable of full operation through a year.
[6] As stated by E-Highway

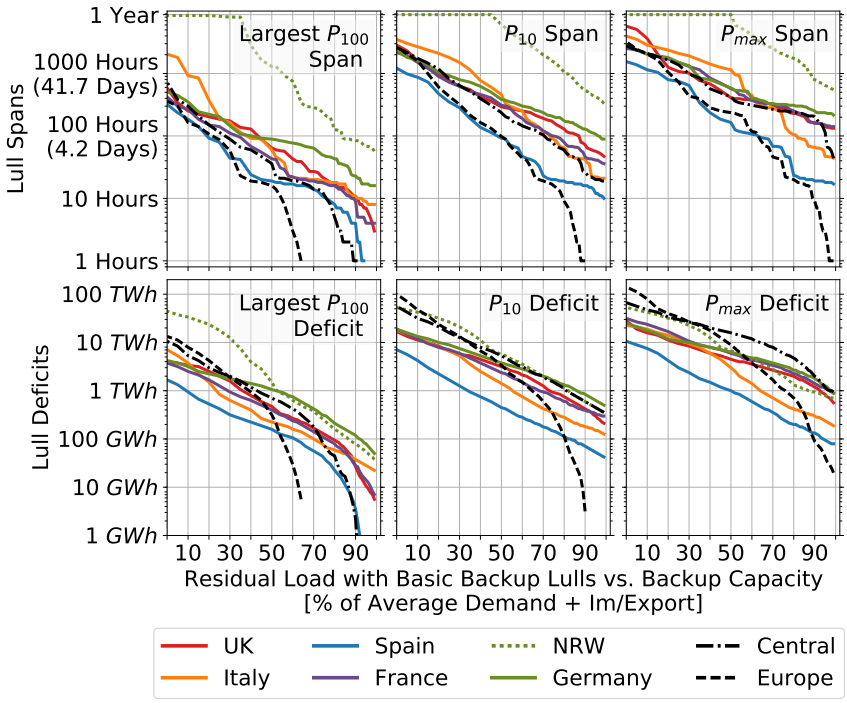

Figure 7.6: Sensitivity of the "Residual Load with Basic Backup" lulls to backup capacity

7.2.3 Discussion

By adding a future-oriented demand profile without any consideration of grid limitations, opportunities to compare the current results to literature sources are rare. Although numerous studies have considered a copper plate over Europe, the only other study known that has looked specifically at the occurrence of lull occurrences in a similar context is that of Raynaud et al [347], introduced in Section 5.1.2. Building atop their analysis discussed in the previous section, Raynaud et al. also formulated a demand estimation function tailored to each European nation which is then used to compare national demands against the VRES generation. As before, however, their context does not match exactly to the lull definitions used here; most notably in the sense that their VRES generation for each nation is scaled such that the total exactly matches the total electricity demand. 'Moderate' and 'Severe' lulls are again investigated, which, in this context, correspond to contiguous time periods where the daily VRES generation is less than $50\,\%$ and $80\,\%$, respectfully, of the total demand of the same day.

With this definition, one of their main results show that the consideration of demand

when evaluating lull occurrence has at most a $10\,\%$ increase on the total number of days a country spends within a lull. The large majority of countries, however, show nearly no change in their total number of moderate or severe lull days and only a few show a change in the mean duration of lull events. Similarly, Weber et al. [352] also find a low sensitivity to the demand profile. Both sources claim that the storage and backup needs across Europe predominantly depend on the VRES generation time series. Of the regional scopes investigated here, Raynaud et al. report that only Germany and England show a slight increase in the average duration of severe lulls, at around 2 days. It is quite clear that these claims are not supported by the current results since, comparing basic residual load lull spans in Figure 7.4 to combined generation lull spans in Figure 7.1, it is clear that the addition of demand to the lull equation has a profound impact on the observed length of lulls. The reasoning behind Raynaud et al.'s low sensitivity when incorporating demand into their lull analysis results from them having not considered a regeneration period as well as their matching of total VRES generation to total demand. This latter aspect means that, by definition, VRES over production in Raynaud et al.'s analysis exactly offsets under production, and thus all countries are designed to be autarkic; which is not the case in the current work.

Besides the length of lull spans, several other researchers have focused their efforts on determining the total amount of backup generation[7] which must be available besides the VRES such that demand satisfaction can be ensured. Towards this end, Rodriguez et al. [354] have taken an approach similar to Raynaud et al. in that they computed normalized multi-year VRES profiles for wind and PV which were scaled to match total generation with total demand. With country-specific wind and PV shares, all hovering around a wind fraction of 0.75, they find that $15.1\,\%$ of the total generation across Europe would need to be satisfied by backup. Performing this evaluation in the European scope of the current context, it is found that only $14.1\,\%$ of European demand would need to be satisfied by backup generation. While close to one another, these quantities are not directly comparable since total VRES production in Rodriguez et al.'s analysis exactly matches demand across Europe, while in the current study the total VRES generation sums to, on average, $103.6\,\%$ of the total demand. It therefore follows that there is slightly less backup utilization in the current analysis. By following the approach of Rodriguez et al., and applying a constant scaling factor to all onshore wind, offshore wind, and PV generation so that their total annual generation adds up to the total annual European demand, it is then found that the backup utilization in the current study would rise to $15.46\,\%$; representing a $2.4\,\%$ difference from the estimate of Rodriguez et al. [354]. Weber et al. [352] also make estimates on the total storage and backup needs within a copper plate Europe, finding that, depending on the fundamental weather data source, a renewable European energy system with $26\,\mathrm{TWh}$ of storage[8] would need to rely on backup generation for between 14 and $18\,\%$ of the total yearly demand; which is well in line with the current result. According to Weber et al., since this storage amounts to $0.6\,\%$ of Europe's average total annual electricity demand then it therefore constitutes a "massive" expansion of storage capacities. Lastly, Rasmussen

[7] Including all dispatchable options such as conventional fossil generators, hydro, and biomass.
[8] Corresponding to the P_{max} European basic residual load lull deficit seen here.

et al. [351] claim that peak storage needed in a highly renewable Europe would reach to 320 TWh, but further conclude that a 6-hour storage equivalent, amounting to 2.94 TWh when scaled to the current scenario, would be perform almost as well. These claims encompass the results found in this work since Rasmussen et al.'s high estimate is far beyond the European P_{max} basic residual load lull deficit, and their lower estimate is significantly below the European P_{100} deficit.

From a high-level perspective, it is commonly concluded in the literature that, even over a European scope, unlimited grid expansion is not sufficient to ensure uninterrupted satisfaction of electricity demand from wind and PV generation [44, 348]. Comparing to the occurrence probabilities of European basic residual load lull spans (Figure 7.4), it is clear that this statement is strongly supported within the current context discussed here. However, considering that the average of all demand-generation year's largest European residual load amounts to 400.1 GW, and that the E-Highway-prescribed dispatchable RES options [9] amount to 481.7 GW, it remains conceivable that only renewable generation would be required to perform this backup function. Of course, this statement hinges upon the copper plate assumption and moreover on the full availability of these backup generators at the time of the maximum residual load. Therefore, the following context will put this statement to the test by incorporating grid limitations and optimizing the orchestration of backup generators using a power flow analysis.

7.3 Context 3: Constrained Grid with Dispatchable Backup

In the final context of the VRES lull analysis, DC optimal power flow analysis is performed using the energy system setup given by E-Highway [296,300] and evaluated by using the PyPSA energy system model framework [368]. A full description of the analysis' basis and evaluation is provided in Section 5.5.3. In summary, the "Constrained Grid with Dispatchable Backup" context differs from the previous contexts in the sense that the optimal hourly dispatch of biomass and hydro generators within each region is included, in addition to the optimized hourly orchestration of imports and exports between regions subject to interregional electricity grid limitations. The lulls in this context (referred to as 'optimized residual load lulls') are determined using the same general lull identification procedure as before (Section 5.4.2) and the temporally-explicit lull threshold is calculated by subtracting the backup and import utilization at each hour from the summation of electricity demand and export (Equation 5.3). As before the lull occurrence probabilities reported here correspond to the probability of observing a lull spanning the given time at least once in a randomly selected year (Section 5.6). Presentation of the results in this context will begin with a report of the observation probabilities of lull spans and deficits in the same form as shown for the previous contexts. After this, the additional results are mapped for each E-Highway region to provide further understanding of how the electricity system is operating in this scenario; this includes the occurrence of lulls,

[9] Biomass, hydro reservoir, and pumped hydro storage

the backup requirements, and the average annual curtailment over all demand-generation years. Finally, a discussion is provided which includes comparison to results and claims seen in the literature.

7.3.1 Lull Occurrence

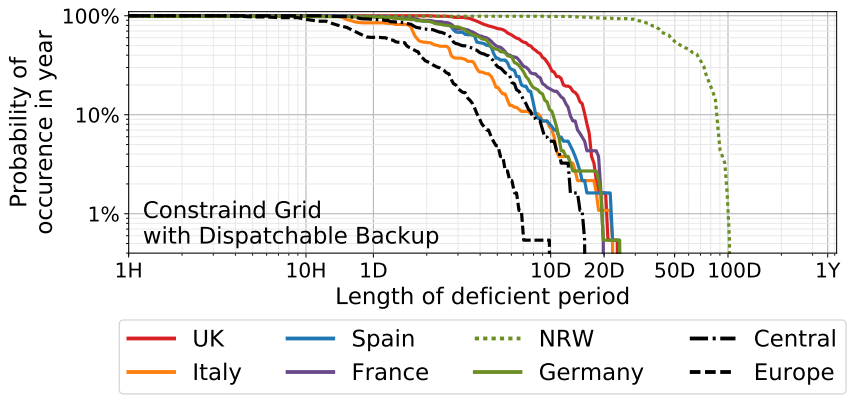

Figure 7.7: Length of VRES lulls in the "Constrained Grid with Dispatchable Backup" context.

Figure 7.7 displays the occurrence of optimized residual load lull spans for the same set of regional scopes as in the previous contexts. In contrast to the combined generation lull spans in Figures 7.1 or the basic residual load spans in Figure 7.4, the national optimized residual load spans are noticeably more clustered together. On the shorter end of this group is Italy, where the largest P_{100} optimized residual load lull span is seen at 13 hours, P_{10} of 8.45 days, P_1 of 21.67 days, and finally P_{max} at 22.33 days. At the other end is the UK, for which the largest P_{100} lull span is seen at 2.04 days, and where P_{10}, P_1, and P_{max} are seen at 15.54, 20.42, and 23.75 days respectively. Germany is situated in the middle of this group, and shows 10.17, 19.21, and 24.46 days for P_{10}, P_1, and P_{max}, and actually has no P_{100} as 1.62 %[10] of the demand-generation years did not observe any lull periods at all. Given the fact that Germany was designed as a net importer of electricity, it is surprising that it shows median optimized residual load lull observation probabilities while the UK, a net exporter of electricity, shows the largest lull observation probabilities of the national group. In any case, since real energy system planners must consider risk-management, it is unlikely that the design of future energy systems is based around the absolute largest possible lulls which, in this analysis, only occur in one out of 185 demand-generation years. Therefore, the national group's convergence around a P_{10} lull span of 10 days[11] and a P_1 lull span of 20 days[12] is a very meaningful

[10] 3 out of 185.
[11] Which should occur in one out of 10 years.
[12] Which should occur in one out of 100 years.

result as these values likely encompass the occurrence rates which are of highest relevance to real energy system designers.

While electricity imports and exports between regions are limited in this context, the lull calculation (Equation 5.3) is still aggregated over each regional scope. As a result of this, Europe is seen to display the shortest optimized residual load lulls. In this case, the largest P_{100} lull span seen in Europe is only 2 hours, after which a P_{10} of 3.71 days, a P_1 of 6.8 days, and a P_{max} of 9.8 days are seen. Compared to the basic residual load lull spans in Figure 7.4, optimized residual load lull spans in the European scope are significantly shorter in Figure 7.7. This is a result of the timely utilization of the backup hydro and biomass generators, which apparently outweighs the detrimental effect of adding grid limitations. In order to distinguish the impact of these two effects, the power flow simulations were repeated with the transmission capacities of all grid lines increased to near infinity. This has the effect of removing all grid limitations, leaving a copper plate over Europe, but still relies on the power flow solver to optimize the use of backup generation. As a result of this test, optimized copper-plate residual load lulls still occurred in $9.73\,\%$ of years, meaning that there is no P_{100} or P_{10} span over Europe. European P_1 and P_{max} optimized copper-plate residual load lull spans are seen at 4.08 and 5.71 days, which are both around $60\,\%$ of their corresponding optimized residual load lull span[13], and around $33\,\%$ of the corresponding basic residual load lull value[14]. In either case, the previously theorized possibility of completely supplying the European electricity system from renewable sources turns out to not be a reality; although this is limited to the context of the current scenario, which does not include long term storage. More importantly, this result finalizes one of the basic but nevertheless key outcomes of this thesis; regardless of how the issue is treated, when considering the residual load VRES lulls will occur over the European scope.

A similar but less pronounced dynamic can be seen for the Central region, whose relatively large spatial scope leads to a more dependable VRES generation profile compared to the national scope. However without many of the fringe European countries included, the observed optimized residual load lull spans are much closer to the national group; partially also due to their large overlap. The region tending to have the longest lull spans in this context is clearly NRW, where a P_{10}, P_1, and P_{max} lull spans are seen at 85.00, 98.92, and 101.96 days respectively. Similar to Germany, however, NRW also does not observe any P_{100} spans as $1.08\,\%$ (2 out of 185) of demand-generation years did not result in any lulls for this region. The underlying reasoning for this observation in NRW will be made clear in the following presentation of optimized residual load lull deficits.

Figure 7.8 shows the occurrence of optimized residual load lull deficits which correspond to the spans given in Figure 7.7. Despite showing the shortest occurrence of optimized residual load lull spans, Europe naturally shows one of the largest occurrence of lull deficits on account of its large annual demand. The largest P_{100} optimized residual load lull deficit in Europe is seen at only $5.96\,\mathrm{GWh}$, the P_{10} at

[13] When grid limitations are included.
[14] When backup orchestration is not active.

1.26 TWh, P_1 at 3.98 TWh, and finally P_{max} at 4.73 TWh. Once again, despite the inclusion of grid dynamics, the European lull deficits are noticeably smaller than Europe's basic residual load lull deficits as a result of the effective dispatch of biomass and hydro generation. As with lull spans, the impacts of grid limitations and explicit backup orchestration are separated from one another by considering power flow simulations without grid limitations; leading to P_1 and P_{max} European optimized copper-plate residual load lull deficits at 237 and 316 GWh. These values are around 94 % less than their corresponding optimized residual load lull deficits[15], and around 99 % less than their corresponding basic residual load lull deficits[16]. Therefore it is once again seen that the optimal dispatch of backup has a stronger beneficial effect on the reduction of lull occurrence than the detrimental effect of adding grid limitations.

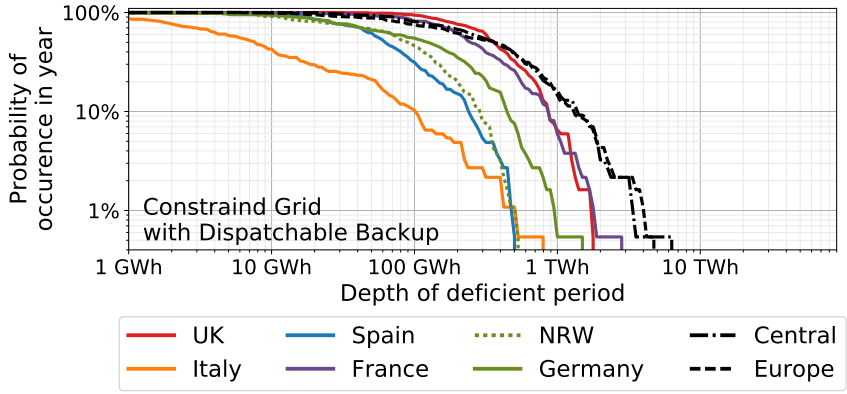

Figure 7.8: Depth of VRES lull deficits in the "Constrained Grid with Dispatchable Backup" context

Returning to the optimized residual load lull deficit outcomes, a greater spread of occurrence probabilities are observed between the regional scopes which is also highly related to the total annual demand of these regions. However the relationship between optimized residual load lull deficit to total demand is not absolute, as can be seen by the Central scope; where the overall largest lull deficits are seen despite only incorporating 49.4 % of the total European demand. In this case the optimized residual load lull deficit occurrences are extremely close to that of the European scope, with the exception of its P_{max} value at 6.31 TWh. This shows that lull occurrences in the Central region would be just as extreme as lull occurrences of the entirety of Europe and, therefore, it makes the most sense for energy system planners to pursue an European-wide solution to their future energy system challenges. Besides this, Italy appears to experience relatively shallow optimized residual load lull deficits where the maximum P_{100} is only 53 MWh, the P_{10} is 100.0 GWh, P_1 is 501.2 GWh, and at last P_{max} is 794.3 GWh. Next is Spain, where the largest P_{100}

[15] Which includes grid limitations/
[16] In which backup orchestration is not active.

lull deficit, P_{10}, P_1, and P_{max} are respectively observed at 2.51, 237.1, 473.2, and 480.1 GWh. The UK and France share a similar lull deficit trend, starting from 31.62 and 11.22 GWh, respectively, at their maximum P_{100} value, sharing a P_{10} of around 840 GWh, and finally increasing to 1.78 and 2.88 TWh, respectfully, at the the P_{max} point. Germany once again takes a median position with 421.7 GWh, 944.1 GWh, and 1.50 TWh for its P_{10}, P_1, and P_{max} optimized residual load lull deficits.

In terms of the NRW trends, it is clear that the observed optimized residual load lull deficit trends for NRW match closely to Spain's. Although, as previously noted, the corresponding lull spans in NRW have the tendency to be between a factor of 5 to 10 longer than Spain's. On closer inspection it is seen that, as a net importer of electricity, NRW has a strong tendency to use all of its internally-produced VRES generation whenever it is available, thus leaving little curtailed generation. Without curtailed VRES generation to rely on to satisfy lull deficits, NRW therefore experiences many long stagnant deficit periods such as in the example given in Figure 5.9. Therefore it is apparent that the optimized residual load lulls in NRW are generally long and shallow; which arise as an artifact of the scenario's design and the lull evaluation method. It will be shown later in this section how this same dynamic is in effect for other regional scope as well that aren't visualized in Figure 7.8; such as Switzerland.

Instead of discussing lull deficits in absolute terms, another interesting perspective to consider is the relative depth of these deficits in relation to each regional scope's total annual demand. Therefore, this is shown in Figure 7.9. The national ordering of lull intensity is more or less the same as seen in Figure 7.8, where Italy tends to have the smallest relative lulls followed by Spain, Germany, France, and the UK. Although, in this case France and the UK are much further apart from one another[17] than previously on account of France's larger annual electricity demand. More noticeably, the European and Central scopes have changed positions significantly; with the European scope now contending with Italy and Spain below the P_{10} probabilities. This shift in position is a result of the greater spatial mixing of VRES generation across these regions leading to smaller relative lull deficits. Across all trends, is seems apparent that P_{10} values are seen between 0.02 and 0.2 % of each region's total annual demand. Similarly, P_1 values are generally between 0.1 and 0.4 % of total annual demand. Therefore, these relative lull deficit values can be of use to energy system planners and researchers as rules-of-thumb when estimating the need for total storage or backup generation besides biomass and hydro in a European electricity system dominated by VRES generation.

7.3.2 Spatially-Explicit Results

Attention is now turned to the spatial relationships within the "Constrained Grid with Dispatchable Backup" context's results. Discussion will focus on the optimized residual load lull span and deficit, largest residual load, annual curtailment, and the additionally-required generation capacity of each E-Highway region. For all

[17] Relatively, speaking.

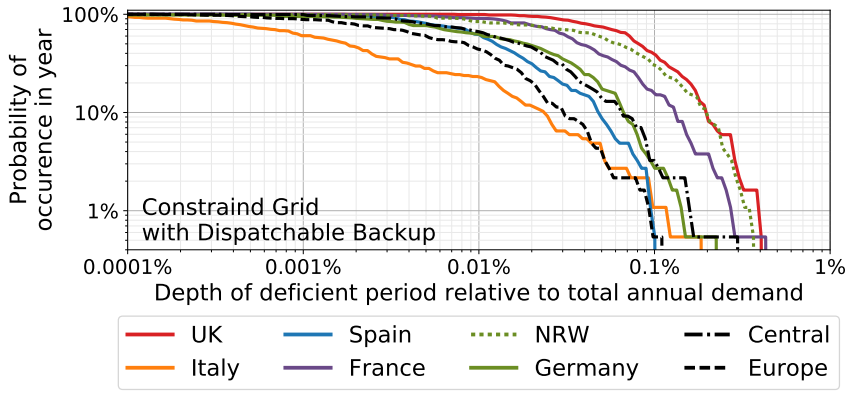

Figure 7.9: Relative depth of VRES lull deficits in the "Constrained Grid with Dispatchable Backup" context

quantities except curtailment, the P_1 quantity is shown as it corresponds to the largest annual value which should be observed once per century. Nevertheless, a complete tabulation of these values are provided in Appendix J for all E-Highway regions and countries.

The first of the observed quantities, the P_1 optimized residual load lull span, is mapped in Figure 7.10. In this figure it is seen that about one-third of the evaluated regions do not observe any lulls at all; including much of the Balkans, as well as Norway, Sweden, and, effectively, Greece[18]. Other regions, such as the Iberian peninsula, southern France, the Baltic countries, Finland, Poland, and Hungary observe lulls that, at most, tend to last between 0 and 20 days. An area near to the center of Europe is apparently the most affected by extreme lulls, which includes NRW, South-Western Germany, Eastern Austria, Northern Italy, Belgium, Luxembourg, and Switzerland. Here, the most extreme lulls can last from 70 days to over 100 days. Individual regions in the UK tend to see maximum optimized residual load lull spans in the range of 20 to 40 days. The regions with the top five spans are Northern and Southern Switzerland, with 105.1 and 102.0 days, NRW with 98.19 days, and finally Paris and Baden-Württemberg, both at 90.29 days. The presence of Switzerland in this group is surprising on account of its large hydro reserves. As previously described for NRW, the long lull spans observed in these regions is an outcome of the specific energy system's design, resulting in only infrequent opportunities to replenish deficiencies from curtailed VRES generation and therefore tending to continue artificially long without experiencing large lull deficits.

Figure 7.11 shows the P_1 optimized residual load lull deficit observed in each region. As with the lull spans shown previously, roughly one-third of the regions do not observe any lulls and thus do not have any deficit. On the Iberian peninsula as

[18] The largest lull span seen in Greece is only 5 hours.

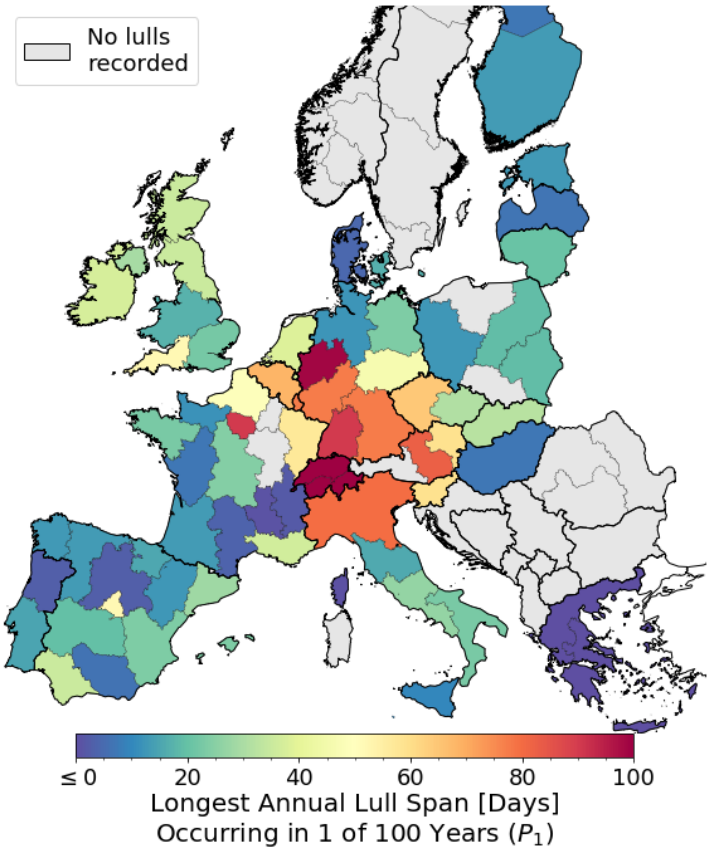

Figure 7.10: P_1 lull span observed in the "Constrained Grid with Dispatchable Backup" context for each E-Highway region

well as in the Baltic countries, Poland, and Finland it is seen that the most extreme deficits are generally within a range of 10 to 30 GWh but, in a few cases, can reach to above 100 GWh. Southern France, which showed a short optimized residual load lull span in the previous figure is here shown to observe a lull deficit as deep as 327.0 GWh; suggesting the occurrence of relatively short but high intensity lull periods. Northern Italy again distinguishes itself as a lull-susceptible zone, although many of the nearby areas which previously showed the longest lull spans, such as Switzerland, have quite low lull deficits in comparison to their neighbors. In fact, the more predominant areas that are at risk of deep lull deficits has moved northward to encompass all of Germany, North-Eastern France, the British Isles, and, especially, Belgium and the Netherlands. This transition is sensible, however, given that these areas correspond to some of the heaviest electricity demands in Europe. Individually summed across Europe, it is seen that a total optimized residual load lull deficit

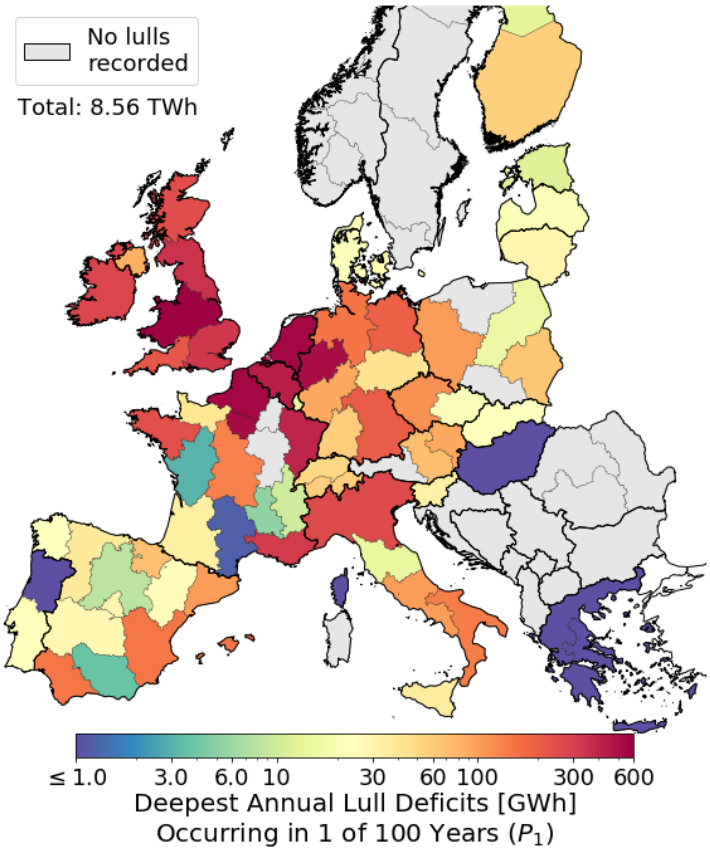

Figure 7.11: Largest lull deficit observed in the "Constrained Grid with Dispatchable Backup" context for each E-Highway region

of 8.56 TWh is seen which, as expected, is higher than the 3.98 TWh found when evaluating lull deficits over the entire European scope.

The following map, Figure 7.12, visualizes the P_1 largest annual residual load observed in each region[19]. In this case all regions are shown to have a value with the exceptions of Sardinia, Corsica, and Montenegro, and the southern tip of Sweden, where a residual load greater than 1 GW was never observed. For all other regions, however, the most extreme residual loads are shown corresponding to the largest backup generation each region should expect to muster if it wanted to be able to settle the most intense residual loads without relying on its neighbors. Despite being much more evenly distributed than the previous maps, many of the same typical regions again show up as also having a high backup requirement. This includes

[19] Calculated for each hour as demand minus onshore and offshore wind, PV, and run-off-river.

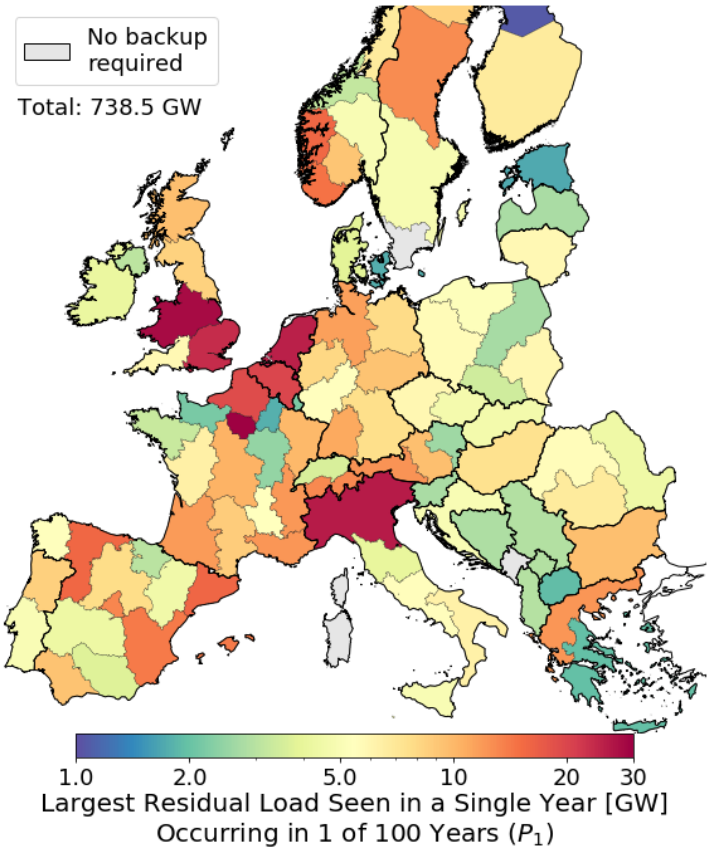

Figure 7.12: P_1 residual load observed in the "Constrained Grid with Dispatchable Backup" context for each E-Highway region

Paris, with a backup need of 29.77 GW, Central England with 28.43 GW, Northern Italy with 25.63 GW, the Netherlands with 25.04 GW, South-Eastern England with 23.37 GW, and Belgium with 19.89 GW. NRW is uncharacteristically absent from this group, where a maximum backup need of only 8.09 GW is seen. In fact, much of Germany is seen to vary between 7.5 and 11.5 GW, totaling to 61.21 GW.

Summing the regionally-evaluated P_1 residual load across all of Europe leads to a total backup requirement of 738.5 GW, printed in the top-left of Figure 7.12. If the P_{10} value were used instead of the P_1, the total backup estimate would reduce to 585.27 GW. As this is evaluated independently for each region, these values do not represent one specific moment, and so searching instead for the hour with the most total backup used summed across all regions, so that a synchronous value is maintained, a P_1 value of 500.89 GW is found. Finally, if the residual load is aggregated

across Europe irrespective of grid limitations, then backup P_1 estimate for Europe would reduce again to 498 GW. Note that this final value is slightly different from the 400.1 GW found when discussing the results of the "Residual Load with Basic Backup" context, as in this case only the residual load is aggregated across Europe. Ultimately all of these values values comment on the total amount of backup capacity which would be required in a European electricity system dominated by VRES generation. The lowest value, 400.1 GW, represents the smallest possible backup capacity that is needed without any grid limitations, while the highest, 738.5 GW, represents the value if every E-Highway region wanted to ensure its own security of supply even in the most extreme cases. The 585.27 GW value corresponds to the situation where the E-Highway regions each choose to ensure their own security of supply in 9 out of 10 years, but would still need to rely on their neighbors occasionally. Note that this represents 119.3 % of the average hourly electricity demand in Europe. The largest synchronous backup requirement of 500.89 GW, 102.1 % of the average electricity demand in Europe, corresponds to the situation where all E-Highway regions cooperate to ensure the security of supply; but also requires frequent reliance on imported electricity in all years for all regions.

As mentioned in Section 5.5.3, some amount of "extra" backup generation capacity had to be given to each region in order to ensure the feasibility of the overall energy system[20]. The necessity for this can be seen clearly by subtracting the total biomass capacity in the evaluated scenario of 184 GW as well as the total hydro reservoir and pumped hydro capacities of 183.74 and 113.94 GW, respectively, from the total backup needs specified in the previous paragraph. Figure 7.13 explicitly displays the P_1 extra generation capacity required by each region. By the definition of the lull threshold equation used for the "Constrained Grid with Dispatchable Backup" context (Equation 5.3), it is seen in this figure that the regions which do not correspond to a need for extra capacity are the same regions which did not observe any lulls. Furthermore, while most regions are seen to need an additional capacity of around 1 to 5 GW, there is a clearly apparent area comprised of much of England, the Netherlands, Belgium, Northern France, and Paris where around 20 GW of generation capacity are needed for each region. It is certainly no coincidence that all of these regions are near to one another and furthermore heavily depend on wind energy, both on- and offshore, and thus have similar wind generation profiles. The need for these extra generators are an indication that the E-Highway scenario does not constitute an optimally designed electricity system when driven by the VRES generation profiles supplied from the wind and PV simulation schemes developed in this work.

Another indication of the suboptimal design of the E-Highway scenario when driven by the VRES profiles developed in this work is given in the average annually curtailed energy within each region; shown in Figure 7.14. Here it is seen that a large swath of significant curtailment begins near Murcia in Spain, continues northward over Western France, encompassing the British Isles, covers Belgium, the Netherlands, Northern Germany, Denmark, Poland, the Baltic states, and finally ends in Finland. Each of these regions have above 10 TWh of curtailed VRES, meaning that

[20] As in, to ensure that it is always possible to satisfy all demands at all time steps.

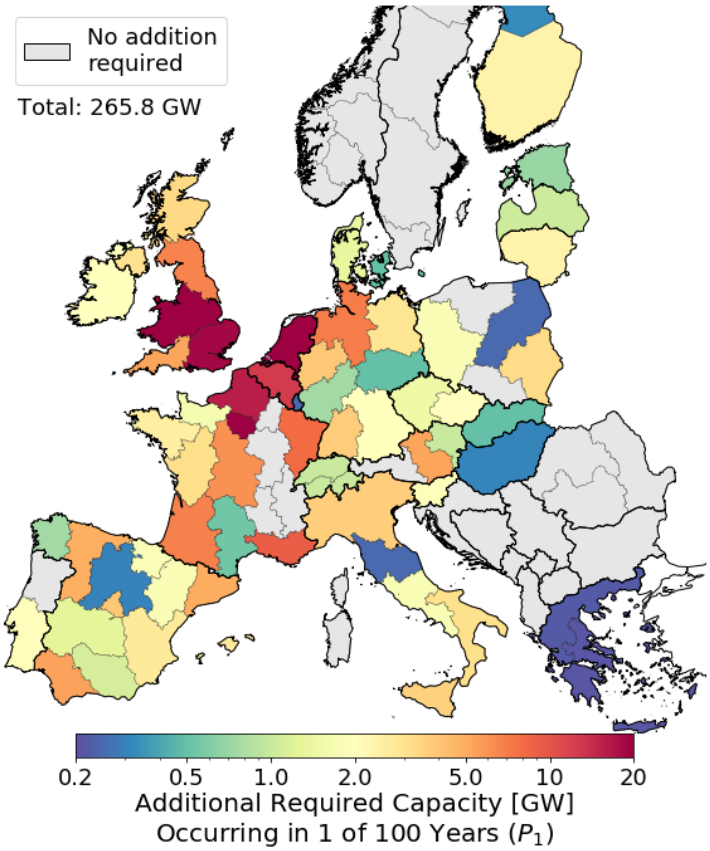

Figure 7.13: Additional backup capacity required to ensure feasibility beyond the specifications of E-Highway

any one of them is, on average, able to offset all of the largest optimized residual load lull deficits seen across Europe. Four regions in particular, mainland Denmark, South-Eastern England, North-Western Germany, and Central England, generate 137.58, 74.99, 73.88, and 60.50 TWh, respectively. Total curtailment across Europe sums to 1066.3 TWh. It is clear that with this setup Denmark curtails an exceedingly high proportion of its VRES generation, 80.51 %, as do some other regions such as Latvia, Estonia, and Poland, seen at 52.71, 47.95, and 41.01 % respectively. However, besides these countries, the average curtailment of each region comes out to around 19 %. This suggests that VRES capacities are over-allocated in many, if not all, of the previously mentioned regions. As a final note, the average curtailment as a percentage of its total VRES generation for each region is given in the Appendix Figure H.1, where it can be seen that there are significantly lower curtailment percentages, in the range of 0 to 5 %, for regions which are near to mountainous zones.

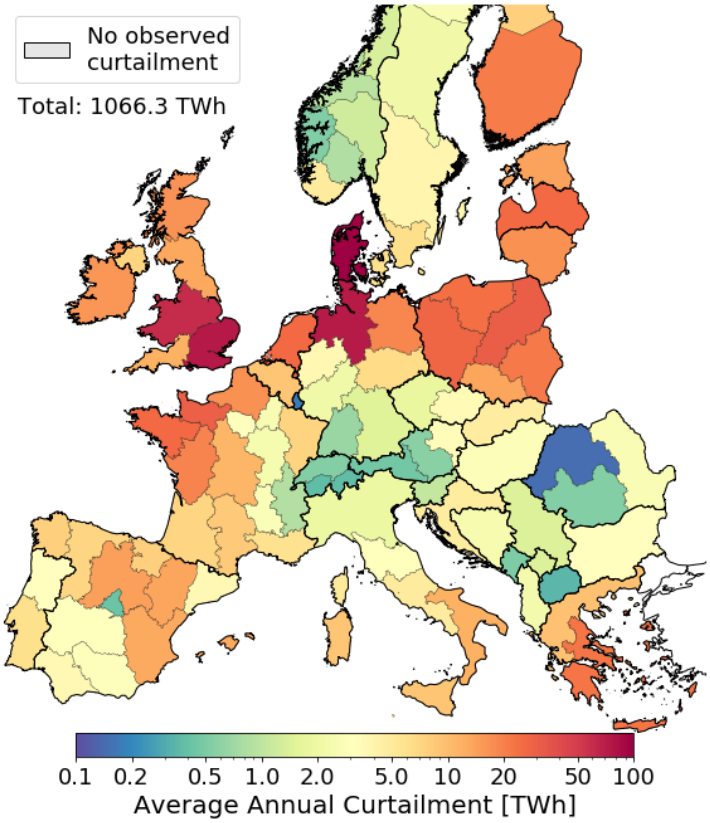

Figure 7.14: Average annual curtailment for each E-Highway region

This is a sensible outcome considering that these are also the regions where a significant portion of pumped hydro storage and generation is available. This heavily suggests that the addition of storage to other parts of this energy system, such as in the UK, the Netherlands, or Northern Germany would greatly enhance VRES utilization, reduce need for extra back-up generation, and suppress the occurrence of lulls throughout the entire system.

7.3.3 Discussion

Searching in the current literature for comparable investigations of lull occurrences across Europe where both grid and dispatch operations are considered dynamically does not reveal any suitable candidates. However, more generalized studies can be found which estimate, for example, the total storage need in Europe or the total need for backup capacity in the context of high shares of VRES generators. Four studies in particular can be identified as having performed a power-flow-like

evaluation of a fully renewable European energy system. Child et al. [358], Becker et al. [359], Rodriguez et al. [354, 357], and Cebulla et al. [350] each modeled Europe with an aggregated grid at the national level. Cebulla et al. differs from the other groups as their national aggregation applies for all countries except Germany which is broken into 16 pieces, and furthermore since they did not include the Balkan region in their analysis unlike the previous authors. All of these studies have varying energy system designs in regards to the total VRES and other generation capacities, transmission line capacities, and total demand assumptions. Nevertheless, despite these differences, many of the estimations made in these studies are comparable to estimates arrived at here.

On the topic of storage, Cebulla et al. [350] evaluated several scenarios and found that an electrical energy storage (EES) capacity of 206 GW would typically be required in a future fully renewable Europe, but that these requirements can also range from 126 GW to 272 GW. These quantities are vaguely comparable to the total amount of additional generation capacity found in the current analysis of 265 GW, shown in Figure 7.13. As discussed in Section 5.4.2, this additional capacity could potentially correspond to storage systems installed across Europe whose total storage potential would match the 8.56 TWh found in Figure 7.11. Alongside their capacity estimate, Cebulla et al. conclude that a typical storage need would reach 30 TWh, and could range between 16 to 54 TWh; all of which are significantly beyond the 8.56 TWh value estimated in this work, even when including the additional 4.56 TWh of pumped hydro storage which is already present in the E-Highway scenario. It is suspected that the reasoning for Cebulla et al.'s higher storage need is a consequence of not including the Balkan states which, in the current analysis, are not seen to observe any lulls and thus are often available to help suppress VRES lulls in the central European nations.

Becker et al. [359] took an in depth look at the effect of varying grid capacities on Europe's total reliance on backup generation. By analyzing a grid with effectively no constraints, they found that the total annual backup generation would sum to 15.1 % of Europe's total annual demand. For a grid which has "70 % effectiveness" of the unconstrained grid, they predict that the total backup generation would rise to 17.8 %. Similarly, Rodriguez et al. [354] make the claim that, for a European grid with a total line capacity of 395 GW, 15.3 % of Europe's total annual demand would have to be satisfied by backup. In the E-Highway scenario used for this analysis, it is seen that the total international line capacities sum to 346 GW, and so the grid used in this work is comparable to that of Rodriguez et al., and likely fall somewhere within the range of "Unconstrained" to "70 % effective" specified by Becker et al. [359]. Summing the total utilization of all non-VRES generation in this work for each demand-generation year, it is seen that an average backup utilization of 15.54 % is found, and so is clearly within the expected range of both studies. Besides Becker et al. and Rodriguez et al., this range of total backup reliance for a highly renewable European energy systems is further supported by Rasmussen et al. [351] and Heide et al. [389].

Although the average backup utilization appears to fit well at the European level,

looking deeper at the study of Rodriguez et al. shows that there are large discrepancies at the national level. Rodriguez et al. show in their results that the typical backup utilization for each nation fluctuates around the average at $15.6\,\%$, with a few outliers such as Norway reported at $10.5\,\%$, and Belgium reported at $19.5\,\%$. In the current result there is a wide disparity of backup utilization values ranging from no backup generation at all, seen in Montenegro, to $105\,\%$ seen in Norway. One key issue leading to this discrepancy is the design issues of the E-Highway scenario when coupled with the current VRES profiles; naturally leading to more energy mismatches than might otherwise be expected had the capacities been optimally designed with these profiles in mind. Additionally, Rodriguez et al. have scaled their total VRES profiles of each nation to exactly offset the annual demand and, therefore, each nation in their study is effectively designed to be autarkic. This results in reduced need for imports and exports in Rodriguez et al.'s study in comparison to here, especially in the case of countries that are, by design, either net exporters or net importers.

At last, the study of Child et al. [358] is addressed, where the optimal transition to a completely renewable European energy system is found using a myopic optimization approach. As a result of their work, Child et al. conclude that a fully renewable energy system is achievable in Europe by 2050 and would correspond to a holistic LCOE value of around 5.1 to $5.5\,\mathrm{ct_{€}\,kWh^{-1}}$. Of this, they also conclude that 2.9 to $3.1\,\mathrm{ct_{€}\,kWh^{-1}}$ corresponds to the effective LCOE contribution from onshore and offshore wind and PV generators. Using the onshore cost model described in Section 3.4, the cost assumptions given in Tables 3.4 and 4.2, and the total utilized generation of wind[21] and PV generators found in the results of the "Constrained Grid with Dispatchable Backup" context, then the effective LCOE contribution of these technologies is calculated here as $4.2\,\mathrm{ct_{€}\,kWh^{-1}}$. While within the total budget specified by Child et al., the LCOE found here is higher compared to their result due to the subnational evaluation performed here, which gives more opportunities for grid limitations, as well as the sub-optimal scenario design leading to excessive VRES curtailment and thus lower VRES generation per installed capacity. It should be noted that the current LCOE value is found while still using the LCOE-sorting convention when selecting individual turbine and PV park locations to satisfy each region's capacity; meaning that a more realistic selection procedure, which would lead to lower FLH, would also lead to a higher LCOE. Given the high curtailment observed in the current result, however, it is not clear how the reduced FLH would impact the effective LCOE.

[21] Including onshore and offshore wind. Offshore wind costs are derived according to the discussion of Caglayan et al. [102].

7.4 Sensitivity to Scaled VRES Capacity

The VRES lull analysis described in the previous sections provides a detailed look into lull occurrence at a level which, until now, has not been available in the literature. Nevertheless, the results produced are intimately tied to the specifics of the selected E-Highway scenario, and would likely change in near unpredictable ways if the energy system were constructed differently. Therefore, a sensitivity analysis is performed which considers how changing the installed VRES capacities might impact lull occurrence. A more detailed analysis should redesign regional capacities via an optimization approach, although implementation of such a procedure is far outside the scope of the current work. Nevertheless, in order to approximate how changing capacities might impact VRES lulls, the capacities specified within the E-Highway scenario (Figure 5.2) are uniformly scaled between $\pm 20\,\%$ in steps of $2\,\%$, and in each case the evaluation performed in the "Constrained Grid with Dispatchable Backup" context (Section 5.5.3) is carried out. By performing this scaling, one expected response of the overall electricity system is that, when capacities are reduced, an increased reliance on backup generation as well as import and exports between regions should be observed, and vice versa.

Due to the need to perform DC optimal power flow for each scaling factor, it is not feasible to perform each of these sensitivity steps for all demand-generation years used in the primary analysis. Therefore, only 2015 was selected for both the demand and generation year for all analyses on account of it's above-average lull observance rate and due to its applicability for further tests which are described in the following section. Because of this, discussion will focus on the relative difference between the sensitivity analysis' lull spans and deficits versus that of the base analysis for the 2015 demand and generation year.

To perform this sensitivity analysis, the following procedure is followed for each E-Highway region for each VRES capacity scaling factor. First, the scaled capacity for each VRES technology is computed from the base E-Highway value and the full LCOE-sorted placement procedure (Section 2.5) is performed. This gives a new set of generator units for each region as compared to the base lull analysis, which therefore must be re-simulated according to the procedures outlined in Section 3 for Wind and Section 4 for PV. As described in Section 5.4, PV capacities are still evenly split between the open-field and rooftop domains. To note, when increasing capacities in Switzerland, the required capacity slightly exceeded the full PV potential. This is not considered to be an issue, however, since additional PV sources are available which were not included in this analysis; such as north-facing roofs and building facades. Furthermore, an additional open-field land eligibility scenario such as the one evaluated for Germany in Section 6.1.4 could have been considered to slightly increase available open-field PV capacity. Therefore, the total PV time-series in the case of Switzerland is simply scaled to match the specified capacity. In any case, at this point new time-series are available for each VRES technology within each region, which then replace the ones used in the base analysis. Since evaluation of this procedure at each scaling percentage results in a new time-series, both the total generation as well as the average FLH are affected. For

instance, when scaling capacities down, the overall wind and PV generation will decrease, however as the LCOE-sorting procedure will select a cheaper subset of turbine and PV park locations in terms of LCOE[22] the FLHs will slightly increase.

Figure 7.15 shows the outcomes of the capacity scaling sensitivity analysis. Along with the change in the longest optimized residual load lull span and deepest lull deficit, this figure also shows the change in the largest residual load, total curtailment, and total utilization of VRES generation. The same regional scopes shown when presenting the base lull occurrences are again given here, in addition to the total value found after summing, or averaging in the case of lull spans, the individual contributions of each E-Highway region.

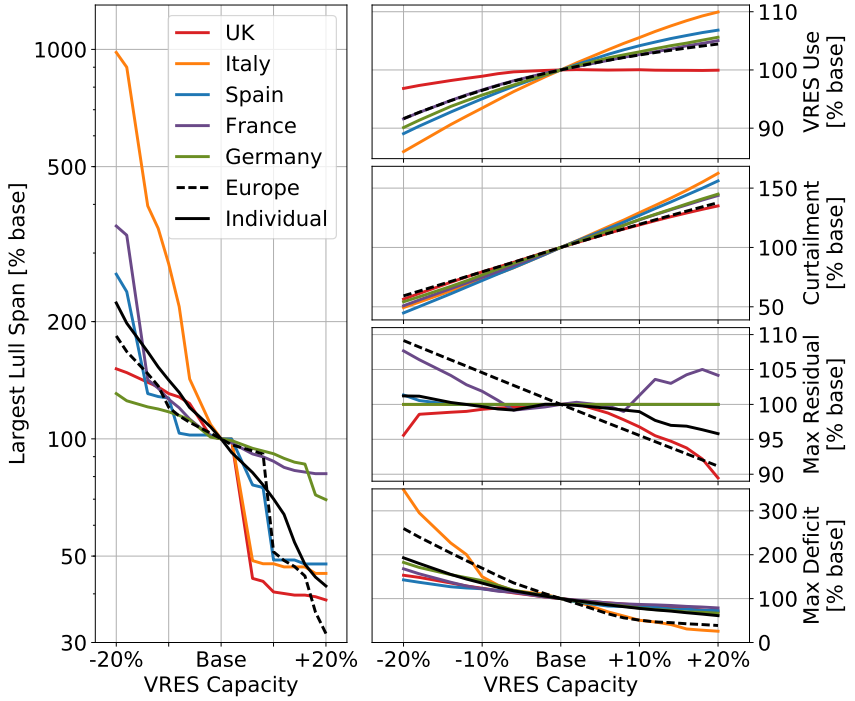

Figure 7.15: VRES lull sensitivity to changes in regional VRES capacity

The left plot of Figure 7.15 gives the change of the largest observed lull throughout the entire sensitivity year. All regional scope are seen to possess an anti-correlated response to VRES capacity changes that are more pronounced for capacity reductions than for capacity increases. For most scopes, a $20\,\%$ capacity reduction would lead to a doubling of the longest lull span observed, with the exception of France,

[22] Generally low LCOE turbine and PV park locations correspond to higher FLH, but this is not always the case.

where lull span increases by a factor of 3.5×, and Italy, with an increase factor of 9.8×. As can be seen by the optimized residual load deficit occurrence trends of Figure 7.8, the large lull growth in Italy is primarily a result of the extraordinarily small lulls Italy experienced in the base analysis. For a 20 % increase in VRES capacity, most regional scopes show a reduction of the longest lull span to 40 % of their base value. France and Germany are exceptions to this, where the lull reduction are limited to 81.4 % and 69.8 %, respectively, on account of their high reliance on imports. Of all countries shown, Germany appears to have the least sensitivity of lull spans to capacity scaling, which is perhaps a result of its geographically central position in the electricity system.

The bottom right plot shows the change in the largest observed optimized residual load lull deficit, which displays a similar asymmetric and anti-correlated trend as the lull spans. In this case the typical response to a 20 % capacity decrease is to increase lull deficits to 160 % of their base value, and to shrink to 70 % of the base when capacities are increased by 20 %. Once again, Italy is seen to be an exception on account of its small base lull deficits. Figure 7.16 shows the sensitivity of the largest lull deficit over the E-Highway regions for scaling factors of −20, −10, 10, and 20 %. From this perspective, Italy's large relative deficit increase when VRES capacities are reduced is seen to come from the central Italian regions, while the northern Italian regions are largely responsible in the opposite case. Nevertheless, it is also seen that countries such as Switzerland, Finland, Estonia and Latvia have an even stronger relative sensitivity than Italy. Referring to the estimation of storage need in Europe in the primary analysis (8.56 TWh when summed regionally), it stands to reason that the size of this storage need would likely rise to around 16.9 TWh if the VRES capacity were to be decreased by 20 %. This estimate is much closer to the values proposed by Cebulla et al. [350], which suggests that a re-optimized distribution of VRES capacities would likely bring the total storage estimates more in line with the literature.

Figure 7.15 also shows that VRES utilization is also impacted by capacity scaling. A common linear response to VRES curtailment is seen for all regions in the range of a 2.5-to-1 % change in total annual curtailment for each change in VRES capacity. Similarly, actual VRES usage, presented in the top right, increases as the capacity increases, but the response is again biased. The UK shows a unique trend where it ceases to utilize more VRES generation when capacities are increased. This is caused by the scenario's design where the UK's role as a net exporter role becomes less important as other nations increase their VRES capacity. In general, however, a 20 % capacity reduction typically corresponds to a 9 % reduction in total VRES usage, while a 20 % capacity increase typically increases VRES usage by 5 %. Notice that, for the −20 % capacity case, the total VRES generation is reduced by slightly less than 20 %[23], since a higher proportion of strong wind and strong PV locations are utilized due to the LCOE-sorting of generator locations, so the relative VRES usage is actually increasing in this case by 13.56 %. This higher usage percentage impacts the effective VRES electricity cost and, returning to the LCOE comparison to Child et al. [358], suggests that reducing the VRES capacity in the

[23] 19.3 %, to be precise.

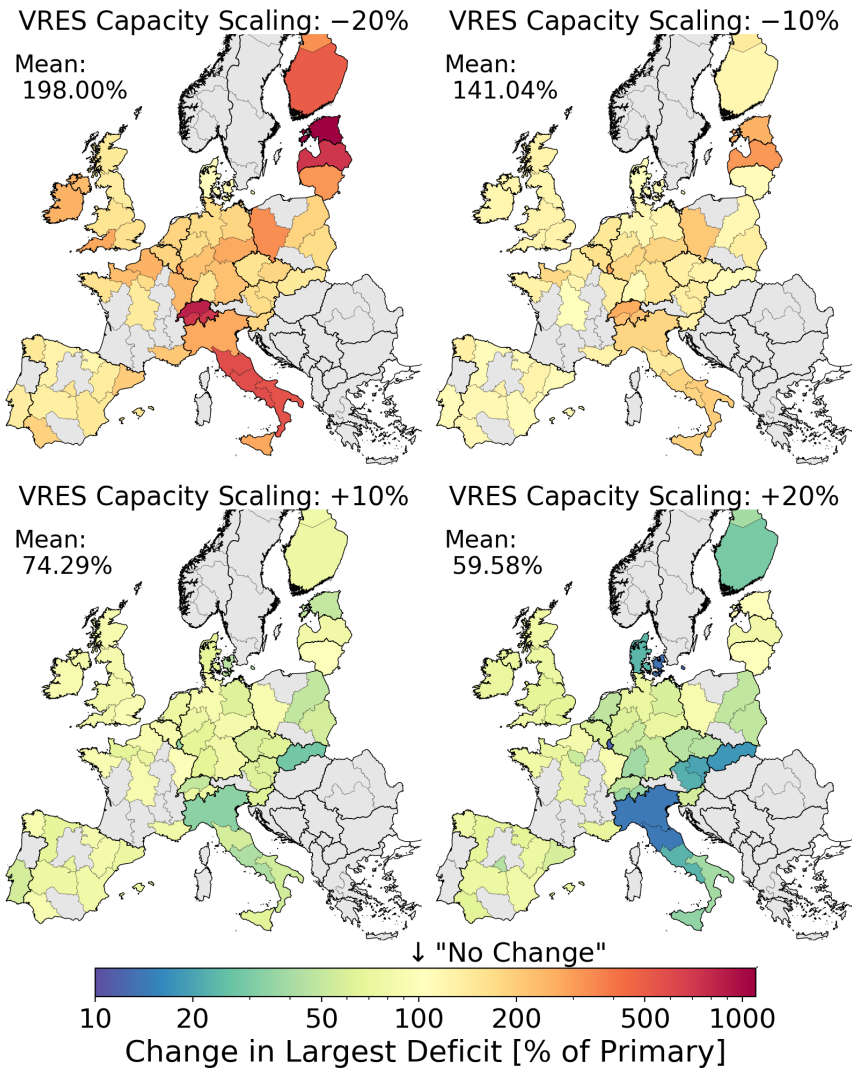

Figure 7.16: Spatial sensitivity of the largest lull deficit to VRES capacity scaling

base analysis by $20\,\%$ would reduce the effective LCOE contribution from VRES generation to $3.7\,\mathrm{ct}_{€}\,\mathrm{kWh}^{-1}$; which, compared to the $4.2\,\mathrm{ct}_{€}\,\mathrm{kWh}^{-1}$ found earlier is significantly closer to the value suggested by Child et al..

Finally, the largest residual load (maximum backup capacity) trend of Figure 7.15 portrays an interesting dynamic. When evaluated across all of Europe, a strong

inverse linear relationship is seen where there is a $1\,\%$ rise in the largest residual load for each $2\,\%$ decrease in VRES capacity. This value is directly translatable to the total European-wide backup estimate of $498\,\mathrm{GW}$ made at the end of the Section 7.3.2 and logically suggests that this value is directly tied to the amount of VRES installed in the system. However this plot also shows that the same quantity, evaluated individually for all regions and summed, shows almost no sensitivity to VRES capacity scaling. This latter value corresponds directly to the maximum backup capacity estimate of $738.5\,\mathrm{GW}$ found from Figure 7.12, and strongly suggests that it is not a sensitive quantity so long as the system is still predominantly based on VRES generation. Other countries, such as France and the UK, show much more varied responses which occur as a result of their unique roles in the energy system shifting. Compared to the largest residual load, summed residual loads (i.e. total backup generation), not shown in Figure 7.15, have a typical sloping trend for almost all regions, which for Europe begins at $181\,\%$ of the base backup usage when $-20\,\%$ VRES capacity is installed, and ending at $55.7\,\%$ of the base backup usage at $20\,\%$ VRES capacity[24]. Translating this to the primary evaluation's average backup reliance of $15.54\,\%$ suggests that this value could rise to around $28\,\%$ or shrink to nearly $9\,\%$ depending on how much VRES capacity is installed. Nevertheless, these values are not out of line with annual backup usage estimates made in the literature, as these are generally given for European systems where total demand and total VRES generation are equal[25].

7.5 Methodology Adjustment Tests

Four additional analyses were performed which each adjust one key piece of the overall methodology in order to observe the effect on the occurrence of lull spans and deficits. These adjustment analyses will be discussed together as their setups are straight forward and the resulting conclusions which pertain to the overarching research questions of this thesis are in the end quite simple. Nevertheless, a more detailed discussion of these analyses can be found in Appendix I. Due to data availability restrictions, however, it is not possible to perform each of these adjustment analyses for all demand-generation years used in the primary analysis. Therefore, only 2015 was selected for both the demand and generation year since it was available for each test and mirrors the capacity scaling sensitivity analysis performed in the previous section. Because of this, discussion will focus on the relative difference between each analysis' lull spans and deficits versus that of the base analysis for the same demand-generation year.

These four adjustment analyses are summarized as follows: First the power flow evaluation is performed with a copper-plate within each country, which equates to the system being evaluated with countries as single nodes. Since this type of evaluation is commonly seen in the literature [350, 354, 357–359], this test will estimate how this simplification of the overall system can impact lull occurrence.

[24] For visual reference, see the 'Individual' curve on the Max Deficit trend in Figure 7.15

[25] In the present work, scaling capacities by $0.94\times$ causes total VRES annual generation to exactly match total annual demand.

Afterwards, the next three sensitivities replace the VRES generation time-series of each E-Highway region with that from another source. In the second adjustment analysis, the EMHIRES datasets for wind [180] and PV [312] are used in place of the wind and PV distribution and simulation schemes developed in this work. This dataset is chosen at is likely to be used by the energy modeling community and therefore this test can show how energy system modeling results can differ when performed with the EMHIRES dataset rather than the VRES time-series developed in this work. In the third adjustment analysis, the time-series arising from applying this work's simulation approach to MCDA-sorted turbine and PV park locations is used. This sorting approach alters the selection order of VRES generator locations within each E-Highway region according to several criteria and, as opposed to the simpler LCOE-sorting used in the base analysis, is slightly more realistic but will lead to less overall FLHs. For this test, the MCDA scoring approach of Tlili et al. [50] is used. Finally, in the fourth adjustment analysis, the time-series arising from using the COSMO-REA6 [194] climate model dataset in place of the MERRA [179] dataset is used. The same LCOE-sorted turbine and PV park location as the base lull analysis are used, and so this analysis directly tests the impact of using the COSMO-REA6 climate model dataset compared to the use of MERRA.

The maps shown in Figure 7.17 display the percent difference of the largest lull deficit observed in each E-Highway region that results from these adjustment analyses in comparison to the base analysis. Regions which previously did not observed a lull are colored gray.

7.5.1 National Copper Plate

In the top left panel of Figure 7.17 it is seen that, with a copper-plate within countries, most regions either show no change in the largest deficit, or else are reduced to around half of their previous lull deficit value. A few regions, however, appear to have large increases in their lull deficit; such as Switzerland, Latvia, Estonia, and Southern Italy; all of which see a deficit increase by nearly a factor of 5. However, when taking a weighted average[26] of the changes seen for this sensitivity, it is seen that there is a typical reduction in deficits to $68.37\,\%$ of that seen in the base analysis. Projecting to the larger context, this result suggests that modeling the European electricity grid with one node per country is likely to under predict the impact of VRES lulls.

7.5.2 VRES Replacement: EMHIRES

The result of replacing the VRES time-series with the EMHIRES dataset is provided in top right panel of Figure 7.17. At first glance, several outliers can be seen in Switzerland, Southern Italy, Latvia, Estonia, and Finland where the percent change can reach as high as $11{,}000\,\%$. These strong differences are thought to arise from the greatly reduced wind energy generation between the EMHIRES dataset and compared to this work. As an example, EMHIRES estimates Estonia's onshore

[26] Weighted by the lull deficits seen in the primary analysis.

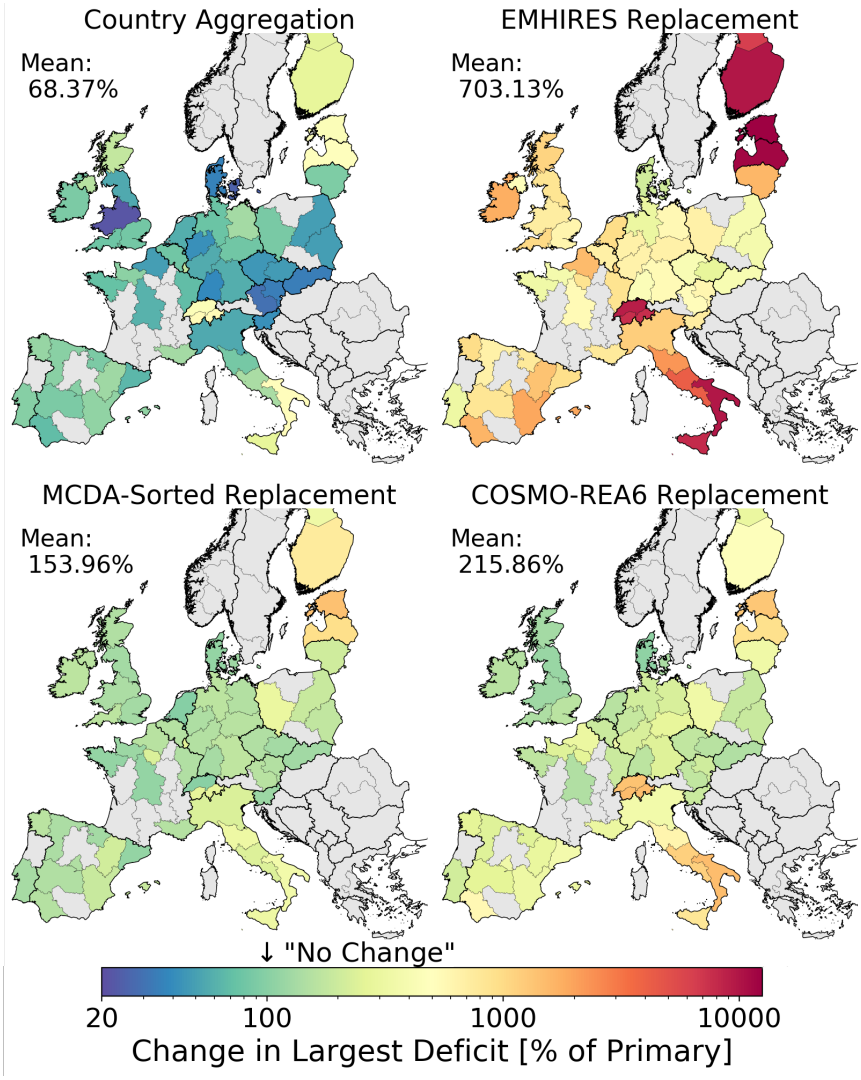

Figure 7.17: Spatial sensitivity of the largest lull deficit to methodology adjustment.

wind FLH at less than $1000\,\mathrm{kWh\,kW^{-1}}$ while, in the primary analysis, Estonia's onshore wind FLH was found at over $3000\,\mathrm{kWh\,kW^{-1}}$. Again, this outcome is a result of EMHIRES' adherence to contemporary turbine designs versus the futuristic turbine designs used in this work. Besides these outliers, Germany and Poland, for instance, appears to show lull deficit increases in the range of 300 to 500 %, while Spain and the UK are more in the range of 500 to 1000 %. Taking the weighted

average leads to a typical increase in lull deficit of 703.1 % compared to the primary analysis when using the EMHIRES dataset.

As shown at several points throughout this work, the relative performance of future generators for the same set of weather conditions will significantly improve in the future. This is especially true for wind turbines, as opposed to PV where the improvements will mostly impact module efficiency rather than performance. Therefore two primary conclusions can be drawn from the this adjustment analysis. First, that the EMHIRES dataset is best used for the analysis of current or at least near-future context electricity systems. Second, that the analyses of future energy systems absolutely must involve the consideration of future-oriented VRES generator designs, or else the expected VRES lulls will be nearly an order magnitude larger than they otherwise would be.

7.5.3 VRES Replacement: MCDA Sorting

The result of the adjustment analysis using MCDA-sorted turbine and PV parks is shown in the bottom left panel of Figure 7.17. As expected, only increases in the largest lull deficits are observed as the MCDA selection procedure selects a larger proportion of generator locations with less than the maximum FLHs. Furthermore, with the exception of Latvia, Estonia, and Finland, where exceptionally large deficit changes are seen, there is a much closer grouping of the various regions in comparison to the previous sensitivity results. Notably this include the regions of Northern Italy and Switzerland. Within this group Italy as a whole apparently observed the most change, rising to around 300 to 400 % of the base value, however, as seen in the optimized residual load lull deficits in Figure 7.8, Italy is also typically the region with the most shallow lulls for which a large relative change is less significant. Changes in Germany are limited to around 200 % versus around 150 % in the UK. Taking the weighted average of these values reveals the typical change in the largest lull deficit to 153.96 % of the primary analysis' value.

Besides the lull deficit, other outcomes of this analysis are interesting as well. Total available VRES generation when using MCDA-sorting has reduced to 94.3 % of that available in the base analysis, while the utilized VRES generation has only reduced to 96.2 %. This means that, in relation to the total available generation, the MCDA-sorting input performs slightly better than the LCOE-sorting input. Connecting this to the "Constrained Grid with Dispatchable Backup" context's results, these outcomes suggest that if MCDA-sorting had been used in the base analysis the total storage need to cover the largest lull deficits would rise from from 8.56 TWh to around 13.57 TWh, a very significant change, and the effective LCOE contribution of the VRES generators would rise from 4.2 $ct_{€}\,kWh^{-1}$ to 4.4 $ct_{€}\,kWh^{-1}$, a far less significant change. It is also seen that the total annual backup generation increases to 121.86 % of the base value, while the largest residual load[27] (largest backup capacity needed) increases to 104.14 %. The first results in a total annual backup utilization which is still easily in range of the literature-expected values pro-

[27] When evaluated individually for each E-Highway region and summed

vided earlier. The second again suggests that the required European-wide backup capacity is not a sensitive quantity. Ultimately, the use of MCDA-sorting compared to LCOE-sorting is seen to invoke noticeable changes to VRES lull occurrence, but these changes are not expected to be overwhelmingly large.

7.5.4 VRES Replacement: COSMO-REA6 Weather Data Source

The outcomes of the final adjustment analysis, where VRES generation time-series are simulated using the COSMO-REA6 dataset as opposed to MERRA are shown in the bottom right panel of Figure 7.17. One might expect that the higher spatial resolution of the COSMO-REA6 dataset should lead to greater spatial mixing of VRES generation, although this is not found to be the case. In fact, a familiar pattern is seen where all of the highly sensitive areas are again seen to have abnormally high increases in lull deficits; including Switzerland, Southern Italy, and much of the Baltic Nations. Besides these regions, however, the impact of switching weather sources typically increases lull deficits to $215.86\,\%$ of the base analysis' value. While this again a significant change, it is not nearly so impactful as not employing futuristic wind turbine and PV module designs, as seen in the EMHIRES adjustment analysis.

Outside of this outcome, however, this adjustment analysis is largely inconclusive due to the biased nature of this comparison. Since the VRES generator locations are chosen as the best-performing options according to a MERRA-derived simulation, it is highly unlikely that these same locations also correspond to the best-performing options from a COSMO-derived simulation. Therefore, as a result of this selection bias, it is expected that the COSMO-derived VRES profiles have fewer FLH than those from MERRA. This is the most likely reason why the expected decrease in lull occurrence due to spatial mixing was not observed, since it was outweighed by the poorer performing selection of turbines and PV parks. Evaluating the interplay between these and other dynamics would require simulating all turbine and PV park locations for all weather years in the COSMO-REA6 dataset, and then identifying the new LCOE-sorting order. As this constitute a much greater degree of analysis and discussion than is reasonable to delve into here, this adjustment analysis is not discussed further.

Chapter 8

Summary

In this final chapter, reiteration of this work's scope, the key results, and the most significant insights gained are summarized, alongside a brief reminder of the fundamental assumptions that drive the observed outcomes. Result robustness is also commented on by referring back to the various sensitivity analyses conducted throughout this thesis. At last, an outlook towards possible improvements to the current approach and the role these results can play within other research efforts are discussed.

8.1 Scope and Objective

Although the exact state of a future European energy system is uncertain, without any doubt VRES generation will play a significant role. Nevertheless, there is much uncertainty in the literature in regards to what design future wind turbines and PV modules will take, how they will be distributed across the landscape, and how much electricity they would generate. Furthermore, probabilistic arrangements of low VRES resource availability at the same time as high demand periods is commonly speculated to lead to extended VRES generation lulls. If not effectively planned for, these lulls could threaten the security of electricity supply, thus proving disastrous to a future VRES based European electricity system. Previous research efforts into this realm have suggested that these lulls can be expected, that the rarest of these could last for weeks at a time, and that they could be managed via the installation of massive storage quantities. However, none of these previous efforts have investigated VRES lulls in such a way that a detailed understanding of lull occurrence is given, both in terms of time spanned and deficient energy, which provides highly actionable quantities to energy system decision makers and other stakeholders.

In light of this, the current work serves to improve upon the VRES potential estimates and to ultimately build up to an in-depth investigation of VRES lull occurrence in Europe by posing three overarching research questions:

- Considering the spatially-varying sociotechnical constraints relating to VRES, what is the technical capacity potential of wind and PV energy in Europe in 2050?
- How much electricity can be expected from these units? At what cost? And how will these quantities vary temporally and spatially?

- When distributed across Europe to form the basis of a fully RES based energy system in 2050, how often could VRES lulls occur? How long will they span? And how deep could their energy deficits be?

To answer these questions, this work begins with the development of fundamental geospatial evaluation tools and dataset which permit a detail geospatial consideration across the European context (Chapter 2). Afterwards, the elementary operating principals of wind turbines (Chapter 3) and PV modules (Chapter 4) are considered and incorporated into methods related to their design, distribution, and simulation. As a result of the computationally-efficient modeling schemes developed in this work, a pan-European evaluation of individual wind turbine and PV park generation profiles over multiple years is possible at the hourly level. Capacity and electricity generation potentials as well as LCOE estimates for onshore wind, open-field PV, and rooftop PV are then produced via the application of these models (Chapter 6); thus addressing the first two overarching research questions. These models are then used to build up to the investigation of VRES lulls (Chapter 5) by constructing fundamentally-derived VRES generation profiles and observing their impact within an evaluation of a reconstructed energy system scenario found in the literature. In the end, the occurrence of VRES lulls are discussed at length in varying contexts (Chapter 7); at last addressing the third and final overarching research question.

The current work has prioritized the development of fundamentally driven VRES distributions and generation profiles which distinguished it from other approaches seen in the literature. While previous studies have performed any of a detailed potential analysis considering land eligibility and the explicit placement of wind turbines and PV parks, performed highly detailed simulations of individual wind turbines or PV modules over multiple years, or else evaluated the operation of the electricity system at the European level, no previous work known to the author has combined these elements into a single analysis. Moreover, an investigation into VRES lulls over Europe that incorporates probabilistic occurrence outcomes has before now not been available in the literature.

Several driving assumptions and other decisions have been made throughout this work, and so a short overview of these is presented. Onshore wind potentials are primarily driven by several exogenous assumptions including: typical turbine cost and design assumptions (Table 3.4), 30 uniformly-enforced land eligibility constraints (Table 3.5), turbine spacing (Section 3.5), and the location-specific design conventions (Equation 3.5). Additionally, central roles are filled by the synthetic power curve method (Section 3.3), which directly influences turbine performance, and the NREL-derived turbine cost model (Section 3.4), impacting fine-grained LCOE estimates. Furthermore, the use of the MERRA climate model dataset for all time series weather parameters and, especially, the GWA for high-resolution wind speed adjustments dictate the spatially-sensitive turbine performance outcomes (Section 3.6). For open-field PV, driving assumptions and practices include: typical module characteristics (Table 4.2), 28 uniformly-enforced land eligibility constraints (Table 4.3), the capacity-to-land coverage factor (Section 4.2.1), and the pre-analyses leading to location-specific tilt angles as well as the ubiquitous instal-

lation of fixed-tilt systems (Section 4.2.1). As with wind, the use of MERRA for all time-series weather parameters and the GSA for high-resolution irradiance adjustments directly influence estimated module performance (Section 4.4). Similar to open-field PV, the driving assumptions and practices include the typical module characteristics (Table 4.2), the capacity-to-roof coverage factor (Section 4.2.2), as well as the use of MERRA and the GSA (Section 4.4). Unique to rooftop PV, however, is the literature-derived relationship between population density and PV-suitable roof area, and the constant distribution of rooftop tilt angles and azimuths (Section 4.3.2). At last, when evaluating VRES lulls, it is clear that the final results are primarily driven by the selection of the E-Highway's "100% RES" energy system scenario (Section 5.3). The manner in which lulls are computed is noteworthy as well, including both the time spent in a lull as well as the time required for VRES generation to offset the deficient energy (Section 5.4.2). Finally, lull occurrence varies considerably between the three investigated contexts of "VRES Only", "Copper Plate", and "Power Flow", which are all evaluated here in order to provide as broad a perspective as possible (Section 5.5).

8.2 Main Conclusions

8.2.1 VRES Potentials

Using the land eligibility and distribution methods in addition to the unit-level simulation schemes, European potentials for onshore wind, open-field PV, and rooftop PV are evaluated and presented; thus addressing the first overarching research questions presented previously. Offshore wind has also been evaluated in a separate thesis from Caglayan [390] and the outcomes of this are later used in the VRES lulls analysis; nevertheless the offshore potentials are not discussed in this work. In summary, the potentials evaluated here offer significantly more generation potential than either of Europe's current electricity demand of 3.5 PWh [10] or its average estimated future demand of 4.3 PWh [300]. Potentials at the European level[1] are:

	Total		$\leq 6\,\mathrm{ct_{€}\,kWh^{-1}}$	$\leq 4\,\mathrm{ct_{€}\,kWh^{-1}}$
	Capacity	Generation	Generation	Generation
Total	28.7 TW	56.2 PWh	42.9 PWh	21.1 PWh
Onshore Wind	13.5 TW	34.3 PWh	22.0 PWh	5.6 PWh
Open-field PV	14.5 TW	21.1 PWh	20.7 PWh	15.5 PWh
Rooftop PV	706 GW	875 TWh	169 TWh	0

Besides the spatially explicit capacity and generation potentials for onshore wind, open-field PV, and rooftop PV, key findings of the VRES potential work show without any doubt that far more generation potential is available in Europe than would conceivably be needed to power a fully renewable European energy system. Nevertheless, these results also stress that a very high level of complexity should always

[1] Country level results can be found in Tables G.1 to G.6

be expected when dealing with VRES generation over large geographic areas. For all technologies, but especially in the case of onshore wind, it is clear that VRES behavior is highly susceptible to the selection of installation location and the individual design of wind turbines and PV systems. Therefore, any future evaluation of the these technologies should specify these details, since the use of out-of-context generator designs and obviously poor performing installation locations can lead to biased conclusions of the role VRES generation can play in future energy systems. Lastly, updated turbine and PV module designs, new weather datasets, or else varying land eligibility and MCDA distribution considerations by region could be implemented in future iterations of this work, and so the importance of developing flexible and high computationally efficient geospatial and simulation models cannot be understated as they strongly facilitate this future work in Europe or elsewhere in the world.

8.2.2 VRES Lulls

To address the third and final overarching research question concerning the occurrence of VRES lulls in Europe, three lull evaluation contexts were considered. In the simplest, the "Intermittent Generation" context, lulls are independently evaluated in reference to the generation profiles of onshore wind, offshore wind, PV, and finally their combination. The "Residual Load with Basic Backup" context evaluates VRES lulls in reference to total VRES generation and its correlation to electricity demand, but neglects any grid limitations. Finally, the "Constrained Grid with Dispatchable Backup" context evaluates VRES lulls in reference to the dynamics of a complete energy system including interregional imports and export subject to grid limitations as well as the optimized dispatch of biomass and hydro generators. The following key conclusions are drawn:

Context 1: "Intermittent Generation"

1. Onshore wind energy lull spans show greater variability between countries than for offshore wind energy lulls. For the countries possessing both on and offshore generation, onshore lulls are slightly longer.

2. Compared to PV energy lull spans, onshore lulls are generally shorter, especially on the European scale, but the rarest onshore lulls are significantly longer than PV lulls.

3. When combining all technologies the resulting VRES generation lulls last at most $20\,\%$ of lull spans from any independent technology. Thus wind and PV are complementary technologies. This suggests that only a mix of these technologies in the future European energy system can lead to an optimal design.

4. The effect of spatial mixing, leading to greatly reduced lull spans, is clearly seen when comparing the pan-European scope against the national scopes,

but little to no difference is seen when comparing the German state of North Rhine-Westphalia to all of Germany. This suggests that such spatial mixing only significantly reduces lull occurrence over international scales.

5. When not accounting for any grid limitations, uninterrupted VRES generation is possible across the European scope equaling 11 % of the average[2] hourly VRES generation.

Context 2: "Residual Load with Basic Backup"

1. When considering electricity demand but no grid limitations, all regions including the entirety of Europe have a non-zero chance of observing lulls in any given year. This is found even with a fully-available[3] backup capacity equivalent to 100 % of the average hourly demand plus export.
2. At the European level, it would require a 66 % backup capacity equivalent to cause at least some years to not observe a lull, and a 90 % backup capacity equivalent to ensure that only 10 % of years observe a lull.
3. The largest residual load over Europe seen in 1 % of years is found at 400.1 GW.

Context 3: "Constrained Grid with Dispatchable Backup"

1. With grid limitations included, the European scope observes a 2 hour lull in all years, with deficits of at least 5.96 GWh.
2. Design-relevant[4] lull spans for all national scopes are clustered between 10 to 20 days. For the European scope this reduces to around 5 days.
3. Lulls lasting 6.8 days and with deficits up to 3.98 TWh can occur at the European scope in 1 % of years. However, when regionally evaluating and summing the 1 % occurring deficits, the European total rises to 8.56 TWh.
4. The Central European scope[5] shows significantly longer lulls than Europe as a whole, at more or less the same deficit intensities. This suggests that only a pan-European approach to combat climate change makes sense since, if only a Central European approach were to be taken, the resulting storage and backup solutions could likely also satisfy the entirety of Europe.
5. The maximum hourly reliance on backup capacity occurring in 1 % of years summed across all regions in Europe comes to 501 GW. However, summing

[2] Over all weather years
[3] As in, capable of 8760 hours of operation per year.
[4] As in, expected to occur between once in 10 years to once in 100 years.
[5] Consisting of Germany, France, Italy, Belgium, the Netherlands, and Luxembourg.

the maximum backup used in an hour for each region, but irrespective of a common hour, raises this backup capacity requirement to 738.5 GW. This latter value correspond to a situation where regions in Europe choose to ensure their own security of electricity supply, while the former corresponds to the requirement if regions fully commit to, and depend on, European cooperation.

6. On average over Europe, the annual total of backup usage sums to 15.54 % of the total annual demand.

8.3 Result Robustness

Many of the result listed above are likely tied to the driving assumptions and practices used in this work, and therefore the robustness of these results comes into question. For example, for obvious fundamental reasons, changes in the land eligibility assumptions are shown to translate directly to new onshore wind and open-field PV capacity potentials. Changes in key fundamental geospatial data are also shown to have a profound impact on land eligibility estimates, and therefore potential, as well; especially in the case of settlements, agriculture, woodlands, electricity grid, and roads. These changes could occur either as a result of new data or actual land-use change. In any case, it is very hard to predict how these alterations would impact generation potentials without redistributing and simulating individual turbines and PV parks. For rooftop PV, it is also shown that more accurate roof orientation data could have a small, but nevertheless measurable, effect on the performances estimated here. For these reasons, it is apparent that, for any large-scale energy system analysis to most accurately reflect reality, researchers should always seek to obtain the highest detailed and most up-to-date geospatial data, in addition to the nearest-to-reality specifications for each geopolitical region under consideration. This also encourages frequent updating of VRES potentials and derived results to incorporate both new data and evolving social attitudes. Nevertheless, with the understanding that total capacity and generation potentials could change with a new eligibility scenario, the potential results are nevertheless considered to be robust since a common European eligibility perspective was considered and the level of geospatial detail either rivals or surpasses other analysis with similar aims. More importantly, average FLH results were often seen to agree with future estimates and thus generation profiles, especially, are expected to be highly dependable.

Of the lull estimations, the scenario selection, and the fact that it is shown to be ill-designed for the current VRES generation profiles[6], strongly influences the results. Nevertheless some items, such as the 15.54 % average total backup utilization, are highly supported in the literature. In the lull sensitivity analyses, the MCDA analysis suggests that this value could rise to 18.94 % and the 0.94 x VRES scaling test[7] translates to 17.28 %. Both of these values are on the higher end of what is sup-

[6] Seeing as how nearly a quarter of all available VRES generation is curtailed in the "Power Flow" lull context

[7] Where total VRES generation is closest to total demand, corresponding best to literature.

ported by literature, but this is not an issue considering that a system design that is optimized to these VRES inputs would likely reduce this backup reliance and thus return it to being in-line with literature. Therefore the backup reliance of a primarily VRES based European energy system summing to around 15 % of the total demand is thought to be highly robust.

Similarly, many literature sources predict that total backup capacity in Europe should be around 100 to 110 % of the average hourly demand. As discussed above, evaluating this quantity across an aggregated European scope, which agrees most with methods in the literature, leads to a design-relevant total backup estimation of 500 GW (≈104 %) and is exactly in the expected range. Furthermore, testing this quantity in the VRES capacity scaling and MCDA input sensitivity analyses results in very little change from the primary analysis. Therefore, it is clear that this result is particularly robust.

The clustering of design-relevant national PFL spans around 10 to 20 days shows regionally varied and highly sensitive responses to VRES capacity scaling. When scaling capacities to −10 %, the longest lull spans typically increase to between 14 and 28 days, and when scaled to −20 % spans increase further to around 20 and 40 days. By comparison, the use of MCDA sorting only increases the longest spans to within 13 and 26 days. For power flow lull deficits, the estimates from 4 to 9 TWh are small compared to storage requirement estimates made in the literature, even when accounting for the 4.56 TWh already present in the scenario in the form of pumped hydro storage. These, too, show a high sensitivity to scenario design as −20 % VRES capacity scaling increase this estimate to between 10 and 17 TWh, while MCDA sorting increases them to within 7 to 14 TWh. Notably, in the EMHIRES input sensitivity, both lull spans and deficits estimates rise to extreme levels; suggesting an 8.7 x increase in the longest spans and an 6.5 x increase in the deepest deficits. As one of the primary differences in this case from the primary analysis is the JRC's use of contemporary turbine and module designs, leading to a clear message that future-oriented energy system analyses absolutely must incorporate future-oriented VRES technology designs. In the end, while it is clear that there is a fair degree of obscurity to these values, it nevertheless appears robust that, in a future-oriented and primarily VRES based European energy system, design-relevant lulls spanning between 2 and 4 weeks, and causing energy deficits in the range of 5 to 15 TWh, should be expected.

8.4 Outlook

Looking to the future, there are numerous ways this work could be improved upon or else could be incorporated into other researcher efforts. It has already been mentioned that a regionally-detailed treatment of the fundamental land eligibility constraints and VRES distribution criteria would improve plausibility in the potential estimates and resulting lull occurrences. Additionally, in case these results are influenced by biases inherent to the MERRA dataset, revalidation of the VRES simulation schemes using higher resolution weather datasets, such as the COSMO-

REA6, should be performed, and then applied to the lull evaluation procedure. Moreover, lull evaluation should also be performed in the context of a European capacity scenario that has been specifically designed around the advanced VRES generation profiles developed here. At last, a higher detailed evaluation of the electricity grid, such as one including the mid-voltage distribution level, would likely reveal more grid limitations and, thus, increase the occurrence of VRES lulls.

Yet even without making these improvements, the current work can still serve as a resource for multiple reasons. On one hand, the validated VRES simulation schemes can be applied as needed to estimate generation profiles for both contemporary and future-oriented wind turbines and PV modules. The land eligibility and unit distribution models, along with the preprocessed Prior datasets, could also be applied to other renewable technologies, such as biomass or geothermal, or even to completely different geospatially-sensitive industries, such as the construction of factories or salt caverns. Furthermore, by expanding the requisite data beyond the current European scope, these models can be applied at a global level. On the other hand, the VRES lull evaluations provide robust indications and trends relevant to future VRES based European energy systems.

Chapter A

Geosptial Modeling

The following is an excerpt from an accompanying publication [25] along with this thesis, and is included here for reference.

A.1 Criteria Description

In the end, 28 general criteria were identified and are shown in Table 2.2. The following sections describe each of the indicated criteria in more detail and provide some common arguments for their consideration in the review literature. A table showing the criteria which were considered by each of the reviewed reports can be found in Appendix A.

A.1.1 Sociopolitical

Within the sociopolitical motivation group, 13 general criteria were identified. The most commonly considered criteria in this group was distance from settlement areas where, as indicated in Table 2.2, distances closer to settlements are considered less desirable. This criterion is generally used to account for both safety issues related to RES technology, as well as to account for visual and audible disruptions to the local population (such as glare from PV panels and noise from wind turbines). Although many studies utilized distance from settlements in a general sense, many also distinguished several sub-definitions; most commonly, this included the distance from urban (or otherwise densely populated) settlements, as well as from rural (sparsely populated) settlements. Distance from airports was the next most commonly included criterion, which was generally considered as a safeguard against dangers to airline passengers (such as increased turbulence in wind turbine wake, or the glare of PV panels affecting pilots), although could also account for effects of airplane turbulence on the RES technologies (such as increased soiling on PV panels). Two sub-criteria were also found for this criterion, namely the distance from large and commercial airports and from smaller airfields. The distance from roadways follows, accounting for safety concerns related to placing an RES technology too close to a roadway (such as potential ice throws and structural failures of wind turbines or, again, glare from PV panels or CSP reflectors). Once again, sub-criteria are found here: the distance from primary roads (such as highways and federal roadways) and from secondary roadways (such as those connecting rural settlements). The distance from agricultural areas refers to distances from agriculture areas such as pastures and farmland, which are considered to prevent the installed technology from interfering with food supply. This criterion was

generally only considered for PV, CSP and biomass systems, as these technologies either interfere or compete with the resources needed by crops, while wind turbines were commonly claimed to be compatible with most types of agriculture [32]. Similar to roadways, the distance from railways was considered a safeguard against dangers to passengers and damage to infrastructure and was most commonly considered for wind turbines. Likewise, distance from power lines was also commonly included to avoid damage to infrastructure and was, once again, most commonly considered for wind turbines. Distance from historical sites was typically included to prevent installations too close to locations of cultural and historic importance, so as to avoid disruptions to visitors to such sites and to prevent the devaluing of a site's significance. This included battlegrounds, castles, monuments, religious sites, and others. No sub-criteria are defined here, as a consensus could not be found in regard to what constitutes a historically significant site. Distance from recreational areas was also generally considered to avoid disruption and danger to visitors. Three sub-criteria were identified here, namely: distance from campgrounds, from urban parks (or 'green' parks) and from tourist attractions. Distance from industrial areas was considered to prevent the placement of a technology too close to industrial areas in order to protect equipment and workers. Distance from mining sites was included to prevent placement too close to mining sites and to protect equipment and workers, and also given that the ground may be unstable in these areas. The general implication in this case saw siting placements further away from mining sites as preferable, although some studies actually used the opposite logic with regard to PV plants, stating that the areas around mining sites presented ideal locations for PV [32]. The distance from radio towers was included to prevent damage to infrastructure and avoid disruption of the signal broadcast from the tower; in general, this constraint was only considered for wind turbines. Similar to distance from power lines, distance from gas lines was considered to avoid damage to infrastructure. As the last criterion in this group, distance from power plants was generally included in order to protect equipment and workers in the area.

A.1.2 Physical

The physical motivation group is characterized by nine general criteria. Most commonly, the terrain slope was considered to measure the average slope of the terrain throughout the area relevant to each location. This criterion was applied to all RES technologies, although the terrain slope in the north-south direction, a sub-criterion of the terrain slope, was only applied to solar and biomass technologies. Following this, distance from water bodies was included on several grounds, including: to protect the installation site from water damage during rainy periods, to avoid contamination of water streams during the construction process and to prevent disturbance of the wildlife dependent on these water bodies. The treatment of water bodies varied heavily between sources however, so three sub-criteria have been extracted from this group. The distance from stagnant water bodies indicates a location's distance from lakes, reservoirs and any other bodies characterized by still water. The distance from running water bodies indicates a location's distance from rivers, streams, canals and other bodies characterized by flowing water. Finally, distance from coasts refers to a location's distance from the nearest coastline, which is

treated separately from stagnant water bodies, as alternative issues must be considered (such as the tide and corrosion from sea spray). Distance from woodlands indicates a location's distance from the nearest forest and was considered for all technologies, as the presence of nearby woodlands can affect resource availability (such as slowing wind speeds and blocking solar irradiance) and the systems themselves can adversely impact local wildlife. Distance from wetlands was considered to avoid terrain unsuitable for construction and ensure the avoidance of riparian zones and wetland areas. Mean Elevation was included under the reasoning that suitability for RES technologies decreases at extreme elevations due to inaccessibility, instillation costs and diminishing resources (in the form of lower air density and increased cloud coverage, for example). The distance from land instability criterion was considered to prevent installation too close to areas which are prone to landslides, mud slides, or earthquakes in order to avoid the damage these events would inflict on an installation site. Distance from ground composition was considered as a criterion to account for certain soil and ground compositions that can affect an RES installation. A notable sub-criterion is given by distance from sand coverage (such as beaches and sand dunes), as the sand might not provide stable land to build on and, when carried by the wind, can cause erosion, soiling (in the case of solar technologies) and disturb plant growth (in the case of biomass). The aspect criterion was considered to account for how the direction of the terrain slope affects an RES installation; for example, how slopes facing in a northerly direction will experience a diminished solar resource, or how slopes facing away from the predominant wind direction will be subject to wind shading. Finally, the vegetation criterion was commonly considered to account for how local flora interact with an RES installation by means of, for example, damage caused by root growth, as the RES installation could disturb the ecosystem of particularly vulnerable vegetation via reduced sunlight (such as by PV panel coverage) and by competition for nutrients (in the case of biomass).

A.1.3 Conservation

The conservation motivation group is characterized by only two main criteria; however, multiple sub-criteria were found in each case. Distance from protected flora, fauna and habitats (FFH) was considered to prevent RES installations from adversely affecting vulnerable ecosystems and commonly relied on national or international designations. As sub-criteria, this criterion is separated into distance from designated habitats (which include bird and bat areas), from animal migration routes, from biospheres and from wildlife refuges. The distance from protected areas criterion was included to prevent RES installations from interfering with protected areas outside of ecological concerns. Sub-criteria in this group include distance from designated landscapes, from protected designated parks, from designated nature reserves and from natural monuments.

A.1.4 Economical

Within the economical motivation group, four general criteria were identified. The resource criterion served as an indicator for how much energy an RES installation at a location would potentially produce. Two sub-criteria were identified according to the quality that was most relevant to the RES technology being investigated: annual mean wind speed in the case of wind turbines and average daily global horizontal irradiance for solar and biomass technologies. The access criterion was commonly included to account for costs associated with providing access to the RES installations during both the construction phase and for maintenance. The implication being that locations that are less accessible with existing infrastructure would incur higher costs as new roadways must be constructed. More often than not, the access criterion was defined according to distance from the nearest roadway, although considering that the opposite implication is used compared to the roadway consideration in the sociopolitical motivation group (where desirability increases with distance) and that the two operate at completely different scales (many kilometers versus hundreds of meters), the access criterion is treated separately than road proximity. Similarly, the connection criterion was considered to account for the installation costs associated with connecting the RES installation to the energy network, the implication being that desirability decreases as distance increases as new transmission infrastructure must be built spanning larger distances. When wind turbines and solar technologies were considered, this criterion was defined by the distance to the nearest electricity grid line, while when biomass was considered the distance to the nearest natural gas pipeline was used. Once again, the connection criterion is treated separately from the power lines and gas network criteria in the sociopolitical motivation group because of the opposite implication and different operating scales. Finally, the land value criterion was used to account for the costs associated with obtaining construction rights at each location, as estimated by the current owners of the land. For similar reasons, as discussed with respect to the distance from historical sites, when this criterion was considered, the definitions of land ownership were highly specific to the local region being investigated and, as such, no general consensus could be extracted.

A.2 Constraint Ranges

In total 28, general criteria were identified as being utilized somewhere within the work flow of the reviewed studies. However, as each study also included an LE investigation, Table 2.2 also provides the inclusion rate of each criterion specifically within the study's LE analysis. As was previously discussed, when criteria are expressed as an exclusion constraint, a value threshold, range, or subset is used to differentiate between which locations are eligible and which should be excluded. In the vast majority of cases, a threshold is given, and therefore in order to get an idea of what threshold values are typically used for each constraint, these values were recorded when reviewing the literature and are summarized in Table A.1. For each of the indicated criteria (and in many cases sub-criteria when a consensus within the literature could be identified), this table gives a typical threshold value that re-

sulted in low exclusions, a threshold that resulted in high exclusions and a typical threshold value used across all observations. Although the low and high exclusion values contain the vast majority of all applications for each constraint, the typical exclusion reported in this table is not intended for any single particular technology, as the chosen threshold for an analysis depends heavily on the technology chosen, the intended application (such as grid-connected or off-grid), and the preferences of the region being investigated. Instead, the typical value is given to indicate the scale at which these constraints require their underlying criterion to offer detailed information; which will come into play in the following discussion, where standardized datasets are produced for Europe.

A.3 Prior Dataset Construction Methods

For each of the created Prior datasets, a slightly unique procedure is followed. In all cases, however, the first step involved initially setting all pixels in the European study area to the ”no indication” value, 254, while all values outside the study area are assigned the ‘no data’ value of 255. Then, for each predetermined edge, starting from the largest and proceeding in reverse order, all locations that have a criterion value less than the given edge are reassigned to the edge’s index given by the table in Appendix C. When a criterion involves a simple value threshold, such as for elevations, the edge is applied directly to the value at each location. However, when the criterion involves a proximity threshold (such as the railway example provided earlier), edge containment is determined by buffering a ‘raw’ indication by the desired edge distance, followed by a rasterization identifying the pixels that lie in the buffered region. We now give more specific detail for each of the constructed Priors.

A.3.1 Sociopolitical Priors

Under the Sociopolitical motivation criteria group, 19 Prior datasets were created.

The settlement proximity Prior describes the distance from all settlement areas and is defined from locations indicated by the Corine Land Cover (CLC) [91] as ”continuous urban fabric” (CLC-code 1.1.1) or as ”Discontinuous urban fabric” (1.1.2). Settlement urban proximity gives distances from specifically dense urban settlements as indicated from features found directly in the European Commission’s (EC) Urban Clusters [92] dataset, which was developed as part of the Geographic Information System of the Commission (GISCO) initiative. In this dataset, urban areas were derived from a population density dataset at 1 km resolution, where only contiguous regions possessing a minimum of 300 inhabitants per at each point and a total population above 1500 were identified as urban.

The Airfield proximity Prior describes distances from small airports and is produced by combining information from both CLC and GISCO’s airport transportation network dataset [93]. In this case the EC’s airport dataset is used to identify the coordinates of activate airports that do not report a large passenger throughput (i.e.,

Table A.1: Typical constraint usage in land eligibility analyses

Group Criterion *Sub-criterion*	Excludes	Low	Typical	High	Unit
Sociopolitical					
Settlements	distances below	0	800	2000	m
Urban Settlements	distances below	0	1000	3000	m
Rural Settlements	distances below	240	500	2000	m
Airports	distances below	0	5	8	km
Large & Commercial	distances below	0	5	25	km
Airfields	distances below	0	3	8	km
Roadways	distances below	50	150	500	m
Primary	distances below	50	200	500	m
Secondary	distances below	50	100	500	m
Agricultural Areas	distances below	0	50	240	m
Railways	distances below	50	150	500	m
Power Lines	distances below	100	200	240	m
Historical Sites	distances below	500	1000	3000	m
Recreational Areas	distances below	0	250	500	m
Leisure & Camping	distances below	0	1000	3000	m
Tourism	distances below	500	800	1000	m
Industrial Areas	distances below	0	300	500	m
Mining Sites	distances below	0	100	500	m
Radio Towers	distances below	400	500	600	m
Gas Lines	distances below	100	150	300	m
Power Plants	distances below	100	150	200	m
Physical					
Slope	values above	30	10	1	°
Water Bodies	distances below	0	300	3000	m
Lakes	distances below	100	400	4000	m
Rivers	distances below	0	200	400	m
Coast	distances below	0	1000	3000	m
Woodlands	distances below	0	300	1000	m
Wetlands	distances below	0	1000	3000	m
Elevation	values above	2000	1800	1500	m
Land Instability	distances below	0	200	500	m
Ground Composition					
Sand	distances below	0	1000	4000	m
Conservation					
Protected FFH	distances below	0	500	2000	m
Habitats	distances below	0	1500	5000	m
Biospheres	distances below	0	300	2000	m
Wildernesses	distances below	0	1000	4000	m
Protected Areas	distances below	0	1000	3000	m
Landscapes & Reserves	distances below	0	500	3000	m
Parks & Monuments	distances below	0	1000	3000	m
Economical					
Resource					
Wind speed	values below	4.0	4.5	7.0	$\mathrm{m\,s^{-1}}$
Irradiance	values below	4.5	5.0	5.5	$\frac{\mathrm{kW\,h}}{\mathrm{m^2\,d}}$
Access	distances above	45	5	1	km
Connection	distances above	40	10	1	km

less than 150,000 passengers per year, or otherwise unreported), which is then connected to the closest contiguous area larger than 1 from the CLC dataset being indicated as ”Airports” (1.2.4). If no appropriate area is found within 2 km, a radius of 800 meters is assumed. Similarly, Airport proximity describes distances from large and commercial airports using the same procedure described for airfields; although in this case, annual passenger count must be greater than 150,000 and, if an appropriate area cannot be identified in the CLC dataset, a radius of 3 km is assumed.

Roadway proximity, roadway main proximity and roadway secondary proximity are all defined from a recent extract of the OpenStreetMap (OSM) [97] database and respectively describe distances from all roadways, major routes and highways, and local and state roadways. In order to remove unwanted features in the OSM dataset (such as footpaths and race tracks), roadway proximity accepts all routes and links classified under the ”highway” key as ”motorway”, ”trunk”, ”primary”, ”secondary”, ”tertiary”, ”service” and ”unclassified”. Meanwhile, roadway-main proximity only considers routes and links indicated as ”motorway”, ”trunk” and ”primary”, while roadway-secondary proximity considers ”secondary” and ”tertiary”.

The agriculture proximity Prior describes distances from all agricultural areas as indicated within the CLC agricultural group (2.x.x). Although not generally required by the LE literature sources, four additional agricultural-based Priors were created to reflect separate agricultural functionality, since this information was readily available from the CLC dataset.

Agriculture arable proximity is defined from CLC indications of ”Non-irrigated arable land” (2.1.1), ”permanently irrigated land” (2.1.2) or ”rice fields” (2.1.3). Agriculture permanent crop proximity is taken from indications of ”vineyards” (2.2.1), ”fruit trees and berry plantations” (2.2.2) and ”olive groves” (2.2.3). Agriculture heterogeneous proximity is taken from all CLC codes in the ”heterogeneous agricultural areas” group (2.4.x). Finally, agriculture pasture proximity simply comes from indications of ”pastures” (2.3.1).

Similar to the roadway priors, railway proximity and power line proximity describe distances from either the railway or the electricity grid network and are also taken from the OSM extract. Filtering is accomplished by selecting routes classified as ”rail” under the ”railway” key, or else as ”line” under the ”power” key.

Leisure proximity, camping proximity, and touristic proximity also describe distances from features as defined in the OSM dataset. Leisure proximity refers to expansive areas to which people may go for recreational or relaxation purposes and were taken as OSM features classified as ”common” or ”park” under the ”leisure” key. Camping proximity describes distances from camp grounds and camp sites and are taken from OSM features classified as ”camp_site” under the ”tourism” key. Touristic proximity describes places of local and cultural importance and are taken from OSM features classified as ”attraction” under the ”tourism” key.

Industrial proximity refers to distances from areas or industrial and commercial activity outside of settlement areas, which are defined from areas indicated by CLC as ”industrial or commercial units” (1.2.1).

As the last Prior in this group, mining proximity refers to distances from mining sites and are defined from areas indicated by the CLC as ”mineral extraction sites” (1.3.1).

A.3.2 Physical Priors

Within the Physical motivation criteria group, 13 Prior datasets were created.

The slope threshold Prior describes areas with an average slope less than the chosen edges, as determined by calculating the pixel-wise gradient of the EuroDEM [94] dataset (another product of the GISCO initiative).

Waterbody proximity refers to distances from all open inland water bodies that are large enough to be classified as a single pixel in the Permanent Water Body [391] dataset developed by the Copernicus group (i.e., comprising the majority of a 20 m pixel) and can refer to lakes, large rivers, reservoirs and other such features. The water-body proximity does not distinguish between stagnant and running water bodies and, moreover, it does not pick up smaller streams and rivers; therefore, additional Prior datasets were created. Lake proximity describes distances from stagnant bodies of water as defined by the HydroLAKES [96] dataset developed by the World Wildlife Fund (WWF). River proximity refers to distances from probable routes of running water, including both large rivers and smaller streams, and is taken from GISCO’s Hydrography [95] dataset. Routes in this dataset were seen to match well with the running bodies of water in the CLC dataset; however, only the route is provided, without any information on the body’s width, so this Prior is best employed in addition to the waterbody proximity Prior in order to account for smaller rivers and streams. The coast proximity Prior describes the distances from coastlines as defined by CLC-indicated ”sea and ocean” (5.2.3) areas.

Similar to the agricultural priors, the woodland proximity Prior describes distances from all woodland areas as indicated by the CLC dataset (3.1.x), but is also broken down into several sub-criterion priors according to the forest’s primary composition, since this information was readily available from the CLC dataset. Woodland-deciduous proximity, woodland-coniferous proximity and woodland-mixed proximity refer, respectively, to areas indicated as ”deciduous forest” (3.1.1), ”coniferous forest” (3.1.2) and ”mixed forest” (3.1.3).

Wetland proximity describes distances from wetlands, marshes and swamps and is taken from all areas indicated in the CLC dataset under the ”wetlands” (4.x.x) category.

Elevation-threshold simply describes the areas that have an average elevation lower than the given edges as read directly by the EuroDEM dataset. While the

Elevation-threshold Prior has the benefit of being much smaller in size than the original EuroDEM dataset (roughly 60 MB vs 20 GB), it does not derive any information beyond what is already communicated by the EuroDEM dataset and so it is suggested to continue using the original EuroDEM whenever possible.

As the final Prior in this group, the sand proximity describes distances from areas that are dominated by sand cover, as classified in the CLC dataset as ”beaches, dunes, [and] sands” (3.3.1).

A.3.3 Conservation Priors

The Conservation motivation group is comprised of 8 Priors representing distances from features extracted from the World Database on Protected Areas (WDPA) [98] dataset.

Protected habitat proximity is defined from WDPA features with an International Union for the Conservation of Nature (IUNC) category of ‘IV’, or else having the word ”habitat” within the area’s English designation.

In a similar manner, Protected wilderness proximity is assigned as WPDA features with an IUNC category of ‘Ib’ or otherwise as having ”wilderness” within the English designation.

Protected biosphere proximity and Protected bird proximity are given as WPDA features with ”bio” or ”bird,” respectively, within the area’s English designation.

Protected park proximity, protected reserve proximity, protected natural-monument proximity and protected landscape proximity refers to WDPA features with an IUNC category of ‘II’, ‘Ia’, ‘III’ or ‘V’, or as having an English designation containing the word ”park,” ”reserve,” ”monument” or ”landscape,” respectively.

Due to the selection of features by both the IUNC category and contents of the English designation, there is significant overlap between these Prior datasets; however, this is to be expected as the original definitions of these areas are already overlapping.

A.3.4 Economic Priors

In the final motivation group, economically-derived criteria, 6 Prior datasets were created, although two of these are simply aliases of previously generated Priors, as they can be used for these criteria as well.

Access distance, referring to distances away from the road network, is one such criterion which is an alias of the general roads proximity Prior. The same applies to Connection distance, describing distances away from the electricity network, is an alias of the power line proximity Prior.

For resource-related criteria like average annual wind speed or mean daily irradiance, several datasets are available, such as the DTU's Global Wind Atlas (GWA) [122] or the World Bank's Global Solar Atlas (GSA) [206]. These datasets are generally provided as a raster and, as such, can already be used directly in the methodology discussed in Section 2.4 Nevertheless, in a similar situation to the dataset used for the elevation Prior, Prior datasets have been constructed from these raw sources in order to expedite their use in LE analyses; however, the original sources should be preferred when available.

The 50m wind speed threshold and 100m wind speed threshold Priors were constructed directly by applying the chosen edges to the GWA's average wind speeds at 50 m and 100 m, respectively.

Similarly, the ghi threshold and dni threshold Priors were constructed from the direct application of the chosen edges onto the GSA's average daily global horizontal irradiance (ghi) and average daily direct normal irradiance (dni) datasets, respectively.

The GWA and GSA are both described at 1 km resolution across the whole world. The spatial interpolation of these datasets to the standard of 100 m was accomplished by using a cubic spline interpolation scheme. The resource-related datasets should be used with caution in LE analyses however, since, as expressed explicitly in the GWA's disclaimer, they are not intended for the direct micro-siting of RES systems.

A.4 Prior Dataset Edge Values

Table A.2: Sociopolitical Prior dataset edges

	Settlement	Settlement Urban	Airport & Airfields	Roads	Roads: Main	Roads: Secondary	Agriculture	Railway	Power line	Leisure	Camping	Touristic	Industrial	Mining
index	km	km	km	km	km	km	km	km	km	km	km	km	km	km
0	0	0	0	0	0	0	0	0	0	0	0	0	0	0
1	0.1	0.1	0.1	0.1	0.05	0.05	0.1	0.05	0.1	0.1	0.1	0.1	0.1	0.1
2	0.2	0.2	0.2	0.2	0.1	0.1	0.2	0.1	0.2	0.2	0.2	0.2	0.2	0.2
3	0.3	0.3	0.3	0.3	0.2	0.2	0.3	0.2	0.3	0.3	0.3	0.3	0.3	0.3
4	0.4	0.4	0.4	0.4	0.3	0.3	0.4	0.3	0.4	0.4	0.4	0.4	0.4	0.4
5	0.5	0.5	0.5	0.5	0.4	0.4	0.5	0.4	0.5	0.5	0.5	0.5	0.5	0.5
6	0.6	0.6	0.6	0.6	0.5	0.5	0.6	0.5	0.6	0.6	0.6	0.6	0.6	0.6
7	0.7	0.7	0.7	0.7	0.6	0.6	0.7	0.6	0.7	0.7	0.7	0.7	0.7	0.7
8	0.8	0.8	0.8	0.8	0.7	0.7	0.8	0.7	0.8	0.8	0.8	0.8	0.8	0.8
9	0.9	0.9	0.9	0.9	0.8	0.8	0.9	0.8	0.9	0.9	0.9	0.9	0.9	0.9
10	1	1	1	1	0.9	0.9	1	0.9	1	1	1	1	1	1
11	1.1	1.1	1.2	1.2	1	1	1.2	1	1.2	1.2	1.2	1.2	1.2	1.2
12	1.2	1.2	1.5	1.4	1.2	1.2	1.4	1.2	1.4	1.4	1.4	1.4	1.4	1.4
13	1.3	1.3	1.8	1.6	1.4	1.4	1.6	1.4	1.6	1.6	1.6	1.6	1.6	1.6
14	1.4	1.4	2	1.8	1.6	1.6	1.8	1.6	1.8	1.8	1.8	1.8	1.8	1.8
15	1.5	1.5	2.2	2	1.8	1.8	2	1.8	2	2	2	2	2	2
16	1.6	1.6	2.5	2.2	2	2	2.5	2	2.5	2.5	2.5	2.5	2.5	2.5
17	1.7	1.7	3	2.5	2.2	2.2	3	2.5	3	3	3	3	3	3
18	1.8	1.8	3.5	2.8	2.5	2.5	4	3	4	4	4	4	4	4
19	1.9	1.9	4	3	2.8	2.8	5	4	5	5	5	5	5	5
20	2	2	4.5	3.5	3	3		5	6					
21	2.2	2.2	5	4	3.5	3.5		6	7					
22	2.4	2.4	5.5	4.5	4	4		7	8					
23	2.6	2.6	6	5	4.5	4.5		8	9					
24	2.8	2.8	7	6	5	5		9	10					
25	3	3	8	7	6	6		10	12					
26	3.5	3.5	9	8	7	7		12	14					
27	4	4	10	10	8	8		14	16					
28	4.5	4.5	15	12	10	10		16	18					
29	5	5		14	12	12		18	20					
30	5.5	5.5		16	14	14		20	25					
31	6	6		18	16	16		25	30					
32	7	7		20	18	18		30	35					
33	8	8			20	20		40	40					
34	9	9			25	25			45					
35	10	10			30	30			50					
36	15	15			40	40								
37	20	20												

Table A.3: Physical Prior dataset edges

	Slope North-Facing	Terrain Slope	Water Body	Lake Proximity	River Proximity	Ocean Proximity	Woodland	Woodland Deciduous	Woodland Coniferous	Woodland Mixed	Wetland	Elevation	Sand
index	°	°	km	km	km	km	km	km	km	km	km	km	km
0	-20.	0	0	0	0	0	0	0	0	0	0	-1	0
1	-19.5	0.5	0.1	0.1	0.05	0.1	0.1	0.1	0.1	0.1	0.1	-0.9	0.05
2	-19.	1	0.2	0.2	0.1	0.2	0.2	0.2	0.2	0.2	0.2	-0.8	0.1
3	-18.5	1.5	0.3	0.3	0.2	0.3	0.3	0.3	0.3	0.3	0.3	-0.7	0.2
4	-18.	2	0.4	0.4	0.3	0.4	0.4	0.4	0.4	0.4	0.4	-0.6	0.3
5	-17.5	2.5	0.5	0.5	0.4	0.5	0.5	0.5	0.5	0.5	0.5	-0.5	0.4
6	-17.	3	0.6	0.6	0.5	0.6	0.6	0.6	0.6	0.6	0.6	-0.4	0.5
7	-16.5	3.5	0.7	0.7	0.6	0.7	0.7	0.7	0.7	0.7	0.7	-0.3	0.6
8	-16.	4	0.8	0.8	0.7	0.8	0.8	0.8	0.8	0.8	0.8	-0.2	0.7
9	-15.5	4.5	0.9	0.9	0.8	0.9	0.9	0.9	0.9	0.9	0.9	-0.1	0.8
10	-15.	5	1	1	0.9	1	1	1	1	1	1	0	0.9
11	-14.5	5.5	1.2	1.2	1	1.2	1.2	1.2	1.2	1.2	1.2	0.1	1
12	-14.	6	1.4	1.4	1.2	1.4	1.4	1.4	1.4	1.4	1.4	0.2	1.2
13	-13.5	6.5	1.6	1.6	1.4	1.6	1.6	1.6	1.6	1.6	1.6	0.3	1.4
14	-13.	7	1.8	1.8	1.6	1.8	1.8	1.8	1.8	1.8	1.8	0.4	1.6
15	-12.5	7.5	2	2	1.8	2	2	2	2	2	2	0.5	1.8
16	-12.	8	2.5	2.5	2	2.5	2.5	2.5	2.5	2.5	2.5	0.6	2
17	-11.5	8.5	3	3	2.5	3	3	3	3	3	3	0.7	2.5
18	-11.	9	4	4	3	4	4	4	4	4	4	0.8	3
19	-10.5	9.5	5	5	4	5	5	5	5	5	5	0.9	4
20	-10.	10			5	10						1	5
21	-9.5	10.5				15						1.1	
22	-9.	11				20						1.2	
23	-8.5	11.5										1.3	
24	-8.	12										1.4	
25	-7.5	12.5										1.5	
26	-7.	13										1.6	
27	-6.5	13.5										1.7	
28	-6.	14										1.8	
29	-5.5	14.5										1.9	
30	-5.	15										2	
31	-4.5	15.5										2.1	
32	-4.	16										2.2	
33	-3.5	16.5										2.3	
34	-3.	17										2.4	
35	-2.5	17.5										2.5	
36	-2.	18										2.6	
37	-1.5	18.5										2.7	
38	-1.	19										2.8	
39	-0.5	19.5										2.9	
40	0.	20										3	
...	...	...											
60	10	60											
...	...	...											
80	20												

Table A.4: Conservation and economic Prior dataset edges

	All Protected Areas	Windspeed 50m	Windspeed 100m	DNI	GHI	Access Distance	Connection Distance
index	km	$m\,s^{-1}$	$m\,s^{-1}$	$W\,m^{-2}$	$W\,m^{-2}$	km	km
0	0	0	0	0	0	0	0
1	0.1	0.25	0.25	0.25	0.25	0.1	0.1
2	0.2	0.5	0.5	0.5	0.5	0.2	0.2
3	0.3	0.75	0.75	0.75	0.75	0.3	0.3
4	0.4	1	1	1	1	0.4	0.4
5	0.5	1.25	1.25	1.25	1.25	0.5	0.5
6	0.6	1.5	1.5	1.5	1.5	0.6	0.6
7	0.7	1.75	1.75	1.75	1.75	0.7	0.7
8	0.8	2	2	2	2	0.8	0.8
9	0.9	2.25	2.25	2.25	2.25	0.9	0.9
10	1	2.5	2.5	2.5	2.5	1	1
11	1.2	2.75	2.75	2.75	2.75	1.2	1.2
12	1.4	3	3	3	3	1.4	1.4
13	1.6	3.25	3.25	3.25	3.25	1.6	1.6
14	1.8	3.5	3.5	3.5	3.5	1.8	1.8
15	2	3.75	3.75	3.75	3.75	2	2
16	2.5	4	4	4	4	2.2	2.5
17	3	4.25	4.25	4.25	4.25	2.5	3
18	4	4.5	4.5	4.5	4.5	2.8	4
19	5	4.75	4.75	4.75	4.75	3	5
20		5	5	5	5	3.5	6
21		5.25	5.25	5.25	5.25	4	7
22		5.5	5.5	5.5	5.5	4.5	8
23		5.75	5.75	5.75	5.75	5	9
24		6	6	6	6	6	10
25		6.25	6.25	6.25	6.25	7	12
26		6.5	6.5	6.5	6.5	8	14
27		6.75	6.75	6.75	6.75	10	16
28		7	7	7	7	12	18
29		7.25	7.25	7.25	7.25	14	20
30		7.5	7.5	7.5	7.5	16	25
31		7.75	7.75	7.75	7.75	18	30
32		8	8	8	8	20	35
33		8.25	8.25	8.25	8.25		40
34		8.5	8.5	8.5	8.5		45
35		8.75	8.75	8.75	8.75		50
36		9	9	9	9		
37		9.25	9.25	9.25	9.25		
38		9.5	9.5	9.5	9.5		
39		9.75	9.75	9.75	9.75		
...		...	...	...	...		
80		20	20	20	20		

A.5 GLAES Work flow Description

The first step within the constructed model involves creating a regional context over which the future computations will operate. Not only does this context determine the geographical area that is extracted from the various exclusion-datasets, but it also defines the raster characteristics (resolution, spatial reference system and extent) of the finalized LE result. Defining this context requires at least three parameters: the boundary of the region to be investigated, the desired output SRS and the desired pixel resolution. There is no methodologically- inherent limitation on the geographic areas, SRSs and resolutions that can be represented by the described model; however, in the case of LE analyses the output SRS would usually be an equal-area projection which preserves relational distances and the resolution should be small enough to capture local details (later analyses in this report use 100 m). When given the necessary inputs, the model represents the regional context as a region mask (RM), which is exemplified in Figure A.1.

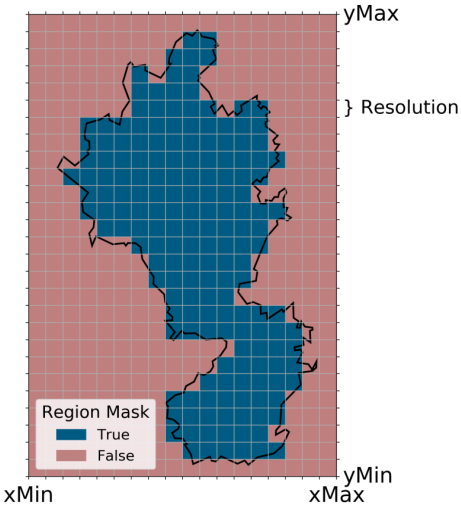

Figure A.1: Example of a region mask used in GLAES

The model first transforms the regional geometry to the desired output SRS and records the enveloping extent (the smallest rectangular extents that contain the region while still fitting the given resolution, as shown in the figure by xMin, yMin, xMax, and yMax). With the output extent, resolution and SRS in hand, a raster dataset comprised of a single band of boolean values is created with these characteristics. The pixels of this raster which are mostly within the original region definition are given the value 1, while all other pixels are given the value 0. In essence,

the RM serves as a basis onto which all exclusion information will be translated, at which point the RM's boolean mask is used to easily determine which of those pixels are within the regional area. After creating the RM, an output availability matrix is also initialized. This matrix shares the same characteristics (SRS, extent, resolution and data type). All pixels in the availability matrix are initially filled with the value 1 indicating that, before any exclusion has been applied, all locations are considered to be $100\,\%$ available. Henceforth, the various exclusion datasets will be processed and the indicated exclusions removed from the availability matrix via element-wise logical operations.

A.5.1 Exclusion Indication

All applications of the exclusion procedure generate a 2-dimensional boolean matrix, matching the characteristics of the RM. In these matrices, true-valued pixels indicate that the associated locations should be excluded from the final availability matrix. Figure 2.7 provides a simplified flow-chart of the implemented procedure. In general, the exclusion procedure functions as follows: first, an indication of the locations to be excluded is made in the dataset's original definition (or as close to it as possible), then those indicated locations are translated into the RM's characteristics, after which the indicated pixels are excluded from the availability matrix. However, considering that raster and vector source represent spatial information in drastically different ways, the procedure must follow one of two initial tracks, depending on the type of input dataset. These two initial tracks are described below. For raster sources, the only parameter required is the indication value or range of indication values that should be marked for exclusion, although an optional buffer distance parameter can be provided as well. The first objective is to generate a new boolean-valued raster source, indicating the to-be-excluded pixels in the source's original SRS and resolution. To minimize memory usage, however, the original source's extent is always clipped to the smallest extent (defined in the source's SRS), which contains the RM's extent. Indication is accomplished by considering each pixel in the original source and determining if its value is equal to, or is otherwise within the range of, the given indication value parameter. This new source, which now contains boolean values indicating whether or not each pixel should be excluded, is then warped using the bilinear method to a new raster in the RM's extent and SRS. By performing the warping procedure after the indication step, the unavoidable error introduced from warping is minimized compared to the reverse order. When a vector dataset is provided, there are no required inputs; however, an optional feature filter, buffer distance, and buffer method parameters can be provided. The most appropriate parameterization to use depends greatly on the characteristics of the dataset that is being processed. As a first step, the original source is spatially filtered and a new vector source is generated that contains only the features of the original vector which overlap the RM's extent. If a feature filter has been provided, another new vector source is produced that only contains the extent-filtered vector's features that also pass the feature filter. Following this, if a buffer distance parameter is provided and the buffer method parameter indicates that the geometry-based method should be used (which is the default pathway in this case), yet another intermediate vector source is then produced. First,

the filtered source's features are segmentized to a distance equivalent to half of the RM's resolution, transformed to the output SRS and then buffered by the given buffer distance. By segmentizing the original geometries, the error introduced when transforming to the output SRS is minimized, as the new geometry will follow the contours of the original more closely than if the geometry was transformed directly. Moreover, since the buffer distance is provided in units of the output SRS, applying the buffer distance to geometries that are expressed in the output SRS ensures that an identical buffer distance is applied everywhere. In any case, the latest intermediate vector source is comprised of geometries that indicate the areas to be excluded. This is then rasterized onto an intermediate boolean-valued raster in the RM's SRS and extent in the same manner described when generating the region mask. Regardless of the original source's type, at this point an intermediate boolean-valued raster has been produced in the RM's characteristics. If a buffer distance parameter was provided and the original source was of the raster type or if the area-based method was indicated in the vector case, then a buffer distance must be applied around all of these indicated pixels. To accomplish this, the intermediate raster is polygonized, converting all contiguous true-valued regions into geometries described in the output SRS. These geometries are then buffered by the given buffer distance, followed by another rasterization of these geometries into a new boolean-valued raster matching the RM's characteristics. Finally, application onto the availability matrix is performed via an element-wise 'or' operation between an inverted version of this output raster and the availability matrix.

A.5.2 Application

With consecutive applications of this procedure using a multitude of exclusion datasets, it can be seen how the availability matrix is updated with each iteration; which always results in a smaller amount of available pixels. Furthermore, the described procedure is general enough that, with proper parameterization, it can be applied to any raster or vector dataset and to any geographical area. Ultimately, the availability matrix will be filled with boolean values, where a value of 1 implies that the pixel remains available after all exclusion indications and a value of 0 implies the pixel has been excluded by at least one exclusion constraint.

A.6 GLAES and Prior Validation

In view of validating the described framework, eight studies that include LE analyses were chosen for replication. To qualify for replication, each study"s LE analysis had to have been conducted within Europe and where the majority of exclusion constraints are closely expressible in terms of the Prior datasets. It was decided that the validation effort would focus on the use of the Prior datasets for reasons of both simplicity and to emphasize how these Prior sources can produce acceptable results despite their lower granularity compared to the raw underlying datasets. Seeing as how the Prior datasets are fixed on their criteria definitions and limited to information contained within their original datasets, they will likely not match perfectly to the datasets and criteria definitions used in the various replication studies.

Therefore, if the result of combining several Prior datasets to recreate previous LE analyses comes close to the reported values, then the overall framework will be considered valid as a more specific choice of datasets and subtle alterations of criteria definitions will surely improve the end result. The procedure taken for each replication was roughly the same in all cases. Following along with the methodology described in Section A.5, a region used by the replication authors is initialized, followed by the application of multiple Prior datasets, along with associated criteria value thresholds. The datasets and thresholds used in each case are given in Table A.5. The number of available pixels is compared against the total number of pixels in the replication region, yielding the percentage of available land remaining. Table A.5 also displays the result of each replication effort

A.6.1 Validation Studies

For each replicated study, a short introduction is given, after which the significant differences from the Prior datasets are summarized. When a course of action was taken to try to account for these discrepancies, the reasoning for this is given as well. The LANUV [53] study investigated onshore wind LE in North Rhine Westphalia, Germany. Typical wind- relevant exclusion constraints were considered, including distances from roads, settlement areas, airports, railways, power lines, rivers and protected areas. They also excluded woodlands, marshlands and seed crop agricultural areas without any buffer distance. Significant deviations from the Prior datasets utilized for the LANUV recreation involved LANUV's exclusion of flood plains, for which no Prior was developed, their exclusion of 450 m from exterior areas with residential use, the exclusion of windbreak areas and the specific exclusion of lignite mining sites, as opposed to general mining sites. Additionally, the LANUV study used a number of proprietary or otherwise unavailable datasets that could not be compared to those used to construct the Priors, which included the dataset on settlement- and residential-use areas.

The UBA [73] study investigated onshore wind LE throughout Germany. Once again, typical wind-relevant exclusion constraints were considered, including distance from urban areas, individual dwellings, state and federal motorways, power lines, railways, industrial and commercial areas, camp sites, lakes and rivers and protected areas. Marshlands and forests were also excluded without a buffer distance. Additionally, all slopes above 30 degrees were excluded. Deviation from the utilized Priors was mostly limited to the way criteria were defined; for example, UBA's criterion defined as distances from individual dwellings versus the settlement proximity Prior's definition of distances from urban land coverage. Most importantly, the UBA study excluded distances from settlement areas up to 600 meters, distances from industrial areas up to 250 meters and distances from campsites up until 900 meters. However, they go on to treat 600-1200 meters from settlement areas, 250-500 meters from industrial areas and 900-2000 meters from campsites as reduced turbine operation zones to prevent exceeding noise limitations. This has been accounted for by increasing the exclusion threshold of each of these priors to a median value. Aside from definition misalignments, the UBA study used criteria definitions very close to those employed in the Priors and, in some cases, the study

Table A.5: Constraints and results of GLAES validation comparisons

Constraint	Unit	LANUV [53]	UBA "South" [73]	UBA "Central" [73]	Sliz [32]	McKenna [29]	Latinopoulos [39]	Höltinger "Med" [67]	Höltinger "Min" [67]	Samsatli [31]	Robinius [47]
Sociopolitical											
Settlements	$<$ m	600	1000	1000	500	800	500	1200	1000	500	
Urban Settle.	$<$ m						1000				800
Airfields	$<$ m	1500		1756		1756					1000
Airports	$<$ m	4000	5000	5000	3000	1000	3000	5100	5100	5000	1000
Main Roads	$<$ m	40	100	100	150	200	150	300	300	200	200
Secondary Roads	$<$ m	40	80	80	100	200	150	300	300		200
Permanent Crops	$<$ m	0					0				
Railways	$<$ m	100	250	250	100	200		300	300		200
Power lines	$<$ m	100	120	120	200			250	250		
Industrial	$<$ m	0	400	400	250	0	0	300	300		300
Mining Quarries	$<$ m	0			100		0	300	300		
Camping sites	$<$ m		1500	1500	450						
Leisure Areas	$<$ m				450						
Touristic Areas	$<$ m				1000						
Physical											
Terrain Slope	$>$ °		30	30		20	14	8.5	11.3	8.5	
Water Body	$<$ m	50	0	0	200						
Lakes	$<$ m							1750	1000		
Rivers	$<$ m	50			250		0	0	0	200	
Woodlands	$<$ m	0	0	0						250	
Wetlands	$<$ m	0	0	0			0				
Elevation	$<$ m							1750	1750		
Conservation											
Habitats	$<$ m	300				0		0	0	0	0
Wilderness	$<$ m	0									
Biospheres	$<$ m	0	0	0		0		0	0		0
Bird Areas	$<$ m	300	200	200		0		0	0		0
Parks	$<$ m	0	200	200	200	1000	0	2000	1000		1000
Reserves	$<$ m	300	200	200	500	200					200
Nat. Monuments	$<$ m	0	500	500				0	0		
Landscapes	$<$ m	0	0	0	200	0	1000	0	0		0
Economic											
Wind speed 50m	$<$ m s^{-1}						4.5			5	
Main Roads	$>$ m									1500	
Secondary Roads	$>$ m									500	
Excluded Area											
Reported	%	96.7	85.9	89.8	65.2	95.1	83.0	89.7	86.1	97.5	66.6
Computed	%	89.1	86.1	91.2	59.6	96.0	76.3	85.9	80.2	96.4	65.0

actually shared the same dataset as well; for example, the CLC [91], as well as the EEA's Nationally Designated Areas (CDDA [392]) and the NATURA2000 [393] were all used. Although the UBA study investigated the entirety of Germany, only the results for central Germany (including North Rhine Westphalia, Rhineland Palatine, Hesse, Thuringia and Saxony), as well as those for south Germany (including Bavaria, Baden Wurttemberg and the Saarland) were evaluated here5.

Sliz [32] investigated onshore wind, open field PV and biomass in central Poland.

Exclusion constraints were highly detailed and included distances from settlement area, industrial zones, leisure areas, existing and planned roads, railways, airports, power lines, gas grid, mines, castles, flood areas, lake, rivers, protected areas and forests. Slope, elevation, and aspect were also considered. Similar to the LANUV study, Sliz's exclusion of proximity to flood areas could not be represented using the Prior datasets. Additionally, some of the criteria definitions differed from our own, including distance from single dwellings as opposed to settlement areas and planned motorways as opposed to existing roadways. Nevertheless, the majority of Silz's criteria definitions employed were close to our own and also employed the CLC6, CDDA and NATURA2000 datasets. Only the LE result for onshore wind in Pomorskie is used for the validation.

The McKenna [29] study also investigated onshore wind LE throughout Germany. Distances from settlements, commercial, mixed-building, federal roadways, railways, airports, protected reserves and protected parks were all excluded. Additionally, industrial areas, habitats, landscapes and biospheres were excluded without any buffer zone. On top of this, locations with a terrain slope greater than 20 degrees were excluded. This study also included the use of CLC and OSM [97] in a similar fashion used here. Besides the criterion defined by distances from mixed building areas, McKenna's criteria definitions matched very well with those employed for the Prior datasets. Unfortunately, McKenna did not report the raw LE result, and instead the available lands are assigned a suitability factor of between 0 and 1 according to their CLC land cover class. The suitability factor-weighted available lands are then summed together to calculate the total available land. This procedure was recreated using the reported weighting structure; however, as McKenna used a previous version of the CLC compared to that used here, small differences are to be expected. Although McKenna investigated the whole of Germany, only North Rhine- Westphalia was evaluated for validation. The Latinopoulos [39] study investigated onshore wind in the Kozani region of northern Greece. Using officially mandated exclusion definitions, Latinopoulos excluded distances from protected landscapes, large, small and traditional settlements, roadways, tourism facilities, industrial areas, airports, and archaeological and historical sites. Mining sites, wetlands and irrigated agricultural lands are also excluded without a buffer distance. Additionally, locations characterized by terrain slopes beyond 25% and an average annual wind speed below 4.5 m/s are also excluded. Many of Latinopoulos' criteria definitions differed from the Prior datasets. For example, the exclusion of distances from large settlements (with populations above 2000 individuals), small settlements (populations below 2000 individuals) and settlements otherwise designated as "traditional" differed significantly from the settlement proximity and settlement urban proximity Priors. In addition to this, Latinopoulos excluded distances from archaeological and historical sites for which there is no representation in the Prior datasets. On the other hand, Latinopoulos also used the CLC and NATURA2000 datasets in the same way that other LE researchers have. Latinopoulos' exclusion based on wind speeds inherently also excluded large lakes as well, as these were not defined in the wind speeds dataset used. Therefore, the lake proximity Prior was utilized in the recreation of this study as well, despite not being explicitly indicated.

Höltinger [67] investigated onshore wind LE in Austria for a trio of exclusion constraint sets representing minimal, median and maximal exclusion scenarios. Two validation efforts are derived from this study, corresponding to the minimal and median sets. As exclusions, Höltinger considered the distances from settlement areas, buildings outside settlement areas, roadways, power lines exceeding 110 kV, railways, built-up areas, forests, airports, lakes and rivers, protected areas and major migration routes. Additionally, a maximal slope ($8.5°$ for the median scenario and $11.3°$ for the minimal) and a maximal elevation defined at the alpine forest line are enforced. Höltinger used many of the same datasets used here, including CLC, OSM, CDDA and NATURA2000, although many of the criteria definitions used here differ significantly from the Priors, alongside the use of several Austria-specific datasets. Most notably, Höltinger's exclusion of animal migration routes and buildings outside settlement areas are completely unrepresented in the Prior datasets. Additionally, Höltinger employed many of the conservation-relevant exclusions on a case-by-case basis, while the Prior datasets cannot distinguish between individual designations. For this validation, only the eastern region of Burgenland is recreated.

Samsatli [31] investigated onshore wind LE in the United Kingdom. Ten exclusion constraints were considered in total, including distances from developed land, roadways, airports, rivers, woodlands, protected areas and power lines. Sites of special scientific interest were also excluded, along with slopes exceeding 15% and average annual wind speeds below 5 m/s at 45m. Samsatli included constraints based off grid connection and accessibility distance, which were expressed as a minimal distance from major roadways (for grid connection) and major and secondary roadways (for accessibility), which explains the use of the roadway Priors in the economic group of Table A.5. Along with these, Samsatli also excluded all locations within five times the rotor diameter of existing turbines. The definition of distances from developed land differed from the settlement proximity Prior's definition, and there was no Prior created to represent distances from preexisting turbines. Furthermore, when considering protected areas, Samsatli only excluded designations of "Sites of Special Scientific Interest" (SSSI), and while these sites are included in the WDPA dataset and therefore also in the various conservation group Priors, they are not specifically selected by any of the conservation group criteria definitions. The protected habitat proximity was found to best match with the SSSIs, however, which is why it was used for validation over the other options. Instead of evaluating the entirety of the UK, only the southwestern portion of England8 was used for validation.

As the final validation study, Robinius [47] also investigate land eligibility for wind turbines in Germany. As the investigator of this study is also an author of this work, this study offered a unique opportunity to compare the operation of the described framework to a conventionally-evaluated LE study where the exact datasets and procedures are known. In this study buffered regions around settlement areas, all airports, roads, railways, industrial areas, and protected parks are all excluded. Furthermore, protected bird zones, landscapes, biospheres, and habitats are excluded without any buffering. Robinius' choice of protected areas differs from the

way they are used in the Prior datasets, nevertheless the CDDA and NATURA2000 datasets are used so the differences are expected to be minimal. Robinius also made use of the CLC and OSM datasets, however in both cases a previous version is used compared to those used to produce the Priors. Once again, instead of recreating the entire study area only the south-west portion of Germany9 is chosen for validation.

A.6.2 Validation Results

Replication results were the least successful with the LANUV report, where a 7.6% difference was observed from the reported left over area. As described above, there were several discrepancies between the datasets and criteria used for the Prior datasets versus those that were employed by LANUV. Most notable, however, was the outcome after applying the constraints related to settlements. After subtracting areas within 600 m of general settlements and within 450 m of rural-use buildings, LANUV reports that 22% of the state's area remains. Comparing this to a value computed by the described framework, after applying a 600 m buffer to the settlement proximity Prior (which also excludes rural settlements), 55% of the state's areas remains. This indicates that the dataset used for the LANUV study differs extensively from the urban area designations in the CLC dataset. Despite the claim that their 17 sources are openly available, they were only found to be obtainable in a form of a web-gui, which could not be extracted and used within our framework. This outcome does not serve to validate or invalidate either implementation, but rather serves as a reinforcement of the point that the use of open and consistent data sources is necessary for broad context LE analyses, as well as for those analyses that depend on them.

Following the LANUV study, the Latinopoulos replication showed the second to worst result, with a 6.7% deviation in the total remaining land. Just as with the LANUV report, several differences from the Prior datasets existed. In this case, key considerations (archaeological and historical sites) could not be included in the replication, and as such it follows that less land would be excluded. In spite of this, it seems that the most likely reason for the discrepancy observed is Latinopoulos' wind speed constraint. Using the same wind speed dataset used by Latinopoulos, it was found that excluding all locations with an average wind speed below 4.5 m/s resulted in only 9% remaining area before considering any other constraints as well. Clearly, this result does not concur with Latinopoulos' reported result and therefore another operation that was not detailed in the publication must have been performed on the wind speeds prior to exclusion, otherwise Latinopoulos must have used a previous version of this dataset. In any case, without further information regarding Latinopoulos' procedure, this discrepancy could not be investigated further.

After these, the Höltinger replications resulted in a 3.8% deviation for the median scenario and a 5.9% deviation for the minimal scenario. Once again, some criteria are missing (animal migration routes) and differing criterion definitions (single dwelling) are present in these recreations. In this case, it was not possible to identify a single dataset as the main cause of the observed discrepancies. Despite these

differences, however, consistency between Höltinger's study and the recreation can be confirmed via visual comparison of the two results. For this purpose, the results of the Höltinger replication are shown in Figure A.2. A comparison between the two replicated scenarios illuminates their difference, where a significantly smaller deviation from the reported value is found for the median scenario compared to the minimal. One way to interpret this result would be that as other exclusion constraints become more confining (for example, the increased exclusion range around settlements), the areas that would have been excluded by the missing constraints are excluded anyway, because they have a higher likelihood of overlapping with the constraints that are included. This dynamic of overlapping constraints presents an interesting investigation point that will be explored in the following section.

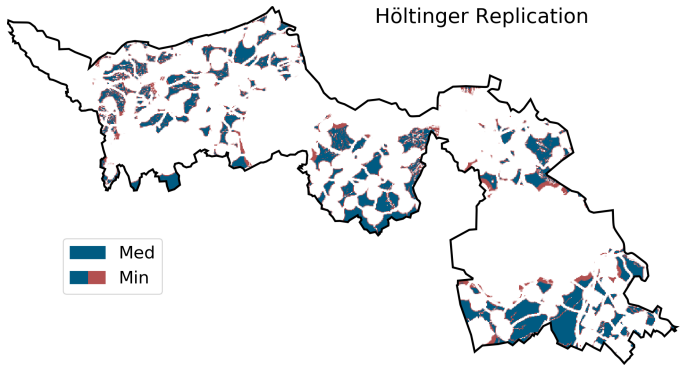

Figure A.2: Example LE replication of Höltinger et al. [67] in Burgenland, Austria

The Silz replication showed a 5.6% deviation for reasons similar to those discussed above. The replication did not include the original exclusion of flood plains, and two criteria definitions differed significantly. However, the resulting discrepancy was less than that of the previous three studies, and so is not discussed in further detail. The four remaining studies, UBA, Samsatli, McKenna and Robinius were found to match very well with -0.2% and -1.4%, 1.1%, 0.9%, and 1.6% deviations respectively. These studies also showed interesting discrepancies, although these were clearly found to have insignificant impacts on the final results. The Samsatli study, for instance, did not include the original exclusion of distances from preexisting wind turbines. Similarly, the UBA study proximity exclusion from single dwellings did not precisely match the settlement proximity Prior used in the replication. Nevertheless, these studies showed general agreement in the datasets used compared to the Prior datasets and their criteria definitions were more often than not a match to our own. Therefore, the significant agreement of these studies with the reported results suggests that the described framework is indeed operating as expected and, furthermore, that the Prior datasets are sufficient for conducting generic LE analyses. Furthermore, these results suggest that if complete knowledge was held concerning the datasets and practices used by investigators of the previously discussed studies, these results could also be replicated with improved accuracy. Taking into consideration that the replication studies with the largest deviations (LANUV and

Latinopoulos) were associated with irreconcilable issues with a particular dataset, that the other replications with relatively large deviations seemed to be missing significant criteria and because the studies that were not subject to these issues (at least not where key criteria were concerned) showed very strong agreement, it can be finally concluded that the described framework is validated and reliable.

Chapter B

Prior Datasets Visualized

The following plots visualize each of the Prior Datasets which were developed in line with this work. For more information on their creation and role in this thesis, see Section 2.3. Note that these plots are visualized at resolution of 2 km, however the datasets themselves have a resolution of 100 m; and so the shown values are averaged over. In some cases, such as in the North Facing Slope Threshold example, this averaging will hide many of nuances available in these datasets. Nevertheless, the general trends and regions of influence for all Prior datasets can be seen.

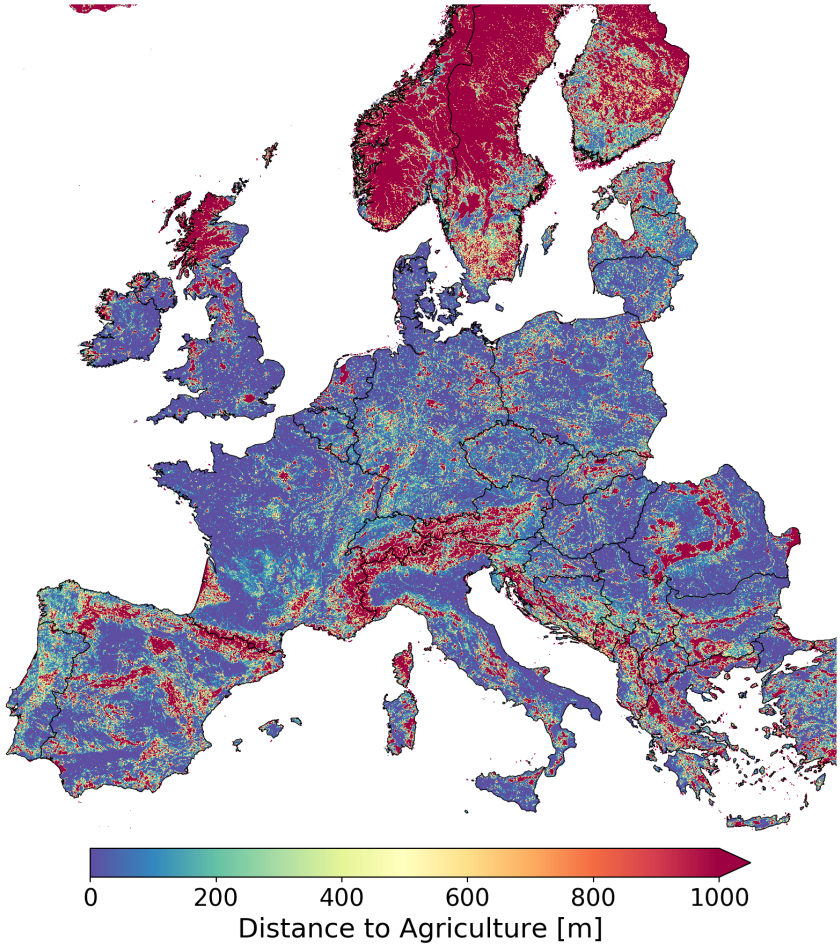

Figure B.1: Prior: Agricultural Proximity. Derived from [91]

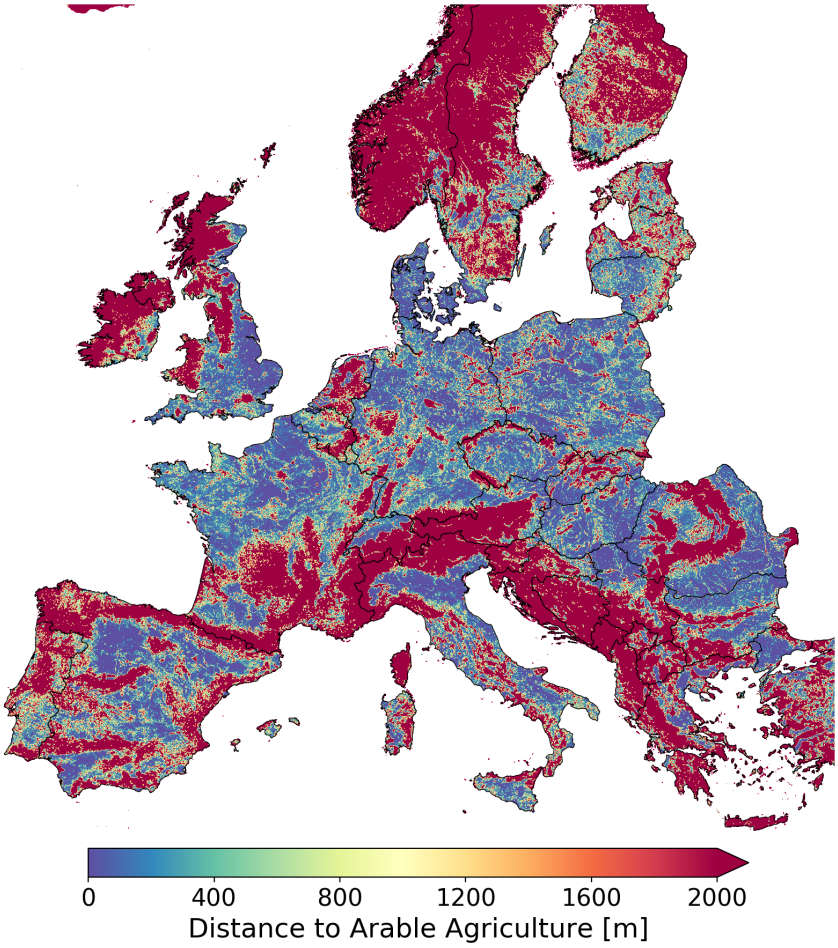

Figure B.2: Prior: Agriculture Arable Proximity. Derived from [91]

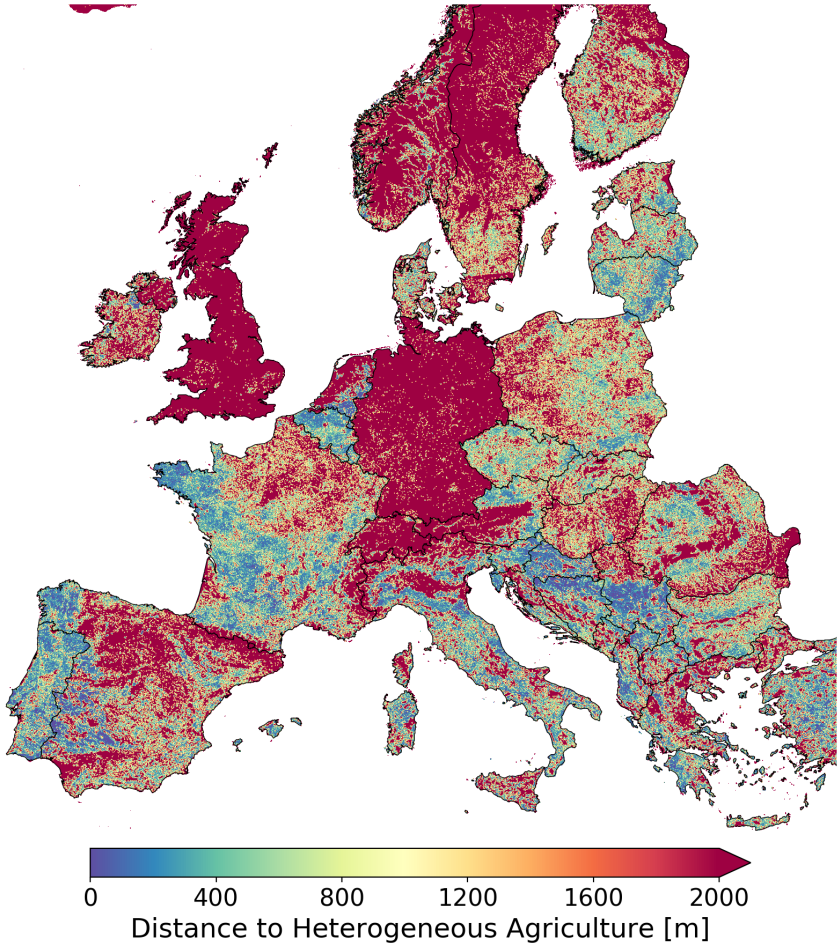

Figure B.3: Prior: Agriculture Heterogeneous Proximity. Derived from [91]

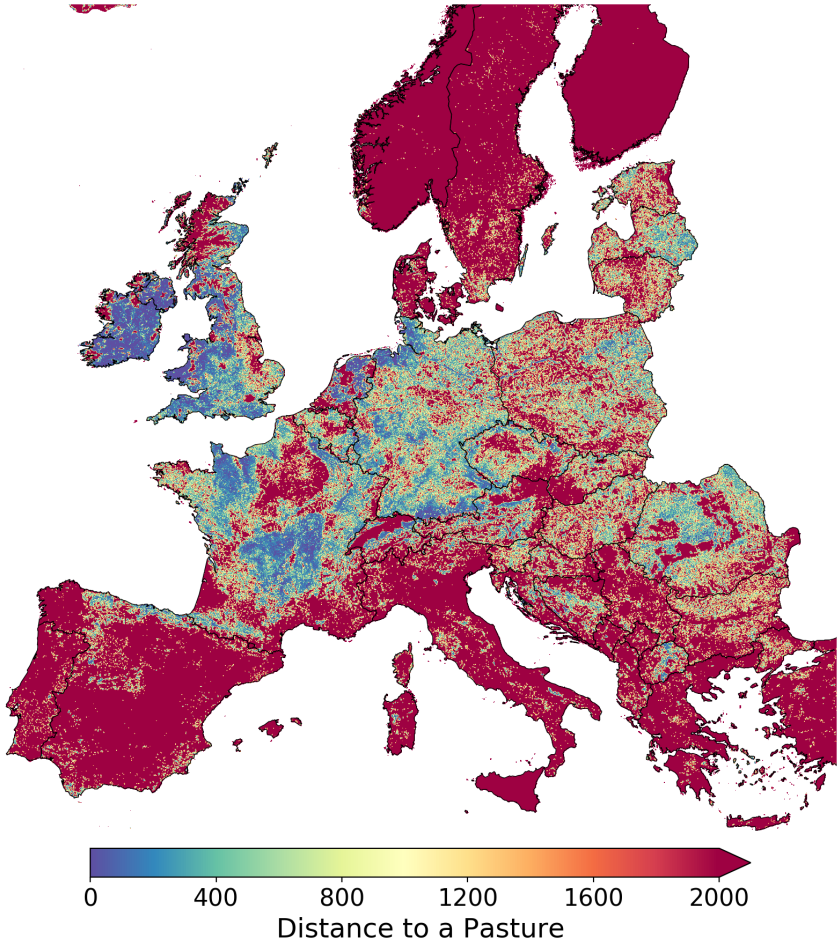

Figure B.4: Prior: Agriculture Pasture Proximity. Derived from [91]

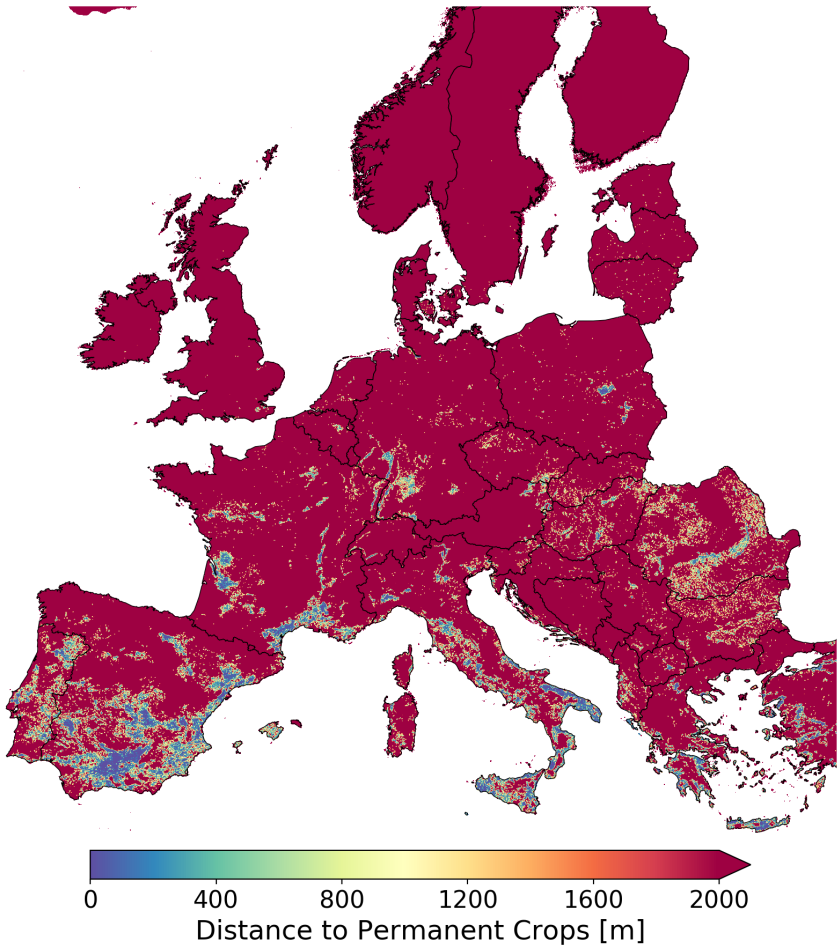

Figure B.5: Prior: Agriculture Permanent Crop Proximity. Derived from [91]

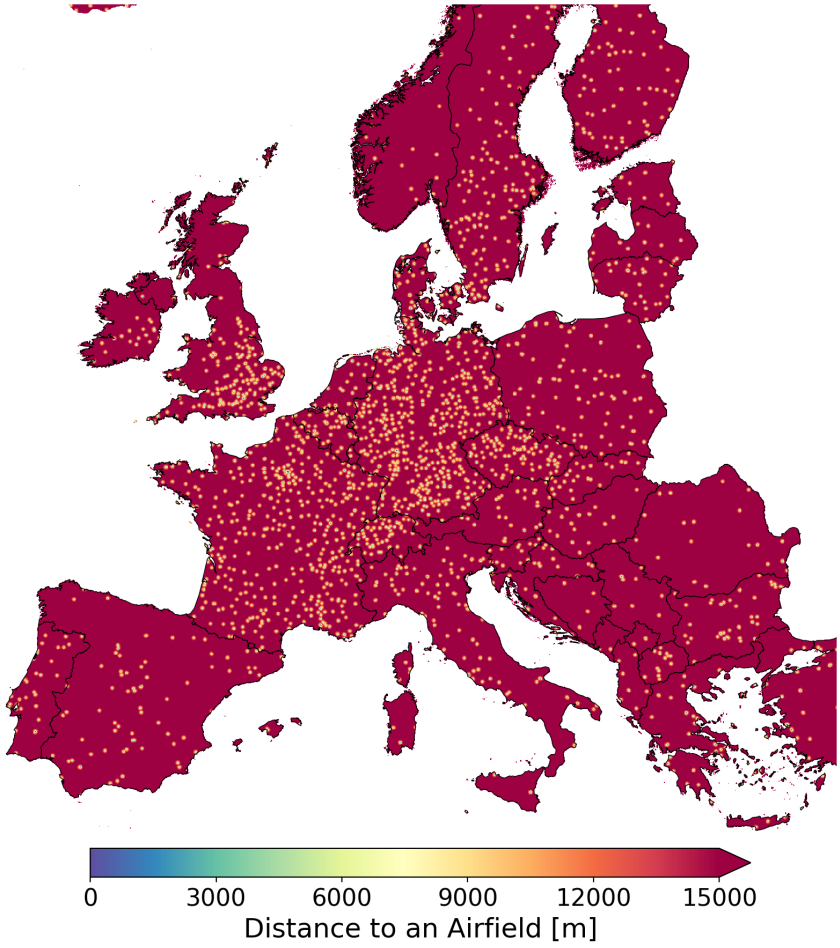

Figure B.6: Prior: Airfield Proximity. Derived from [91, 93]

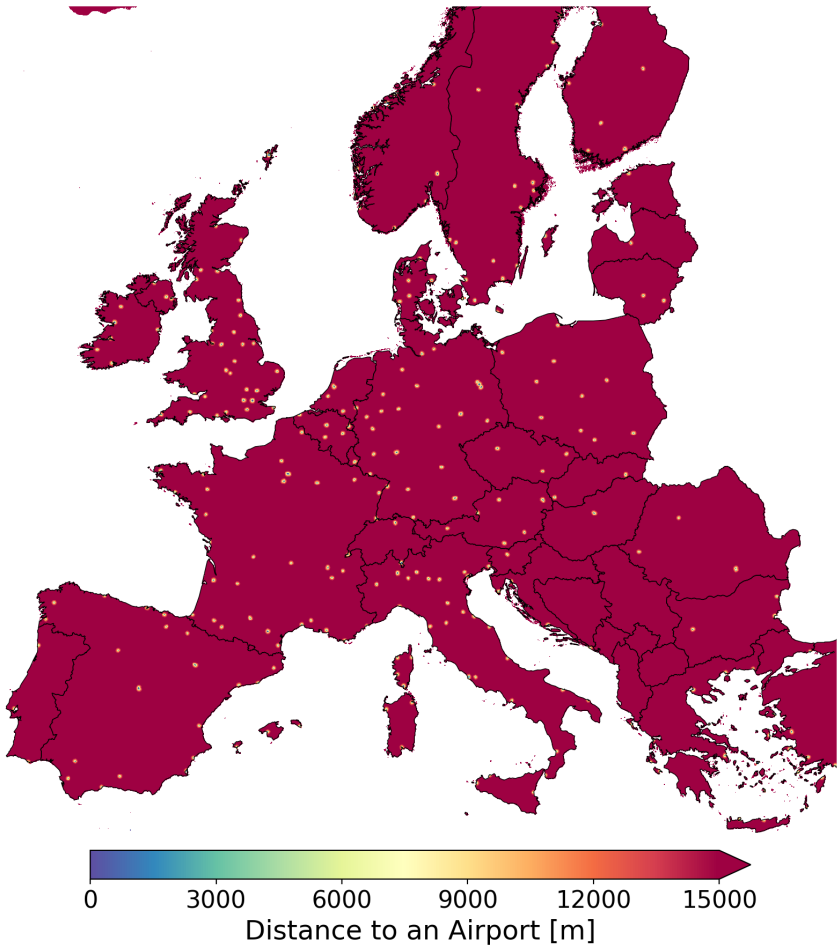

Figure B.7: Prior: Airport Proximity. Derived from [91, 93]

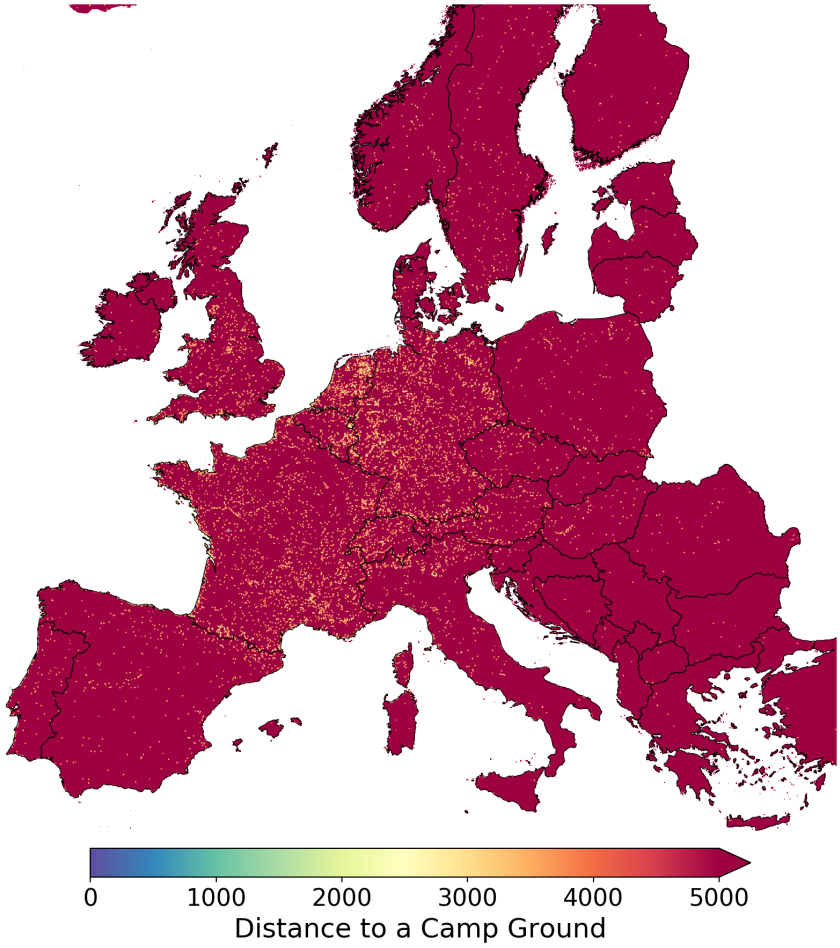

Figure B.8: Prior: Camping Proximity. Derived from [97]

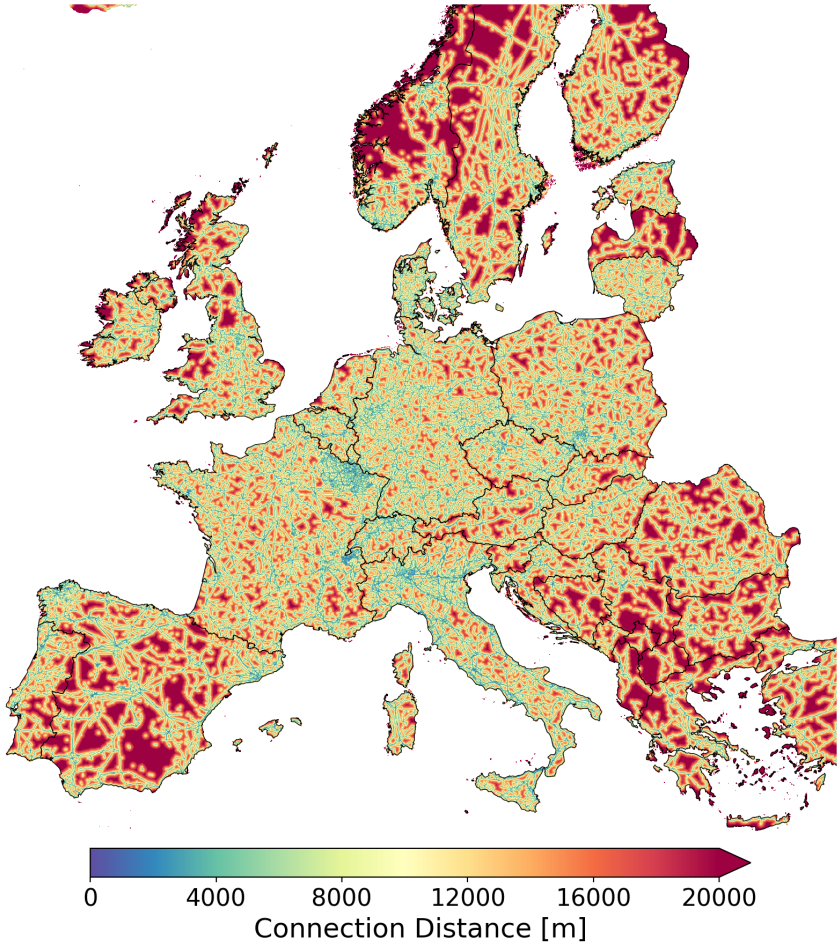

Figure B.9: Prior: Connection Distance. Derived from [97]

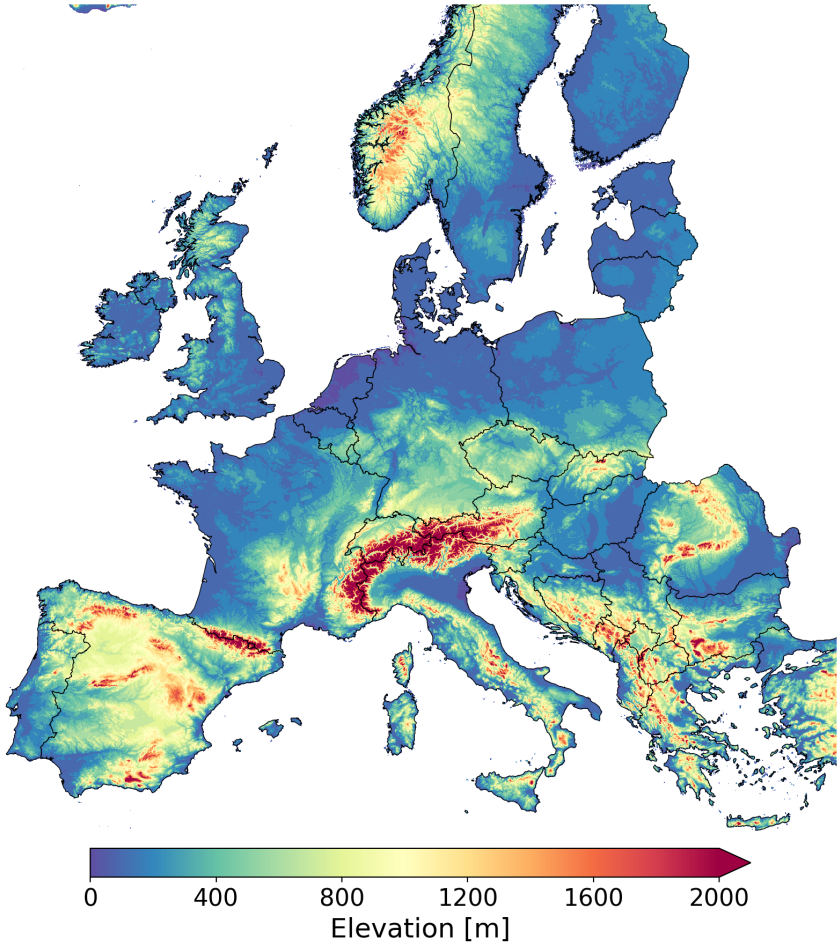

Figure B.10: Prior: Elevation Threshold. Derived from [94]

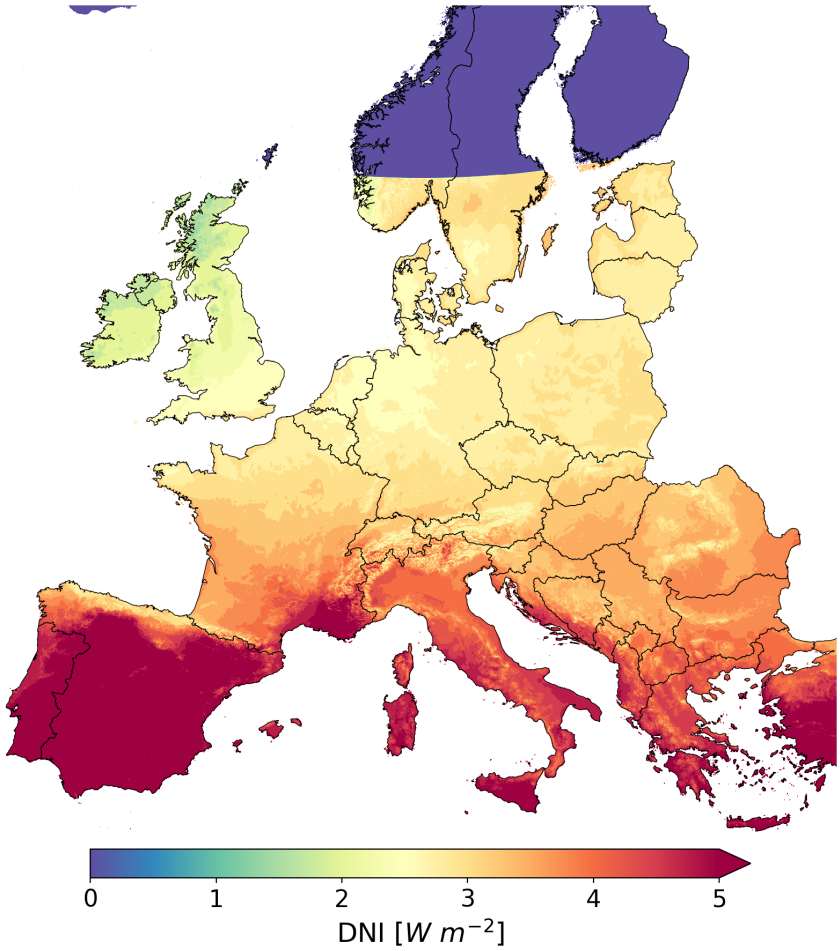

Figure B.11: Prior: Direct Normal Irradiance (DNI) Threshold. Derived from [206]

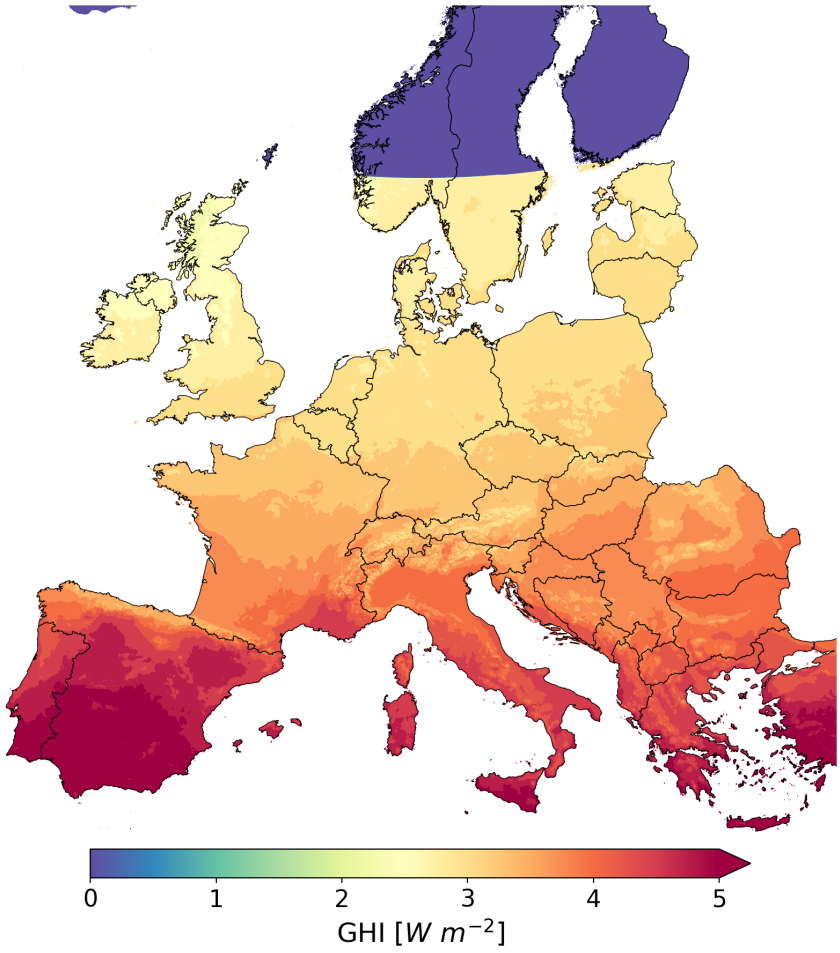

Figure B.12: Prior: Global Horizontal Irradiance (GHI) Threshold. Derived from [206]

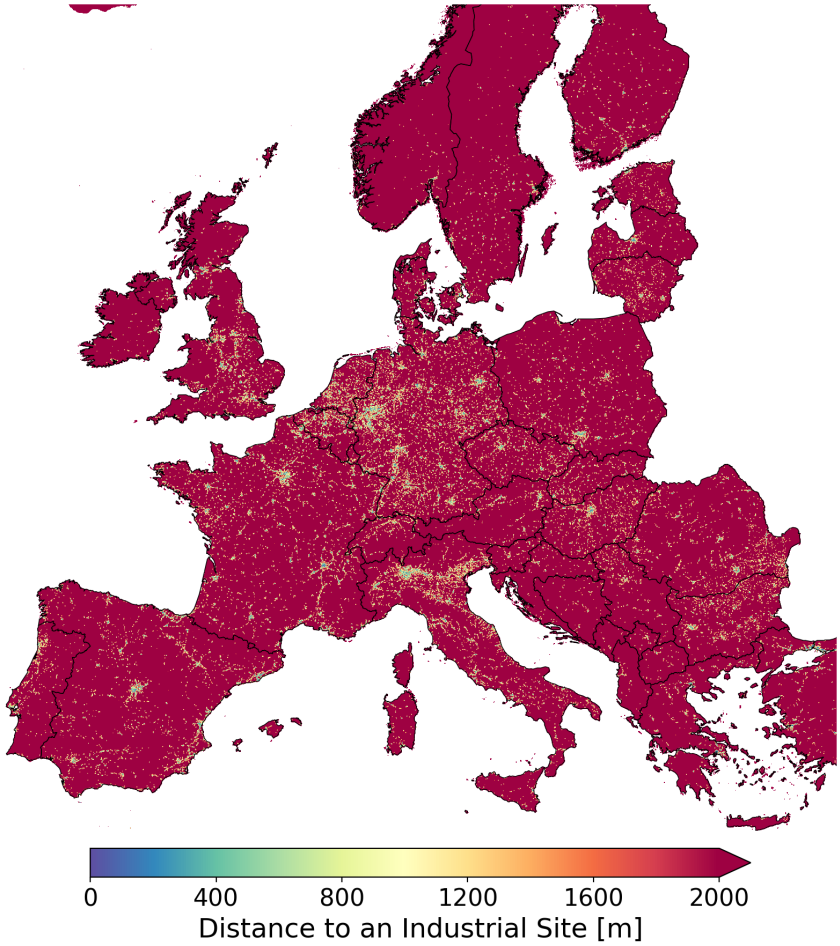

Figure B.13: Prior: Industrial Proximity. Derived from [91]

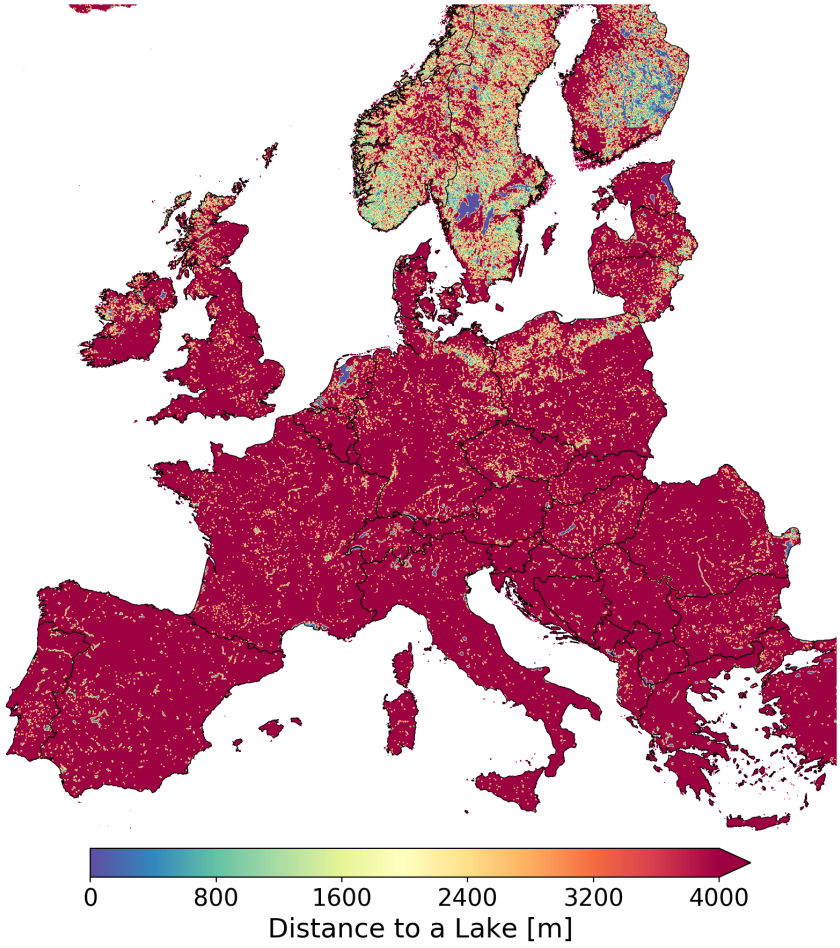

Figure B.14: Prior: Lake Proximity. Derived from [96]

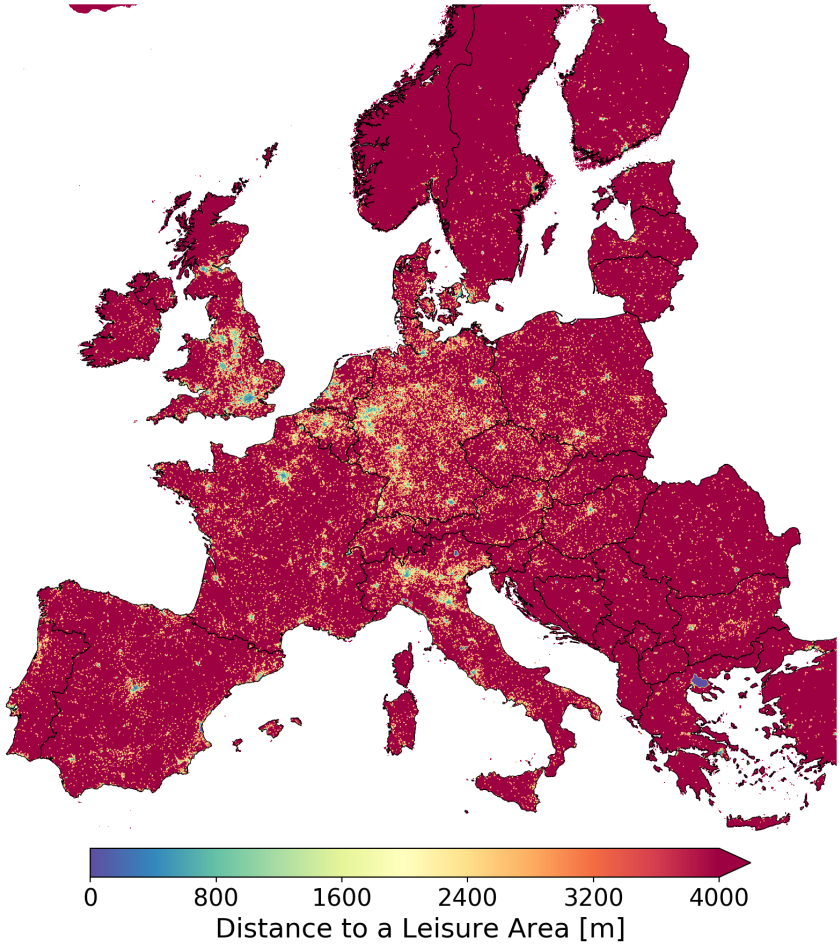

Figure B.15: Prior: Leisure Proximity. Derived from [97]

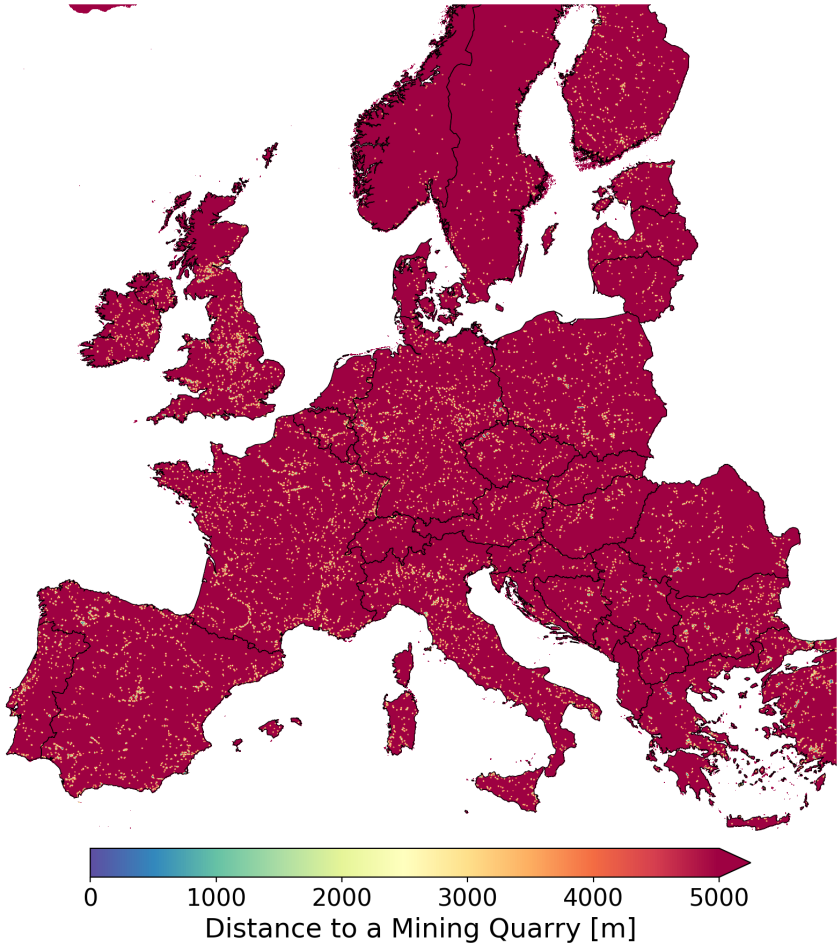

Figure B.16: Prior: Mining Proximity. Derived from [91]

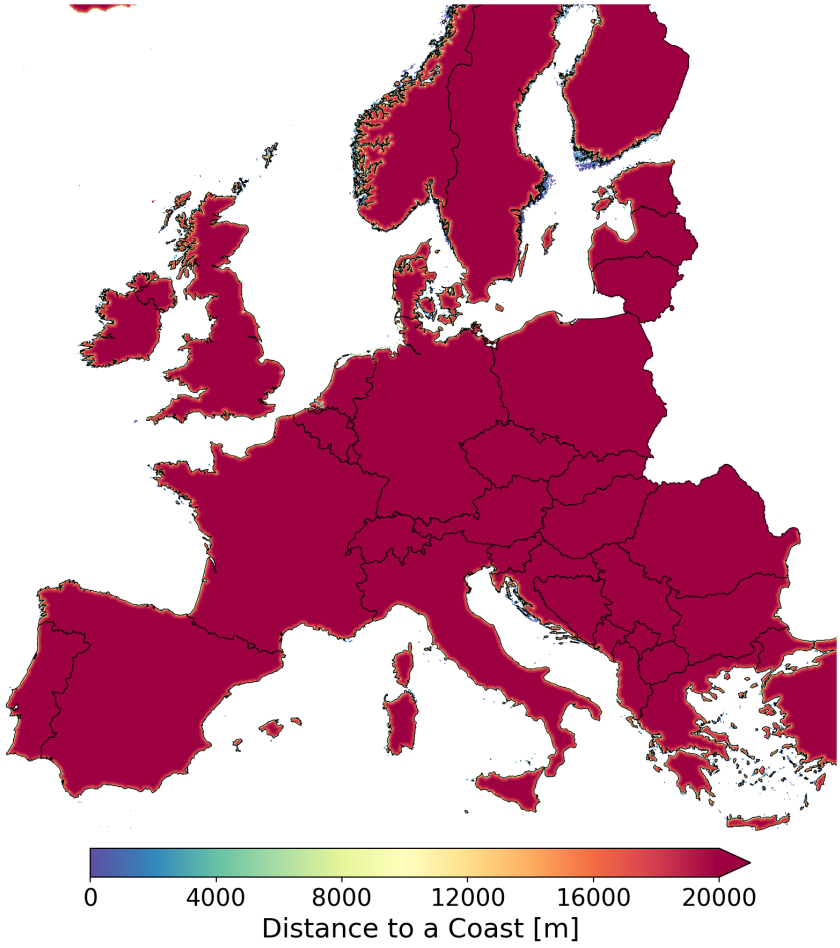

Figure B.17: Prior: Coasts Proximity. Derived from [91]

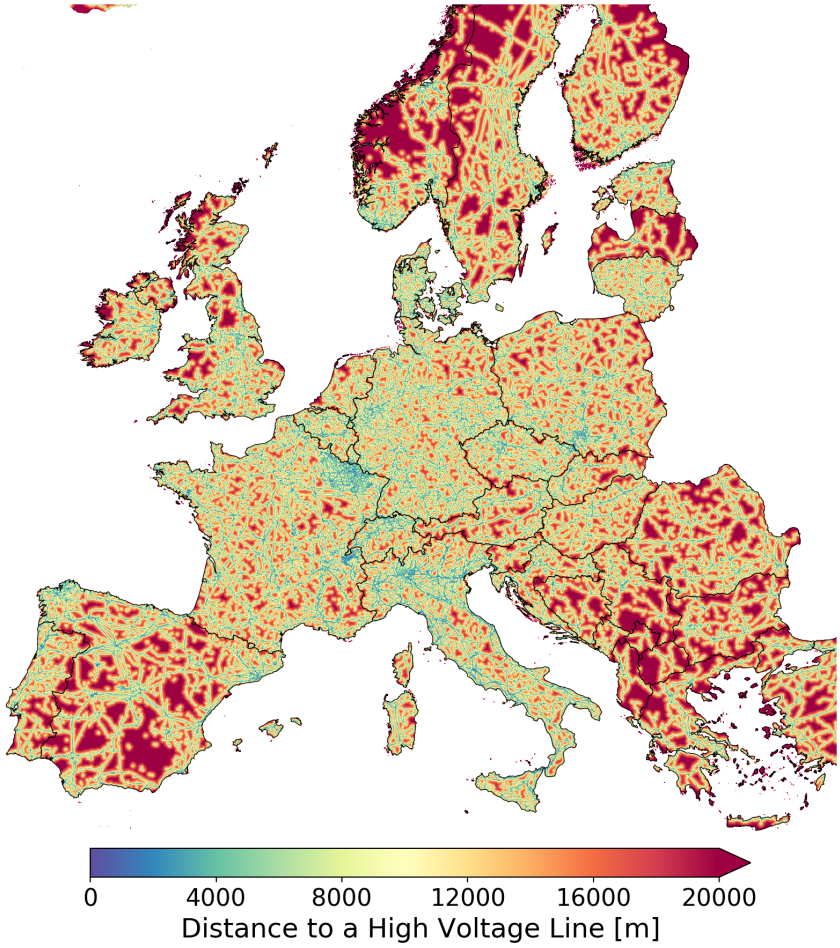

Figure B.18: Prior: Power Line Proximity. Derived from [97]

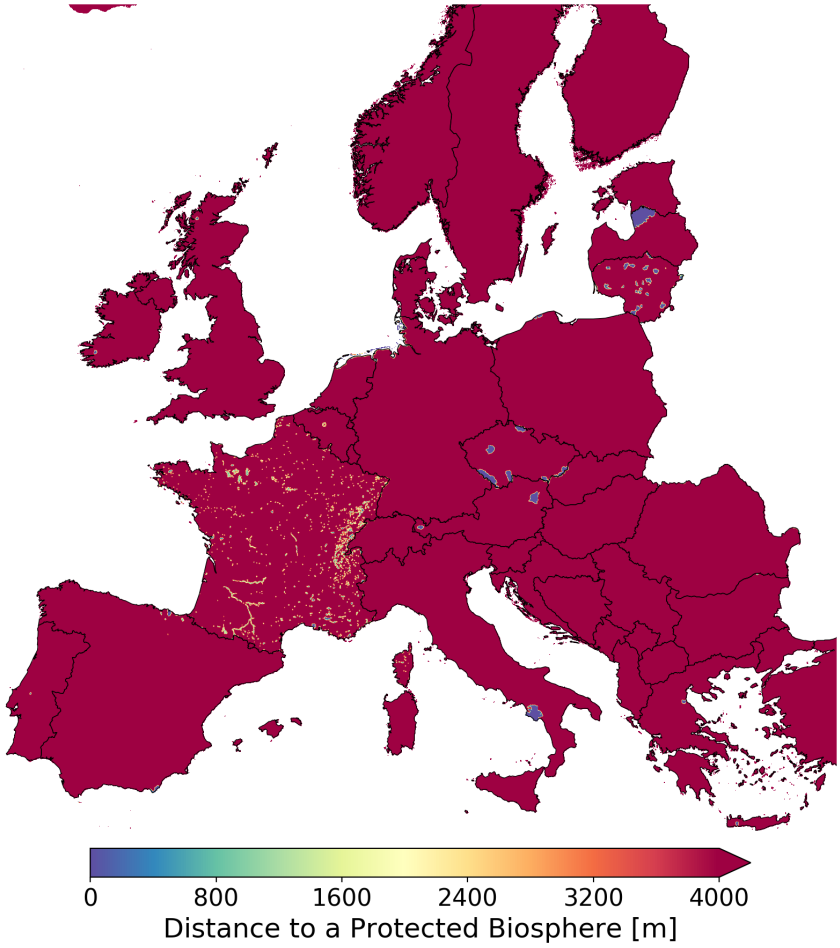

Figure B.19: Prior: Protected Biosphere Proximity. Derived from [98]

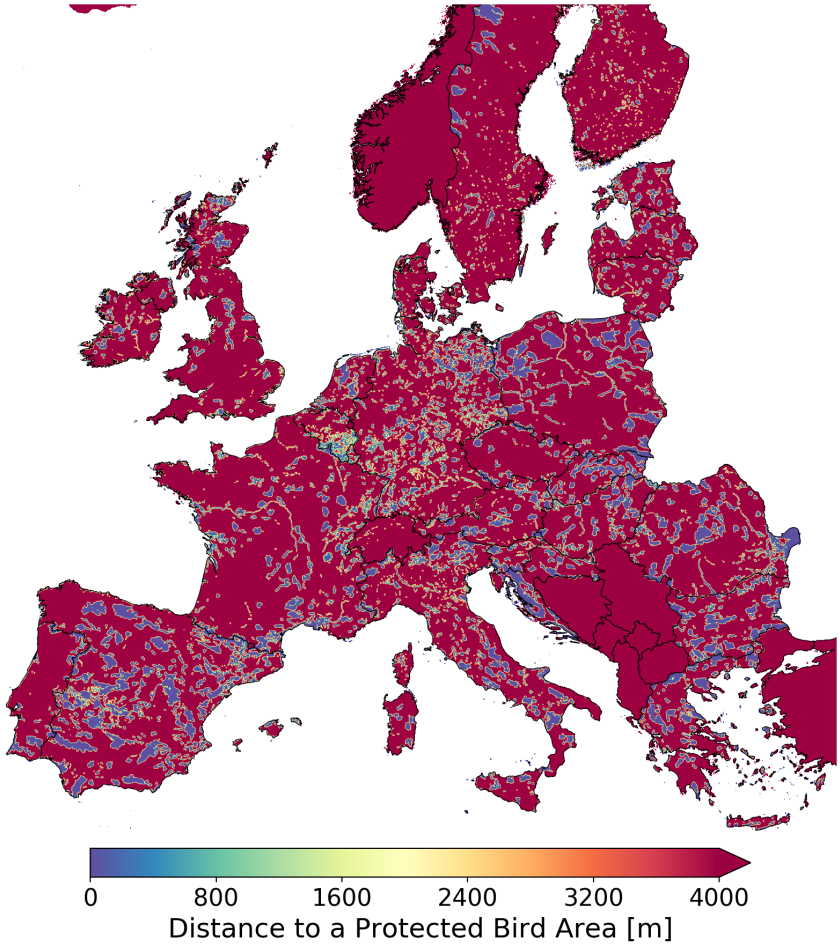

Figure B.20: Prior: Protected Bird Proximity. Derived from [98]

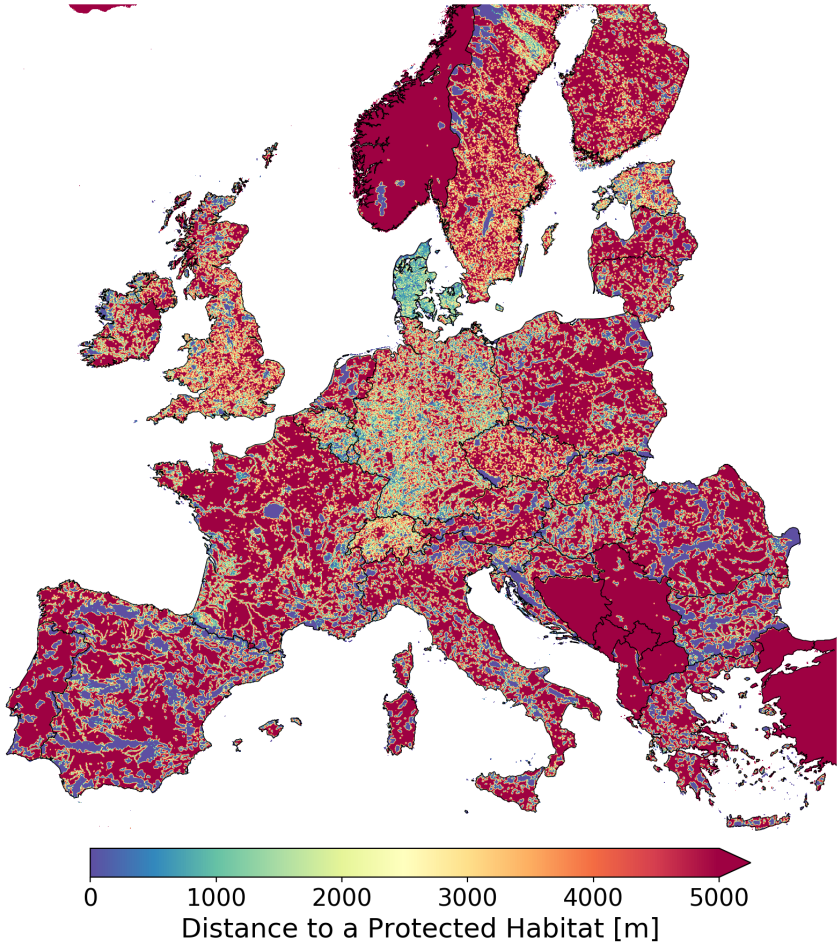

Figure B.21: Prior: Protected Habitat Proximity. Derived from [98]

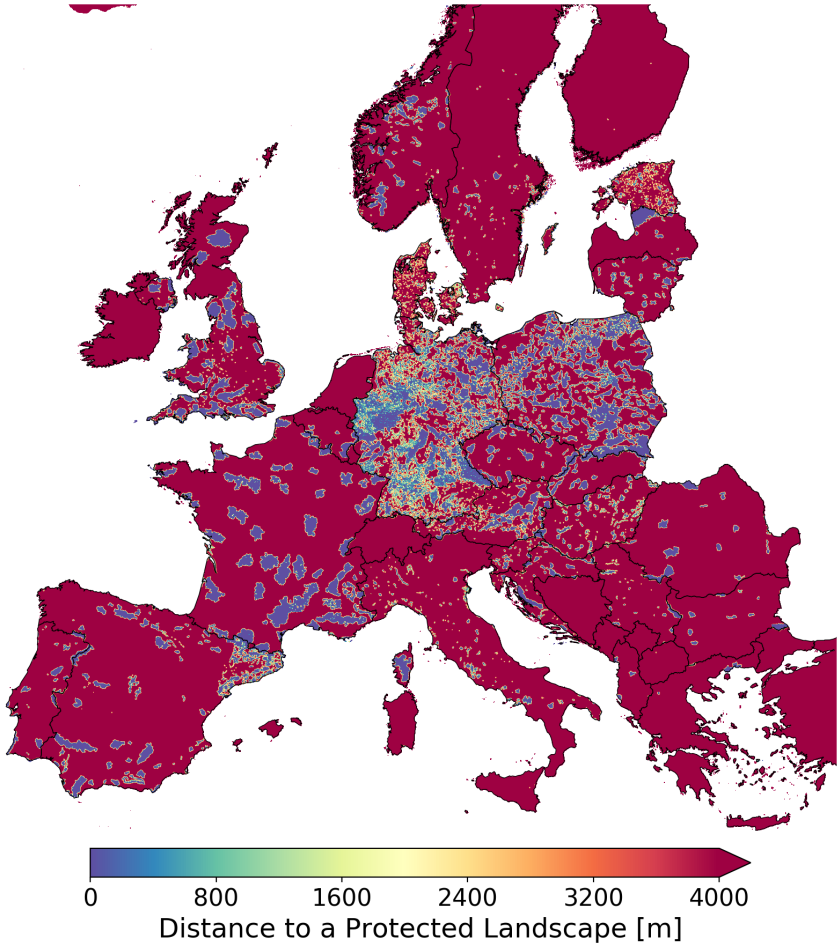

Figure B.22: Prior: Protected Landscape Proximity. Derived from [98]

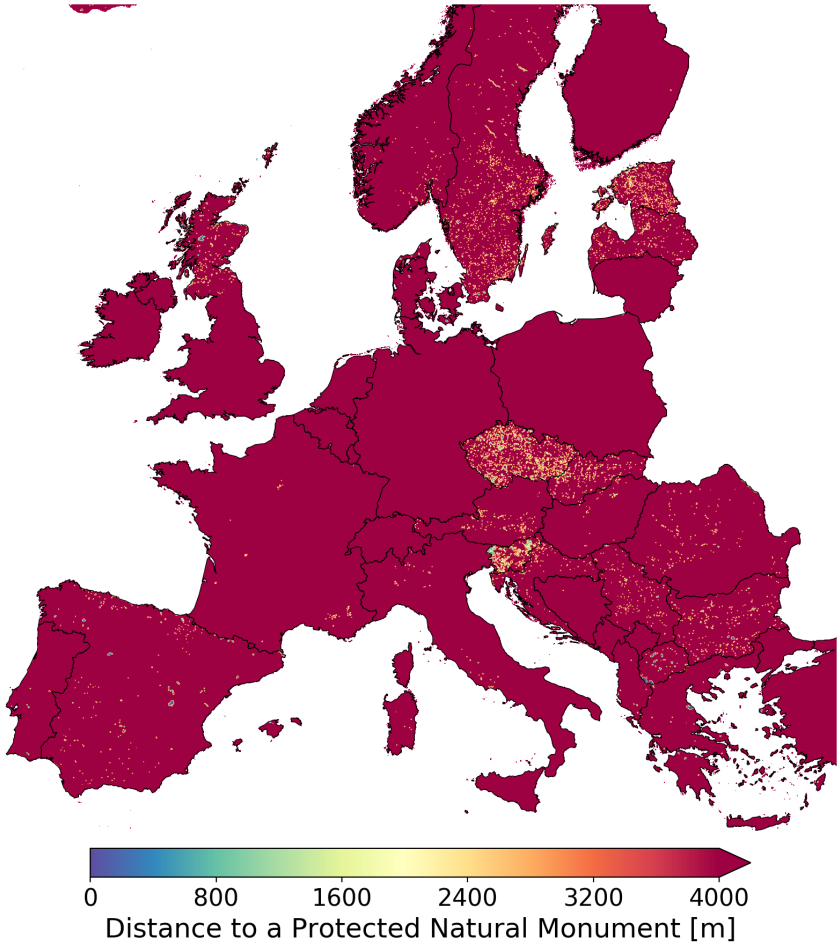

Figure B.23: Prior: Protected Natural Monument Proximity. Derived from [98]

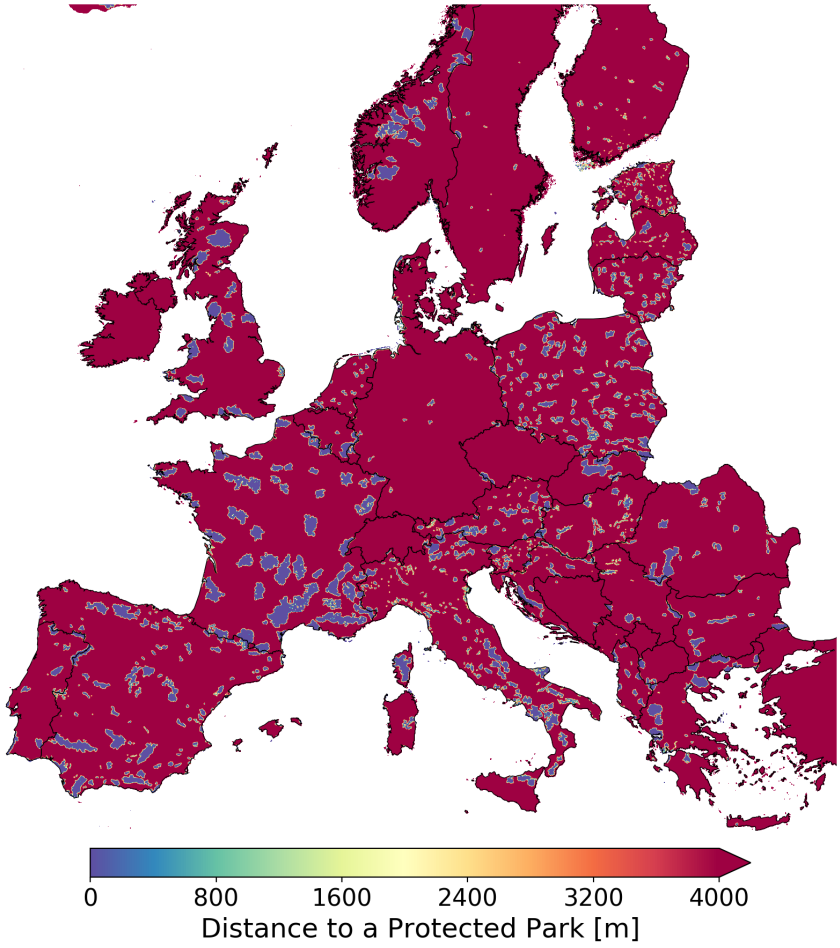

Figure B.24: Prior: Protected Park Proximity. Derived from [98]

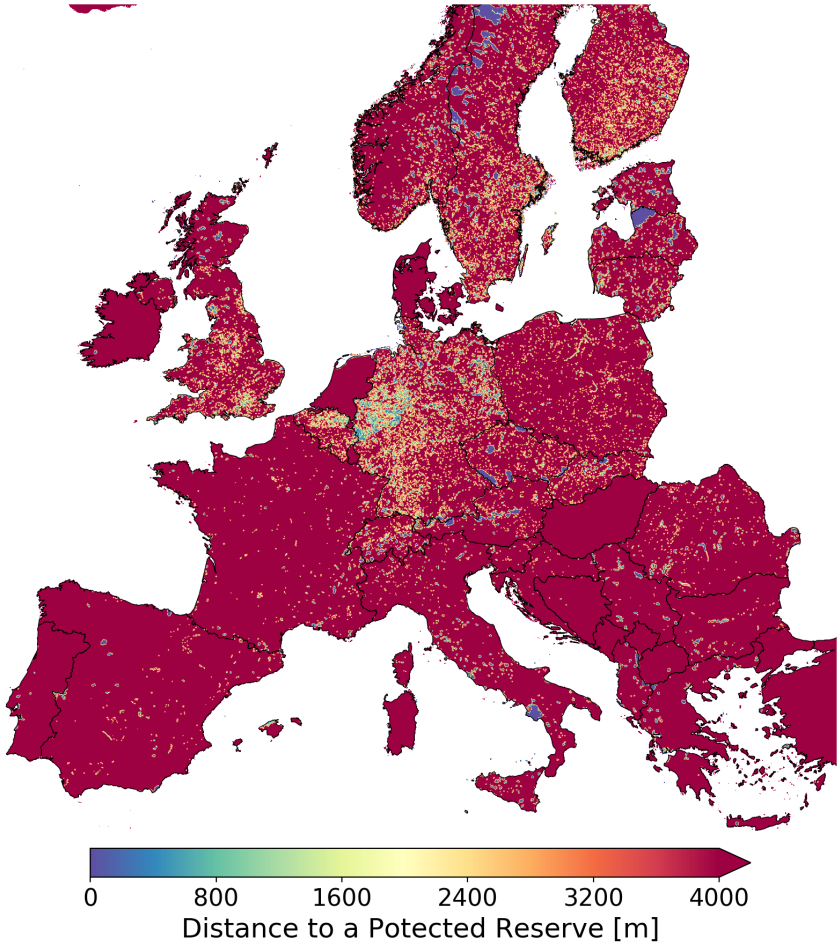

Figure B.25: Prior: Protected Reserve Proximity. Derived from [98]

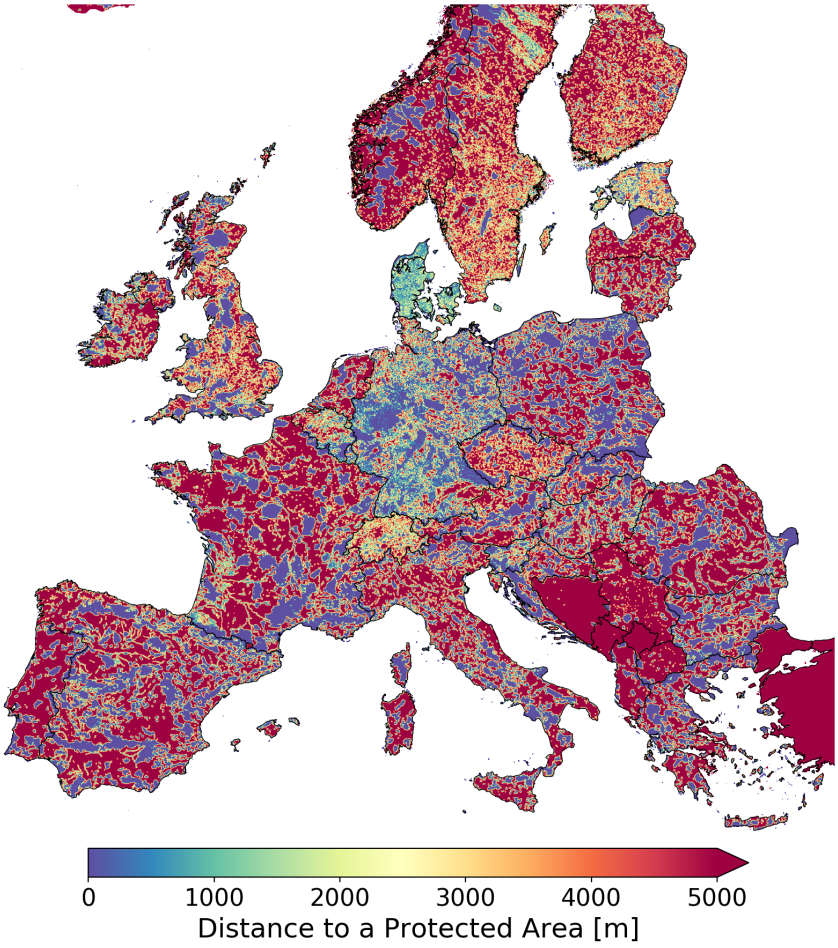

Figure B.26: Prior: Proximity to any protected area. Derived from [98]

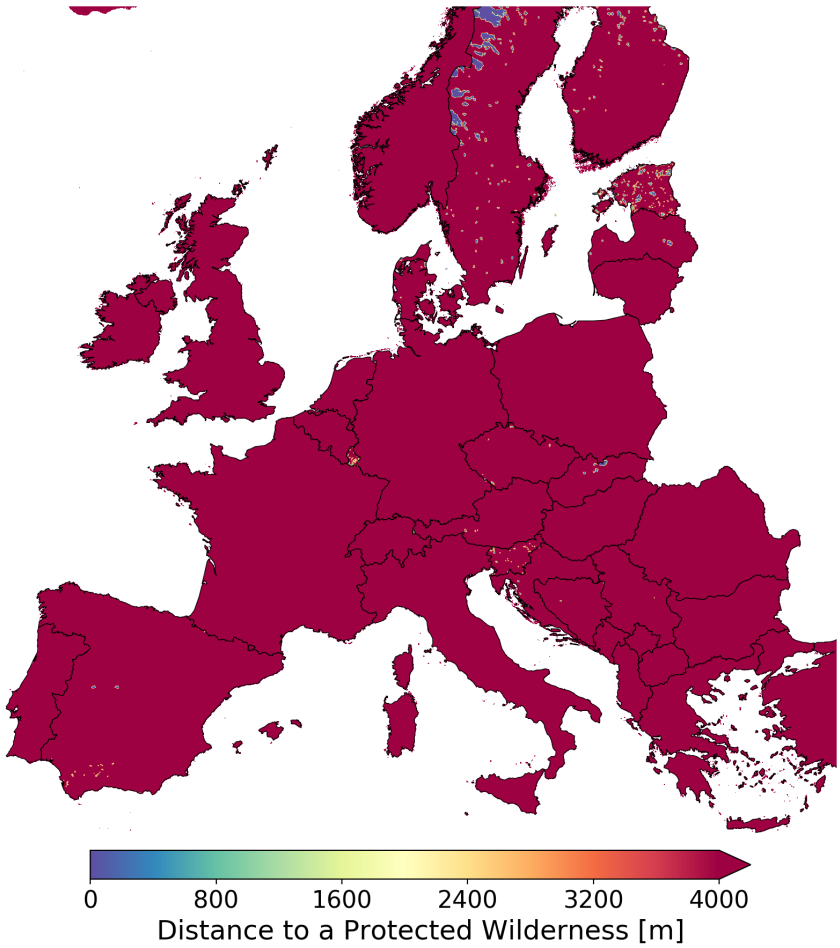

Figure B.27: Prior: Protected Wilderness Proximity. Derived from [98]

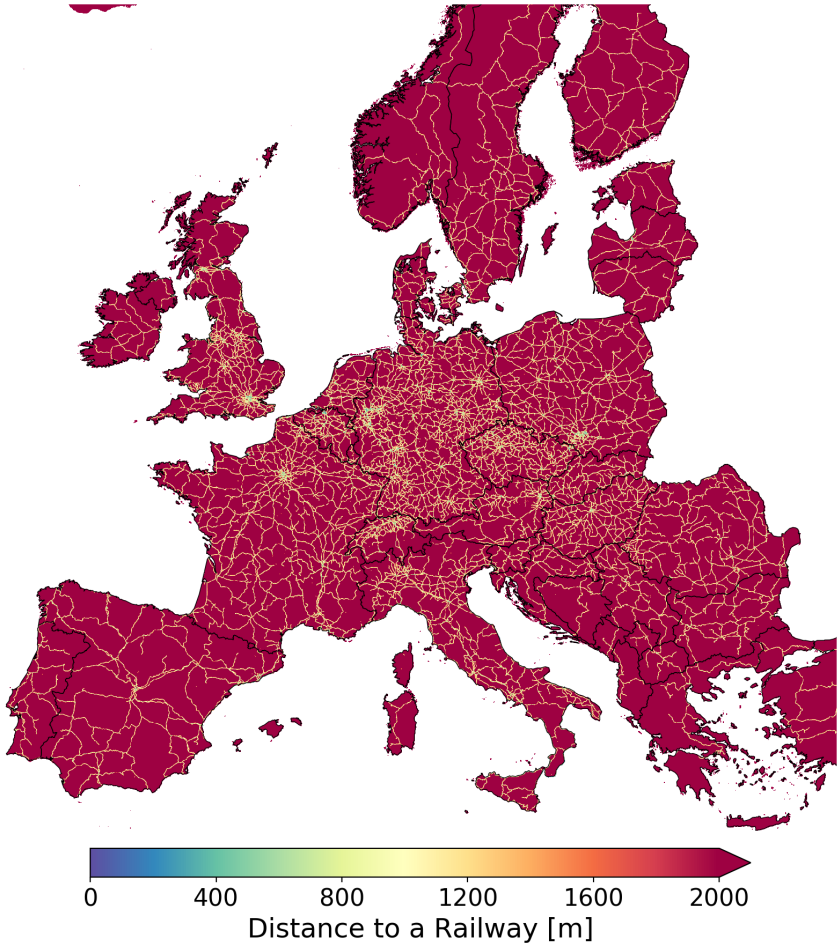

Figure B.28: Prior: Railway Proximity. Derived from [97]

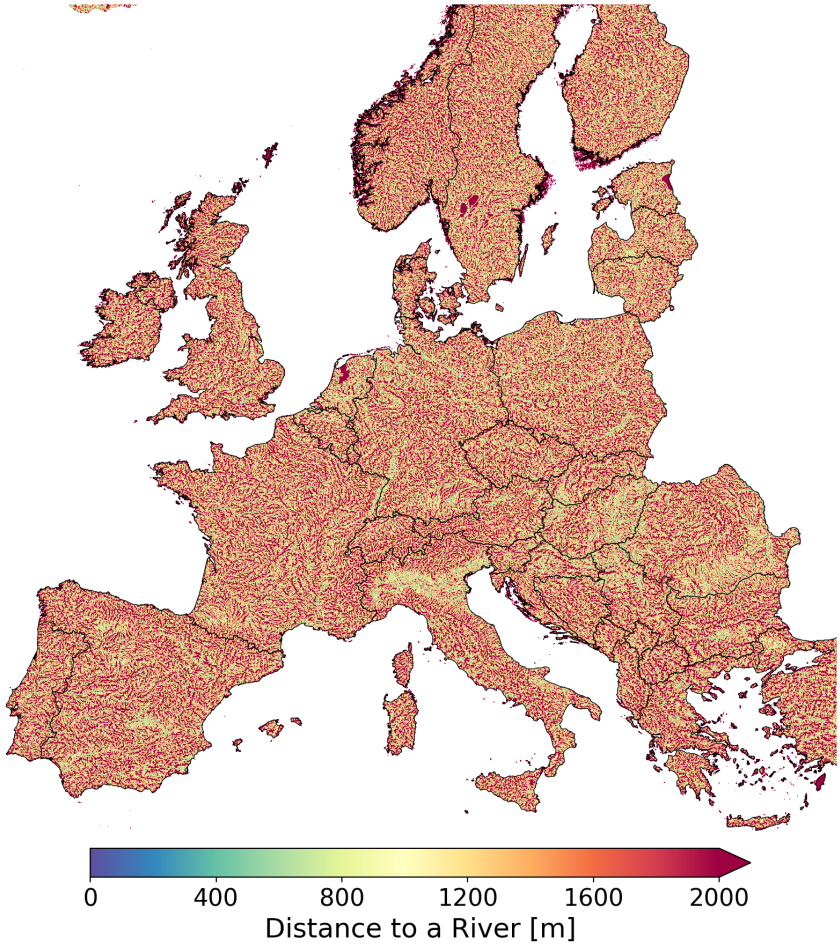

Figure B.29: Prior: River Proximity. Derived from [95]

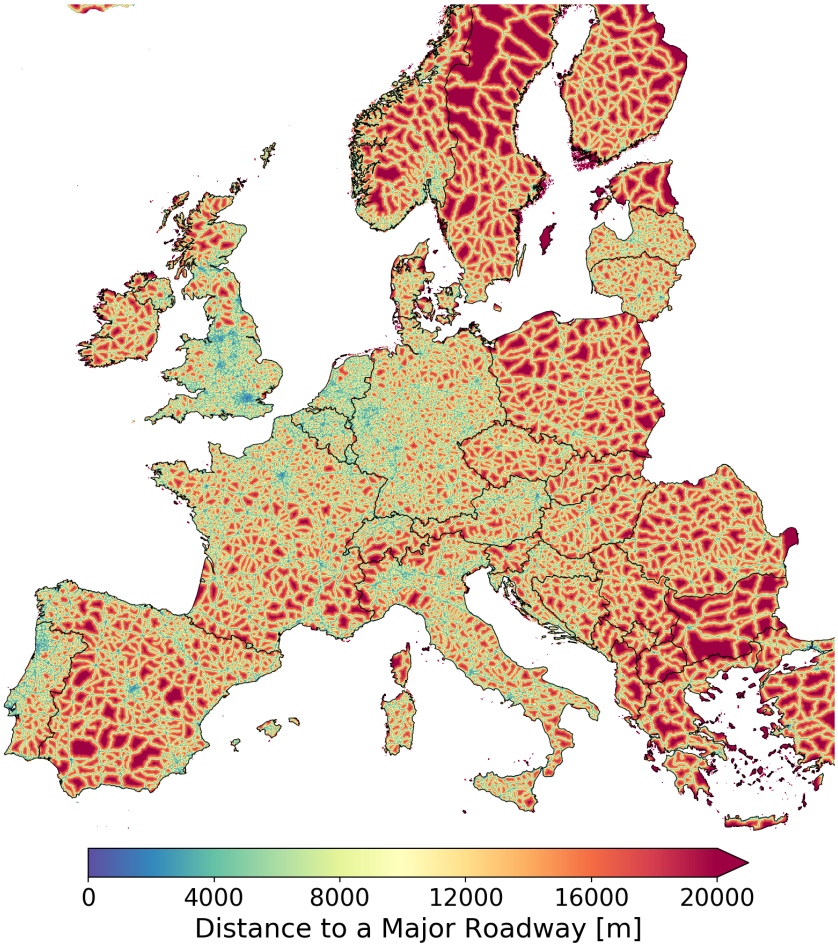

Figure B.30: Prior: Roads Main Proximity. Derived from [97]

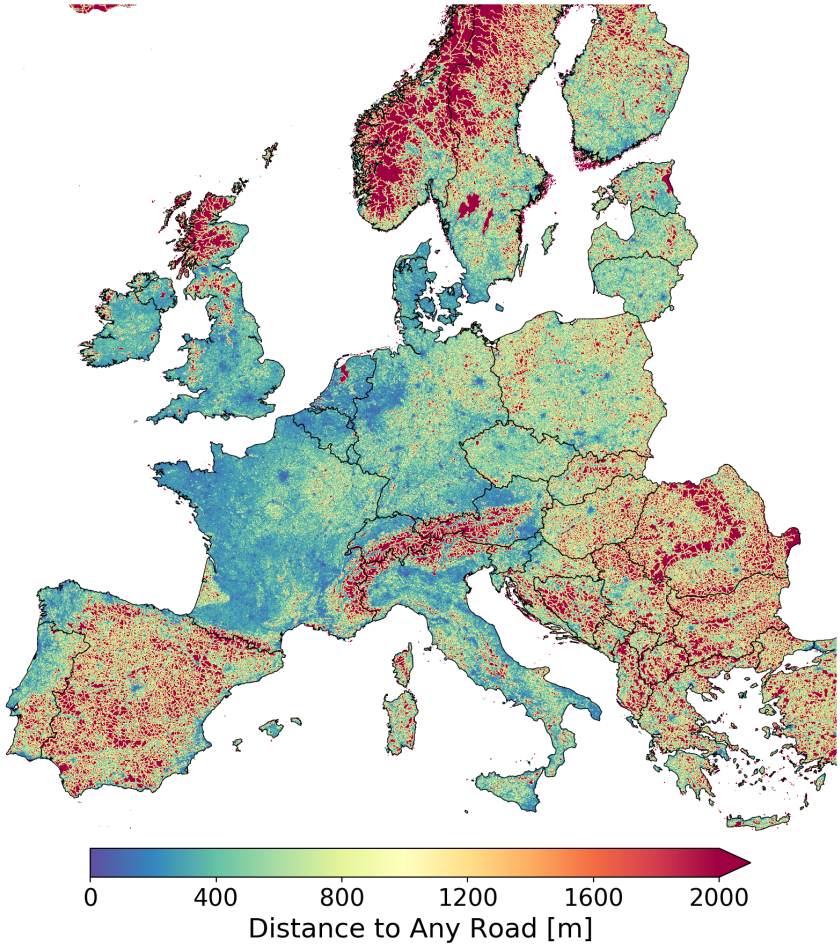

Figure B.31: Prior: Roads Proximity. Derived from [97]

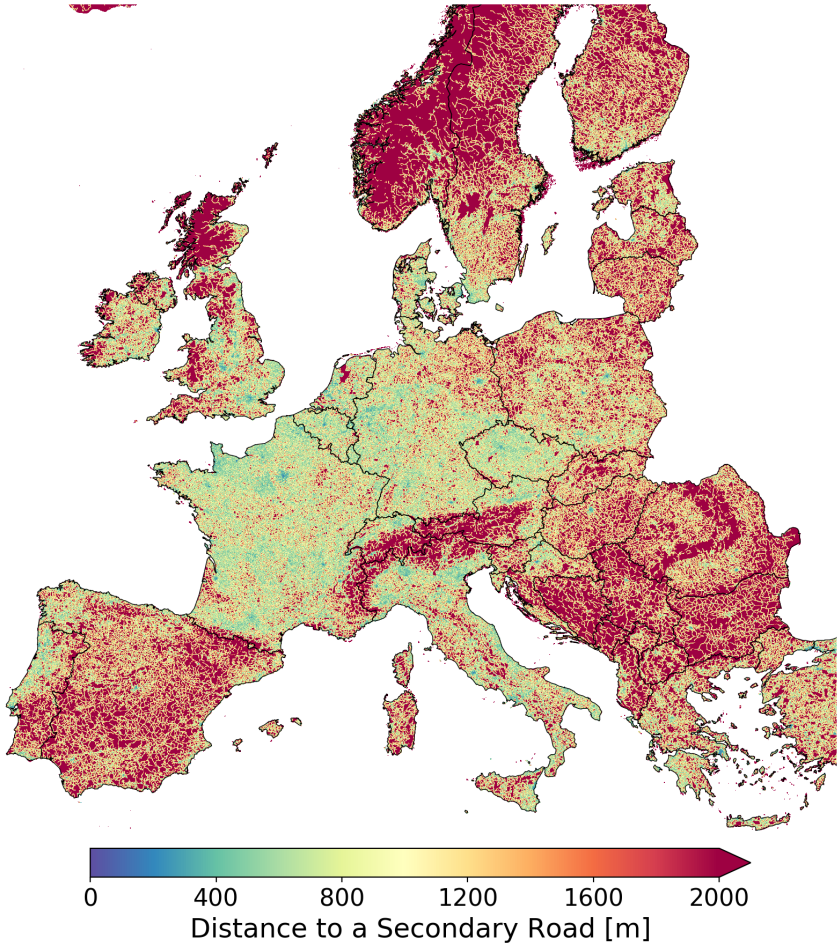

Figure B.32: Prior: Roads Secondary Proximity. Derived from [97]

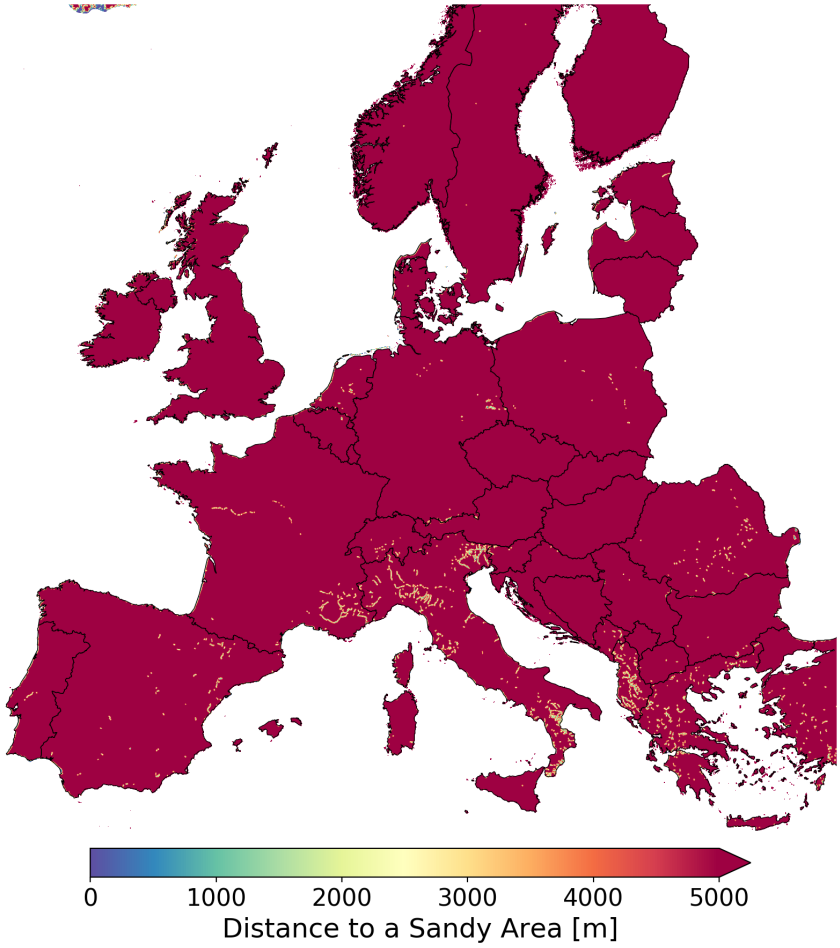

Figure B.33: Prior: Sand Proximity. Derived from [91]

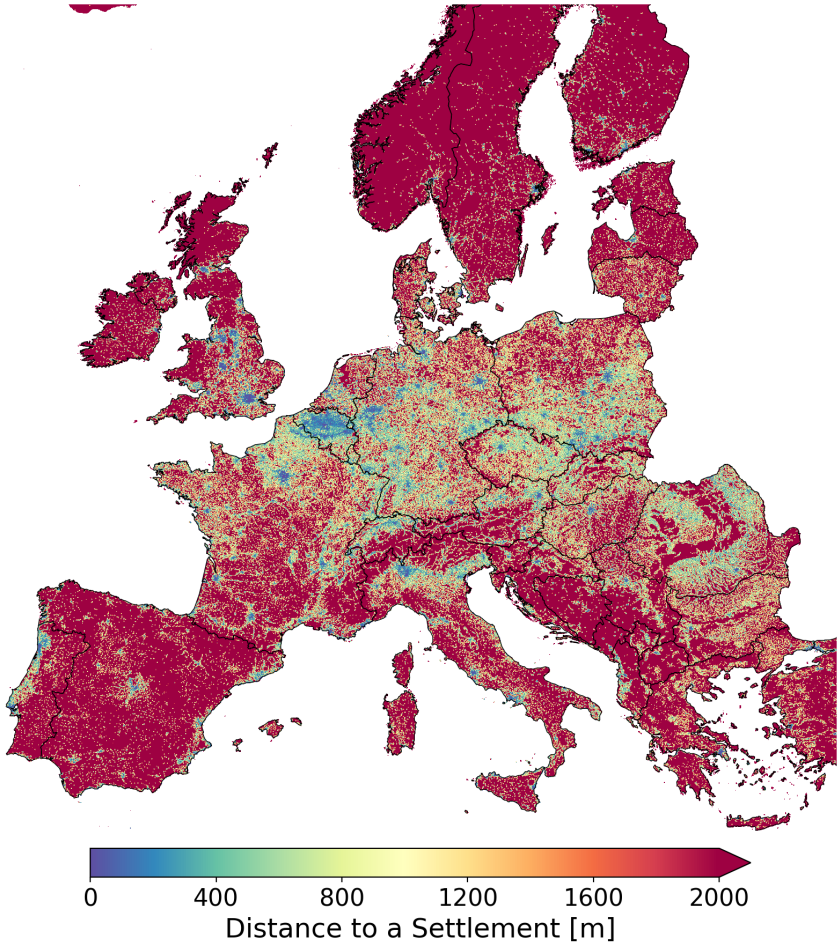

Figure B.34: Prior: Settlement Proximity. Derived from [91]

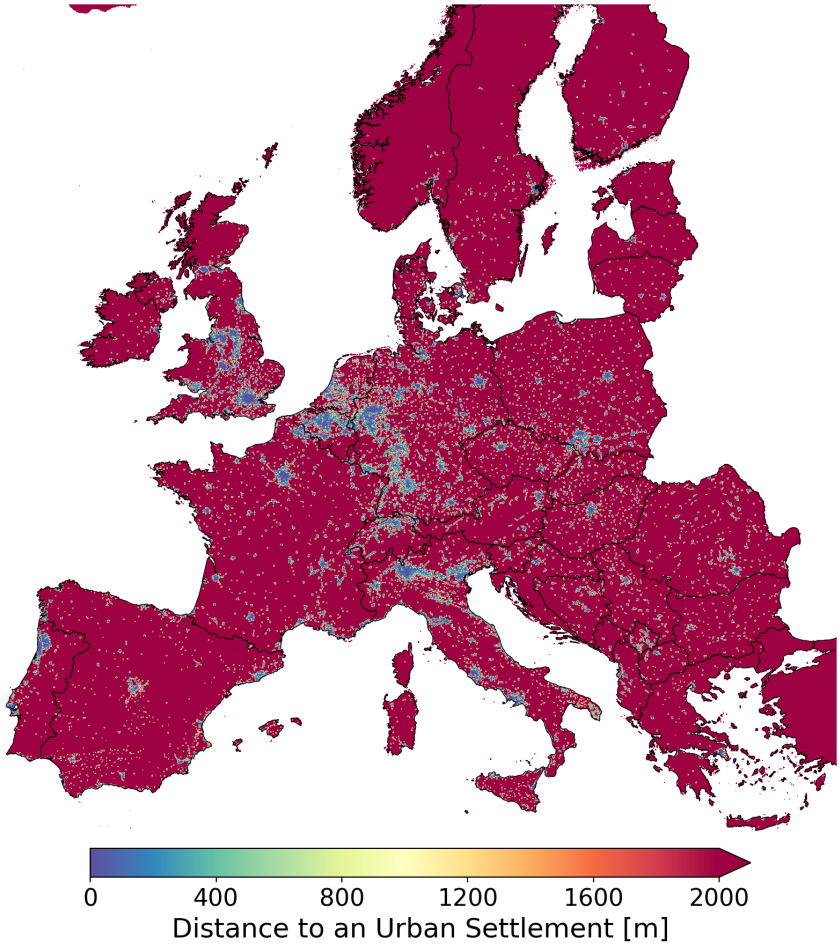

Figure B.35: Prior: Settlement Urban Proximity. Derived from [92]

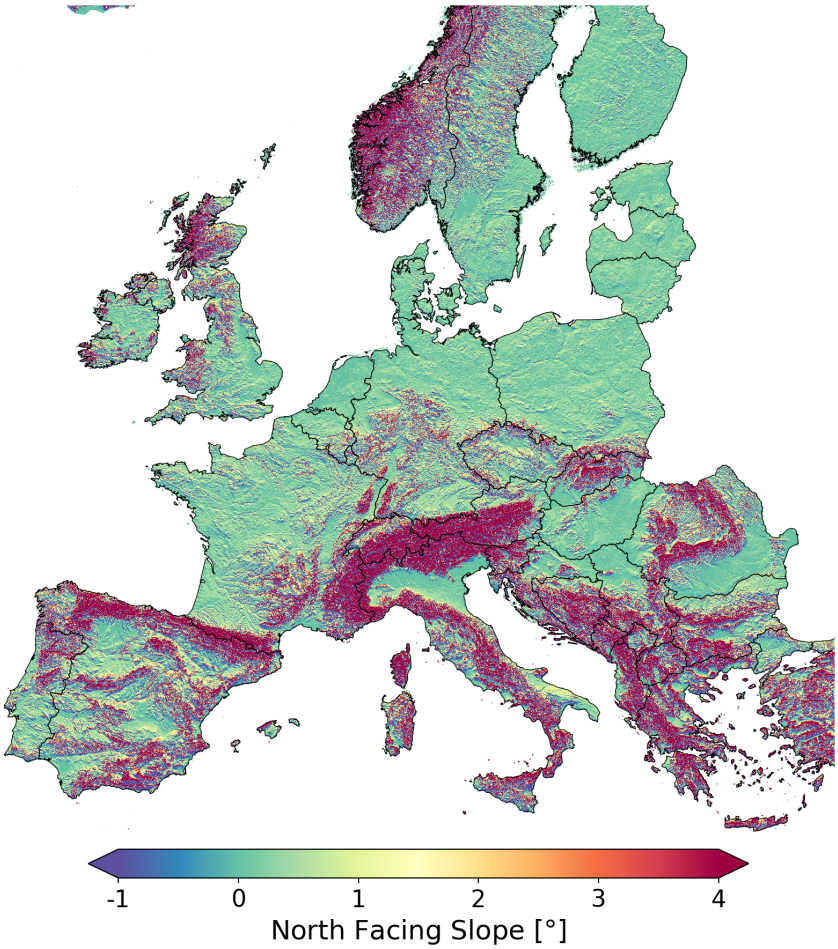

Figure B.36: Prior: Slope North Facing Threshold. Derived from [94]

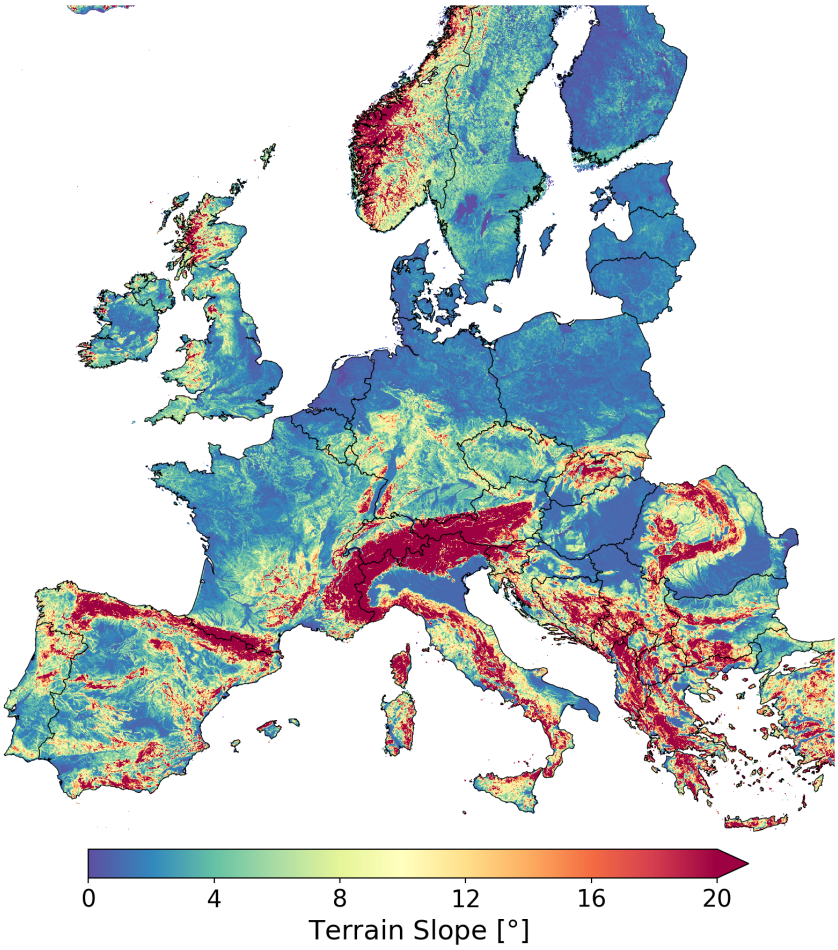

Figure B.37: Prior: Slope Threshold. Derived from [94]

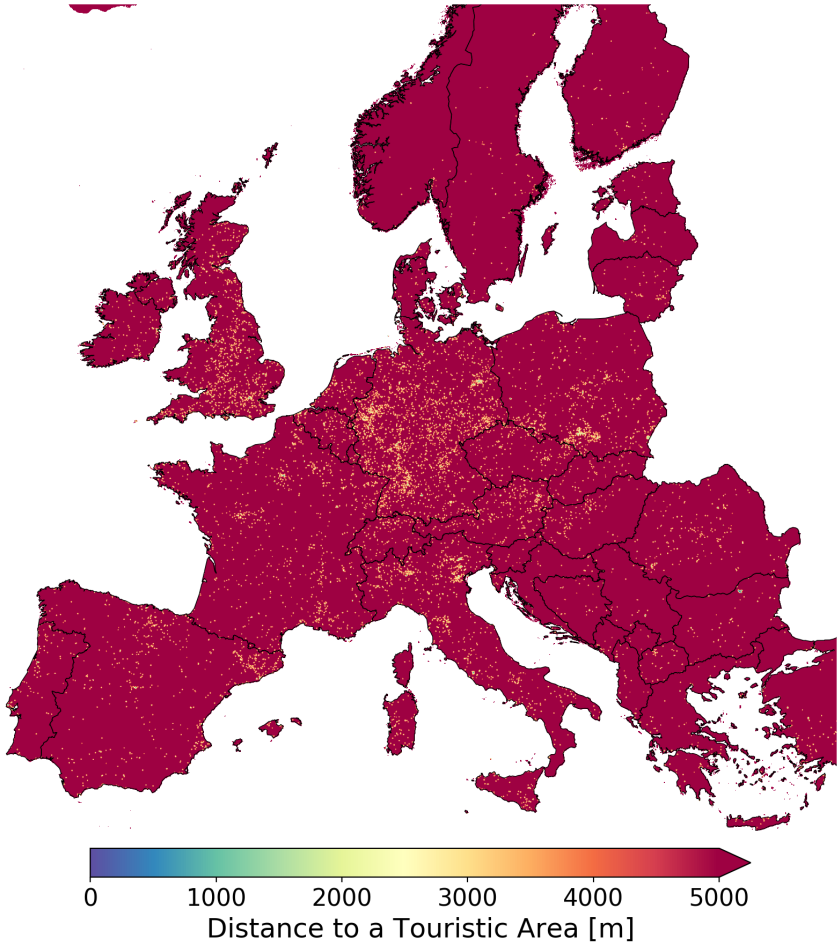

Figure B.38: Prior: Touristic Proximity. Derived from [97]

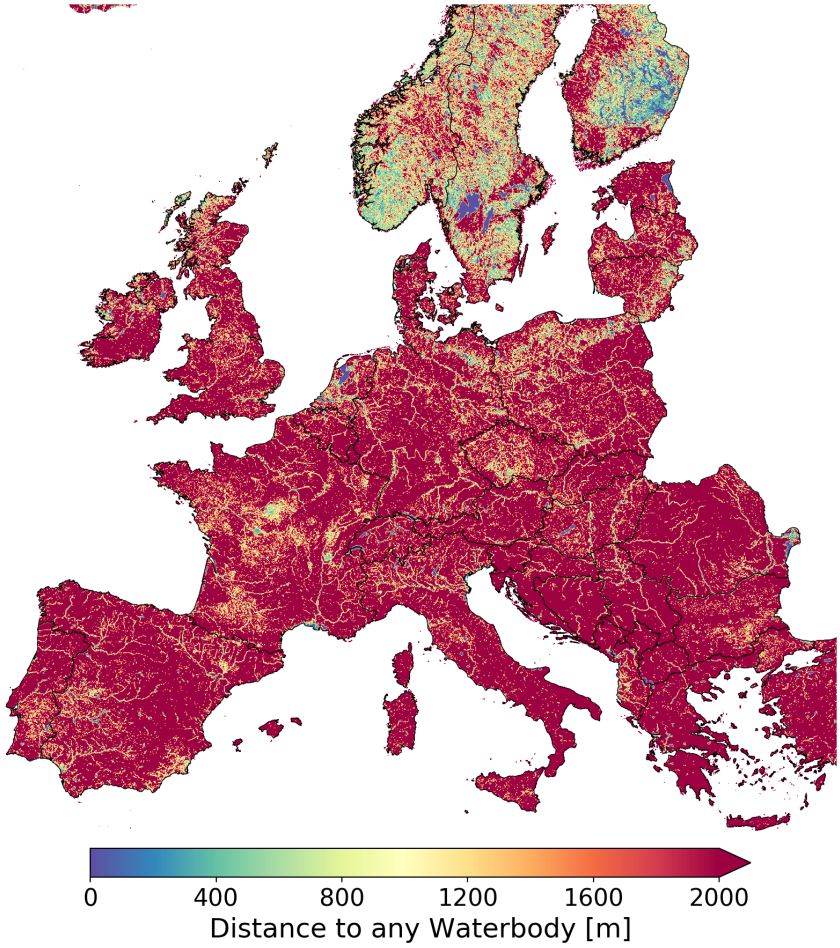

Figure B.39: Prior: Water Body Proximity. Derived from [391]

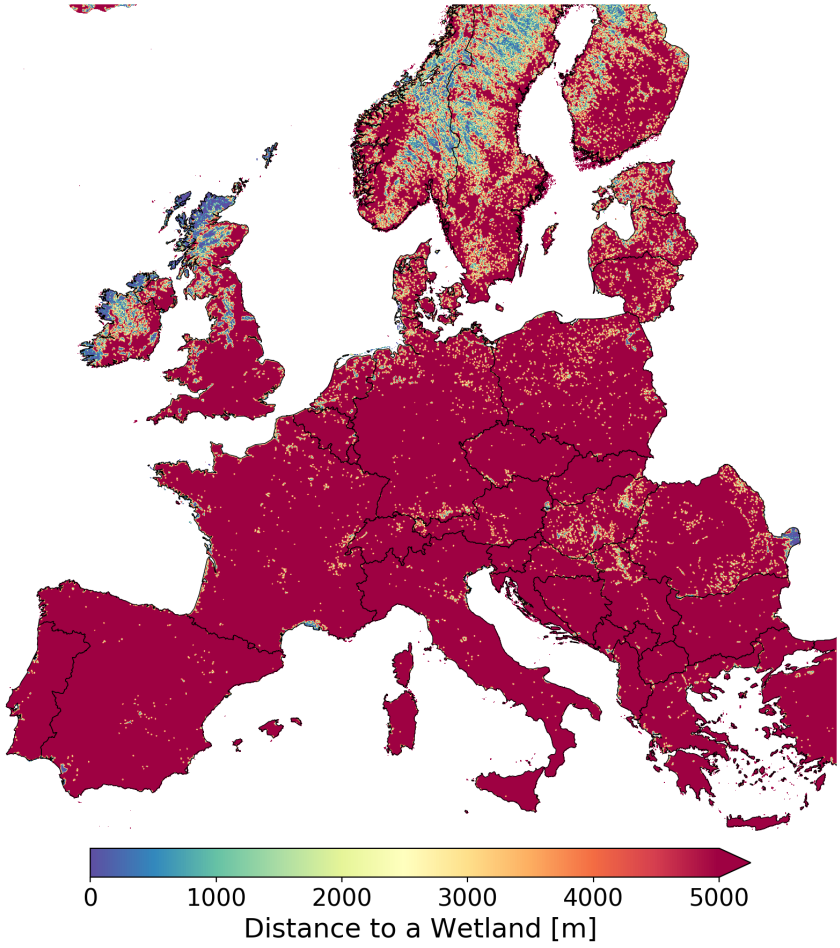

Figure B.40: Prior: Wetland Proximity. Derived from [91]

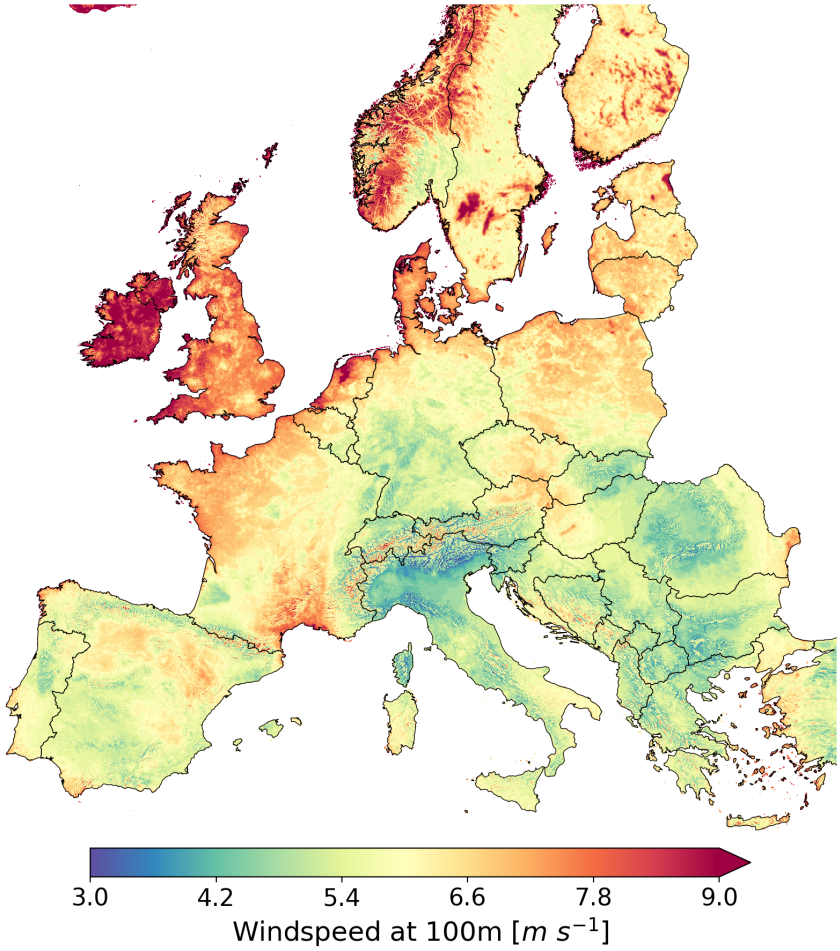

Figure B.41: Prior: Wind Speed 100 m Threshold. Derived from [122]

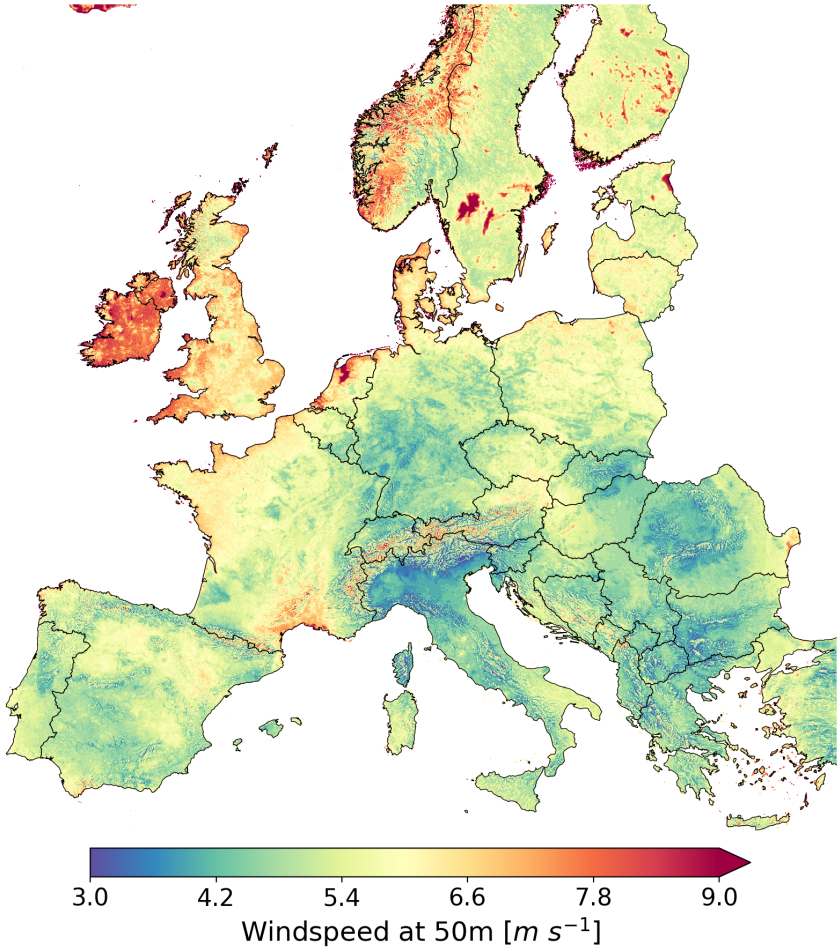

Figure B.42: Prior: Wind Speed 50 m Threshold. Derived from [122]

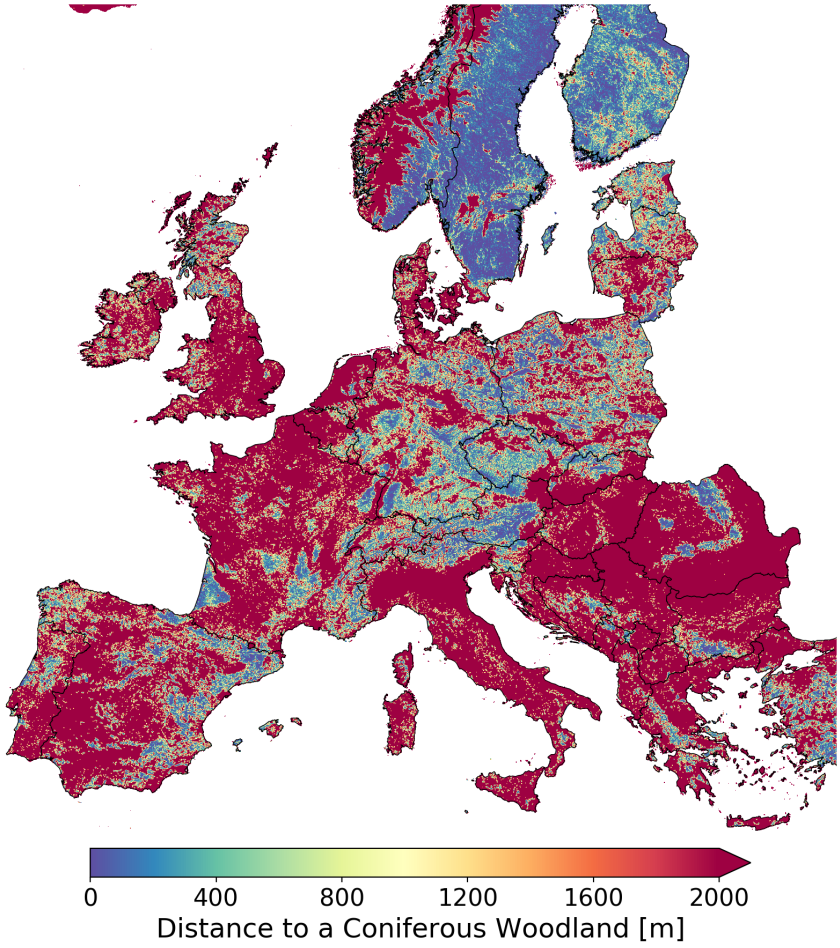

Figure B.43: Prior: Woodland Coniferous Proximity. Derived from [91]

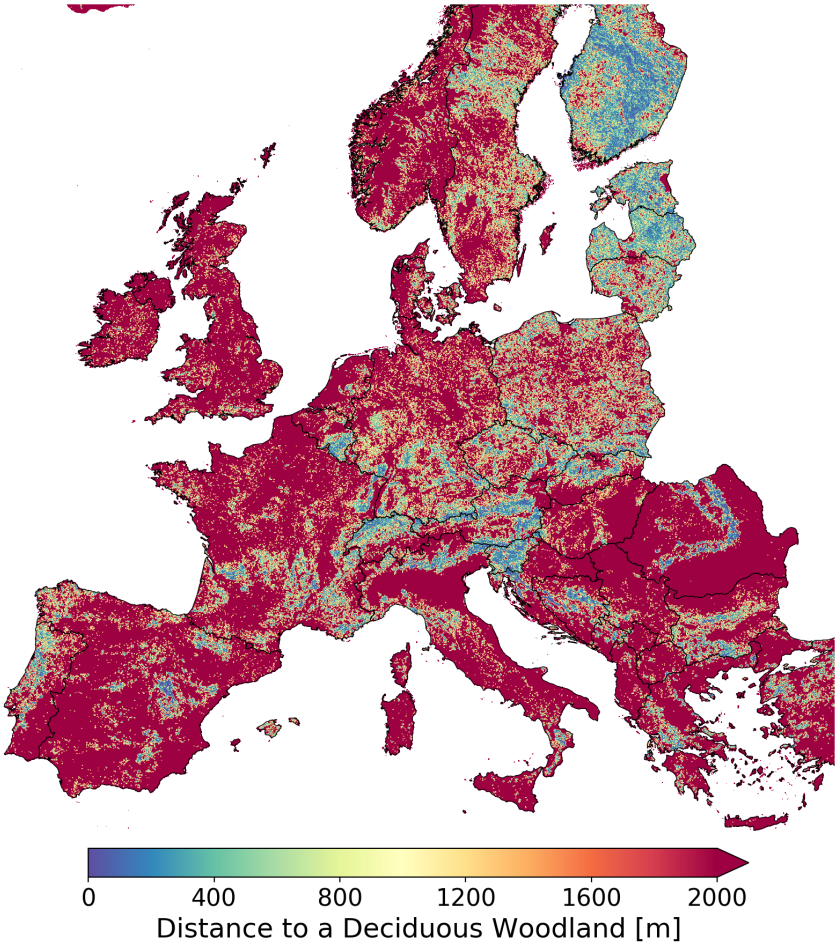

Figure B.44: Prior: Woodland Deciduous Proximity. Derived from [91]

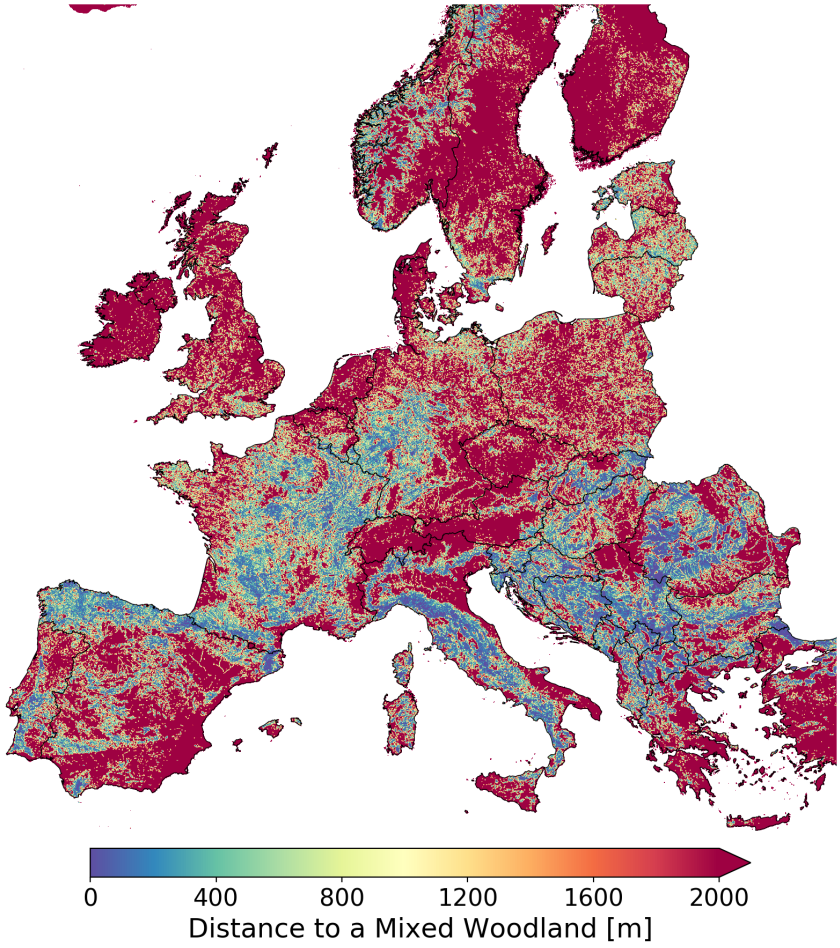

Figure B.45: Prior: Woodland Mixed Proximity. Derived from [91]

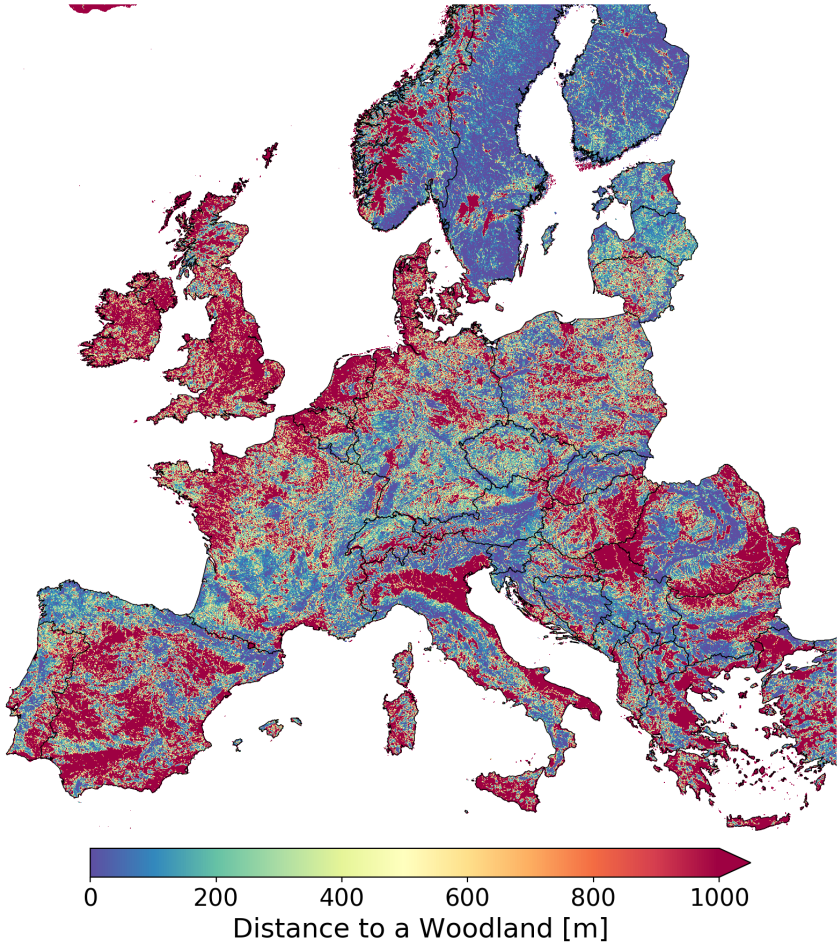

Figure B.46: Prior: Woodland Proximity. Derived from [91]

Chapter C

Extra Backgound Topics

C.1 The Beaufort Wind Speed Scale

Table C.1: The Beaufort wind speed scale with associated energy densities [116].

Type of Wind	Wind Speed	Energy Density
Calm	$<$0.3 m s^{-1}	$\approx$ 0 W m^{-2}
Light air	0.3 - 1.5 m s^{-1}	0 - 4 W m^{-2}
Light breeze	1.5 - 3.3 m s^{-1}	4 - 43 W m^{-2}
Gentle breeze	3.3 - 5.5 m s^{-1}	43 - 200 W m^{-2}
Moderate breeze	5.5 - 7.9 m s^{-1}	200 - 590 W m^{-2}
Fresh breeze	8.0 - 10.7 m s^{-1}	590 - 1,500 W m^{-2}
Strong breeze	10.7 - 13.8 m s^{-1}	1,500 - 3,200 W m^{-2}
High wind	13.8 - 17.1 m s^{-1}	3,200 - 6,000 W m^{-2}
Gale	17.1 - 20.7 m s^{-1}	6,000 - 10,700 W m^{-2}
Strong Gale	20.8 - 24.4 m s^{-1}	10,700 - 17,500 W m^{-2}
Storm	24.4 - 28.4 m s^{-1}	17,500 - 27,600 W m^{-2}
Violent storm	28.4 - 32.6 m s^{-1}	27,600 - 41,800 W m^{-2}
Hurricane force	$>$32.6 m s^{-1}	$>$41,800 W m^{-2}

C.2 Roughness Lengths

The following table suggests roughness lengths suggested by Silva et al. [129] for different land cover types, and is intended to be used in Equation 3.4.

C.3 Weather and Climate Models

To evaluate the generation profiles of wind turbines, PV modules and other VRES technologies, access to weather variables such as wind speed, irradiance, temperature, and others is paramount. Without detailed weather data, estimates made on the performance of these technologies are likely to not incorporate the temporal and spatial fluctuations which have been discussed in previous sections; especially in the context of modeling VRES generation lulls. Therefore, careful consideration must be taken when decided on how and where to source this information.

Three options are available to obtain weather variables: weather station measure-

Table C.2: Roughness value ranges suggested by Silva et al. [129].

Predominant Land Cover	Likely Value	Value Range
Continuous urban fabric	1.2	1.1 - 1.3
Forest	0.75	0.6 - 1.2
Green urban areas	0.6	0.5 - 0.6
Transitional woodland/shrub	0.6	0.5 - 0.6
Burnt areas	0.6	0.5 - 0.6
Discontinuous urban fabric	0.5	0.3 - 0.5
Industrial or commercial units	0.5	0.3 - 0.5
Agro-forestry areas	0.3	0.1 - 0.5
Permanent crops	0.1	0.1 - 0.3
Roads and rails and associated land	0.075	0.05 - 0.1
Non-irrigated arable land	0.05	0.03 - 0.05
Permanently irrigated land	0.05	0.03 - 0.05
Marshes	0.05	0.03 - 0.05
Sclerophylous vegetation	0.03	0.03 - 0.1
Natural grassland and pastures	0.03	0.03 - 0.1
Dump sites and Mining sites	0.005	0.005 - 0.01
Airports	0.005	0.005 - 0.01
Sparsely vegetated areas	0.005	0.005 - 0.01
Glaciers and perpetual snow	0.001	
Peatbogs	0.0005	
Salines	0.0005	
Intertidal flats	0.0005	
Beaches, dunes, and sand plains	0.0003	0.0003 - 0.06
Water courses	0.001	
Water bodies	0.0005	
Costal lagoons	0.0005	
Ocean	0.0002	

ments, satellite-imagery derived data, and climate model outputs. Thanks to the World Meteorological Organization (WMO), the US's National Oceanic and Atmospheric Administration (NOAA), and affiliates, measured weather station data is available across the globe [128]. This data is not applicable to the current use case, however, since it inhomogeneously located across the European area, collected via a variety of measurement techniques made at different stations, and contains missing or erroneous data. Satellite imagery, by comparison, can be used to estimate spatially broad and temporally fine-grained weather variables such as surface temperature [394] and irradiance [395]. However, since a complete set of weather data is required to model VRES systems, it is of high importance that all of these variables are taken from the same source in order to maintain internal consistency of the resulting VRES generation profiles. Unfortunately, no satellite-derived weather products offers the full collection of the requisite parameters in a single package. Furthermore, the use of these techniques are only available so long as recorded

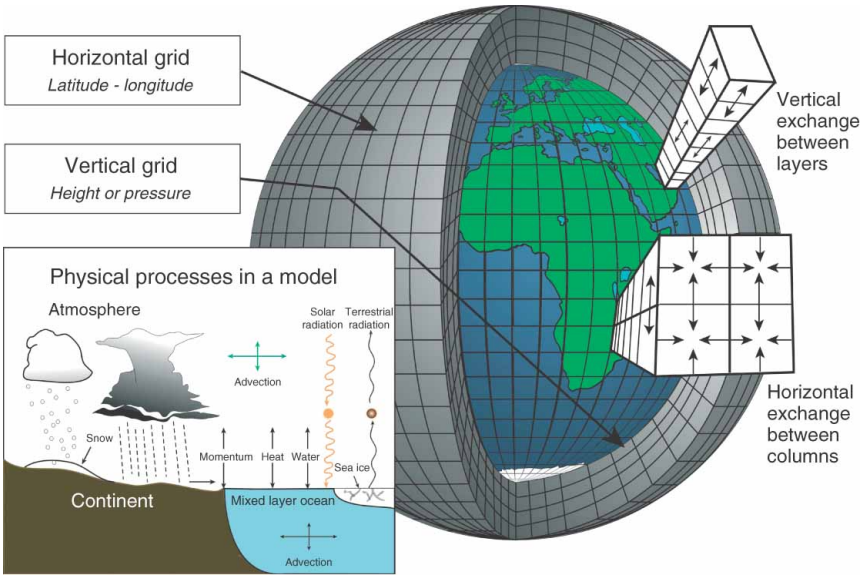

Figure C.1: Visual representation of a global climate model. Figure extracted from [396].

imagery exists and, as a result, many satellite weather products only offer a few years of weather data. This leaves the final option, the output of climate models.

Climate modeling has been an active area of science for nearly half a century and, as a result, climate models have progressed to the point of being extremely intricate. Nevertheless, climate models remain a simplification of the climactic dynamics, and this always must be kept in mind when making use of the tremendous amount of data they produce. Figure C.1 provides an explanatory representation of a global climate model. As shown, climate models must spatially partition the atmosphere into a three dimensional lattice of grid cells. Numerous fundamentally-approximate physical dynamics are then modeled within and between these cells; including precipitation, fluid flows, temperature gradients, photosynthetic activity, and many others. A key issue here is that little to no distinction can be made within grid cells; meaning that each cell is computed to have a single, for example, wind speed. For climate models with fine spatial resolution, these output values for each cell can be more reasonably treated as though they were observations, however for models with coarse resolution a downscaling procedure would be additionally required. In any case, these calculations are performed once over all cells in reference to a short moment of time, typically on the order or minutes to seconds, which are then used as input variables to compute the updated variables in the following moment. After a set number of time steps, commonly amounting to 1 hour, the instantaneous weather variables within each cell are stored on file. These outputs constitute the climate model's output dataset.

Numerous climate models exist, and they differ in regards to their spatial resolution and scope, the physics they include and the submodules they use, and finally their time step. Furthermore, climate models can be separated into two groups: global climate models (GCM) and regional climate models (RCM). GCMs are typically lower spatially resolved, historically around 70 to 40 km between cells, and focus on the synoptic scale meteorology physics which are most impactful on the global scale. As the name suggests, they model the entire globe as a sphere. RCM only model a specific region, which can be as small as a city or as large as a continent, and depending on the model in question can incorporate much more detailed physical processes that operate on the mesoscale or even the microscale. For this purpose, their spatial resolution is often much finer than GCMs; commonly offering resolutions between 2 and 12 km. Of course, weather is highly stochastic and so the use of a different climate models, and even different parameterizations of the same climate model, can lead to a very different outcomes at small spatial scales and over short time frames. Therefore, in order to better compare the outputs of RCMs and their parameterizations, the CORDEX initiative was created to normalize the regional domain and set of output variables [397].

The common work flow used in the weather modeling community is the following. Near-present real weather measurements and satellite information is gathered to form a driving set of weather variables which 'seed' a GCM. The GCM then simulates the state of the global climate during a 'reanalysis' period, commonly lasting between 1980 and the current date. This reanalysis data is then checked against other real measurements and observations to ensure the output's realism. RCMs, which do not maintain a complete global view, then use GCM outputs to nudge the RCM to follow along with the global developments estimated by the GCM. In effect, the RCM is capable of downscaling the GCM data by filling out the weather dynamics which occur at smaller scales. When researchers are confident in the output of the GCMs and RCMs, the models can be run into the future as 'projections', for which assumptions must be made regarding the aerosol contents in the atmosphere, or into the past as 'hindcasts'.

In the context of this work and similar works, the outputs of climate models are integral to the evaluation of energy systems and the impacts of VRES generation. Climate modeling is still a developing science, however, and so vigilance must be taken to avoid inherent biases of these models [16, 17, 186, 187] and, moreover, to update climate-model-based VRES estimates along with the progressive nature of this field.

C.4 LCOE Calculation Method

LCOE computations are performed using the following general approach where a fundamental formula for calculating the LCOE is simplified using several assumptions. Equation C.1 displays the fundamental LCOE equation.

$$\sum_{t=0}^{years} \frac{I_t + Op_t}{(1+r)^t} = \sum_{t=0}^{years} \frac{LCOE * G_t}{(1+r)^t} \tag{C.1}$$

Where I_t indicates all investment-related expenditures in year t and Op_t indicates all operational-related expenditures in year t. These costs are scaled by a constant interest rate, r, which has a compounding effect for each additional year in the system's economic lifetime. G_t refers to total electricity generation in year t in kWh. Finally, $LCOE$ refers to a constant value at which the generated electricity must be sold for in order to exactly offset all investment and operational costs. In order to find LCOE this equation must be solved for $LCOE$, as shown in Equation C.2.

$$LCOE = \frac{\sum_{t=0}^{years} I_t + Op_t/(1+r)^t}{\sum_{t=0}^{years} G_t/(1+r)^t} \tag{C.2}$$

Computing Equation C.2 is easily performed if all expenditure and generation values are known throughout a system's economic lifespan, however this information is generally not available. Therefore several simplifying assumptions are made in order to make the LCOE computable with the information which will be available. The first of these assumptions is that all capital costs are paid in the first year of operation. Capital costs estimations of all the VRE generators considered in this work will be detailed in each technology's respective modeling section. Secondly, the assumption is made that the operational costs in each year are equal to a constant percentage of the total capital cost. Again, the exact factor which is used will depend on the VRE generator type in question and will be discussed in later sections. Finally, the assumption is made that the yearly generation values used should all be equal to the average generation value. Once again, the methods used to obtain average generation values will be detailed for each technology in the coming sections. In general, however, these values will be obtained by means of multi-year simulations of the Wind or PV system in question. With these assumptions, Equation C.1 takes the form of Equation C.3; where I indicates the total capital cost, α refers to the operational cost factor, and G_{avg} indicates the average generation.

$$LCOE = \frac{I \cdot \sum_{t=0}^{years} (1+\alpha)/(1+r)^t}{G_{avg} \cdot \sum_{t=0}^{years} 1/(1+r)^t} \tag{C.3}$$

This equation can be further simplified to that given in Equation C.4, where T now indicates the total economic lifetime of the system. Another interpretation of Equation C.4 is given by C.5 which is expressed in terms of the specific cost of the system, I_{sp}, given in €/kW, and the system's average FLH. These two equations represent the final LCOE equations used in the remainder of this work.

$$LCOE = \frac{I}{G_{avg}} \cdot \left(\frac{r}{(1+r)^{-T}} + \alpha \right) \tag{C.4}$$

$$LCOE = \frac{I_{sp}}{FLH} \cdot \left(\frac{r}{(1+r)^{-T}} + \alpha \right) \tag{C.5}$$

Chapter D

Wind Energy Modeling

D.1 Synthetic Wind Turbine Constants

Table D.1: Synthetic power curve fitting constants. Previously published in Ryberg et al. [109].

%	A_{cf}	B_{cf}	%	A_{cf}	B_{cf}	%	A_{cf}	B_{cf}
1	−0.584,630	0.298,395	35	0.089,884	0.331,396	69	0.179,021	0.356,938
2	−0.419,940	0.288,554	36	0.104,825	0.330,433	70	0.175,836	0.358,507
3	−0.391,026	0.296,708	37	0.115,079	0.330,222	71	0.174,338	0.359,783
4	−0.389,457	0.306,946	38	0.119,641	0.330,932	72	0.172,826	0.361,062
5	−0.405,802	0.318,660	39	0.124,266	0.331,594	73	0.171,831	0.362,248
6	−0.404,320	0.326,210	40	0.129,406	0.332,135	74	0.171,274	0.363,357
7	−0.392,369	0.330,959	41	0.135,250	0.332,527	75	0.171,008	0.364,420
8	−0.381,924	0.335,307	42	0.141,521	0.332,818	76	0.171,555	0.365,349
9	−0.363,300	0.337,792	43	0.146,831	0.333,249	77	0.171,811	0.366,329
10	−0.343,517	0.339,634	44	0.151,369	0.333,788	78	0.171,747	0.367,368
11	−0.317,832	0.339,947	45	0.155,791	0.334,317	79	0.172,059	0.368,349
12	−0.291,175	0.339,762	46	0.160,274	0.334,814	80	0.172,037	0.369,401
13	−0.269,508	0.340,070	47	0.164,556	0.335,321	81	0.171,353	0.370,576
14	−0.253,212	0.341,045	48	0.168,360	0.335,894	82	0.170,385	0.371,812
15	−0.237,163	0.341,822	49	0.172,509	0.336,394	83	0.169,653	0.373,019
16	−0.222,626	0.342,677	50	0.176,535	0.336,900	84	0.167,779	0.374,431
17	−0.206,083	0.343,045	51	0.180,574	0.337,385	85	0.166,319	0.375,801
18	−0.182,945	0.342,120	52	0.184,264	0.337,910	86	0.165,007	0.377,203
19	−0.159,519	0.340,946	53	0.188,553	0.338,307	87	0.163,899	0.378,624
20	−0.137,017	0.339,791	54	0.192,156	0.338,806	88	0.163,928	0.379,897
21	−0.116,739	0.338,917	55	0.194,822	0.339,454	89	0.165,921	0.380,865
22	−0.101,093	0.338,734	56	0.197,050	0.340,169	90	0.168,181	0.381,818
23	−0.086,576	0.338,621	57	0.198,232	0.341,055	91	0.168,264	0.383,199
24	−0.074,753	0.338,868	58	0.198,694	0.342,060	92	0.168,549	0.384,629
25	−0.063,226	0.339,079	59	0.198,578	0.343,159	93	0.171,687	0.385,673
26	−0.051,254	0.339,143	60	0.198,261	0.344,285	94	0.178,577	0.386,181
27	−0.039,703	0.339,222	61	0.197,871	0.345,417	95	0.183,538	0.387,207
28	−0.028,335	0.339,261	62	0.196,978	0.346,626	96	0.178,848	0.390,208
29	−0.015,586	0.339,001	63	0.195,416	0.347,943	97	0.172,858	0.393,784
30	−0.002,372	0.338,596	64	0.193,265	0.349,355	98	0.150,698	0.400,896
31	0.012,792	0.337,801	65	0.190,900	0.350,794	99	0.131,285	0.408,730
32	0.034,139	0.335,896	66	0.188,335	0.352,264	100	0.110,124	0.421,266
33	0.054,711	0.334,097	67	0.185,694	0.353,743			
34	0.073,012	0.332,644	68	0.182,301	0.355,351			

D.2 Simulation Validation

Simulation validation performed here focuses on onshore applications since this was specifically developed in line with this work. The reader is again referred to the work of Caglayan et al. [102] for a similar validation discussion of the simulation procedure when applied for offshore. Furthermore, as cost projections and economic evaluation of future wind turbines in the far future is highly speculative, validation of the onshore methodologies focuses on the turbine design and simulation procedures. Therefore, measured turbine generation data from three independent sources are considered in addition to summary production data and estimations for Germany from numerous sources. Lastly, since the majority of the later stages of this work rely predominantly on the weather data from MERRA dataset, validation is only discussed in regards to the usage of this source.

D.2.1 Hourly Comparison

The first two data sources which will be discussed constitute hourly measurement data from two wind parks in Europe. The Princess Alexia wind park in the Netherlands, commissioned in September of 2013 and consisting of 36 Senvion 3.4M104 wind turbines totaling 122 MW, is the first of these. Turbines in the Princess Alexia park are characterized by a 3400 kW nameplate capacity, a 98 m hub height, and a 104 m rotor diameter. Furthermore, via manually reviewing satellite imagery data, each turbine in this park was located with precise latitude and longitude coordinates and measured generation data for the entire park was retrieved for 2015 and 2016 from the data portal provided by the European Energy Exchange (EEX) [398]. The second park considered is the La Haute Borne wind park in western France. In operation since 2009, the La Haute wind park consists of 4 Senvion MM82 wind turbines, characterized by a 2050 kW nameplate capacity, 80 m hub height and 82 m rotor diameter. Detailed location and measurement data for the La Haute park's wind turbines is provided through by the ENGIE Group [137, 138] and includes sub hourly production data between 2009 until 2017 for each turbine, in addition to measured wind speed, wind direction, temperature, grid voltage, and other parameters. For the sake of this validation, only aggregated hourly generation data across the whole park for 2015 and 2016 is considered to match the availability of the Princess Alexia data. Finally, only hours in which measurements were reposted for all four turbines in the park were considered in the comparison; resulting in slightly below 13,000 values to consider.

For both parks, comparison is performed by simulating each of the located turbines for the time frames where measurement data exists, aggregating generation across the park, and recording the deviance from the reported generation. Figure D.1 provides a sample of the resulting time series, where measured and simulated time series for the two parks is shown. For the full time frame, Table D.2 provides statistical summaries of each comparison. From the figure, it is generally seen that the onshore simulation model does an acceptable job at recreating the measured generation from these parks, as the range of generation and significant fluctuations are recreated well. Princess Alexia estimations, shown at the bottom, however, ap-

pear to fit much better than the La Haute simulations, shown in the top plot. Indeed, when viewed across longer time frames the model is shown to slightly under predict the generation from the Princess Alexia park by $5.05\,\%$, while it under predicts the generation from the La Haute park by $37.65\,\%$. The large discrepancy of the La Haute park is expected to be an outcome of the LRA spatial adjustment procedure which fixes the long run average of the MERRA wind speed values to the value dictated by GWA. Therefore, under and over predictions of the model are highly dependent on the downscaling accuracy of GWA. Due to the availability of wind speed data for the La Haute turbines, this hypothesis was directly tested by using the actual observed time-averaged wind speeds instead of the GWA estimate for spatial adjustment resulting in the line shown in red in Figure D.1. After making this average wind speed correction, the total percent error was reduced to an over prediction of $3.77\,\%$. In both cases, a strong correlation is observed, however the normalized root mean squared error (RMSE) shows that the error in hourly fluctuations can be quite high; reaching, for example, $48\,\%$ of the average generation value for the Princess Alexia park. This discrepancy is due to the inability of the MERRA dataset to recreate local context wind fluctuations due to its large context area for each grid cell.

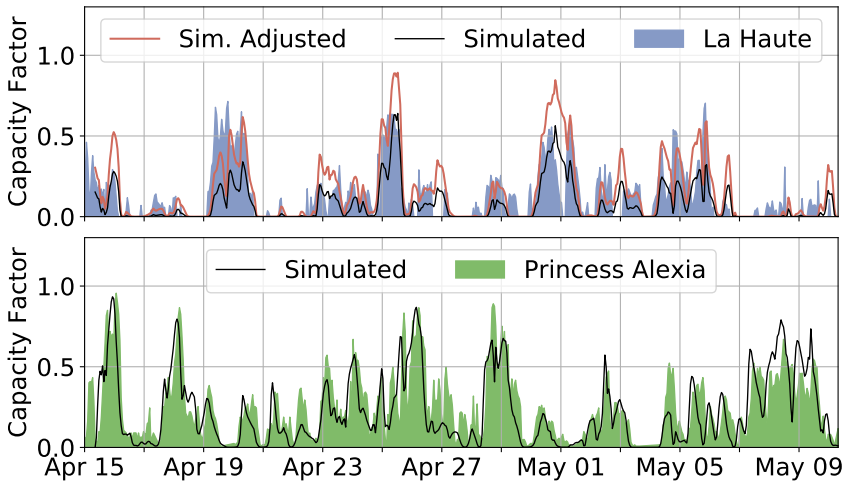

Figure D.1: Visual comparison of hourly generation values against the measured Princess Alexia and La Haute generation data. A large total percent error was found when applying the proposed method to the La Haute park, however when correcting the average wind speed to the actually observed value, the overall error was reduced considerably. Figure previously published in Ryberg et al. [109].

Table D.2: Summary of various statistical measures when comparing simulated and measured generation data from the La Haute and Princess Alexia wind parks

Measure	**Princess Alexia**	**La Haute**	**La Haute - Corrected**
Absolute Error [%]	−5.05	−37.65	3.77
Normalized RMSE [%]	47.91	63.40	61.23
Correlation	0.88	0.80	0.81

D.2.2 Regional Comparison

In addition to the hourly comparisons, monthly generation estimations are compared to 86 turbines spread across Denmark between 2002 and 2011. Measured generation data and turbine characteristic data are obtained from the "Master Data Register of Wind Turbines" originating from the Danish Energy Agency [399]. This dataset includes capacity, hub height, rotor diameter, installation date, and location of over 6100 wind turbines installed in Denmark; of which only onshore turbines with greater than 2000 kW capacity and a known power curve are considered for comparison. After filtering to the 86 known turbines, a variety of designs remain; spanning capacities from 2 to 3.6MW, rotor diameters from 73 to 120 m, hub heights from 68 to 94 m, and specific powers from 312 to 473 $\mathrm{W\,m^{-2}}$. For the known turbines, the percent error of estimated monthly generation values compared against the reported measurements is found, and the result is shown in Figure D.2.

When comparing the generation histograms shown to the left of Figure D.2, a transition is seen at 300 MWh below which a smaller population of modeled observations is seen and above which an over population is found. This over prediction is also seen in the percent error per turbine histogram, shown in blue to the right of Figure D.2, where the most likely observations are found between −20 and 30 %, with a over estimating tail extending beyond 80 %. Unlike the hourly comparisons, miss-

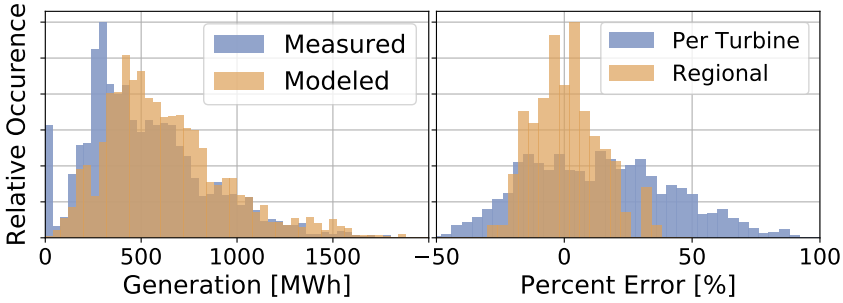

Figure D.2: Monthly validation against 86 Turbines in Denmark, simulated from 2002 until the end of 2011. Figure previously published in Ryberg et al. [109].

ing or otherwise clearly erroneous data cannot be easily removed from the comparisons as only monthly sums are reported, and these measurement values are certain to include dynamics which cannot be predicted in the current state of this model; such as downtime and curtailment. From this perspective an overestimation would be expected, but to what degree is uncertain without detailed knowledge of the data gathering and processing procedures used by the Danish Energy Agency. Therefore, these results are not conclusive of a systematic over prediction of the simulation scheme in Denmark. Nevertheless, when taking a regional perspective it seen that over and under predictions for individual turbines tend to balance each other. This is shown by the orange distribution on the right of Figure D.2, when generation is aggregated for all turbines within each reported month the resulting distribution is nearly symmetrically centered around a $0\,\%$ error with tails extending to $\pm 30\,\%$. As a result of this observation, in addition to the agreements observed for the hourly validations, it is concluded that the simulation model behaves reliably well for estimating hourly generation.

D.2.3 Design Comparison

Finally, as future wind turbine designs will slightly improve upon those which are available today, it is also of interest to determine whether the model behaves reasonably well for simulating turbines in a future context. Therefore, outputs of the model are compared against average FLH values for the entirety of Germany as reported by other sources that span a variety of turbine design contexts. Figure D.3 presents the outcome of these comparisons. The solid lines in this figure represent the average FLH value for a homogeneous turbine design used for all available locations in Germany, as identified by the procedure discussed in Section 3.5. These trends clearly show how the expected FLH is sensitive to the turbine

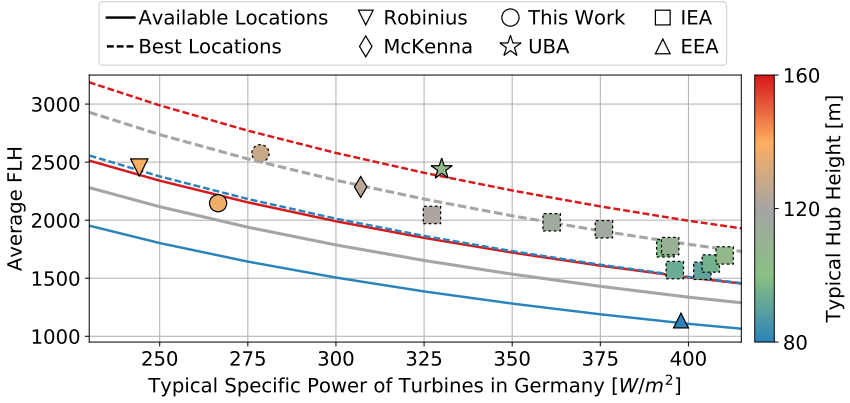

Figure D.3: Average German FLH estimated with the model compared to similar estimations and historical values. Figure previously published in Ryberg et al. [109].

design; that when the typical hub height of turbines increases, or when the typical specific power decreases, higher FLH values should be observed compared to the use of contemporary turbine designs. The circle with a solid border shows the average FLH across Germany resulting from the full analysis conducted here, which takes into account location-specific turbine designs and displayed at the capacity-weighted values for specific power and hub height. However, these estimations will of course include contributions from weak wind locations that are unlikely to be considered in a realistic scenario, so the dashed lines and dash-bordered circle are also shown which represent the German FLH average when only the best $40\,\%$[1] of potential turbines are considered. As expected, the dashed trends show higher FLH for the same specific power and hub height values since only turbines at the best locations contribute to the averaged value. In comparing the solid-bordered and dash-bordered circle, it is also expected that the best turbines are those with higher specific power and lower hub heights, since these turbines designs correspond to locations with a larger average wind speed.

For the other points found in Figure D.3, the average FLH is always taken as the reported value while the typical specific power and typical hub height values are also determined from a capacity-weighted average of the turbines considered in the respective sources. The values derived from the German Environmental Agency (UBA) [73], McKenna et al. [43], European Environmental Agency (EEA) [42], and Robinius et al. [156] represent the average German FLH in an expressed future context. From these points it is seen that, when a comparable context of turbine design in Germany is used, estimations of the model shows close agreement with the EEA value, is significantly more conservative than the values given by McKenna et al. and by UBA, and is in the same range as the value predicted by Robinius et al. The square points show the average FLH of real grid connected turbines in Germany as reported by the International Energy Agency's (IEA) annual reports on wind energy statistics [146], where averages for Germany are taken between 2009 and 2017. Although the IEA values are subject to the inter-annual variability of wind speeds, they clearly show the progression of increasing FLH resulting from improved turbine design which is reflected by the model used in this analysis. Furthermore, the FLH values reported by IEA represent the average FLH of installed turbines, which will naturally exclude poor performing locations, so are more comparable to the dashed design trends. These trend lines are found to be in the same range as the values reported by IEA. From these comparisons, it is evident that the model predicts similar average FLH values across Germany to both estimated and reported values when similar turbine designs are used. Moreover, while the progressive turbine design scenario investigated here will result in significantly higher FLH values compared to these other studies, this discrepancy appears to be well in line with a reasonable trend of improving performance.

[1] Sorting by estimated LCOE

Chapter E

Solar Energy Modeling

E.1 PV Simulation Validation

Since all major compoent models of the PV Simulation scheme have been independently validated in numerous works, these issues are not discussed in detail here. Nevertheless, it remains to be proven that the chosen simulation scheme, when it is applied in its entirety, is capable of reproducing results reported in the literature. Two sources will be focused on in the following section. The first performs hourly-resolved simulations for each European country, which can be directly compared against, and the other provides highly spatially resolved multi-annual FLH averages which can be recreated. The comparisons will be discussed in this order.

For the hourly comparisons, the study of Pfenninger et al. [16] is of prime interest since it incorporated a highly detailed validation effort and, moreover, the results of et al. 's work are openly available as country-level capacity factor time series values between the years 1985 and 2015. Pfenninger et al.'s validation effort consisted of comparing simulations against measured data of several thousand PV systems dispersed across Europe, and ultimately relied upon country-specific correction factors for their final method. Therefore, the first level of validation for the PV simulation scheme developed here is addressed via a direct comparison to the results of Pfenninger et al. [16]. In order to accomplish this, the simulated system design was chosen to reflect that which was used by Pfenninger; such as fixed-tilt, $180°$ azimuth, and tilt angle as a function of latitude. Nevertheless, many details of Pfenninger's evaluation were not known; such as the precise module characteristics which should be used or the exact locations which were simulated. In the end, the PV simulation scheme was applied on a $5\,\mathrm{km}$ grid across Europe, and then averaged across national contexts for each time step to produce a dataset mirroring that of Pfenninger's. A $5\,\mathrm{km}$ was chosen in this case as it equates to nearly $192{,}000$ simulation points across the European scope, and therefore offers a highly resolved coverage of the generation profiles which will be observed. Furthermore, the "*First_Solar_FS_272*" module from the Go Solar California module database [244] was selected as it appeared to best match the characteristics of the module chosen by Pfenninger. The final outcome of this effort is shown in Table E.1, showing the summary statistics for each country ordered by the absolute error, and Figure E.1, showing the normalized RMSE of each hour for each country in the same order.

Table E.1 shows that, in general, the PV simulation scheme can produce very similar results to Pfenninger's. Under these contexts, 28 out of the 33 countries investi-

Table E.1: Comparison of PV simulation scheme to results from Pfenninger et al.

Region	**Correlation**	**RMSE** [capacity factor]	**Error** [%]
France	0.997	0.016	−0.260
United Kingdom	0.996	0.015	−2.646
Italy	0.996	0.022	4.445
Germany	0.997	0.017	−4.602
Czech Republic	0.997	0.022	−7.250
Poland	0.997	0.014	0.138
Bulgaria	0.996	0.018	0.528
Serbia	0.995	0.020	−0.858
Romania	0.996	0.019	1.585
Finland	0.991	0.021	1.607
Bosnia and Herz.	0.997	0.016	−1.955
Hungary	0.996	0.019	2.031
Lithuania	0.996	0.016	2.123
Norway	0.989	0.025	−2.296
Slovenia	0.994	0.023	−2.406
Denmark	0.992	0.024	2.600
Albania	0.997	0.020	2.956
Slovakia	0.997	0.018	−3.127
Montenegro	0.995	0.024	−3.221
Sweden	0.993	0.019	4.130
Croatia	0.994	0.025	4.150
Macedonia	0.993	0.029	4.380
Belgium	0.994	0.023	−4.918
Greece	0.994	0.030	6.248
Netherlands	0.996	0.023	−6.448
Spain	0.996	0.027	6.541
Latvia	0.988	0.030	6.637
Ireland	0.997	0.019	−6.705
Estonia	0.993	0.025	7.075
Austria	0.997	0.022	−7.097
Portugal	0.996	0.030	7.218
Luxembourg	0.989	0.035	−7.284
Switzerland	0.997	0.036	-12.283

gated showed a less than $5\,\%$ error and an average correlation of 0.992. Moreover, key PV countries such as Italy, Spain, Portugal, Portugal, Germany, and France were all found with a error below $2\,\%$. In regards to the spread of observed values, 29 out of 33 countries were found to possess an error in the resulting standard deviation below $5\,\%$. These results strongly suggest that simulation scheme developed here is capable of producing result at least as valid as those estimated by Pfenninger's model.

For the few countries which did not exhibit such strong comparison results, such as Norway, Switzerland, and Finland, the resulting errors do not necessarily invalidate the proposed model for use in these regions. On one hand, this outcome could be the result of set-up differences between the analyses. As an example, from Figure 4.15 it is apparent that both Norway and Switzerland exhibit rapid spatial variation in the relevant weather parameters for PV generation, as seen by the rapid change in optimal tilt angle It stands to reason that differences in the specific locations simulated should have a larger impact on the estimations made in these two countries as compared to the other countries where there is less spatial variability in climatic conditions. On the other hand, all three of these countries can be described as regions where frequent cloud coverage can be expected and, especially in the case of Norway and Finland, high zenith angles. Therefore, estimations from these countries are heavily influenced by the DNI estimation method employed; where Pfenninger has used the BRL method [400,401] to compute DHI from GHI, then allowing for compared to the use of DIRINT [224], here. As discussed by Loutzenhiser [205], no DNI estimation model behaves exceptionally well, and they all exhibit relatively large errors during over cast and times of high zenith angles; since so much of the received irradiance at these times comes from complex diffuse sources.

Figure E.1 takes a deeper look into the validity of the proposed model in relation to the time of day, where the root mean squared error [RMSE] normalized to the average generation and shown as a percentage is given for all daily hours for each country. The top-down order of Figure E.1 is chosen to match the order of Table E.1. For the countries in the top half of this figure, a typical trend wherein a high RMSE, in the range of $10\,\%$ to $20\,\%$, is seen in the early mornings and late evenings, while a much lower RMSE, around $5\,\%$, is seen during mid day. Since the RMSE values shown here are of a relative nature, these high errors are not concerning since these time periods contribute very little to the overall generation. For the bottom half of the the figure, a trimodal trend is observed for many countries wherein there are three clear peaks in RMSE: one in the early morning, one in the late evening, and also one at midday. Norway and Finland represent clear examples of this, however this trend can also be seen for Switzerland, Estonia, Latvia, Sweden, and Lithuania. As before, the set-up uncertainties could lead to the discrepancy seen for these later countries, as could the use of the different irradiance models between the two approaches. Despite this, the errors seen are for the most part small, and considering this alongside the result shown in Table E.1 leads to the conclusion that the PV simulation model behaves as expected, and is at least as valid as the model of Pfenninger et al. [16].

In addition to Pfenninger's study, the Global Solar Atlas (GSA) [206] provides a highly spatially resolved estimate of annually-average FLHs for optimally tilted PV models on a $1\,\mathrm{km}$ grid across the globe[1]. Since the current work can also simulate PV modules at an extremely high spatial resolution, the GSA's estimates can also be directly compared against. According to their description of their methodology, errors in the GSA's irradiance estimations are expected to be in the range of 4 to $8\,\%$ over Europe, and other weather parameters such as wind speed and tempera-

[1] Up until $60\,°$ latitude.

ture are sourced from a climate model simulation. Furthermore, for PV simulation, solar position, terrain-specific albedo, angle of incidence losses, dynamic terrain shading, and typical losses from snow, soiling, power conversion, and cable losses are all included. In order to compare simulation results against the GSA, the same 5 km grid and module mentioned above was simulated between the years 1994 until 2015, since these are the years which correspond to the GSA's estimates in Europe. One difference between the simulations performed when comparing to Pfenninger et al. versus the GSA, is that the optimal tilt angles computed for Figure 4.15 are used in these latter comparisons. In the end the average FLH for each simulated grid point is found, and directly compared against the estimate of GSA at that location. The outcomes of these comparisons are plotted in Figure E.2 to accentuate the close agreement, and mapped in Figure E.3 to display the spatial trends.

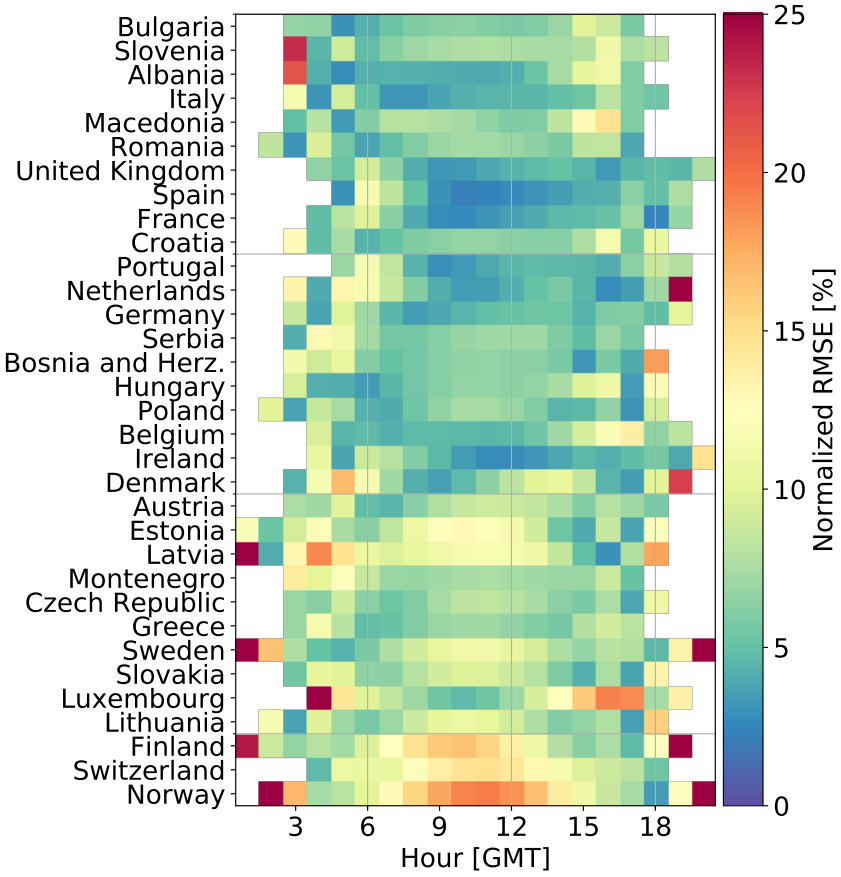

Figure E.1: PV Hourly RMSE compared to Pfenninger et al. [16].

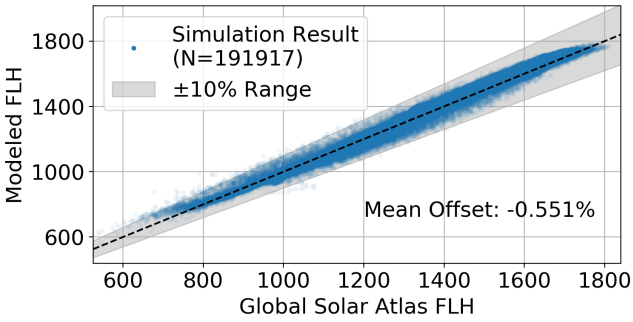

Figure E.2: Result of spatial PV FLH comparison to the Global Solar Atlas [206]

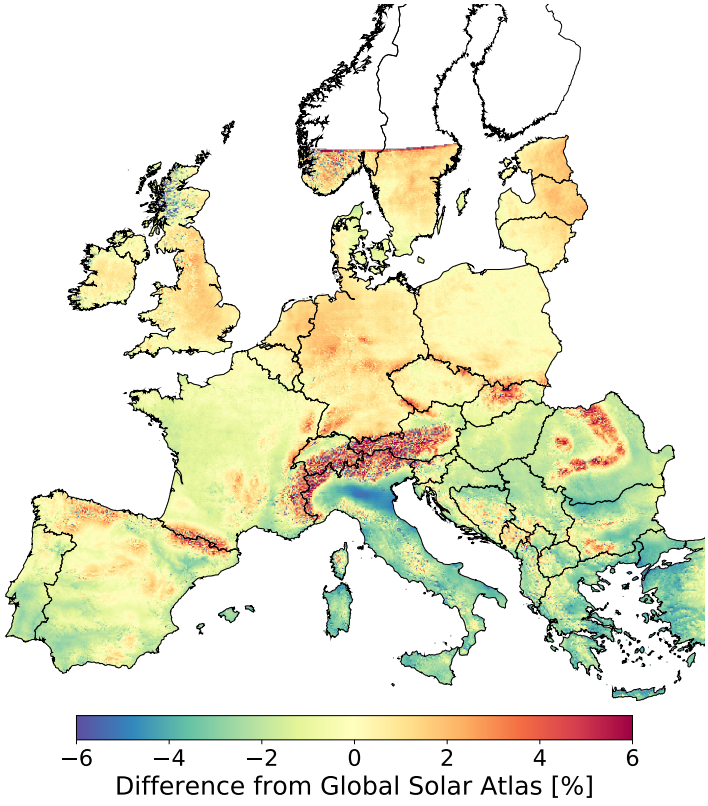

Figure E.3: Spatially resolved PV FLH comparison to the Global Solar Atlas [206]

Considering Figure E.2, it is clear that a very strong correlation between these two sources can be seen; with the average percent difference across all simulation locations at $0.551\,\%$. The vast majority of location are withing a percent difference of $\pm 6\,\%$, although a few locations, primarily those at low FLHs, are seen to have a bias towards over production up to difference of $10\,\%$. In these latter cases, this deviation arises from the different optimal tilt outcomes between the GSA and this work, where it appears that the GSA did not consider diffuse irradiance in their optimal tilt equation. As a result of this the GSA's system tilt angles are steeper than the ones used here, meaning they don't take advantage of the larger sky view as is performed here. In the end, the modules simulated at these locations perform better than the estimates of GSA due to the superior tilt angle selection. Comparing the map of these differences in Figure E.3, it is clear that these differences are found in the regions with high terrain complexity, such as the Alps and central Norway. As seen in the Figure 4.15, these regions correspond to the regions mentioned previously where low tilt angles are selected in the current work to better capture the diffuse radiation. Besides these regions, Figure E.3 makes it clear that differences between the current work's PV simulation scheme and that of the GSA produce very similar results.

As a result of these comparisons, it is seen that the current work shows very strong agreement to two well known PV simulation models in the literature. The comparison to Pfenninger et al. showed a strong temporal correlation, while the comparison to the GSA shows a strong spatial correlation. Therefore, it is concluded that the PV simulation scheme of this work operates as intended and can be depended upon for high fidelity PV simulations in Europe.

Chapter F

Lull Modeling

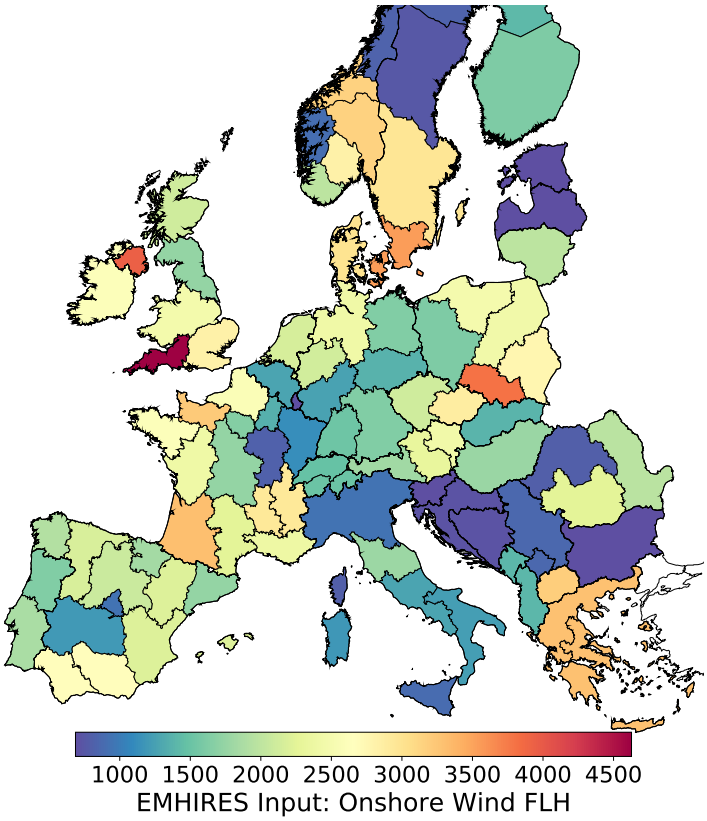

Figure F.1: Average Onshore Wind FLH from aggregated EMHIRES data [180] for weather year 2015

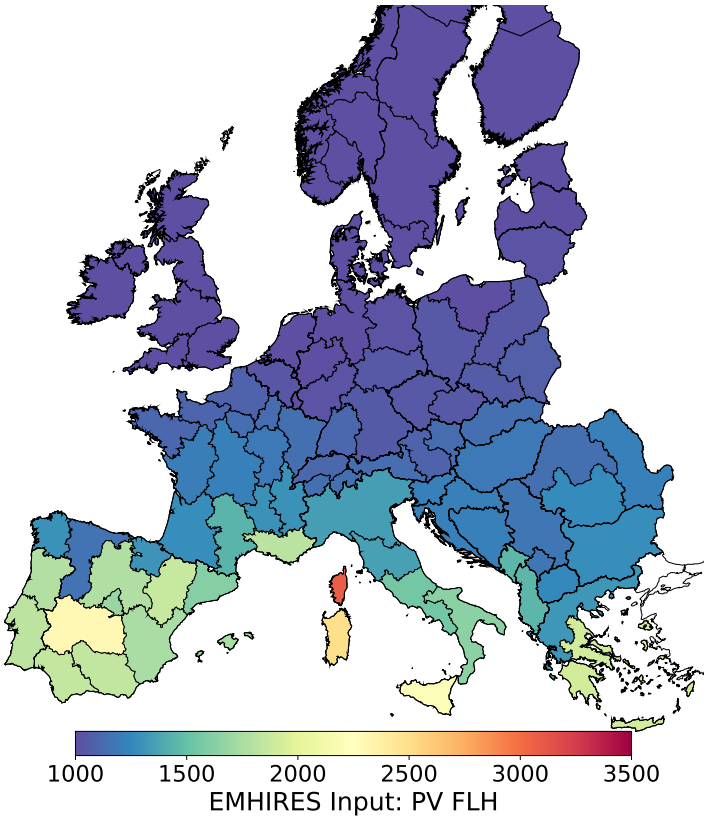

Figure F.2: Average PV FLH from aggregated EMHIRES data [312] for weather year 2015

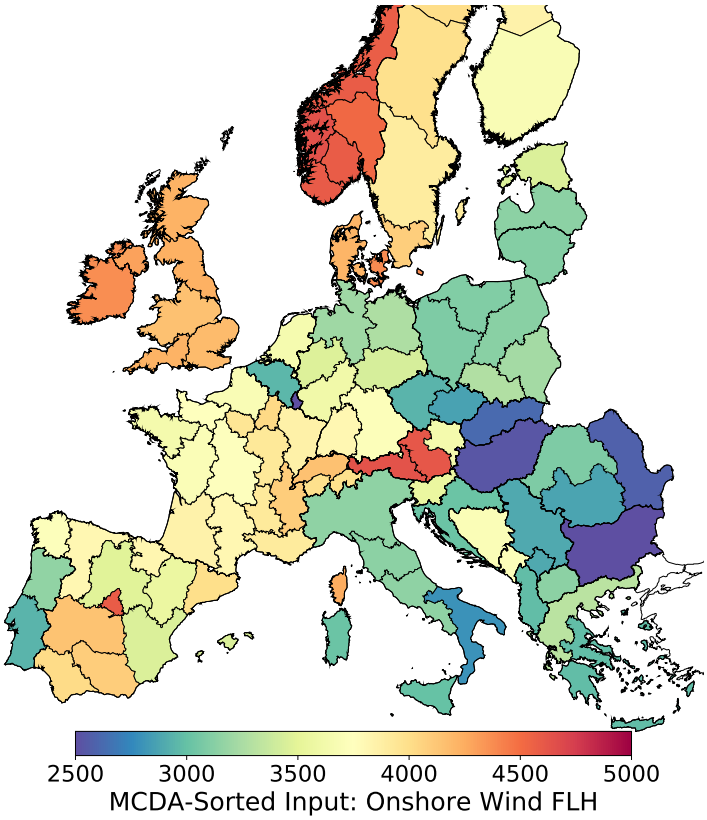

Figure F.3: Average Onshore Wind FLH from MCDA-sorted turbine locations for weather year 2015

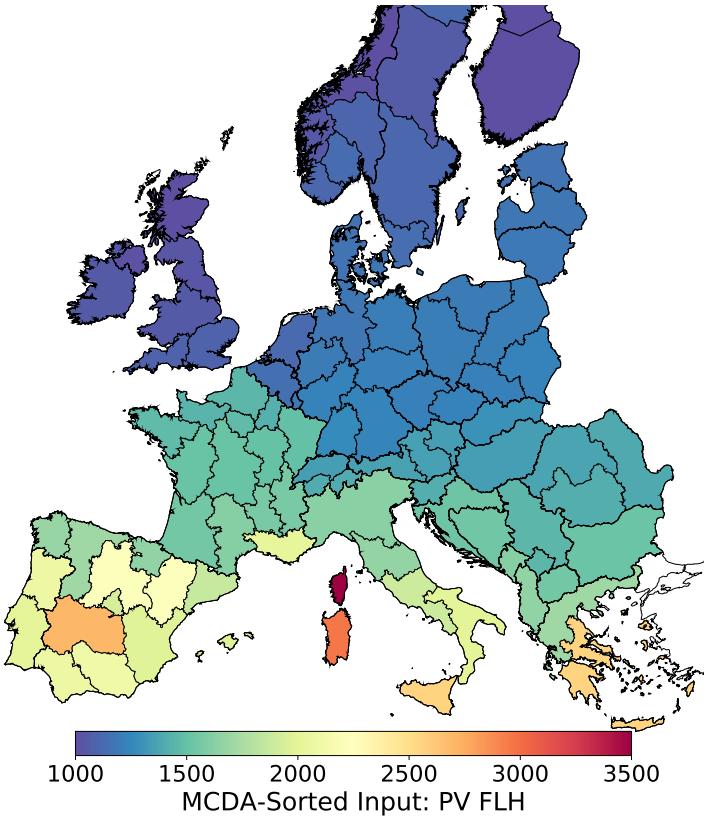

Figure F.4: Average PV FLH from MCDA-sorted park locations for weather year 2015

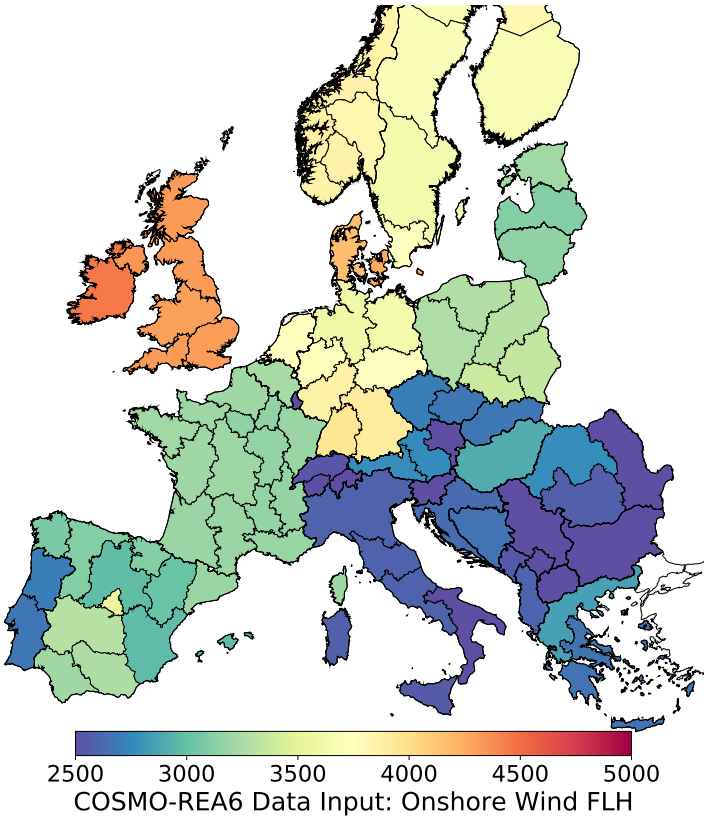

Figure F.5: Average Onshore Wind FLH from COSMO-REA6 weather data [123] in weather year 2015

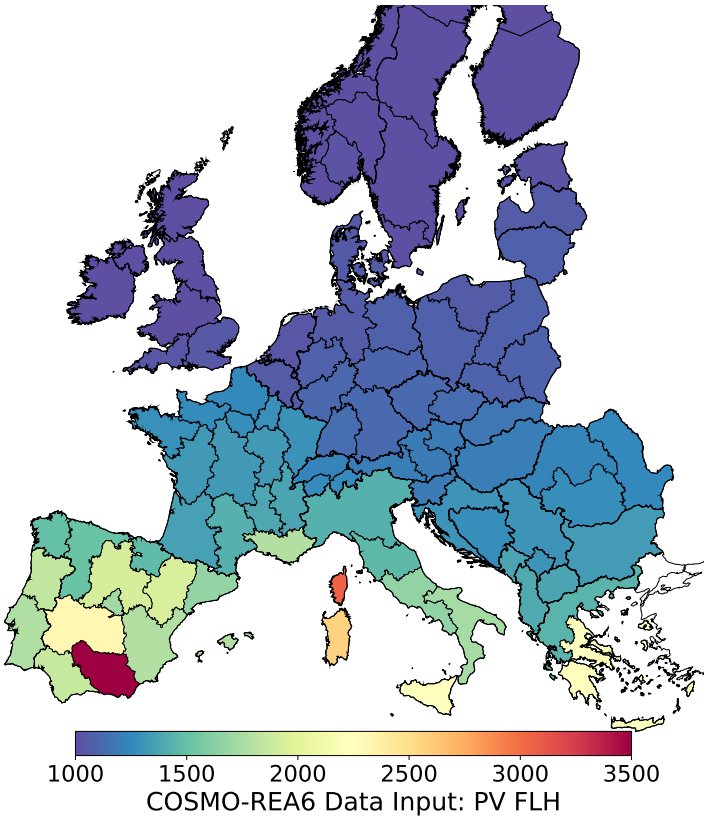

Figure F.6: Average PV FLH from COSMO-REA6 weather data [123] in weather year 2015

Chapter G

Extra VRES Potentials Results

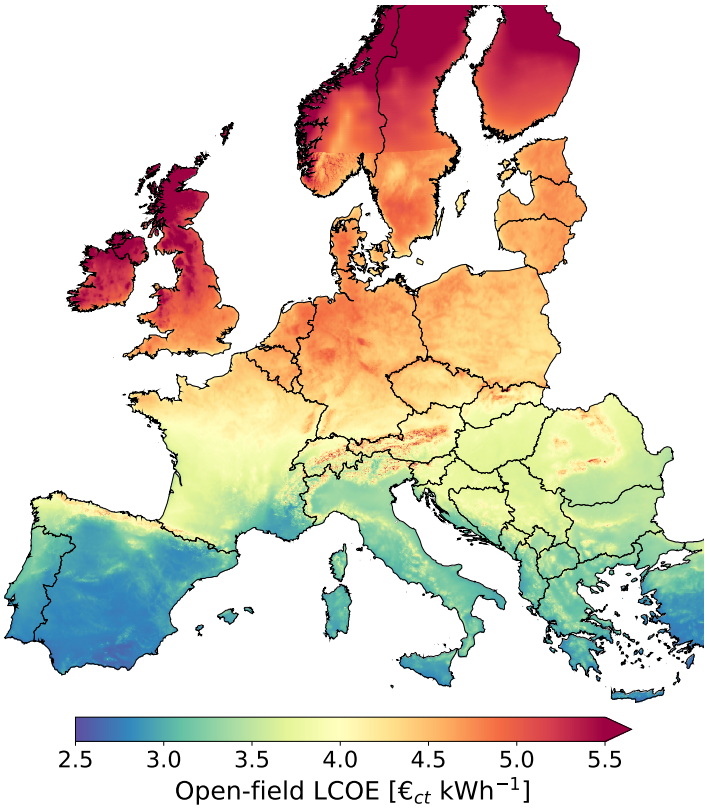

Figure G.1: Average estimated LCOE for open-field PV parks mapped across Europe. Land eligibility is not included.

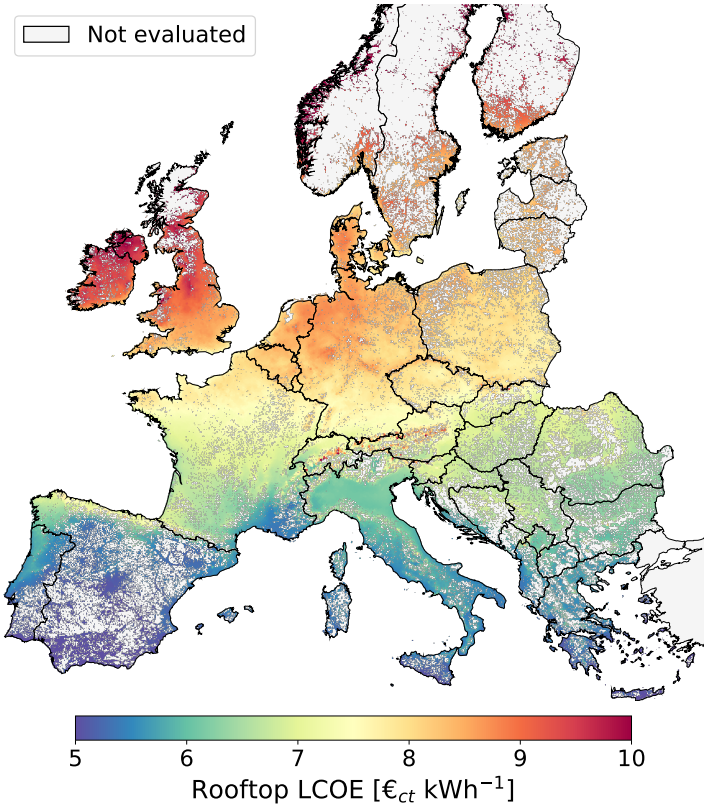

Figure G.2: Average estimated LCOE for rooftop PV zones mapped across Europe. Note that land eligibility is not accurately represented due to the display resolution.

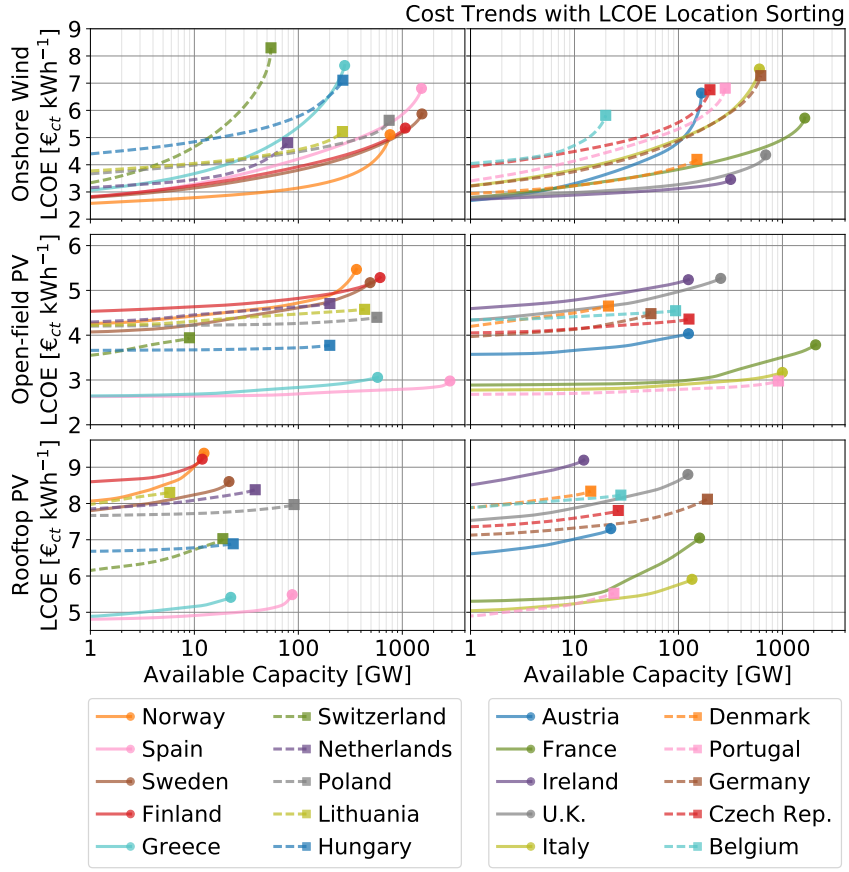

Figure G.3: Average LCOE trends for onshore wind, open-field PV, and rooftop PV versus installed capacity per country. Placements sorted by LCOE. Onshore wind results previously published in Ryberg et al. [109].

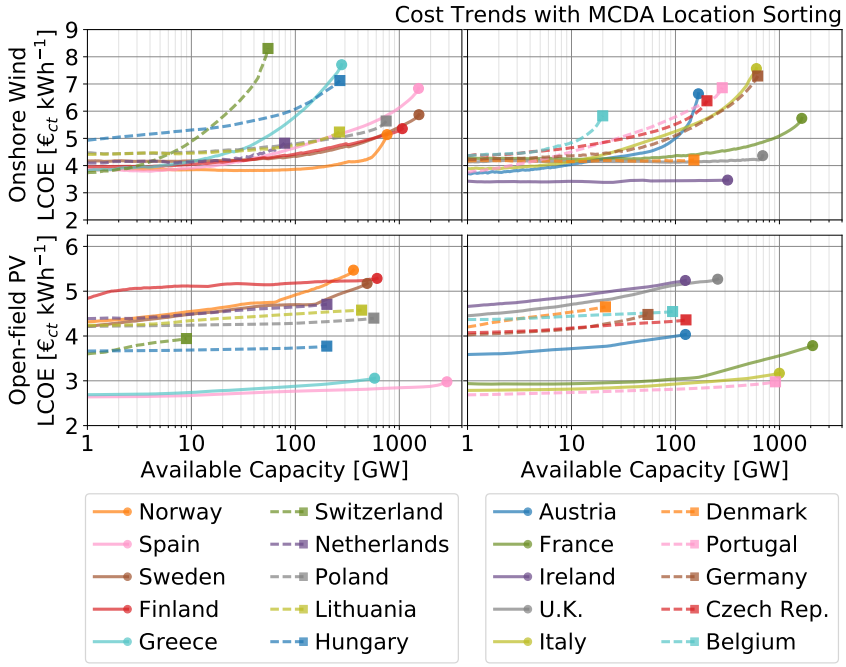

Figure G.4: Average LCOE trends for onshore wind, open-field PV, and rooftop PV versus installed capacity per country. Placements sorted by the MCDA approach of Tlili et al. [50].

Table G.1: Impact of economic limitations on onshore wind capacity. Previously published in Ryberg et al. [109].

	Available Capacity [GW]			
Area	Maximal	$\leq 10 \frac{€_{ct}}{kWh}$	$\leq 6 \frac{€_{ct}}{kWh}$	$\leq 4 \frac{€_{ct}}{kWh}$
Europe	13,418	12,896	7315	1177
France	1640	1623	1103	68
Sweden	1545	1532	895	69
Spain	1530	1458	534	26
Finland	1069	1069	851	48
Norway	762	744	572	250
Poland	747	743	554	4.3
United Kingdom	690	685	655	260
Germany	618	569	145	8.5
Italy	600	536	153	6.8
Romania	554	505	73	2.4
Ireland	318	318	318	292
Portugal	282	266	98	2.8
Greece	279	237	69	8.6
Serbia	274	249	31	1.8
Hungary	268	263	61	0.05
Lithuania	265	265	226	2.9
Latvia	238	238	185	2.8
Bulgaria	231	198	20	0.31
Bosnia & Herz	209	190	79	15
Czech Republic	201	191	74	0.54
Estonia	178	178	151	6.3
Austria	166	150	94	15
Denmark	151	151	151	53
Croatia	135	132	44	3.3
Slovakia	85	73	28	0.71
Netherlands	79	79	69	19
Albania	58	48	15	2.3
Montenegro	55	51	25	4.0
Macedonia	55	39	6.7	0.42
Switzerland	55	44	13	1.9
Slovenia	31	26	5.0	0.52
Kosovo	27	23	4.1	0.48
Belgium	20	20	13	0.28
Luxembourg	2.6	2.5	0.18	0.05

Table G.2: Impact of economic limitations on onshore wind generation. Previously published in Ryberg et al. [109].

	Available Generation [TWh]			
Area	Maximal	$\leq 10 \frac{€_{ct}}{kWh}$	$\leq 6 \frac{€_{ct}}{kWh}$	$\leq 4 \frac{€_{ct}}{kWh}$
Europe	34,341	33,622	22,008	4614
France	4306	4284	3173	256
Sweden	3990	3972	2593	262
Spain	3496	3398	1503	103
Finland	2940	2940	2440	183
Norway	2327	2302	1951	999
Poland	1941	1935	1529	16
United Kingdom	2262	2254	2192	996
Germany	1330	1261	404	32
Italy	1309	1221	443	28
Romania	1163	1093	205	10
Ireland	1254	1254	1254	1176
Portugal	648	627	274	11
Greece	601	542	211	35
Serbia	567	533	94	7.6
Hungary	583	576	161	0.19
Lithuania	733	733	645	10
Latvia	637	637	519	10
Bulgaria	456	409	55	1.3
Bosnia & Herz	505	481	251	62
Czech Republic	453	440	202	2.0
Estonia	494	494	433	23
Austria	434	414	298	65
Denmark	501	501	501	197
Croatia	321	317	129	14
Slovakia	188	171	80	2.9
Netherlands	238	238	216	71
Albania	126	113	47	9.6
Montenegro	136	130	77	16
Macedonia	107	85	21	1.7
Switzerland	116	102	40	8.0
Slovenia	66	60	16	2.3
Kosovo	56	49	13	1.9
Belgium	52	51	38	1.0
Luxembourg	5.3	5.1	0.49	0.15

Table G.3: Impact of economic limitations on open-field PV capacity potential

	Available Capacity [GW]			
	Maximum	$\leq 6\ \frac{€_{ct}}{kWh}$	$\leq 4\ \frac{€_{ct}}{kWh}$	$\leq 3\ \frac{€_{ct}}{kWh}$
Europe	14,475	13,926	9559	438
Spain	2871	2871	2871	173
France	2085	2085	1325	18.2
Italy	995	995	995	44.9
Portugal	917	917	917	90.1
Finland	601	400	0.00	0.00
Croatia	588	588	588	0.00
Greece	573	573	573	111
Poland	566	566	0.00	0.00
Serbia	559	559	559	0.00
Sweden	486	345	0.00	0.00
Bosnia and Herz.	474	474	474	0.00
Lithuania	431	431	0.00	0.00
Latvia	407	407	0.00	0.00
Romania	355	355	296	0.00
Norway	327	121	0.00	0.00
Bulgaria	259	259	259	0.00
United Kingdom	254	251	1.09	0.00
Netherlands	201	201	0.17	0.00
Hungary	201	201	156	0.00
Estonia	196	196	0.00	0.00
Macedonia	131	131	131	0.00
Czech Republic	126	126	0.88	0.00
Austria	125	125	45.9	0.00
Ireland	124	124	0.00	0.00
Albania	102	102	102	0.00
Kosovo	98.6	98.6	98.6	0.00
Montenegro	96.9	96.9	96.9	0.00
Belgium	94.0	94.0	0.00	0.00
Slovakia	81.4	81.4	2.80	0.00
Slovenia	59.9	59.9	59.9	0.00
Germany	54.4	54.4	1.54	0.00
Denmark	20.9	20.9	0.00	0.00
Switzerland	8.98	8.98	5.39	0.00
Luxembourg	6.20	6.20	0.00	0.00

Table G.4: Impact of economic limitations on open-field PV generation potential

	Available Generation [TWh]			
	Maximum	$\leq 6\ \frac{€_{ct}}{kWh}$	$\leq 4\ \frac{€_{ct}}{kWh}$	$\leq 3\ \frac{€_{ct}}{kWh}$
Europe	21,117	20,663	15,546	836
Spain	4914	4914	4914	330
France	3039	3039	2027	34.0
Italy	1660	1660	1659	83.9
Portugal	1606	1606	1606	172
Finland	579	408	0.00	0.00
Croatia	873	873	873	0.00
Greece	1009	1009	1009	216
Poland	688	688	0.00	0.00
Serbia	833	833	833	0.00
Sweden	486	370	0.00	0.00
Bosnia and Herz.	714	714	714	0.00
Lithuania	471	471	0.00	0.00
Latvia	441	441	0.00	0.00
Romania	506	506	427	0.00
Norway	290	126	0.00	0.00
Bulgaria	407	407	407	0.00
United Kingdom	276	274	1.55	0.00
Netherlands	246	246	0.23	0.00
Hungary	281	281	220	0.00
Estonia	208	208	0.00	0.00
Macedonia	210	210	210	0.00
Czech Republic	166	166	1.22	0.00
Austria	173	173	66.2	0.00
Ireland	136	136	0.00	0.00
Albania	171	171	171	0.00
Kosovo	154	154	154	0.00
Montenegro	152	152	152	0.00
Belgium	117	117	0.00	0.00
Slovakia	109	109	3.89	0.00
Slovenia	86.9	86.9	86.9	0.00
Germany	69.4	69.4	2.14	0.00
Denmark	25.1	25.1	0.00	0.00
Switzerland	12.5	12.5	7.65	0.00
Luxembourg	7.85	7.85	0.00	0.00

Table G.5: Impact of economic limitations on rooftop PV capacity potential

	Available Capacity [GW]			
	Maximum	$\leq 10 \frac{€_{ct}}{kWh}$	$\leq 8 \frac{€_{ct}}{kWh}$	$\leq 6 \frac{€_{ct}}{kWh}$
Europe	706	701	513	107
Germany	111	111	73.1	0.00
France	93.0	93.0	88.1	10.4
Italy	78.7	78.7	78.7	30.0
United Kingdom	71.8	71.7	18.2	0.00
Poland	53.0	53.0	25.9	0.00
Spain	50.9	50.9	50.9	38.2
Romania	28.4	28.4	28.4	0.00
Netherlands	22.4	22.4	11.1	0.00
Belgium	16.3	16.3	5.01	0.00
Czech Republic	15.4	15.4	15.4	0.00
Portugal	13.9	13.9	13.9	13.7
Hungary	13.8	13.8	13.8	0.00
Greece	13.0	13.0	13.0	10.9
Austria	13.0	13.0	13.0	0.00
Sweden	12.6	11.8	0.53	0.00
Serbia	11.7	11.7	11.7	0.00
Switzerland	11.0	11.0	11.0	0.00
Bulgaria	9.48	9.48	9.48	0.24
Denmark	8.36	8.36	1.16	0.00
Slovakia	8.23	8.23	8.23	0.00
Norway	7.21	4.73	0.00	0.00
Ireland	7.15	7.15	0.34	0.00
Finland	6.94	4.97	0.00	0.00
Croatia	6.20	6.20	6.20	0.73
Bosnia and Herz.	4.69	4.69	4.69	0.04
Albania	3.54	3.54	3.54	2.73
Slovenia	3.53	3.53	3.53	0.00
Lithuania	3.38	3.38	0.00	0.00
Macedonia	2.58	2.58	2.58	0.02
Latvia	2.21	2.21	0.12	0.00
Estonia	1.66	1.66	0.00	0.00
Luxembourg	0.83	0.83	0.83	0.00
Montenegro	0.81	0.81	0.81	0.22

Table G.6: Impact of economic limitations on rooftop PV generation potential

	Available Generation [TWh]			
	Maximum	$\leq 10 \frac{€_{ct}}{kWh}$	$\leq 8 \frac{€_{ct}}{kWh}$	$\leq 6 \frac{€_{ct}}{kWh}$
Europe	875	871	674	169
Germany	125	125	85.0	0.00
France	117	117	112	16.2
Italy	113	113	113	46.8
United Kingdom	76.2	76.1	21.1	0.00
Poland	58.3	58.3	29.3	0.00
Spain	79.1	79.1	79.1	61.0
Romania	36.4	36.4	36.4	0.00
Netherlands	25.0	25.0	12.8	0.00
Belgium	18.0	18.0	5.63	0.00
Czech Republic	18.0	18.0	18.0	0.00
Portugal	22.0	22.0	22.0	21.7
Hungary	17.1	17.1	17.1	0.00
Greece	20.9	20.9	20.9	17.7
Austria	16.1	16.1	16.1	0.00
Sweden	12.8	12.1	0.60	0.00
Serbia	15.7	15.7	15.7	0.00
Switzerland	13.6	13.6	13.6	0.00
Bulgaria	13.3	13.3	13.3	0.36
Denmark	8.98	8.98	1.30	0.00
Slovakia	9.81	9.81	9.81	0.00
Norway	6.58	4.64	0.00	0.00
Ireland	7.19	7.19	0.38	0.00
Finland	6.36	4.74	0.00	0.00
Croatia	8.22	8.22	8.22	1.09
Bosnia and Herz.	6.23	6.23	6.23	0.06
Albania	5.30	5.30	5.30	4.13
Slovenia	4.56	4.56	4.56	0.00
Lithuania	3.34	3.34	0.00	0.00
Macedonia	3.70	3.70	3.70	0.03
Latvia	2.18	2.18	0.13	0.00
Estonia	1.61	1.61	0.00	0.00
Luxembourg	0.94	0.94	0.94	0.00
Montenegro	1.15	1.15	1.15	0.33

Chapter H

VRES Lull Extra Results

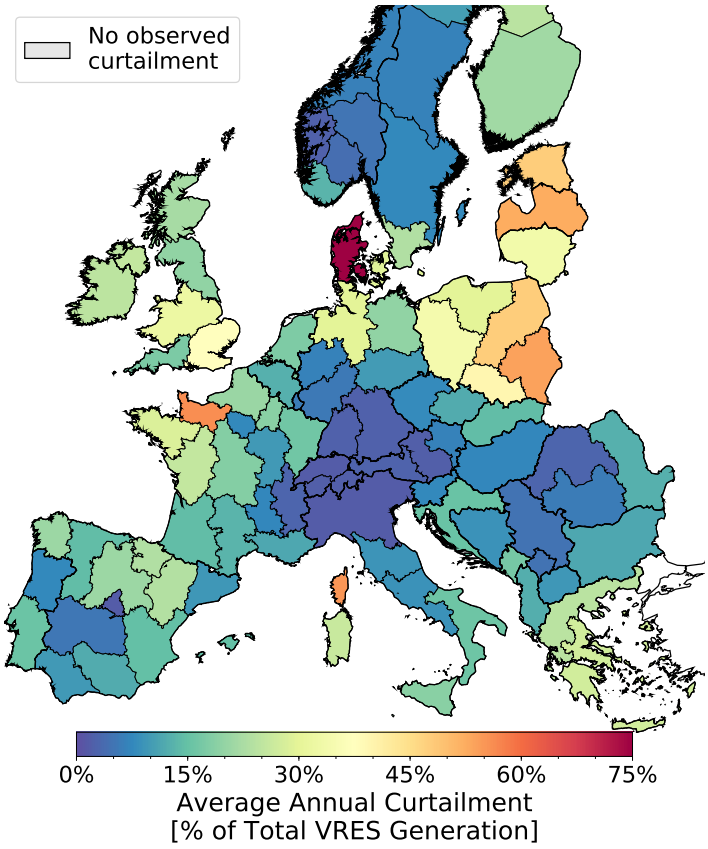

Figure H.1: Maximum curtailment percentage of each E-Highway Region in the Power Flow context

Chapter I

Sensitivity Analyses

The VRES lull analysis described in the previous sections provides a detailed look into lull occurrence at a level which, until now, has not been available in the literature. Nevertheless, the results produced will be intimately tied to the specifics of the selected E-Highway scenario, and would likely change in hard-to-predict ways if the energy system were constructed differently. Therefore, in addition to the results available in the primary analysis, several sensitivity analyses are performed to better understand how lull observations could change.

In all, 5 sensitivity analysis are performed which each alter one key piece of the primary analysis' "Power Flow" context (Section 5.5.3). Due to data availability restrictions, it is not possible to perform each of these sensitivity analyses for all demand-generation years used in the primary analysis. Therefore, only 2015 was selected for both the demand and generation year for all sensitivity analyses on account of it's above-average lull observance rate and due to its applicability for all performed sensitivities. This also allows a better comparability in between the sensitivity results. Because of this, discussion will focus on the relative difference between the sensitivity analysis' lull spans and deficits versus that of the primary analysis for the same demand-generation year.

In the following sections the setup of each performed sensitivity analyses is described, followed a short discussion of the observed changes compared to the primary analysis and their implications. The chosen sensitivities are as follows: First the effect of altering VRES capacity across all E-Highway regions is investigated to see the impact of increased or decreased VRES generation on the overall system. Next the power flow evaluation is performed with copper plates within each country, which equates to the system being evaluated with countries as single nodes. Since this type of evaluation is commonly seen in the literature, this test will estimate how this simplification of the overall system can impact lull occurrence. Afterwards, the next three sensitivities replace the VRES generation time-series of each E-Highway region with that from another source. These sources include: the EMHIRES datasets for wind [180] and PV [312] are used, the time-series arising from applying this work's simulation approach to MCDA-sorted[1] turbine and PV park locations, and finally the time-series arising from using the COSMO-REA6 [194] climate model dataset in place of the MERRA [179] dataset[2].

[1] Which alters the order of selected locations within each E-Highway region according to several criteria. As opposed to the simpler LCOE-sorting used in the primary analysis.

[2] Using the same LCOE-sorted locations as in the primary analysis

I.1 Installed Capacity Scaling

I.1.1 Set Up

The first sensitivity analysis considers how changing the installed VRES capacities might impact lull occurrence. A more detailed analysis should redesign regional capacities via optimization, although implementation of such a procedure is far outside the scope of the current work. Nevertheless, in order to approximate how changing capacities might impact VRES lulls, the capacities specified within the E-Highway scenario (Figure 5.2) will be uniformly scaled between $\pm 20\,\%$. By performing this scaling, one expected response of the overall energy system is that, when capacities are reduced, an increased reliance on backup generation as well as import and exports between regions should be observed, and vice versa.

Every second percentage within this range is evaluated for this sensitivity and, in each case as well as for each region, the following procedure is followed. First, the scaled capacity for each VRES technology is computed from the base E-Highway value and the full LCOE-sorted placement procedure (Section 2.5) is performed. This gives a new set of generator units for each region as compared to the base lull analysis, which therefore must be re-simulated according to the procedures outlined in Section 3 for Wind and Section 4 for PV. As described in 5.4, PV capacities are still evenly split between the open-field and rooftop domains. To note, when increasing capacities in Switzerland, the required capacity slightly exceeded the full PV potential. This is not considered to be an issue, however, since additional PV sources are available which were not included in this analysis; such as north-facing roofs and building facades. Furthermore, an additional open-field land eligibility scenario such as the one evaluated for Germany in Section 6.1.4 could have been considered to slightly increase available open-field PV capacity. Therefore, the total PV time-series in the case of Switzerland is simply scaled to match the specified capacity. In any case, at this point new time-series are available for each VRES technology within each region, which simply replace the ones used in the base analysis. Since evaluation of this procedure at each scaling percentage results in a new time-series, both the total generation as well as the average FLH are affected. For instance, when scaling capacities down, the overall wind and PV generation will decrease, however as the LCOE-sorting procedure will select a cheaper subset of turbine and PV park locations in terms of LCOE[3] the FLHs will slightly increase.

I.1.2 Outcomes

Figure I.1 shows the outcomes of the capacity scaling sensitivity. Along with the change in the longest PFL span and deepest PFL deficit, this figure also shows the the change in the largest residual load, total curtailment, and total utilization of VRES generation. The same regional scopes shown when presenting the primary lull occurrence results are again given here, in addition to the total value found after

[3] Generally low LCOE turbine and PV park locations correspond to higher FLH, but this is not always the case.

summing, or averaging in the case of PFL spans, the individual contributions of each E-Highway region.

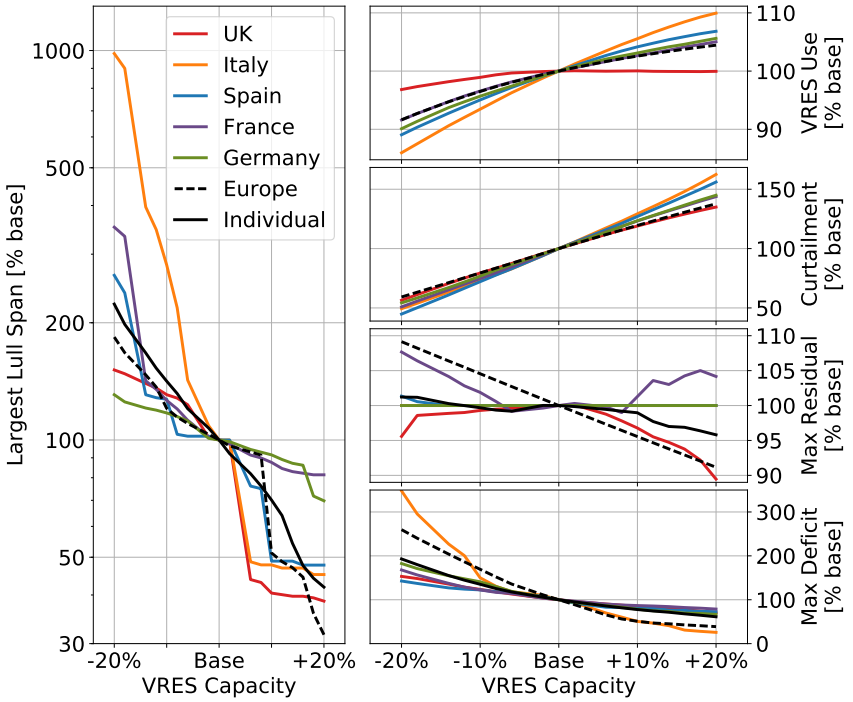

Figure I.1: VRES lull sensitivity to changes in regional VRES capacity

The left plot of Figure I.1 gives the change of the largest observed lull throughout the entire sensitivity year. All regional scope are seen to possess an anti-correlated response to VRES capacity changes that are more pronounced for capacity reductions than for capacity increases. For most scopes, a $20\,\%$ capacity reduction would lead to a doubling of the longest lull span observed, with the exception of France, where lull span increases by a factor of $3.5\,\mathrm{x}$, and Italy, with an increase factor of $9.8\,\mathrm{x}$. As can be seen by the PFL deficit occurrence trend of Figure 7.8, the large lull growth in Italy is primarily a function of the extraordinarily small lulls Italy experienced in the primary analysis. For a $20\,\%$ increase in VRES capacity, most regional scopes show a reduction of the longest lull span to $40\,\%$ of the base value. France and Germany are exceptions to this, where the lull reduction are limited to $81.4\,\%$ and $69.8\,\%$, respectively, on account of their high reliance on imports. Of all countries shown, Germany appears to have the least lull spans sensitivity to capacity scaling, which is perhaps a result of its geographically central position in the energy system.

The bottom right plot shows the change in the largest lull deficit observed, which

displays a similar asymmetric anti-correlated trend as the lull spans. In this case the typical response to a $20\,\%$ capacity decrease is to increase lull deficits to $160\,\%$ of their base value, and to shrink to $70\,\%$ of the base when capacities are increased by $20\,\%$. Once again, Italy is seen to be an exception on account of its small PFL deficits. Figure I.2 shows the sensitivity of the largest lull deficit over the E-Highway regions for scaling factors of -20, -10, 10, and $20\,\%$. From this perspective, the Italy's large relative deficit increase when VRES capacities are reduced is seen to come from the central Italian regions, while the northern Italian regions are largely responsible in the opposite case. Nevertheless, it is also seen that countries such as Switzerland, Finland, Estonia and Latvia have an even stronger relative sensitivity than Italy. Referring to the estimation of storage need in Europe in the primary analysis ($8.56\,\text{TWh}$ when summed regionally), it stands to reason that the size of this storage need would likely rise to around $16.9\,\text{TWh}$ if the VRES capacity were to be decreased by $20\,\%$. This estimate is much closer to the values proposed by Cebulla et al. [350], which suggests that a re-optimized distribution of VRES capacities would likely bring the total storage estimates more in line with the literature.

VRES utilization is also impacted by capacity scaling. Total VRES generation, not shown, gives a nearly uniform direct linear trend for all regions, which is slightly less than a one-to-one relationship of total VRES generation and VRES Capacity. Ultimately, in the $-20\,\%$ case, total VRES production sums to around $84\,\%$ of electricity demand, while, in the opposite case, sums to $125\,\%$. Shown in Figure 7.8, there is a common linear response to VRES curtailment for all regions in the range of a 2.5-to-$1\,\%$ change in total annual curtailment for each change in VRES capacity. Similarly, actual VRES usage, presented in the top right, increases as the capacity increases, but the response is again biased. A $20\,\%$ capacity reduction typically corresponds to a $9\,\%$ reduction in total VRES usage, while a $20\,\%$ capacity increase typically increases VRES usage by $5\,\%$. Notice that, for the $-20\,\%$ capacity case, the total VRES generation is reduced by slightly less than $20\,\%$, since a higher proportion of strong wind and strong PV locations are utilized, so the relative VRES usage is actually increasing in this case by $13.56\,\%$. This higher usage percentage impacts the effective VRES electricity cost and, returning to the LCOE comparison to Child et al. [358], suggests that reducing the VRES capacity in the base analysis by $20\,\%$ would reduce the effective LCOE contribution from VRES generation to $3.7\,\text{ct}_€\,\text{kWh}^{-1}$; which, compared to the $4.2\,\text{ct}_€\,\text{kWh}^{-1}$ is significantly closer to the value suggested by Child et al.

Finally, the largest residual (maximum backup capacity) trend portrays an interesting dynamic. When evaluated across all of Europe, a strong inverse linear relationship is seen where there is a $1\,\%$ rise in the largest residual for each $2\,\%$ decrease in VRES capacity. This value is directly translatable to the total European backup estimate of $498\,\text{GW}$ made at the end of the Section 7.3.2, which agreed very well with the literature, and logically suggests that this value is directly tied to the amount of VRES installed in the system. However this plot also shows that the same quantity, evaluated individually for all regions and summed, shows almost no sensitivity to VRES capacity scaling. This latter value corresponds directly to the $738.5\,\text{GW}$ backup capacity estimate found from Figure 7.12, and strongly suggests that it is

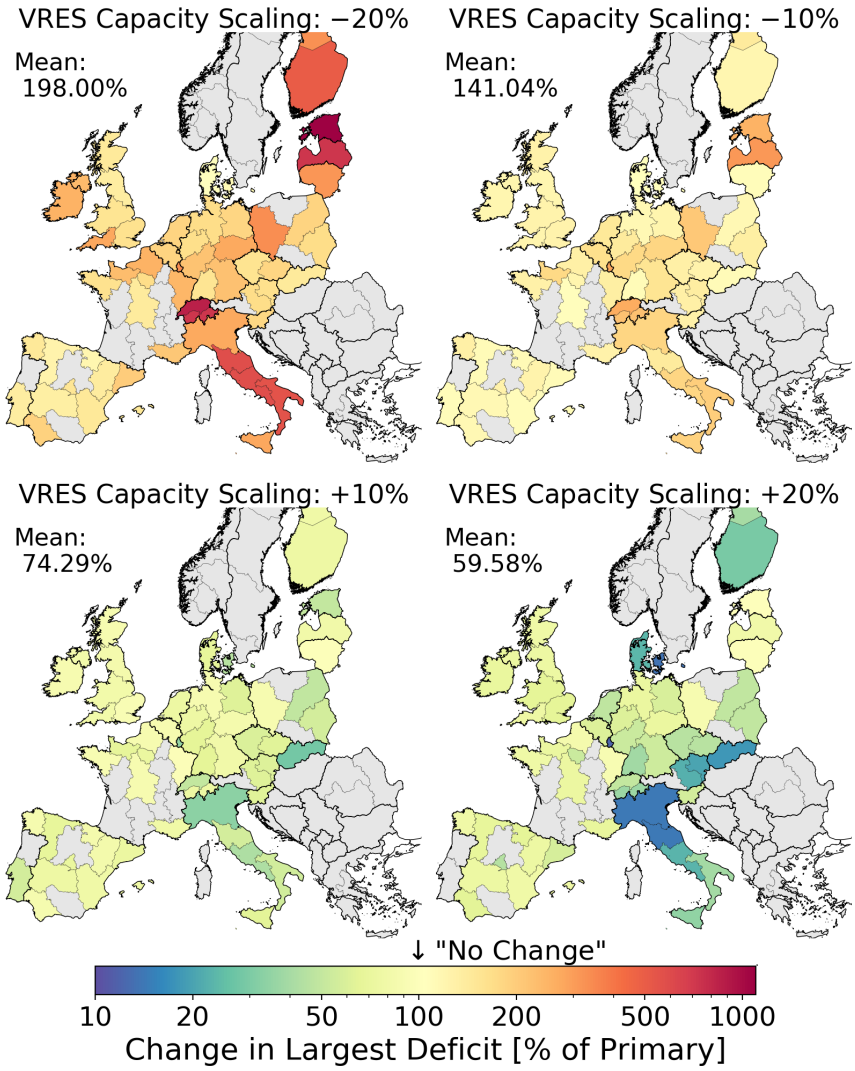

Figure I.2: Spatially sensitivity of the largest lull deficit to VRES capacity scaling

not a sensitive quantity so long as the system is still predominantly based on VRES generation. Other countries, such as France and the UK, show much more varied responses which occur as a result of their unique roles in the energy system shifting. Compared to the required backup capacity, summed residual loads (i.e. total backup generation), not shown in Figure I.1, are seen to have a typical sloping trend for almost all regions, which, for Europe, begins at $181\,\%$ of the base backup

usage when $-20\,\%$ VRES capacity is installed, and ending at $55.7\,\%$ of the base backup usage at $20\,\%$ VRES capacity[4]. Translating this to the primary evaluation's average backup reliance of $15.54\,\%$ suggests that this value could to rise to around $28\,\%$ or shrink to nearly $9\,\%$ depending on how much VRES capacity is installed. Nevertheless, these values are not out of line with annual backup usage estimates made in the literature, as these are generally given for European systems where total demand and total VRES generation are equal[5].

I.2 National Aggregation

The next sensitivity sheds light on the impact of regionalization on the outcome of lull occurrence by simplifying the system to single-node nations. Evaluating large scale energy systems with nations as single nodes is common in the literature; such as Wohland et al. [348], Schlachtberger et al. [356], Rasmussen et al. [351], and Rodriguez et al. [357]. Nevertheless, by neglecting grid dynamics within countries, this is likely to greatly reduce the impact of VRES variability on the end result. Therefore, the outcome of this sensitivity will shed light on how the results of these previous analysis might change if a higher spatial resolution were considered. In the same way, these results also suggest how the results obtained from the analysis made in this work might change if a higher spatial resolution scenario were developed.

One explicit method to perform this sensitivity would require aggregating all capacities and clustering the grid lines to fit the national-node setup. However, for this sensitivity, a simpler approach is taken wherein the full gridded Power Flow procedure is carried out with the one adjustment of removing all grid impediments within nations; i.e. by setting line capacities to, effectively, infinite. This allows each nation to operate as if it were a single node and, additionally, allows for the direct comparison of the resulting differences at the regional level. Besides this change, all capacities, cost, and time-series remain the same as the primary analysis.

The map shown in Figure I.3 provides the outcome of this result, as well as the latter sensitivities for ease of comparison, in reference to the percent difference from the primary analysis. Regions which previously did not observed a lull are colored gray.

In Figure I.3 it is seen that most regions either show no change in the largest deficit, or else are reduced to around half of their previous value. A few regions, however, appear to have large increases in their deficit; such as Switzerland, Latvia, Estonia, and Southern Italy; all of which see a deficit increase by nearly a factor of 5. However, when taking a weighted average[6] of the changes seen for this sensitivity, it is seen that there is a typical reduction in deficits to $68.37\,\%$ of that seen in the base analysis. Projecting to the larger context, this sensitivity result suggests that

[4] For visual reference, see the 'Individual' curve on the Max Deficit trend

[5] In the present work, scaling capacities by $0.94\,\mathrm{x}$ causes total VRES annual generation to exactly match total annual demand.

[6] Weighted by the lull deficits seen in the primary analysis.

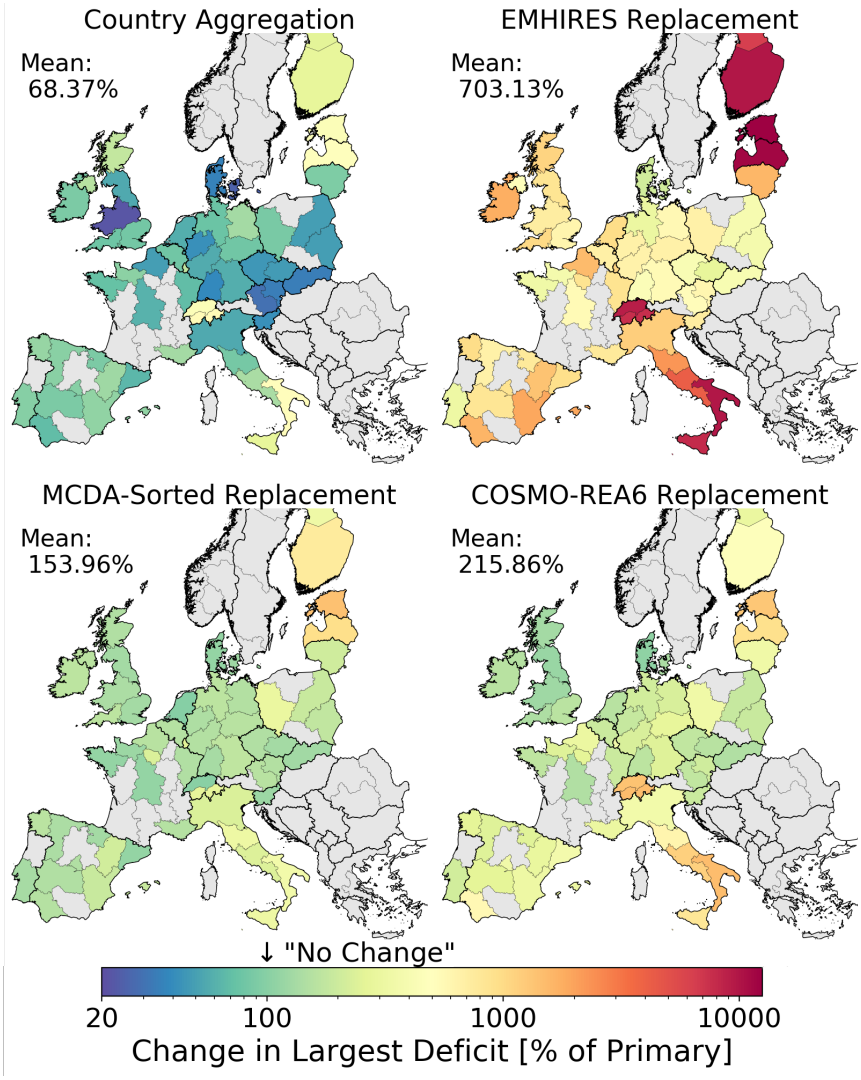

Figure I.3: Spatially sensitivity of the largest lull deficit

modeling the European electricity grid with one node per country is likely to under predict the impact of VRES lulls.

I.3 VRES Replacement: EMHIRES Input

For the first VRES replacement sensitivity, the new VRES time-series is taken directly from the literature. To assist with the work of research groups dealing with energy system design, the JRC has developed their EMHIRES dataset [180, 312]. As this dataset is recently released and moreover made freely available, it is likely to be used by other research group in the future and thus this sensitivity serves as a potential point of reference. Key features of this dataset include the simulation of onshore and offshore wind turbines as well as PV modules across Europe using the same MERRA weather data set used here. Furthermore, EMHIRES' simulation schemes are quite close to the ones used here. One key difference between simulation schemes, however, is their use of a contemporary design context of the wind turbines and PV modules. Additionally, when simulating wind turbines, JRC performs a spatial adjustment like the long-run-average adjustment discussed in Section 3.6, although they do not specify land-cover-dependent roughness lengths when performing vertical projection as is performed here. Nevertheless, the fact that both sources make use of the MERRA dataset mean that the resulting wind and PV time-series are highly correlated with one another.

Ultimately, the EMHIRES dataset provides capacity factor time-series over 37 weather years for onshore wind, offshore wind, and PV at the NUTS2 level across Europe. Use of this dataset allows for a high fidelity consideration of VRES generation. At the same time, however, this dataset also requires adhering to the technological and spatial assumptions of JRC. JRC's contemporary stance means that the wind turbines and PV modules simulated will produce FLHs comparable to those produced today. Therefore this sensitivity analysis can also be viewed as a comparison between the use of contemporary versus future-oriented VRES generator designs. Similarly, as the NUTS2 regions are still quite large, a single time-series at this level is still an over simplification of the spatial variability of VRES generators in these regions. As JRC does not perform land eligibility, placement, and unit selection procedures as is done here, the time-series available in this dataset will be comprised of a mix of eligible, ineligible, strong FLH, and weak FLH locations that likely will not reflect an opportunistic distribution.

With these features in mind, this sensitivity analysis is constructed by identifying which NUTS2 regions are within each E-Highway region and combing their time-series profiles. As the E-Highway regions are largely defined by political boundaries and do not cross international borders, there was no instance where a NUTS2 region spanned more than one E-Highway region. Since it is not known how much wind and PV potential JRC intended within each NUTS2 region, the capacity factor time-series are combined via an area-weighted average when multiple NUTS2 regions are located within a single E-Highway region. These combined time-series are then scaled to match the E-Highway's specified capacities. In the end, the average FLH for onshore wind and PV are shown in Figure F.1 and F.2; which, especially for wind, are noticeably less than the FLHs arrived at from the simulation schemes developed in this work.

The result of this sensitivity is also provided in Figure I.3. At first glance, several outliers can be seen of Switzerland, Southern Italy, Latvia, Estonia, and Finland where the percent change can reach as high as $11{,}000\,\%$. These strong differences are thought to arise from the greatly reduced wind energy generation between the the EMHIRES dataset and compared to this work. As an example, EMHIRES estimates Estonia's onshore wind FLH at less than $1000\,\mathrm{kWh\,kW^{-1}}$ while, in the primary analysis, Estonia's onshore wind FLH was found at over $3000\,\mathrm{kWh\,kW^{-1}}$. Again, this outcome is a result of EMHIRES' adherence to contemporary turbine designs. Besides these outliers, Germany and Poland, for instance, appears to show lull deficit increases in the range of 300 to $500\,\%$, while Spain and the UK are more in the range of 500 to $1000\,\%$. Taking the base-deficit-weighted average leads to the typical increased lull deficit of $703.1\,\%$ compared to the primary analysis when using the EMHIRES dataset.

As shown at several points throughout this work, the relative performance of future generators for the same set of weather conditions will significantly improve in the future. This is especially true for wind turbines, as opposed to PV where the improvements will mostly impact module efficiency rather than performance. Therefore two primary conclusions can be drawn from the this sensitivity analysis. First, that the EMHIRES dataset is best used for the analysis of current or at least near-future context energy systems. Second, that the analyses of future energy systems absolutely must involve the consideration of future-oriented VRES generator designs, or else the expected VRES lulls will be nearly an order magnitude larger than they otherwise would be.

I.4 VRES Replacement: MCDA Location Sorting

The LCOE-sorting of available turbines and PV parks provides an intuitive selection of generators, but at the same time most likely leads to higher performance estimations than would normally be expected since other factors influence VRES generator siting besides the expected LCOE. Therefore, a sensitivity is performed wherein generator sorting is performed using a MCDA approach such as the ones developed by Tlili et al. [50], Al-Yahyai [54], and Höfer [38]. A proper MCDA application should involve the specific definition of criteria scoring functions which are uniquely tailored to each geopolitical region across Europe. However, since such a procedure is far beyond the scope of this sensitivity analysis, this is only intended as an exemplary MCDA evaluation to suggest how much the situation *might* change.

For this sensitivity, the weighting structure used by Tlili et al. [50], discussed in Section 2.1.3, is applied across the European scope. Using the classic MCDA approach, the scoring conventions, shown in Figure 2.1, operate on multiple criteria and, in each case, produce a subscore between zero and one. In total, five criteria are involved depending on technology: including average wind speed at $100\,\mathrm{m}$, average hourly GHI, distance from the nearest roadway, distance from the nearest power line, and distance from the nearest settlement. All distance based criteria apply to both onshore wind and open-field PV, although GHI is only used for PV

while wind speed is only used for wind. As with the land eligibility analysis, the Prior datasets created in line with this work and described in Section 2.3 have been used to determine subscores.

Once new scores are computed for all onshore wind turbine and open-field PV park locations, the full procedure described for the primary analysis is carried out using MCDA-sorting in place of LCOE-sorting. Although the total capacities within each region will not have changed, the distribution of VRES generators will change and therefore the FLHs and generation profiles will change as well. As a result, the resulting FLHs for all E-Highway regions are displayed in Figures F.3 and F.4.

The result of this sensitivity is shown in the bottom left panel of Figure I.3. As expected, only increases in the largest lull deficits are observed as the MCDA selection procedure selects a higher proportion of suboptimal generator locations. Furthermore, with the exception of Latvia, Estonia, and Finland, where exceptionally large deficit changes are seen, there is a much closer grouping of the various regions in comparison to the previous sensitivity results. Notably this include the regions of Northern Italy and Switzerland. Within this group Italy as a whole apparently observed the most change, rising to around 300 to $400\,\%$ of the base value, however, as seen in Figure 7.8, Italy is also typically the region with the most shallow lulls for which a large relative change is less significant. Changes in Germany are limited to around $200\,\%$ versus around $150\,\%$ in the UK. Taking the weighted average of these values reveals the typical change in the largest lull deficit to $153.96\,\%$ of the primary analysis' value.

Besides the lull deficit, other outcomes of this sensitivity are interesting as well. Total available VRES generation when using MCDA-sorting has reduced to $94.3\,\%$ of that available in the base analysis, while the utilized VRES generation has only reduced to $96.2\,\%$. This means that, in relation to the total available generation, the MCDA-sorting input performs slightly better than the LCOE-sorting input. Connecting this to the PFL results discussion, these results suggest that, if MCDA-sorting had been used in the primary analysis, the total storage need to cover the largest deficits would rise from from $8.56\,\mathrm{TWh}$ to $13.57\,\mathrm{TWh}$, a very significant change, and the effective LCOE contribution of the VRES generators would rise from $4.2\,\mathrm{ct_{€}\,kWh^{-1}}$ to $4.4\,\mathrm{ct_{€}\,kWh^{-1}}$, a far less significant change. It is also seen that the total annual backup generation increases to $121.86\,\%$ of the base value, while the largest maximum backup capacity needed increases to $104.14\,\%$. Both of these changes are interesting, the first results in a total annual backup utilization which is still easily in range of the literature-expected values provided earlier, and the second again suggests that the required European-wide backup capacity is not a sensitive quantity. Ultimately, the use of MCDA-sorting compared to LCOE-sorting is seen to invoke noticeable changes to VRES lull occurrence, but these changes are not expected to be overwhelmingly large.

I.5 VRES Replacement: COSMO Weather Dataset

As described throughout Sections 3.6 and 4.4, the wind turbine and PV simulation procedures were developed and validated with the MERRA dataset in mind, nevertheless it is possible to use almost any other climate model dataset with only slight changes to the overall procedure. Therefore, the final sensitivity analysis tests this against the use of the COSMO-REA6 dataset on account of its $6\,\mathrm{km}$ spatial resolution across Europe, roughly 100 times that of MERRA, vertically resolved wind speed data, and explicitly specified direct normal irradiance. Ideally, as both the MERRA and COSMO-REA6 datasets recreate weather events across Europe during 2015, then, if both datasets were flawless and if the long-run-average adjustment procedures used here were sufficiently accurate, then use of either dataset should not impact the observation of lull occurrences. In reality, however, the use of the COSMO-REA6 is likely to lead to more prominent spatial mixing in the wind and PV generation profiles due to its vastly improved spatial resolution; which should have the effect of reducing the occurrence of lulls as seen in the previous comparison against Weber et al. [352] in Section 7.1.3.

In order to perform this sensitivity analysis, the wind and PV simulation schemes are carried out using the COSMO dataset following the discussions in Sections 3.6 and 4.4. As described, slight variations from the original scheme using MERRA are incorporated including: Hourly-performed vertical interpolation of wind speeds instead of log-law projection, bilinear wind speed spatial interpolation instead of LRA adjustment, and transmissivity-based GHI correction. Despite the fact that FLH distribution between wind turbine and PV park location change as a result of the new underlying weather data, the same locations as in the primary analysis are still simulated for the sake of consistency. As a result of performing these simulations using the weather year 2015, the resulting FLH can be observed for each E-Highway region in Figure F.5 for onshore wind and Figure F.6 for PV.

The outcomes of this final sensitivity analysis are also shown in the bottom right panel of Figure I.3. Contrary to the expectation stated above, a familiar pattern in seen where all of the highly sensitive areas are again seen to have abnormally high increases in lull deficits; including Switzerland, Southern Italy, and much of the Baltic Nations. Besides these regions, however, the impact of switching weather sources typically increases lull deficits to $215.86\,\%$ of the primary analysis' value. While this again a significant change, it is not nearly so impactful as not employing futuristic wind turbine and PV module designs, as seen in the EMHIRES sensitivity analysis.

Outside of this outcome, however, this sensitivity is largely inconclusive due to the biased nature of this comparison. Since the VRES generator locations are chosen as the best-performing options according to a MERRA-derived simulation, it is highly unlikely that these same locations also correspond to the best-performing options from a COSMO-derived simulation. Therefore, as a result of this selection bias, it is expected that the COSMO-derived VRES profiles have fewer FLH than those from MERRA. This is the most likely reason why the expected decrease in

lull occurrence due to spatial mixing was not observed, since it was outweighed by the poorer performing selection of turbines and PV parks. Evaluating the interplay between these and other dynamics would constitute a much greater degree of analysis and discussion than is reasonable to delve into here. For this reason, this sensitivity analysis is not discussed further.

Chapter J

Scenario Averages and Simulation Results

The following tables provide a comprehensive summary of scenario inputs, simulation results, and lull occurrences as described in Chapter 5. Values are provided for all E-Highway regions (See Figure 5.1 for reference) as well as for countries as a whole. Note that, except for values labeled as P_x, all values shown represent averages across all 185 demand-generation combination years. As described in the beginning of Section 7, the P_x notation refers to an x percentage of demand-generation years which observed the indicated value. For instance, P_1 would refer to a value which is observed in only $1\,\%$ of demand-generation years. This could also be interpreted as referring to a value which likely to occur at a rate of once per 100 years.

Table J.1: Summary table for E-Highway inputs, simulation results, VRES Only lulls, and Copper Plate lulls

		Europe	Albania	Austria				Belgium	Bosnia
			70_al		49_at	50_at	51_at	28_be	63_ba
E-Highway Inputs:									
Total Annual Demand and Capacities									
Demand	TWh	4277	15.0	84.8	20.4	27.1	37.3	121	12.7
Biomass	GW	184	0.00	3.50	0.75	1.25	1.50	4.75	0.25
Hydro	GW	298	2.98	16.4	11.7	3.02	1.65	2.31	2.60
Onshore Wind	GW	760	2.43	6.88	0.99	1.00	4.89	10.9	2.60
Offshore Wind	GW	115						3.00	
PV	GW	692	1.18	12.1	4.24	3.66	4.19	24.1	1.29
VRES Simulation Outcomes:									
Total Generation Potentials									
Onshore Wind	TWh	2899	9.41	32.8	5.11	5.13	22.6	30.8	11.8
Offshore Wind	TWh	516	0.00	0.00	0.00	0.00	0.00	12.8	0.00
PV	TWh	987	1.96	16.0	5.64	4.85	5.53	26.9	1.93
'VRES Only' Lull Context									
Onshore Wind									
P_{100}	Hours		68.0	32.0	33.0	32.0	30.0	191	49.0
P_{10}	Hours		203	92.0	89.0	89.0	95.0	490	185
P_1	Hours		251	104	98.0	98.0	125	772	259
Offshore Wind									
P_{100}	Hours							101	
P_{10}	Hours							373	
P_1	Hours							606	
PV									
P_{100}	Hours		44.0	66.0	64.0	68.0	68.0	236	66.0
P_{10}	Hours		185	229	209	236	236	727	185
P_1	Hours		259	301	301	310	330	926	209
All VRES									
P_{100}	Hours		30.0	14.0	16.0	16.0	15.0	41.0	20.0
P_{10}	Hours		75.0	42.0	42.0	43.0	43.0	236	68.0
P_1	Hours		114	60.0	62.0	64.0	77.0	340	141
'Copper Plate' Lull Context									
Years Without Lull [%]			0.00	0.00	100	0.00	0.00	0.00	0.00
Span									
P_{100}	Hours		15.0	11.0		1146	216	984	7.00
P_{10}	Hours		44.0	95.0		1700	1015	3315	46.0
P_1	Hours		87.0	164		1806	1146	3631	104
Deficit									
P_{100}	GWh		2.99	5.96		188	84.1	1122	1.00
P_{10}	GWh		10.6	70.8		355	501	4467	6.68
P_1	GWh		23.7	133		447	631	5012	16.8

Table J.2: Result summary table for power flow operation variables and lulls

		Europe	Albania 70_al	Austria	49_at	50_at	51_at	Belgium 28_be	Bosnia 63_ba
Power Flow Orchestration									
Generation Used									
Onshore	TWh	2173	7.22	28.6	4.66	4.65	19.3	26.5	9.52
Offshore	TWh	198	0.00	0.00	0.00	0.00	0.00	8.06	0.00
PV	TWh	965	1.85	15.9	5.63	4.82	5.42	26.8	1.79
ROR	TWh	378	7.08	42.1	5.73	14.4	21.9	1.70	13.9
Biomass	TWh	146	0.00	4.39	0.60	1.65	2.14	6.30	0.01
Hydro	TWh	539	9.97	37.8	29.2	8.59	0.00	3.79	6.64
Misc.									
Curtailed	TWh	1065	2.29	4.32	0.46	0.52	3.35	9.25	2.44
Hydro Stored	TWh	152	0.00	23.3	17.5	5.84	0.00	2.76	0.94
Import	TWh	0.00	0.61	19.7	19.1	6.88	2.15	52.9	0.48
Export	TWh	0.00	11.7	40.7	27.0	8.03	14.1	2.12	18.7
Unsatisfied	TWh	3.12	0.00	0.03	0.00	0.01	0.02	0.17	0.00
Max. Residual Load									
P_{100}	GW		2.97	18.1	12.4	4.25	1.49	9.51	2.59
P_{10}	GW		2.97	19.9	12.4	4.77	2.62	12.0	2.84
P_1	GW		2.97	24.8	12.4	9.62	2.62	19.9	2.84
"Power Flow" Lull Context									
Years Without Lull [%]			100	5.95	100	5.95	10.3	0.00	100
Span									
P_{100}	Hours							89.0	
P_{10}	Hours			1181		1600	1146	984	
P_1	Hours			1417		1979	1417	1649	
Deficit									
P_{100}	GWh							3.55	
P_{10}	GWh			56.2		21.1	35.5	200	
P_1	GWh			133		70.8	89.1	447	
Deficit vs. Annual Demand									
P_{100}	%							0.00	
P_{10}	%			0.06		0.08	0.09	0.16	
P_1	%			0.15		0.26	0.24	0.36	

Table J.3: Summary table for E-Highway inputs, simulation results, VRES Only lulls, and Copper Plate lulls [Continued]

		Bulgaria	Croatia	Czech Republic			Denmark		
		66_bg	62_hr		39_cz	40_cz		38_dk	72_dk
E-Highway Inputs:									
Total Annual Demand and Capacities									
Demand	TWh	31.8	23.9	71.8	40.7	31.1	42.7	23.3	19.4
Biomass	GW	4.75	0.00	5.00	2.75	2.25	3.75	2.50	1.25
Hydro	GW	9.96	5.00	2.61	1.79	0.82	0.00	0.00	0.00
Onshore Wind	GW	4.40	6.25	10.2	3.45	6.78	18.7	13.9	4.83
Offshore Wind	GW						25.6	25.6	
PV	GW	5.39	3.78	13.0	7.26	5.78	2.04	1.22	0.82
VRES Simulation Outcomes:									
Total Generation Potentials									
Onshore Wind	TWh	13.8	22.7	33.8	11.7	22.1	74.2	54.3	19.9
Offshore Wind	TWh	0.00	0.00	0.00	0.00	0.00	115	115	0.00
PV	TWh	8.23	5.77	15.6	8.64	6.97	2.35	1.40	0.95
'VRES Only' Lull Context									
Onshore Wind									
P_{100}	Hours	70.0	79.0	92.0	89.0	92.0	95.0	95.0	104
P_{10}	Hours	203	320	320	310	320	373	373	361
P_1	Hours	384	361	408	408	408	606	606	553
Offshore Wind									
P_{100}	Hours						95.0	95.0	
P_{10}	Hours						301	301	
P_1	Hours						447	447	
PV									
P_{100}	Hours	44.0	44.0	89.0	68.0	89.0	283	283	283
P_{10}	Hours	209	185	421	396	421	1111	1111	1111
P_1	Hours	351	185	536	536	536	1294	1181	1294
All VRES									
P_{100}	Hours	17.0	21.0	23.0	21.0	39.0	95.0	95.0	101
P_{10}	Hours	66.0	98.0	137	107	133	340	340	283
P_1	Hours	111	129	164	141	174	373	384	351
'Copper Plate' Lull Context									
Years Without Lull [%]		0.00	0.00	0.00	0.00	0.00	0.00	0.00	0.00
Span									
P_{100}	Hours	52.0	58.0	351	1862	145	121	84.0	7996
P_{10}	Hours	461	222	1806	3631	684	421	275	8759
P_1	Hours	796	553	2040	3978	926	663	361	8759
Deficit									
P_{100}	GWh	22.4	22.4	299	841	70.8	501	158	8414
P_{10}	GWh	158	112	1413	1778	398	1189	447	11885
P_1	GWh	299	150	1884	2113	531	1413	631	12589

Table J.4: Result summary table for power flow operation variables and lulls [Continued]

		Bulgaria	Croatia	Czech Republic			Denmark		
		66_bg	62_hr		39_cz	40_cz		38_dk	72_dk
Power Flow Orchestration									
Generation Used									
Onshore	TWh	10.7	18.4	28.5	9.95	18.5	41.7	28.0	13.8
Offshore	TWh	0.00	0.00	0.00	0.00	0.00	3.89	3.89	0.00
PV	TWh	8.07	5.22	15.5	8.62	6.91	2.34	1.39	0.95
ROR	TWh	5.51	3.10	1.97	1.36	0.62	0.00	0.00	0.00
Biomass	TWh	0.00	0.00	8.16	4.82	3.34	1.43	1.01	0.42
Hydro	TWh	17.9	13.5	4.35	3.19	1.16	0.00	0.00	0.00
Misc.									
Curtailed	TWh	3.23	4.84	5.36	1.77	3.59	144	138	6.14
Hydro Stored	TWh	0.22	0.95	2.44	1.66	0.78	0.00	0.00	0.00
Import	TWh	1.31	1.59	18.5	14.9	6.36	1.08	0.47	1.77
Export	TWh	11.4	16.9	2.38	0.48	4.70	27.2	22.1	6.28
Unsatisfied	TWh	0.00	0.00	0.02	0.02	0.00	0.01	0.00	0.00
Max. Residual Load									
P_{100}	GW	7.38	4.99	7.30	4.50	2.77	3.74	2.50	1.24
P_{10}	GW	9.19	4.99	9.08	6.00	3.04	4.71	2.97	1.75
P_1	GW	9.62	4.99	10.7	6.00	4.71	5.60	3.87	1.75
"Power Flow" Lull Context									
Years Without Lull [%]		100	100	10.3	12.4	14.1	14.1	15.1	25.4
Span									
P_{100}	Hours								
P_{10}	Hours			705	1146	475	57.0	53.0	133
P_1	Hours			1217	1552	749	107	107	408
Deficit									
P_{100}	GWh								
P_{10}	GWh			50.1	44.7	7.08	11.9	7.94	8.41
P_1	GWh			133	112	21.1	39.8	21.1	26.6
Deficit vs. Annual Demand									
P_{100}	%								
P_{10}	%			0.07	0.11	0.02	0.03	0.06	0.08
P_1	%			0.19	0.27	0.07	0.09	0.17	0.25

Table J.5: Summary table for E-Highway inputs, simulation results, VRES Only lulls, and Copper Plate lulls [Continued]

		Estonia	Finland			France			
		73_ee		74_fi	75_fi		14_fr	15_fr	16_fr
E-Highway Inputs:									
Total Annual Demand and Capacities									
Demand	TWh	12.5	82.6	8.36	74.2	649	56.4	33.8	57.7
Biomass	GW	1.00	3.75	0.75	3.00	28.2	3.50	2.00	1.50
Hydro	GW	0.79	2.38	0.89	1.49	31.6	2.78	6.29	3.02
Onshore Wind	GW	8.14	29.5	6.46	23.1	124	6.30	8.43	4.92
Offshore Wind	GW								
PV	GW	0.80	5.83	1.35	4.48	107	11.2	8.08	13.1
VRES Simulation Outcomes:									
Total Generation Potentials									
Onshore Wind	TWh	28.1	115	26.8	88.0	513	27.0	35.5	21.6
Offshore Wind	TWh	0.00	0.00	0.00	0.00	0.00	0.00	0.00	0.00
PV	TWh	0.91	5.95	1.33	4.63	165	17.3	13.0	22.0
'VRES Only' Lull Context									
Onshore Wind									
P_{100}	Hours	114	64.0	44.0	64.0	44.0	36.0	47.0	35.0
P_{10}	Hours	490	209	209	222	137	125	133	129
P_1	Hours	846	236	267	351	174	169	174	169
Offshore Wind									
P_{100}	Hours								
P_{10}	Hours								
P_1	Hours								
PV									
P_{100}	Hours	705	1046	1146	955	42.0	42.0	41.0	43.0
P_{10}	Hours	1417	1552	1600	1552	114	114	114	137
P_1	Hours	1552	1649	1700	1600	137	159	159	229
All VRES									
P_{100}	Hours	111	35.0	35.0	37.0	17.0	15.0	16.0	15.0
P_{10}	Hours	340	129	121	129	27.0	22.0	30.0	35.0
P_1	Hours	796	137	133	141	33.0	25.0	39.0	60.0
'Copper Plate' Lull Context									
Years Without Lull [%]		0.00	0.00	100	0.00	0.00	0.00	56.8	0.00
Span									
P_{100}	Hours	244	98.0		222	111	244		1046
P_{10}	Hours	772	408		1181	624	1506	7.00	2303
P_1	Hours	926	606		1700	1217	1862	16.0	2447
Deficit									
P_{100}	GWh	100	119		422	944	106		562
P_{10}	GWh	316	668		1413	5957	750	2.11	1679
P_1	GWh	447	841		1778	10000	1189	6.68	2113

Table J.6: Result summary table for power flow operation variables and lulls [Continued]

		Estonia	Finland			France			
		73_ee		74_fi	75_fi		14_fr	15_fr	16_fr
Power Flow Orchestration									
Generation Used									
Onshore	TWh	14.1	85.9	19.1	66.8	370	20.0	27.5	16.5
Offshore	TWh	0.00	0.00	0.00	0.00	0.00	0.00	0.00	0.00
PV	TWh	0.91	5.95	1.32	4.62	159	17.1	12.5	21.1
ROR	TWh	0.00	8.46	3.16	5.30	50.7	5.24	15.5	8.41
Biomass	TWh	0.39	1.75	0.37	1.38	35.7	3.01	2.03	2.08
Hydro	TWh	0.00	2.68	0.00	2.68	42.7	1.90	12.7	2.06
Misc.									
Curtailed	TWh	14.0	28.9	7.73	21.2	150	7.15	8.46	5.99
Hydro Stored	TWh	0.00	0.00	0.00	0.00	18.3	0.00	7.39	0.00
Import	TWh	2.62	6.14	0.01	10.5	64.0	13.9	0.93	14.8
Export	TWh	5.56	28.3	19.7	13.0	55.0	4.73	30.1	7.35
Unsatisfied	TWh	0.00	0.01	0.00	0.01	0.82	0.00	0.00	0.09
Max. Residual Load									
P_{100}	GW	0.99	5.23	0.75	4.45	53.6	5.05	8.28	3.22
P_{10}	GW	1.24	6.43	0.99	5.47	85.9	5.17	8.28	8.78
P_1	GW	1.71	7.91	1.08	6.81	94.2	11.8	8.78	12.3
"Power Flow" Lull Context									
Years Without Lull [%]		33.0	6.49	10.8	23.2	0.00	88.6	96.2	1.08
Span									
P_{100}	Hours					14.0			
P_{10}	Hours	118	137	125	145	301	28.0		606
P_1	Hours	310	244	169	310	461	320	87.0	872
Deficit									
P_{100}	GWh					11.2			
P_{10}	GWh	3.98	16.8	3.76	15.0	841	0.08		141
P_1	GWh	11.9	63.1	12.6	56.2	1778	33.5	1.19	316
Deficit vs. Annual Demand									
P_{100}	%					0.00			
P_{10}	%	0.03	0.02	0.09	0.02	0.13	0.00		0.24
P_1	%	0.09	0.08	0.29	0.07	0.27	0.06	0.00	0.54

Table J.7: Summary table for E-Highway inputs, simulation results, VRES Only lulls, and Copper Plate lulls [Continued]

		France							
		17_fr	18_fr	19_fr	20_fr	21_fr	22_fr	23_fr	24_fr
E-Highway Inputs:									
Total Annual Demand and Capacities									
Demand	TWh	45.3	36.9	36.8	35.3	50.5	20.5	123	18.8
Biomass	GW	3.25	4.00	1.00	1.00	0.75	0.50	1.50	2.50
Hydro	GW	0.00	0.54	6.18	11.2	0.29	0.00	0.00	0.00
Onshore Wind	GW	16.2	12.9	4.53	1.87	21.6	12.2	3.85	4.46
Offshore Wind	GW								
PV	GW	6.84	6.54	6.57	8.44	5.15	2.60	15.5	3.08
VRES Simulation Outcomes:									
Total Generation Potentials									
Onshore Wind	TWh	65.0	52.6	19.9	8.74	84.6	49.8	17.1	19.7
Offshore Wind	TWh	0.00	0.00	0.00	0.00	0.00	0.00	0.00	0.00
PV	TWh	10.4	9.87	10.3	13.2	7.68	3.82	22.6	4.62
'VRES Only' Lull Context									
Onshore Wind									
P_{100}	Hours	47.0	46.0	34.0	28.0	53.0	44.0	32.0	34.0
P_{10}	Hours	159	141	129	121	169	141	129	129
P_1	Hours	180	174	169	169	180	174	174	169
Offshore Wind									
P_{100}	Hours								
P_{10}	Hours								
P_1	Hours								
PV									
P_{100}	Hours	21.0	41.0	42.0	42.0	21.0	20.0	41.0	42.0
P_{10}	Hours	137	137	114	114	114	114	137	137
P_1	Hours	159	159	185	164	137	141	159	159
All VRES									
P_{100}	Hours	17.0	16.0	15.0	16.0	23.0	26.0	16.0	14.0
P_{10}	Hours	53.0	43.0	25.0	21.0	89.0	87.0	38.0	33.0
P_1	Hours	68.0	53.0	41.0	62.0	111	121	60.0	42.0
'Copper Plate' Lull Context									
Years Without Lull [%]		0.00	0.00	0.00	0.00	0.00	0.00	0.00	0.00
Span									
P_{100}	Hours	52.0	25.0	21.0	2.00	64.0	35.0	8759	41.0
P_{10}	Hours	275	141	180	19.0	310	111	8759	310
P_1	Hours	461	292	330	43.0	475	197	8759	536
Deficit									
P_{100}	GWh	47.3	18.8	11.2	0.28	84.1	13.3	59566	14.1
P_{10}	GWh	211	89.1	75.0	10.0	335	56.2	63096	75.0
P_1	GWh	473	224	112	15.0	562	141	63096	168

Table J.8: Result summary table for power flow operation variables and lulls [Continued]

		France							
		17_fr	18_fr	19_fr	20_fr	21_fr	22_fr	23_fr	24_fr
Power Flow Orchestration									
Generation Used									
Onshore	TWh	45.6	41.1	17.2	7.90	58.2	19.9	14.2	17.3
Offshore	TWh	0.00	0.00	0.00	0.00	0.00	0.00	0.00	0.00
PV	TWh	10.4	9.85	10.3	13.2	7.67	3.69	22.6	4.60
ROR	TWh	0.00	0.00	5.94	7.46	0.00	0.00	0.00	0.00
Biomass	TWh	2.78	5.15	0.81	0.83	0.67	0.44	3.17	3.15
Hydro	TWh	0.00	0.37	4.22	20.2	0.00	0.00	0.00	0.00
Misc.									
Curtailed	TWh	19.4	11.5	2.75	0.86	26.4	30.1	3.05	2.41
Hydro Stored	TWh	0.00	0.00	0.00	10.1	0.00	0.00	0.00	0.00
Import	TWh	4.50	1.31	5.13	11.1	6.24	5.81	83.4	1.65
Export	TWh	18.0	20.9	6.75	15.3	22.4	9.30	0.11	7.94
Unsatisfied	TWh	0.00	0.05	0.00	0.00	0.10	0.03	0.14	0.00
Max. Residual Load									
P_{100}	GW	3.22	4.30	4.55	12.1	1.47	0.99	2.74	2.50
P_{10}	GW	3.22	7.13	4.55	12.1	2.74	0.99	18.3	2.50
P_1	GW	6.43	10.4	5.47	12.1	3.30	2.18	29.8	2.50
"Power Flow" Lull Context									
Years Without Lull [%]		95.1	0.54	96.8	97.3	0.00	0.00	0.00	100
Span									
P_{100}	Hours					25.0	5.00	129	
P_{10}	Hours		421			421	133	1752	
P_1	Hours	169	587	20.0	47.0	553	275	2167	
Deficit									
P_{100}	GWh					0.71	0.47	2.37	
P_{10}	GWh		47.3			112	20.0	224	
P_1	GWh	3.16	133	5.31	10.0	237	39.8	531	
Deficit vs. Annual Demand									
P_{100}	%					0.00	0.00	0.00	
P_{10}	%		0.13			0.22	0.10	0.18	
P_1	%	0.01	0.36	0.01	0.03	0.46	0.19	0.43	

Table J.9: Summary table for E-Highway inputs, simulation results, VRES Only lulls, and Copper Plate lulls [Continued]

		France				Germany			
		25_fr	26_fr	27_fr	99_fr		31_de	32_de	33_de
E-Highway Inputs:									
Total Annual Demand and Capacities									
Demand	TWh	51.1	71.4	8.13	3.42	666	111	63.1	145
Biomass	GW	2.00	3.25	1.25	0.25	27.8	3.75	5.00	3.00
Hydro	GW	0.00	0.00	1.30	0.00	12.8	0.82	0.02	1.16
Onshore Wind	GW	6.12	17.5	2.55	0.76	98.3	32.2	26.2	12.5
Offshore Wind	GW					27.2	27.2		
PV	GW	7.30	8.23	1.20	3.15	98.6	14.9	10.3	11.0
VRES Simulation Outcomes:									
Total Generation Potentials									
Onshore Wind	TWh	26.4	70.0	11.7	3.70	326	101	84.1	43.0
Offshore Wind	TWh	0.00	0.00	0.00	0.00	128	128	0.00	0.00
PV	TWh	10.8	11.9	1.76	5.55	116	17.0	12.1	12.7
'VRES Only' Lull Context									
Onshore Wind									
P_{100}	Hours	36.0	50.0	29.0	22.0	133	137	137	133
P_{10}	Hours	125	159	125	104	396	505	396	384
P_1	Hours	169	180	174	133	643	643	643	624
Offshore Wind									
P_{100}	Hours					118	118		
P_{10}	Hours					301	301		
P_1	Hours					396	396		
PV									
P_{100}	Hours	42.0	41.0	42.0	42.0	68.0	68.0	89.0	89.0
P_{10}	Hours	137	125	137	114	373	624	447	587
P_1	Hours	164	137	159	185	820	820	820	820
All VRES									
P_{100}	Hours	15.0	18.0	15.0	16.0	44.0	89.0	72.0	44.0
P_{10}	Hours	22.0	46.0	43.0	37.0	129	229	180	125
P_1	Hours	30.0	77.0	50.0	62.0	174	292	292	169
'Copper Plate' Lull Context									
Years Without Lull [%]		0.00	0.00	2.16	0.00	0.00	0.00	0.00	0.00
Span									
P_{100}	Hours	872	174		17.0	229	84.0	84.0	8497
P_{10}	Hours	2600	1111	19.0	52.0	1146	229	340	8759
P_1	Hours	2848	1919	60.0	89.0	1806	320	475	8759
Deficit									
P_{100}	GWh	473	211		2.51	2239	237	158	33497
P_{10}	GWh	1679	1189	1.68	6.31	10593	750	501	42170
P_1	GWh	2239	2371	5.62	10.6	12589	1122	750	42170

Table J.10: Result summary table for power flow operation variables and lulls [Continued]

		France				Germany			
		25_fr	26_fr	27_fr	99_fr		31_de	32_de	33_de
Power Flow Orchestration									
Generation Used									
Onshore	TWh	19.9	53.5	9.18	2.01	281	90.7	64.9	39.2
Offshore	TWh	0.00	0.00	0.00	0.00	65.4	65.4	0.00	0.00
PV	TWh	10.4	11.5	1.72	2.14	116	17.0	12.0	12.7
ROR	TWh	8.18	0.00	0.00	0.00	23.5	1.08	0.00	0.60
Biomass	TWh	2.62	6.66	2.24	0.08	21.7	2.32	2.56	3.94
Hydro	TWh	0.00	0.00	1.16	0.00	25.2	1.06	0.00	2.16
Misc.									
Curtailed	TWh	6.91	16.9	2.54	5.10	108	73.9	19.2	3.81
Hydro Stored	TWh	0.00	0.00	0.83	0.00	17.8	0.65	0.00	1.42
Import	TWh	14.0	11.0	1.08	0.36	170	15.4	11.3	88.1
Export	TWh	4.16	11.5	6.41	1.18	27.0	80.9	27.8	0.03
Unsatisfied	TWh	0.15	0.26	0.00	0.00	0.31	0.04	0.04	0.15
Max. Residual Load									
P_{100}	GW	1.98	6.73	1.79	0.25	40.2	4.55	4.99	4.15
P_{10}	GW	5.80	12.3	1.79	0.25	53.0	6.81	7.91	8.10
P_1	GW	10.1	19.2	1.79	0.37	58.1	11.6	7.91	8.10
"Power Flow" Lull Context									
Years Without Lull [%]		0.54	0.00	99.5	96.2	1.62	3.78	7.57	1.08
Span									
P_{100}	Hours		43.0						
P_{10}	Hours	624	820			244	180	275	2040
P_1	Hours	1374	1181		13.0	461	292	570	2374
Deficit									
P_{100}	GWh		6.68						
P_{10}	GWh	224	299			422	75.0	70.8	282
P_1	GWh	398	531		0.30	944	150	200	501
Deficit vs. Annual Demand									
P_{100}	%		0.01						
P_{10}	%	0.43	0.41			0.06	0.07	0.11	0.19
P_1	%	0.77	0.74		0.01	0.14	0.13	0.31	0.34

Table J.11: Summary table for E-Highway inputs, simulation results, VRES Only lulls, and Copper Plate lulls [Continued]

		Germany				Greece			Hungary
		34_de	35_de	36_de	37_de		68_gr	69_gr	58_hu
E-Highway Inputs:									
Total Annual Demand and Capacities									
Demand	TWh	62.9	89.9	88.2	105	67.8	23.6	44.2	59.4
Biomass	GW	4.50	3.75	3.00	4.75	3.75	2.00	1.75	7.25
Hydro	GW	4.44	1.09	4.33	0.95	10.1	10.1	0.00	0.95
Onshore Wind	GW	14.7	6.63	2.22	3.99	25.9	7.39	18.5	4.90
Offshore Wind	GW								
PV	GW	13.5	10.9	11.4	26.5	15.1	5.40	9.67	14.0
VRES Simulation Outcomes:									
Total Generation Potentials									
Onshore Wind	TWh	49.8	24.0	8.58	14.9	93.6	28.5	65.0	14.4
Offshore Wind	TWh	0.00	0.00	0.00	0.00	0.00	0.00	0.00	0.00
PV	TWh	15.9	12.8	13.9	31.6	25.7	8.85	16.9	18.8
'VRES Only' Lull Context									
Onshore Wind									
P_{100}	Hours	133	125	104	111	66.0	49.0	68.0	125
P_{10}	Hours	396	384	340	351	185	164	203	421
P_1	Hours	643	624	408	587	292	283	292	490
Offshore Wind									
P_{100}	Hours								
P_{10}	Hours								
P_1	Hours								
PV									
P_{100}	Hours	66.0	92.0	68.0	89.0	20.0	20.0	39.0	44.0
P_{10}	Hours	361	384	373	373	66.0	66.0	66.0	301
P_1	Hours	820	820	796	820	114	68.0	137	351
All VRES									
P_{100}	Hours	44.0	25.0	20.0	20.0	19.0	18.0	19.0	20.0
P_{10}	Hours	121	89.0	66.0	68.0	66.0	49.0	66.0	159
P_1	Hours	169	137	92.0	95.0	111	68.0	111	209
'Copper Plate' Lull Context									
Years Without Lull [%]		0.00	0.00	0.00	0.00	0.00	0.00	0.00	0.00
Span									
P_{100}	Hours	89.0	8497	8497	3743	133	30.0	320	1181
P_{10}	Hours	396	8759	8759	4630	536	154	1181	2374
P_1	Hours	553	8759	8759	4920	772	259	1752	2523
Deficit									
P_{100}	GWh	119	8414	18836	5309	251	14.1	335	501
P_{10}	GWh	398	12589	21135	7079	1122	59.6	1334	1884
P_1	GWh	596	14125	21135	7499	1496	112	1585	2113

Table J.12: Result summary table for power flow operation variables and lulls [Continued]

		Germany				Greece			Hungary
		34_de	35_de	36_de	37_de		68_gr	69_gr	58_hu
Power Flow Orchestration									
Generation Used									
Onshore	TWh	43.2	21.9	7.92	13.4	62.0	19.1	42.8	12.0
Offshore	TWh	0.00	0.00	0.00	0.00	0.00	0.00	0.00	0.00
PV	TWh	15.8	12.8	13.9	31.6	24.8	8.50	16.3	18.4
ROR	TWh	0.33	0.10	5.15	16.2	3.49	2.45	1.04	4.35
Biomass	TWh	3.35	3.44	2.39	3.68	0.09	0.05	0.04	3.44
Hydro	TWh	9.01	2.47	8.47	2.08	19.9	19.9	0.00	0.00
Misc.									
Curtailed	TWh	6.64	2.11	0.67	1.50	32.5	9.73	22.8	2.78
Hydro Stored	TWh	6.48	1.90	5.84	1.55	4.32	4.32	0.00	0.00
Import	TWh	12.3	43.3	56.2	46.9	2.87	2.74	4.55	27.1
Export	TWh	14.7	0.17	0.02	7.11	41.0	24.9	20.5	2.97
Unsatisfied	TWh	0.01	0.02	0.01	0.04	0.00	0.00	0.00	0.00
Max. Residual Load									
P_{100}	GW	8.88	4.82	7.30	5.66	10.1	10.1		6.89
P_{10}	GW	9.40	5.54	7.82	7.64	13.8	12.0	1.75	7.21
P_1	GW	9.40	5.54	11.1	7.64	14.2	12.3	1.96	7.47
"Power Flow" Lull Context									
Years Without Lull [%]		7.03	3.78	4.32	6.49	98.9	98.9	98.9	98.4
Span									
P_{100}	Hours								
P_{10}	Hours	624	1552	1700	1600				
P_1	Hours	1111	1862	2167	1862	5.00	5.00	5.00	169
Deficit									
P_{100}	GWh								
P_{10}	GWh	18.8	42.2	28.2	94.4				
P_1	GWh	42.2	89.1	56.2	200	0.42	0.22	0.21	0.30
Deficit vs. Annual Demand									
P_{100}	%								
P_{10}	%	0.03	0.05	0.03	0.09				
P_1	%	0.07	0.11	0.06	0.19	0.00	0.00	0.00	0.00

Table J.13: Summary table for E-Highway inputs, simulation results, VRES Only lulls, and Copper Plate lulls [Continued]

		Ireland 96_ie	Italy	52_it	53_it	54_it	55_it	56_it	98_it
E-Highway Inputs:									
Total Annual Demand and Capacities									
Demand	TWh	43.1	431	200	43.6	91.5	47.9	34.9	13.1
Biomass	GW	0.25	14.8	6.75	2.75	1.00	2.50	1.25	0.50
Hydro	GW	1.91	22.0	15.4	1.40	2.87	1.01	0.96	0.33
Onshore Wind	GW	13.6	41.3	4.02	4.25	4.12	14.8	7.29	6.84
Offshore Wind	GW								
PV	GW	3.84	101	42.5	8.58	21.2	12.0	11.8	5.00
VRES Simulation Outcomes:									
Total Generation Potentials									
Onshore Wind	TWh	60.1	157	16.2	17.1	16.6	53.1	28.0	26.4
Offshore Wind	TWh	0.00	0.00	0.00	0.00	0.00	0.00	0.00	0.00
PV	TWh	3.88	169	69.0	14.2	35.9	20.4	20.6	8.76
'VRES Only' Lull Context									
Onshore Wind									
P_{100}	Hours	118	26.0	18.0	18.0	18.0	38.0	25.0	25.0
P_{10}	Hours	384	111	98.0	98.0	98.0	137	111	111
P_1	Hours	570	137	125	125	125	310	137	137
Offshore Wind									
P_{100}	Hours								
P_{10}	Hours								
P_1	Hours								
PV									
P_{100}	Hours	185	21.0	20.0	21.0	22.0	21.0	42.0	20.0
P_{10}	Hours	899	68.0	68.0	68.0	68.0	68.0	114	68.0
P_1	Hours	1015	70.0	118	114	104	104	209	92.0
All VRES									
P_{100}	Hours	84.0	16.0	16.0	16.0	16.0	16.0	16.0	15.0
P_{10}	Hours	236	19.0	21.0	19.0	21.0	34.0	41.0	34.0
P_1	Hours	396	43.0	43.0	43.0	43.0	66.0	46.0	66.0
'Copper Plate' Lull Context									
Years Without Lull [%]		0.00	0.00	0.00	0.00	0.00	0.00	0.00	0.00
Span									
P_{100}	Hours	244	137	3027	111	3978	19.0	19.0	12.0
P_{10}	Hours	796	1255	3417	872	8497	125	141	28.0
P_1	Hours	1255	1752	3523	1506	8759	185	236	68.0
Deficit									
P_{100}	GWh	282	531	5957	50.1	3162	20.0	18.8	2.66
P_{10}	GWh	750	4217	8414	335	5012	94.4	84.1	9.44
P_1	GWh	1000	7079	8913	562	5309	141	119	16.8

Table J.14: Result summary table for power flow operation variables and lulls [Continued]

		Ireland 96_ie	Italy	52_it	53_it	54_it	55_it	56_it	98_it
Power Flow Orchestration									
Generation Used									
Onshore	TWh	44.0	122	14.5	14.7	12.7	41.5	20.4	18.1
Offshore	TWh	0.00	0.00	0.00	0.00	0.00	0.00	0.00	0.00
PV	TWh	3.87	164	68.7	13.6	34.9	20.1	18.9	7.77
ROR	TWh	1.04	24.8	20.0	1.32	2.37	0.74	0.22	0.14
Biomass	TWh	0.25	6.70	4.14	0.82	0.24	0.90	0.47	0.12
Hydro	TWh	2.55	41.2	30.7	2.02	5.63	1.46	0.57	0.73
Misc.									
Curtailed	TWh	16.1	40.3	1.94	3.03	4.94	12.0	9.21	9.24
Hydro Stored	TWh	2.05	11.5	9.02	0.00	1.55	0.00	0.62	0.28
Import	TWh	10.3	112	79.4	13.5	41.9	3.78	4.82	0.31
Export	TWh	17.0	27.4	8.05	2.32	4.63	20.6	9.92	13.8
Unsatisfied	TWh	0.18	0.05	0.02	0.00	0.01	0.01	0.01	0.00
Max. Residual Load									
P_{100}	GW	4.15	35.4	22.1	3.78	3.87	3.26	1.47	0.83
P_{10}	GW	4.15	44.0	25.6	4.06	5.60	6.00	3.26	0.83
P_1	GW	4.15	45.6	25.6	4.06	5.60	6.36	4.99	0.83
"Power Flow" Lull Context									
Years Without Lull [%]		0.00	0.00	41.1	58.9	59.5	50.8	1.08	100
Span									
P_{100}	Hours	66.0	13.0						
P_{10}	Hours	505	203	1461	137	267	340	121	
P_1	Hours	899	520	1919	384	643	553	236	
Deficit									
P_{100}	GWh	3.98	0.05						
P_{10}	GWh	150	100	70.8	2.24	13.3	26.6	12.6	
P_1	GWh	282	501	266	14.1	100	141	35.5	
Deficit vs. Annual Demand									
P_{100}	%	0.01	0.00						
P_{10}	%	0.34	0.02	0.03	0.01	0.01	0.05	0.04	
P_1	%	0.65	0.12	0.13	0.03	0.11	0.29	0.10	

Table J.15: Summary table for E-Highway inputs, simulation results, VRES Only lulls, and Copper Plate lulls [Continued]

		Latvia 78_lv	Lithuania 77_lt	Lux. 29_lu	Maced. 67_mk	Monten. 64_me	Netherlands 30_nl	Norway	79_no
E-Highway Inputs:									
Total Annual Demand and Capacities									
Demand	TWh	21.0	28.0	7.38	8.44	3.22	161	102	15.2
Biomass	GW	1.75	1.75	0.00	0.00	0.00	4.00	0.50	0.25
Hydro	GW	0.00	1.79	1.65	1.94	3.99	0.00	59.8	14.6
Onshore Wind	GW	13.8	15.2	0.74	0.37	0.52	15.0	12.2	1.47
Offshore Wind	GW						15.9	3.00	3.00
PV	GW	1.13	1.34	1.03	1.37	0.49	22.2	5.36	0.73
VRES Simulation Outcomes:									
Total Generation Potentials									
Onshore Wind	TWh	44.3	48.8	1.70	1.46	2.29	54.7	60.7	7.37
Offshore Wind	TWh	0.00	0.00	0.00	0.00	0.00	70.8	14.3	14.3
PV	TWh	1.28	1.54	1.19	2.14	0.76	24.4	5.79	0.82
'VRES Only' Lull Context									
Onshore Wind									
P_{100}	Hours	121	107	197	79.0	52.0	121	32.0	29.0
P_{10}	Hours	505	361	587	216	203	434	129	118
P_1	Hours	796	749	772	301	320	820	229	229
Offshore Wind									
P_{100}	Hours						107	79.0	79.0
P_{10}	Hours						310	283	283
P_1	Hours						384	320	320
PV									
P_{100}	Hours	490	384	340	44.0	89.0	236	663	384
P_{10}	Hours	1294	1255	872	251	283	872	1461	1461
P_1	Hours	1374	1294	955	301	283	955	1700	1700
All VRES									
P_{100}	Hours	118	107	62.0	18.0	19.0	60.0	15.0	42.0
P_{10}	Hours	421	283	191	44.0	50.0	222	68.0	129
P_1	Hours	749	351	292	68.0	87.0	310	111	216
'Copper Plate' Lull Context									
Years Without Lull [%]		0.00	0.00	0.00	0.00	0.00	0.00	0.00	100
Span									
P_{100}	Hours	259	361	955	1806	68.0	292	15.0	
P_{10}	Hours	1417	1461	3417	2936	301	2103	145	
P_1	Hours	1700	2936	3978	3120	408	2600	351	
Deficit									
P_{100}	GWh	178	224	63.1	94.4	2.51	944	16.8	
P_{10}	GWh	841	1059	237	316	11.9	4732	178	
P_1	GWh	1122	1259	282	376	17.8	5309	282	

Table J.16: Result summary table for power flow operation variables and lulls [Continued]

		Latvia 78_lv	Lithuania 77_lt	Lux. 29_lu	Maced. 67_mk	Monten. 64_me	Netherlands 30_nl	Norway 79_no	
Power Flow Orchestration									
Generation Used									
Onshore	TWh	18.2	31.9	1.54	1.18	1.83	49.8	54.4	6.70
Offshore	TWh	0.00	0.00	0.00	0.00	0.00	49.2	9.97	9.97
PV	TWh	1.27	1.53	1.18	2.07	0.71	24.3	5.65	0.81
ROR	TWh	3.79	0.00	0.00	0.00	0.00	0.00	61.8	15.2
Biomass	TWh	0.69	0.94	0.00	0.00	0.00	4.91	0.00	0.00
Hydro	TWh	0.00	3.03	2.85	3.93	0.00	0.00	108	42.2
Misc.									
Curtailed	TWh	26.1	17.0	0.18	0.35	0.51	26.5	10.7	4.99
Hydro Stored	TWh	0.00	2.44	1.44	0.00	0.00	0.00	0.08	0.03
Import	TWh	4.17	8.13	4.19	3.05	0.98	46.5	2.21	0.39
Export	TWh	7.19	15.0	1.40	1.79	0.31	14.2	139	60.1
Unsatisfied	TWh	0.00	0.01	0.00	0.00	0.00	0.19	0.00	0.00
Max. Residual Load									
P_{100}	GW	1.75	3.53	1.63	1.94		4.55	38.4	14.6
P_{10}	GW	2.23	4.01	2.08	1.94		13.6	44.0	14.6
P_1	GW	2.77	5.86	2.20	1.94		25.0	45.1	14.7
"Power Flow" Lull Context									
Years Without Lull [%]		29.7	17.3	23.2	100	100	0.00	99.5	99.5
Span									
P_{100}	Hours						52.0		
P_{10}	Hours	89.0	185	1374			553		
P_1	Hours	159	490	1862			926		
Deficit									
P_{100}	GWh						0.56		
P_{10}	GWh	7.50	11.2	7.50			251		
P_1	GWh	21.1	29.9	14.1			531		
Deficit vs. Annual Demand									
P_{100}	%						0.00		
P_{10}	%	0.04	0.04	0.10			0.15		
P_1	%	0.10	0.11	0.19			0.33		

Table J.17: Summary table for E-Highway inputs, simulation results, VRES Only lulls, and Copper Plate lulls [Continued]

		Norway						Poland	
		80_no	81_no	82_no	83_no	84_no	85_no		41_pl
E-Highway Inputs:									
Total Annual Demand and Capacities									
Demand	TWh	13.6	12.1	38.0	11.3	10.4	1.43	172	39.0
Biomass	GW	0.25	0.00	0.00	0.00	0.00	0.00	14.2	2.50
Hydro	GW	9.94	14.9	7.10	4.52	8.11	0.57	3.79	0.00
Onshore Wind	GW	1.86	1.06	2.88	1.79	2.04	1.07	81.9	18.1
Offshore Wind	GW								
PV	GW	0.69	0.63	1.51	0.62	0.91	0.27	24.2	5.38
VRES Simulation Outcomes:									
Total Generation Potentials									
Onshore Wind	TWh	9.29	5.40	14.2	8.95	10.1	5.42	266	58.8
Offshore Wind	TWh	0.00	0.00	0.00	0.00	0.00	0.00	0.00	0.00
PV	TWh	0.78	0.66	1.68	0.64	0.92	0.29	27.7	6.14
'VRES Only' Lull Context									
Onshore Wind									
P_{100}	Hours	28.0	31.0	34.0	29.0	32.0	31.0	98.0	98.0
P_{10}	Hours	121	114	154	121	129	114	283	283
P_1	Hours	229	229	229	229	229	229	536	536
Offshore Wind									
P_{100}	Hours								
P_{10}	Hours								
P_1	Hours								
PV									
P_{100}	Hours	384	520	384	705	872	684	114	114
P_{10}	Hours	1461	1417	1461	1417	1461	1461	663	705
P_1	Hours	1752	1649	1752	1600	1752	1752	772	872
All VRES									
P_{100}	Hours	15.0	12.0	13.0	14.0	13.0	14.0	53.0	53.0
P_{10}	Hours	62.0	35.0	44.0	64.0	42.0	79.0	185	185
P_1	Hours	79.0	42.0	64.0	87.0	62.0	114	209	209
'Copper Plate' Lull Context									
Years Without Lull [%]		97.3	100	0.00	0.00	90.3	0.00	0.00	0.00
Span									
P_{100}	Hours			8759	2523		15.0	154	251
P_{10}	Hours			8759	3978		72.0	606	899
P_1	Hours	5.00		8759	4100	9.00	111	772	1015
Deficit									
P_{100}	GWh			47315	200		0.50	841	299
P_{10}	GWh			47315	668		1.88	2985	944
P_1	GWh	0.32		47315	794	1.06	2.99	3981	1259

Table J.18: Result summary table for power flow operation variables and lulls [Continued]

		Norway						Poland	
		80_no	81_no	82_no	83_no	84_no	85_no		41_pl
Power Flow Orchestration									
Generation Used									
Onshore	TWh	8.46	4.89	13.0	8.02	8.92	4.47	148	27.6
Offshore	TWh	0.00	0.00	0.00	0.00	0.00	0.00	0.00	0.00
PV	TWh	0.77	0.65	1.66	0.63	0.87	0.27	27.4	6.13
ROR	TWh	10.4	15.6	7.42	4.72	8.37	0.00	6.86	0.00
Biomass	TWh	0.00	0.00	0.00	0.00	0.00	0.00	9.14	1.56
Hydro	TWh	13.6	28.1	14.2	3.83	5.39	0.27	4.00	0.00
Misc.									
Curtailed	TWh	0.84	0.53	1.20	0.95	1.25	0.98	118	31.2
Hydro Stored	TWh	0.00	0.02	0.00	0.00	0.03	0.00	3.44	0.00
Import	TWh	0.12	0.52	12.4	1.59	0.25	0.09	19.2	12.3
Export	TWh	24.5	40.8	5.87	4.42	13.3	3.66	39.2	8.54
Unsatisfied	TWh	0.00	0.00	0.00	0.00	0.00	0.00	0.03	0.00
Max. Residual Load									
P_{100}	GW	7.05	14.9	4.99	3.11	5.73	0.40	17.9	2.50
P_{10}	GW	9.08	15.6	4.99	3.18	6.50	0.40	20.8	2.74
P_1	GW	9.30	15.8	4.99	3.18	6.81	0.40	23.1	2.74
"Power Flow" Lull Context									
Years Without Lull [%]		100	100	100	100	100	100	14.1	20.0
Span									
P_{100}	Hours								
P_{10}	Hours							154	180
P_1	Hours							222	461
Deficit									
P_{100}	GWh								
P_{10}	GWh							70.8	5.96
P_1	GWh							168	15.0
Deficit vs. Annual Demand									
P_{100}	%								
P_{10}	%							0.04	0.02
P_1	%							0.10	0.04

Table J.19: Summary table for E-Highway inputs, simulation results, VRES Only lulls, and Copper Plate lulls [Continued]

		Poland				Portugal			Romania
		42_pl	43_pl	44_pl	45_pl		12_pt	13_pt	
E-Highway Inputs:									
Total Annual Demand and Capacities									
Demand	TWh	27.4	40.2	38.0	27.5	70.9	36.2	34.7	68.3
Biomass	GW	2.75	2.00	4.00	3.00	2.75	1.25	1.50	9.25
Hydro	GW	0.00	1.45	0.00	2.34	8.65	7.17	1.48	8.62
Onshore Wind	GW	10.6	7.91	23.1	22.2	11.9	3.84	8.02	4.83
Offshore Wind	GW								
PV	GW	4.27	5.63	5.62	3.32	13.8	8.33	5.47	11.0
VRES Simulation Outcomes:									
Total Generation Potentials									
Onshore Wind	TWh	35.1	26.5	74.2	71.6	42.1	14.3	27.8	19.0
Offshore Wind	TWh	0.00	0.00	0.00	0.00	0.00	0.00	0.00	0.00
PV	TWh	4.93	6.49	6.42	3.73	23.9	14.2	9.64	15.4
'VRES Only' Lull Context									
Onshore Wind									
P_{100}	Hours	95.0	92.0	98.0	98.0	58.0	55.0	60.0	60.0
P_{10}	Hours	283	283	301	292	180	185	180	197
P_1	Hours	536	536	536	536	244	244	236	209
Offshore Wind									
P_{100}	Hours								
P_{10}	Hours								
P_1	Hours								
PV									
P_{100}	Hours	129	114	114	114	22.0	43.0	41.0	44.0
P_{10}	Hours	643	570	663	727	150	159	159	229
P_1	Hours	705	643	872	1015	209	209	209	351
All VRES									
P_{100}	Hours	52.0	39.0	72.0	92.0	17.0	17.0	19.0	18.0
P_{10}	Hours	164	145	191	216	39.0	39.0	60.0	68.0
P_1	Hours	203	203	209	292	43.0	39.0	68.0	180
'Copper Plate' Lull Context									
Years Without Lull [%]		0.00	0.00	0.00	0.00	0.00	0.00	0.00	0.00
Span									
P_{100}	Hours	259	1862	145	41.0	154	21.0	749	520
P_{10}	Hours	955	8759	396	174	606	159	2681	2303
P_1	Hours	1217	8759	520	229	872	185	3523	2600
Deficit									
P_{100}	GWh	188	1259	158	25.1	106	18.8	282	266
P_{10}	GWh	668	4467	562	150	473	50.1	1334	1496
P_1	GWh	944	5309	750	211	596	84.1	1995	1884

Table J.20: Result summary table for power flow operation variables and lulls [Continued]

		Poland				Portugal			Romania
		42_pl	43_pl	44_pl	45_pl		12_pt	13_pt	
Power Flow Orchestration									
Generation Used									
Onshore	TWh	13.6	13.0	46.5	47.5	33.0	11.2	21.8	15.8
Offshore	TWh	0.00	0.00	0.00	0.00	0.00	0.00	0.00	0.00
PV	TWh	4.84	6.29	6.40	3.73	23.6	14.1	9.54	15.2
ROR	TWh	0.00	1.59	0.00	5.26	13.9	12.6	1.25	0.00
Biomass	TWh	1.73	1.18	2.42	2.26	1.51	0.56	0.95	3.13
Hydro	TWh	0.00	1.43	0.00	2.57	19.5	16.5	2.99	21.3
Misc.									
Curtailed	TWh	21.6	13.7	27.7	24.1	9.36	3.23	6.13	3.36
Hydro Stored	TWh	0.00	1.21	0.00	2.23	16.1	13.8	2.34	1.72
Import	TWh	11.2	19.1	5.67	2.57	12.2	9.81	6.04	18.8
Export	TWh	4.00	1.19	23.0	34.1	16.7	14.8	5.52	4.24
Unsatisfied	TWh	0.01	0.00	0.02	0.00	0.00	0.00	0.00	0.00
Max. Residual Load									
P_{100}	GW	2.74	3.41	3.96	5.29	11.3	8.38	2.97	12.7
P_{10}	GW	3.74	3.41	5.73	5.29	12.5	8.38	4.30	15.8
P_1	GW	6.00	3.41	5.73	5.29	13.4	8.58	5.05	16.9
"Power Flow" Lull Context									
Years Without Lull [%]		18.4	99.5	18.9	100	61.6	96.2	61.6	100
Span									
P_{100}	Hours								
P_{10}	Hours	159		169		111		125	
P_1	Hours	461		301		229	64.0	361	
Deficit									
P_{100}	GWh								
P_{10}	GWh	26.6		42.2		3.98		3.98	
P_1	GWh	63.1		100		25.1	0.42	25.1	
Deficit vs. Annual Demand									
P_{100}	%								
P_{10}	%	0.10		0.11		0.01		0.01	
P_1	%	0.23		0.26		0.04	0.00	0.07	

Table J.21: Summary table for E-Highway inputs, simulation results, VRES Only lulls, and Copper Plate lulls [Continued]

		Romania			Serbia	Slovakia	Slovenia	Spain	
		59_ro	60_ro	61_ro	65_rs	46_sk	57_si		01_es
E-Highway Inputs:									
Total Annual Demand and Capacities									
Demand	TWh	17.1	33.6	17.5	31.4	26.5	14.9	498	13.5
Biomass	GW	2.50	3.25	3.50	1.00	2.75	0.75	17.2	0.75
Hydro	GW	3.90	3.61	1.11	1.93	0.31	0.32	34.0	8.24
Onshore Wind	GW	0.10	0.64	4.09	1.43	5.23	0.47	69.4	7.29
Offshore Wind	GW								
PV	GW	2.96	4.38	3.64	4.99	6.88	2.33	103	1.56
VRES Simulation Outcomes:									
Total Generation Potentials									
Onshore Wind	TWh	0.49	2.86	15.6	5.81	16.7	1.95	292	31.0
Offshore Wind	TWh	0.00	0.00	0.00	0.00	0.00	0.00	0.00	0.00
PV	TWh	4.10	6.21	5.10	7.22	8.80	3.18	187	2.59
'VRES Only' Lull Context									
Onshore Wind									
P_{100}	Hours	37.0	44.0	60.0	43.0	87.0	49.0	18.0	18.0
P_{10}	Hours	125	169	197	203	361	141	107	107
P_1	Hours	169	191	216	361	396	267	133	133
Offshore Wind									
P_{100}	Hours								
P_{10}	Hours								
P_1	Hours								
PV									
P_{100}	Hours	44.0	46.0	66.0	44.0	114	89.0	19.0	21.0
P_{10}	Hours	164	229	236	244	351	320	66.0	79.0
P_1	Hours	330	351	301	330	461	421	159	114
All VRES									
P_{100}	Hours	19.0	18.0	20.0	16.0	20.0	19.0	13.0	15.0
P_{10}	Hours	89.0	70.0	89.0	39.0	125	75.0	20.0	64.0
P_1	Hours	114	137	185	62.0	244	89.0	20.0	72.0
'Copper Plate' Lull Context									
Years Without Lull [%]		0.00	0.00	0.00	0.00	0.00	0.00	0.00	100
Span									
P_{100}	Hours	15.0	8759	57.0	13.0	98.0	21.0	72.0	
P_{10}	Hours	68.0	8759	320	89.0	684	505	310	
P_1	Hours	114	8759	520	209	820	606	520	
Deficit									
P_{100}	GWh	2.82	6683	20.0	2.82	44.7	3.76	376	
P_{10}	GWh	7.50	7499	106	20.0	299	59.6	1496	
P_1	GWh	10.6	7943	200	44.7	398	89.1	2239	

Table J.22: Result summary table for power flow operation variables and lulls [Continued]

		Romania			Serbia	Slovakia	Slovenia	Spain	
		59_ro	60_ro	61_ro	65_rs	46_sk	57_si		01_es
Power Flow Orchestration									
Generation Used									
Onshore	TWh	0.41	2.39	13.0	4.77	13.6	1.57	218	23.2
Offshore	TWh	0.00	0.00	0.00	0.00	0.00	0.00	0.00	0.00
PV	TWh	4.04	6.14	5.04	6.88	7.34	2.54	183	2.48
ROR	TWh	0.00	0.00	0.00	16.2	6.26	8.32	36.1	3.86
Biomass	TWh	0.31	2.78	0.05	0.04	2.67	1.26	16.6	0.40
Hydro	TWh	8.77	10.00	2.50	5.46	0.50	0.59	41.4	5.73
Misc.									
Curtailed	TWh	0.15	0.54	2.67	1.39	4.64	1.01	77.9	7.89
Hydro Stored	TWh	0.00	1.72	0.00	1.93	0.50	0.22	18.8	3.53
Import	TWh	5.94	16.6	2.15	5.65	2.57	2.55	54.0	3.33
Export	TWh	3.59	1.37	5.23	5.68	8.71	1.67	32.4	22.0
Unsatisfied	TWh	0.00	0.00	0.00	0.00	0.00	0.00	0.19	0.01
Max. Residual Load									
P_{100}	GW	5.47	6.81	0.91	1.92	3.04	1.07	40.2	4.01
P_{10}	GW	5.66	6.81	4.40	2.90	4.60	1.31	51.2	4.50
P_1	GW	5.66	6.81	4.40	2.90	4.66	2.77	56.1	5.35
"Power Flow" Lull Context									
Years Without Lull [%]		100	100	100	100	53.0	15.1	0.00	8.11
Span									
P_{100}	Hours							16.0	
P_{10}	Hours					461	899	197	185
P_1	Hours					772	1417	520	310
Deficit									
P_{100}	GWh							2.51	
P_{10}	GWh					6.31	10.0	237	11.9
P_1	GWh					23.7	33.5	473	23.7
Deficit vs. Annual Demand									
P_{100}	%							0.00	
P_{10}	%					0.02	0.07	0.05	0.09
P_1	%					0.09	0.22	0.09	0.17

Table J.23: Summary table for E-Highway inputs, simulation results, VRES Only lulls, and Copper Plate lulls [Continued]

		Spain							
		02_es	03_es	04_es	05_es	06_es	07_es	08_es	09_es
E-Highway Inputs:									
Total Annual Demand and Capacities									
Demand	TWh	39.8	21.9	33.1	14.6	84.4	71.9	25.9	60.0
Biomass	GW	1.75	2.75	1.25	2.00	1.25	0.25	1.50	1.75
Hydro	GW	9.12	1.03	0.61	1.85	4.85	0.45	1.61	1.70
Onshore Wind	GW	5.89	13.6	5.69	11.1	3.59	0.19	2.06	3.31
Offshore Wind	GW								
PV	GW	7.90	7.83	5.10	4.82	12.6	12.4	15.8	12.4
VRES Simulation Outcomes:									
Total Generation Potentials									
Onshore Wind	TWh	25.5	54.9	24.6	45.6	16.0	0.96	9.46	14.9
Offshore Wind	TWh	0.00	0.00	0.00	0.00	0.00	0.00	0.00	0.00
PV	TWh	13.4	14.5	8.40	8.94	22.4	22.9	30.2	23.1
'VRES Only' Lull Context									
Onshore Wind									
P_{100}	Hours	18.0	19.0	18.0	19.0	18.0	18.0	19.0	19.0
P_{10}	Hours	107	114	107	111	104	62.0	104	104
P_1	Hours	133	174	133	174	133	104	133	133
Offshore Wind									
P_{100}	Hours								
P_{10}	Hours								
P_1	Hours								
PV									
P_{100}	Hours	20.0	19.0	19.0	19.0	20.0	19.0	19.0	20.0
P_{10}	Hours	68.0	66.0	66.0	70.0	68.0	70.0	89.0	114
P_1	Hours	92.0	137	68.0	114	111	159	159	159
All VRES									
P_{100}	Hours	14.0	14.0	13.0	14.0	15.0	19.0	17.0	15.0
P_{10}	Hours	19.0	28.0	20.0	38.0	20.0	66.0	21.0	19.0
P_1	Hours	21.0	43.0	27.0	47.0	39.0	137	39.0	39.0
'Copper Plate' Lull Context									
Years Without Lull [%]		0.00	0.00	0.00	87.6	0.00	0.00	0.00	0.00
Span									
P_{100}	Hours	9.00	3.00	174		8497	8759	14.0	8497
P_{10}	Hours	17.0	16.0	846		8759	8759	18.0	8759
P_1	Hours	19.0	19.0	1146	6.00	8759	8759	20.0	8759
Deficit									
P_{100}	GWh	1.78	0.67	70.8		18836	35481	11.9	3350
P_{10}	GWh	8.41	7.50	335	0.01	22387	35481	16.8	5957
P_1	GWh	11.2	11.2	447	1.26	22387	37584	17.8	6683

Table J.24: Result summary table for power flow operation variables and lulls [Continued]

		Spain							
		02_es	03_es	04_es	05_es	06_es	07_es	08_es	09_es
Power Flow Orchestration									
Generation Used									
Onshore	TWh	18.8	40.8	17.7	32.2	12.6	0.73	7.13	11.4
Offshore	TWh	0.00	0.00	0.00	0.00	0.00	0.00	0.00	0.00
PV	TWh	12.9	14.2	7.57	8.56	22.2	22.7	29.5	22.9
ROR	TWh	10.3	0.00	0.00	4.03	0.00	0.00	15.1	0.12
Biomass	TWh	1.00	2.05	1.11	2.73	1.22	0.33	1.63	2.14
Hydro	TWh	17.1	0.97	0.00	2.52	7.38	0.00	2.72	1.25
Misc.									
Curtailed	TWh	7.19	14.5	7.72	13.8	3.62	0.43	3.04	3.70
Hydro Stored	TWh	6.27	0.76	0.00	2.32	1.09	0.00	0.71	0.79
Import	TWh	4.48	0.13	8.19	0.08	42.2	49.2	1.21	25.6
Export	TWh	18.4	35.5	1.46	33.2	0.08	1.04	30.8	2.66
Unsatisfied	TWh	0.01	0.00	0.02	0.01	0.03	0.01	0.02	0.05
Max. Residual Load									
P_{100}	GW	10.8	3.15	1.24	2.71	6.07	0.25	3.57	3.92
P_{10}	GW	11.6	3.15	2.74	3.22	7.82	3.87	3.57	5.73
P_1	GW	15.8	7.82	3.04	4.50	16.0	13.3	4.35	9.40
"Power Flow" Lull Context									
Years Without Lull [%]		5.41	94.6	8.65	2.16	1.62	19.5	0.00	0.00
Span									
P_{100}	Hours							15.0	41.0
P_{10}	Hours	203		203	150	505	796	310	587
P_1	Hours	320	64.0	373	301	684	1255	475	846
Deficit									
P_{100}	GWh							0.47	2.00
P_{10}	GWh	20.0		31.6	13.3	42.2	13.3	15.0	66.8
P_1	GWh	37.6	7.94	66.8	25.1	100	29.9	28.2	150
Deficit vs. Annual Demand									
P_{100}	%							0.00	0.00
P_{10}	%	0.05		0.09	0.09	0.05	0.02	0.06	0.11
P_1	%	0.09	0.04	0.20	0.17	0.12	0.04	0.11	0.25

Table J.25: Summary table for E-Highway inputs, simulation results, VRES Only lulls, and Copper Plate lulls [Continued]

		Spain		Sweden					Switzerland
		10_es	11_es		86_se	87_se	88_se	89_se	
E-Highway Inputs:									
Total Annual Demand and Capacities									
Demand	TWh	35.1	97.7	132	3.95	11.8	89.5	26.3	77.3
Biomass	GW	2.00	2.00	5.50	0.75	3.00	1.25	0.50	1.25
Hydro	GW	1.28	3.23	21.4	7.69	10.0	3.66	0.00	13.6
Onshore Wind	GW	2.57	14.2	24.2	4.89	5.28	11.1	2.99	1.38
Offshore Wind	GW			3.00				3.00	
PV	GW	6.88	15.2	8.92	1.58	1.58	4.46	1.30	15.0
VRES Simulation Outcomes:									
Total Generation Potentials									
Onshore Wind	TWh	11.7	57.0	103	21.1	22.7	45.6	13.3	6.07
Offshore Wind	TWh	0.00	0.00	12.5	0.00	0.00	0.00	12.5	0.00
PV	TWh	12.8	27.7	9.58	1.73	1.63	4.80	1.42	19.6
'VRES Only' Lull Context									
Onshore Wind									
P_{100}	Hours	18.0	19.0	39.0	39.0	39.0	39.0	39.0	27.0
P_{10}	Hours	104	114	191	209	191	185	191	79.0
P_1	Hours	133	174	292	310	292	292	267	150
Offshore Wind									
P_{100}	Hours			137				137	
P_{10}	Hours			373				373	
P_1	Hours			643				643	
PV									
P_{100}	Hours	20.0	19.0	705	643	926	749	663	66.0
P_{10}	Hours	92.0	68.0	1333	1333	1333	1333	1217	330
P_1	Hours	159	141	1552	1506	1649	1552	1417	421
All VRES									
P_{100}	Hours	15.0	13.0	27.0	26.0	27.0	21.0	26.0	19.0
P_{10}	Hours	19.0	22.0	77.0	89.0	92.0	72.0	121	44.0
P_1	Hours	38.0	39.0	114	137	145	101	174	70.0
'Copper Plate' Lull Context									
Years Without Lull [%]		0.00	0.00	0.00	100	100	0.00	0.00	0.00
Span									
P_{100}	Hours	1417	351	52.0			8759	6665	1979
P_{10}	Hours	2936	1752	292			8759	8759	2600
P_1	Hours	3216	2040	434			8759	8759	2681
Deficit									
P_{100}	GWh	299	335	79.4			37584	3548	891
P_{10}	GWh	891	1778	473			47315	7079	2239
P_1	GWh	1122	2512	794			50119	7499	2512

Table J.26: Result summary table for power flow operation variables and lulls [Continued]

		Spain		Sweden					Switzerland
		10_es	11_es		86_se	87_se	88_se	89_se	
Power Flow Orchestration									
Generation Used									
Onshore	TWh	8.97	44.2	92.8	18.5	20.6	41.7	12.0	5.44
Offshore	TWh	0.00	0.00	7.42	0.00	0.00	0.00	7.42	0.00
PV	TWh	12.6	27.5	9.56	1.73	1.63	4.80	1.41	19.3
ROR	TWh	0.00	2.72	9.91	2.39	6.78	0.74	0.00	18.6
Biomass	TWh	2.06	1.93	0.26	0.00	0.01	0.09	0.16	1.51
Hydro	TWh	0.00	3.79	49.3	9.94	27.2	12.2	0.00	36.1
Misc.									
Curtailed	TWh	2.99	13.0	15.1	2.65	2.14	3.96	6.31	0.91
Hydro Stored	TWh	0.00	3.28	0.00	0.00	0.00	0.00	0.00	13.6
Import	TWh	13.0	23.1	11.1	0.01	0.05	30.9	7.69	29.0
Export	TWh	1.49	2.41	48.8	28.6	44.4	1.02	2.41	19.1
Unsatisfied	TWh	0.00	0.04	0.00	0.00	0.00	0.00	0.00	0.01
Max. Residual Load									
P_{100}	GW	1.98	3.70	21.3	7.64	9.96	4.88	0.50	14.7
P_{10}	GW	1.98	5.29	23.9	8.00	13.0	4.88	0.50	16.7
P_1	GW	3.74	14.1	25.3	8.38	13.0	4.88	0.50	16.7
"Power Flow" Lull Context									
Years Without Lull [%]		93.5	0.00	100	100	100	100	100	49.2
Span									
P_{100}	Hours		13.0						
P_{10}	Hours		361						1600
P_1	Hours	159	570						2523
Deficit									
P_{100}	GWh		0.42						
P_{10}	GWh		59.6						18.8
P_1	GWh	3.55	150						106
Deficit vs. Annual Demand									
P_{100}	%		0.00						
P_{10}	%		0.06						0.02
P_1	%	0.01	0.15						0.13

Table J.27: Summary table for E-Highway inputs, simulation results, VRES Only lulls, and Copper Plate lulls [Continued]

		Switzerland		United Kingdom					
		47_ch	48_ch		90_uk	91_uk	92_uk	93_uk	94_uk
E-Highway Inputs:									
Total Annual Demand and Capacities									
Demand	TWh	60.3	17.0	439	162	39.5	158	43.9	22.0
Biomass	GW	1.00	0.25	12.5	4.75	0.50	4.00	1.75	1.50
Hydro	GW	1.63	11.9	11.6	0.06	0.00	6.24	0.35	4.98
Onshore Wind	GW	0.51	0.87	93.1	19.4	13.8	27.9	11.8	13.9
Offshore Wind	GW			37.2	22.3		11.2	1.86	1.86
PV	GW	12.0	3.03	59.9	18.6	9.29	19.6	7.69	3.47
VRES Simulation Outcomes:									
Total Generation Potentials									
Onshore Wind	TWh	2.31	3.76	396	82.2	59.1	117	50.9	59.8
Offshore Wind	TWh	0.00	0.00	162	96.5	0.00	48.5	7.80	8.81
PV	TWh	15.5	4.15	63.3	20.0	10.0	20.4	8.01	3.53
'VRES Only' Lull Context									
Onshore Wind									
P_{100}	Hours	29.0	26.0	107	111	107	114	107	107
P_{10}	Hours	79.0	79.0	361	373	330	373	330	330
P_1	Hours	150	150	505	520	505	520	505	505
Offshore Wind									
P_{100}	Hours			62.0	107		150	164	118
P_{10}	Hours			236	310		447	505	340
P_1	Hours			373	421		587	643	461
PV									
P_{100}	Hours	66.0	44.0	259	185	185	283	283	301
P_{10}	Hours	361	185	749	727	727	872	846	846
P_1	Hours	447	283	1046	1046	1046	1146	1146	1146
All VRES									
P_{100}	Hours	39.0	17.0	41.0	35.0	27.0	44.0	43.0	72.0
P_{10}	Hours	89.0	43.0	137	133	137	164	137	180
P_1	Hours	137	64.0	267	267	150	267	159	292
'Copper Plate' Lull Context									
Years Without Lull [%]		0.00	100	0.00	0.00	0.00	0.00	0.00	0.00
Span									
P_{100}	Hours	8759		275	796	229	899	283	31.0
P_{10}	Hours	8759		1919	6272	872	6085	1552	121
P_1	Hours	8759		3978	8497	1255	8759	3523	141
Deficit									
P_{100}	GWh	19953		3548	2239	224	2371	376	11.9
P_{10}	GWh	22387		12589	9441	944	9441	1189	47.3
P_1	GWh	22387		16788	14962	1413	17783	1778	84.1

Table J.28: Result summary table for power flow operation variables and lulls [Continued]

		Switzerland		United Kingdom					
		47_ch	48_ch		90_uk	91_uk	92_uk	93_uk	94_uk
Power Flow Orchestration									
Generation Used									
Onshore	TWh	2.05	3.39	319	68.3	47.0	91.4	43.2	48.6
Offshore	TWh	0.00	0.00	54.5	35.4	0.00	13.3	2.33	3.53
PV	TWh	15.2	4.14	63.1	20.0	10.0	20.3	7.94	3.50
ROR	TWh	8.35	10.3	4.42	0.00	0.00	2.38	0.13	1.90
Biomass	TWh	1.27	0.24	13.2	5.10	0.48	3.80	2.06	1.73
Hydro	TWh	4.33	31.7	15.0	0.00	0.00	3.98	0.00	11.0
Misc.									
Curtailed	TWh	0.53	0.38	185	75.0	12.1	60.5	13.3	16.5
Hydro Stored	TWh	1.62	11.9	7.25	0.00	0.00	2.71	0.00	4.54
Import	TWh	43.8	6.02	46.6	37.7	4.13	32.3	4.73	2.62
Export	TWh	0.93	39.0	70.2	4.29	22.2	6.94	16.6	46.6
Unsatisfied	TWh	0.00	0.00	1.08	0.24	0.16	0.31	0.13	0.18
Max. Residual Load									
P_{100}	GW	2.62	12.1	27.1	6.73	1.75	9.08	1.98	7.21
P_{10}	GW	3.61	13.1	49.4	14.6	3.04	23.4	8.00	9.51
P_1	GW	3.61	13.1	56.1	23.4	5.86	28.4	8.48	9.62
"Power Flow" Lull Context									
Years Without Lull [%]		50.8	57.3	0.00	0.00	0.00	0.00	0.00	0.00
Span									
P_{100}	Hours			49.0	27.0	98.0	50.0	66.0	82.0
P_{10}	Hours	1600	1600	373	361	796	340	447	475
P_1	Hours	2447	2523	490	536	1255	421	846	846
Deficit									
P_{100}	GWh			31.6	6.31	7.50	12.6	2.00	5.96
P_{10}	GWh	9.44	9.44	841	188	126	282	141	133
P_1	GWh	50.1	56.2	1679	335	224	562	335	251
Deficit vs. Annual Demand									
P_{100}	%			0.01	0.00	0.02	0.01	0.00	0.03
P_{10}	%	0.01	0.19	0.19	0.11	0.32	0.18	0.32	0.60
P_1	%	0.07	1.14	0.38	0.20	0.56	0.35	0.75	1.13

Table J.29: Summary table for E-Highway inputs, simulation results, VRES Only lulls, and Copper Plate lulls [Continued]

		United Kingdom 95_uk
E-Highway Inputs:		
Total Annual Demand and Capacities		
Demand	TWh	13.2
Biomass	GW	0.00
Hydro	GW	0.00
Onshore Wind	GW	6.28
Offshore Wind	GW	
PV	GW	1.24
VRES Simulation Outcomes:		
Total Generation Potentials		
Onshore Wind	TWh	27.6
Offshore Wind	TWh	0.00
PV	TWh	1.27
'VRES Only' Lull Context		
Onshore Wind		
P_{100}	Hours	95.0
P_{10}	Hours	310
P_1	Hours	490
Offshore Wind		
P_{100}	Hours	
P_{10}	Hours	
P_1	Hours	
PV		
P_{100}	Hours	244
P_{10}	Hours	820
P_1	Hours	1015
All VRES		
P_{100}	Hours	82.0
P_{10}	Hours	244
P_1	Hours	301
'Copper Plate' Lull Context		
0.00		
Years Without Lull [%]		*Span*
P_{100}	Hours	180
P_{10}	Hours	727
P_1	Hours	984
Deficit		
P_{100}	GWh	79.4
P_{10}	GWh	266
P_1	GWh	299

Table J.30: Result summary table for power flow operation variables and lulls [Continued]

		United Kingdom 95_uk
Power Flow Orchestration		
Generation Used		
Onshore	TWh	20.2
Offshore	TWh	0.00
PV	TWh	1.27
ROR	TWh	0.00
Biomass	TWh	0.00
Hydro	TWh	0.00
Misc.		
Curtailed	TWh	7.41
Hydro Stored	TWh	0.00
Import	TWh	1.73
Export	TWh	10.1
Unsatisfied	TWh	0.06
Max. Residual Load		
P_{100}	GW	0.50
P_{10}	GW	1.94
P_1	GW	3.08
"Power Flow" Lull Context		
Years Without Lull [%]		0.00
Span		
P_{100}	Hours	62.0
P_{10}	Hours	447
P_1	Hours	705
Deficit		
P_{100}	GWh	1.78
P_{10}	GWh	44.7
P_1	GWh	84.1
Deficit vs. Annual Demand		
P_{100}	%	0.01
P_{10}	%	0.34
P_1	%	0.63

Bibliography

[1] D. J. Wuebbles, D. W. Fahey, K. A. Hibbard, D. J. Dokken, B. C. Stewart, and T. K. Maycock, “Climate Science Special Report: Fourth National Climate Assessment, Volume I,” U.S. Global Change Research Program (USGCRP), Washington, DC, USA, Tech. Rep., 2017.

[2] R. Pachauri and L. Meyer, “Climate Change 2014: Synthesis Report. Contribution Of Working Groups I, Ii And Iii To The Fifth Assessment Report Of The Intergovernmental Panel On Climate Change,” International Panel on Climate Change, IPCC, Geneva, Switzerland, Tech. Rep., 2014. [Online]. Available: https://www.ipcc.ch/site/assets/uploads/2018/02/SYR_AR5_FINAL_full.pdf

[3] J. Cook, N. Oreskes, P. T. Doran, W. R. L. Anderegg, B. Verheggen, E. W. Maibach, J. S. Carlton, S. Lewandowsky, A. G. Skuce, S. A. Green, D. Nuccitelli, P. Jacobs, M. Richardson, B. Winkler, R. Painting, and K. Rice, “Consensus On Consensus: A Synthesis Of Consensus Estimates On Human-caused Global Warming,” *Environmental Research Letters*, vol. 11, no. 4, p. 048002, apr 2016. [Online]. Available: http://stacks.iop.org/1748-9326/11/i=4/a=048002?key=crossref.80d294a6c5d3b7882bc7dc12487e9f39

[4] A. Borunda and K. Elliott, “See How A Warmer World Primed California For Large Fires,” *National Geographic*, nov 2018. [Online]. Available: https://www.nationalgeographic.com/environment/2018/11/climate-change-california-wildfire/

[5] “Report Of The Conference Of The Parties On Its Twenty-first Session, Held In Paris From 30 November To 13 December 2015,” United Nations Framework Convention on Climate Change, Paris, Tech. Rep., 2015. [Online]. Available: https://unfccc.int/resource/docs/2015/cop21/eng/10a01.pdf

[6] “Communication From The Commission To The European Parliament, The Council, The European Economic And Social Committee And The Committee Of The Regions,” Brussels, Belgium, 2011. [Online]. Available: https://eur-lex.europa.eu/legal-content/EN/TXT/?uri=CELEX:52011DC0112

[7] European Commission, “Two Years After Paris – Progress Towards Meeting The Eu’s Climate Commitments,” European Commission, Brussels, Belgium, Tech. Rep., 2017. [Online]. Available: https://eur-lex.europa.eu/legal-content/EN/TXT/?uri=COM:2017:646:FIN

[8] D. Hales, “Renewables 2018 Global Status Report,” REN21, Paris, Tech. Rep., 2018.

[9] "BP Statistical Review Of World Energy," British Petroleum (BP), London, UK, Tech. Rep., 2018. [Online]. Available: https://www.bp.com/content/dam/bp/en/corporate/pdf/energy-economics/statistical-review/bp-stats-review-2018-full-report.pdf

[10] International Energy Agency (IEA), "Key World Energy Statistics," International Energy Agency (IEA), Tech. Rep., 2018. [Online]. Available: https://webstore.iea.org/download/direct/2291?fileName=Key_World_2018.pdf

[11] M. Taylor, P. Ralon, and A. Ilas, "The power to change: Solar and wind cost reduction potential to 2025," International Renewable Energy Agency (IRENA), Tech. Rep., 2016, iSBN: 978-92-95111-97-4. [Online]. Available: http://www.irena.org/-/media/Files/IRENA/Agency/Publication/2016/IRENA_Power_to_Change_2016.pdf

[12] M. Schmela, A. Beauvais, N. Chevillard, M. G. Paredes, M. Heisz, R. Rossi, M. Schmela, D. Whitten, J. Baca, F. Telemcioglu, S. Blume, R. L. Sauaia, and S. Betz, "Global Market Outlook For Solar Power / 2018 - 2022," SolarPower Europe, Onehemisphere, Sweden, Tech. Rep., 2018. [Online]. Available: http://www.solarpowereurope.org/wp-content/uploads/2018/09/Global-Market-Outlook-2018-2022.pdf

[13] International Energy Agency (IEA), "World Energy Outlook 2018," International Energy Agency (IEA), Tech. Rep., 2018. [Online]. Available: https://www.iea.org/weo2018/

[14] P. Moriarty and D. Honnery, "Can Renewable Energy Power The Future?" *Energy Policy*, vol. 93, pp. 3–7, jun 2016. [Online]. Available: https://linkinghub.elsevier.com/retrieve/pii/S030142151630088X

[15] C. M. Grams, R. Beerli, S. Pfenninger, I. Staffell, and H. Wernli, "Balancing Europe's Wind-power Output Through Spatial Deployment Informed By Weather Regimes," *Nature Climate Change*, 2017.

[16] S. Pfenninger and I. Staffell, "Long-term patterns of European PV output using 30 years of validated hourly reanalysis and satellite data," *Energy*, vol. 114, pp. 1251–1265, nov 2016.

[17] I. Staffell and S. Pfenninger, "Using Bias-corrected Reanalysis To Simulate Current And Future Wind Power Output," *Energy*, 2016.

[18] K. Zhou, C. Fu, and S. Yang, "Big Data Driven Smart Energy Management: From Big Data To Big Insights," *Renewable and Sustainable Energy Reviews*, vol. 56, pp. 215–225, apr 2016. [Online]. Available: https://linkinghub.elsevier.com/retrieve/pii/S1364032115013179

[19] B. Resch, G. Sagl, T. Tornros, A. Bachmaier, J. B. Eggers, S. Herkel, S. Narmsara, and H. Gundra, "GIS-based Planning And Modeling For Renewable Energy: Challenges And Future Research Avenues," *Isprs International Journal of Geo-Information*, vol. 3, no. 2, pp. 662–692, 2014.

[20] M. Huber, D. Dimkova, and T. Hamacher, "Integration Of Wind And Solar Power In Europe: Assessment Of Flexibility Requirements," *Energy*, vol. 69, pp. 236–246, 2014. [Online]. Available: http://dx.doi.org/10.1016/j.energy.2014.02.109

[21] C. Klessmann, A. Held, M. Rathmann, and M. Ragwitz, "Status And Perspectives Of Renewable Energy Policy And Deployment In The European Union—what Is Needed To Reach The 2020 Targets?" *Energy Policy*, vol. 39, no. 12, pp. 7637–7657, 2011. [Online]. Available: http://www.sciencedirect.com/science/article/pii/S0301421511006355http://dx.doi.org/10.1016/j.enpol.2011.08.038

[22] M. Wolsink, "Wind Powerwind Power: Basic Challenge Concerning Social Acceptance," in *Encyclopedia Of Sustainability Science And Technology. Volume 17*, R. A. Meyers, Ed. New York, NY: Springer New York, 2012, pp. 12 218–12 254. [Online]. Available: https://doi.org/10.1007/978-1-4419-0851-3_88

[23] D. Rudolph, S. V. Larsen, and H. Nielsen, "International Experiences With Opposition To Wind Energy Siting Decisions: Lessons For Environmental And Social Appraisal Au - Cashmore, Matthew," *Journal of Environmental Planning and Management*, pp. 1–24, jun 2018, doi: 10.1080/09640568.2018.1473150. [Online]. Available: https://doi.org/10.1080/09640568.2018.1473150

[24] B. Moller, "Spatial Analyses Of Emerging And Fading Wind Energy Landscapes In Denmark," *Land Use Policy*, vol. 27, no. 2, pp. 233–241, 2010.

[25] D. S. Ryberg, M. Robinius, and D. Stolten, "Methodological Framework for Determining the Land Eligibility of Renewable Energy Sources," *ArXiv*, dec 2017. [Online]. Available: http://arxiv.org/abs/1712.07840

[26] S. D. Ã. Pohekar and M. Ramachandran, "Application Of Multi-criteria Decision Making To Sustainable Energy Planning - A Review," *Renewable & Sustainable Energy Reviews*, vol. 8, no. 4, pp. 365–381, 2004.

[27] E. Loken and E. L. Ã, "Use Of Multicriteria Decision Analysis Methods For Energy Planning Problems," *Renewable & Sustainable Energy Reviews*, vol. 11, no. 7, pp. 1584–1595, 2007.

[28] M. Iqbal, M. Azam, M. Naeem, A. S. Khwaja, and A. Anpalagan, "Optimization Classification, Algorithms And Tools For Renewable Energy: A Review," *Renewable & Sustainable Energy Reviews*, vol. 39, pp. 640–654, 2014.

[29] R. McKenna, S. Hollnaicher, and W. Fichtner, "Cost-potential curves for onshore wind energy: A high-resolution analysis for Germany," *Applied Energy*, vol. 115, pp. 103–115, feb 2014. [Online]. Available: http://dx.doi.org/10.1016/j.apenergy.2013.10.030https://linkinghub.elsevier.com/retrieve/pii/S0306261913008507

[30] M. Robinius, A. Otto, K. Syranidis, D. S. Ryberg, P. Heuser, L. Welder, T. Grube, P. Markewitz, V. Tietze, and D. Stolten, "Linking The Power And Transport Sectors - Part 2: Modelling A Sector Coupling Scenario For Germany," *Energies*, vol. 10, 2017.

[31] S. Samsatli, I. Staffell, and N. J. Samsatli, "Optimal Design And Operation Of Integrated Wind-hydrogen-electricity Networks For Decarbonising The Domestic Transport Sector In Great Britain," *International Journal of Hydrogen Energy*, vol. 41, no. 1, pp. 447–475, jan 2016. [Online]. Available: http://dx.doi.org/10.1016/j.ijhydene.2015.10.032https://linkinghub.elsevier.com/retrieve/pii/S0360319915300574

[32] B. Sliz-Szkliniarz, "Assessment Of The Renewable Energy-mix And Land Use Trade-off At A Regional Level: A Case Study For The Kujawsko-pomorskie Voivodship," *Land Use Policy*, vol. 35, pp. 257–270, 2013. [Online]. Available: http://dx.doi.org/10.1016/j.landusepol.2013.05.018

[33] L.-I. Tegou, H. Polatidis, and D. A. Haralambopoulos, "Distributed Generation With Renewable Energy Systems: The Spatial Dimension For An Autonomous Grid," in *47th conference of the European Regional Science Association, ERSA. Paris, France*, 2007, pp. 1731–1744.

[34] O. A. Omitaomu, B. R. Blevins, W. C. Jochem, G. T. Mays, R. Belles, S. W. Hadley, T. J. Harrison, B. L. Bhaduri, B. S. Neish, and A. N. Rose, "Adapting A GIS-based Multicriteria Decision Analysis Approach For Evaluating New Power Generating Sites," *Applied Energy*, vol. 96, pp. 292–301, 2012. [Online]. Available: http://dx.doi.org/10.1016/j.apenergy.2011.11.087

[35] R. van Haaren, V. Fthenakis, R. V. Haaren, and V. Fthenakis, "GIS-based Wind Farm Site Selection Using Spatial Multi-criteria Analysis (smca): Evaluating The Case For New York State," *Renewable and Sustainable Energy Reviews*, vol. 15, no. 7, pp. 3332–3340, 2011. [Online]. Available: http://dx.doi.org/10.1016/j.rser.2011.04.010

[36] N. Y. Aydin, E. Kentel, and H. Sebnem Duzgun, "Gis-based Site Selection Methodology For Hybrid Renewable Energy Systems: A Case Study From Western Turkey," *Energy Conversion and Management*, vol. 70, pp. 90–106, jun 2013. [Online]. Available: http://dx.doi.org/10.1016/j.enconman.2013.02.004https://linkinghub.elsevier.com/retrieve/pii/S0196890413000848

[37] C. Franco, M. Bojesen, J. L. Hougaard, K. Nielsen, C. Franco, M. Bojesen, J. L. Hougaard, and K. Nielsen, "A Fuzzy Approach To A Multiple Criteria And Geographical Information System For Decision Support On Suitable Locations For Biogas Plants," *Applied Energy*, vol. 140, no. March, pp. 304–315, 2015. [Online]. Available: http://dx.doi.org/10.1016/j.apenergy.2014.11.060

[38] T. Höfer, Y. Sunak, H. Siddique, and R. Madlener, "Wind Farm Siting Using A Spatial Analytic Hierarchy Process Approach: A Case Study Of The Städteregion Aachen," *Applied Energy*, vol. 163, pp. 222–243, 2016.

[39] D. Latinopoulos and K. Kechagia, “A GIS-based Multi-criteria Evaluation For Wind Farm Site Selection. A Regional Scale Application In Greece,” *Renewable Energy*, vol. 78, pp. 550–560, jun 2015. [Online]. Available: http://dx.doi.org/10.1016/j.renene.2015.01.041https://linkinghub.elsevier.com/retrieve/pii/S0960148115000592

[40] K. B. Atici, A. B. Simsek, A. Ulucan, and M. U. Tosun, “A Gis-based Multiple Criteria Decision Analysis Approach For Wind Power Plant Site Selection,” *Utilities Policy*, vol. 37, pp. 86–96, dec 2015. [Online]. Available: http://dx.doi.org/10.1016/j.jup.2015.06.001https://linkinghub.elsevier.com/retrieve/pii/S0957178715000351

[41] M. Vasileiou, E. Loukogeorgaki, and D. G. Vagiona, “GIS-based Multi-criteria Decision Analysis For Site Selection Of Hybrid Offshore Wind And Wave Energy Systems In Greece,” *Renewable and Sustainable Energy Reviews*, vol. 73, no. January, pp. 745–757, jun 2017. [Online]. Available: http://dx.doi.org/10.1016/j.rser.2017.01.161https://linkinghub.elsevier.com/retrieve/pii/S1364032117301892

[42] C. Coppens, H. Gordijn, M. Piek, P. Ruyssenaars, J.-j. Schrander, P. de Smet, R. Swart, M. Hoogwijk, M. Papalexandrou, E. de Visser, J. Horalek, P. Kurfürst, F. Pagh Jensen, B. Svenning Petersen, M. Harfoot, R. Milego, N.-E. Clausen, and G. Giebel, “Europe’s onshore and offshore wind energy potential: An assessment of environmental and economic constraints,” European Environmental Agency, Report, June 2009.

[43] R. McKenna, S. Hollnaicher, P. Ostman v. d. Leye, and W. Fichtner, “Cost-potentials for large onshore wind turbines in Europe,” *Energy*, vol. 83, pp. 217–229, apr 2015. [Online]. Available: https://linkinghub.elsevier.com/retrieve/pii/S0360544215001681

[44] W. Zappa and M. van den Broek, “Analysing The Potential Of Integrating Wind And Solar Power In Europe Using Spatial Optimisation Under Various Scenarios,” *Renewable and Sustainable Energy Reviews*, vol. 94, no. August, pp. 1192–1216, 2018. [Online]. Available: https://doi.org/10.1016/j.rser.2018.05.071

[45] Y. Y. Deng, M. Haigh, W. Pouwels, L. Ramaekers, R. Brandsma, S. Schimschar, J. Grözinger, and D. de Jager, “Quantifying A Realistic, Worldwide Wind And Solar Electricity Supply,” *Global Environmental Change*, vol. 31, pp. 239–252, mar 2015. [Online]. Available: https://linkinghub.elsevier.com/retrieve/pii/S0959378015000072

[46] A. Myhr, C. Bjerkseter, A. Ågotnes, and T. A. Nygaard, “Levelised Cost Of Energy For Offshore Floating Wind Turbines In A Life Cycle Perspective,” *Renewable Energy*, vol. 66, pp. 714–728, jun 2014. [Online]. Available: https://linkinghub.elsevier.com/retrieve/pii/S0960148114000469

[47] M. Robinius, “Strom- Und Gasmarktdesign Zur Versorgung Des Deutschen Straßenverkehrs Mit Wasserstoff Von Der Fakultät Für Maschinenwesen Der

Rheinisch-westfälischen Technischen Hochschule Aachen Zur Erlangung Des Akademischen Grades Eines Doktors Der Ingenieurwissensch," Doctoral, RWTH Aachen, 2015.

[48] T. Jäger, R. McKenna, and W. Fichtner, "The feasible onshore wind energy potential in Baden-Württemberg: A bottom-up methodology considering socio-economic constraints," *Renewable Energy*, vol. 96, pp. 662–675, oct 2016. [Online]. Available: https://linkinghub.elsevier.com/retrieve/pii/S0960148116304244

[49] H.-J. Wagner and J. Mathur, *Introduction to Wind Energy Systems: Basics, Technology and Operation*. Springer Science & Business Media, 2009, ISBN: 978-3-642-32976-0.

[50] O. Tlili, C. Mansilla, M. Robinius, D. S. Ryberg, D. G. Caglayan, J. Linssen, J. André, Y. Perez, and D. Stolten, "Downscaling of future national capacity scenarios of the French electricity system to the regional level," *Energy Systems*, sep 2020. [Online]. Available: http://link.springer.com/10.1007/s12667-020-00406-8

[51] J. J. W. Watson and M. D. Hudson, "Regional Scale Wind Farm And Solar Farm Suitability Assessment Using GIS-assisted Multi-criteria Evaluation," *Landscape and Urban Planning*, vol. 138, pp. 20–31, 2015. [Online]. Available: http://dx.doi.org/10.1016/j.landurbplan.2015.02.001

[52] J. J. Wang, Y. Y. Jing, C. F. Zhang, and J. H. Zhao, "Review On Multi-criteria Decision Analysis Aid In Sustainable Energy Decision-making," *Renewable & Sustainable Energy Reviews*, vol. 13, no. 9, pp. 2263–2278, 2009.

[53] LANUV, "Potenzialstudie Erneuerbare Energien Nrw; Teil 1-windenergie," Landesamt für Natur, Umwelt und Verbraucherschutz Nordrhein-Westfalen, Tech. Rep., 2013.

[54] S. Al-Yahyai, Y. Charabi, A. Gastli, and A. Al-Badi, "Wind Farm Land Suitability Indexing Using Multi-criteria Analysis," *Renewable Energy*, vol. 44, pp. 80–87, 2012. [Online]. Available: http://dx.doi.org/10.1016/j.renene.2012.01.004

[55] S. M. J. Baban and T. Parry, "Developing And Applying A Gis-assisted Approach To Locating Wind Farms In The Uk," *Renewable Energy*, vol. 24, no. 1, pp. 59–71, 2001.

[56] A. Bennui, P. Rattanamanee, U. Puetpaiboon, P. Phukpattaranont, and K. Chetpattananondh, "Site Selection For Large Wind Turbine Using Gis," in *PSU-UNS International Conference on Engineering and Environment*, 2007, pp. 561–566.

[57] J. Clifton and B. Boruff, "Site Options For Concentrated Solar Power Generation In The Wheatbelt," *Perth, Australia, Prepared for the Wheatbelt Development Commission*, 2010.

[58] H. A. Effat, “Spatial Modeling Of Optimum Zones For Wind Farms Using Remote Sensing And Geographic Information System, Application In The Red Sea, Egypt,” *Journal of Geographic Information System*, vol. 06, no. 04, pp. 358–374, 2014.

[59] T. Funabashi, “A GIS Approach For Estimating Optimal Sites For Grid-connected Photovoltaic (pv) Cells In Nebraska,” 2011.

[60] M. S. García-cascales, M. T. Lamata, J. M. Sanchez-Lozano, M. S. Garcia-Cascales, and M. T. Lamata, “Identification And Selection Of Potential Sites For Onshore Wind Farms Development In Region Of Murcia, Spain,” *Energy*, vol. 73, pp. 311–324, 2014.

[61] V. Gass, J. Schmidt, F. Strauss, and E. Schmid, “Assessing The Economic Wind Power Potential In Austria,” *Energy Policy*, vol. 53, no. 2013, pp. 323–330, 2013. [Online]. Available: http://dx.doi.org/10.1016/j.enpol.2012.10.079

[62] A. Gastli, Y. Charabi, and S. Zekri, “GIS-based assessment of combined CSP electric power and seawater desalination plant for Duqum—Oman,” *Renewable and Sustainable Energy Reviews*, vol. 14, no. 2, pp. 821–827, feb 2010. [Online]. Available: https://linkinghub.elsevier.com/retrieve/pii/S1364032109002159

[63] P. V. Gorsevski, S. C. Cathcart, G. Mirzaei, M. M. Jamali, X. Y. Ye, and E. Gomezdelcampo, “A Group-based Spatial Decision Support System For Wind Farm Site Selection In Northwest Ohio,” *Energy Policy*, vol. 55, pp. 374–385, 2013. [Online]. Available: http://dx.doi.org/10.1016/j.enpol.2012.12.013

[64] S. Grassi, N. Chokani, and R. S. Abhari, “Large Scale Technical And Economical Assessment Of Wind Energy Potential With A GIS Tool: Case Study Iowa,” *Energy Policy*, vol. 45, pp. 73–85, 2012. [Online]. Available: http://dx.doi.org/10.1016/j.enpol.2012.01.061

[65] H. S. Hansen, “GIS-based multi-criteria analysis of wind farm development,” in *ScanGIS 2005 - Proceedings of the 10th Scandinavian Research Conference on Geographical Information Sciences*, 2005.

[66] J. Hohn, E. Lehtonen, S. Rasi, J. Rintala, J. Höhn, E. Lehtonen, S. Rasi, and J. Rintala, “A Geographical Information System (GIS) Based Methodology For Determination Of Potential Biomasses And Sites For Biogas Plants In Southern Finland,” *Applied Energy*, vol. 113, no. 2014, pp. 1–10, 2014.

[67] S. Holtinger, B. Salak, T. Schauppenlehner, P. Scherhaufer, J. Schmidt, S. Höltinger, B. Salak, T. Schauppenlehner, P. Scherhaufer, and J. Schmidt, “Austria’s Wind Energy Potential - A Participatory Modeling Approach To Assess Socio-political And Market Acceptance,” *Energy Policy*, vol. 98, pp. 49–61, 2016. [Online]. Available: http://dx.doi.org/10.1016/j.enpol.2016.08.010

[68] J. R. Janke, “Multicriteria GIS Modeling Of Wind And Solar Farms In Colorado,” *Renewable Energy*, vol. 35, no. 10, pp. 2228–2234, 2010. [Online]. Available: http://dx.doi.org/10.1016/j.renene.2010.03.014

[69] W. Krewitt and J. Nitsch, “The Potential For Electricity Generation From Onshore Wind Energy Under The Constraints Of Nature Conservation: A Case Study For Two Regions In Germany,” *Renewable Energy*, vol. 28, no. 10, pp. 1645–1655, 2003.

[70] R. G. Lehman, *Concentrated Solar Thermal Facilities: A GIS Approach For Land Planning*. University of Southern California, 2011.

[71] P. Lejeune and C. Feltz, “Development Of A Decision Support System For Setting Up A Wind Energy Policy Across The Walloon Region (southern Belgium),” *Renewable Energy*, vol. 33, no. 11, pp. 2416–2422, 2008.

[72] A. Lopez, B. Roberts, D. Heimiller, N. Blair, G. Porro, A. Lopez, B. Roberts, N. Blair, and G. Porro, “U.S. Renewable Energy Technical Potentials : A GIS-Based Analysis,” National Renewable Energy Laboratory, Golden, Colorado. USA, Tech. Rep. July, 2012.

[73] I. U. Lütkehus, H. U. Salecker, and K. U. Adlunger, *Potenzial Der Windenergie An Land - Studie Zur Ermittlung Des Bundesweiten Flächen- Und Leistungspotenzial*. Umweltbundesamt, 2013, ISBN: 9788578110796, ISSN: 09953914.

[74] J. G. Ma, N. R. Scott, S. D. DeGloria, and A. J. Lembo, “Siting Analysis Of Farm-based Centralized Anaerobic Digester Systems For Distributed Generation Using GIS,” *Biomass & Bioenergy*, vol. 28, no. 6, pp. 591–600, 2005.

[75] R. Mari, L. Bottai, C. Busillo, F. Calastrini, B. Gozzini, and G. Gualtieri, “A GIS-based Interactive Web Decision Support System For Planning Wind Farms In Tuscany (Italy),” *Renewable Energy*, vol. 36, no. 2, pp. 754–763, 2011. [Online]. Available: http://dx.doi.org/10.1016/j.renene.2010.07.005

[76] A. D. Mekonnen and P. V. Gorsevski, “A Web-based Participatory GIS (PGIS) For Offshore Wind Farm Suitability Within Lake Erie, Ohio,” *Renewable & Sustainable Energy Reviews*, vol. 41, no. January, pp. 162–177, 2015. [Online]. Available: http://dx.doi.org/10.1016/j.rser.2014.08.030

[77] A. N. Michał SZUREK Jan BLACHOWSKI, M. Szurek, J. Blachowski, and A. Nowacka, “GIS-based method for wind farm location multi-criteria analysis,” *Mining Science*, vol. 21, pp. 65–81, 2014.

[78] A. Ouammi, V. Ghigliotti, M. Robba, A. Mimet, and R. Sacile, “A Decision Support System For The Optimal Exploitation Of Wind Energy On Regional Scale,” *Renewable Energy*, vol. 37, no. 1, pp. 299–309, 2012. [Online]. Available: http://dx.doi.org/10.1016/j.renene.2011.06.027

[79] N. Phuangpornpitak and S. Tia, “Feasibility Study Of Wind Farms Under The Thai Very Small Scale Renewable Energy Power Producer (vspp) Program,” *9th Eco-Energy and Materials Science and Engineering Symposium*, vol. 9, pp. 159–170, 2011. [Online]. Available: http://dx.doi.org/10.1016/j.egypro.2011.09.017

[80] I. J. Ramírez-Rosado, E. García-Garrido, L. A. Fernández-Jiménez, P. J. Zorzano-Santamaría, C. Monteiro, and V. Miranda, "Promotion Of New Wind Farms Based On A Decision Support System," *Renewable Energy*, vol. 33, no. 4, pp. 558–566, apr 2008. [Online]. Available: http://linkinghub.elsevier.com/retrieve/pii/S0960148107001140

[81] L. C. Rodman and R. K. Meentemeyer, "A Geographic Analysis Of Wind Turbine Placement In Northern California," *Energy Policy*, vol. 34, no. 15, pp. 2137–2149, 2006.

[82] J. Schallenberg-Rodriguez, J. N. D. Pino, and J. Notario, "Evaluation Of Onshore Wind Techno-economical Potential In Regions And Islands," *Applied Energy*, vol. 124, no. July 2014, pp. 117–129, 2014.

[83] A. Sultana and A. Kumar, "Optimal Siting And Size Of Bioenergy Facilities Using Geographic Information System," *Applied Energy*, vol. 94, pp. 192–201, 2012. [Online]. Available: http://dx.doi.org/10.1016/j.apenergy.2012.01.052

[84] L.-I. Tegou, H. Polatidis, and D. A. Haralambopoulos, "Environmental Management Framework For Wind Farm Siting: Methodology And Case Study," *Journal of Environmental Management*, vol. 91, no. 11, pp. 2134–2147, nov 2010. [Online]. Available: https://www.ncbi.nlm.nih.gov/pubmed/20541310http://dx.doi.org/10.1016/j.jenvman.2010.05.010https://linkinghub.elsevier.com/retrieve/pii/S0301479710001398

[85] F. Trieb, "Expert System For Solar Thermal Power Stations," Institute of Technical Thermodynamics (DLR), Report, 2001.

[86] T. Tsoutsos, I. Tsitoura, D. Kokologos, and K. Kalaitzakis, "Sustainable Siting Process In Large Wind Farms Case Study In Crete," *Renewable Energy*, vol. 75, pp. 474–480, 2015. [Online]. Available: http://dx.doi.org/10.1016/j.renene.2014.10.020

[87] K. Ummel and D. Wheeler, "Desert power: the economics of solar thermal electricity For Europe," North Africa, and the Middle East Center for Global Development, Tech. Rep., 2008. [Online]. Available: https://www.cgdev.org/publication/desert-power-economics-solar-thermal-electricity-europe-north-africa-and-middle-east

[88] M. Vandenbergh, F.-P. Neirac, and H. Turki, "A GIS approach for the siting of solar thermal power plants application to Tunisia," *Le Journal de Physique IV*, vol. 09, no. PR3, pp. Pr3–223–Pr3–228, mar 1999. [Online]. Available: http://www.edpsciences.org/10.1051/jp4:1999333

[89] T. Wanderer and S. Herle, "Creating A Spatial Multi-criteria Decision Support System For Energy Related Integrated Environmental Impact Assessment," *Environmental Impact Assessment Review*, vol. 52, pp. 2–8, apr 2015. [Online]. Available: http://dx.doi.org/10.1016/j.eiar.2014.09.002https://linkinghub.elsevier.com/retrieve/pii/S0195925514000900

[90] Y. Zhou, W.X.Wu, and G. Liu, “Assessment Of Onshore Wind Energy Resource And Wind-generated Electricity Potential In Jiangsu, China,” *Energy Procedia*, vol. 5, pp. 418–422, 2011. [Online]. Available: https://linkinghub.elsevier.com/retrieve/pii/S1876610211010083

[91] Copernicus. European Environmental Agency (EEA), “corine Land Cover (clc) 2012, Version 18.5.1 [dataset],” ”land.copernicus.eu/pan-european/corine-land-cover/clc/2012/view”, 2012, accessed: 2017-04-01.

[92] Geographic Information System of the COmmission (GISCO), “Clusters: Urban 2011 [dataset],” http://ec.europa.eu/eurostat/web/gisco/geodata/reference-data/population-distribution-demography/clusters, 2016, accessed: 2017-04-01. [Online]. Available: http://ec.europa.eu/eurostat/web/gisco/geodata/reference-data/population-distribution-demography/clusters

[93] Geographic Information System of the COmmission (GISCO), “Transport Networks: Airports 2013 [dataset],” http://ec.europa.eu/eurostat/web/gisco/geodata/reference-data/transport-networks, 2013, accessed: 2017-04-01. [Online]. Available: http://ec.europa.eu/eurostat/web/gisco/geodata/reference-data/transport-networks

[94] European Environmental Agency (EEA), “Digital Elevation Model Over Europe (eu-dem) [dataset],” ”https://www.eea.europa.eu/data-and-maps/data/eu-dem”, 2013, accessed: 2017-04-01. [Online]. Available: https://www.eea.europa.eu/data-and-maps/data/eu-dem

[95] Geographic Information System of the COmmission (GISCO), “Hydrography (laea) [dataset],” http://ec.europa.eu/eurostat/web/gisco/geodata/reference-data/elevation/hydrography-laea, 2014, accessed: 2017-04-01. [Online]. Available: http://ec.europa.eu/eurostat/web/gisco/geodata/reference-data/elevation/hydrography-laea

[96] M. L. L. Messager, B. Lehner, G. Grill, I. Nedeva, and O. Schmitt, “Estimating The Volume And Age Of Water Stored In Global Lakes Using A Geo-statistical Approach,” *Nature Communications*, vol. 7, p. 13603, 2016.

[97] OpenStreetMap contributors, “Openstreetmap [dataset],” https://www.openstreetmap.org, 2017, accessed 2017-04-01.

[98] UNEP-WCMC and IUCN, “Protected Planet: The World Database On Protected Areas (wdpa)[on-line],” Available at: www.protectedplanet.net, 2016, accessed: 2017-04-01.

[99] N. Dudley, “Guidelines For Applying Protected Area Management Categories,” IUNC, Gland, Switzerland, Tech. Rep., 2008. [Online]. Available: https://portals.iucn.org/library/sites/library/files/documents/PAG-021.pdf

[100] D. S. Ryberg, Z. Tulemat, M. Robinius, and D. Stolten, “Geospatial Land Availability For Energy Systems (glaes),” GitHub Repository, 2017. [Online]. Available: http//github.com/FZJ-IEK3-VSA/glaes

[101] P.-M. Heuser, D. S. Ryberg, T. Grube, M. Robinius, and D. Stolten, "Techno-economic Analysis Of A Potential Energy Trading Link Between Patagonia And Japan Based On Co2 Free Hydrogen," *International Journal of Hydrogen Energy*, jan 2019. [Online]. Available: https://linkinghub.elsevier.com/retrieve/pii/S0360319918341582

[102] D. G. Caglayan, D. S. Ryberg, H. Heinrichs, J. Linßen, D. Stolten, and M. Robinius, "The techno-economic potential of offshore wind energy with optimized future turbine designs in Europe," *Applied Energy*, vol. 255, p. 113794, dec 2019. [Online]. Available: https://linkinghub.elsevier.com/retrieve/pii/S0306261919314813

[103] N. Weber, "Assessment of the Technical and Economic Potential of Salt Deposits for Hydrogen Storage," Master's thesis, RWTH Aachen University & Forschungszentrum Jülich, 9 2018.

[104] GDAL Development Team, *Gdal - Geospatial Data Abstraction Library, Version 2.1.1*, Open Source Geospatial Foundation, 2017.

[105] E. Jones, T. Oliphant, P. Peterson, and Others, "{scipy}: Open Source Scientific Tools For {python}," 2017.

[106] D. Ryberg, M. Robinius, and D. Stolten, "Evaluating Land Eligibility Constraints Of Renewable Energy Sources In Europe," *Energies*, vol. 11, no. 5, p. 1246, may 2018. [Online]. Available: http://www.mdpi.com/1996-1073/11/5/1246

[107] A. Okabe, B. Boots, K. Sugihara, and S. N. Chiu, *Spatial Tessellations: Concepts And Applications Of Voronoi Diagrams*, 2nd ed. Wiley, 2000, ISBN: 978-0-471-98635-5.

[108] D. S. Ryberg, Z. Tulemat, D. Stolten, and M. Robinius, "Uniformly constrained land eligibility for onshore European wind power," *Renewable Energy*, vol. 146, no. 0960-1481, pp. 921–931, jun 2019. [Online]. Available: https://linkinghub.elsevier.com/retrieve/pii/S0960148119309619

[109] D. S. Ryberg, D. G. Caglayan, S. Schmitt, J. Linßen, D. Stolten, and M. Robinius, "The future of European onshore wind energy potential: Detailed distribution and simulation of advanced turbine designs," *Energy*, vol. 182, pp. 1222–1238, sep 2019. [Online]. Available: https://linkinghub.elsevier.com/retrieve/pii/S0360544219311818

[110] A. Troccoli, *Management Of Weather And Climate Risk In The Energy Industry*. Springer, 2008, ISBN: 978-90-481-3692-6.

[111] R. B. Stull, *An introduction to boundary layer meteorology*. Springer Science & Business Media, 2012, vol. 13.

[112] J. C. Kaimal and J. J. Finnigan, *Atmospheric boundary layer flows: their structure and measurement*. Oxford university press, 1994.

[113] M. A. El-Sharkawi, *Wind Energy: An Introduction*, 1st ed. CRC Press, 2015, ISBN: 9781482263992.

[114] J. F. Manwell, J. G. McGowan, and A. L. Rogers, *Wind Energy Explained*. John Wiley & Sons, Ltd, dec 2009.

[115] T. Letcher, *Wind Energy Engineering*, 1st ed. Academic Press, 2017.

[116] Meteorology, World Meteorological Organization. Commission for Maritime, *The Beaufort Scale Of Wind Force : (technical And Operational Aspects)*. Geneva : WMO, 1970., 1970, report submitted by the President of the Commission for Maritime Meteorology to the WMO Executive Committee at its twenty-second session.;Bibliography: pages 21-22. [Online]. Available: https://search.library.wisc.edu/catalog/999768644902121

[117] A. Picard, R. S. Davis, M. Gläser, and K. Fujii, "Revised Formula For The Density Of Moist Air ({cipm}-2007)," *Metrologia*, vol. 45, no. 2, pp. 149–155, feb 2008.

[118] J. Wright, A. Johnson, and M. Moldover, "Design and uncertainty analysis for a PVTt gas flow standard," *Journal of Research of the National Institute of Standards and Technology*, vol. 108, no. 1, p. 21, jan 2003. [Online]. Available: https://nvlpubs.nist.gov/nistpubs/jres/108/1/j80wri.pdf

[119] S. E. Tuller and A. C. Brett, "The Characteristics of Wind Velocity that Favor the Fitting of a Weibull Distribution in Wind Speed Analysis," *Journal of Climate and Applied Meteorology*, vol. 23, no. 1, pp. 124–134, jan 1984. [Online]. Available: http://journals.ametsoc.org/doi/abs/10.1175/1520-0450%281984%29023%3C0124%3ATCOWVT%3E2.0.CO%3B2

[120] D. Deaves and I. Lines, "The Nature And Frequency Of Low Wind Speed Conditions," *Journal of Wind Engineering and Industrial Aerodynamics*, vol. 73, no. 1, pp. 1–29, jan 1998. [Online]. Available: http://linkinghub.elsevier.com/retrieve/pii/S016761059700278X

[121] I. Troen and E. L. Petersen, *European wind atlas*. Risø National Laboratory, 1989.

[122] Technical University of Denmark, "DTU Global Wind Atlas 1km resolution [Dataset]. Version 1.0," online, 2015, accessed: 2017-04-01. [Online]. Available: https://irena.masdar.ac.ae/gallery/#map/103

[123] C. Bollmeyer, J. D. Keller, C. Ohlwein, S. Wahl, S. Crewell, P. Friederichs, A. Hense, J. Keune, S. Kneifel, I. Pscheidt, S. Redl, and S. Steinke, "Towards a high-resolution regional reanalysis for the european CORDEX domain," *Quarterly Journal of the Royal Meteorological Society*, vol. 141, no. 686, pp. 1–15, dec 2014.

[124] J. Sumner and C. Masson, "Influence of atmospheric stability on wind turbine power performance curves," *Journal of Solar Energy Engineering*, vol. 128, no. 4, p. 531, 2006.

[125] I. Antoniou, S. M. Pedersen, and P. B. Enevoldsen, "Wind Shear and Uncertainties in Power Curve Measurement and Wind Resources," *Wind Engineering*, vol. 33, no. 5, pp. 449–468, oct 2009.

[126] B. Storm, J. Dudhia, S. Basu, A. Swift, and I. Giammanco, "Evaluation of the weather research and forecasting model on forecasting low-level jets: implications for wind energy," *Wind Energy*, vol. 12, no. 1, pp. 81–90, jan 2009.

[127] Y. Zhang, D. J. Seidel, and S. Zhang, "Trends In Planetary Boundary Layer Height Over Europe," *Journal of Climate*, vol. 26, no. 24, pp. 10 071–10 076, dec 2013.

[128] S. Nave, "June 2018: Monthly Climatic Data For The World," National Oceanic and Atmospheric Administration, Tech. Rep. 6, 2018.

[129] J. Silva, C. Ribeiro, and R. Guedes, "Roughness length classification of corine land cover classes," Jan 2007, megajoule Consultants.

[130] The European Wind Energy Association (EWEA), "Upwind "design Limits And Solutions For Very Large Wind Turbines: A 20 Mw Turbine Is Feasible"," Tech. Rep., 2011.

[131] G. Thomaßen and M. Deutsch, "Future cost of onshore wind. Recent auction results, long-term outlook and implications for upcoming German auctions." Agora Energiewende, Agora Energiewende. Anna-Louisa-Karsch-Straße 2. 10178 Berlin, Germany, Tech. Rep., April 2017. [Online]. Available: https://www.agora-energiewende.de/fileadmin2/Projekte/2017/Future_Cost_of_Wind/Agora_Future-Cost-of-Wind_WEB.pdf

[132] International Electrotechnical Commission and others, "Wind turbines: Part 1: Design requirements; 2005," 2005.

[133] DNV/Riso, *Guidelines For Design Of Wind Turbines*, 2002, ISBN: 8755028705, ISSN:1751-7214.

[134] Vestas, *Vestas: 4 MW Platform*, Vestas, Vestas Wind Systems A/S. Hedeager 42. 8200 Aarhus N. Denmark, 2018.

[135] A. Rauh and W. Seelert, "The betz optimum efficiency for windmills," *Applied Energy*, vol. 17, no. 1, pp. 15–23, jan 1984.

[136] The Wind Power, "Power curves database," Dataset, 2018, accessed: 2017-11-01. [Online]. Available: https://www.thewindpower.net/store_manufacturer_turbine_en.php?id_type=7

[137] ENGIE Group, "la-haute-borne-data-2013-2016 [Dataset]," online, 2017, accessed: 2018-03-01. License: Licence Ouverte v2.0 (Etalab). [Online]. Available: https://opendata-renewables.engie.com/explore/dataset/la-haute-borne-data-2013-2016/

[138] ENGIE Group, “La Haute Borne static information [Dataset],” online, 2017, accessed: 2018-03-01. License: Licence Ouverte v2.0 (Etalab). [Online]. Available: https://opendata-renewables.engie.com/explore/dataset/static-information/

[139] P. Tavner, C. Edwards, A. Brinkman, and F. Spinato, “Influence Of Wind Speed On Wind Turbine Reliability,” *Wind Engineering*, vol. 30, no. 1, pp. 55–72, jan 2006. [Online]. Available: http://journals.sagepub.com/doi/10.1260/030952406777641441

[140] K. S. Hansen, R. J. Barthelmie, L. E. Jensen, and A. Sommer, “The Impact Of Turbulence Intensity And Atmospheric Stability On Power Deficits Due To Wind Turbine Wakes At Horns Rev Wind Farm,” *Wind Energy*, vol. 15, no. 1, pp. 183–196, jan 2012. [Online]. Available: http://doi.wiley.com/10.1002/we.512

[141] G. Ren, J. Liu, J. Wan, F. Li, Y. Guo, and D. Yu, “The analysis of turbulence intensity based on wind speed data in onshore wind farms,” *Renewable Energy*, vol. 123, pp. 756–766, aug 2018.

[142] S.-D. Kwon, “Uncertainty Analysis Of Wind Energy Potential Assessment,” *Applied Energy*, vol. 87, no. 3, pp. 856–865, mar 2010. [Online]. Available: https://linkinghub.elsevier.com/retrieve/pii/S0306261909003717

[143] C. L. Archer, A. Vasel-Be-Hagh, C. Yan, S. Wu, Y. Pan, J. F. Brodie, and A. E. Maguire, “Review and evaluation of wake loss models for wind energy applications,” *Applied Energy*, vol. 226, pp. 1187–1207, sep 2018.

[144] F. Seim, A. R. Gravdahl, and M. S. Adaramola, “Validation of kinematic wind turbine wake models in complex terrain using actual windfarm production data,” *Energy*, vol. 123, pp. 742–753, mar 2017.

[145] The Wind Power, “Wind turbines database,” Dataset, 2018, accessed: 2017-11-01. [Online]. Available: https://www.thewindpower.net/store_manufacturer_turbine_en.php?id_type=4

[146] International Energy Agency, “IEA Wind, Task 26: Data Viewer,” Online, 2018. [Online]. Available: https://community.ieawind.org/task26/dataviewer

[147] M. Holmes, “Global carbon fibre market remains on upward trend,” *Reinforced Plastics*, vol. 58, no. 6, pp. 38–45, nov 2014.

[148] International Energy Agency (IEA), “Technology roadmap wind energy,” 2013.

[149] Siemans AG, “The Onshore Direct Drive platform – your solution for every situation,” article-No. WPON-B10021-00-7600.

[150] G. A. M. van Kuik, J. Peinke, R. Nijssen, D. Lekou, J. Mann, J. N. Sørensen, C. Ferreira, J. W. van Wingerden, D. Schlipf, P. Gebraad, H. Polinder, A. Abrahamsen, G. J. W. van Bussel, J. D. Sørensen, P. Tavner, C. L. Bottasso, M. Muskulus, D. Matha, H. J. Lindeboom, S. Degraer, O. Kramer, S. Lehnhoff, M. Sonnenschein, P. E. Sørensen, R. W. Künneke, P. E. Morthorst,

and K. Skytte, “Long-term research challenges in wind energy – a research agenda by the European Academy of Wind Energy,” *Wind Energy Science*, vol. 1, no. 1, pp. 1–39, feb 2016.

[151] B. Valpy, P. English, A. Martinez, and E. Simonot, “Future renewable energy costs: offshore wind,” KIC InnoEnergy, Tech. Rep., 2014. [Online]. Available: http://www.innoenergy.com/wp-content/uploads/2014/09/KIC_IE_OffshoreWind_anticipated_innovations_impact1.pdf

[152] Enercon, “Advancing To New Heights,” *WindBlatt*, p. 1, feb 2017. [Online]. Available: https://www.enercon.de/fileadmin/Redakteur/Medien-Portal/windblatt/pdf/WB_02-17_GB_ANSICHT.pdf

[153] T. Kellner, “Friends In High Places: “space Frame” Wind Tower Takes Renewables To Tough Locations,” *GE Reports*, mar 2014. [Online]. Available: https://www.ge.com/reports/post/79185604909/friends-in-high-places/

[154] E. De Vries, “Windtech: Mixing Steel And Concrete To Go Higher,” *Wind Power Monthly*, nov 2017. [Online]. Available: https://www.windpowermonthly.com/article/1448423/windtech-mixing-steel-concrete-go-higher

[155] Siemens, “An Innovative Solution For High Hub Heights: Bolted Steel Shell Tower,” Siemens Wind Power, Hamburg, Germany, Tech. Rep., 2011. [Online]. Available: https://www.energy.siemens.com/us/pool/hq/power-generation/renewables/wind-power/Bolted_Steel_Shell_Tower_brochure_EN.pdf

[156] M. Robinius, A. Otto, K. Syranidis, D. S. Ryberg, P. Heuser, L. Welder, T. Grube, P. Markewitz, V. Tietze, and D. Stolten, “Linking the Power and Transport Sectors—Part 2: Modelling a Sector Coupling Scenario for Germany,” *Energies*, vol. 10, no. 7, p. 957, jul 2017. [Online]. Available: http://www.mdpi.com/1996-1073/10/7/957

[157] R. Wiser, K. Jenni, J. Seel, E. Baker, M. Hand, E. Lantz, A. Smith, V. Berkhout, A. Duffy, B. Cleary, R. Lacal-Arántegui, and L. Husabø, “Forecasting Wind Energy Costs And Cost Drivers: The Views Of The World’s Leading Experts,” Lawrence Berkeley National Laboratory, resreport June, jun 2016. [Online]. Available: https://escholarship.org/uc/item/0s43r9w4

[158] A. Ilas, P. Ralon, A. Rodriguez, and M. Taylor, “Renewable power generation costs in 2017,” International Renewable Energy Agency (IRENA), Tech. Rep., 2018, iSBN 978-92-9260-040-2. [Online]. Available: https://www.irena.org/-/media/Files/IRENA/Agency/Publication/2018/Jan/IRENA_2017_Power_Costs_2018.pdf

[159] European Climate Foundation, “Roadmap 2050; a Practical Guide to a Prosperous, Low-carbon Europe,” European Climate Foundation, Tech. Rep., 2010. [Online]. Available: http://www.roadmap2050.eu/attachments/files/Volume1_fullreport_PressPack.pdf

[160] R. Lacal Arantegui, A. Jaeger-waldau, M. Vellei, B. Sigfusson, D. Magagna, M. Jakubcionis, M. Perez Fortes Del Mar, S. Lazarou, J. Giuntoli, E. Weidner Ronnefeld, G. De Marco, A. Spisto, and C. Gutierrez Moles, "ETRI 2014 - Energy Technology Reference Indicator projections for 2010-2050," Joint Research Center, Tech. Rep., 2014. [Online]. Available: http://publications.jrc.ec.europa.eu/repository/handle/JRC92496

[161] P. Nielsen, "Vindmollers okonomi," EMD International, Tech. Rep., 2010. [Online]. Available: https://www.emd.dk/files/Vindm%C3%B8llers%20%C3%B8konomi_EMD-Feb2010.pdf

[162] L. Fried, S. Shukla, S. Sawyer, and S. Teske, "Global wind energy outlook: 2016," Global Wind Energy Council, Tech. Rep., Oct. 2016. [Online]. Available: http://files.gwec.net/files/GlobalWindEnergyOutlook2016

[163] G. H. Oettinger, "Energy roadmap 2050," European Comission, Tech. Rep., 2012. [Online]. Available: https://ec.europa.eu/energy/en/topics/energy-strategy-and-energy-union/2050-energy-strategy

[164] S. Lindenberg, B. Smith, K. O'Dell, E. DeMeo, and B. Ram, "20by 2030 Increasing Wind Energy's Contribution to U.S. Electricity Supply," US Department of Energy, Tech. Rep., Jul. 2008. [Online]. Available: https://www.nrel.gov/docs/fy08osti/41869.pdf

[165] J. Moccia, A. Arapogianni, J. Wilkes, C. Kjaer, R. Gruet, S. Azau, and J. Scola, "Pure power. wind energy targets for 2020 and 2030," The European Wind Energy Association, Tech. Rep., 2011. [Online]. Available: http://www.ewea.org/fileadmin/files/library/publications/reports/Pure_Power_III.pdf

[166] C. Kost, J. N. Mayer, J. Thomsen, N. Hartmann, C. Senkpiel, S. Philipps, S. Nold, S. Lude, and T. Schlegl, "Stromgestehungskosten Erneuerbare Energien," Fraunhofer-institut für Solare Energiesysteme (ISE), Tech. Rep., Nov. 2013. [Online]. Available: https://www.ise.fraunhofer.de/content/dam/ise/de/documents/publications/studies/DE2013_ISE_Studie_Stromgestehungskosten_Erneuerbare_Energien.pdf

[167] G. Doyle and G. Vantsiotis, "Costs of low-carbon generation technologies," Mott MacDonald, Tech. Rep., May 2011, report for the Committee on Climate Change. Brighton.

[168] T. J. Stehly, D. M. Heimiller, and G. N. Scott, "2016 Cost of Wind Energy Review," National Renewable Energy Lab.(NREL), Golden, CO (United States), Tech. Rep., 2017.

[169] M. I. Blanco, "The economics of wind energy," *Renewable and Sustainable Energy Reviews*, vol. 13, no. 6-7, pp. 1372–1382, aug 2009.

[170] C. Kruck and E. Ludger, "Perspektiven der Stromerzeugung aus Solar- und Windenergienutzung für eine nachhaltige Energieversorgung in Deutschland," Universit a t Stuttgart, Institut für Energiewirtschaft und Rationelle Energieanwendung (IER), Tech. Rep., 2004.

[171] L. J. Fingersh, M. M. Hand, and A. S. Laxson, "Wind turbine design cost and scaling model," National Renewable Energy Laboratory Internal Report, Tech. Rep., 2006.

[172] B. Maples, M. Hand, and W. Musial, "Comparative assessment of direct drive high temperature superconducting generators in multi-megawatt class wind turbines," National Renewable Energy Lab.(NREL), Golden, CO (United States), Tech. Rep., 2010.

[173] A. Vitina, S. Lüers, A.-K. Wallasch, V. Berkhout, A. Duffy, B. Cleary, L. I. Husabø, D. E. Weir, R. Lacal-Arántegui, M. M. Hand, E. Lantz, K. Belyeu, R. Wiser, M. Bolinger, and B. Hoen, "IEA Wind Task 26: Wind Technology, Cost, and Performance Trends in Denmark, Germany, Ireland, Norway, the European Union, and the United States: 2007–2012," National Renewable Energy Laboratory, Tech. Rep., Jun. 2015, nREL/TP-6A20-64332.

[174] P. Hjuler-Jensen, P. E. Morthorst, S. Skriver, M. Rasmussen, H. Larsen, L. H. Hansen, P. Nielsen, and J. Lemming, "Economics of wind turbines in Denmark–investment and operation and maintenance costs for selected generations of turbines," Risoe National Lab, Roskilde, Denmark, Tech. Rep., Oct. 2002.

[175] P. Capros, A. De Vita, N. Tasios, P. Siskos, M. Kannavou, A. Petropoulos, S. Evangelopoulou, M. Zampara, D. Papadopoulos, L. Paroussos, K. Fragiadakis, S. Tsani, P. Fragkos, N. Kouvaritakis, L. Höglund-Isaksson, W. Winiwarter, P. Purohit, A. Gomez-Sanabria, S. Frank, N. Forsell, M. Gusti, P. Havlik, M. Obersteiner, H. P. Witzke, and M. Kesting, "EU Reference Scenario 2016 Energy, transport and GHG emissions Trends to 2050," European Commission, Tech. Rep., 2016.

[176] S. A. Kalogirou, "Artificial Neural Networks In Renewable Energy Systems Applications: A Review," *Renewable and Sustainable Energy Reviews*, vol. 5, no. 4, pp. 373–401, dec 2001. [Online]. Available: http://linkinghub.elsevier.com/retrieve/pii/S1364032101000065

[177] T. L. Saaty, *What Is The Analytic Hierarchy Process?* Springer, 1988, pp. 109–121.

[178] K. Rehfeldt, L. Rehfeldt, and P. Graichen, "Vergütung von windenergieanlagen an land über das referenzertragsmodel," Agora Energiewende, Tech. Rep., March 2014. [Online]. Available: https://www.agora-energiewende.de/fileadmin/Projekte/2012/Studie_Referenzertragsmodell_Wind_korrigiert_WEB.pdf

[179] R. Gelaro, W. McCarty, M. J. Suárez, R. Todling, A. Molod, L. Takacs, C. A. Randles, A. Darmenov, M. G. Bosilovich, R. Reichle *et al.*, "The modern-era retrospective analysis for research and applications, version 2 (merra-2)," *Journal of Climate*, vol. 30, no. 14, pp. 5419–5454, 2017.

[180] I. Gonzalez Aparicio, A. Zucker, F. Careri, F. Monforti, T. Huld, and J. Badger, "Emhires Dataset. Part I: Wind Power Generation European

Meteorological Derived High Resolution Res Generation Time Series For Present And Future Scenarios," Joint Research Center, Tech. Rep., 2016. [Online]. Available: https://setis.ec.europa.eu/sites/default/files/reports/emhires_dataset_part_i_wind_power_generation_0.pdf

[181] International Energy Agency, "Energy Technology Perspectives 2017 - Executive Summary," International Energy Agency (IEA), Tech. Rep., 2017.

[182] The Wind Power, "World wind farms database," Dataset, 2018, accessed: 2017-11-01. [Online]. Available: https://www.thewindpower.net/store_continent_en.php?id_zone=1000

[183] A. Emami and P. Noghreh, "New Approach On Optimization In Placement Of Wind Turbines Within Wind Farm By Genetic Algorithms," *Renewable Energy*, 2010.

[184] L. Welder, D. Ryberg, L. Kotzur, T. Grube, M. Robinius, and D. Stolten, "Spatio-temporal optimization of a future energy system for power-to-hydrogen applications in Germany," *Energy*, vol. 158, pp. 1130–1149, sep 2018. [Online]. Available: https://linkinghub.elsevier.com/retrieve/pii/S036054421830879X

[185] O. Tlili, C. Mansilla, M. Robinius, K. Syranidis, M. Reuss, J. Linssen, J. André, Y. Perez, and D. Stolten, "Role of electricity interconnections and impact of the geographical scale on the French potential of producing hydrogen via electricity surplus by 2035," *Energy*, 2019.

[186] M. K. Tippett, L. Trenary, T. DelSole, K. Pegion, and M. L. L'Heureux, "Sources Of Bias In The Monthly Cfsv2 Forecast Climatology," *Journal of Applied Meteorology and Climatology*, vol. 57, no. 5, pp. 1111–1122, may 2018. [Online]. Available: http://journals.ametsoc.org/doi/10.1175/JAMC-D-17-0299.1

[187] C. W. Frank, S. Wahl, J. D. Keller, B. Pospichal, A. Hense, and S. Crewell, "Bias correction of a novel european reanalysis data set for solar energy applications," *Solar Energy*, vol. 164, pp. 12–24, apr 2018.

[188] J. Olauson and M. Bergkvist, "Modelling The Swedish Wind Power Production Using Merra Reanalysis Data," *Renewable Energy*, vol. 76, pp. 717–725, apr 2015. [Online]. Available: https://linkinghub.elsevier.com/retrieve/pii/S0960148114008167

[189] D. Laslett, C. Creagh, and P. Jennings, "A Simple Hourly Wind Power Simulation For The South-west Region Of Western Australia Using Merra Data," *Renewable Energy*, vol. 96, pp. 1003–1014, oct 2016. [Online]. Available: https://linkinghub.elsevier.com/retrieve/pii/S0960148116304359

[190] M. McPherson, T. Sotiropoulos-Michalakakos, L. Harvey, and B. Karney, "An Open-access Web-based Tool To Access Global, Hourly Wind And Solar Pv Generation Time-series Derived From The Merra Reanalysis Dataset," *Energies*, vol. 10, no. 7, p. 1007, jul 2017. [Online]. Available: http://www.mdpi.com/1996-1073/10/7/1007

[191] L. C. Cradden, F. McDermott, L. Zubiate, C. Sweeney, and M. O'Malley, "A 34-year Simulation Of Wind Generation Potential For Ireland And The Impact Of Large-scale Atmospheric Pressure Patterns," *Renewable Energy*, vol. 106, pp. 165–176, jun 2017. [Online]. Available: https://linkinghub.elsevier.com/retrieve/pii/S0960148116311296

[192] M. Kubik, D. Brayshaw, P. Coker, and J. Barlow, "Exploring The Role Of Reanalysis Data In Simulating Regional Wind Generation Variability Over Northern Ireland," *Renewable Energy*, vol. 57, pp. 558–561, sep 2013. [Online]. Available: https://linkinghub.elsevier.com/retrieve/pii/S0960148113001213

[193] D. Carvalho, A. Rocha, M. Gómez-Gesteira, and C. Silva Santos, "Offshore Wind Energy Resource Simulation Forced By Different Reanalyses: Comparison With Observed Data In The Iberian Peninsula," *Applied Energy*, vol. 134, pp. 57–64, dec 2014. [Online]. Available: https://linkinghub.elsevier.com/retrieve/pii/S0306261914008216

[194] C. Bollmeyer, J. D. Keller, C. Ohlwein, S. Wahl, S. Crewell, P. Friederichs, A. Hense, J. Keune, S. Kneifel, I. Pscheidt, S. Redl, and S. Steinke, "Towards A High-resolution Regional Reanalysis For The European Cordex Domain," *Quarterly Journal of the Royal Meteorological Society*, vol. 141, no. 686, pp. 1–15, jan 2015. [Online]. Available: http://doi.wiley.com/10.1002/qj.2486

[195] P. Henckes, A. Knaut, F. Obermüller, and C. Frank, "The Benefit Of Long-term High Resolution Wind Data For Electricity System Analysis," *Energy*, vol. 143, pp. 934–942, jan 2018. [Online]. Available: https://linkinghub.elsevier.com/retrieve/pii/S0360544217317280

[196] T. V. Jensen and P. Pinson, "Re-europe, A Large-scale Dataset For Modeling A Highly Renewable European Electricity System," *Scientific Data*, vol. 4, p. 170175, nov 2017. [Online]. Available: http://www.nature.com/articles/sdata2017175

[197] R. Becker and D. Thrän, "Optimal Siting Of Wind Farms In Wind Energy Dominated Power Systems," *Energies*, vol. 11, no. 4, p. 978, apr 2018. [Online]. Available: http://www.mdpi.com/1996-1073/11/4/978

[198] S. Rose and J. Apt, "Quantifying Sources Of Uncertainty In Reanalysis Derived Wind Speed," *Renewable Energy*, vol. 94, pp. 157–165, aug 2016. [Online]. Available: https://linkinghub.elsevier.com/retrieve/pii/S0960148116302129

[199] International Electrotechnical Commission, "Iec61400: Wind Energy Generation Systems – Part 12-1: Power Performance Measurements Of Electricity Producing Wind Turbines," Geneva, 2017. [Online]. Available: https://webstore.iec.ch/publication/26603

[200] G. Smart, A. Smith, E. Warner, I. Bakken Sperstad, B. Prinsen, and R. Lacal-Arántegui, "Iea wind task 26 - offshore wind farm

baseline documentation," IEA Wind, Tech. Rep., 2016. [Online]. Available: www.nrel.gov/docs/fy16osti/66262.pdf

[201] W. A. B. John A. Duffie, *Solar Engineering of Thermal Processes*. JOHN WILEY & SONS INC, 2013, ISBN: 0470873663, EAN: 9780470873663. [Online]. Available: https://www.ebook.de/de/product/18917192/john_a_duffie_william_a_beckman_solar_engineering_of_thermal_processes.html

[202] S. R. Wenham, M. A. Green, M. E. Watt, R. Corkish, and A. Sproul, *Applied Photovoltaics 3rd Edition*, 2012, ISBN: 9781849711425.

[203] D. R. Myers, *Solar Radiation: Practical Modeling For Renewable Energy Applications*, A. Ghassemi, Ed. CRC Press, 2013, ISBN:9781466503274.

[204] R. Santbergen, "Optical Absorption Factor Of Solar Cells For Pvt Systems," Ph.D. dissertation, Technische Universiteit Eindhoven, 2008. [Online]. Available: https://pure.tue.nl/ws/files/3351299/200811936.pdf

[205] P. Loutzenhiser, H. Manz, C. Felsmann, P. Strachan, T. Frank, and G. Maxwell, "Empirical validation of models to compute solar irradiance on inclined surfaces for building energy simulation," *Solar Energy*, vol. 81, no. 2, pp. 254–267, feb 2007. [Online]. Available: https://linkinghub.elsevier.com/retrieve/pii/S0038092X06000879

[206] World Bank Group, "Global Solar Atlas [dataset]," "http://globalsolaratlas.info/", 2016, accessed: 2017-04-01.

[207] C. Frohlich and J. Lean, "Solar Radiative Output And Its Variability: Evidence And Mechanisms," *The Astronomy and Astrophysics Review*, vol. 12, no. 4, pp. 273–320, dec 2004. [Online]. Available: http://link.springer.com/10.1007/s00159-004-0024-1

[208] F. Espenak, "Earth At Perihelion And Aphelion: 2001 To 2100," 2016. [Online]. Available: http://www.astropixels.com/ephemeris/perap2001.html

[209] G. Kopp and J. L. Lean, "A New, Lower Value Of Total Solar Irradiance: Evidence And Climate Significance," *Geophysical Research Letters*, vol. 38, no. 1, jan 2011. [Online]. Available: http://doi.wiley.com/10.1029/2010GL045777

[210] C. A. Gueymard, "The Sun's Total And Spectral Irradiance For Solar Energy Applications And Solar Radiation Models," *Solar Energy*, vol. 76, no. 4, pp. 423–453, apr 2004. [Online]. Available: http://linkinghub.elsevier.com/retrieve/pii/S0038092X03003967

[211] M. Pidwirny, "Atmospheric Effects On Incoming Solar Radiation," in *Fundamentals of Physical Geography*, 2006.

[212] D. Griffiths, *Introduction To Electrodynamics*, 3rd ed., 1999, ISBN: 013805326X.

[213] J. Lorente, A. Redañ, and X. De Cabo, "Influence Of Urban Aerosol On Spectral Solar Irradiance," *Journal of Applied Meteorology*, vol. 33, no. 3, pp. 406–415, mar 1994. [Online]. Available: http://journals.ametsoc.org/doi/abs/10.1175/1520-0450{%}281994{%}29033{%}3C0406{%}3AIOUAOS{%}3E2.0.CO{%}3B2

[214] P. Koronakis, G. Sfantos, A. Paliatsos, J. Kaldellis, J. Garofalakis, and I. Koronaki, "Interrelations Of Uv-global/global/diffuse Solar Irradiance Components And Uv-global Attenuation On Air Pollution Episode Days In Athens, Greece," *Atmospheric Environment*, vol. 36, no. 19, pp. 3173–3181, jul 2002. [Online]. Available: http://linkinghub.elsevier.com/retrieve/pii/S1352231002002339

[215] C. P. Jacovides, M. D. Steven, and D. N. Asimakopoulos, "Spectral Solar Irradiance And Some Optical Properties For Various Polluted Atmospheres," *Solar Energy*, vol. 69, no. 3, pp. 215–227, 2000. [Online]. Available: http://linkinghub.elsevier.com/retrieve/pii/S0038092X00000621

[216] C. C. Gonzalez and R. G. Ross, "Performance Measurement Reference Conditions for Terrestrial Photovoltaics," in *Proceedings of the Annual Meeting - American Section of the International Solar Energy Society*, 1980.

[217] R. A. Rohde, "Solar Spectrum.svg," 2008. [Online]. Available: http://commons.wikimedia.org/wiki/File:Solar_spectrum_ita.svg

[218] C. Gueymard, D. Myers, and K. Emery, "Proposed Reference Irradiance Spectra For Solar Energy Systems Testing," *Solar Energy*, vol. 73, no. 6, pp. 443–467, dec 2002. [Online]. Available: http://linkinghub.elsevier.com/retrieve/pii/S0038092X03000057

[219] "The Sun As A Source Of Energy: Part 3: Calculating Solar Angles." [Online]. Available: https://www.itacanet.org/the-sun-as-a-source-of-energy/part-3-calculating-solar-angles/

[220] A. Tim Umoette, "Development Of Site Specific Optimal Tilt Angle Model For Fixed Tilted Plane Pv Installation In Akwa Ibom State, Nigeria," *Science Journal of Energy Engineering*, vol. 4, no. 6, p. 50, 2016. [Online]. Available: http://www.sciencepublishinggroup.com/journal/paperinfo?journalid=269{&}doi=10.11648/j.sjee.20160406.11

[221] M. Hartner, A. Ortner, A. Hiesl, and R. Haas, "East To West - The Optimal Tilt Angle And Orientation Of Photovoltaic Panels From An Electricity System Perspective," *Applied Energy*, 2015.

[222] C. A. Gueymard, "Direct And Indirect Uncertainties In The Prediction Of Tilted Irradiance For Solar Engineering Applications," *Solar Energy*, vol. 83, no. 3, pp. 432–444, mar 2009. [Online]. Available: https://linkinghub.elsevier.com/retrieve/pii/S0038092X08002983

[223] S. A. Khalil and A. M. Shaffie, "Performance Of Statistical Comparison Models Of Solar Energy On Horizontal And Inclined Surface," vol. 2, no. 1, pp. 8–25, 2013.

[224] R. R. Perez, P. Ineichen, E. L. Maxwell, R. D. Seals, and A. Zelenka, "Dynamic global-to-direct irradiance conversion models," in *ASHRAE Transactions*, 1992.

[225] E. L. Maxwell, "A quasi-physical model for converting hourly global horizontal to direct normal insolation," Tech. Rep., Aug. 1987.

[226] R. Perez, P. Ineichen, R. Seals, J. Michalsky, and R. Stewart, "Modeling daylight availability and irradiance components from direct and global irradiance," *Solar Energy*, vol. 44, no. 5, pp. 271–289, 1990. [Online]. Available: https://linkinghub.elsevier.com/retrieve/pii/0038092X9090055H

[227] R. Perez, R. Stewart, R. Seals, and T. Guertin, "The Development And Verification Of The Perez Diffuse Radiation Model," Atmospheric Sciences Research Center, Albany, NY, Tech. Rep. October, 1988.

[228] K. Mertens and K. Hanser, "Photovoltaics : Fundamentals, Technology And Practice," in *Photovoltaics : Fundamentals, Technology and Practice*, 2013.

[229] J. L. Gray, "The Physics Of The Solar Cell," in *Handbook of Photovoltaic Science and Engineering*, 2011.

[230] B. Sopori, P. Rupnowski, V. Mehta, V. Budhraja, S. Johnston, N. Call, H. Mountinho, M. Al-Jassim, A. Shaikh, M. Seacrist, and D. Carlson, "Performance Limitations Of Mc-si Solar Cells Caused By Defect Clusters," in *ECS Transactions*, 2009.

[231] "Photovoltaics Report 08/2018," Fraunhofer Institute for Solar Energy Systems, ISE, Freiburg, Germany, Tech. Rep., 2018. [Online]. Available: https://www.ise.fraunhofer.de/content/dam/ise/de/documents/publications/studies/Photovoltaics-Report.pdf

[232] K. L. Chopra, P. D. Paulson, and V. Dutta, "Thin-film Solar Cells: An Overview," *Progress in Photovoltaics: Research and Applications*, vol. 12, no. 23, pp. 69–92, mar 2004. [Online]. Available: http://doi.wiley.com/10.1002/pip.541

[233] A. Polman, M. Knight, E. C. Garnett, B. Ehrler, and W. C. Sinke, "Photovoltaic Materials: Present Efficiencies And Future Challenges," *Science*, vol. 352, no. 6283, pp. aad4424–aad4424, apr 2016. [Online]. Available: http://www.sciencemag.org/cgi/doi/10.1126/science.aad4424

[234] T. Ishii, K. Otani, T. Takashima, and Y. Xue, "Solar Spectral Influence On The Performance Of Photovoltaic (pv) Modules Under Fine Weather And Cloudy Weather Conditions," *Progress in Photovoltaics: Research and Applications*, pp. n/a–n/a, nov 2011. [Online]. Available: http://doi.wiley.com/10.1002/pip.1210

[235] S. Nann and K. Emery, "Spectral Effects On Pv-device Rating," *Solar Energy Materials and Solar Cells*, vol. 27, no. 3, pp. 189–216, aug 1992. [Online]. Available: http://linkinghub.elsevier.com/retrieve/pii/0927024892900832

[236] W. D. Soto, S. Klein, and W. Beckman, "Improvement and validation of a model for photovoltaic array performance," *Solar Energy*, vol. 80, no. 1, pp. 78–88, jan 2006.

[237] L. D. King, A. J. Kratochvil, and E. W. Boyson, "Photovoltaic Array Performance Model," Sandia Nathional Labs, Tech. Rep., 01 2004.

[238] PV Performance Modelling Colaborative, "Spectral Response." [Online]. Available: https://pvpmc.sandia.gov/modeling-steps/2-dc-module-iv/effective-irradiance/spectral-response/

[239] A. Jain, "Exact analytical solutions of the parameters of real solar cells using lambert w-function," *Solar Energy Materials and Solar Cells*, vol. 81, no. 2, pp. 269–277, feb 2004.

[240] PV Performance Modelling Colaborative, "Single Diode Equivalent Circuit Models." [Online]. Available: https://pvpmc.sandia.gov/modeling-steps/2-dc-module-iv/diode-equivalent-circuit-models/

[241] D. Faiman, "Assessing The Outdoor Operating Temperature Of Photovoltaic Modules," *Progress in Photovoltaics: Research and Applications*, 2008.

[242] J. S. Stein, "Pv Performance Modeling Methods And Practices Results From The 4th Pv Performance Modeling Collaborative Workshop," International Energy Agency: Photovoltaic Power Systems Programme, Tech. Rep., 2017.

[243] D. M. Tobnaghi, R. Madatov, and D. Naderi, "The Effect of Temperature on Electrical Parameters of Solar Cells," *International Journal of Advanced Research in Electrical Electronics and Instrumentation Engineering*, 2007.

[244] Go Solar California, "PV Module List - Full Data," Online, Sep. 2018. [Online]. Available: http://www.gosolarcalifornia.ca.gov/equipment/pv_modules.php

[245] Go Solar California, "PV Module Listing Request Procedure," Nov. 2017, online. [Online]. Available: http://www.gosolarcalifornia.ca.gov/equipment/documents/PV_Module_Listing_Request_Procedure.pdf

[246] "Iec 61646: 2008 - thin-film terrestrial photovoltaic (pv) modules–design qualification and type approval," International Electrotechnical Commission, Tech. Rep., 2008.

[247] "Iec61215: 2005 - crystalline silicon terrestrial photovoltaic (pv) modules–design qualification and type approval," International Electrotechnical Commission, Tech. Rep., 2005.

[248] B. H. King, C. W. Hansen, D. Riley, C. D. Robinson, and L. Pratt, "Procedure to Determine Coefficients for the Sandia Array Performance Model (SAPM)," Sandia National Laboratories, Albuquerque, New Mexico. USA, Tech. Rep. SAND2016-5284, 2016. [Online]. Available: https://prod-ng.sandia.gov/techlib-noauth/access-control.cgi/2016/165284.pdf

[249] J. S. Stein, J. Sutterlueti, S. Ransome, C. W. Hansen, and B. H. King, "Outdoor Pv Performance Evaluation Of Three Different Models: Single-diode, Sapm And Loss Factor Model," Sandia National Laboratory, Albuquerque, NM. USA, Tech. Rep., 2013. [Online]. Available: https://www.osti.gov/servlets/purl/1111299

[250] W. Shockley and H. J. Queisser, "Detailed Balance Limit Of Efficiency Of P-n Junction Solar Cells," *Journal of Applied Physics*, 1961.

[251] S. Rühle, "Tabulated Values Of The Shockley-queisser Limit For Single Junction Solar Cells," *Solar Energy*, 2016.

[252] L. Mazzarella, M. Werth, K. Jäger, M. Jošt, L. Korte, S. Albrecht, R. Schlatmann, and B. Stannowski, "Infrared Photocurrent Management In Monolithic Perovskite/silicon Heterojunction Tandem Solar Cells By Using A Nanocrystalline Silicon Oxide Interlayer," *Optics Express*, 2018.

[253] K. Tanabe, "A Review Of Ultrahigh Efficiency Iii-v Semiconductor Compound Solar Cells: Multijunction Tandem, Lower Dimensional, Photonic Up/down Conversion And Plasmonic Nanometallic Structures," *Energies*, vol. 2, no. 3, pp. 504–530, jul 2009. [Online]. Available: http://www.mdpi.com/1996-1073/2/3/504

[254] M. Yamaguchi, T. Takamoto, K. Araki, and N. Ekins-Daukes, "Multijunction Iii–v Solar Cells: Current Status And Future Potential," *Solar Energy*, vol. 79, no. 1, pp. 78–85, jul 2005. [Online]. Available: http://linkinghub.elsevier.com/retrieve/pii/S0038092X04002944

[255] C. Battaglia, A. Cuevas, and S. De Wolf, "High-efficiency Crystalline Silicon Solar Cells: Status And Perspectives," *Energy & Environmental Science*, vol. 9, no. 5, pp. 1552–1576, 2016. [Online]. Available: http://xlink.rsc.org/?DOI=C5EE03380B

[256] R. Santbergen and R. van Zolingen, "The Absorption Factor Of Crystalline Silicon Pv Cells: A Numerical And Experimental Study," *Solar Energy Materials and Solar Cells*, vol. 92, no. 4, pp. 432–444, apr 2008. [Online]. Available: http://linkinghub.elsevier.com/retrieve/pii/S0927024807004023

[257] D. L. King, J. A. Kratochvil, and W. E. Boyson, "Measuring Solar Spectral And Angle-of-incidence Effects On Photovoltaic Modules And Solar Irradiance Sensors," in *PVSC 25th*, 1997.

[258] M. Brandemuehl and W. Beckman, "Transmission of diffuse radiation through CPC and flat plate collector glazings," *Solar Energy*, vol. 24, no. 5, pp. 511–513, 1980.

[259] R. Ramaprabha and B. Mathur, "Modelling And Simulation Of Solar Pv Array Under Partial Shaded Conditions," in *2008 IEEE International Conference on Sustainable Energy Technologies*. IEEE, nov 2008, pp. 7–11. [Online]. Available: http://ieeexplore.ieee.org/document/4746963/

[260] Y.-J. Wang and P.-C. Hsu, "Analytical Modelling Of Partial Shading And Different Orientation Of Photovoltaic Modules," *IET Renewable Power Generation*, vol. 4, no. 3, p. 272, 2010. [Online]. Available: https://digital-library.theiet.org/content/journals/10.1049/iet-rpg.2009.0157

[261] M. R. Maghami, H. Hizam, C. Gomes, M. A. Radzi, M. I. Rezadad, and S. Hajighorbani, "Power Loss Due To Soiling On Solar Panel: A Review," *Renewable and Sustainable Energy Reviews*, vol. 59, pp. 1307–1316, jun 2016. [Online]. Available: https://linkinghub.elsevier.com/retrieve/pii/S1364032116000745

[262] D. S. Ryberg and J. Freeman, "Integration, Validation, And Application Of A Pv Snow Coverage Model In Sam," National Renewable Energy Laboratory Internal Report, Tech. Rep., 2017. [Online]. Available: https://www.nrel.gov/docs/fy17osti/68705.pdf

[263] D. G. Lorente, S. Pedrazzi, G. Zini, A. Dalla Rosa, and P. Tartarini, "Mismatch Losses In Pv Power Plants," *Solar Energy*, vol. 100, pp. 42–49, feb 2014. [Online]. Available: https://linkinghub.elsevier.com/retrieve/pii/S0038092X13005070

[264] A. Chouder and S. Silvestre, "Analysis Model Of Mismatch Power Losses In Pv Systems," *Journal of Solar Energy Engineering*, vol. 131, no. 2, p. 024504, 2009. [Online]. Available: http://solarenergyengineering.asmedigitalcollection.asme.org/article.aspx?articleid=1458176

[265] N. Kaushika and A. Rai, "An Investigation Of Mismatch Losses In Solar Photovoltaic Cell Networks," *Energy*, vol. 32, no. 5, pp. 755–759, may 2007. [Online]. Available: http://linkinghub.elsevier.com/retrieve/pii/S0360544206001423

[266] J. Rabanal-Arabach, A. Schneider, and E. Cabrera, "Minimization Of Electrical Losses Of Pv Modules Located In Places With High Solar Irradiance," *Energy Procedia*, vol. 77, pp. 402–406, aug 2015. [Online]. Available: https://linkinghub.elsevier.com/retrieve/pii/S1876610215008243

[267] E. Kabalci, A. Boyar, and Y. Kabalci, "Design And Analysis Of A Micro Inverter For Pv Plants," in *2017 9th International Conference on Electronics, Computers and Artificial Intelligence (ECAI)*. IEEE, jun 2017, pp. 1–6. [Online]. Available: http://ieeexplore.ieee.org/document/8166459/

[268] R. Hasan, S. Mekhilef, M. Seyedmahmoudian, and B. Horan, "Grid-connected Isolated Pv Microinverters: A Review," 2017.

[269] S. Harb, M. Kedia, H. Zhang, and R. S. Balog, "Microinverter And String Inverter Grid-connected Photovoltaic System - A Comprehensive Study," in *Conference Record of the IEEE Photovoltaic Specialists Conference*, 2013.

[270] M. A. Hossain, Y. Xu, T. J. Peshek, L. Ji, A. R. Abramson, and R. H. French, "Microinverter Thermal Performance In The Real-world: Measurements And Modeling," *PLOS ONE*, vol. 10, no. 7, p. e0131279, jul 2015. [Online]. Available: https://dx.plos.org/10.1371/journal.pone.0131279

[271] J. Good and J. X. Johnson, "Impact Of Inverter Loading Ratio On Solar Photovoltaic System Performance," *Applied Energy*, vol. 177, pp. 475–486, sep 2016. [Online]. Available: https://linkinghub.elsevier.com/retrieve/pii/S0306261916307395

[272] R. R. Hernandez, M. K. Hoffacker, M. L. Murphy-Mariscal, G. C. Wu, and M. F. Allen, "Solar Energy Development Impacts On Land Cover Change And Protected Areas," *Proceedings of the National Academy of Sciences*, vol. 112, no. 44, pp. 13 579–13 584, nov 2015. [Online]. Available: http://www.pnas.org/lookup/doi/10.1073/pnas.1517656112

[273] S. Nonhebel, "Renewable Energy And Food Supply: Will There Be Enough Land?" *Renewable and Sustainable Energy Reviews*, vol. 9, no. 2, pp. 191–201, apr 2005. [Online]. Available: http://linkinghub.elsevier.com/retrieve/pii/S1364032104000498

[274] K. Calvert and W. Mabee, "More Solar Farms Or More Bioenergy Crops? Mapping And Assessing Potential Land-use Conflicts Among Renewable Energy Technologies In Eastern Ontario, Canada," *Applied Geography*, vol. 56, pp. 209–221, jan 2015. [Online]. Available: http://dx.doi.org/10.1016/j.apgeog.2014.11.028https://linkinghub.elsevier.com/retrieve/pii/S0143622814002835

[275] E. Marcheggiani, H. Gulinck, and A. Galli, "Detection Of Fast Landscape Changes: The Case Of Solar Modules On Agricultural Land Bt - Computational Science And Its Applications – Iccsa 2013," B. Murgante, S. Misra, M. Carlini, C. M. Torre, H.-Q. Nguyen, D. Taniar, B. O. Apduhan, and O. Gervasi, Eds. Berlin, Heidelberg: Springer Berlin Heidelberg, 2013, pp. 315–327.

[276] Fraunhofer Institute For Solar Energy Systems (ISE), "Harvesting The Sun For Power And Produce – Agrophotovoltaics Increases The Land Use Efficiency By Over 60 Percent," Freiburg, Germany, nov 2017. [Online]. Available: https://www.ise.fraunhofer.de/content/dam/ise/en/documents/press-releases/2017/2017_ISE_e_PR_1yearAPV.pdf

[277] Ong, Sean and Campbell, Clinton and Denholm, Paul and Margolis, Robert and Heath, Garvin, "Land-Use Requirements for Solar Power Plants in the United States," National Renewable Energy Laboratory, techreport NREL/TP-6A20-56290, Jun. 2013.

[278] E. Lorenzo, L. Narvarte, and J. Muñoz, "Tracking and back-tracking," *Progress in Photovoltaics: Research and Applications*, vol. 19, no. 6, pp. 747–753, feb 2011.

[279] A. Senpinar and M. Cebeci, "Evaluation Of Power Output For Fixed And Two-axis Tracking Pvarrays," *Applied Energy*, vol. 92, pp. 677–685, apr 2012. [Online]. Available: https://linkinghub.elsevier.com/retrieve/pii/S0306261911004880

[280] R. Eke and A. Senturk, "Performance Comparison Of A Double-axis Sun Tracking Versus Fixed Pv System," *Solar Energy*, vol. 86, no. 9, pp. 2665–2672, sep 2012. [Online]. Available: https://linkinghub.elsevier.com/retrieve/pii/S0038092X12002174

[281] T. Huld, T. Cebecauer, M. Šúri, and E. D. Dunlop, "Analysis Of One-axis Tracking Strategies For Pv Systems In Europe," *Progress in Photovoltaics: Research and Applications*, vol. 18, no. 3, pp. 183–194, may 2010. [Online]. Available: http://doi.wiley.com/10.1002/pip.948

[282] H. Wirth, "Recent Facts About Photovoltaics In Germany," Fraunhofer Institute for Solar Energy Systems ISE, Freiburg, Germany, Tech. Rep., 2018. [Online]. Available: https://www.ise.fraunhofer.de/content/dam/ise/en/documents/publications/studies/recent-facts-about-photovoltaics-in-germany.pdf

[283] K. I. Chowdhury, "Performance Comparison Between Fixed Panel, Single-axis And Dual-axis Sun Tracking Solar Panel System," Bachelor Thesis, BRAC University, 2017. [Online]. Available: http://dspace.bracu.ac.bd/xmlui/bitstream/handle/10361/9118/12221046{%}2C12221071{%}2C12121101_EEE.pdf?sequence=1{&}isAllowed=y

[284] K. Brecl and M. Topič, "Self-shading Losses Of Fixed Free-standing Pv Arrays," *Renewable Energy*, vol. 36, no. 11, pp. 3211–3216, nov 2011. [Online]. Available: https://linkinghub.elsevier.com/retrieve/pii/S096014811100125X

[285] Fraunhofer ISE, "Current And Future Cost Of Photovoltaics ," Fraunhofer ISE, Tech. Rep., 2015.

[286] M. Taylor and P. Ralon, "Irena Cost And Competitiveness Indicators Rooftop Solar Pv," International Renewable Energy Agency (IRENA), Abu Dhabi, Tech. Rep., 2017. [Online]. Available: http://www.irena.org/publications

[287] E. Vartiainen, G. Masson, and C. Breyer, "The True Competitiveness Of Solar Pv: A European Case Study," European Technology and Innovation Platform for Photovoltaics, Tech. Rep., 2017. [Online]. Available: http://www.etip-pv.eu/fileadmin/Documents/ETIP_PV_Publications_2017-2018/LCOE_Report_March_2017.pdf

[288] J. Leloux, L. Narvarte, M. Collares-Pereira, and A. Desportes, "Analysis Of The State Of The Art Of Pv Systems In Europe," Universidad Politécnica de Madrid, Tech. Rep., 2015.

[289] C. L. Kwan, "Influence Of Local Environmental, Social, Economic And Political Variables On The Spatial Distribution Of Residential Solar Pv Arrays Across The United States," *Energy Policy*, vol. 47, pp. 332–344, aug 2012. [Online]. Available: https://linkinghub.elsevier.com/retrieve/pii/S0301421512003795

[290] K. Mainzer, S. Killinger, R. McKenna, and W. Fichtner, “Assessment of rooftop photovoltaic potentials at the urban level using publicly available geodata and image recognition techniques,” *Solar Energy*, vol. 155, pp. 561–573, oct 2017.

[291] K. Adam, V. Hoolohan, J. Gooding, T. Knowland, C. S. Bale, and A. S. Tomlin, “Methodologies For City-scale Assessment Of Renewable Energy Generation Potential To Inform Strategic Energy Infrastructure Investment,” *Cities*, vol. 54, pp. 45–56, may 2016. [Online]. Available: http://dx.doi.org/10.1016/j.cities.2015.10.015https://linkinghub.elsevier.com/retrieve/pii/S0264275115001687

[292] International Energy Agency (IEA), “Energy technology perspectives 2016: towards sustainable urban energy systems Annex H,” IEA, Tech. Rep., 2016. [Online]. Available: http://www.iea.org/etp/etp2016/annexes/

[293] S. Freitas, C. Catita, P. Redweik, and M. Brito, “Modelling Solar Potential In The Urban Environment: State-of-the-art Review,” *Renewable and Sustainable Energy Reviews*, vol. 41, pp. 915–931, jan 2015. [Online]. Available: https://linkinghub.elsevier.com/retrieve/pii/S1364032114007461

[294] S. Ullah, “Characterization Of Pv Technology Over Roofs And Their Constraints For A Geographical Analysis,” Masters Thesis, Universitat Politècnica de Catalunya, 2013.

[295] L. Bergamasco and P. Asinari, “Scalable Methodology For The Photovoltaic Solar Energy Potential Assessment Based On Available Roof Surface Area: Further Improvements By Ortho-image Analysis And Application To Turin (italy),” *Solar Energy*, 2011.

[296] G. Sanchis, “Europe’s Future Secure And Sustainable Electricity Infrastructure: E-highway2050 Project Results,” European Union, Tech. Rep., 2015. [Online]. Available: http://www.e-highway2050.eu/fileadmin/documents/e_highway2050_booklet.pdf

[297] “Best Research-cell Efficiencies,” Golden, Colorado. USA. [Online]. Available: https://www.nrel.gov/pv/assets/pdfs/pv-efficiency-chart.20181221.pdf

[298] ITRPV, *International Technology Roadmap For Photovoltaic (itrpv), Ninth Edition, 2018 Results*, 2018, ISBN: 9781424413911, ISSN: 0018-9162. [Online]. Available: http://www.itrs.net/Links/2013ITRS/2013Chapters/2013Litho.pdf

[299] D. Stetter, “Enhancement Of The Remix Energy System Model: Global Renewable Energy Potentials , Optimized Power Plant Siting And Scenario Validation,” Ph.D. dissertation, 2012.

[300] K. Bruninx, D. Orlic, D. Couckuyt, N. Grisey, B. Betraoui, T. Anderski, Y. Surmann, N. T. Franck, G. Keane, B. Hickman, D. Huertas-hernando, M. Wilk, and R. Jankowski, “E-highway 2050: Modular Development Plan Of The Pan-european Transmission System 2050:

D 2.1 - Data Sets Of Scenarios For 2050," European Union, Tech. Rep., 2014. [Online]. Available: http://www.e-highway2050.eu/fileadmin/documents/Results/D2_1_Data_sets_of_scenarios_for_2050_20072015.pdf

[301] P. R. Defaix, W. G. van Sark, E. Worrell, and E. de Visser, "Technical Potential For Photovoltaics On Buildings In The Eu-27," *Solar Energy*, 2012.

[302] K. Bódis, T. Huld, I. Pinedo Pascua, N. Taylor, and A. Jäger-Waldau, "Technical Potential Of Rooftop Photovoltaics In Eu Member States , Regions And Cities," Joint Research Center, Ispra, Italy, Tech. Rep., 2017.

[303] M. Šúri, T. A. Huld, and E. D. Dunlop, "PV-GIS: A Web-based Solar Radiation Database For The Calculation Of Pv Potential In Europe," *International Journal of Sustainable Energy*, 2005.

[304] M. Šúri, T. A. Huld, E. D. Dunlop, and H. A. Ossenbrink, "Potential Of Solar Electricity Generation In The European Union Member States And Candidate Countries," *Solar Energy*, 2007.

[305] T. Huld, "Pvmaps: Software Tools And Data For The Estimation Of Solar Radiation And Photovoltaic Module Performance Over Large Geographical Areas," *Solar Energy*, vol. 142, pp. 171–181, jan 2017. [Online]. Available: https://linkinghub.elsevier.com/retrieve/pii/S0038092X16306089

[306] T. Huld, G. Friesen, A. Skoczek, R. P. Kenny, T. Sample, M. Field, and E. D. Dunlop, "A Power-rating Model For Crystalline Silicon Pv Modules," *Solar Energy Materials and Solar Cells*, vol. 95, no. 12, pp. 3359–3369, dec 2011. [Online]. Available: https://linkinghub.elsevier.com/retrieve/pii/S0927024811004442

[307] T. Huld, R. Gottschalg, H. G. Beyer, and M. Topič, "Mapping The Performance Of Pv Modules, Effects Of Module Type And Data Averaging," *Solar Energy*, vol. 84, no. 2, pp. 324–338, feb 2010. [Online]. Available: https://linkinghub.elsevier.com/retrieve/pii/S0038092X0900293X

[308] B. Ridley, J. Boland, and P. Lauret, "Modelling Of Diffuse Solar Fraction With Multiple Predictors," *Renewable Energy*, vol. 35, no. 2, pp. 478–483, feb 2010. [Online]. Available: https://linkinghub.elsevier.com/retrieve/pii/S0960148109003012

[309] P. Lauret, J. Boland, and B. Ridley, "Bayesian Statistical Analysis Applied To Solar Radiation Modelling," *Renewable Energy*, vol. 49, pp. 124–127, jan 2013. [Online]. Available: https://linkinghub.elsevier.com/retrieve/pii/S0960148112000602

[310] K. Mainzer, K. Fath, R. McKenna, J. Stengel, W. Fichtner, and F. Schultmann, "A high-resolution determination of the technical potential for residential-roof-mounted photovoltaic systems in Germany," *Solar Energy*, vol. 105, pp. 715–731, jul 2014.

[311] A. M. Held, “Modelling The Future Development Of Renewable Energy Technologies In The European Electricity Sector Using Agent-based Simulation,” Dissertation, Karlsruher Institut fuer Technologie, Karlsruhe (Germany), 2011.

[312] I. Gonzalez Aparicio, T. Huld, F. Careri, F. Monforti, and A. Zucker, *Emhires Dataset Part II : Solar Power Generation*, 2017, ISBN: 9789279692857, ISSN: 1831-9424.

[313] “Ghs Population Grid, Derived From Gpw4, Multitemporal (1975, 1990, 2000, 2015),” Online, 2015. [Online]. Available: http://data.europa.eu/89h/jrc-ghsl-ghs_pop_gpw4_globe_r2015a

[314] W. F. Holmgren, R. W. Andrews, A. T. Lorenzo, and J. S. Stein, “PVLIB python 2015,” in *Proceedings of the IEEE 42nd Photovoltaic Specialist Conference (PVSC)*, 2015, pp. 1–5.

[315] E. Nuño, P. Maule, A. Hahmann, N. Cutululis, P. Sørensen, and I. Karagali, “Simulation Of Transcontinental Wind And Solar Pv Generation Time Series,” *Renewable Energy*, vol. 118, pp. 425–436, apr 2018. [Online]. Available: https://linkinghub.elsevier.com/retrieve/pii/S0960148117311400

[316] T. Alexis, S. Marc, D. Philippe, B. Jordi, C. Silvia, C. Anna, D. Claudia, T. Dimitri, and T. Peter, “Optimal Wind-solar Energy Mix In Italy: Impact Of Climate Variability,” *arXiv*, vol. arXiv:1812, dec 2018. [Online]. Available: http://arxiv.org/abs/1812.09181

[317] S. Collins, P. Deane, B. Ó Gallachóir, S. Pfenninger, and I. Staffell, “Impacts Of Inter-annual Wind And Solar Variations On The European Power System,” *Joule*, vol. 2, no. 10, pp. 2076–2090, oct 2018. [Online]. Available: https://linkinghub.elsevier.com/retrieve/pii/S254243511830285X

[318] P. Juruš, K. Eben, J. Resler, P. Krč, I. Kasanický, E. Pelikán, M. Brabec, and J. Hošek, “Estimating Climatological Variability Of Solar Energy Production,” *Solar Energy*, vol. 98, pp. 255–264, dec 2013. [Online]. Available: https://linkinghub.elsevier.com/retrieve/pii/S0038092X13004088

[319] R. Urraca, T. Huld, A. Gracia-Amillo, F. J. Martinez-de Pison, F. Kaspar, and A. Sanz-Garcia, “Evaluation Of Global Horizontal Irradiance Estimates From Era5 And Cosmo-rea6 Reanalyses Using Ground And Satellite-based Data,” *Solar Energy*, 2018.

[320] I. Reda and A. Andreas, “Solar Position Algorithm for Solar Radiation Applications ,” National Renewable Energy Laboratory, techreport, Jan 2008, nREL/TP-560-34302. [Online]. Available: https://www.nrel.gov/docs/fy08osti/34302.pdf

[321] European Environmental Agency, “Digital Elevation Model over Europe (EU-DEM) [Dataset],” https://www.eea.europa.eu/data-and-maps/data/eu-dem, 2013, accessed: 2017-04-01.

[322] M. J. Reno, C. W. Hansen, and J. S. Stein, "Global Horizontal Irradiance Clear Sky Models: Implementation and Analysis," Sandia National Labs, techreport SAND2012-2389, Mar. 2012.

[323] J. W. Spencer, "Fourier Series Representation of the Position of the Sun," *Search*, vol. 2, no. 5, 1971.

[324] F. Kasten and A. T. Young, "Revised optical air mass tables and approximation formula," *Applied Optics*, vol. 28, no. 22, p. 4735, nov 1989. [Online]. Available: https://www.osapublishing.org/abstract.cfm?URI=ao-28-22-4735

[325] D. Erbs, S. Klein, and J. Duffie, "Estimation of the diffuse radiation fraction for hourly, daily and monthly-average global radiation," *Solar Energy*, vol. 28, no. 4, pp. 293–302, 1982. [Online]. Available: https://linkinghub.elsevier.com/retrieve/pii/0038092X82903024

[326] B. Y. Liu and R. C. Jordan, "The interrelationship and characteristic distribution of direct, diffuse and total solar radiation," *Solar Energy*, vol. 4, no. 3, pp. 1–19, jul 1960. [Online]. Available: https://linkinghub.elsevier.com/retrieve/pii/0038092X60900621

[327] C. L. Brest and S. N. Goward, "Deriving Surface Albedo Measurements From Narrow Band Satellite Data," *International Journal of Remote Sensing*, vol. 8, no. 3, pp. 351–367, mar 1987. [Online]. Available: https://www.tandfonline.com/doi/full/10.1080/01431168708948646

[328] R. Perez, R. Seals, P. Ineichen, R. Stewart, and D. Menicucci, "A new simplified version of the perez diffuse irradiance model for tilted surfaces," *Solar Energy*, vol. 39, no. 3, pp. 221–231, 1987. [Online]. Available: https://linkinghub.elsevier.com/retrieve/pii/S0038092X87800312

[329] J. E. Hay and J. A. Davies, "Calculations of the solar radiation incident on an inclined surface," in *Proc. of First Canadian Solar Radiation Data Workshop, 59*. Ministry of Supply and Services, Canada, 1980.

[330] D. Reindl, W. Beckman, and J. Duffie, "Evaluation Of Hourly Tilted Surface Radiation Models," *Solar Energy*, vol. 45, no. 1, pp. 9–17, 1990. [Online]. Available: http://linkinghub.elsevier.com/retrieve/pii/0038092X9090061G

[331] F. Huneke, C. P. Linkenheil, and M. Niggemeier, "Kalte Dunkelflaute Robustheit Des Stromsystems Bei Extremwetter," Greenpeace Energy eG, Berlin, Germany, Tech. Rep., 2017. [Online]. Available: https://www.energybrainpool.com/fileadmin/download/Studien/Studie_2017-06-26_GPE_Studie_Kalte-Dunkelflaute_Energy-Brainpool.pdf

[332] Z. Yang, J. Zhang, M. C. Kintner-Meyer, X. Lu, D. Choi, J. P. Lemmon, and J. Liu, "Electrochemical Energy Storage For Green Grid," 2011.

[333] C. Wahlquist, "South Australia's Tesla Battery On Track To Make Back A Third Of Cost In A Year," *The Guardian*, sep 2018.

[Online]. Available: https://www.theguardian.com/technology/2018/sep/27/south-australias-tesla-battery-on-track-to-make-back-a-third-of-cost-in-a-year

[334] F. Crotogino, S. Donadei, U. Bünger, and H. Landinger, "Large-scale Hydrogen Underground Storage For Securing Future Energy Supplies," in *18th World Hydrogen Energy Conference 2010 - WHEC 2010 Parallel Sessions Book 4: Storage Systems / Policy Perspectives, Initiatives and Co-operations*, 2010.

[335] M. Paulescu, E. Paulescu, P. Gravila, and V. Badescu, "Weather Modeling And Forecasting Of Pv Systems Operation," *Green Energy and Technology*, 2013.

[336] G. Pérez-Landa, P. Ciais, M. J. Sanz, B. Gioli, F. Miglietta, J. L. Palau, G. Gangoiti, and M. M. Millán, "Atmospheric Chemistry And Physics Mesoscale Circulations Over Complex Terrain In The Valencia Coastal Region, Spain-part 1: Simulation Of Diurnal Circulation Regimes," Tech. Rep., 2007. [Online]. Available: www.atmos-chem-phys.net/7/1835/2007/

[337] C. Talbot, E. Bou-Zeid, and J. Smith, "Nested Mesoscale Large-eddy Simulations With Wrf: Performance In Real Test Cases," *Journal of Hydrometeorology*, 2012.

[338] A. Yamaguchi and T. Ishihara, "Assessment Of Offshore Wind Energy Potential Using Mesoscale Model And Geographic Information System," *Renewable Energy*, vol. 69, pp. 506–515, sep 2014. [Online]. Available: https://www.sciencedirect.com/science/article/pii/S0960148114001153

[339] W. R. Holland, "The Role Of Mesoscale Eddies In The General Circulation Of The Ocean—numerical Experiments Using A Wind-driven Quasi-geostrophic Model," *Journal of Physical Oceanography*, vol. 8, no. 3, pp. 363–392, may 1978. [Online]. Available: http://journals.ametsoc.org/doi/abs/10.1175/1520-0485{%}281978{%}29008{%}3C0363{%}3ATROMEI{%}3E2.0.CO{%}3B2

[340] M. A. Handschy, S. Rose, and J. Apt, "Is It Always Windy Somewhere? Occurrence Of Low-wind-power Events Over Large Areas," *Renewable Energy*, vol. 101, pp. 1124–1130, feb 2017. [Online]. Available: https://linkinghub.elsevier.com/retrieve/pii/S0960148116308680

[341] B. Matek and K. Gawell, "The Benefits Of Baseload Renewables: A Misunderstood Energy Technology," *The Electricity Journal*, vol. 28, no. 2, pp. 101–112, mar 2015. [Online]. Available: https://www.sciencedirect.com/science/article/pii/S104061901500024X

[342] C. L. Archer, M. Z. Jacobson, C. L. Archer, and M. Z. Jacobson, "Supplying Baseload Power And Reducing Transmission Requirements By Interconnecting Wind Farms," *Journal of Applied Meteorology and Climatology*, vol. 46, no. 11, pp. 1701–1717, nov 2007. [Online]. Available: http://journals.ametsoc.org/doi/abs/10.1175/2007JAMC1538.1

[343] F. Ueckerdt and R. Kempener, "From Baseload To Peak: Renewables Provide A Reliable Solution." IRENA, Tech. Rep., 2015. [Online]. Available: www.irena.org

[344] J. W. Hurrell, Y. Kushnir, G. Ottersen, and M. Visbeck, "An Overview Of The North Atlantic Oscillation," in *Geophysical Monograph Series*, 2003.

[345] J. Marshall, Y. Kushnir, D. Battisti, P. Chang, A. Czaja, R. Dickson, J. Hurrell, M. McCartney, R. Saravanan, and M. Visbeck, "North Atlantic Climate Variability: Phenomena, Impacts And Mechanisms," *International Journal of Climatology*, 2001.

[346] G. Colantuono, Y. Wang, E. Hanna, and R. Erdélyi, "Signature Of The North Atlantic Oscillation On British Solar Radiation Availability And Pv Potential: The Winter Zonal Seesaw," *Solar Energy*, vol. 107, pp. 210–219, sep 2014. [Online]. Available: https://linkinghub.elsevier.com/retrieve/pii/S0038092X14002850

[347] D. Raynaud, B. Hingray, B. François, and J. Creutin, "Energy Droughts From Variable Renewable Energy Sources In European Climates," *Renewable Energy*, vol. 125, pp. 578–589, sep 2018. [Online]. Available: https://linkinghub.elsevier.com/retrieve/pii/S0960148118302829

[348] J. Wohland, M. Reyers, J. Weber, and D. Witthaut, "More Homogeneous Wind Conditions Under Strong Climate Change Decrease The Potential For Inter-state Balancing Of Electricity In Europe," *Earth System Dynamics*, vol. 8, no. 4, pp. 1047–1060, nov 2017. [Online]. Available: https://www.earth-syst-dynam.net/8/1047/2017/

[349] P. Ravestein, G. van der Schrier, R. Haarsma, R. Scheele, and M. van den Broek, "Vulnerability Of European Intermittent Renewable Energy Supply To Climate Change And Climate Variability," *Renewable and Sustainable Energy Reviews*, vol. 97, pp. 497–508, dec 2018. [Online]. Available: https://linkinghub.elsevier.com/retrieve/pii/S1364032118306415

[350] F. Cebulla, T. Naegler, and M. Pohl, "Electrical Energy Storage In Highly Renewable European Energy Systems: Capacity Requirements, Spatial Distribution, And Storage Dispatch," *Journal of Energy Storage*, vol. 14, pp. 211–223, dec 2017. [Online]. Available: https://linkinghub.elsevier.com/retrieve/pii/S2352152X17302815

[351] M. G. Rasmussen, G. B. Andresen, and M. Greiner, "Storage And Balancing Synergies In A Fully Or Highly Renewable Pan-european Power System," *Energy Policy*, vol. 51, pp. 642–651, dec 2012. [Online]. Available: https://linkinghub.elsevier.com/retrieve/pii/S0301421512007677

[352] J. Weber, J. Wohland, M. Reyers, J. Moemken, C. Hoppe, J. G. Pinto, and D. Witthaut, "Impact Of Climate Change On Backup Energy And Storage Needs In Wind-dominated Power Systems In Europe," *PLOS ONE*, vol. 13, no. 8, p. e0201457, aug 2018. [Online]. Available: https://dx.plos.org/10.1371/journal.pone.0201457

[353] B. François, B. Hingray, D. Raynaud, M. Borga, and J. Creutin, "Increasing Climate-related-energy Penetration By Integrating Run-of-the River Hydropower To Wind/solar Mix," *Renewable Energy*, vol. 87, pp. 686–696, mar 2016. [Online]. Available: https://linkinghub.elsevier.com/retrieve/pii/S0960148115304171

[354] R. A. Rodríguez, S. Becker, G. B. Andresen, D. Heide, and M. Greiner, "Transmission Needs Across A Fully Renewable European Power System," *Renewable Energy*, vol. 63, pp. 467–476, mar 2014. [Online]. Available: https://linkinghub.elsevier.com/retrieve/pii/S0960148113005351

[355] R. A. Rodriguez, M. Dahl, S. Becker, and M. Greiner, "Localized Vs. Synchronized Exports Across A Highly Renewable Pan European Transmission Network," *Energy, Sustainability and Society*, vol. 5, no. 1, p. 21, dec 2015. [Online]. Available: http://energsustainsoc.springeropen.com/articles/10.1186/s13705-015-0048-6

[356] D. Schlachtberger, T. Brown, S. Schramm, and M. Greiner, "The Benefits Of Cooperation In A Highly Renewable European Electricity Network," *Energy*, vol. 134, pp. 469–481, sep 2017. [Online]. Available: https://linkinghub.elsevier.com/retrieve/pii/S0360544217309969

[357] R. A. Rodriguez, S. Becker, and M. Greiner, "Cost-optimal Design Of A Simplified, Highly Renewable Pan-european Electricity System," *Energy*, vol. 83, pp. 658–668, apr 2015. [Online]. Available: https://linkinghub.elsevier.com/retrieve/pii/S0360544215002212

[358] M. Child, D. Bogdanov, and C. Breyer, "The Role Of Storage Technologies For The Transition To A 100% Renewable Energy System In Europe," *Energy Procedia*, vol. 155, pp. 44–60, nov 2018. [Online]. Available: https://linkinghub.elsevier.com/retrieve/pii/S1876610218310221

[359] S. Becker, R. Rodriguez, G. Andresen, S. Schramm, and M. Greiner, "Transmission Grid Extensions During The Build-up Of A Fully Renewable Pan-european Electricity Supply," *Energy*, vol. 64, pp. 404–418, jan 2014. [Online]. Available: https://linkinghub.elsevier.com/retrieve/pii/S0360544213008438

[360] M. Doquet, C. Fourment, and J. Roudergues, "Generation Amp; Transmission Adequacy Of Large Interconnected Power Systems: A Contribution To The Renewal Of Monte-carlo Approaches," in *2011 IEEE Trondheim PowerTech*, jun 2011, pp. 1–6.

[361] K. Syranidis, P. Markowitz, J. Linssen, M. Robinius, and D. Stoltcn, "Flexible Demand For Higher Integration Of Renewables Into The European Power System," in *2018 15th International Conference on the European Energy Market (EEM)*. IEEE, jun 2018, pp. 1–6. [Online]. Available: https://ieeexplore.ieee.org/document/8469962/

[362] K. Syranidis, "On The Integration Of Renewable Energy Sources Into The Future European Power System," Doctoral Thesis, RWTH Aachen University, 2019.

[363] V. Khare, S. Nema, and P. Baredar, "Solar–wind Hybrid Renewable Energy System: A Review," *Renewable and Sustainable Energy Reviews*, vol. 58, pp. 23–33, may 2016. [Online]. Available: https://linkinghub.elsevier.com/retrieve/pii/S1364032115016068

[364] C. Christiansen and T. Lam, "Co-location Investigation: A Study Into The Potential For Co-locating Wind And Solar Farms In Australia," Australian Renewable Energy Agency (ARENA), Tech. Rep., 2016. [Online]. Available: http://www.aecom.com/au/wp-content/uploads/2016/03/Wind-solar-Co-location-Study-Final.pdf

[365] I. Mamia and J. Appelbaum, "Shadow Analysis Of Wind Turbines For Dual Use Of Land For Combined Wind And Solar Photovoltaic Power Generation," *Renewable and Sustainable Energy Reviews*, vol. 55, pp. 713–718, mar 2016. [Online]. Available: https://linkinghub.elsevier.com/retrieve/pii/S1364032115012617

[366] S. Schiebahn, T. Grube, M. Robinius, V. Tietze, B. Kumar, and D. Stolten, "Power To Gas: Technological Overview, Systems Analysis And Economic Assessment For A Case Study In Germany," 2015.

[367] K. Syranidis, M. Robinius, and D. Stolten, "Control Techniques And The Modeling Of Electrical Power Flow Across Transmission Networks," *Renewable and Sustainable Energy Reviews*, vol. 82, pp. 3452–3467, feb 2018. [Online]. Available: https://linkinghub.elsevier.com/retrieve/pii/S1364032117314740

[368] T. Brown, J. Hörsch, and D. Schlachtberger, "Pypsa: Python For Power System Analysis," *Journal of Open Research Software*, vol. 6, jan 2018. [Online]. Available: http://openresearchsoftware.metajnl.com/articles/10.5334/jors.188/

[369] Gurobi Optimization, LLC, "Gurobi Optimizer Reference Manual," 2018. [Online]. Available: http://www.gurobi.com

[370] A. Schröder, F. Kunz, J. Meiss, R. Mendelevitch, and C. von Hirschhausen, "Current And Prospective Costs Of Electricity Generation Until 2050," Deutsches Institut für Wirtschaftsforschung, Berlin, Germany, Tech. Rep., 2013. [Online]. Available: https://www.diw.de/documents/publikationen/73/diw_01.c.424566.de/diw_datadoc_2013-068.pdf

[371] M. M. Hoogwijk, "On The Global And Regional Potential Of Renewable Energy Sources," Ph.D. dissertation, 2004.

[372] J. Bosch, I. Staffell, and A. D. Hawkes, "Temporally-explicit And Spatially-resolved Global Onshore Wind Energy Potentials," *Energy*, vol. 131, pp. 207–217, 2017.

[373] K. Eurek, P. Sullivan, M. Gleason, D. Hettinger, D. Heimiller, and A. Lopez, "An improved global wind resource estimate for integrated assessment models," *Energy Economics*, vol. 64, pp. 552–567, may 2017. [Online]. Available: https://linkinghub.elsevier.com/retrieve/pii/S014098831630336X

[374] S. H. Siyal, U. Mörtberg, D. Mentis, M. Welsch, I. Babelon, and M. Howells, "Wind Energy Assessment Considering Geographic And Environmental Restrictions In Sweden: A Gis-based Approach," *Energy*, 2015.

[375] C. V. Hernández, T. Telsnig, and A. V. Pradas, "JRC Wind Energy Status Report 2016 Edition," 2017.

[376] R. C. Pietzcker, D. Stetter, S. Manger, and G. Luderer, "Using The Sun To Decarbonize The Power Sector: The Economic Potential Of Photovoltaics And Concentrating Solar Power," *Applied Energy*, 2014, i can use this for comparing openfield potentials.

[377] W. Peters, S. Schicketanz, M. Hanusch, A. Rohr, M. Kothe, P. Kinast, M. Reichmuth, C. Lorenz, A. Scheuermann, A. Schiffler, G. Schröder, K. Einig, and B. Zaspel-Heisters, "Räumlich differenzierte Flächenpotentiale für erneuerbare Energien in Deutschland," 2015.

[378] A. von Oehsen, Y.-M. M. Saint-Drenan, T. Stetz, M. Braun, A. van Oehsen, Y.-M. M. Saint-Drenan, T. Stetz, A. von Oehsen, Y.-M. M. Saint-Drenan, T. Stetz, and M. Braun, "Vorstudie zur Integration großer Anteile Photovoltaik in die elektrische Energieversorgung," 2012.

[379] J. Nitsch, W. Krewitt, M. Nast, and P. Viebahn, "Ökologisch optimierter Ausbau der Nutzung erneuerbarer Energien in Deutschland," *. . . Energie, Bericht für das . . .*, 2004.

[380] S. Nowak, M. Gutschner, D. Ruoss, P. Toggweiler, and T. Schoen, "Potential for Buildings Integrated photovoltaics," International Energy Agency (IEA), Tech. Rep., 2002, Report IEA: PVPS T7-4.

[381] S. Izquierdo, M. Rodrigues, and N. Fueyo, "A Method For Estimating The Geographical Distribution Of The Available Roof Surface Area For Large-scale Photovoltaic Energy-potential Evaluations," *Solar Energy*, 2008.

[382] A. Korfiati, C. Gkonos, F. Veronesi, A. Gaki, S. Grassi, R. Schenkel, S. Volkwein, M. Raubal, and L. Hurni, "Estimation of the Global Solar Energy Potential and Photovoltaic Costwith the use of Open Data," *International Journal of Sustainable Energy Planning and Management*, vol. 09, 2016. [Online]. Available: https://journals.aau.dk/index.php/sepm/article/view/1218

[383] X. García, J. Domínguez, J. Linares, and O. López, "Un informe sobre el potencial de las energías renovables en la España peninsular," Greenpeace, Tech. Rep., 2005. [Online]. Available: http://www.greenpeace.org/espana/Global/espana/report/other/renovables-2050.pdf

[384] T. Grau, M. Huo, and K. Neuhoff, "Survey of photovoltaic industry and policy in Germany and China," *Energy Policy*, vol. 51, pp. 20–37, dec 2012. [Online]. Available: https://linkinghub.elsevier.com/retrieve/pii/S0301421512003345

[385] Umweltbundesamt und Energiesystemtechnik and Fraunhofer-Institut für Windenergie, "Energieziel 2050 : 100 % Strom aus erneuerbaren Quellen," 2010.

[386] W. Kaltschmitt, *M. Kaltschmitt, A. Wiese (Hrsg.): Erneuerbare Energieträger in Deutschland*. Springer-Verlag Heidelberg, 1993.

[387] V. Quaschning, *Systemtechnik einer klimaverträglichen Elektrizitätsversorgung in Deutschland für das 21. Jahrhundert*, 2000, ISBN: 3-318-343706-6.

[388] M. Lödl, G. Kerber, R. Witzmann, C. Hoffmann, and M. Metzger, "Abschätzung des Photovoltaik-Potentials auf Dachflächen in Deutschland," in *11th Symposium Energieinnovation, 10-12 February 2010, Graz, Austria*, 2010.

[389] D. Heide, M. Greiner, L. von Bremen, and C. Hoffmann, "Reduced Storage And Balancing Needs In A Fully Renewable European Power System With Excess Wind And Solar Power Generation," *Renewable Energy*, vol. 36, no. 9, pp. 2515–2523, sep 2011. [Online]. Available: https://linkinghub.elsevier.com/retrieve/pii/S0960148111000851

[390] D. G. Caglayan, "Design of a Future Hydrogen Infrastructure to Supply Electricity and Hydrogen Demand Across Europe," Doctoral Thesis, RWTH Aachen University, 2020.

[391] Copernicus. European Environmental Agency (EEA), "high Resolution Layer: Permanent Water Bodies (pwb) [dataset]," "land.copernicus.eu/pan-european/high-resolution-layers/permanent-water-bodies", 2012, accessed: 2017-04-01.

[392] European Environmental Agency (EEA), "Nationally Designated Areas (cdda) [dataset]," "https://www.eea.europa.eu/data-and-maps/data/nationally-designated-areas-national-cdda-12", 2016, accessed: 2017-04-01.

[393] European Environmental Agency (EEA), "Natura 2000 Data - The European Network Of Protected Sites [dataset]," "https://www.eea.europa.eu/data-and-maps/data/natura-8", 2016, accessed: 2017-04-01.

[394] J. D. Kalma, T. R. McVicar, and M. F. McCabe, "Estimating Land Surface Evaporation: A Review Of Methods Using Remotely Sensed Surface Temperature Data," *Surveys in Geophysics*, vol. 29, no. 4, pp. 421–469, 2008. [Online]. Available: https://doi.org/10.1007/s10712-008-9037-z

[395] R. Müller, U. Pfeifroth, C. Träger-Chatterjee, R. Cremer, J. Trentmann, and R. Hollmann, "Surface Solar Radiation Data Set - Heliosat (sarah) - Edition 1," *EUMETSAT Satellite Application Facility on Climate Monitoring (CM SAF)*, 2015.

[396] P. N. Edwards, "History of climate modeling," *Wiley Interdisciplinary Reviews: Climate Change*, vol. 2, no. 1, pp. 128–139, jan 2011. [Online]. Available: http://doi.wiley.com/10.1002/wcc.95

[397] J. P. Evans, “CORDEX - An international climate downscaling initiative,” in *MODSIM 2011 - 19th International Congress on Modelling and Simulation - Sustaining Our Future: Understanding and Living with Uncertainty*, 2011.

[398] European Energy Exchange (EEX), “Transparency in Energy Markets,” online, 2017, accessed: 2017-08-23. [Online]. Available: https://www.eex.com/de/about/eex/transparency-in-energy-markets

[399] Danish Energy Agency, “Master Data Register of Wind Turbines,” online, 2017, accessed: 2017-10-19. [Online]. Available: https://ens.dk/en/our-services/statistics-data-key-figures-and-energy-maps/overview-energy-sector

[400] P. Lauret, J. Boland, and B. Ridley, “Bayesian statistical analysis applied to solar radiation modelling,” *Renewable Energy*, vol. 49, pp. 124–127, jan 2013. [Online]. Available: https://linkinghub.elsevier.com/retrieve/pii/S0960148112000602

[401] B. Ridley, J. Boland, and P. Lauret, “Modelling of diffuse solar fraction with multiple predictors,” *Renewable Energy*, vol. 35, no. 2, pp. 478–483, feb 2010. [Online]. Available: https://linkinghub.elsevier.com/retrieve/pii/S0960148109003012

Band / Volume 507
Integration of Renewable Energy Sources into the Future European Power System Using a Verified Dispatch Model with High Spatiotemporal Resolution
C. Syranidou (2020), VIII, 242 pp
ISBN: 978-3-95806-494-2

Band / Volume 508
Solar driven water electrolysis based on silicon solar cells and earth-abundant catalysts
K. Welter (2020), iv, 165 pp
ISBN: 978-3-95806-495-9

Band / Volume 509
Electric Field Assisted Sintering of Gadolinium-doped Ceria
T. P. Mishra (2020), x, 195 pp
ISBN: 978-3-95806-496-6

Band / Volume 510
Effect of electric field on the sintering of ceria
C. Cao (2020), xix, 143 pp
ISBN: 978-3-95806-497-3

Band / Volume 511
Techno-ökonomische Bewertung von Verfahren zur Herstellung von Kraftstoffen aus H_2 und CO_2
S. Schemme (2020), 360 pp
ISBN: 978-3-95806-499-7

Band / Volume 512
Enhanced crosshole GPR full-waveform inversion to improve aquifer characterization
Z. Zhou (2020), VIII, 136 pp
ISBN: 978-3-95806-500-0

Band / Volume 513
Time-Resolved Photoluminescence on Perovskite Absorber Materials for Photovoltaic Applications
F. Staub (2020), viii, 198 pp
ISBN: 978-3-95806-503-1

Band / Volume 514
Crystallisation of Oxidic Gasifier Slags
J. P. Schupsky (2020), III, 127, XXII pp
ISBN: 978-3-95806-506-2

Band / Volume 515
Modeling and validation of chemical vapor deposition for tungsten fiber reinforced tungsten
L. Raumann (2020), X, 98, XXXVIII pp
ISBN: 978-3-95806-507-9

Band / Volume 516
Zinc Oxide / Nanocrystalline Silicon Contacts for Silicon Heterojunction Solar Cells
H. Li (2020), VIII, 135 pp
ISBN: 978-3-95806-508-6

Band / Volume 517
Iron isotope fractionation in arable soil and graminaceous crops
Y. Xing (2020), X, 111 pp
ISBN: 978-3-95806-509-3

Band / Volume 518
Geophysics-based soil mapping for improved modelling of spatial variability in crop growth and yield
C. Brogi (2020), xxi, 127 pp
ISBN: 978-3-95806-510-9

Band / Volume 519
Measuring and modelling spatiotemporal changes in hydrological response after partial deforestation
I. Wiekenkamp (2020), xxxvii, 276 pp
ISBN: 978-3-95806-512-3

Band / Volume 520
Characterization of Root System Architectures from Field Root Sampling Methods
S. Morandage (2020), xxii, 157 pp
ISBN: 978-3-95806-511-6

Band / Volume 521
Generation Lulls from the Future Potential of Wind and Solar Energy in Europe
D. S. Ryberg (2020), xxvii, 398 pp
ISBN: 978-3-95806-513-0

Weitere ***Schriften des Verlags im Forschungszentrum Jülich*** unter
http://wwwzb1.fz-juelich.de/verlagextern1/index.asp

Energie & Umwelt / Energy & Environment
Band / Volume 521
ISBN 978-3-95806-513-0

Mitglied der Helmholtz-Gemeinschaft

JÜLICH
Forschungszentrum